Mapping Intermediates in Hydrogen Evolution with [Cp*Rh] Catalysts and Carbon Monoxide Release from [$Mn(CO)_3$] Complexes

By
Wade C. Henke
B.S., University of Kansas, 2017

Submitted to the graduate degree program in Chemistry and the Graduate Faculty of the University of Kansas in partial fulfillment of the requirements for the degree Doctor of Philosophy.

_____

Chair: Prof. James Blakemore

_____

Prof. Mikhail Barybin

_____

Prof. Christopher Elles

_____

Prof. Ward Thompson

_____

Prof. Zarko Boskovic

Date Defended: 12 April 2022

The dissertation committee for Wade C. Henke certifies that this is the approved version of the following dissertation:

Mapping Intermediates in Hydrogen Evolution with [Cp*Rh] Catalysts and Carbon Monoxide Release from [$Mn(CO)_3$] Complexes

_____

Chair: Prof. James Blakemore

Date Approved: 25 April 2022

Abstract

Pentamethylcyclopentadienyl rhodium ([Cp*Rh]) and manganese tricarbonyl ([$Mn(CO)_3$]) complexes represent workhorse families of compounds with key applications in catalytic hydrogen evolution and light-driven carbon monoxide (CO) release, respectively. Investigations with these model molecular systems are motivated by our limited knowledge concerning the fundamental mechanisms involved in storing energy in chemical bonds and releasing carbon monoxide using visible light. In Part I of this dissertation, synthetic, electrochemical, structural, and spectroscopic studies have been applied to map the elementary electron- and proton-transfer steps leading to catalytic dihydrogen evolution. Time-resolved pulse radiolysis and stopped-flow spectroscopic studies reveal that the sole product of initial protonation of Cp*Rh(bpy) is $[Cp^*Rh(H)(bpy)]^+$, followed by tautomerization to form $[(\eta^4\text{-}Cp^*H)Rh(bpy)]^+$. Spectroscopic monitoring of the second proton transfer event reveals both the hydride and related Cp*H complex are involved in further reactivity and confirm that [(Cp*H)Rh] is not an off-cycle intermediate, but can be an active participant in catalytic H_2 evolution. In Part II, synthetic, electrochemical, structural, and spectroscopic studies have been applied to elucidate the redox and electronic properties of a family of monometallic, as well as homo- and hetero-bimetallic complexes, bearing the $[Mn(CO)]_3$ unit. In particular, we have elucidated the early intermediates involved in visible-light-driven speciation of a series of $[Mn(CO)_3(^Rbpy)]$ complexes bearing 4,4′-disubstituted 2,2′-bipyridyl ligands (^Rbpy, R = ^{t}Bu, H, CF_3, NO_2). Ultrafast transient absorption spectroscopy measurements with UV-visible monitoring reveals loss of a CO ligand on the femtosecond timescale, followed by solvent coordination on the picosecond timescale. Taken together, the findings described in this dissertation of [Cp*Rh] and $[Mn(CO)_3]$ complexes provide a foundation for future investigations that could yield more detailed mechanistic insight into H_2 generation and controlled CO release.

Acknowledgements

Though I am not currently in the proper athletic shape to run an actual marathon (maybe someday!), I have been fortunate to experience graduate school, and I think these two things have many parallels. In the following quote by Joe Henderson, an American marathon runner and writer, I have replaced the word "marathon" with "graduate school." *"You can never be sure. That's what makes graduate school both fearsome and fascinating. The deeper you go into the unknown, the more uncertain you become. But then you finish. And you wonder later, "How did I do that?" This question compels you to keep making the journey from the usual to the magical."* If you ask me there certainly appear to be some parallels. However, in my eyes, one of the major differences between these events is that in graduate school you need a great team. I am very fortunate to have been surrounded by a great team of peers, labmates, professors, and family, and they have each played a significant role in my graduate education. I want to thank each of them here.

First, I would like to express my appreciation and thankfulness to my advisor James D. Blakemore. James, I have been incredibly fortunate to have you as my advisor and mentor during graduate school. This all started in your undergraduate inorganic chemistry class; I vividly remember sitting in your class, and you asking me, "What are you doing this Summer?" This was a moment that changed my life. During the Summer of 2016, I began undergraduate research in your lab, and I fell in love with inorganic chemistry under the lens of fundamental energy storage. Around this time, you also asked if I was planning to attend graduate school. As a first-generation college student, I never thought of graduate school as a reality, so thank you for your encouragement. With your help, I applied to graduate schools, and I was accepted into two programs: The University of Oregon and The University of Kanas. After visiting both programs,

I knew your group was going to be the place I was going to grow and learn the most as a chemist. Choosing you as my academic advisor and mentor has been one of the best decisions in my entire life. You took time to personally teach me how to use a Schlenk line and glovebox, and how to perform electrochemical measurements. Our many meetings together taught me how to read, write, and speak the language of chemistry. I have always appreciated your willingness to help your students and the fact that you never give up on anyone. From a personal standpoint, this involved crafting materials to apply for many programs and scholarships, like the Chemical Biology Training Grant and the Kansas Academy of Science Graduate Program. Thank you for being a great advisor, mentor, and role model, and I hope we can work together in the future!

Thank you to my committee members Professor Chris Elles and Professor Misha Barybin. Chris and Misha, thank you for serving on my research advisory, comprehensive examination, and dissertation defense committees. Your guidance has been invaluable during my time at KU, and you have provided me with excellent scholastic and professional advice. I appreciate the interactions we had, and your accessibility and willingness to help me become a better scientist. Misha, I was very fortunate to have you as a professor for your exciting courses about organometallic reaction mechanisms and nuclear magnetic resonance. You have an excellent teaching style which made traditionally difficult topics accessible because of your expertise. Chris, I am grateful that you taught me the basics of ultrafast spectroscopy and allowed me to work with your group on some very exciting projects. James and Chris, I also appreciate you for allowing me to travel to Argonne National Laboratory as a young graduate student. This experience granted me a brief, but exciting glimpse into the atmosphere of the national lab system.

Thank you to Professor Tim Jackson for serving on my comprehensive examination committee. I enjoyed his structure, bonding, and spectroscopic methods course, and I will always remember

that the doughnut is bigger than you think (in life, and the case of the Taurus ring on the d_{z^2} orbital). Thank you to Professor Audrey Lamb for serving on my comprehensive exam committee. I was fortunate to have Audrey as a professor for a few courses during my time in the NIH Chemical Biology Training Grant. I also really appreciated the time she let me join in with her lab for virtual beamtime at SSRL. Experiences like this cultivated my love for X-ray crystallography even more. I would like to thank Professor Ward Thompson for his guidance, wisdom, and helpful discussions about reaction mechanisms and chemical kinetics, and for serving on my dissertation committee. I would also like to thank Professor Zarko Boskovic for helpful discussions about X-ray crystallography and for serving on my dissertation committee.

Next, I would like to thank Professor Davide Lionetti for his mentorship in the lab and for constantly answering my many questions. I will always remember his love for synthetic chemistry, teaching students, molecular orbital theory, and ducks. Davide is the most well-rounded synthetic chemist I have had the pleasure to work with. He taught me how to work with pyrophoric reagents and strong acids. He also helped me understand concepts in the classroom. One particular instance I remember well, I asked him why aqua regia was red-orange in color. We then spent an hour drawing the molecular orbital diagram for NOCl to see that the HOMO-LUMO gap was narrow; I am sure this was very easy for him, but this was an invaluable experience for me, and my love of molecular orbital theory has grown exponentially since then. I also want to thank him for teaching me the basics of X-ray crystallography and refining these data for publication. Davide, you played a key role during my graduate education, I miss working and learning with you, and I am a better chemist because of you. Thank you for your guidance and expertise.

Another person who was instrumental during my time at KU is Dr. Victor W. Day. I have never met someone who is so passionate and good at a subject; he is truly an expert. Without his help,

we wouldn't have published 26 crystal structures together. Victor, I appreciate that you always took the time to teach me fundamental concepts about crystallography. Thank you for being so generous with your time, and your patience. Thank you for spending many hours showing me how the diffractometer works, how to collect and refine data, and how to speak the language of X-ray crystallography. I will miss your group parties which were only complete with the Shrek soundtrack, pool tournaments, and sambuca. I have enjoyed working with you, Victor, and I will miss working with you very much.

Thank you to Justin Douglas and Sarah Neuenswander for teaching me how to use the EPR and NMR instruments. Thank you both so much for your help over the years and your willingness to discuss EPR and NMR data, simulations, and new techniques.

Next, I would like to thank my labmates that I had the opportunity to interact with while I was in the group. I would like to thank David Sconyers for teaching me about electrochemistry and how to perform and troubleshoot CV experiments. I also want to take the chance to thank him for some great memories during the time we attended the Orlando, Fl ACS National meeting; I will always remember the turtle boogie board fondly, and I still will not rub sunscreen on your back. Thank you to Yun Peng for teaching me how to use the glovebox as an undergraduate. I appreciated our discussions about [Rh] chemistry and different video games.

A big thank you to my labmates Amit Kumar and Julie Hopkins who were constant role models for me during my time in graduate school. Amit and Julie have been helping me since the beginning in the group, and they have provided me with constant motivation and support during graduate school. I will always remember dancing on the table (if you can imagine this) with Amit at the Sandbar after his comprehensive exam. I will also remember singing karaoke to Julie after she

passed her comprehensive exam; it turns out tequila is both great for a celebration and as a song. Amit, you are one of the hardest workers I have had the opportunity to know, and your knowledge and love of chemistry make everyone around you better. Julie, you are the best synthetic organometallic chemist I have ever met, and I was very fortunate to start in the group at the same time as you. I am really happy that you stayed for your Ph.D. at KU, and our McLain's writing days for our papers and dissertations were always a blast. Thank you for always talking with me about ideas and ways to approach things; I always really appreciated these conversations. Amit and Julie, thank you both!

Next, I would like to thank my labmate Chelsea Comadoll. You are a great chemist, and I am so glad that you joined the group. You are one of the most mentally tough people I know, and I had such a great time teaching CHEM 661 with you. I am certain I would not have survived that semester without you because it was the most challenging group I have encountered. Thank you for always letting me talk to you about synthetic and mechanistic work. You are a brilliant organic, inorganic, and organometallic chemist. Thank you to Riddhi Golwankar who has been a wonderful lab and desk mate. I am happy that we have been able to sit next to each other during graduate school because this has made it very easy to talk with you about ideas in the lab, your crystal structures, and Poppy. Thank you to Joe Karnes, for always telling me good morning and asking how I am doing. These conversations brought me joy. I will always remember you trying that hot sauce in Branson; I am still sorry about this.

Thank you to Shaun Kelsey for great conversations and for talking with me about synthesis and lab equipment. I also appreciate you helping me move during my last year at KU; gestures like this mean a lot to me, and I appreciate you, buddy. Emily Mikeska, thank you for talking with me about X-ray crystallography and teaching me how to mount crystals. I appreciated the times when

you, Amit, and I were working with Victor to learn how to use the diffractometer. Christian Nilles, thank you for talking about catalysis with me, sharing an appreciation for carbonyl complexes, and telling me about your catalytic runs at CEBC. Davis Curry and Alex Ervin, even though we haven't had the chance to work together much, I can tell from the interactions that we have had that you are both hard workers and will be great chemists in the group.

I have also had the privilege to work with some tremendous undergraduate students. Thank you to Will Moore and Jonah Stiel for being my mentees during my time at KU. Will, you are a fantastic synthetic chemist and an incredibly hard worker. I am glad to see that you are excelling in Bill's group at UC Irvine. Jonah, thank you for your hard work on several challenging synthetic projects. I am happy that we have been able to publish together, and I know you are going to continue being a star in graduate school. Working with Emma Cosner and Claire Dopp has also been a pleasure. Emma and Clair are both some of the hardest working and brilliant undergraduate students I have gotten to work with during graduate school.

Next, thank you to my Aunts, Nancy, Marsha, and Sharon, Uncles, Pete and Paul, and Cousins, Julie, Mike, Kristi, and Pat for their continual support. I have always appreciated the constant encouragement. Maddie and I are really excited to see everyone in Chicago!

Next, a major thanks to my Mom, Dad, and Mamama for their continual and unwavering support. Thank you so much for encouraging my pursuit of graduate school. I am glad that you always encouraged me to keep up with my education; I clearly remember when I was younger when you told me how important learning and keeping good grades were. I also remember Dad saying, "School gets harder every year." I can confirm he is correct. Graduate school has been a very challenging five years, but this is an experience that will forever be a part of me now. Thank

you for always letting me visit you all while you were in Kansas City and now down in Warsaw; these visits and our phone calls on Sundays have helped my mental health so much and allowed me to talk about my week and experiences. Our talks prepared me to tackle the next week and were uplifting. Now, coming down to visit you all at the lake feels like a vacation. I have enjoyed our conversations while fishing and enjoying nature. Mom, thank you for always being so easy to talk to, for watching scary movies with me, and always being encouraging. Dad, thank you for continually providing me guidance and for working on motorcycles and cars with me. Mamama, thank you for always being such a positive influence in my life; thank you for your advice, humor, love, and delicious homemade chicken-fried steak. Mom, Dad, and Mamama thank you for your constant cheer and support, and I love you so much!

A major thanks too to my mother-in-law, Darcy, father-in-law, Darren, sisters-in-law, Eliza and Emily, brother-in-law, Joe, and grandmothers-in-law, Jerri and Marilyn, for constantly inspiriting and cheering for me. Nearly every Saturday morning for the past five years, we have met at Roubinek HQ to enjoy coffee, lunch, and great conversation. Often, these moments provided me with refuge from intense weeks, something exciting to look forward to, and allowed me to spend some time relaxing with loved ones. Darcy and Darren, twelve years ago you both took me into your family with open arms and have provided me continuous encouragement in my pursuit of education; thank you so much for this. Joe, Eliza, and Emily, I am so thankful to have you as my siblings and thank you for being a great support system during my time at KU. I have enjoyed playing board games with you and talking about our weeks together. Jerri and Marilyn, thank you both for always rooting for and supporting me during graduate school. I love you all so much!

Lastly, and most importantly, I would like to thank my wife, Maddie Roubinek. Maddie, I want to express how thankful I am for you. You have been, and continue to be, the everlasting light

guiding me to the completion of this goal. You changed my life forever when we met twelve years ago, and I am so grateful that you are my best friend and wife. Day-after-day, good news or bad news, you sat beside me and have continued to provide me with unwavering support toward the completion of my goals. Thank you for being my biggest cheerleader, ultimate pillar of support, and source of inspiration; I am so lucky to have you by my side every day. During the past five years, there were a lot of late nights, early mornings, and a lot of time spent trying to reach this goal. Thank you for your encouragement, patience, solace, and unconditional positive regard. Completing my Ph.D. would have never happened without you, and because of that, if you read further, you will see that this is all dedicated to you. I love you always ♡.

Dedication

This dissertation is dedicated to my best friend and wife, Madeline Roubinek. Without her support, encouragement, and love this would have never been possible. Maddie is the light of my life, my person that I hold most dear, and the woman I love with all my heart.

This poem and dissertation are for her.

–Wade C. Henke

You Changed My Life Forever

My dearest Maddie,

I was on a trajectory to despondency.
The moment you said hello to me.
You changed my life forever.

This led me to a revelation.
I changed my focus to education.
You changed my life forever.

Your love and solace vitalized me.
You encouraged my pursuit of chemistry.
You changed my life forever.

Thank you for supporting me.
With your help, I have graduated with my Ph.D.
Thank you, you changed my life forever.

♡

Love always, Wade

Table of Contents

Part II

List of Figures

List of Tables

Mänskligheten står ... inför ett stort problem att hitta nya råvaror och nya energikällor som aldrig kommer att ta slut. Under tiden får vi inte slösa bort det vi har, utan måste lämna så mycket som möjligt till kommande generationer.

Humanity stands ... before a great problem of finding new raw materials and new sources of energy that shall never become exhausted. In the meantime we must not waste what we have, but must leave as much as possible for coming generations.

--Svante A. Arrhenius

(Nobel Laureate in Chemistry, 1903)

Chapter 1

Introduction to Mapping Intermediates in Hydrogen Evolution with [Cp*Rh] Catalysts and Carbon Monoxide Release from [$Mn(CO)_3$] Complexes

1.1 Introduction

One of humanity's most formidable challenges is learning to store energy harvested from renewable resources.[1] Currently, our sources of renewable energy are intermittent and suffer from a fundamental storage problem; there is a need to store energy obtained from renewable resources indefinitely for future use. One potential solution to this problem involves storing energy in the form of chemical bonds. However, storing energy quickly, selectively, and efficiently in this fashion is challenging and not well-understood. To improve future systems by rational design, synthetic and mechanistic studies are needed to understand the elementary steps leading to desirable reactivity while disfavoring side-reactions that can sometimes occur. The elementary steps that define reaction mechanisms provide a detailed map for converting starting materials into products. Although reaction mechanisms cannot ever be proven with philosophical certainty, compelling support may establish credibility for a particular mechanism, which can then serve as a model for the rational design of future systems. Within this context, this dissertation focuses on a series of synthetic, electrochemical, structural, and time-resolved spectroscopic studies aimed at mapping the intermediates involved in catalytic hydrogen evolution and light-driven carbon monoxide release using model [Cp*Rh] (Cp* = pentamethylcyclopentadienyl) and manganese tricarbonyl ([$Mn(CO)_3$]) complexes, respectively.

Part I of this dissertation, which includes Chapters 2–4, describes the synthetic, structural, electrochemical, and time-resolved spectroscopic studies of reduced and protonated intermediates involved in catalytic dihydrogen evolution using [Cp*Rh] complexes. In Chapter 2, the prominent role of electrochemistry in the field of organometallic chemistry is discussed.[2] This chapter is designed to introduce the reader to the development, execution, and application of electrochemical techniques, and provides a brief history of the field. Electrochemical measurements have become

workhorse experimental techniques in organometallic chemistry and have enabled advances in the fundamental understanding of the behavior of redox-active molecules in electrochemical systems. Notably, electrochemistry is a versatile technique, and through use of a potentiostat, various electrochemical experiments can be performed alone or in concert to obtain thermodynamic, kinetic, and/or mechanistic information. Chapter 2 also aims to assist the reader with understanding experimental design in electrochemistry by reviewing the most commonly used electrochemical methods. Examples are included for a variety of molecular systems to provide the reader with examples that illustrate the interpretation of electrochemical data.

In Chapter 3, synthetic, structural, electrochemical, and spectroscopic studies are used to bring attention to ligands based upon the 4,5-diazafluorene core and show that these ligands can be used under highly reducing conditions using the [Cp*Rh] platform as a model, at least when derivatized appropriately.[3] The ligands 4,5-diazafluoren-9-one (dafone), 4,5-diazafluorene (daf), and 9,9′-dimethyl-4,5-diazafluorene (Me_2daf) are an important class of emerging ligands in organometallic chemistry, but the structural and electronic properties of these ligands have received less attention than they deserve; moreover, these ligands have traditionally been utilized in oxidative applications.[4,5,6,7,8,9] In particular, we show that 9,9′-dimethyl-4,5-diazafluorene can stabilize low-valent complexes through charge delocalization into its conjugated π-system.[10] Using the new platform of [Cp*Rh] complexes developed in this work, three formal oxidation states (+III, +II, and +I) are accessible; we show that the methylation in Me_2daf is protective, blocking Brønsted acid-base chemistry commonly encountered with other daf-based ligands. Electronic absorption spectroscopy and single-crystal X-ray diffraction analysis of a family of eleven new compounds, including the unusual Cp*Rh(Me_2daf), reveal features consistent with charge delocalization driven by π-backbonding into the LUMO of Me_2daf, reminiscent of behavior displayed by the much more

common 2,2′-bipyridyl ligand. Taken together with spectrochemical data demonstrating clean conversion between oxidation states, our findings show that 9,9′-dialkylated daf-type ligands are promising building blocks for applications in reductive chemistry and catalysis.

In Chapter 4, time-resolved spectroscopic studies are used to interrogate protonation reactions involving organometallic [Cp*Rh] complexes. Protonation reactions are ubiquitous in redox chemistry and often result in the generation of reactive metal hydrides. However, some organometallic species supported by η^5-pentamethylcyclopentadienyl (Cp*) ligands have recently been shown to undergo ligand-centered protonation by direct proton transfer from acids or tautomerization of metal hydrides, resulting in the generation of complexes bearing the uncommon η^4-cyclopentadiene (Cp*H) ligand.[11,12,13,14,15] In this chapter, we report time-resolved pulse radiolysis (PR) and stopped-flow spectroscopic studies that examine the kinetics and atomistic details involved in the elementary electron- and proton-transfer steps leading to complexes ligated by Cp*H, using Cp*Rh(bpy) as a molecular model. Stopped-flow measurements coupled with infrared and UV-visible detection reveal that the sole product of initial protonation of Cp*Rh(bpy) is $[Cp^*Rh(H)(bpy)]^+$, an elusive hydride complex that was rigorously characterized in this work for the first time. Tautomerization of this hydride leads to the clean formation of $[(Cp^*H)Rh(bpy)]^+$. Variable temperature and isotopic labeling experiments provide confirmation of this assignment of the reactivity and yield experimental activation parameters and mechanistic insight for hydride-to-proton tautomerism for the first time. Spectroscopic monitoring of the second proton transfer event reveals both the hydride and related Cp*H complex can be involved in further reactivity, confirming that [(Cp*H)Rh] is not an off-cycle intermediate, but, instead, that it can be an active participant in catalytic hydrogen evolution. Understanding the roles of these protonated intermediates under conditions relevant to catalysis is of interest for improving future

systems by rational design, since protonation reactions are required for virtually all reactivity paradigms that would generate chemical fuels from feedstocks like CO_2 or N_2.

In Part II of this dissertation, which includes Chapters 5-7, we build on the mechanistic work from Part I and discuss the synthetic, structural, electrochemical, and time-resolved spectroscopic studies focused on reactions of the [$Mn(CO)_3$] platform. In Chapter 5, we discuss tuning the kinetics of light-driven carbon monoxide (CO) release and solvent binding in a family of [$Mn(CO)_3$] complexes. [$Mn(CO)_3$] complexes are promising catalysts for carbon dioxide (CO_2) reduction,[16,17] but the complexes in this family are often photo-sensitive and decompose rapidly upon exposure to visible light.[18] In Chapter 5, synthetic and photochemical studies are used to probe the initial steps of light-driven speciation for $Mn(CO)_3(^{R}bpy)Br$ complexes bearing a range of 4,4′-disubstituted 2,2′-bipyridyl ligands (^{R}bpy, R = ^{t}Bu, H, CF_3, NO_2). Transient absorption spectroscopy measurements for the $Mn(CO)_3(^{R}bpy)Br$ coordination compounds with R = ^{t}Bu, H, and CF_3 in acetonitrile reveal ultrafast loss of a CO ligand on the femtosecond timescale, followed by solvent coordination on the picosecond timescale. The $Mn(CO)_3(^{NO2}bpy)Br$ complex is unique among the four compounds in having a longer-lived excited state that apparently does not undergo CO release or subsequent solvent coordination. The kinetics of photolysis and solvent coordination for the light-sensitive complexes depends on the electronic properties of the di-substituted bipyridyl ligand. The results implicate roles for both metal-to-ligand charge transfer (MLCT) and dissociative ligand field (dd) excited states in the ultrafast photochemistry. Taken together, the findings in this chapter suggest that more robust catalysts could be prepared with appropriately designed complexes that avoid crossing between the excited states that drive photochemical CO loss.

Complementary to Chapter 3, in Chapter 6, we discuss the use of 4,5-diazafluorene (daf) and 9,9′-dimethyl-4,5-diazafluorene (Me_2daf) as redox-active supporting ligands for $[Mn(CO)_3]$- and $[Ru(diimine)_3]^{2+}$ complexes.[19] Daf and Me_2daf are structurally similar to the important ligand 2,2′-bipyridine (bpy), but significantly less is known about the redox and spectroscopic properties of metal complexes containing Me_2daf as a ligand than those containing bpy.[20] The new complexes $Mn(CO)_3Br(daf)$, $Mn(CO)_3Br(Me_2daf)$, and $[Ru(Me_2daf)_3](PF_6)_2$ have been prepared and fully characterized to understand the influence of the Me_2daf framework on their chemical and electrochemical properties. Structural data for all three complexes were obtained by single-crystal X-ray diffraction analysis and reveal a distinctive widening of the daf and Me_2daf chelate angles in comparison to those for bpy in the analogous $Mn(CO)_3(bpy)Br$ and $[Ru(bpy)_3]^{2+}$ complexes. Electronic absorption data for these complexes confirm the electronic similarity of daf, Me_2daf, and bpy, as the spectra are dominated in each case by metal-to-ligand charge transfer (MLCT) bands in the visible region. However, the electrochemical properties of the complexes reveal that the redox-active Me_2daf framework in $Mn(CO)_3Br(Me_2daf)$ and $[Ru(Me_2daf)_3](PF_6)_2$ undergoes reduction at a slightly more negative potential than that of bpy in $Mn(CO)_3(bpy)Br$ and $[Ru(bpy)_3]^{2+}$. Taken together, the results in this chapter indicate that Me_2daf could be useful for the preparation of a variety of new redox-active compounds, as it retains the useful redox-active nature of bpy but lacks the acidic, benzylic C–H bonds that can induce secondary reactivity in complexes bearing daf.

In Chapter 7, we discuss the synthesis, structural studies, and redox chemistry of a family of bimetallic $[Mn(CO)_3]$ and $[Re(CO)_3]$ complexes,[21] motivated by the observation that monometallic $[Mn(CO)_3]$ and $[Re(CO)_3]$ complexes represent a workhorse family of compounds with applications in a variety of fields.[16,22,23,24,25,26,27] In the work reported here, the coordination,

structural, and electrochemical properties of a family of mono- and bimetallic [$Mn(CO)_3$] and [$Re(CO)_3$] complexes are explored; in particular, a novel heterobimetallic complex featuring both a [$Mn(CO)_3$] unit and a [$Re(CO)_3$] unit supported by a bridging 2,2′-bipyrimidine (bpm) ligand have been synthesized, structurally characterized, and compared to analogous monomeric and homobimetallic complexes. To enable a comprehensive structural analysis for the series of complexes, we have carried out new single-crystal X-ray diffraction studies of seven compounds: $Re(CO)_3Cl(bpm)$, *anti*-[{$Re(CO_3)Cl$}$_2$(bpm)], $Mn(CO)_3Br(bpz)$ (bpz = 2,2′-bipyrazine), $Mn(CO)_3Br(bpm)$, *syn*- and *anti*-[{$Mn(CO_3)Br$}$_2$(bpm)], and *syn*-[$Mn(CO_3)Br(bpm)Re(CO)_3Br$]). Electrochemical studies reveal that the bimetallic complexes undergo reduction at much more positive potentials ($\Delta E \geq 380$ mV) than their monometallic analogues. This redox behavior is consistent with the introduction of the second tricarbonyl unit which inductively withdraws electron density from the bridging, redox-active bpm ligand, resulting in more positive reduction potentials. [$Re(CO_3)Cl$]$_2$(bpm) was reduced with cobaltocene; the electron paramagnetic resonance spectrum of the product exhibits an isotropic signal (near $g = 2$) characteristic of a ligand-centered bpm radical. Our findings in this chapter highlight the facile synthesis as well as the structural characteristics and unique electrochemical behavior of this family of complexes.

In summary, this dissertation, in two parts, highlights the critical intermediates that ultimately lead to catalytic hydrogen evolution from [Cp*Rh] complexes and the photodecomposition of [$Mn(CO)_3$] complexes which results in CO release. While these particular complexes will most likely not solve the world's energy problems, they do serve as a set of well-behaved model complexes; understanding the mechanisms by which hydrogen evolution and carbon monoxide release occurs with these complexes could represent a springboard for the design and study of even better systems in the future. Of particular note, harnessing the reactivity of the Cp*H moiety in

Earth-abundant transition metal systems could represent an especially attractive opportunity to access new redox molecular mediators for small-molecule activation. Additionally, [$Mn(CO)_3$] complexes will serve as excellent model complexes for ultrafast photochemical experiments to be performed with X-ray free-electron laser (XFEL) equipment and thus will continue to merit significant attention in the years ahead.

1.2 References

(1) Lewis, N. S.; Nocera, D. G., *PNAS* **2006,** *103* (43), 15729.

(2) Hopkins Leseberg, J.A, Henke, W.C., and Blakemore, J.D.* *Comprehensive Organometallic Chemistry IV*, Meyer, K. and Holland, P., Eds.; Elsevier: Amsterdam, forthcoming, 37 pages; *in press*

(3) Henke, W.; Stiel, J.; Day, V.; Blakemore, J., *Chem. Eur. J.* **2022**.

(4) a) Jiang, H.; Stepowska, E.; Song, D., *Dalton Trans.* **2008,** (43), 5879-5881. b) Tan, R.; Chiu, F. S. N.; Hadzovic, A.; Song, D., *Organometallics* **2012,** *31* (6), 2184-2192. c) Annibale, V. T.; Dalessandro, D. A.; Song, D., *J. Am. Chem. Soc.* **2013,** *135* (43), 16175-16183. d) R. Batcup, V. T. Annibale and D. Song, *Dalton Trans.* **2014**, *43*, 8951-8958. e) Annibale, V. T.; Song, D., *Organometallics* **2014,** *33* (11), 2776-2783. f) Janes, T.; Osten, K. M.; Pantaleo, A.; Yan, E.; Yang, Y.; Song, D., *Chem. Commun.* **2016,** *52* (22), 4148-4151. g) Janes, T.; Annibale, V. T.; Song, D., *J. Organomet. Chem.* **2018,** *872*, 79-86.

(5) Jiang, H.; Song, D., *Organometallics* **2008,** *27* (14), 3587-3592.

(6) Stepowska, E.; Jiang, H.; Song, D., *Chem. Commun.* **2010,** *46* (4), 556-558.

(7) Jiang, H.; Stepowska, E.; Song, D., *Eur. J. Inorg. Chem.* **2009,** *2009* (14), 2083-2089.

(8) Campbell, A. N.; White, P. B.; Guzei, I. A.; Stahl, S. S., *J. Am. Chem. Soc.* **2010,** *132* (43), 15116-15119.

(9) a) Diao, T.; Wadzinski, T. J.; Stahl, S. S., *Chem. Sci.* **2012,** *3* (3), 887-891.b) Gao, W.; He, Z.; Qian, Y.; Zhao, J.; Huang, Y., *Chem. Sci.* **2012,** *3* (3), 883-886.

(10) Creutz, C., *Comments Inorg. Chem.* **1982**, *1*, 293-311.

(11) Quintana, L. M. A.; Johnson, S. I.; Corona, S. L.; Villatoro, W.; Goddard, W. A.; Takase, M. K.; VanderVelde, D. G.; Winkler, J. R.; Gray, H. B.; Blakemore, J. D., *PNAS* **2016,** *113* (23), 6409-6414.

(12) Pitman, C. L.; Finster, O. N. L.; Miller, A. J. M., *Chem. Commun.* **2016,** *52* (58), 9105-9108.

(13) Peng, Y.; Ramos-Garcés, M. V.; Lionetti, D.; Blakemore, J. D., *Inorg. Chem.* **2017,** *56* (17), 10824-10831.

(14) Schild, D. J.; Drover, M. W.; Oyala, P. H.; Peters, J. C., *J. Am. Chem. Soc.* **2020,** *142* (44), 18963-18970.

(15) Chalkley, M. J.; Oyala, P. H.; Peters, J. C., *J. am. Chem. Soc.* **2019,** *141* (11), 4721-4729.

(16) Bourrez, M.; Molton, F.; Chardon-Noblat, S.; Deronzier, A., *Angew. Chem. Int. Ed.* **2011,** *50*, 9903-9906.

(17) Smieja, J. M.; Sampson, M. D.; Grice, K. A.; Benson, E. E.; Froehlich, J. D.; Kubiak, C. P., *Inorg. Chem.* **2013,** *52*, 2484-2491.

(18) Carrington, S. J.; Chakraborty, I.; Mascharak, P. K., *Dalton Trans.* **2015,** *44*, 13828-13834.

(19) Henke, W. C.; Hopkins, J. A.; Anderson, M. L.; Stiel, J. P.; Day, V. W.; Blakemore, J. D., *Molecules* **2020,** *25* (14), 3189.

(20) Henderson, L. J.; Fronczek, F. R.; Cherry, W. R., *J. Am. Chem. Soc.* **1984,** *106*, 5876-5879.

(21) Henke, W. C.; Kerr, T. A.; Sheridan, T. R.; Henling, L. M.; Takase, M. K.; Day, V. W.; Gray, H. B.; Blakemore, J. D., *Dalton Transactions* **2021,** *50* (8), 2746-2756.

(22) (a) Stufkens, D. J.; Vlček, A., *Coord. Chem. Rev.* **1998,** *177* (1), 127-179. (b) El Nahhas, A.; Consani, C.; Blanco-Rodríguez, A. M.; Lancaster, K. M.; Braem, O.; Cannizzo, A.; Towrie, M.; Clark, I. P.; Záliš, S.; Chergui, M.; Vlček, A., *Inorg. Chem.* **2011,** *50* (7), 2932-2943.

(23) (a) Wallace, L.; Rillema, D. P., *Inorg. Chem.* **1993,** *32* (18), 3836-3843. (b) Shaver, R. J.; Perkovic, M. W.; Rillema, D. P.; Woods, C., *Inorg. Chem.* **1995,** *34* (22), 5446-5454.

(24) Léval, A.; Junge, H.; Beller, M., *Catal. Sci. Technol.* **2020,** *10* (12), 3931-3937.

(25) (a) Schatzschneider, U., *Inorg. Chim. Acta* **2011,** *374* (1), 19-23. (b) Alberto, R.; Schibli, R.; Egli, A.; Schubiger, A. P.; Abram, U.; Kaden, T. A *J. Am. Chem. Soc.* **1998,** *120* (31), 7987-7988.

(26) M. N. Pinto, I. Chakraborty, C. Sandoval and P. K. Mascharak, *J. Controlled Release*, 2017, **264**, 192-202.

(27) (a) Hawecker, J.; Lehn, J.-M.; Ziessel, R., *J. Chem Soc., Chem. Commun.* **1984,** (6), 328-330. (b) Sullivan, B. P.; Bolinger, C. M.; Conrad, D.; Vining, W. J.; Meyer, T. J., *J. Chem. Soc., Chem. Commun.* **1985,** (20), 1414-1416.

Part I

Chapter 2

Electrochemistry in Organometallic Chemistry

This chapter is adapted from a published book chapter: Hopkins Leseberg, J.A,[#] Henke, W.C.,[#] and Blakemore, J.D.* "Electrochemistry in Organometallic Chemistry" in *Comprehensive Organometallic Chemistry IV*, Meyer, K. and Holland, P., Eds.; Elsevier: Amsterdam, forthcoming, 37 pages; *in press.*

[#]These authors contributed equally

2.1 Introduction

Many organometallic systems are redox active, featuring multiple accessible oxidation states that may each have their own unique properties. To study these redox-active systems, electrochemical techniques have been widely adopted by organometallic chemists to better understand the synthetic, kinetic, and thermodynamic properties that involve changes in oxidation state. Electrochemical research is typically complemented by study of reactions with chemical redox reagents and isolation of products. These parallel approaches to studying organometallic redox chemistry represent a truly powerful combination.

Organometallic electrochemistry emerged in the 1950s. Notably, soon after the synthesis of ferrocene by Kealy and Pauson,[1] studies on the redox chemistry of this species as well as the first polarographic investigation by Wilkinson, Rosenblum, Whiting, and Woodward enabled the correct assignment of the now famous "sandwich" structure of the compound.[2] Since these early days, studies of both aqueous and non-aqueous organometallic electrochemistry have flourished, enabled by the wide availability of potentiostats in laboratories.[3,4] Readers of this review may be unfamiliar with common electrochemical methods, and in this case, we suggest further reading in the wide variety of high quality books[5] and reviews[6,7,8] that are available to guide the reader through the fundamentals of workhorse electrochemical techniques such as cyclic voltammetry (CV) and controlled potential electrolysis (CPE). References throughout this review are cited to assist readers in identification of appropriate further resources.

The potentiostat, which readily enables the three-electrode cell configuration for electrochemical work wherein potentials can be measured with respect to a well-known reference electrode potential, can be thought of as a ready means of understanding free energy (ΔG) changes

associated with organometallic redox reactions. Using the Nernst equation (2.1),[9] the reduction potential (*E*) of a given compound (analyte) present in solution may be determined by consideration of the standard potential (E^o) of the compound and the concentrations of the oxidized and reduced forms of the analyte present in solution. Conversely, knowing the concentrations of these forms at the surface of the working electrode as well as the standard potential, one can readily calculate the effective potential of a given mixture. Thus, using the potentiostat to determine the reduction potential *E* of a given species or mixture, the free energy change ΔG associated with electron transfer to a second redox active species can be calculated from the difference in reduction potentials (ΔE) using equation (2.2).

$$E = E^o - \frac{RT}{nF} ln \frac{[ox]}{[red]} \tag{2.1}$$

$$\Delta G = -nF\Delta E \tag{2.2}$$

The values of *E* are best determined using a potentiostat during cyclic voltammetry (CV) experiments. Determination of *E* from cyclic voltammetry experiments is particularly illuminating for synthetic chemists interested in exploring the accessible oxidation states of their compounds, because such a determination allows for the selection of suitable chemical redox reagents for the oxidation, or reduction, of organometallic complexes. A list of suitable oxidants and reductants for chemical synthesis were tabulated for this purpose in a popular *Chemical Reviews* article by Connelly and Geiger.[10]

In addition to thermodynamic insights of the type described above, monitoring of redox reactions by voltammetry can often provide significant kinetic and mechanistic information about chemical reactivity that precedes or, more commonly, follows electron transfer from an electrode.

Organometallic chemists can unite the study of chemical kinetics with electrochemical methods by leveraging the powerful concepts of electrochemical kinetic Zone Diagrams and methods like foot-of-the-wave analysis (FOWA) that were developed and popularized by Savéant, Costentin, and others.[11,12] In such efforts, examining the shape of a redox 'wave' in a cyclic voltammogram and comparing it to those of standard waves organized into so-called Zone Diagrams can provide key insights into the kinetic regime and mechanism associated with the given redox process of an organometallic analyte. FOWA is an excellent companion method to such approaches, particularly when catalytic processes are involved, as it allows for the determination of observed rate constants under a variety of conditions, particularly those involving "fast" catalysts that may rapidly consume substrates or display product inhibition.

Information on the design of experiments with CV to interrogate (electro)catalysis are described in detail in Sections 1.5 and 1.6 of this chapter. Details that can be studied include quantification of key catalyst properties such as the overpotential required to achieve a given transformation with a certain catalyst.[13] Such electroanalytical work to interrogate catalysis is often also paired with bulk electrolysis efforts that are aimed at generation of isolable and/or useful quantities of electrocatalytically generated products; information on such efforts is also given at appropriate points in Sections 1.5 and 1.6. In these sections, examples are taken from areas of current interest in redox catalysis, including both small-molecule substrate activations of relevance to energy science as well as select electrosynthetic organic reactions.

In this chapter, our goal has been to weave together the elementary concepts needed to carry out and interpret results from electrochemical studies of organometallic compounds. The individual sections of the chapter have been organized to provide the reader with information on the diverse facets of the vibrant field of organometallic electrochemistry. Effort has been made to

treat these facets in a balanced way, such that this chapter will provide both the key historical developments that underpin a given area as well as recount more recent developments that may be of use to researchers interested in applying electrochemical methods in their own work. We highlight the usefulness of pairing chemical and electrochemical methods in order to understand, in a comprehensive manner, the redox chemistry of organometallic species. Specific examples are given to highlight both practical aspects and fundamental considerations for gaining insights into stoichiometric and catalytic chemistries. Our hope is that this primer inspires further growth and development in the field of organometallic electrochemistry.

2.2 Developments in Electrodes, Materials, and Methods

2.2.1. Early Electrochemical Studies

The foundational work that initiated the field of electrochemistry dates back to the late 18th century; these very early studies will not be reviewed here in detail.[14] Rapid development of the field as we know now it began with studies in the mid-20th century focused primarily on main-group organometallic compounds.[15,16] These studies, taking place before the synthesis and structural identification of ferrocene, largely focused on the reductive chemistry of Hg and Mg compounds with direct current (DC) polarography. DC polarography was the dominant electroanalytical method prior to the 1960s and utilized a mercury electrode (in the form of metallic Hg(0)) as the working surface for measurements. However, Hg(0) can undergo a thermodynamically accessible oxidation to Hg(I); this feature made studying many oxidation processes difficult via this method.[6]

The synthesis and determination of the sandwich structure of ferrocene marked a significant development in the field of organometallic chemistry, in that this compound displays chemically stable iron(II) form as well as a stable oxidized form containing iron(III), known as ferrocenium.[6,17] The first electrochemical characterization of ferrocene, which demonstrated the interconversion of these oxidation states, was a landmark study that heavily contributed to the development of modern organometallic electrochemistry. [2,3,4,6,18]

The first major studies of organometallic electrochemistry can be attributed to Raymond Dessy's research group.[6] The Dessy group published a series of papers in 1966 detailing their work in organometallic electrochemistry[19] using Hg electrodes to study cathodic processes as well as the use of polarography,[20] cyclic voltammetry, bulk cathodic electrolysis, and monitoring of solutions via voltammetry and "back electrolysis" to recover the compounds under study.[21] Building on these initial studies, systematic electrochemical investigations have become a key method for studying the redox chemistry of organometallic compounds.

2.2.2. Major Advances in Materials and Measurement

Following the foundational early studies, experimental work in electrochemistry was expanded significantly by two key advances: the use of solid electrodes and the operational-amplifier-based potentiostat. Solid electrodes with reproducible and reliable surface properties, features thought to be impossible to achieve in prior years, were developed by Ralph Adams at the University of Kansas; such electrodes enable facile electrochemical investigation of redox processes without the requirement of mercury or other challenging electrode materials.[22] The advent of solid electrodes expanded the accessible positive potential range and obviated the need for toxic Hg for electrodes. The second major advancement in technology in this period was the use of the operational-

amplifier-based three-electrode potentiostat.[23,24,25,26,27] The employment of the three-electrode system, now universally applied in electroanalytical work, minimizes resistive errors especially in lower polarity solvents of relevance to organometallic chemistry carried out in solvents like tetrahydrofuran or acetonitrile. These technological advances have enabled the current popularity of studying non-aqueous redox processes of organometallic compounds.

Parallel to these improvements in experimental conditions, numerical approaches to solving the mathematical relationships underpinning diffusion and electron transfer kinetics enabled a once qualitative technique to become a quantitative analytical tool for investigating organometallic redox processes. In 1964, Nicholson and Shain used a numerical integration approach to map the features encountered in cyclic voltammetry data arising in the cases of several common redox mechanisms. To this day, the relationships established in this work are bedrock features of the quantitative cyclic voltammetry analyses used in modern research with electrochemistry.[28]

Building on the redox mechanisms outlined by Nicholson and Shain, the work of Jean-Michel Savéant in "molecular electrochemistry" constitutes a major contribution to the systematic quantification of heterogeneous electron transfer chemistry and interpretation of data for cases where electron transfer at an electrode is coupled with follow-up chemical reactivity.[29] This work emphasizes the critical aspects of electron transfer and reaction kinetics, enabling study of complicated reaction schemes that involve short-lived electrochemically generated complexes that can be quantitatively investigated over periods of time that are readily interrogated with electrochemical methods.

Several helpful resources regarding the values of standard reduction potentials and the behavior of various elements under electrochemical conditions also appeared for the first time in the mid-

twentieth century. Marcel Pourbaix introduced the use of potential-pH diagrams, now known as Pourbaix diagrams, which were first reported in 1945 to understand electrochemical reactions in aqueous media at an electrode. Pourbaix diagrams enable prediction of thermodynamic equilibrium states of reactions involving a specific element and its ions, and key solid, liquid, and gas phase compounds in aqueous media.[30] Similarly, in 1952, Wendell Latimer published potential diagrams that used the then-standard "oxidation potentials" to summarize thermodynamic data for inorganic compounds, including heat of formation, free energy of formation, entropies and equilibrium constants.[31] The eponymous Latimer diagrams summarize the key information needed to predict the relative stability of oxidation states at a given pH, and represent electrochemical equilibria for compounds with multiple oxidation states. Bard, Parsons and Jordan expanded and modernized the work of Latimer in a noted volume published in 1985,[32] providing a thorough tabulation of standard reduction potentials in aqueous solution to assist in predictions of chemical reactions and behavior of metal-solution interfaces. Modern data available at the time was used in the updated volume, and transitioned potential values to current notations and conventions used by IUPAC, particularly the standard reporting of half-reaction potentials as reductions.

2.2.3. Modern Electrochemical Methods and Techniques

Early developments in electrochemical methodology and technology have led to a plethora of modern techniques using electrochemistry. A compilation of modern electrochemical techniques can be found in Kissinger and Heineman's *Laboratory Techniques in Electroanalytical Chemistry*.[33]

The advent of gloveboxes with inert atmosphere has significantly advanced the facile study of air- and moisture-sensitive organometallic compounds. Accordingly, there is often interest among

researchers to carry out electrochemical investigations inside the glovebox. There are two common configurations that enable this.

The first setup involves keeping both the potentiostat and electrochemical cell inside the glovebox, which requires either specialized USB feedthrough ports through the dry box wall to reach the operating computer or a wireless, WiFi-enabled potentiostat. The wireless potentiostat obviates the need for cables; the user can place the potentiostat in the glovebox and control it from a nearby computer.[34] However, in this configuration, it is advisable to exercise extreme caution and minimize exposure of the potentiostat to organic solvent vapors, as these can damage the electronics. Common sources of vibrations present near gloveboxes, like vacuum pumps and refrigerator compressors, may also cause electronic noise and contribute to unexpected current flows by agitation of solutions under investigation.[35] Careful grounding of the potentiostat is another important consideration in this configuration; this can be done by grounding the instrument to the outside of the dry box. This approach can allow the glovebox to function as a Faraday cage, reducing electronic noise that originates from outside the glovebox that could impact electrochemical studies.

The second setup is the placement of the potentiostat outside the dry box, with connection of the electrochemical cell to the potentiostat through the glovebox wall using custom feedthroughs, or a more standard port with a KF-40 flange that can accommodate the needed cables. Alternatively, some gloveboxes come equipped with bulkhead connections built into side-panels, ready for wire-clips to be attached inside and outside for experiments. The longer cables needed for this cell-inside, potentiostat-outside configuration may be problematic for Electrochemical Impedance Spectroscopy (EIS) measurements, as they can introduce additional capacitance to the total electrochemical system.[35] The use of short, shielded cables with the fewest possible

connections can minimize electrical noise as well as capacitance. In both configurations, electrical devices placed near the instrument or electrochemical cell may cause spurious signals arising from electrical or magnetic fields; for example, stir plates left on during voltammetry can induce significant noise or non-chemical contributions to the data. Finally, static electricity can also be present in gloveboxes; use of shielded cables minimizes this type of interference.

In potential step methods, the electrode potential is rapidly changed from a value at which no Faradaic current is flowing to a potential value at which the potential difference is sufficient to induce electron transfer. Potential step chronoamperometry measures the current passed at the working electrode at a fixed potential.[43] Using the Cottrell equation (2.3) this method can be used to determine the number of electrons involved in an electron transfer reaction (n) and diffusion coefficient of the species undergoing electron transfer (typically, D_0). In a chronoamperometry measurement, an average value of current (i) is determined over a range of time at an electrode. From this measurement of the diffusion coefficient of electroactive species if the number of electrons transferred is known and vice versa. However, often D_0 and n are both unknown. D_0 can be estimated for most freely diffusing small-molecule/organometallic species to be on the order of 10^{-5} cm^2 s^{-1}. Alternatively, diffusion coefficients can be experimentally determined with hydrodynamic measurements using a rotating disk electrode to carry out Koutecký-Levich Analysis.[36,37] The number of electrons can be determined indirectly using chemical reduction with stoichiometric reductants[10] and characterization of chemically prepared reduced forms. Once either of the D_0 or n variables are known, the other variable can be calculated using the chronoamperometry measurement and the Cottrell equation.

$$i = \frac{nFAD_O^{1/2}C_O^*}{\pi^{1/2}t^{1/2}} \qquad (2.3)$$

Potential step chronocoulometry enables measurement of the charge (Q) passed following a potential step versus time. Charge (Q) is often quantified directly in the instrument with this method, although integrating the current (i) flowing during the potential step can also return the total charge passed at a given time through mathematical means.[43] Chronoamperometry, the measurement of current passed during a potential step versus time, is advantageous when the goal is to monitor current as a function of time, while chronocoulometry is useful for monitoring the total charge passed as a function of time. Although chronocoulometry and chronoamperometry are similar and related because charge passed and current flow are related by calculus, the two techniques are especially useful for different purposes depending on context. Chronoamperometry is often utilized for investigation of catalytic processes because changes in current flow (changes in the rate of a redox reaction), read out directly in chronoamperometry as current vs. time, are often straightforward to observe and interpret. For example, marked drop-off in current flow may suggest substrate consumption or catalyst decomposition during controlled potential electrolysis used for interrogating a molecular electrocatalyst. Chronocoulometry, on the other hand, reads out the total charge passed vs. time during a given experiment, making it useful for instantaneous determinations of expected product yields from redox reactions or calculation of predicted turnover numbers during a CPE investigation of a molecular electrocatalyst. However, as chronocoulometry records the total charge passed versus time, it can be more difficult to observe data trends that indicate changes in the chemical processes occurring during electrolysis. Chronocoulometry uses circuitry in the potentiostat to determine the number of electrons transferred, whereas chronoamperometry directly measures the current flow as a function of time, giving a mathematical (error-minimizing) benefit to use of chronoamperometry for measurements related to rates and chronocoulometry for measurements related to product yields.

Controlled potential electrolysis[38] (CPE) is an electrochemical technique in which the working electrode is held at a constant potential and monitored until completion of the redox reaction. Controlled potential methods such as bulk electrolysis requires a potentiostat that is capable of passing relatively large amounts of current and maintaining often substantial cell voltages. Additionally, placement of the working and counter electrodes is important in bulk electrolysis work to minimize uncompensated resistance; two-compartment cells are often useful for separation of the working and counter electrodes with a glass frit. Careful determination of the reduction potential of the target electroactive species by voltammetry is typically essential to ensure high current efficiency and complete conversion of the oxidized or reduced starting species. Comparison of the number of Coulombs passed during an electrolysis to the amount of product formed is then used to determine the Faradaic efficiency of the system.

Potential sweep methods are techniques that apply a range of applied potentials over time, in which the resulting current passed at the working electrode is measured as a function of potential. The effective midpoint potential ($E^{0\prime}$) of a target species can be measured by varying the potential over a range to identify the potential associated with electron transfer. The most commonly used potential sweep methods are cyclic voltammetry (CV) and linear sweep voltammetry. Linear sweep voltammetry (LSV)[43] is a technique in which the potential is varied linearly with time and the current passed is measured. In LSV of an electroactive species, if the scan begins well positive of the $E^{0\prime}$, essentially only non-Faradaic current will flow and [ox]>[red]. However, once the potential sweeps to the reduction potential current starts to flow, [ox] and [red] are equal at $E^{0\prime}$. As the potential sweeps negative of $E^{0\prime}$, however, [ox]<[red] at the electrode surface.

CV is a method in which the potential is varied over a range like in LSV, but the potential scan is reversed after the $E^{0\prime}$ and towards the initial potential. The intricacies and powerful opportunities

afforded by CV will be discussed here and in depth in later sections.[43] For those unfamiliar with running CV experiments, we direct the reader to several foundational books and articles which will provide practical guidance for organometallic chemists beginning to utilize electrochemistry. In particular, the books presented by Zoski,[39] Bard and Faulkner,[43] and Constentin and Savéant[29] can provide the reader with a comprehensive guide to the theory, instrumentation, and electrochemical techniques necessary for the investigation of organometallic complexes. Popular educational articles[8] and resources[40] are available that provide initial information on selecting solvents, electrolytes, electrodes, and use of electrochemical cells to perform a CV experiment.

Differential pulse voltammetry (DPV)[41] allows interrogation of a system via an approach similar to linear sweep voltammetry, but involving a more complex pulse sequence that minimizes non-Faradaic currents in the final data output. This technique, like CV and LSV, can be used for a variety of mechanistic and kinetic measurement applications.[42] DPV can be preferred over CV methods because the series of pulses applied at steadily changing potentials minimizes background from background charging of the electrode.[43]

Square wave voltammetry[42,44] is similar to DPV and utilizes a discontinuous potential change in which its current output is obtained as a symmetrical peak, unlike the current output obtained in linear sweep voltammetry that displays the direct influence of diffusion. Like DPV, square wave is a technique that is useful for detection of very low concentrations of analytes. The use of discontinuous potential in this technique allows measurement of Faradaic currents at the points in which current from double layer charging at the electrode is negligible.

Digital computer simulations of voltammetry data[33,45,46] can be employed as a complement to experimental cyclic voltammetry to help decipher and quantify coupled electron transfer reactions.

Simulations of cyclic voltammograms can be performed by changing variables such as electrode area, solution concentration, scan rate and switching potential, in order to extract kinetic information from voltammograms. Mathematically derived differential equations can be applied to organometallic systems to describe the concentration of a species in solution as a function of time. Other variables that are described by these differential equations include diffusion, convection, and migration; however, understanding these variables can be complex due to heterogenous chemical processes occurring at the electrode surface and homogenous chemical reactions occurring in the bulk solution.[47] Some simulation packages available include: ELSIM,[48,49,50,51] DigiSim,[52] DigiElch,[53] CVSIM[54] and CVPLOT.[54] An exhaustive list of packages and description can be found in *Digital Simulation in Electrochemistry*.[47]

Low temperature cyclic voltammetry[55] is an attractive technique for interrogating mechanistic pathways that create electrogenerated transient intermediate species. Additionally, this technique enables electrochemists to quantify thermodynamic parameters such as enthalpy change and kinetic parameters such as diffusion rate and heterogenous electron transfer rates of electron transfer reactions, and aids in the understanding of intricate coupled chemical reactions. Two cells are suitable for this technique, the *dip-type* cell that have an elongated cell body suitable for immersion in a coolant and *jacketed* cell that has a second outer jacket with feed throughs for coolants. Special care needs to be taken to choose an appropriate solvent and supporting electrolyte that can be used at low temperatures; a comprehensive list can be found in *Laboratory Techniques in Electroanalytical Chemistry*.[33] An additional challenge is that solution resistance increases at low temperatures; it is therefore often necessary to electronically compensate for the solution resistance.[33]

Spectroelectrochemistry[56] is a technique that allows for simultaneous electrochemical and spectroscopic interrogation of a compound. Spectroelectrochemistry enables the observation of spectral changes *in situ* to understand the reactions occurring at an electrode surface. These cells contain an optically transparent electrode (OTE) that are constructed of a conductive material such as platinum, gold, carbon, or a semiconductor material such as doped tin oxide on glass or quartz. Various spectroscopic techniques such as electronic absorption spectroscopy, infrared spectroscopy and Raman spectroscopy can be used in parallel with electrochemical methods.[43]

The use of chemically modified electrodes,[57] in which electrodes are purposefully modified via adsorption, coating or attachment of molecules to the electrode surface, is also a robust area of inquiry relevant to numerous fields. Modified electrodes are studied for their interesting properties in applications such as electrocatalysis, display devices, analytical applications and photoelectrochemical applications.

Alternating current (AC) voltammetry is a small-amplitude method that involves the application of sinusoidal wave voltage to an electrochemical cell. This method enables deciphering of contributions to electrochemical behaviors of, separately, the analyte concentration, the identity of solution components, kinetics of charge transfer, and the nature of the double layer capacitance at the electrode/electrolyte interface. This technique can be used primarily for mechanistic studies and allows separation of Faradaic and non-Faradaic current responses.[33]

Modern electrochemical methods and techniques will be discussed in further detail in the context of organometallic electrochemistry throughout this chapter.

2.3 Chemical Reactivity at the Working Electrode Surface

2.3.1 Electrochemically and Chemically Reversible Electron Transfers

Electron transfer can be homogenous or heterogenous in nature. Homogenous electron transfer is the transfer of an electron from one solubilized molecule to another. The movement of an electron from the highest occupied molecular orbital (HOMO) of a donor molecule and the lowest unoccupied molecular orbital (LUMO) of a given acceptor should be thermodynamically favored to take place. The kinetics of homogeneous electron transfer are most commonly discussed in the context of Marcus Theory.[58] On the other hand, heterogenous electron transfer typically occurs in molecular electrochemistry, an electron being transferred from a solid electrode to a solubilized molecule in solution that is located near the electrode surface. This type of electron transfer is associated with electrochemical reduction/oxidation in which the driving force for electron transfer to a compound in solution is based on the potential applied to the electrode by the potentiostat.

Electron transfer reactions are ubiquitous in organometallic electrochemistry and it is therefore often important to understand how electron transfer to/from an electrode affects the structure and composition of organometallic complexes. Electron transfer reactions are broadly classified as either "reversible" or "irreversible" processes. However, these classifications should be more specific: electron transfer reactions can be classified as either *electrochemically (ir)reversible* and/or *chemically (ir)reversible*. *Chemical reversibility* refers to processes in which the electroactive species are stable and homogenous in their reduced and oxidized forms.[8] *Electrochemical reversibility* speaks to the rate of electron transfer kinetics between the electrode surface and the electroactive species, with fast rates of electron transfer giving rise to *electrochemically reversible* behavior. *Electrochemically reversible* systems are referred to as

Nernstian, meaning that they obey the Nernst equation (2.1) by virtue of equilibrium concentrations being fully established at the electrode surface.[8,43] *Processes that are both electrochemically* and *chemically reversible* have a potential separation between cathodic and anodic peaks (ΔE_p) of 57 mV in cyclic voltammetry, a value derived first in the work of Nicholson and Shain for electron transfer rates at the fast limit. The term *quasi-reversible* refers to electron transfers that appear chemically reversible but have $\Delta E_p > 57$ mV, or for cases where the forward and backward rates are similar but not quite equal.

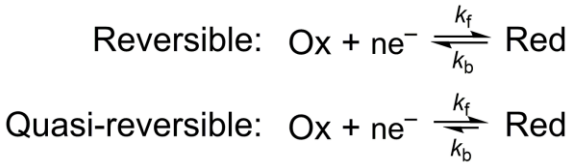

Scheme 2.1: Reversible electron transfer ($k_f = k_b$) and quasi-reversible electron transfer ($k_f \sim k_b$).

Reversible electron transfers can be described with the E mechanism notation used by Nicholson and Shain, referring to the involvement of a single electron transfer step.[28] The most well-known example of an organometallic complex that engenders an E mechanism upon oxidation and reduction is ferrocene/ferrocenium; ferrocene is ubiquitous in organometallic electrochemistry in part due to its ability to undergo fast electron transfer with minimal redox-induced structural change. Cycling of the oxidation state of the ferrocenium/ferrocene couple results in very little structural distortion, giving rise to fast electron transfer and therefore it is typically electrochemically reversible.[59] This has led to the widespread adoption of ferrocenium/ferrocene ($Fc^{+/0}$) as an internal reference for the reporting of electrochemical potentials for redox events.[60] This is because the reversible behavior of the $Fc^{+/0}$ couple holds true for a range of solvents; there is little to no structural rearrangement upon electron transfer, and

therefore there are no significant influences of solvent interactions that would otherwise affect the appearance of the voltammogram. Although ferrocene is traditionally viewed as highly stable and is therefore used as a standard for normalizing potential, readers should be aware that ferrocene can be oxidized to a dication[61] or reduced to an anion,[62] or degrade from reactions with electrogenerated species.

As the reader progresses ahead in this chapter toward the CV and CPE sections, please note that midpoint potentials ($E_{1/2}$ values) for redox processes may be reported, at various points, versus the ferrcenium/ferrocene couple ($Fc^{+/0}$) as well as versus SHE, the standard hydrogen electrode. This is because, in order to for a reported potential to be a standard reduction potential (E^0), the conditions of the measurement of the potential must satisfy the Nernst equation (see equation 2.2), wherein the temperature is 25 ºC, any gases involved are present at 1 atm, and the molarity of the analytes are 1 M.[63] These conditions are not always readily achievable or desireable in organometallic chemistry, and thus midpoint potentials measured for various redox processes are often simply reported as $E_{1/2}$ values vs. $Fc^{+/0}$ or other reference potentials. In order to convert between V vs SHE and V vs $Fc^{+/0}$, E^0 would need to be rigorously determined for ferrocene in water. However, ferrocene is insoluble in water, limiting the ability to rigorously determine the E^0 of $Fc^{+/0}$ or other insoluble redox active species in terms of V vs $Fc^{+/0}$, limiting the precise and rigorous interconversion between V vs SHE and V vs $Fc^{+/0}$.

Thermodynamic half-cell potentials for processes like proton reduction, oxygen reduction, and water oxidation are typically discussed with referencing of V vs SHE instead of V vs $Fc^{+/0}$ because such small-molecule reactions often do not have well-defined standard potentials in non-aqueous solvents. We note, however, that the conversion between the two references (SHE and $Fc^{+/0}$) has been estimated to be $Fc^{+/0}$ = +400 mV vs SHE.[10]

Under non-aqueous conditions, the midpoint potential, $E_{1/2}$, measured using cyclic voltammetry of the $Fc^{+/0}$ couple can provide an estimate of the formal potential, $E^{0'}$, of the $Fc^{+/0}$ couple.[64] The midpoint potential and formal potential of the ferrocenium/ferrocene couple are virtually equivalent because of the electrochemically and chemically reversible nature of the redox chemistry of these species. Therefore, a traditional measurement to determine the standard reduction potential of ferrocenium/ferrocene (carried out so as to satisfy all the requirements of the Nernst equation) in which the potential of a half-cell prepared with a 1:1 mixture of ferrocenium and ferrocene would be compared to a reference potential can be reliably concluded to be comparable to that of the operationally much simpler measurement of the midpoint potential of the $Fc^{+/0}$ redox system via CV.

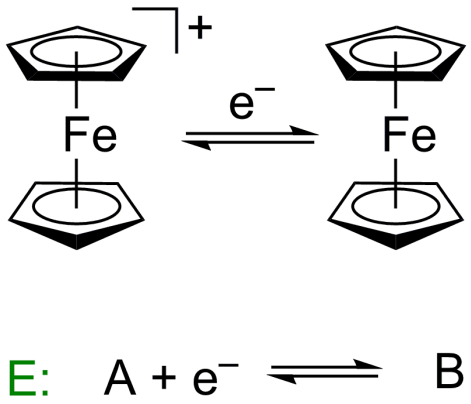

Scheme 2.2: One-electron reduction of ferrocenium/ferrocene. General E mechanism. Electrode electron transfer reaction.

2.3.2 Coupled Chemical Reactions

Chemical reactions are often coupled to electron transfer, because gain or loss of electrons by a metal complex can cause structural changes and/or changes in the frontier orbitals in the complex.

An extensive review of examples of electrochemically induced redox chemistry is beyond the scope of this chapter, but a thorough list of examples is given in a review from Geiger.[6] Electronic changes often induce chemical processes due to the instability of formed intermediate species that result from electron transfer. *Irreversible* electron transfer processes involve a charge transfer that is rate limiting. A *non-reversible* electron transfer processes involve thermodynamically reversible process as well as a redox-induced chemical reaction.

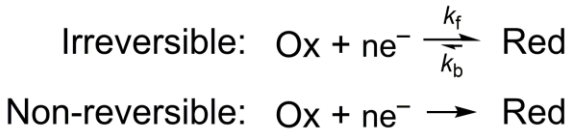

Scheme 2.3: Irreversible electron transfer ($k_f >> k_b$) and non-reversible electron transfer.

2.3.3 EC Mechanism

There are multiple mechanisms by which electron transfers and chemical processes can be coupled together at an electrode.[28] The simplest of these is the EC mechanism, in which an electron transfer is followed by a first-order or pseudo-first-order reaction that occurs in solution. If the initial electron transfer is fast, the follow-up homogeneous chemical reaction often does not interfere with the electrochemical response in a kinetic sense. In the case of the EC mechanism, the redox-induced chemical reaction is the only rate limiting factor except for diffusion.[29]

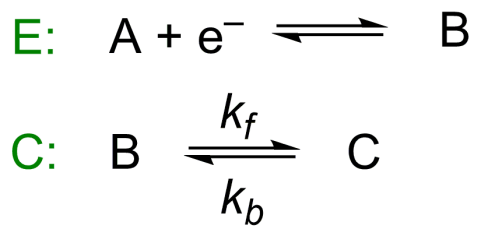

Scheme 2.4: General EC mechanism. Electrode electron transfer flowed by a first-order or pseudo-first-order homogenous reaction.

The zone diagrams developed by Savéant are helpful to understand redox reactions that engender a general EC mechanism. Zone diagrams serve to identify the relationship between the rate of diffusion, the kinetic properties of the reduction-induced reaction (as a function of equilibrium constant, K) and the ratio of the coupled chemical reaction rate and diffusion rate (quantified in a dimensionless parameter, λ). The scan rate at which the CV is measured is inversely proportional to λ. This inverse relationship means that as the scan rate is increased for a CV measurement, the λ parameter decreases. When scan rate is high in a reduction, λ is small, allowing less time for the reduced form of the organometallic complex to diffuse in solution, and therefore there is less time for the coupled chemical reaction to occur at the electrode surface and influence the electron transfer equilibrium that is measured as current. At faster scan rates, the anodic peak current associated with reoxidation increases until it appears to be quasi-reversible, indicating that the coupled chemical reaction has had insufficient time to occur. Conversely, at low scan rates the coupled chemical reaction appears as an irreversible process, because there is sufficient time for the coupled chemical reaction to occur at the electrode surface, and the back reaction is eliminated.[29] Two examples of kinetic zone diagrams are shown in Figure 2.1; for a complete set of the diagrams discussed in this chapter please refer to Savéant and Costentin's

Elements of Molecular and Biomolecular Electrochemistry: An Electrochemical Approach To Electron Transfer Chemistry.[29]

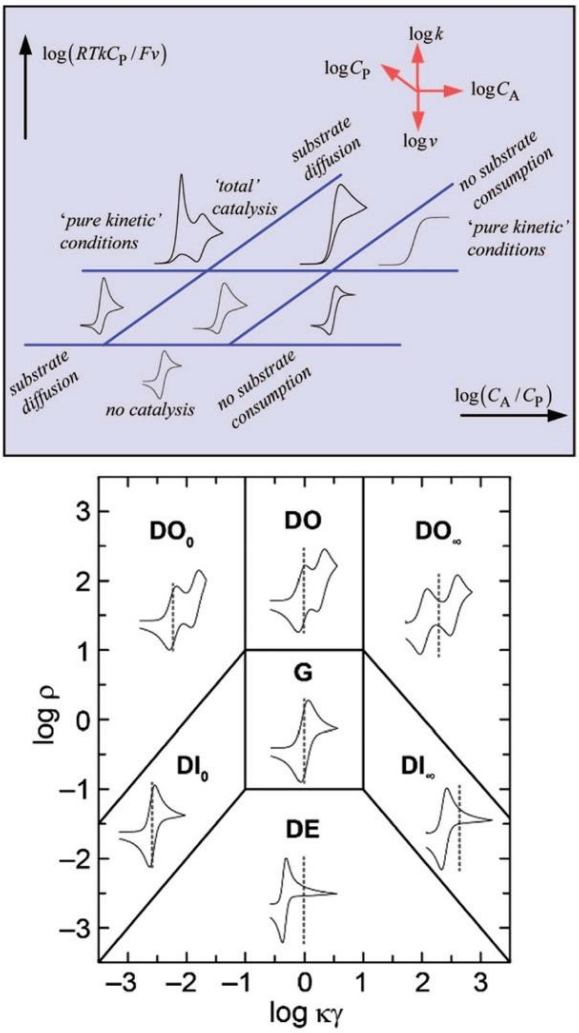

Figure 2.1: Examples of Zone diagrams. Upper Panel: Kinetic zone diagram of expected shapes of CV response for a catalytic reaction first order in substrate (C_A) and catalyst (C_P). Reprinted (adapted) with permission from Savéant, J.-M., *Chem. Rev.* **2008,** *108* (7), 2348-2378. Copyright 2008, American Chemical Society. Lower Panel: Kinetic zone diagram for the EC_rEC_i mechanism. Reprinted (adapted) with permission from Elias, J. S.; Costentin, C.; Nocera, D. G., *J. Am. Chem. Soc.* **2018,** *140* (42), 13711-13718. Copyright 2018, American Chemical Society.

A well-defined organometallic system that demonstrates this behavior with an EC mechanism is the series of [Cp*Rh] bis(2-pyridyl)methane complexes studied by our own group.[65,66] In this organometallic system, a $1e^-$ quasi-reversible reduction is followed by a second $1e^-$ reduction that is coupled to a rearrangement of the bis(2-pyridyl)methane ligand. Figure 2.2 shows the voltammograms of the benzyl (Bn) analog of **1** at 50, 1000, and 2500 mVs^{-1} (left panel) associated with the reduction-induced ligand rearrangement shown (right panel). The second reduction at E_{pc} = −1.40 V vs $Fc^{+/0}$ exhibits characteristics of an EC mechanism in which there is an expected increase in cathodic current with increasing scan rate coupled with observation of the anodic process at only higher scan rates. As described by Savéant, λ is large at slower scan rates allowing ample time for the redox induced ligand rearrangement to occur. At higher scan rates the observation of the reoxidation event in the form of the anodic feature at leading to an electrochemically quasi-reversible process. At higher scan rates the relative increase in anodic current is a result of the small value of λ. In other words, the increased scan rate enables the rate of the coupled chemical step to be overtaken, enabling direct observation of redox couple for the species that can otherwise be considered transient. As a complement to this experimental voltammetric study, digital simulations of the experimental data were performed using DigiElch in order to measure the first-order rate constant (k^+) for the ligand reorientation or "flip" chemical step. Multiple scan-rate dependent voltammograms were simulated to extract, from the behavior of the anodic feature, quantitative values of k^+.

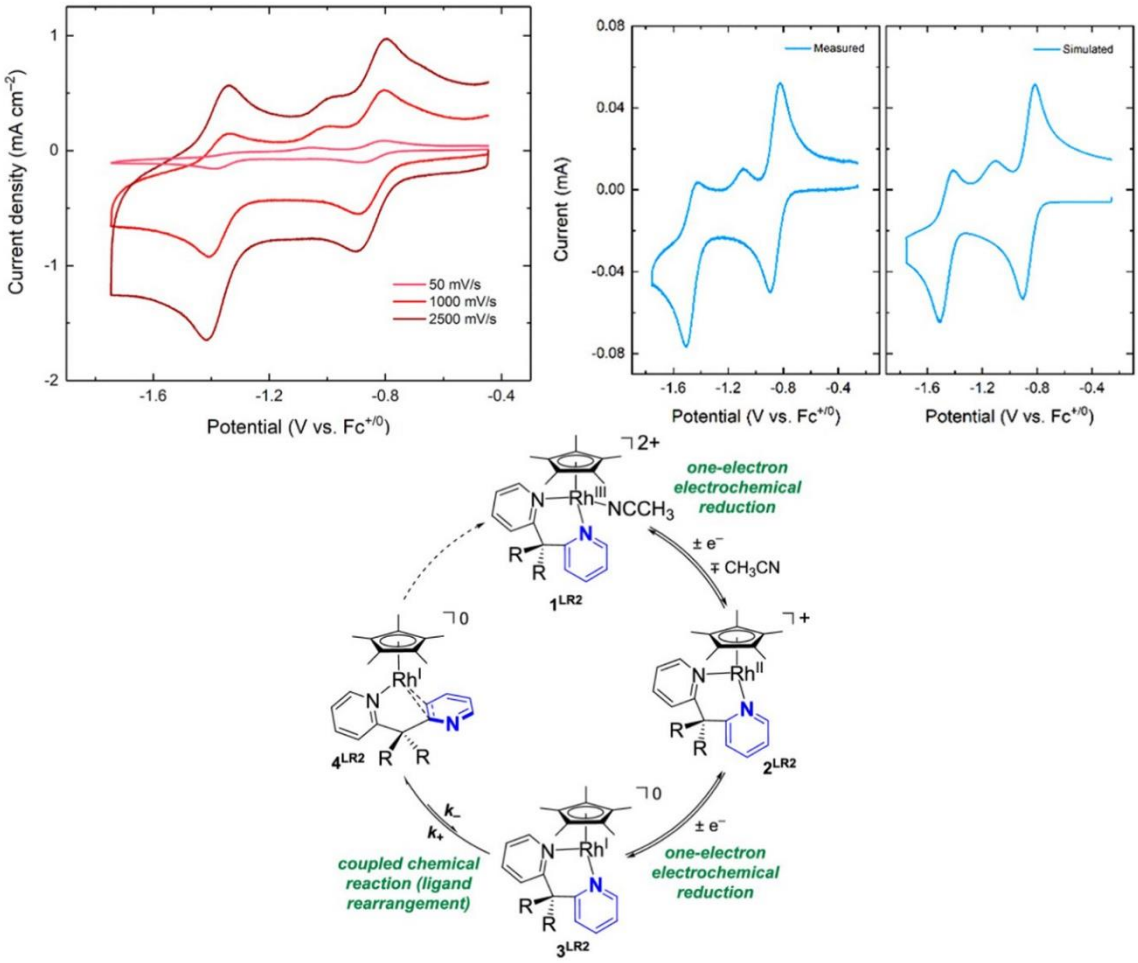

Figure 2.2: Top left panel: cyclic voltammetry of **1** (R = benzyl, Bn) at increasing scan rates. Conditions: electrolyte, 0.1 M $TBAPF_6$ in CH_3CN; working electrode, highly oriented pyrolytic graphite. Upper right panel: experimental and simulated voltammograms of **1** (R = methyl, Me). Lower scheme: electrochemical reduction pathway for **1**. Adapted from work described in citation 65. Copyright 2021, American Chemical Society.

2.3.4 ECC Mechanism

An electrochemical process that involves an electron transfer step followed by two sequential chemical reactions is referred to as an ECC mechanism. One of the most common ECC

mechanistic scenarios results from the generation of an organometallic radical, followed by the loss of a ligand, and then dimerization to give the final product. This can occur by $1e^-$ oxidation or reduction of a substrate, which ultimately results in a ligand or metal centered radical. Radicals are notoriously reactive species, and once generated electrochemically, often go on to react with another species present. A notable organometallic complex that undergoes $1e^-$ reduction to form a metal centered radical is $Mn(CO)_3Br(^{H}bpy)$, a well-known CO_2 reduction catalyst. The electrochemical and electrocatalytic behavior of $Mn(CO)_3Br(^{H}bpy)$ was first established by Deronzier, Chardon-Noblat, and co-workers using CV (see Figure 2.3).[67]

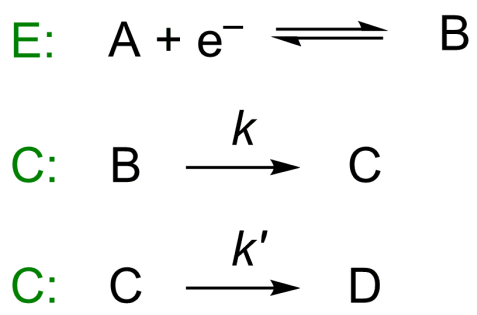

Scheme 2.5: General ECC mechanism. Electrode electron transfer followed by two first-order or pseudo-first-order homogenous reactions.

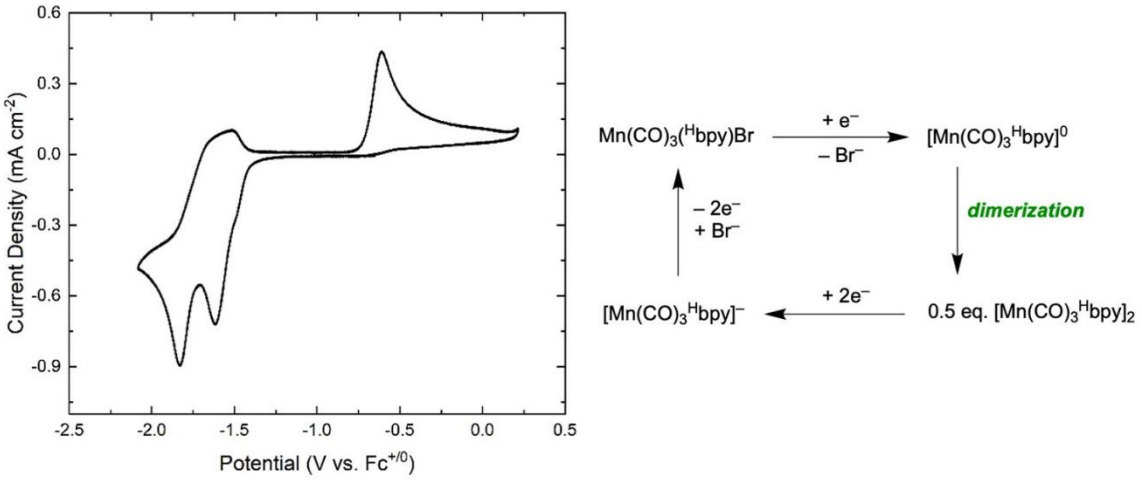

Figure 2.3: CV of $Mn(CO)_3Br(^{H}bpy)$ in 0.1 M $TBAPF_6$/MeCN electrolyte at 100 mVs^{-1} (left). Accompanying chemical scheme for the sequential irreversible reductions and more positive oxidation associated with $Mn(CO)_3Br(^{H}bpy)$ (right).

At first glance, the cyclic voltammogram of $Mn(CO)_3Br(^{H}bpy)$ seems to be quite complicated; this is attributable to the multiple chemical reactions involved in the redox behavior of this complex. Scanning toward more negative potentials, two sequential and essentially irreversible reductions are observed with cathodic peak potentials of –1.61 V vs $Fc^{+/0}$ and –1.83 V vs $Fc^{+/0}$, followed by an oxidation at more positive potentials with an anodic peak potential at –0.61 V vs $Fc^{+/0}$. Based on mechanistic work with this complex, the first irreversible reduction of $Mn(CO)_3Br(^{H}bpy)$ can be reliably assigned to result in a $19e^-$ complex.[68] This $19e^-$ complex then loses Br^- to generate a $17e^-$ species with a Mn-centered radical. Two of these Mn-centered radicals can recombine to dimerize and produce $Mn_2(CO)_6(^{H}bpy)_2$ (Mn–Mn dimer) in an overall ECC-type mechanism. The second reduction feature in the CV is attributed to the reduction of the Mn–Mn dimer, which cleaves the metal-metal bond to generate the 18 e^- complex, $[Mn(CO)_3(^{H}bpy)]^-$ in an overall EC process. Lastly, scanning to more positive potentials, $[Mn(CO)_3(^{H}bpy)]^-$ is re-oxidized to form the starting complex, $Mn(CO)_3Br(^{H}bpy)$.

2.3.5 CE Mechanism

The CE mechanism involves a rapid, reversible first-order or pseudo-first-order chemical reaction followed by an electron transfer. For CE mechanisms the electroactive starting material (A) is the product of chemical conversion of the starting material (species C in Scheme 2.6) in the chemical reaction labelled as step C.

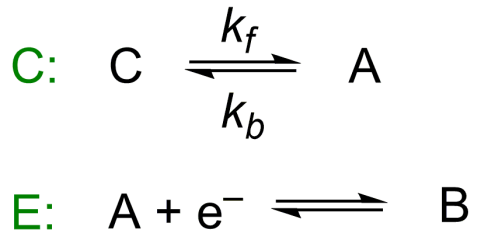

Scheme 2.6: General CE mechanism. A first/pseudo first-order homogenous reaction preceding an electrode electron transfer.

CE mechanisms in which the pre-equilibrium is sufficiently fast to not influence the electrochemical response kinetically can be described using the equilibrium constant (K) and kinetic parameter λ.[29] In the case of one-electron reversible waves that engender a CE mechanism when the equilibrium constant is large, the couple appears reversible regardless of λ. However, when K is small, the appearance of the CV becomes more complex and depends on the value of λ. The preceding reaction (C step) influences the electrochemical response (E step) when k_f is small. The CV response is controlled by the rate at which the species C is converted to the electroactive species A (k_f). The kinetics and thermodynamics of the conversion of C to A can influence the height and shape of the CV. As previously stated, the inverse relationship between scan rate and λ means that as the scan rate is increased for a CV measurement, the λ parameter decreases. The case of CE with a small λ engenders (fast scan rate and/or slow reaction) a reversible wave in

which the height is influenced by the equilibrium constant. If the equilibrium constant is proportional to the peak heights of the CV, meaning for a CE case with a small K and small λ value there will be a reversible wave with small peak current. As λ increases as a result of slower scan rate the anodic wave takes the form of a plateauing wave which has a plateauing current independent of scan rate. An even slower scan rate and larger λ parameter results in a CV that gradually increases in reversibility until reaching a quasi-reversible wave.[29]

A distinct CE mechanism was observed in the titration of the solvent rhodium complex $[Cp^*Rh(PQN)NCCH_3]^{2+}$ (PQN) = (diphenylphosphino)quinoline) with tetrabutylammonium chloride (TBACl).[69] This titration was performed to understand the role of halide ligands in influencing the redox properties of [Cp*Rh] complexes supported by bidentate chelates. The CV of $[Cp^*Rh(PQN)NCCH_3]^{2+}$ reveals two distinct quasi-reversible one-electron couples ($Rh^{III/II}$ and $Rh^{II/I}$, –0.93 V and –1.16 V vs $Fc^{+/0}$ respectively). Increasing the concentration of TBACl to $[Cp^*Rh(PQN)NCCH_3]^{2+}$ clearly results in the diminution of the two original waves and gives rise to a new single $2e^-$ wave ($Rh^{III/II}$ = –1.19 V vs $Fc^{+/0}$) that corresponds to the electrochemical profile of $[Cp^*Rh(PQN)Cl]^+$; this was verified when this species was isolated through chemical synthesis and studied independently. This behavior confirms the rapid chemical conversion (C step) of $[Cp^*Rh(PQN)NCCH_3]^{2+}$ to $[Cp^*Rh(PQN)Cl]^+$ by displacement of the ligated CH_3CN with chloride followed by an electron transfer to reduce the rhodium(III) complex (E step) giving rise to an EC mechanism observed in Figure 2.4.[70]

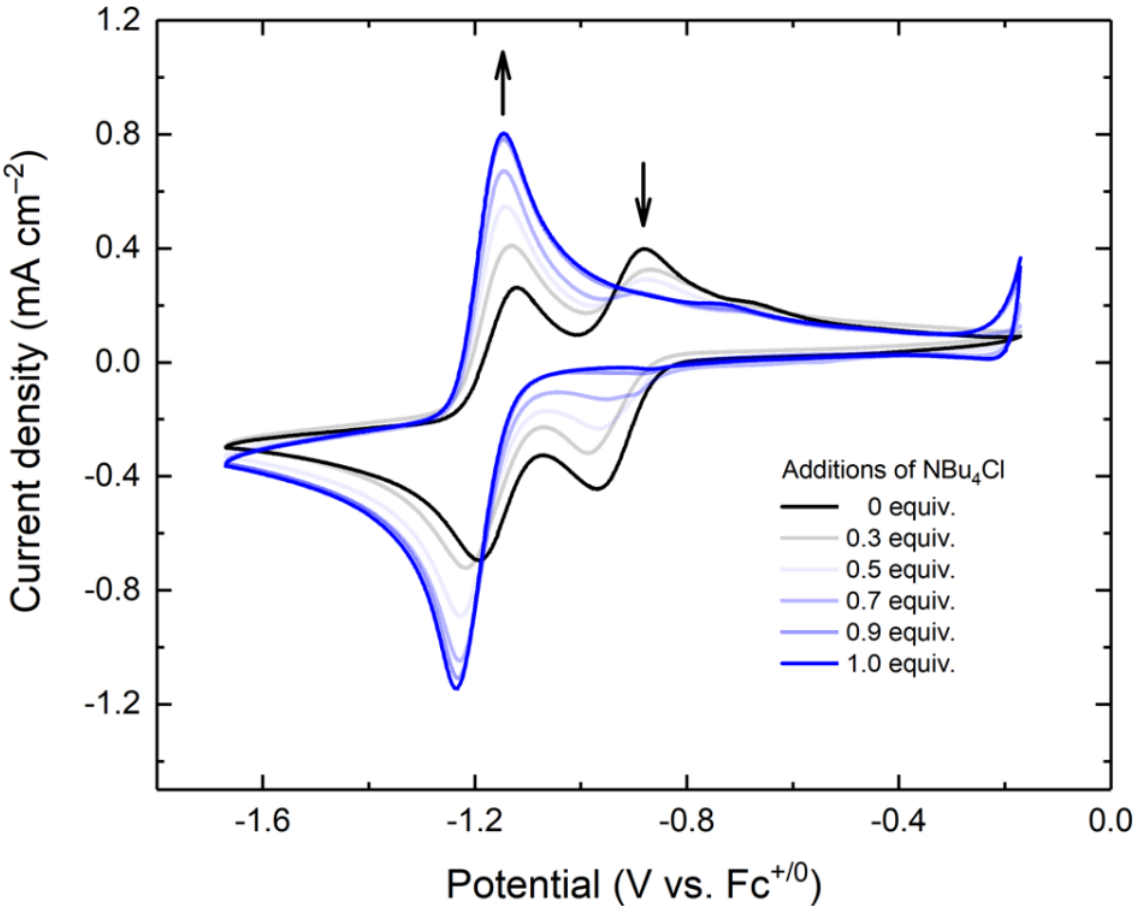

Figure 2.4: Electrochemical response of $[Cp^*Rh(PQN)NCCH_3]^{2+}$ in CH_3CN upon increasing additions of tetrabutylammonium chloride. Growth of the reduction process with $E_{1/2} = -1.19$ V indicates coordination of chloride to $[Cp^*Rh(PQN)NCCH_3]^{2+}$ by displacement of bound CH_3CN, generating $[Cp^*Rh(PQN)Cl]^+$. Reprinted (adapted) with permission from citation 69. Copyright 2019, American Chemical Society.

2.3.6 ECE Mechanism

The ECE mechanism is the case in which an electroactive species undergoes an electron transfer reaction followed by a coupled chemical reaction, like that of an EC reaction. However, the intermediate formed by the chemical step then undergoes a second electron transfer (Scheme 2.7). An ECE reduction occurs when the intermediate C formed has a standard reduction potential that is more positive than that of the standard reduction potential for the conversion of the initial electroactive species A to generate B. Each molecule of B is chemically converted to C, and following the chemical conversion, C is instantaneously reduced by the electrode to generate the final species, D. This instantaneous reduction of C means that the ECE mechanism results in the appearance of a "$2e^-$ wave" which is often misinterpreted as arising from a truly simultaneous transfer of $2e^-$. However, virtually all ECE reductions actually involve two separate $1e^-$ reduction steps. Like many of the other mechanisms discussed here, the appearance of the CV can sometimes be influenced by varying the scan rate. In the ECE case, the λ kinetic parameter is interrelated with the rate of the chemical reaction that controls conversion of B to C. In the ECE case, at faster scan rates where λ is small, a quasi-reversible wave is predicted to be observed, corresponding to the one-electron process for reduction of A to B and re-oxidation of B to A. As the scan rate is decreased, however, λ increases, giving rise to irreversibility with respect to the original A/B wave and increase of the cathodic peak current, attributable to time being allowed for conversion of B to C and subsequent reduction of C to D. At slow scan rates the CV should then have the expected two-fold increase in the magnitude of the cathodic peak current. In certain systems which have appropriate kinetics of the chemical step associated with conversion of B to C, accumulation of the intermediate C at the electrode during scans can give rise to trace crossing; such behavior is attributable to the greater quantity of the intermediate C present at the surface during the reverse

scan than the cathodic scan, giving rise to cathodic current during the anodic scan.[29] However, at typical electrodes and scan rates of relevance to molecular organometallic chemistry, this trace crossing associated with the ECE mechanism is not commonly observed and thus the absence of the behavior should not be taken as evidence against net $2e^-$, ECE-type behavior.

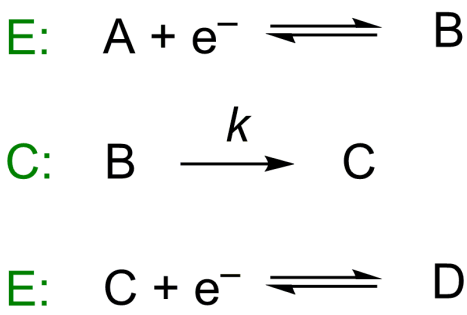

Scheme 2.7: General ECE mechanism (reduction shown). Electrode electron transfer flowed by a first/pseudo first-order homogenous reaction which undergoes a second electron transfer.

A well-defined family of Cp*Rh complexes illustrates the ECE mechanism engendering two sequential $1e^-$ reductions.[65,71,72,73,74] Electrochemical studies on the $[Cp^*Rh(PQN)L]^{n+}$ (PQN = 8-(diphenylphosphino)quinoline) complex exhibits interesting activity with substitution of the monodentate ligand (Figure 2.5). The $[Cp^*Rh^{III}(PQN)Cl]^+$ analog undergoes an initial $1e^-$ reduction generates a transient $[Cp^*Rh^{II}(PQN)Cl]^0$ following the initial E step, the Rh(II) complex undergoes a chemical loss of the monodentate Cl^- to form the intermediate $[Cp^*Rh^{II}(PQN)]^+$, which is immediately followed by a second $1e^-$ reduction to generate $[Cp^*Rh^{I}(PQN)]^0$. This ECE mechanism gives rise to a CV with the appearance of a quasi-reversible $2e^-$ reduction. In the absence of chloride, however, the reduction of the solvento species, $[Cp^*Rh^{III}(PQN)NCCH_3]^{2+}$ takes place at a potential more positive than that for $[Cp^*Rh^{III}(PQN)Cl]^+$ due to its dicationic nature. The shift in this potential is a result of the chemical reaction step (loss of CH_3CN rather

than Cl^-) being insufficient to cause the transient $[Cp^*Rh^{II}(PQN)NCCH_3]^+$ complex to be reduced at a more positive potential compared to the $[Cp^*Rh^{III}(PQN)NCCH_3]^{2+}$ complex. Due to this phenomenon two discrete reductions are observable and results in the metastable $[Cp^*Rh^{II}(PQN)NCCH_3]^+$ complex generated near the electrode. The oxidation of the $[Cp^*Rh^{I}(PQN)]^0$ analog results in a very similar CV profile due to the generation of the $[Cp^*Rh^{III}(PQN)NCCH_3]^{2+}$ in CH_3CN solvent. The third reduction in each CV is attributed to the reduction of the PQN ligand.[73]

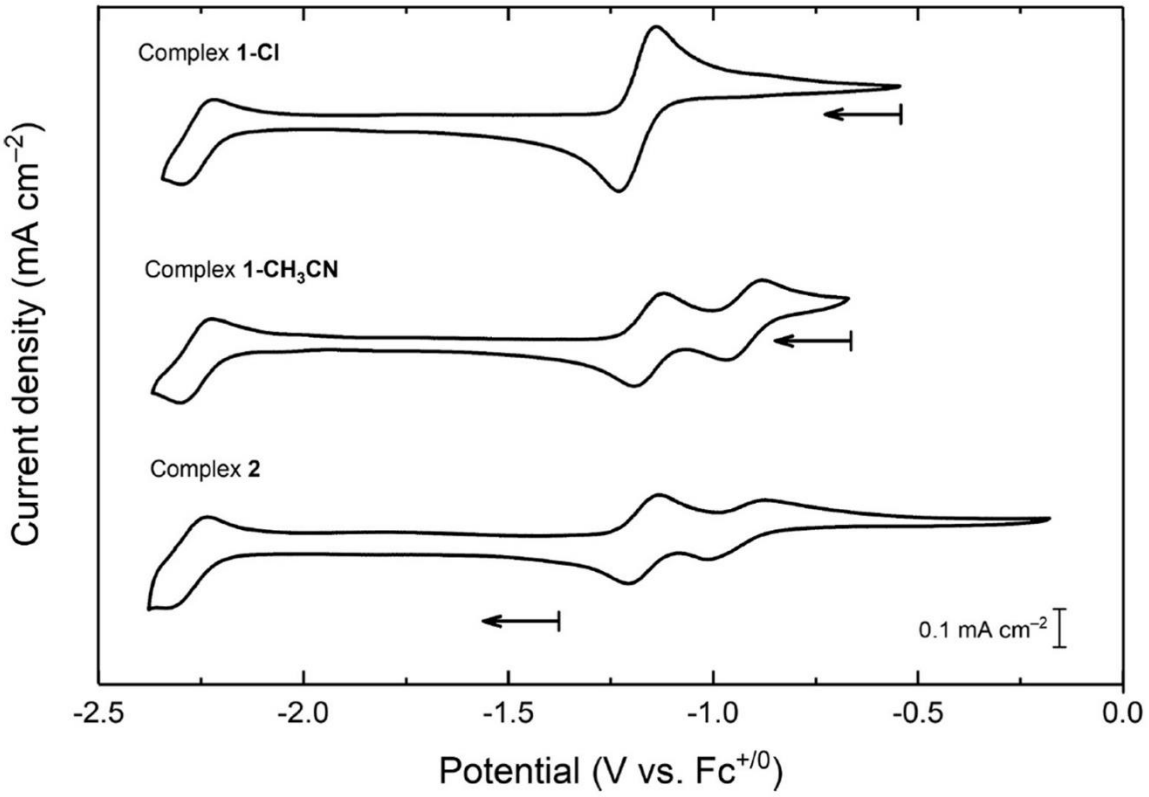

Figure 2.5: CV of $[Cp^*Rh^{III}(PQN)Cl]^+$ (upper panel) $[Cp^*Rh^{III}(PQN)NCCH_3]^{2+}$ (middle panel) and $[Cp^*Rh^{I}(PQN)]^0$ (lower panel). Reprinted (adapted) with permission from citation 69. Copyright 2019, American Chemical Society.

2.3.7 Substitution Mechanism

In inorganic and organometallic chemistry intermolecular substitution reactions typically occur by associative or dissociative mechanisms. In an associative mechanism, a ligand forms a bond to the metal center prior to the ejection of the exiting ligand. Conversely, in a dissociative mechanism, a ligand is initially expelled from the metal center to generate space for an incoming ligand to bind. Electrochemical oxidation or reduction has been shown to accelerate some intermolecular organometallic substitution reactions, and therefore gives useful mechanistic insights.

In an example from the work of Kochi and co-workers, organometallic intermolecular ligand substitution is enhanced and observed using electrochemical methods.[75] This series of reactions, monitored by CV, demonstrate that the acetonitrile ligand bound to (η^5-MeCp)Mn(CO)$_2$(NCMe) (Mn-NCMe) may be substituted with various alkyl and arylphosphines when an oxidative bias is applied (see Figure 2.6). The initial CV of Mn-NCMe displays a well-behaved quasi-reversible 1e- redox couple at 0.22 V vs $Fc^{+/0}$. However, when 1 equiv. of triphenylphosphine (PPh_3) is added to the system, the quasi-reversibility of the initial redox couple ceases, but the $1e^-$ oxidation of Mn-NCMe to the $17e^-$ species $[Mn\text{-}NCMe]^+$ persists and a new redox couple begins to grow in at 0.55 V vs $Fc^{+/0}$. This behavior suggests that once [Mn-NCMe] is oxidized to $[Mn\text{-}NCMe]^+$, substitution of the NCMe for PPh_3 is facile and results in the rapid consumption of $[Mn\text{-}NCMe]^+$ to generate the intermolecular substitution product (η^5-MeCp)Mn(CO)$_2$(PPh_3) (Mn-PPh_3). As increasing equivalents of PPh_3 are added to the electrochemical cell, $[Mn\text{-}NCMe]^+$ is consumed more rapidly until only the current corresponding to the substitution product is observed during CV. To confirm that it is indeed MeCp)Mn(CO)$_2$(PPh_3) being generated, an authentic sample of (MeCp)Mn(CO)$_2$(PPh_3) was found to be oxidized at the latter potential. This exemplifies a class

of substitution reactions that take place when inner-sphere ligands become labile upon oxidation or reduction of different organometallic complexes.

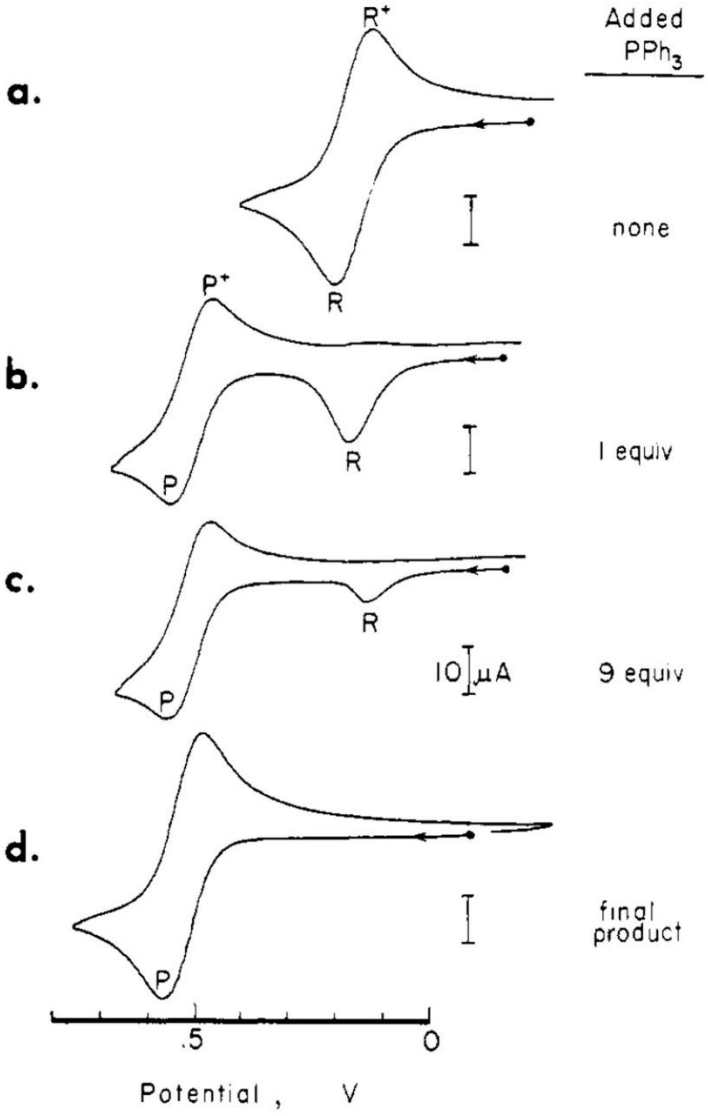

Figure 2.6: (**a**) Initial CV of (η^5-MeCp)Mn(CO)$_2$(NCMe). (**b** and **c**) Potentiometric titration of (η^5-MeCp)Mn(CO)$_2$(NCMe) (R) with PPh_3 to generate (η^5-MeCp)Mn(CO)$_2$(PPh_3) (P) under electrochemical conditions. (**d**) CV of isolated (η^5-MeCp)Mn(CO)$_2$(PPh_3). CVs are taken at 200 mVs^{-1} with MeCN solvent at 0.1 M TEAP electrolyte. Reprinted with permission from 75. Copyright 1983 American Chemical Society.

2.3.8 DISP Mechanism

The DISP mechanism, or disproportionation mechanism, is similar to that of the ECE mechanism previously discussed, but involves a second disproportionation pathway following the non-electrode-based generation of the intermediate C. For DISP mechanisms the second electron is transferred from B to C rather than from the electrode to C as in an ECE mechanism. In the ECE mechanism the $E^0_{C/D}$ is at a more positive potential than $E^0_{A/B}$, implying that the disproportionation reaction K_D is favorable. The two electron transfers engendered in the ECE mechanism are both fast, therefore it is assumed that the thermodynamically favorable disproportionation reaction is fast. The chemical conversion of B to C is the rate determining step and λ behaves in the same manner as in ECE mechanism. As discussed for the ECE mechanism at faster scan rates λ is low, which gives rise to a quasi-reversible wave. As the scan rate is gradually decreased, λ increases giving rise to increasing irreversibility and increase of the cathodic peak current and slow scan rates the CV reaches complete irreversibility and has appearance of a $2e^-$ reduction in magnitude of the peak current. Under pure kinetic conditions the ECE and DISP mechanisms are indistinguishable by CV, but when pure kinetic conditions are not achieved it is possible to distinguish between ECE and DISP mechanisms. Non-pure kinetic conditions in DISP do not lead to crossing as seen in the ECE case discussed above. The absence of trace crossing in the DISP mechanism is due to the slow reaction of B to C, consequently the intermediate C is formed far from the electrode surface which allows ample time for the disproportionation to occur before C reaches the electrode. This prevents the accumulation of C at the electrode surface during scans, and therefore there is no possible contribution of cathodic current during the anodic scan as is possible during the ECE-type mechanism.[29]

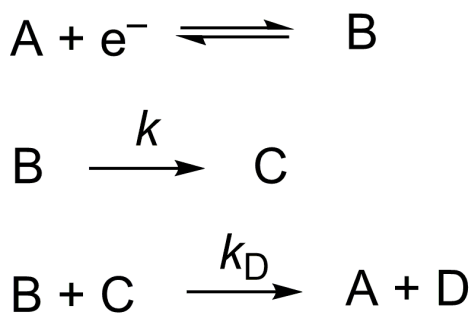

Scheme 2.8: DISP mechanism. Electrode electron transfer followed by a first-order or pseudo-first-order homogenous reaction in which a second electron is transferred from species B to C.

An example of an organometallic system with an ECE-DISP mechanism is the series of substituted rhodium(III) porphyrin complexes studied by Savéant et al (Figure 2.7).[76] This rhodium(III) porphyrin family engenders chemical irreversibility that is attributed to the disproportionation of the rhodium(II) complexes caused by ligand exchange reactions. During reduction $^{+}Rh(III)L_2$ is reduced by $1e^{-}$ to the corresponding $Rh(II)L_2$ followed by the loss of one L ligand. The loss of L generates a second Rh(II)L which is reduced at a more positive potential than the initial Rh(III) complex by $1e^{-}$. This electrochemical reduction thus involves a disproportionation step because the second electron step occurs concurrently with electrode reduction.

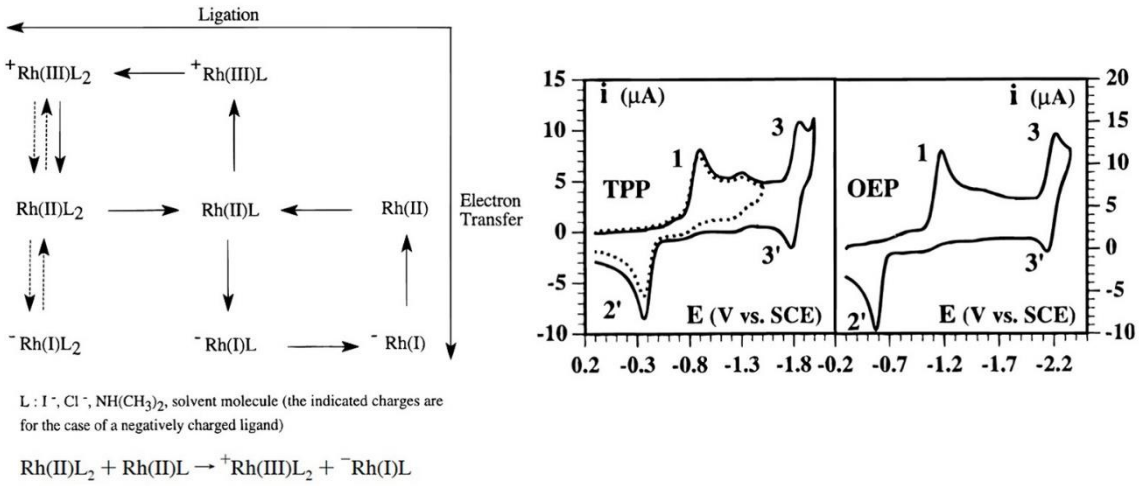

Figure 2.7: Reduction scheme of Rh(III) porphryin complexes in which disproportionation occurs with the reduction to Rh(II)L_2. Disproportionation scheme of Rh(II)L_2 shown below. (Left.) Cyclic voltammetry of rhodium(III) tetraphenylporphyrin (TPP) and rhodium(III) octaethylporphyrin (OEP) (Right.) Reprinted (adapted) with permission from citation 76. Copyright 1997, American Chemical Society.

2.4 Using Electrochemistry to Explore Chemical Reactivity with Stoichiometric Redox Reagents

2.4.1. Synthesis via Controlled Potential Electrolysis

Controlled potential electrolysis (CPE) is a well-established electrochemical method used for synthesis of electron transfer products.[10,77,78,79 80,81,82] There are advantages and disadvantages to this electrochemical synthetic method. CPE allows a wide range of precise potentials accessible for reduction/oxidation of organometallic compounds with minimal side reactivity that leads to byproducts. However, CPE can be problematic because of the need for a large amount of electrolyte salt in solution, which can be difficult to separate from the product.[10]

2.4.2. Synthesis via Chemical Redox Reagents

An alternative method for synthesis of electron transfer products is use of chemical redox reagents, chosen based on CV to determine the reduction potential of the electroactive species (Figure 2.8). The utilization of a homogeneous reductant/oxidant eliminates the necessity for a large excess of supporting electrolyte salt that must be separated. Another advantage of chemical methods is the fast time scale and large reaction scale compared to electrochemical methods. Chemical reduction and oxidation can be performed at low temperatures to reduce side reactivity and improve selectivity. Although it should be noted that low temperature electrolysis experiments are possible, it is necessary to be strategic when selecting the solvent and supporting electrolyte for work at low temperature. A list of appropriate solvents and electrolyte systems for work at reduced temperatures can be found in Kissinger and Heineman's *Laboratory Techniques in Electroanalytical Chemistry.*[83] Another notable difference between chemical and electrochemical synthetic methods is the former can be done in non-polar solvents. This may be advantageous for precipitation of products, or for use of a non-coordinating solvent to prevent ligand exchange/displacement.[10]

However, the use of chemical redox reagents have notable disadvantages.[10] Chemical reagents have a fixed reduction/oxidation potential, which can be disadvantageous for target complexes for which there is no good match of a chemical redox agent with chemical compatibility and the correct potential, whereas electrochemical methods enable precise choice of potential. Chemical reagents also introduce a redox byproduct, which may give undesired reactivity. Particularly problematic are reagents that give inner-sphere electron transfer leading to installation of ligands such as NO when using the oxidant $[NO]^+$ or chloride derived from trityl chloride.[10,84] In choosing

a redox reagent for chemical reduction or oxidation, one must take solubility into account as well as considering the reduction potential of the electroactive species and fixed potential of the redox reagent. It is important to note that for a Nernstian system (see section 1.3.1) a 99% reaction completion for a 1e⁻ transfer requires a reducing agent to have E^o 118 mV negative of the E^0 and an oxidizing agent to have $E°$ 118 mV positive of the E^0 (Figure 2.8).[10]

Formal Potentials (V *vs* Fc) of Selected Oxidizing Agents

oxidant	solvent	$E^{o\prime}$	correction	ref
$[N(C_6H_2Br_3\text{-}2,4,6)_3]^+$	MeCN	1.36	*a*	228
Ce(IV)	$HClO_4$	1.30	*b*	*c*
	H_2O	0.88	*b*	*c*
$[N(C_6H_3Br_2\text{-}2,4)_3]^+$	MeCN	1.14	*a*	228
$[WCl_6]$	CH_2Cl_2	*ca.* 1.1	*d*	132
$[NO]^+$	CH_2Cl_2	1.00	none	195
$[Ru(phen)_3]^{3+}$	MeCN	0.87	*e*	108
$[NO]^+$	MeCN	0.87	none	195
[thianthrene]$^+$	MeCN	0.86	*f*	*g*
$[N(C_6H_4Br\text{-}4)_3]^+$	CH_2Cl_2	0.70	*d*	*h*
	MeCN	0.67	*i*	*j*
$[Fe(bipy)_3]^{3+}$	MeCN	0.66	*e*	111
Ag^+	CH_2Cl_2	0.65	*d*	63
$[Mo(tfd)_3]$	MeCN	0.55	*f*	*k*
$[IrCl_4(PMe_2Ph)_2]$	MeCN	*ca.* 0.5	*l*	123
$[Fe(\eta\text{-}C_5H_4COMe)_2]^+$	CH_2Cl_2	0.49	none	*h*
$[CuTf_2]$	MeCN	0.40	*f*	88
Ag^+	THF	0.41	*m*	63
$[Ni(tfd)_2]$	CH_2Cl_2	0.33	none	*h*
$[PtCl_6]^{2-}$	H_2O	0.31	*b*	*n*
$[Fe(\eta\text{-}C_5H_4COMe)Cp]^+$	CH_2Cl_2	0.27	none	*h*
Ag^+	acetone	0.18	*o*	63
Cl_2	MeCN	0.18	*b*	*p*
DDQ	MeCN	0.13	*i*	308
Br_2	MeCN	0.07	*b*	*p*
$[N_2C_6H_4NO_2\text{-}4]^+$	sulfolane	*ca.* 0.05	*f*	*q*
Ag^+	MeCN	0.04	*f*	63
$[C_3\{C(CN)_2\}_3]^-$	MeCN	0.03−0.06	*r*	304
$[FeCp_2]^+$		0.0		
$[N_2C_6H_4F\text{-}4]^+$	MeCN	−0.07	*f*	*q*
$[CPh_3]^+$	MeCN	−0.11	*f*	*s*
I_2	MeCN	−0.14	*f*	*t*
TCNE	MeCN	−0.27	*f*	*u*
TCNQ	MeCN	−0.30	*f*	*u*
$[FeCp^*_2]^+$	MeCN	−0.59	none	*h*
	CH_2Cl_2	−0.48	none	*h*
$[C_7H_7]^+$	MeCN	−0.65	*f*	*s*

[a] Use measured difference from potential of $[N(C_6H_4Br\text{-}4)_3]^+$ which is 0.70 V *vs* Fc. [b] Fc = 0.40 V *vs* NHE in H_2O. [c] Smith, G. F.; Getz, C. A. *Ind. Eng. Chem., Anal. Ed.* **1938**, *10*, 191. [d] Fc = 0.46 V *vs* SCE (CH_2Cl_2/[NBu_4][PF_6]). [e] Fc = 0.32 V *vs* sodium SCE. [f] Fc = 0.40 V *vs* SCE (MeCN/[NBu_4][PF_6]). [g] Hammerich, O.; Parker, V. D. *Electrochim. Acta* **1973**, *18*, 537. [h] Data from authors' laboratories. [i] Fc = 0.38 V *vs* SCE (MeCN/[NEt_4][ClO_4]). [j] Reynolds, R.; Line, L. L.; Nelson, R. F. *J. Am. Chem. Soc.* **1974**, *96*, 1087. [k] Davison, A.; Edelstein, N.; Holm, R. H.; Maki, A. H. *J. Am. Chem. Soc.* **1964**, *86*, 2799. [l] 0.9 V *vs* Ag/AgCl in MeCN/0.1 M $NaClO_4$; conversion to Fc approximate. [m] Fc = 0.56 V *vs* SCE (THF/[NBu_4][PF_6]). [n] Kravtsov, V. I.; Simakov, B. V. *Elektrokhimiya* **1966**, *2*, 646. [o] Fc = 0.48 V *vs* SCE (acetone/[NBu_4][PF_6]). [p] Parsons, R. *Handbook of Electrochemical Constants*; Butterworth: London, 1959; p 73. [q] Elofson, R. M.; Gadallah, F. F. *J. Org. Chem.* **1969**, *34*, 854. [r] Fc potential uncertain; no supporting electrolyte specified. [s] Volz, H.; Lotsch, W. *Tetrahedron Letts.* **1969**, 2275. [t] Nelson, I. V.; Iwamoto, R. T. *J. Electroanal. Chem.* **1964**, *7*, 218. [u] Gross-Lannert, R.; Kaim, W.; Olbrich-Deussner, B. *Inorg. Chem.* **1990**, *29*, 5046.

Formal Potentials (V *vs* Fc) of Selected Reducing Agents

reductant	solvent	$E^{o\prime}$	correction	ref
$[C_{10}H_8]^-$	THF	−3.10	*a*	366b
	glyme	−3.05	*a*	366b
	DMF	−2.95	*b*	*c*
Na	THF, glyme	−3.04	*a*	*d*
Li	NH_3	−2.64	*e*	*f*
Li(Hg)	H_2O	−2.60	*e*	*g*
K	NH_3	−2.38	*e*	*f*
Na(Hg)	nonaqueous	−2.36	*e*	*h*
[anthracene]$^-$	glyme	−2.47	*i*	*j*
$[FeCp^*(\eta\text{-}C_6Me_6)]$	dmf	−2.30	*b*	437
Na	NH_3	−2.25	*e*	*f*
[benzophenone]$^-$	THF	−2.30	none	*k*
	DMF	−2.17	*b*	*l*
[acenaphthalene]$^-$	THF	−2.26	*a*	366b
	glyme	−2.17	*i*	*i*
$[FeCp(\eta\text{-}C_6Me_6)]$	glyme	−2.09	*m*	402
$[CoCp^*_2]$	CH_2Cl_2	−1.94	*n*	*o*
	MeCN	−1.91	*p*	*q*
$[Fe(CO)_2Cp]^-$	THF, MeCN	*ca.* −1.8 (irr)	*p*, *r*	448, 449
$[CoCp_2]$	CH_2Cl_2	−1.33	none	*k*
	glyme	−1.31	*m*	404a
$[Cr(\eta\text{-}C_6H_6)_2]$	CH_2Cl_2	−1.15	none	8
$[FeCp^*_2]$	CH_2Cl_2	−0.59	*n*	*q*
	MeCN	−0.48	*p*	*s*
hydrazine	DMSO	−0.41	*t*	357
$[FeCp_2]$		0.0		
NEt_3	MeCN	*ca.* 0.47	*u*	393

[a] $E^{o\prime}$ *vs* [biphenyl]$^{0/-}$; [biphenyl]$^{0/-}$ = −2.69 V *vs* SCE (DMF/[NBu_4][ClO_4]) (Grzeszczuk, M.; Smith, D. E. *J. Electroanal. Chem.* **1983**, *157*, 205); Fc = 0.45 *vs* SCE (DMF/[NBu_4][ClO_4]). [b] Fc = 0.45 V *vs* SCE (DMF/[NBu_4][PF_6]). [c] Aten, A. C; Buthker, C.; Hoijtink, G. J. *Trans. Faraday Soc.* **1959**, *55*, 324. [d] Hoijtink, G. J.; de Boer, E.; van der Meij, P. H.; Weijland, W. P. *Recl. Trav. Chim.* **1956**, *75*, 487. [e] Fc = 0.40 V *vs* NHE in H_2O. [f] Strehlow, H. *The Chemistry of Nonaqueous Solvents*; Lagowski, J. J., Ed.; Academic Press: New York, 1966. [g] Lebed, V. I.; Aleksandrov, V. V. *Russ. J. Phys. Chem.* **1964**, *38*, 1414. [h] Balej, J. *Electrochim. Acta* **1976**, *21*, 953. [i] $E^{o\prime}$ *vs* Ag^+/Ag; $[Cr(\eta\text{-}C_6H_6)_2]^{+/0}$ = −1.25 V *vs* Ag^+/Ag; Fc = 1.12 V *vs* $[Cr(\eta\text{-}C_6H_6)_2]^{+/0}$ (ref 8). [j] Dessy, R. E.; King, R. B.; Waldrop, M. *J. Am. Chem. Soc.* **1966**, *88*, 5112. [k] Data from authors' laboratories. [l] Jensen, B. S.; Parker, V. D. *J. Chem. Soc., Chem. Commun.* **1974**, 367. [m] Fc = 0.51 V *vs* SCE (glyme/[NBu_4][PF_6]). [n] Fc = 0.46 V *vs* SCE (CH_2Cl_2/[NBu_4][PF_6]). [o] Koelle, U.; Khouzami, F. *Angew. Chem., Int. Ed. Engl.* **1980**, *19*, 640. [p] Fc = 0.40 V *vs* SCE (MeCN/[NBu_4][PF_6]). [q] Gennett, T.; Milner, D. F.; Weaver, M. J. *J. Phys. Chem.* **1985**, *89*, 2787. [r] Fc = 0.56 V *vs* SCE (THF/[NBu_4][PF_6]). [s] Robbins, J. L.; Edelstein, N.; Spencer, B; Smart, J. C. *J. Am. Chem. Soc.* **1982**, *104*, 1882. [t] Fc = 0.43 V *vs* SCE (DMSO/[NBu_4][PF_6]). [u] Fc = 0.31 V *vs* SCE (MeCN/Na[ClO_4]).

Figure 2.8: List of chemical redox agents as summarized by Connelly and Geiger in 1996. Chemical oxidants (left) chemical reductants (right). Reprinted (adapted) with permission from 10. Copyright 1996 American Chemical Society.

2.4.3. Literature Examples of Combined Use of Cyclic Voltammetry and Chemical Redox Reagents

An example of utilizing chemical reducing agents as a supporting complement to cyclic voltammetry is a titanium polymerization catalyst with added $AlEt_3$.[85] This work features cyclic voltametric studies of the titanium catalyst **Ti-1** shown in Figure 2.9 in which the complex undergoes a single irreversible $1e^-$ reduction at –2.12 V vs. $Fc^{+/0}$. The cyclic voltammogram of **Ti-1** in the presence of $AlEt_3$ changes the appearance to include an oxidative feature at E_{pa} at –1.32 V vs $Fc^{+/0}$. Chemical reduction of **Ti-1** in the presence of $AlEt_3$ yields bimetallic complex **Ti-2** (Figure 2.9). The anodic feature at E_{pa} at –1.32 V vs $Fc^{+/0}$ in the electrochemistry corresponds to the oxidation of **Ti-2.** This assignment is supported by matching spectral profiles of the spectroelectrochemical data of the parallel addition of $AlEt_3$ to **1** and the UV-vis data of the chemically prepared complex **Ti-1**.

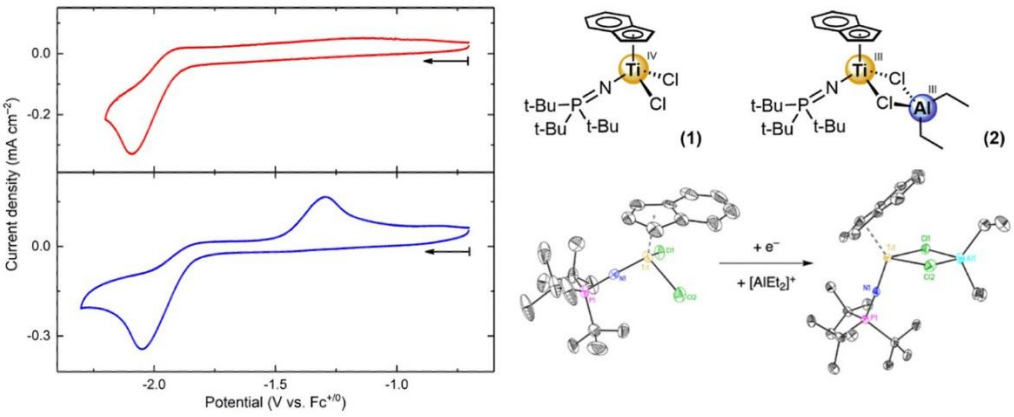

Figure 2.9: Cyclic voltammetry data for **Ti-1 (**red trace upper panel) and cyclic voltammetry of **Ti-1** with the addition of 6 equivalents of $AlEt_3$ (blue lower panel) (left panel.) Structures of compound **Ti-1** and **Ti-2** (top panel) and solid-state structures of complex **Ti-1** and **Ti-2**. Reprinted (adapted) with permission from citation 85. Copyright 2019, American Chemical Society.

Cyclic voltammetry published by Kubiak et al of a $Mn(bpy\text{-}tBu)(CO)_3Br$ complex exhibits two sequential, irreversible $1e^-$ reductions at –1.39 V and –1.57 V vs SCE. The first reduction is assigned to metal centered with concomitant loss of Br^- resulting in the formation of a Mn–Mn dimer[67] and the second reduction is attributed to formation of $[Mn(bpy\text{-}tBu)(CO)_3]^-$.[86] The feature at –0.30 V vs SCE is assigned to the oxidative cleavage of the Mn–Mn bond. The identity of the second reduction at –1.57 V vs SCE was interrogated by reduction of $Mn(bpy\text{-}tBu)(CO)_3Br$ by two equivalents of potassium graphite (KC_8, $E^0 \sim -3.1$ V vs. $Fc^{+/0}$ in THF)[10] in the presence of 18-crown-6 to yield the doubly reduced $[Mn(bpy\text{-}tBu)(CO)_3][K(18\text{-crown-6})(THF)]$ (Figure 2.10). Note the use of a much stronger reducing agent than formally needed for the reduction, which is common. The solid-state structure of the doubly reduced form was used to the assignment of the second $1e^-$ reduction as the formation of $[Mn(bpy\text{-}tBu)(CO)_3]^-$.

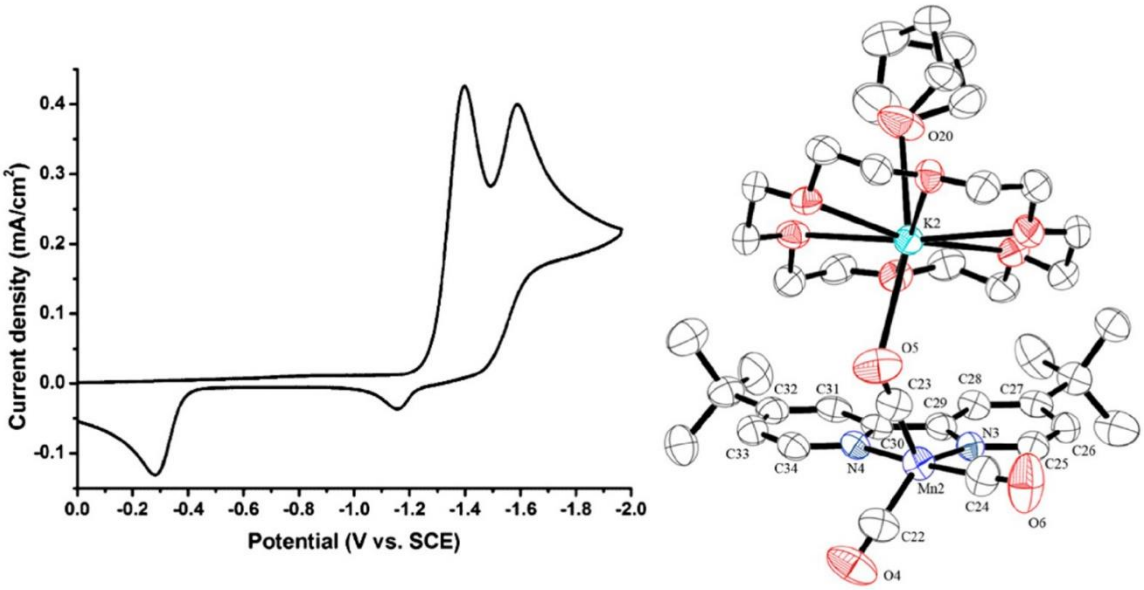

Figure 2.10: Cyclic voltammogram of $Mn(bpy\text{-}tBu)(CO)_3Br$ (left) Solid state structure of chemically prepared doubly reduced $[Mn(bpy\text{-}tBu)(CO)_3][K(18\text{-crown}_6)(THF)]$ (right.) Reprinted (adapted) with permission from citation 86. Copyright 2013, American Chemical Society.

Another literature example of combining cyclic voltammetry methods and chemical reductants comes from a study of dimeric tungsten species.[87] The CV of complex **W-1** in Figure 2.11 exhibits an irreversible oxidation at –2.21 V vs $Fc^{+/0}$ followed by a corresponding reduction feature indicating an EC process in which a new tungsten species is formed *in situ.* To interrogate the identity of this species formed the starting material **W-1** was chemically reduced by potassium graphite (KC_8, E^0 ~ –3.1 V vs. $Fc^{+/0}$ in THF)[10] and it was possible to isolate and crystallographically characterize **W-3**. The CV of isolated **W-3** reveals a quasi-reversible couple at –2.29 V vs. $Fc^{+/0}$ that matches the oxidation feature in the CV of **W-1**. The paper hypothesizes that the *in situ* formation of **W-3** is most likely a result of disproportionation reactions.

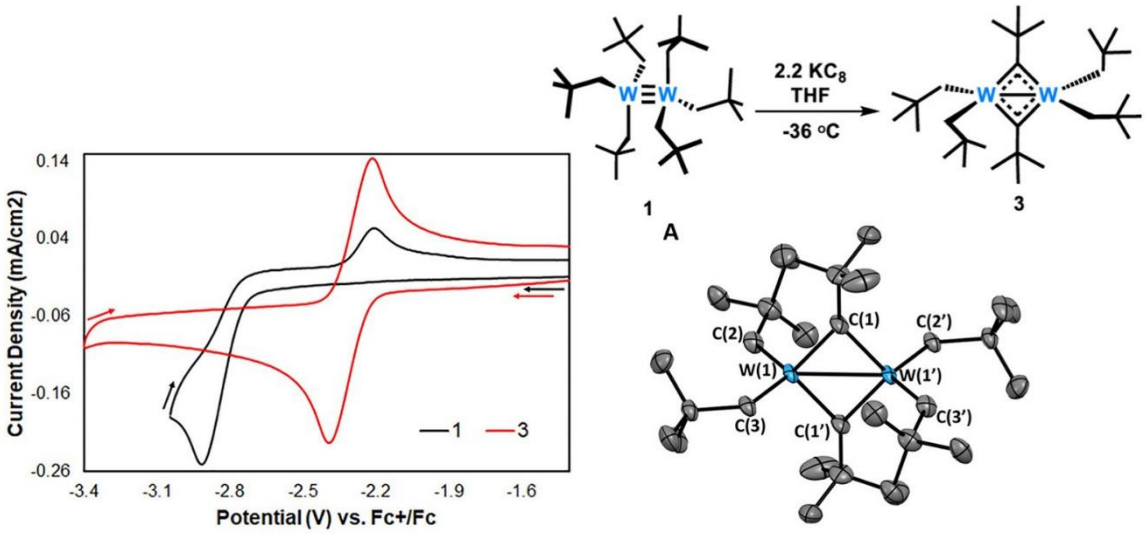

Figure 2.11: Cyclic voltammogram of **W-1** and **W-3** (left) chemical reduction of **W-1** with KC_8 to **W-3** (middle) solid state structure of **W-3** (right). Reprinted (adapted) with permission from citation 87. Copyright 2020, American Chemical Society.

A family of [Cp*Rh](Me$_2$dpma)] (Me$_2$dpma = dimethylbis(2-pyridyl)methane) complexes were studied for their redox properties as they relate to the [Cp*Rh(bpy)] system (Figure 2.12).[66]

The cyclic voltammetry of **1-NCCH$_3$** displays an initial quasi-reversible 1e$^-$ reduction from Rh(III) to Rh(II) at –0.85 V vs $Fc^{+/0}$, and continuing to scan cathodically a second irreversible 1e$^-$ reduction occurs at –1.50 vs $Fc^{+/0}$. The irreversibility of this reduction suggests an EC process. To probe the identity of the species formed upon electrochemical reduction the **1-Cl** and **1-NCCH$_3$** complexes were treated with chemical reductants. Treatment of **1-Cl** with cobaltocene ($CoCp_2$, $E_{1/2}$ = –1.30 V vs $Fc^{+/0}$)[10] yielded the expected Rh(II) reduction product with minimal chemical change as indicated by the 1e$^-$ quasi-reversible couple. The **1-NCCH$_3$** complex was used to interrogate the EC process of the doubly reduced product to avoid side reactivity seen with the 2e$^-$ chemical reduction of **1-Cl**. Treatment of **1-NCCH$_3$** with a stronger reducing agent, sodium amalgam (Na(Hg), E^0 = –2.4 V vs $Fc^{+/0}$),[10] generated the doubly reduced Rh(I) product **3**. Upon the addition of the second electron there is a significant ligand rearrangement in which one pyridine moiety "flips" on the bidentate Me_2dpma ligand. This assignment of the doubly reduced species identifies the chemical step upon the second reduction. The origin of this rearrangement is attributed to the ability of the Me_2dpma ligand to stabilize the low-valent Rh(I) center with strong π-backbonding by way of facial coordination of the pyridine moiety.

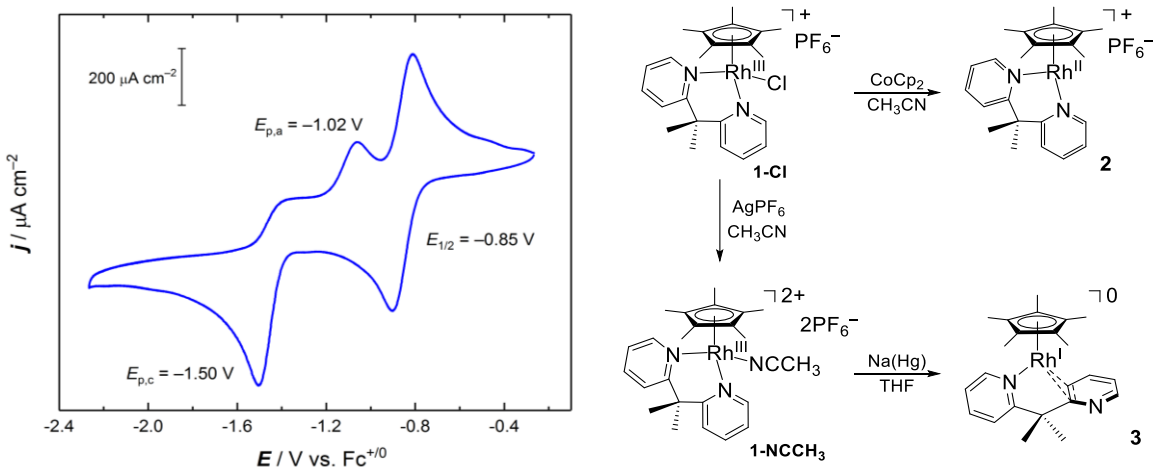

Figure 2.12: Cyclic voltammogram of **1-NCCH$_3$** (left) reduction scheme of **1-Cl** with $CoCp_2$ to **2** and **1-NCCH$_3$** with Na(Hg) to **3** (right).

2.5 Fundamental Concepts of Organometallic Electrocatalysis

2.5.1 Motivation for Studying Organometallic Electrocatalysts in the Context of Energy Science

Energy consumption is anticipated to continue increasing as the Earth's population grows, motivating work to develop new renewable energy sources and technologies that can produce fuels and chemicals with reneable energy. The most abundant renewable energy source available is sunlight, which provides enough energy (1.2×10^{14} kWh) in 80 minutes to sustain the global power demand for over a year.[88,89,90] While there is plenty of potential energy available in the form of sunlight, utilizing this energy is challenging due to its intermittency, variable intensity, and uneven distribution across the surface of the Earth. Development of model molecular electrocatalysts capable of converting electrical energy into stored fuels and chemicals can provide fundamental insights into how such catalysts convert energy. Considering that harnessing renewable energy

sources is an important goal of contemporary chemistry, organometallic chemistry has been heavily utilized in recent years for development of new electrocatalysts. Electrocatalysts are typically classified as heterogeneous or homogeneous, and there are many relevant examples of studying both classes of catalysts using electrochemical techniques, particularly cyclic voltammetry (CV) and controlled potential electrolysis (CPE). In this section, priority will be given to discussion of homogeneous molecular catalysts because these are i) more relevant to organometallic chemistry and ii) mechanistic discussions are more certain for cases in which catalyst (or precatalyst) structures are well defined.

CV and CPE experiments are regularly used to interrogate candidate organometallic systems for oxidative or reductive electrocatalytic applications. This section will provide a brief overview of catalytic CV and CPE experiments to investigate organometallic complexes as potential electrocatalysts. CV techniques can also be employed to assist in distinguishing heterogeneous versus homogenous catalysis. CV and controlled potential electrolysis experiments are often used synergistically to extract important thermodynamic, kinetic, and mechanistic information about these electrocatalytic transformations. When these electrocatalytic experiments are combined with product detection, Faradaic efficiency (FE), turnover number (TON), and turnover frequency (TOF) parameters can be extracted. In this section, we will discuss some of the most popular areas of organometallic electrocatalysis, including literature examples that utilize organometallic complexes capable of electrocatalytic water (WO) and ammonia oxidation (AO), and proton (HER), carbon dioxide (CO_2R), dinitrogen reduction reactions (N_2RR), and electroorganic transformations (EOT).

2.5.2 Investigating Organometallic Electrocatalysis using CV

2.5.2.1 Electrocatalytic Parameters and Thermodynamic Overpotential Determined by CV

For catalytic CV experiments, the observations and parameters associated with the generation of a catalytic response are well detailed in the viewpoint provided by Appel and Helm.[13] Their work provides insight and information about the parameters gleaned from a set of catalytic CV experiments regarding electrocatalytic overpotential. Specifically, parameters associated with the electrocatalytic response such as peak catalytic current (i_{cat}), half the peak catalytic current ($i_{cat/2}$), and catalytic potential ($E_{cat/2}$) are used in this area to determine the thermodynamic overpotential of a molecular catalyst (see Figure 2.13). The i_{cat} is the maximum current that flows in a catalytic CV experiment; for a plateauing catalytic wave, this is assigned as the maximum current anywhere in the plateauing region of the wave, while for a non-plateauing wave, this is assigned as the absolute maximum current of the wave. $i_{cat/2}$ is defined as half the catalytic current, and the potential at which this current is observed is termed $E_{cat/2}$. Selection of $E_{cat/2}$ in this manner ensures that there is minimal variation in the catalytic rate when determining a catalytic potential.

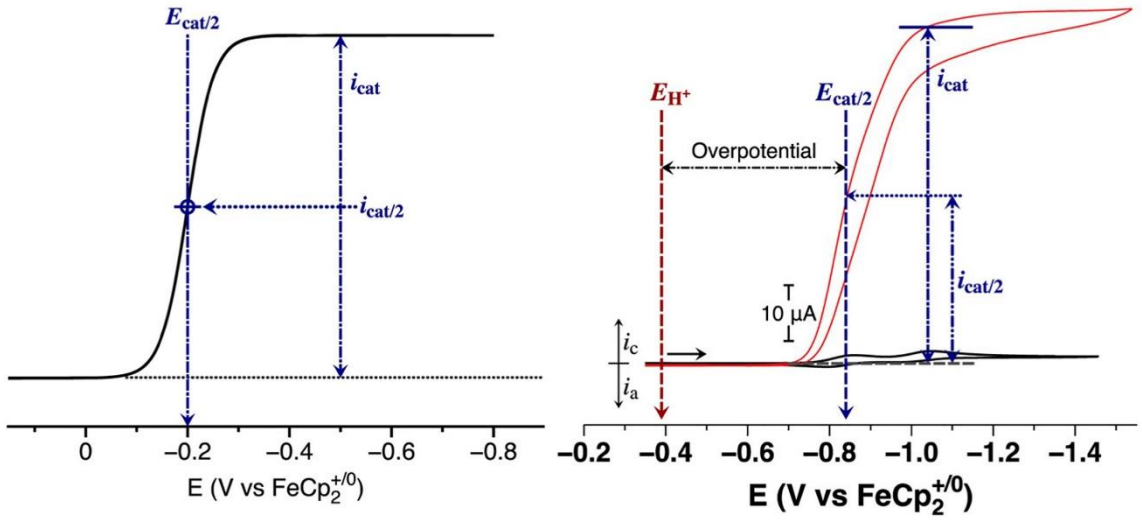

Figure 2.13: Simulated catalytic wave for a molecular catalyst showing the selection of i_{cat}, $i_{cat/2}$, and $E_{cat/2}$ (left). Experimental CV illustrating determination of $E_{cat/2}$ (and overpotential) for H_2 production (right). Reprinted with permission from 13. Copyright 2014 American Chemical Society.

The information provided by these CV experiments also provides essential information about the overpotential for a catalytic reaction, which is the driving force beyond the thermodynamic minimum needed to carry out a particular chemical transformation. The thermodynamic overpotential is most accurate when the Nernst equation is satisfied and can be determined using the following equations:

$$E_X = E_X^o + \frac{RT}{nF} \ln \frac{[HB^+]}{[B]} \tag{2.4}$$

$$E_X = E_X^o - 0.05916\,V \times pH \tag{2.5}$$

Notably, overpotential can be determined in aqueous or non-aqueous solvents, but the thermodynamic potential of a catalytic reaction at standard conditions (defined as the equilibrium potential (E^{o}_{X})), pH of the system, and the $E_{cat/2}$ must be defined. Acetonitrile is generally the preferred solvent because E^{o}_{X} can be determined[91] and there is well defined pK_a scale for this purpose.[92,93,94]

As an example, if the reader is interested in proton reduction to dihydrogen using an acid such as protonated dimethylformamide, $[DMFH]^+$, as the substrate, a series of cyclic voltammograms would be run at standard-state conditions, with a buffered solution of DMF/$[DMFH]^+$, and under 1 atm of H_2. Under these conditions, i_{cat}, $i_{cat/2}$, and $E_{cat/2}$ can be determined to calculate the thermodynamic overpotential. Though the observation of a catalytic response during a CV experiment does not depend on satisfying the Nernst equation for a particular transformation, an accurate calculation of the thermodynamic overpotential can only extracted when this is possible.

A relevant example uses the organometallic complex $[Cp^*RhCl(^{tBu}bpy)]^+$ (where Cp* is η^5-(1,2,3,4,5-pentamethylcyclopentadienyl) and ^{tBu}bpy is 4,4′-bis-*tert*butyl-2,2′-bipyridine) as a proton reduction catalyst for the production of dihydrogen (see Figure 2.14).[72] In the absence of acid, the CV of $[Cp^*RhCl(^{tBu}bpy)]^+$ exhibits a quasi-reversible redox event centered at -1.25 V vs. $Fc^{+/0}$ in MeCN. When acid is added, the quasi-reversible behavior of the Rh^{III}/Rh^{I} redox couple ceases, and a catalytic response is observed. The loss of reversibility here indicates that the acid is reacting with the reduced Rh^{I} species and the resulting current enhancement is consistent with catalytic behavior. The current enhancement results from the Rh^{III} starting material being reduced to Rh^{I}, which then interacts with the acid substrate, evolving dihydrogen, and subsequently regenerating the Rh^{III} starting complex. Since the potential at the electrode surface is still sufficiently reducing, this process continues as long as the potential of the electrode remains at

values sufficient to drive the reduction processes involved in the chemistry. With these CVs in hand, the i_{cat} (–4.16 mA cm^{-2}), $i_{cat/2}$ (–2.08 16 mA cm^{-2}), $E_{cat/2}$ (–1.33 V), and overpotential (0.569 V) were determined for the catalytic process. Taking these parameters into account, the CPE experiments were carried out under identical conditions with polarization at –1.36 V vs $Fc^{+/0}$ over the course of 90 minutes. Other $[Cp^*RhCl(^{R}bpy)]^{+}$ (R = 4,4-bis-substituted-2,2'-bipyridyl, H and CF_3) complexes have also shown this catalytic behavior in the presence of a proton source. These catalytic CV experiments are not limited to proton reduction and have been carried out in the exploration of catalytic applications involving WO, AO, HER, CO_2R, and N_2RR.

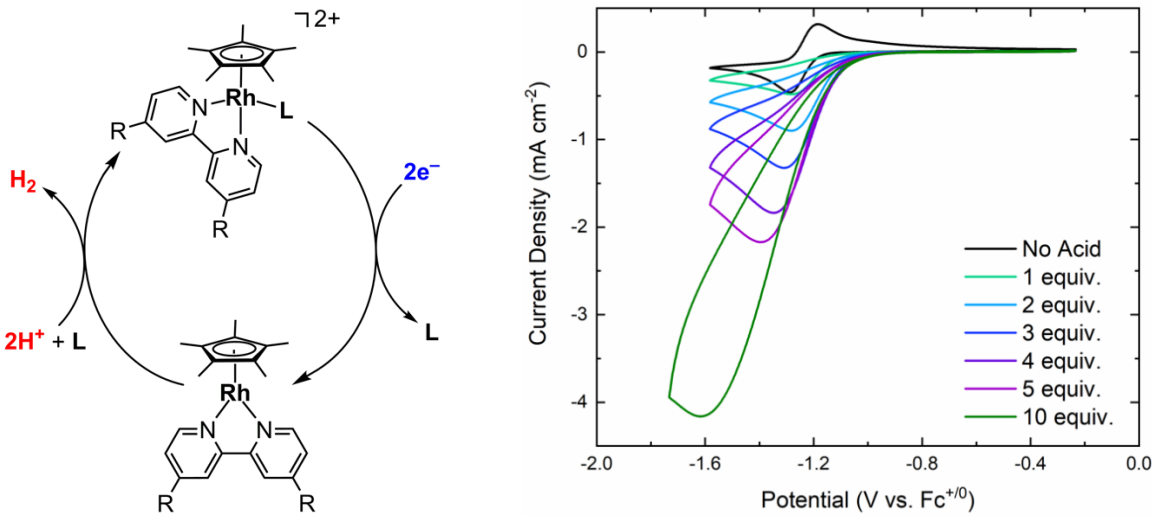

Figure 2.14: Pathway for HER using $[Cp^*Rh(^{R}bpy)]$ showing the energy loading and energy storage steps (left). Cyclic voltammograms with $[Cp^*RhCl(^{tBu}bpy)]^{+}$, 1-5 equiv. of $PhNH_2/[PhNH_3]OTf$, and 1 atm of H_2 at a scan rate of 100 mVs^{-1} (right).

2.5.2.2 Kinetic Considerations in Electrocatalysis: Foot of the Wave Analysis

To extract kinetic and latent mechanistic information from CV experiments, one employs a method pioneered by Constentin, Savéant, and co-workers known as foot-of-the-wave analysis

(FOWA).[95] This method simplifies the analysis because the earliest part of the catalytic wave inevitably has pseudo-first order kinetics because the substrate will be in vast excess compared to the catalyst.[96] FOWA minimizes the effects of secondary phenomena such as catalyst inhibition, decomposition, or saturation, and maximizes the information provided by the current that flows. Under ideal conditions, an observed rate constant can be computed using:

$$\frac{i_{cat}}{i_p} = \frac{2.24\left[\frac{RT}{Fv}2k_{obs}C_A\right]^{\frac{1}{2}}}{1+exp\left[\frac{F}{RT}(E-E^o)\right]} \tag{2.6}$$

where i_{cat} is the peak catalytic current, i_p is the peak current of the redox process of the catalyst in the absence of substrate, R is the ideal gas constant, F is Faraday's constant, T is temperature, ν is the scan rate, k_{obs} is the observed rate constant, C_A is the initial concentration of substrate, E is the present potential and $E^o = E_{cat/2}$ which is the thermodynamic potential for the catalytic wave. Plotting i_{cat}/i_p as a function of $1/\{1+\exp[(F/RT)(E-E^o)]\}$ produces a line with a slope equal to $2.24((RT/F\nu)2k_{obs}C_A)^{1/2}$, that can be used to extract the observed rate of catalysis (see Figure 2.15). These experiments can be repeated at various substrate concentrations, and at several different scan rates, to extract an average rate constant for the desired electrocatalytic reaction. The average k_{obs} is computed from a linear regression of the scan rate dependent data with a fixed slope of zero, since the intrinsic chemical kinetics should not depend on scan rate. This kinetic technique has become a recognized approach to determining substrate order and observed rates when mapping out the mechanistic details of electrocatalysts. FOWA has been used in various electrocatalytic kinetic studies for WO,[97] AO,[98] HER,[99] CO_2R,[100] and N_2RR.[101]

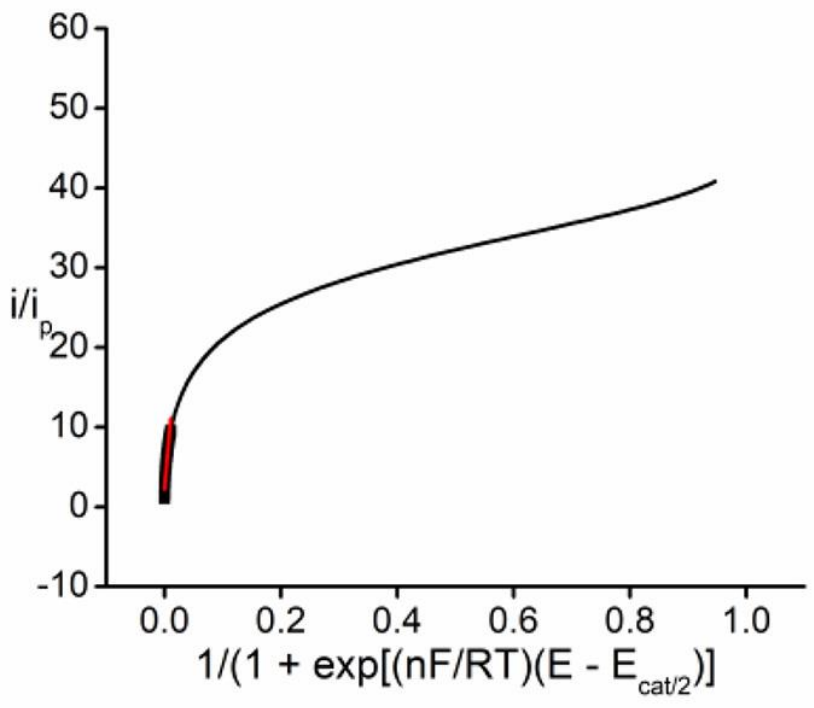

Figure 2.15: An example FOWA plot of i_{cat}/i_p as a function of $1/\{1+\exp[(F/RT)(E–E^o)]\}$. The pseudo-first order rate constant is extracted from the initial linear region of the plot. Reprinted with permission from 100. Copyright 2018 American Chemical Society.

2.5.2.3 Distinguishing Homogenous from Heterogeneous Catalysis with Electrochemical Methods

In organometallic catalysis, it is often desirable to confirm the identity or composition of a molecular catalyst. An important step in identifying the "true," or active, catalyst is distinguishing whether the materials in the electrochemical cell behaves as a homogenous or heterogeneous electrocatalyst. While there is an excellent precedent to explore heterogeneous materials in electrocatalysis because of their ease of separation from products, crucial structural, electronic, and mechanistic information is typically lost because traditional spectroscopic techniques such as NMR, IR, and electronic absorption spectroscopies are limited in the interrogation of these

systems. However, there are several techniques and methods that may be used to investigate catalytic systems in an effort to distinguish homogenous from heterogeneous catalysts.[102] These methods include strategic catalyst poisoning, [103] X-ray photoelectron spectroscopy,[104] and transmission electron microscopy.[105] However, the *in situ* generation of new molecular species during electrocatalysis provides a unique challenge when there is a concern about distinguishing between homogeneous and heterogeneous catalysis. Distinguishing between homogeneous and heterogeneous electrocatalysts may be accomplished with electrochemical techniques such as a two-cell CV experiment, or by using an electrochemical quartz crystal microbalance (EQCM).[104]

In a two-cell CV experiment, homogeneous catalysis is distinguished from heterogeneous catalysis by running a series of CV scans under catalytic conditions. The first cell will contain the candidate catalyst, substrate, and electrolyte solution. When running this experiment, typical catalytic current enhancement should be observed. Following this series of scans, the working electrode is transferred to a second electrochemical cell which contains only substrate and electrolyte solution. A series of CVs identical to those run in the first cell are then run. If there is still a large current enhancement observed, this suggests the deposition of heterogeneous material behaving as the catalyst at the surface of the electrode. If the current enhancement is absent in the fresh solution, this provides support for molecular homogeneous catalysis.

Another method for distinguishing heterogeneous from homogeneous catalysis is by using an electrochemical quartz crystal microbalance (EQCM).[104,106,107] This piezoelectric gravimetric technique can detect small mass changes at the surface of the working electrode as a function of scan rate during common electrochemical experiments, such as CV. In the case of formation of a heterogeneous catalyst, a change in mass at the surface of the electrode would be detectable during a catalytic CV experiment. Conversely, for a homogenous system, there would not be a detectable

change in the mass at the working electrode surface. An example from our group highlights the possible distinction of heterogeneous catalysis from homogeneous catalysis in the analysis of a well-known molecular cobaloxime complex which catalyzes hydrogen production. The deposition of heterogeneous cobalt material on the surface of the working electrode could be detected during a CV experiment with an EQCM and is distinctive from an electrochemical blank containing only electrolyte solution (See Figure 2.16).

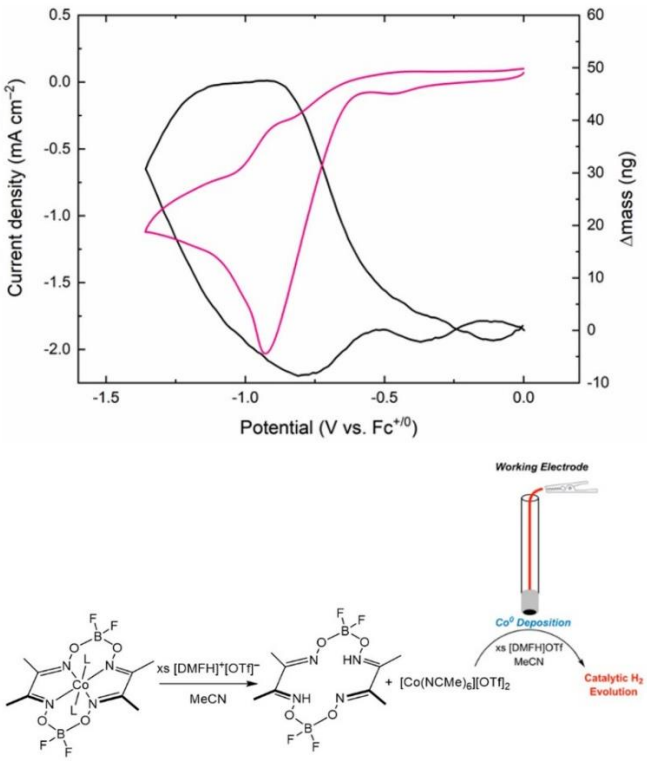

Figure 2.16: Upper panel: cyclic voltammetry data (pink trace) and gravimetry data (black trace) showing involvement of heterogeneous, electrodeposited material under potentials at which nominally molecular catalysis is indicated by CV data alone. See reference 104 for details. Lower scheme: After the addition of acid to a (bis-difluoroboryl)cobaloxime, spectral evidence from

chemical work supports the presence of the demetallated, protonated macrocycle and cobalt(hexakis-acetonitrile) ($[Co(NCMe)_6]^{2+}$). When conducting a CV of (bis-difluoroboryl)cobaloxime in the presence of acid during an EQCM experiment, the observation of a catalytic wave is observed, as well as the deposition of cobalt metal on the surface of the working electrode. The cobalt metal is generated by reduction of $[Co(NCMe)_6]^{2+}$, a reaction that can be probed by independent electrochemical work with $[Co(NCMe)_6]^{2+}$.

2.5.3 Investigating Organometallic Electrocatalysis using Controlled Potential Electrolysis

To generate the product(s) associated with the current enhancement observed during electrocatalytic CV experiments, CPE experiments are commonly employed. For a detailed explanation of bulk and controlled potential electrolysis methods, Bard and Faulkner dedicate a chapter to the discussion of these techniques.[43] Briefly, a CPE is typically carried out in an electrochemical cell designed specifically for the product being analyzed (See Figure 2.17). Common design principles among the CPE cells include two separated compartments, with a known volume and headspace, capable of a gas-tight seal, and the ability to have headspace withdrawn after electrolysis is complete.

Using the first CPE cell as an example, a typical experiment is set up where the left compartment contains the candidate electrocatalyst, the substrate, electrolyte solution, a large surface area working electrode, and reference electrode, while the right compartment contains a sacrificial reductant (for reductive catalysis) or oxidant (oxidative catalysis), electrolyte solution, and the counter electrode. The experiment is set up to apply a bias, ideally at the determined $E_{cat/2}$ from the electrocatalytic CV experiments, for a fixed amount of time, typically ranging from 30

min., up to 24 hours. Once the experiment is complete, the amount of product produced may be quantified via various detection methods. Based on the amount of charge passed during the electrolysis, and the amount of product detected, the Faradaic efficiency, turnover number, and turnover frequency can also be calculated. The Faradaic efficiency is determined by converting the charge passed, into moles of electrons passed, and then into the theoretical amount of product that should be produced. The actual yield is then divided by this theoretical yield to obtain the FE. The TON is determined by computing the moles of product per moles of catalyst. Finally, the TOF is determined by dividing the amount of product produced over unit time.

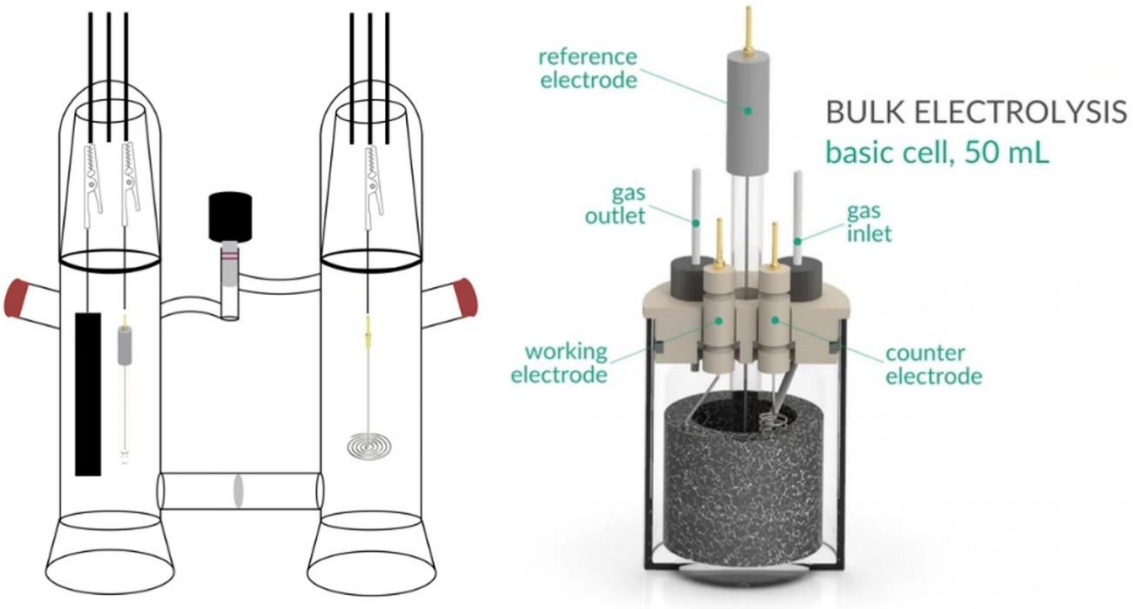

Figure 2.17: Example controlled potential electrolysis cells that can be used to conduct WO, AO, HER, CO_2R, N_2RR, or EOT reactions. Cells can be custom made to specialize in gaseous product detection (left[108]) or ordered directly from a supplier if the goal is complete liquid or solid isolation (right, from redoxme[109]).

2.5.4 Product Analysis in Organometallic Electrochemistry

To analyze the product(s) produced during organometallic electrocatalysis, quantitative methods of analysis are employed.[110] Products generated in electrocatalytic reactions may be gaseous, liquid, or solid. Common laboratory techniques and instruments such as gas chromatography (GC), liquid chromatography-mass spectrometry (LC-MS), nuclear magnetic resonance (NMR), electron paramagnetic resonance (EPR), UV-Vis, and gravimetry may be used to determine the amount of product generated during electrocatalytic experiments. For gaseous product detection and quantification of common electrocatalytic products such as O_2, N_2, H_2, and CO, gas chromatography is capable of rapid product detection and quantification when a calibration curve can be established for the particular product being examined. Likewise, when samples contain liquid or dissolved solids in solution, LC-MS techniques can be used to identify and quantify products. Furthermore, solid and liquid samples that can be dissolved in deuterated solvents may also be examined via NMR and integrated in reference to a known standard, such as trimethoxybenzene, to quantify the product produced. For paramagnetic products, EPR can be used to quantify the amount of product produced by using spin quantitation.[111] Some electrolysis products, such as ammonia, can undergo a quantitative reaction that gives a product that can be quantitated colorimetrically, using UV-Vis since the molar absorptivity of the generated product is known. Lastly, for solid samples that cannot be reasonably dissolved, gravimetric methods may be used to weigh out the product produced from the CPE experiment.

2.6 Applications of Organometallic Electrocatalysis for Select Transformations

2.6.1 Electrocatalytic Water Oxidation

Solar fuel cells are one possible solution to the renewable energy storage challenge, and the basic design makes use of a solar photovoltaic assembly used in combination with an efficient WO electrocatalyst at the anode and a HER electrocatalyst at the cathode to generate H_2.[88] The allure of a clean energy future powered by sunlight and water continues to spark interest in electrocatalytic WO, which has been the topic of many reviews.[112,113,114,115] As inspiration, metalloenzymes found in nature often serve as role models for the development and investigation of organometallic electrocatalysts. For instance, the oxygen-evolving complex (OEC) in photosystem II is responsible for oxidizing water to dioxygen, with release of four protons and four electrons.[116] When written according to the standard of the IUPAC, the reduction potential for the interconversion of water and oxygen is +1.23 V vs SHE (see Table 2.1).[32,117] However, if you wish to discuss the potential for the oxidation, which may be useful in computing electrochemical cell potentials, the value will be -1.23 V; this is the minimum voltage needed to drive WO. For example, using a platinized platinum electrode as a cathode, the equilibrium potential of the H_2/H^+ couple is set to 0 V vs SHE. At the anode, two equivalents of water is oxidized to dioxygen, four protons, and four electrons at +1.23 V vs SHE. Thus, using equation 2.2, the four electron oxidation of water to dioxygen and dihydrogen is shown to be endothermic by approximately 113 kcal/mol under aqueous conditions (see equations 2.7-2.10).[113]

Overall: $2H_2O \rightarrow O_2 + 2H_2$ (2.7)

Cathode: $2H^+ + 2e^- \rightarrow H_2$ (2.8)

Anode: $2H_2O \rightarrow O_2 + 4H^+ + 4e^-$ (2.9)

$$\Delta G = -nF\Delta E = -(4\ mol\ e^-)\left(96485\ \frac{C}{mol\ e^-}\right)(0 - 1.23\ V) = +475\ \frac{kJ}{mol} = +113\ \frac{kcal}{mol} \quad (2.10)$$

The calculation shown here is readily extended to other reactions too, but with the caveat that the reversible potentials for the reactions at the cathode and the anode must be known for a specific set of conditions that satisfy the Nernst equation. Partial oxidation of water is also possible, generating products such as hydroxyl radicals, hydrogen peroxide, and peroxyl radicals, along with the appropriate number of protons and electrons. The mechanisms for formation of these partial oxidation products are also important to understand, because they may be generated as undesired side products during WO.

Thermodynamic Half-Reactions	Potential, E^0 (V vs SHE)
$O_2 + 4H^+ + 4e^- \rightleftharpoons 2H_2O$	+1.23
$H_2O_2 + 2H^+ + 2e^- \rightleftharpoons 2H_2O$	+1.76
$HO\cdot + H^+ + e^- \rightleftharpoons H_2O$	+2.38
$HOO\cdot + 3H^+ + 3e^- \rightleftharpoons 2H_2O$	+1.65

Table 2.1: Standard thermodynamic electrochemical half-reaction potentials for water in aqueous solution.[32,43]

Heterogeneous metal oxides of manganese, ruthenium, and iridium have long been recognized as electrocatalysts for WO.[118,119,120] On the other hand, homogeneous catalysts were discovered much more recently; such homogeneous systems offer numerous advantages with regard to

mechanistic studies, detection of reactive intermediates, and development of tunable catalysts. In 1982, Meyer and co-workers were the first to synthesize and characterize a molecular ruthenium electrocatalyst for water-oxidation.[121] Since then, other homogeneous and heterogeneous molecular catalysts of ruthenium,[122,123] iridium,[124,125,126] and other metals,[127,128] have allowed for more in-depth analysis of the steps involved in WO. For example, Brudvig, Crabtree, and co-workers,[129] Macchioni and co-workers[130] and several other groups have developed iridium-based catalyst precursors supported by Cp* or Cp rings along with a variety of other ligands, including diimines, halides, waters, carbonyls, and phosphines (see Figure 2.18 for some example complexes). Most of these complexes serve as precatalysts for water oxidation, in that initial electrochemical oxidation generates the active catalytic species that can then undergo further oxidation, triggering catalytic water oxidation. One notable example precatalyst, $[Cp^*Ir(H_2O)_3]^{2+}$, undergoes oxidation to form a heterogeneous "blue layer" on the electrode surface that is readily observed by a variety of techniques, including cyclic voltammetry.[131] In other cases, catalyst activation leads to formation of homogeneous species that can catalyze water oxidation in solution (i.e., without formation of solids or particulate species). Distinguishing between homogeneous and heterogeneous catalysis, a recognized challenge in organometallic chemistry, is made especially challenging under these conditions for water oxidation catalysis driven by organometallic precatalysts. The electrochemical quartz crystal microbalance has been shown to be a useful tool for observing formation of insoluble heterogeneous species, both for oxidative reactions like water oxidation driven by organometallic precursors[132] as well as reductive reactions like hydrogen evolution and metal electrodeposition.[133,134,135] Along a similar line, dynamic light scattering is useful for formation of particulates or particles in solution. Application of specialized techniques like these, in concert with detailed electroanalytical and mechanistic/kinetic/chemical work, can

strongly inform studies of water oxidation catalysis. Approaching molecular electrocatalytic systems from multiple viewpoints and with multiple chemical and electrochemical techniques can thus be an appealing strategy, especially when dealing with challenging reactions like water oxidation.

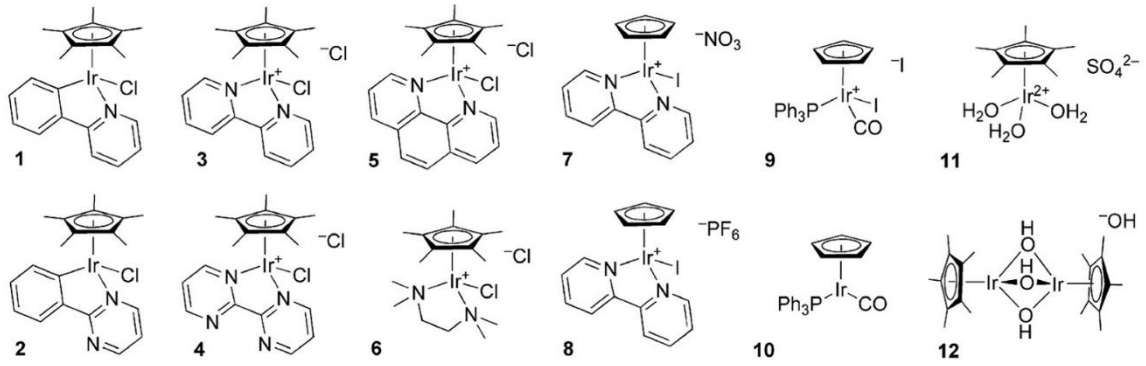

Figure 2.18: Select iridium(III) organometallic precatalysts for electrochemical WO. Reprinted with permission from reference 129. Copyright 2010, American Chemical Society.

2.6.2 Electrocatalytic Ammonia Oxidation

Electrocatalytic AO and WO are comparable in many ways; both reactions involve the removal of several electrons and protons, the formation of a new bond between heteroatoms, and the evolution of a gaseous product (N_2 or O_2). Likewise, electrocatalytic AO represents an alternative fuel cell design where AO would be carried out at an anode and proton reduction at a cathode to generate energy. However, unlike WO, electrocatalytic AO is still an emerging field and has been the topic of a recent review by Wu and co-workers[136] and perspective by Bullock and co-workers.[137] Complete ammonia oxidation is best summarized as a thermodynamic electrochemical half reaction where ammonia is converted into dinitrogen, six protons, and six electrons at –0.057 V vs SCE (see Table 2.2). Partial ammonia oxidation is also possible, generating other products

such as hydrazine and hydroxylamine along with the relevant number of protons and electrons, on route to complete ammonia oxidation.

Thermodynamic Half-Reactions[24]	Potential E^0 (V vs SHE)
$N_2 + 6H^+ + 6e^- \rightleftharpoons 2NH_3$	– 0.06
$N_2 + 8H^+ + 6e^- \rightleftharpoons 2NH_4^+$	+0.28
$N_2 + 4H_2O + 4e^- \rightleftharpoons N_2H_4 + 4OH^-$	–1.16
$N_2 + 5H^+ + 4e^- \rightleftharpoons N_2H_5+$	–0.23
$3N_2 + 2e^- \rightleftharpoons 2N_3^-$	–3.40

Table 2.2: Standard thermodynamic electrochemical half-reaction potentials for dinitrogen in aqueous solution.[32,43]

Heterogeneous materials have been employed in electrocatalytic AO, but these instances rely heavily on precious metals and thus proposed mechanisms are not secure. The first report of a molecular electrocatalyst for AO was reported by Smith, Hamann, and co-workers, where they used a derivative of a Ru-based WO catalyst bearing an electron-donating ^{Me2N}bpy ligand.[138] Subsequently, other electrocatalysts for water oxidation have been repurposed for ammonia oxidation. Recent work from the Peters group makes use of a previously reported alkane oxidation catalyst.[139] The labile acetonitrile (MeCN) ligands of the starting complex are readily exchanged in the presence of ammonia, shown here in the solid-state structure of $[(bpyPy_2Me)Fe(MeCN)(NH_3)](OTf)_2$ (see Figure 2.19). Compared to $[(TPA)Fe(MeCN)_2](OTf)_2$ (TPA is tris(2-pyridylmethyl)amine),[98] a catalytic CV experiment shows a dramatic increase in a catalytic current for this newly reported complex and FOWA was performed to determine the

observed rate of AO. The CPE cell was loaded with 0.05 mM [Fe] catalyst, 20 mM of NH_3, and 50 mM NH_4OTf in MeCN as the supporting electrolyte. After applying a bias of 0.85 V vs $Fc^{+/0}$ for 24 hours, product analysis revealed the formation of N_2 at the working electrode and H_2 at the counter electrode in all instances, as well as the highest TON to date for a molecular AO electrocatalyst. Future work in the field of electrocatalytic AO requires probing the rational design, kinetics, and thermodynamics of molecular complexes.

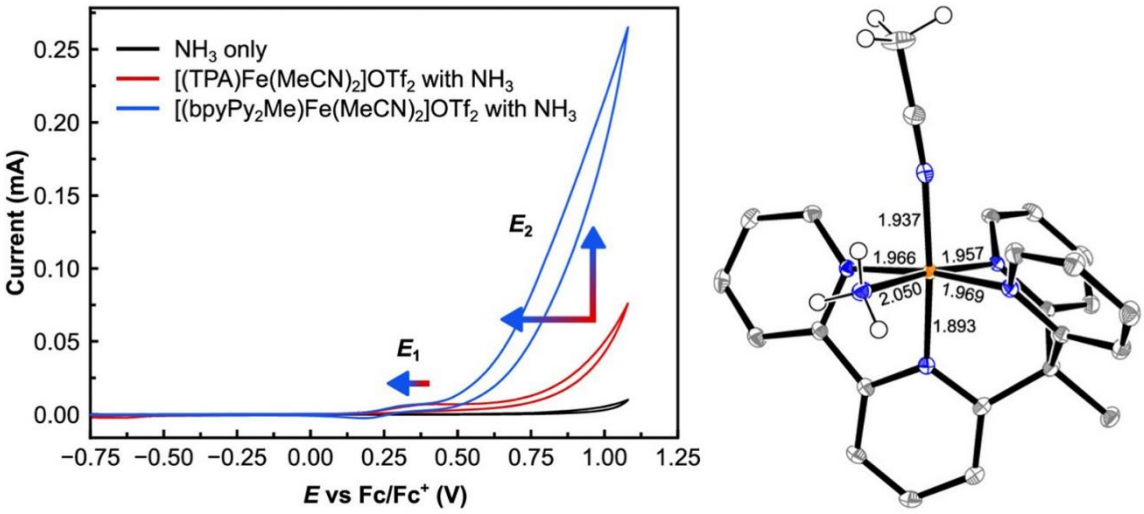

Figure 2.19: Solid-state structure of $[(bpyPy_2Me)Fe(MeCN)(NH_3)](OTf)_2$ (left). Thermal ellipsoids shown at 50% probability. Triflate and hydrogen atoms are omitted for clarity. CV of MeCN solutions containing 400 equiv. of NH_3, 0.05 M NH_4OTf, 0.5 M of $[(bpyPy_2Me)Fe(MeCN)_2](OTf)_2$ or $[(TPA)Fe(MeCN)_2](OTf)_2$. Reprinted with permission from reference 139. Copyright 2021, American Chemical Society.

2.6.3 Electrocatalytic Proton Reduction

In the electrocatalytic HER, two protons and two electrons are coupled with the help of a catalyst to generate dihydrogen. This is simpler than the multielectron N_2 and O_2 reactions,

electrocatalytic HER has been the topic of significant work spanning decades. Electrocatalytic HER continues to draw major interest in the solar fuels community because understanding the elementary steps involved in this simple energy storage reaction could help in the rational design of future electrocatalysts.[140,141] Complete proton reduction to dihydrogen is represented by the thermodynamic electrochemical half reaction where two protons and two electrons are coupled together to generate dihydrogen at 0.00 V vs SHE (see Table 2.3).[32]

Thermodynamic Half-Reaction	Potential E^0 (V vs SHE)
$2H^+ + 2e^- \rightleftharpoons H_2$	0.00

Table 2.3: Standard thermodynamic electrochemical half-reaction potentials for protons in aqueous solution.[32,43]

Gray, Winkler, Brunschwig and co-workers have discussed possible mechanisms for dihydrogen evolution,[142] as have other researchers in this vibrant area of electrocatalysis research. HER catalysis typically involves either a homolytic or heterolytic pathway to the production of dihydrogen. The heterolytic pathway involves a proton and a hydride reacting to generate dihydrogen, while the homolytic pathway involves homolytic cleavage of two hydride species which undergo recombination to produce dihydrogen. Heterogeneous noble metals, such as platinum, are prominent electrocatalysts for the reduction of protons to dihydrogen.[143] Other heterogeneous materials, such as metal nanoparticles, have also shown promise for the electrocatalytic production of dihydrogen.[144] Molecular cobaloxime complexes have also been

shown to be highly active for the production of dihydrogen.[145] While these systems are competent and efficient HER electrocatalysts, they may generate Co nanoparticles in the presence of acid which generates ambiguity in the identity of the true electrocatalyst.[104] Thus, well-defined homogeneous model systems that show activity toward electrocatalytic HER have been desirable.

While many redox-active systems are capable of electrocatalytic HER, the homogeneous Rh-based electrocatalyst, $[Cp^*RhCl(^{H}bpy)]^+$, developed by Kölle and Grätzel is one of the most well-known.[146] CV of $[Cp^*RhCl(^{H}bpy)]^+$ reveals a quasi-reversible $2e^-$ redox couple centered at approximately –1.21 V vs $Fc^{+/0}$. Addition of two equivalents of acid to Cp*Rh(bpy) results in the quantitative production of dihydrogen, and further experiments confirm its catalytic ability. This led to a systematic examination of a series of $[Cp^*RhCl(^{R}bpy)]^+$ (^{R}bpy is 4,4´-disubstituted-2,2´-bipyridyl; R = H, tBu, and CF_3) complexes by Blakemore and co-workers in an effort to determine if electrocatalytic dihydrogen evolution could be modulated using substituents on the bpy ligand.[72] Initial catalytic CV experiments for these complexes were discussed in section 1.5.2.1. These experiments assisted in the determination of the parameters needed to carry out a series of CPE experiments. To systematically compare the catalytic ability of each complex, CPE experiment were conducted with identical conditions with 1 mM of [Rh] catalyst and 10 mM anilinium triflate in the WE portion of the cell, ferrocene was added to the CE portion of the cell as a sacrificial reductant, 0.1 M $TBAPF_6$ in MeCN was used as the supporting electrolyte, and a bias of –1.36 V vs $Fc^{+/0}$ was applied for 90 minutes.

Over the course of the experiment, steady current flow is observed for each complex over time (see Figure 2.20). Notably, each of the complexes has significantly more current flowing than the blank and the amount of current flowing is different based on the identity of the complex. When the experiment is first started, the first few seconds appears to show rapid consumption of acid,

but this is actually the initial charging of the WE, and following this period, steady current flows over time. Upon completion of the experiment, the presence of dihydrogen was confirmed in all instances by GC. When the identity of the substituents was –tBu, –H, or $–CF_3$, the complexes produced 2.6 mL, 3.5 mL, and 1.5 mL of dihydrogen, with corresponding TONs of 3.4, 4.4, and 2.7, respectively.

As an aside, keeping the bias at the same potential across the series of complexes results in what could be perceived as an "unfair" although uniformly direct comparison of these catalysts' abilities to produce dihydrogen. This is because from the perspective of the Nernst equation, when the potential is moved from $E_{cat/2}$ of a given individual complex, the amount of reduced species present at the electrode at any one point in time is changed. In other words, catalysis for each of these systems will be optimal when polarizing at $E_{cat/2}$, and thus comparing the kinetic performance of the catalysts at a common potential value that doesn't align with the value of $E_{cat/2}$ for all the catalysts introduces an additional concentration/potential dependence to this study. On the other hand, a common potential polarization for all the comparisons made here does satisfy a pratical aspect of testing and comparing these model catalysts under comparable conditions. Regardless of this potential ambiguity, however, based on the amount of charge transferred and the amount of dihydrogen detected, all three complexes were confirmed (in this study) to be electrocatalysts with FE exceeding 90% in all three systems. This study encapsulates the challenges and opportunities in comparing across a family of catalysts that may have unique redox chemistries.

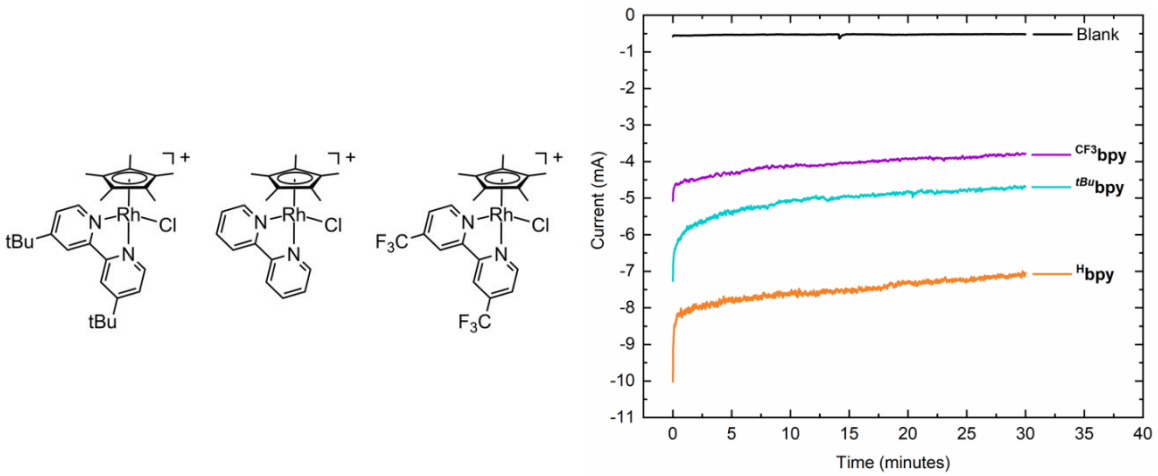

Figure 2.20: [Cp*RhCl(^{R}bpy)]$^{+}$ complexes with electron donating and withdrawing substituents (left). Comparison of CPE steady-state current as a function of time with an applied bias of –1.36 V vs $Fc^{+/0}$ with 10 mM anilinium triflate as the proton source (right).

2.6.4 Electrocatalytic Carbon Dioxide Reduction

Electrocatalytic CO_2 reduction continues to draw attention from the organometallic chemistry community because organometallic compounds are uniquely well-suited to understanding the bonding and activation of carbon-containing small molecules.[147] Use of CO_2 as input for preparation of useful chemicals could also decrease the environmental impact of chemical industry, motivating work in this area further. CO_2 has many potential reduction pathways and products, with one of the most common targets being carbon monoxide (CO) because of its use as an industrial synthon. More elaborate reactions could be used to produce carbon-based fuels or other chemicals. The thermodynamic electrochemical half-reaction for some key CO_2 reduction products involving two, four, six, or eight electron pathways are shown below (see Table 2.4).[32,148]

$$CO_2 + 2H^+ + 2e^- \xrightarrow{[catalyst]} CO + H_2O$$

Thermodynamic Half-Reactions	Potential E^0 (V vs SHE)
$CO_2 + 2H^+ + 2e^- \rightleftharpoons CO + H_2O$	–0.106
$CO_2 + 2H^+ + 2e^- \rightleftharpoons HCO_2H$	–0.199
$CO_2 + H_2O + 2e^- \rightleftharpoons HCO_2^- + OH^-$	–1.078
$CO_2 + 2H_2O + 2e^- \rightleftharpoons CO + 2OH^-$	–0.934
$CO_2 + 4H^+ + 4e^- \rightleftharpoons CH_2O + H_2O$	–0.070
$CO_2 + 3H_2O + 4e^- \rightleftharpoons CH_2O + 4OH^-$	–0.898
$CO_2 + 6H^+ + 6e^- \rightleftharpoons CH_3OH + H_2O$	+0.016
$CO_2 + 8H^+ + 8e^- \rightleftharpoons CH_4 + 2H_2O$	+0.169
$CO_2 + 5H_2O + 6e^- \rightleftharpoons CH_3OH + 6OH^-$	–0.812
$CO_2 + 6H_2O + 8e^- \rightleftharpoons CH_4 + 8OH^-$	–0.569
$2CO_2 + 2H^+ + 2e^- \rightleftharpoons C_2H_2O_4$	–0.475
$2CO_2 + 2e^- \rightleftharpoons C_2O_4^{2-}$	–0.590
$2CO_2 + 12H^+ + 12e^- \rightleftharpoons C_2H_4 + 4H_2O$	+0.064
$2CO_2 + 12H^+ + 12e^- \rightleftharpoons C_2H_6O + 3H_2O$	+0.084
$CO_2 + 4H^+ + 4e^- \rightleftharpoons C + 2H_2O$	+0.206
$CO_2 + 2H_2O + 4e^- \rightleftharpoons C + 4OH^-$	–0.627

Table 2.4: Standard thermodynamic electrochemical half-reaction potentials for CO_2 in aqueous solution.[32]

Heterogeneous electrode materials such as carbon, copper, and gold are capable of reducing CO_2 directly, but with various reaction pathways and significant overpotentials.[149] The use of these materials precludes the use of spectroscopic methods, making the development of future heterogeneous materials more difficult. Many homogeneous molecular complexes bearing first- and third-row transition metals have been synthesized with the goal of using them as CO_2 reduction catalysts. A notable example from Savéant and co-workers uses a molecular catalyst, tetraphenylporphyrin Fe(III) chloride (TPPFe(III)Cl), which undergoes three sequential one electron reductions to generate the active electrocatalyst for CO_2 reduction (see Figure 2.21).[150] In

the presence of trifluoroacetic acid and CO_2, the reversible behavior in the CV of the Fe(TPP) complex ceases and a substantial catalytic wave is observed at around -1.5 V vs. SCE. Preparative scale CPE results in the selective production of CO at 96% FE.

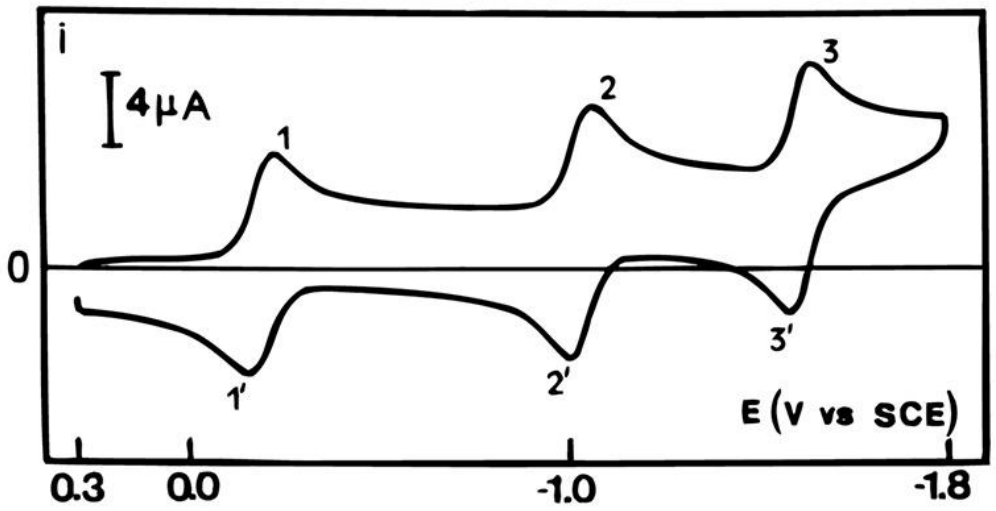

Figure 2.21: CV of TPPFe(III)Cl at 100 mVs^{-1} using 0.1 M $TEAClO_4$ in dimethylformamide as the supporting electrolyte and a glassy carbon working electrode. The sequential reductions of TPPFe(III)Cl at these negative potentials suggests that it was a prime candidate for electrocatalytic CO_2 reduction. Adapted with permission from 150. Copyright 1996 American Chemical Society.

However, the tricarbonyl complexes of the group 7 metals Re and Mn are perhaps the most famous CO_2 reduction electrocatalysts. The initial design of this class of homogeneous molecular CO_2 electrocatalysts began in the 1980s with the initial report of *fac*-$Re(CO)_3Cl(^{H}bpy)$ by Lehn and co-workers[151] and Meyer and co-workers.[152] Approximately thirty years later, Deronzier, Chardon-Noblat, and co-workers introduced the manganese analogue of the complex, *fac*-$Mn(CO)_3Br(^{H}bpy)$ as a significantly more Earth-abundant electrocatalyst for CO_2 reduction.[67] Both *fac*-$Re(CO)_3Cl(^{H}bpy)$ and *fac*-$Mn(CO)_3Br(^{H}bpy)$ are comparable and competent catalysts for

the generation of CO from CO_2. Recent work in this area has focused on tuning the electron density at the [Re] and [Mn] metal centers by using 4,4´-disubstituted-bpy (^{R}bpy) ligands.[86,100,153]

The high cost of Re has resulted in an influx of reports on *fac*-$Mn(CO)_3Br(^{R}bpy)$ complexes. Some *fac*-$Mn(CO)_3Br(^{R}bpy)$ derivatives have been used to address potential shortcomings of Mn(I) complexes, including the known visible-light photosensitivity and redox-induced dimerization of *fac*-$Mn(CO)_3Br(^{R}bpy)$ to form $Mn_2(CO)_6(^{R}bpy)_2$.[154,155] Kubiak and co-workers demonstrated that the dimerization of *fac*-$Mn(CO)_3Br(^{R}bpy)$ complexes can be impeded by utilizing bulky bipyridine ligands bearing mesityl groups in the 6 and 6´ positions of the bpy ligand (^{mes}bpy). CV of *fac*-$Mn(CO)_3(NCMe)(^{mes}bpy)$ reveals a quasi-reversible $2e^-$ redox couple centered at -1.55 V vs $Fc^{+/0}$ (see Figure 2.22).[156] In a catalytic CV experiment, *fac*-$Mn(CO)_3(NCMe)(^{mes}bpy)$ is reduced in the presence of methanol and CO_2. Interestingly, the onset of the catalytic wave does not occur at the initial $2e^-$ reduction, but rather, there is a kinetic potential shift that indicate the binding of CO_2, before being reduced again at -2.0 V to induce catalysis. Preparative CPE experiments reveal *fac*-$Mn(CO)_3(NCMe)(^{mes}bpy)$ is a competent CO_2 reduction electrocatalyst and selectively produces CO at 98% FE. Future work in the area of electrocatalytic CO_2 reduction will likely focus on kinetic, mechanistic, and thermodynamic studies in areas that extend beyond the common two-electron reduction products.

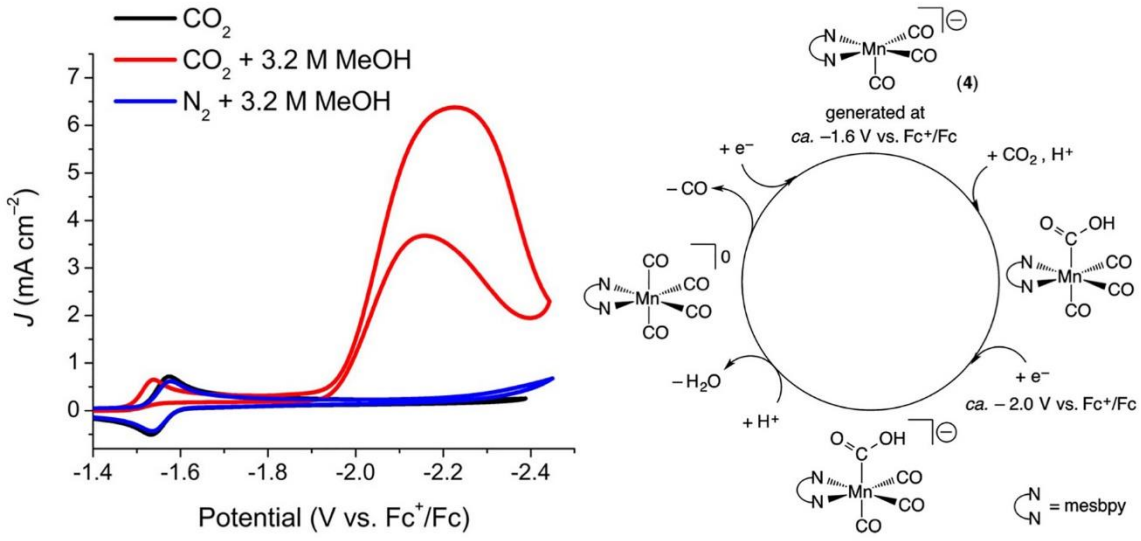

Figure 2.22: Catalytic CV experiment demonstrating that catalysis only occurs when *fac*-$Mn(CO)_3(NCMe)(^{mes}bpy)$ is in the presence of CO_2 and MeOH (left). A proposed catalytic cycle for the electrocatalytic generation of CO using $Mn(CO)_3(NCMe)(^{mes}bpy)$ (right). Reprinted with permission from 156. Copyright 2014 American Chemical Society.

2.6.5 Electrocatalytic Dinitrogen Reduction

Functionalizing dinitrogen is a particularly challenging process, and this is manifested in its physicochemical characteristics.[157] However, since dinitrogen comprises more than 79% of the Earth's atmosphere, chemical or electrochemical generation of reduced nitrogen products, such as ammonia, could be a useful way to utilize this abundant resource. On an industrial scale, nitrogen fixation is accomplished using the Haber-Bosch process where dihydrogen (produced from the steam reformation of methane), dinitrogen (obtained from air), and a doped heterogeneous Fe-based catalyst are used to produce ammonia.[158] The Haber-Bosch process itself is quite efficient, converting >97% of the chemical inputs into ammonia, a fact made more incredible when considering that this reaction accounts for nearly half of the Earth's total ammonia production

including both natural and artificial reactivity. However, the Haber-Bosch process as currently performed is the source of copious amounts of CO_2, and requires reaction temperatures exceeding 400 °C and pressures surpassing 200 atm. As a result, the redox process of reducing dinitrogen to ammonia has attracted increased interest from the electrocatalysis community; from this perspective, ammonia could either be used in fuel cells, producing only dinitrogen and water in an ideal scenario, or in its traditional role as a crop fertilizer. In nature, nitrogen fixation occurs by using the enzyme nitrogenase to reduce dinitrogen at room temperature and ambient pressure.[159,160] Toward this goal, the thermodynamic electrochemical half-reactions for some key dinitrogen reduction products involving, two, four, or six electrons are shown above (see Table 2.2 in AO).[32]

Figure 2.23: Reduction of dinitrogen using protons and electrons in combination with an electrocatalyst to generate ammonia.

While the electrocatalytic transformations (WO, HER, and CO_2R) discussed so far have many examples, electrocatalytic N_2RR with homogeneous catalysts is rare.[161] The first report of a true electrocatalytic N_2RR came from the Peters group in 2016 using $[(P_3^B)Fe]^+$ as a precatalyst and HBArF as an acid source.[162] Catalytic CV experiments revealed the onset of a catalytic wave at the $[(P_3^B)Fe]^+$ / $[(P_3^B)Fe(N_2)]$ couple at –1.5 V vs $Fc^{+/0}$, but greater enhancement was observed at the $[(P_3^B)Fe(N_2)]^{0/-1}$ couple at -2.2 V vs $Fc^{+/0}$. This potential is well within the range to observe HER as well as N_2RR. CPE of this complex revealed the presence of ammonia (2.3 equiv.) (as well as substantial amounts of H_2), confirming the catalytic ability of the complex. More recently, better kinetic control was achieved to improve the selectivity and turnover of this reaction by using

a metallocene molecular mediator to facilitate the reduction of dinitrogen.[163,164] Improvement was achieved through the use of Cp^*_2Co as a mediator, resulting in a catalytic wave with onset at ~ -2.0 V vs. $Fc^{+/0}$. CPE of $[(P_3^B)Fe]^+$, with $[Ph_2NH_2]^+$ and a cocatalytic amount of Cp_2Co, at an applied bias of -2.1 V vs $Fc^{+/0}$ resulted in 4 equiv. of ammonia. Future work in this area depends on the synthesis of new heterogeneous or homogeneous electrocatalysts capable of N_2RR. This will be accomplished by developing systems and conditions that can operate negative enough to engender N_2RR, but at the same time disfavor the kinetics that prefers the HER.

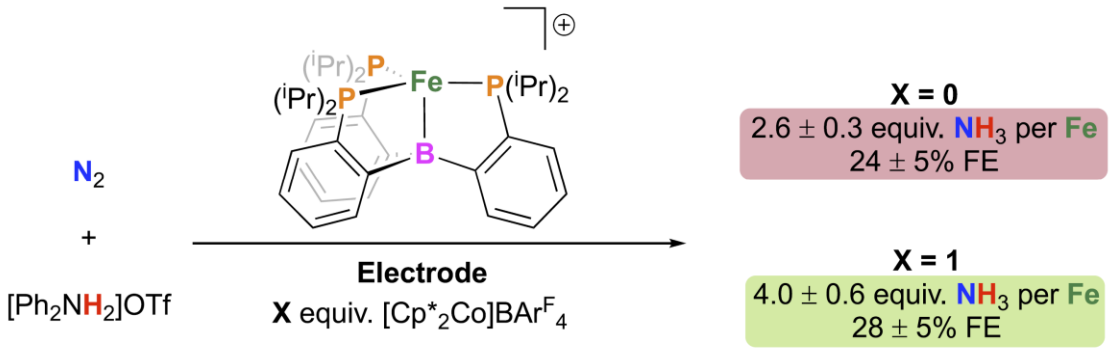

Figure 2.24: First molecular electrocatalyst for N_2RR in the presence of a cocatalytic amount of $[Cp^*_2Co]^+$. Reprinted with permission from reference 161. Copyright 2020, American Chemical Society.

2.6.6 Electrocatalytic Organic Transformations

Organometallic electrochemistry is typically associated with redox-induced small molecule activation where electrocatalysts are used to access and store energy. However, these techniques also are readily extended to electrocatalytic organic (electroorganic) transformations, which are rapidly gaining popularity.[165] Fortunately, organic chemists are beginning to think of electrochemistry as an essential method for driving synthetic processes. In this field,

organometallic electrocatalysts typically behave as redox mediators, shuttling electrons from the surface of the working electrode to an organic substrate on the way to product generation.[163,166] In some instance, these electrocatalysts may also engender regio-, chemo-, and stereoselectivity in the products (see Figure 2.25).[167] In these reactions organic substrates are oxidized or reduced at a controlled potential, resulting in the generation of intermediate radical species that undergo further chemical reactivity before generating the product(s). To this end, electroorganic syntheses mediated by organometallic complexes have attracted the interest of commodity chemical and pharmaceutical industries because of the tunability, scalability, and potential energy control provided by electrochemical techniques. Indeed, selective manipulation and installation of functional groups on organic substrates with electrochemical methods offers a distinct new approach that is likely to continue surging in activity.

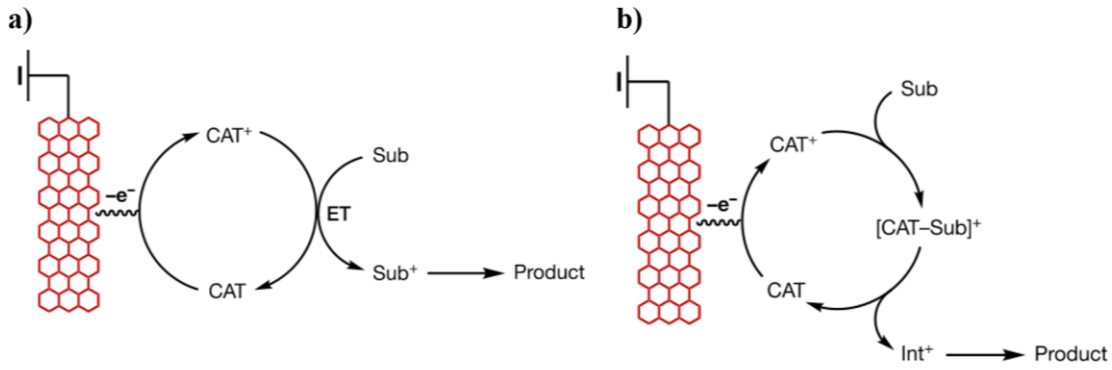

Figure 2.25: (**a**) a molecular mediator (CAT), in the context of oxidation, donating an electron to the working electrode, and later being reduced by the substrate (SUB) in route to product generation. (**b**) a molecular mediator, in the context of oxidation, donating an electron to the working electrode, stabilizing the substrate to form a catalyst–substrate complex, and then generating an intermediate on route to product generation. Figure adapted with permission from 167.

The earliest preparative scale electrochemical experiment was performed by Faraday in 1834, where an acetic acid solution was placed under anodic oxidative bias to generate ethane.[168] This experiment went on to inspire the Kolbe electrolysis in 1847, where abundant carboxylic acids were oxidized and used to produce alkyl radicals.[169] Around the same time, the first reductive preparative scale electroorganic experiment was also reported; this involved the reductive dehalogenation of trichlormethane sulfonic acid to methanesulfonic acid.[170] In the last twenty years, electrochemical methods have become more accessible to synthetic organic chemists due to the widespread availability of potentiostats and advancements in electrochemical techniques and methods, and this has resulted in an uptick in catalytic electroorganic synthesis literature reports.[171] Common functional groups such as aldehydes, ketones, esters, and olefins have been studied under electrocatalytic oxidative and reductive conditions with success. Hydrogenation of olefins and alkynes has also been studied, taking advantage of reactive transition metal hydrides typically implicated in HER electrocatalysis.[172]

A common theme in organic electrocatalysis is the use of a redox mediator to drive a chemical transformation. In an example of organometallic electroorganic synthesis, Xu and co-workers have taken advantage of the reliable one-electron redox chemistry of ferrocene.[173] In their work, ferrocene is a mediator in the electrocatalytic C–H and N–H functionalization of functionalized (aza)indoles. A catalytic CV experiment shows that the addition of the model urea-based substrate in the presence of ferrocene does not result in any significant change to the appearance of the CV which displays the reversible oxidation of ferrocene to ferrocenium (see Figure 2.26). However, when sodium methoxide is added, a catalytic wave is observed and the return reduction has ceased, suggesting that the ferrocenium is consumed by the urea-based substrate. A possible mechanism involves a pre-equilibrium with deprotonation of the urea-based complex, resulting in a nitrogen-

centered anion which then undergoes oxidation by intermolecular electron transfer with the electrogenerated ferrocenium. The oxidation generates a nitrogen centered radical that is capable of intramolecular cyclization with the neighboring alkyne which ultimately results in the formation of highly substituted indoles, while also regenerating ferrocene. Electrochemical methods for this redox-induced synthetic organic chemistry are advantageous because waste byproducts associated with the use of stoichiometric oxidants and reductants are eliminated. Future work in this area needs to focus on systematic studies of appropriate redox mediators capable of driving more complicated organic transformations. Important reactions, such as those involving the activation of aliphatic C-H bonds near amine and amide functionalities, is currently an active area in electroorganic synthesis.[174]

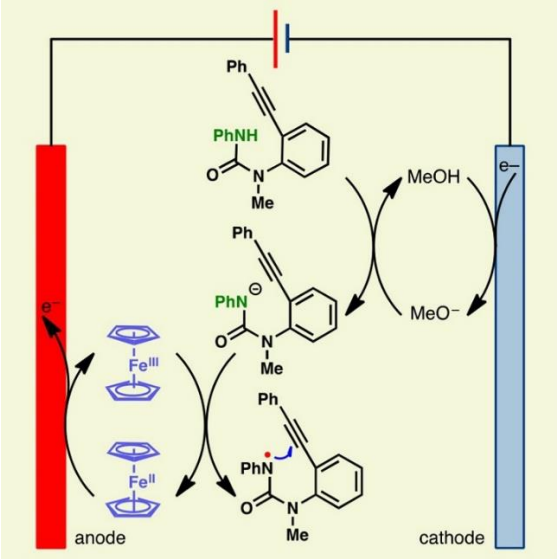

Figure 2.26: A proposed mechanism for the catalytic electrosynthesis of highly substituted indoles (right). Figure reprinted from reference 171 (right). Copyright 2017 American Chemical Society.

2.6.7 Analyses for Benchmarking Electrocatalysts

The significant increase in the production of new electrocatalysts over the years has contributed to the need for methods that can reliably benchmark in order to determine what is a "good" electrocatalyst. To this end, the derived Butler-Volmer[43] and Tafel[175] equations are two common analyses for benchmarking electrocatalysts, especially in the realm of heterogeneous catalysis. These methods are typically used to benchmark WO, HER, and CO_2RR catalysts, but can be performed for AO, N_2RR, and EOT reactions. Demonstrating high rates of activity and low overpotentials are the desired outcomes of catalyst benchmarking efforts. The main assessment methods are Butler-Volmer and Tafel analyses, and the reader may consult resources that give the full details.[43,176] Briefly, the Butler-Volmer equation describes the relationship between the current and potential between the surface of the electrode and the bulk sample for an elementary redox reaction. However, at high overpotentials, the Butler-Volmer equations simplifies to the Tafel equation. The resulting Butler-Volmer and Tafel analyses provide kinetic and thermodynamic insight into systems by relating the rate of electrocatalysis to the overpotential.

In the realm of molecular electrocatalysis, alternative methods for benchmarking catalysts and understanding their kinetic behaviors are typically utilized. One such method is Foot-of-the-Wave (FOWA) analysis, a method developed by Savéant, Costentin, and co-workers.[177] Summarizing this method, FOWA examines the "foot" of catalytic (and therefore irreversible) waves at points early in the onset of the catalytic current, in order to extract the instantaneous reaction rate from the voltammetric data.[178] One assumption that underlies typical FOWA is that the key redox-active intermediate involved in the rate-determining step of catalysis behaves in a Nernstian fashion, and thus its concentration can be considered directly controlled at the electrode surface by the applied

potential. FOWA is distinguished as a very helpful method for extraction of rate information at short times, when catalyst deactivation, substrate consumption, and/or product inhibition are avoided. Notably, when voltammetric data is collected in such a way as to avoid these issues, other analyses based on Zone Diagrams and mathematical treatments are possible. The reader is encouraged to consult resources that give the full details on these methods.[29]

Significant work has also been accomplished in the last few years to better understand equilibrium potentials (E^{o}_{X}) of feedstocks capable of interconverting chemical and electrical energy in non-aqueous, organic solvents. These measurements establish a metric for evaluating and comparing different electrocatalysts for a given process in non-aqueous solvents. Work by Roberts and Bullock has provided an accurate determination of the H^+/H_2 equilibrium potential for various acids in MeCN (see Table 2.5).[179] These experiments use a Pt electrode, which is an excellent catalyst for reversible hydrogen reduction, even in organic solvents. In related work, Mayer and Helm have also established E^{o}_{X} values (referenced to $Fc^{+/0}$ in acetonitrile and DMF) for electrocatalytic oxygen reduction and carbon dioxide reduction.[180] Determining these values in non-aqueous solvents has allowed the determination of accurate potentials for catalytic responses during electrocatalysis.

Half-Reactions	**Potential, E^0 (V vs $Fc^{+/0}$) MeCN**	**Potential, E^0 (V vs $Fc^{+/0}$) DMF**
$2H^+ + 2e^- \rightleftharpoons H_2$	-0.028	-0.662
$O_2 + 4H^+ + 4e^- \rightleftharpoons 2H_2O$	+1.29	+0.60
$CO_2 + 2H^+ + 2e^- \rightleftharpoons CO + H_2O$	-0.12	-0.73

Table 2.5: Thermodynamic equilibrium potentials for the reduction of protons, oxygen, and CO_2 in MeCN and DMF.[179,180]

2.7 Conclusion

The widespread availability of sensitive and robust potentiostats has led to substantial growth in the electrochemical investigation of redox processes in diverse compounds that are of interest to organometallic chemists. Modern electrochemical materials, methods and techniques have assisted in interpreting chemical reactivity that can be promoted at electrode surfaces. Cyclic voltammetry and controlled potential electrolysis experiments have provided important insights, and continue to be workhorse methods in organometallic electrochemistry. Voltammetry experiments can reveal the potentials of redox events whose nature is then probed with stoichiometric redox reagents in chemical syntheses. The thermodynamic, kinetic, and mechanistic data provided by cyclic voltammetric experiments has informed design principles that can be used to generate organometallic complexes and catalysts with tailored properties. Further, the shapes of redox waves in cyclic voltammetry responses can provide crucial information about the nature of electron transfer events and chemical reactions in solution, offering insights difficult to obtain by other techniques. This is particularly important in the field of electrocatalysis, in which efficiency and selectivity of a given catalyst can be investigated by coupling electrolysis methods to product analysis. Considering all the useful opportunities afforded by electrochemical methods, the future of organometallic electrochemistry is bright.

2.8 Acknowledgments

The authors thank the US National Science Foundation (OIA-1833087), the US Department of Energy, Office of Science, Office of Basic Energy Sciences, Early Career Research Program (DE-SC0019169), and the Kansas Academy of Science for funding different aspects of our group's work in redox chemistry and catalysis.

2.9 References

(1) Kealy, T.; Pauson, P. A. *Nature* **1951**, *168,* 1039–1040.

(2) Wilkinson, G.; Rosenblum, M.; Whiting, M. C.; Woodward, R. B. *J. Am. Chem. Soc.* **1952**, *74*, 2125-2126.

(3) Kuwana, T.; Bublitz, D. E.; Hoh, G. *Chem. Ind-London* **1959**, *20*, 635-636.

(4) Kuwana, T.; Bublitz, D. E.; Hoh, G. *J. Am. Chem. Soc.* **1960**, *82*, 5811-5817.

(5) Astruc, D. *Electron Transfer and Radical Processes in Transition-Metal Chemistry*; VCH Publishers: New York, 1995.

(6) Geiger, W. E. *Organometallics* **2007,** *26*, 5738-5765

(7) Werlé, C.; Meyer K., *Organometallics* **2019,** *38*, 1181-1185.

(8) Elgrishi, N.; Rountree, K. J.; McCarthy, B. D.; Rountree, E. S.; Eisenhart, T. T.; Dempsey, J. L., *J. Chem. Ed.* **2018,** *95* (2), 197-206.

(9) Nernst, W., *Z. Phys. Chem. NF.* **1888,** *2U* (1), 613-637.

(10) Connelly, N. G.; Geiger, W. E., *Chem. Rev.* **1996,** *6* (2), 877-910.

(11) Savéant, J. M.; Su, K. B., *J. Electroanal. Chem.* **1984,** *171* (1), 341-349.

(12) (a) Costentin, C.; Drouet, S.; Robert, M.; Saveant, J. M. *J. Am. Chem. Soc.* **2012**, *134*, 11235−11242. (b) Costentin, C.; Saveant, J. M. *ChemElectroChem.* **2014**, *1*, 1226−1236. (c) Costentin, C.; Drouet, S.; Robert, M.; Saveant, J. M. *Science* **2012**, *338*, 90−94.

(13) Appel, A. M.; Helm, M. L., *ACS Catalysis* **2014,** *4* (2), 630-633.

(14) Stock, J. T., Electrochemistry in Retrospect. In *Electrochemistry, Past and Present*, American Chemical Society: 1989; Vol. 390, pp 1-17.

(15) Mann, C. K.; Barnes, K. K. Electrochemical Reactions in Nonaqueous Systems; Marcel Dekker: New York, 1970; pp 403-418.

(16) Morris, M. D. In Electroanalytical Chemistry; Bard, A. J., Ed.; Marcel Dekker: New York, 1974; Vol. 7, pp 80-121.

(17) Kauffman, G. B., *J. Chem. Ed.* **1983,** *60* (3), 185-186.

(18) Page, J. A.; Wilkinson, G., *J. Am. Chem. Soc.* **1952,** *74* (23), 6149-6150.

(19) (a) Dessy, R. E.; Kitching, W.; Chivers, T., *J. Am. Chem. Soc.* **1966,** *88* (3), 453-459. (b) Dessy, R. E.; Kitching, W.; Psarras, T.; Salinger, R.; Chen, A.; Chivers, T., *J. Am. Chem. Soc.* **1966,** *88* (3), 460-467. (c) Dessy, R. E.; Chivers, T.; Kitching, W., *J. Am. Chem. Soc.***1966,** *88* (3), 467-470. (d) Dessy, R. E.; Stary, F. E.; King, R. B.; Waldrop, M., *J. Am. Chem. Soc.***1966,** *88* (3), 471-476. (e) Dessy, R. E.; King, R. B.; Waldrop, M., *J. Am. Chem. Soc.***1966,** *88* (22), 5112-5117. (f) Dessy, R. E.; Weissman, P. M.; Pohl, R. L., *J. Am. Chem. Soc.***1966,** *88* (22), 5117-5121. Dessy, R. E.; Pohl, R. L.; King, R. B., *J. Am. Chem. Soc.* **1966,** *88* (22), 5121-5124. (g) Dessy, R. E.; Weissman, P. M., *J. Am. Chem. Soc.* **1966,** *88* (22), 5124-5129. (h) Dessy, R. E.; Weissman, P. M., *J. Am. Chem. Soc.* **1966,** *88* (22), 5129-5131. (i) Psarras, T.; Dessy, R. E., *J. Am. Chem. Soc.* **1966,** *88* (22), 5132-5135. (j) Dessy, R. E.; Pohl, R. L., *J. Am. Chem. Soc.* **1968,** *90* (8), 1995-2001. (k) Dessy, R. E.; Kornmann, R. L.; Smith, C.; Haytor, R., *J. Am. Chem. Soc.* **1968,** *90* (8), 2001-2004. (l) Dessy, R. E.; Pohl, R. L., *J. Am. Chem. Soc.* **1968,** *90*

(8), 2005-2008. (m) Dessy, R. E.; Wieczorek, L., *J. Am. Chem. Soc.* **1969,** *91* (18), 4963-4974. (n) Dessy, R. E.; Charkoudian, J. C.; Abeles, T. P.; Rheingold, A. L., *J. Am. Chem. Soc.***1970,** *92* (13), 3947-3956. (o) Dessy, R. E.; Charkoudian, J. C.; Rheingold, A. L., *J. Am. Chem. Soc.* **1972,** *94* (3), 738-745. (p) Dessy, R. E.; Rheingold, A. L.; Howard, G. D., *J. Am. Chem. Soc.* **1972,** *94* (3), 746-752. (q) Dessy, R. E.; Bares, L. A., *Acc. Chem. Res.* **1972,** *5* (12), 415-421.

(20) (a) Huebert, B. J.; Smith, D. E., *J. Electroanal. Chem.* **1971,** *31* (2), 333-348. For later work on the reduction of cyclooctatetraene see: Petersen, R. A.; Evans, D. H., *J. Electroanal. Chem.* **1987,** *222* (1), 129-150. (b) Smith, D. E. In Electroanalytical Chemistry; Bard, A. J., Ed.; Marcel Dekker Inc.: New York, 1966; Vol. 1, pp 102-110.

(21) (a) Gutmann, V.; Schöber, G., *Monatsh. Chem. Verw. Teile Anderer Wiss.* **1957,** *88* (2), 206-215. (b) Vlček, A. A., *Collect. Czech. Chem. Commun.* **1965**, *30*, 952-960. (c) Mašek, J. *Collect. Czech. Chem. Commun.* **1965**, *30*, 4117-4126. (d) Denisovich, L. I.; Gubin, S. P.; Chapovski Yu, A.; Ustynok, N. A. Bull. Acad. Sci. USSR, DiV. Chem. Sci. 1968, 891. (e) Piazza, G.; Paliani, G., Z. Phys. Chem. **1970,** *71*, 91-101. (f) Mann, C. K.; Barnes, K. K. Electrochemical Reactions in Nonaqueous Systems; Marcel Dekker: New York, 1970; pp 403-418.

(22) Adams, R. N. Electrochemistry at Solid Electrodes; Marcel Dekker: New York, 1969

(23) Booman, G. L., *Anal. Chem.* **1957,** *29* (2), 213-218.

(24) Smith, D. E. In Electroanalytical Chemistry; Bard, A. J., Ed.; Marcel Dekker Inc.: New York, 1966; Vol. 1, pp 102-110.

(25) DeFord, D. D. American Chemical Society 133rd Meeting, San Francisco, April 1958

(26) Smith, D. E., A.C. *Analytical Chemistry* **1963,** *35* (12), 1811-1820.

(27) Schwarz, W. M.; Shain, I., *Anal. Chem.* **1963,** *35* (12), 1770-1778.

(28) Nicholson, R. S.; Shain, I., *Anal. Chem.* **1964,** *36* (4), 706-723.

(29) Savéant, Jean-Michel; Costentin, C. *Elements of molecular and biomolecular electrochemistry: an electrochemical approach to electron transfer chemistry*, 2nd ed.; John Wiley & Sons: Hoboken, NJ, 2019.

(30) Pourbaix, M. *Atlas of Electrochemical Equilibria in Aqueous Solutions*, 2nd ed.; National Association of Corrosion Engineers: Houston, 1974.

(31) Latimer, W. M. *Oxidation potentials*, 2nd ed.; Prentice-Hall: New York, 1952.

(32) Bard, A. J.; Jordan, J.; Parsons, R. *Standard potentials in aqueous solutions*; Marcel Dekker: New York, 1985.

(33) Kissinger, P. T.; Heineman, W. R. *Laboratory techniques in electroanalytical chemistry*; Marcel Dekker: New York, 1984.

(34) https://pineresearch.com/shop/products/potentiostats/wavenow-series/wavenow-wireless/

(35)https://pineresearch.com/shop/kb/applications/general-electrochemistry/potentiostat-glovebox-installation/

(36) Treimer, S.; Tang, A.; Johnson, D. C., *Electroanalysis* **2002,** *14* (3), 165-171.

(37) https://pineresearch.com/shop/kb/theory/hydrodynamic-electrochemistry/koutecky-levich-analysis/

(38) Gunasingham, H. In Electrochemistry, Past and Present; Stock, J. T., Orna, M. V., Eds.; ACS Symposium Series; American Chemical Society: Washington, DC, 1989; Vol. 390, Chapter 17.

(39) Zoski, C. G., Ed. Handbook of Electrochemistry; Elsevier: Amsterdam, The Netherlands, 2006.

(40) Graham, D. J. Standard Operating Procedures for Cyclic Voltammetry. https://sop4cv.com/index.html (accessed Jun 2021).

(41) Flato, J. B., *Anal. Chem.* **1972,** *44* (11), 75A-87A.

(42) Laborda, E.; González, J.; Molina, Á., *Electrochem. Commun.* **2014,** *43*, 25-30.

(43) Bard, A.J., Faulkner, L.R., Electrochemical Methods: Fundamentals and Applications, New York: Wiley, 2001, 2nd ed.

(44) Barker, G. C.; Jenkins, I. L., *Analyst* **1952,** *77* (920), 685-696.

(45) Rudolph, M., *J. Electroanal. Chem.* **2003,** *543* (1), 23-39.

(46) Feldberg, S. W., *J. Am. Chem. Soc.* **1966,** *88* (3), 390-393.

(47) D. Britz, Jörg Strutwolf, *Digital simulation in electrochemistry*, Berlin New York : Springer, Berlin New York, **2016**.

(48) Bieniasz, L. K., *Comput. Chem.* **1992,** *16* (1), 11-14.

(49) Bieniasz, L. K., *mput. Chem.* **1993,** *17* (4), 355-368.

(50) Bieniasz, L. K., *mput. Chem.* **1997,** *21* (1), 1-12.

(51) https://home.cyf-kr.edu.pl/~nbbienia/elsim3ad.html

(52) Rudolph, M.; Reddy, D. P.; Feldberg, S. W., *Anal. Chem.* **1994,** *66* (10), 589A-600A.

(53) http://www.digielch.de/

(54) D. K. Gosser in *Cyclic voltammetry : simulation and analysis of reaction mechanisms*, *Vol.* New York, N.Y. : VCH, New York, N.Y., 1993.

(55) López, I.; Le Poul, N., *Coord. Chem. Rev.* **2021,** *436*, 213823-21844.

(56) Kuwana, T.; Darlington, R. K.; Leedy, D. W., *Anal. Chem.* **1964,** *36* (10), 2023-2025.

(57) Bard, A. J., *J. Chem. Ed.* **1983,** *60* (4), 302.

(58) Marcus, R. A., On the Theory of Oxidation-Reduction Reactions Involving Electron Transfer. I. *J. Chem Phys* **1956,** *24* (5), 966-978.

(59) Johnson, M. D. Comprehensive Organometallic Chemistry; Wilkinson, G., Stone, F. G. A., Abel, E. W., Eds.; Pergammon Press: Oxford, 1982; Vol. 4, p 479.

(60) Gagne, R. R.; Koval, C. A.; Lisensky, G. C., Ferrocene as an internal standard for electrochemical measurements. *Inorg. Chem.* **1980,** *19* (9), 2854-2855.

(61) Malischewski, M.; Adelhardt, M.; Sutter, J.; Meyer, K.; Seppelt, K., *Science* **2016,** *353* (6300), 678-682.

(62) Goodwin, C. A. P.; Giansiracusa, M. J.; Greer, S. M.; Nicholas, H. M.; Evans, P.; Vonci, M.; Hill, S.; Chilton, N. F.; Mills, D. P., *Nature Chemistry* **2021,** *13* (3), 243-248.

(63) Bard, A.J., Faulkner, L.R., Electrochemical Methods: Fundamentals and Applications, New York: Wiley, 2001, 2nd ed. pp 49-51.

(64) Bard, A.J., Faulkner, L.R., Electrochemical Methods: Fundamentals and Applications, New York: Wiley, 2001, 2nd ed. pp 52-53.

(65) Hopkins Leseberg, J. A.; Lionetti, D.; Day, V. W.; Blakemore, J. D., *Organometallics* **2021,** *40* (2), 266-277.

(66) Lionetti, D.; Day, V. W.; Lassalle-Kaiser, B.; Blakemore, J. D., *Chem. Commun.* **2018,** *54* (14), 1694-1697.

(67) Bourrez, M.; Molton, F.; Chardon-Noblat, S.; Deronzier, A., *Angew. Chem. Int. Ed.* **2011,** *50* (42), 9903-9906.

(68) Hartl, F.; Rossenaar, B. D.; Stor, G. J.; Stufkens, D. J., *Recl. Trav. Chim. Pays-Bas* **1995,** *114* (11-12), 565-570.

(69) Hopkins, J. A.; Lionetti, D.; Day, V. W.; Blakemore, J. D., *Organometallics* **2019,** *38* (6), 1300-1310.

(70) See Supporting Information Figure S48 of publication for electrochemical control experiment to confirm the absence of a chloride in TBAPF6/CH3CN electrolyte.

(71) Lionetti, D.; Day, V. W.; Blakemore, J. D., *Organometallics* **2017,** *36* (10), 1897-1905.

(72) Henke, W. C.; Lionetti, D.; Moore, W. N. G.; Hopkins, J. A.; Day, V. W.; Blakemore, J. D., *ChemSusChem* **2017,** *10* (22), 4589-4598.

(73) Hopkins, J. A.; Lionetti, D.; Day, V. W.; Blakemore, J. D., *J. Organomet. Chem.* **2020,** *921*, 121294.

(74) Boyd, E. A.; Lionetti, D.; Henke, W. C.; Day, V. W.; Blakemore, J. D., *Inorg. Chem.* **2019,** *58* (6), 3606-3615.

(75) Hershberger, J. W.; Klingler, R. J.; Kochi, J. K., *J. Am. Chem. Soc.* **1983**, *105*, 61.

(76) Grass, V.; Lexa, D.; Momenteau, M.; Savéant, J.-M., *J. Am. Chem. Soc.* **1997,** *119* (15), 3536-3542.

(77) F. Goodridge and C. King, *Techniques of Electroorganic Synthesis'(ed. NL Weinberg) John Wiley, New York* **1974**.

(78) Harrar, J. E. In *Electroanalytical Chemistry*; Bard, A. J., Ed.; Marcel Dekker: New York, 1975; Vol. 8.

(79) A. J. Bard and C. G. Zoski, *Electroanalytical Chemistry: A Series of Advances: Volume 23*, CRC press, **2010**.

(80) T. Shōno, *Electroorganic synthesis*, Academic press, **1991**.

(81) Kyriacou, D. K. *Basics of Electroorganic Synthesis*; Wiley-Interscience: New York, 1981.

(82) A. J. Fry, *Synthetic organic electrochemistry*, John Wiley & Sons, **1989**.

(83) Kissinger, P. T.; Heineman, W. R. *Laboratory techniques in electroanalytical chemistry*; Marcel Dekker: New York, 1984. pp 504-506

(84) Robinson, J. R.; Gordon, Z.; Booth, C. H.; Carroll, P. J.; Walsh, P. J.; Schelter, E. J., *J. Am. Chem. Soc.* **2013,** *135* (50), 19016-19024.

(85) Barr, J. L.; Kumar, A.; Lionetti, D.; Cruz, C. A.; Blakemore, J. D., *Organometallics* **2019,** *38* (9), 2150-2155.

(86) Smieja, J. M.; Sampson, M. D.; Grice, K. A.; Benson, E. E.; Froehlich, J. D.; Kubiak, C. P., *Inorg. Chem.* **2013,** *52* (5), 2484-2491.

(87) Chapovetsky, A.; Patel, P.; Liu, C.; Sattelberger, A. P.; Kaphan, D. M.; Delferro, M., *Organometallics* **2020,** *39* (24), 4430-4436.

(88) Lewis, N. S.; Nocera, D. G., *PNAS.* **2006,** *103* (43), 15729-15735.

(89) International Energy Agency. Data and Statistics for World Electricity Generation by Source, 2018.

(90) International Energy Agency: World Energy Outlook, 2015.

(91) Roberts, J. A. S.; Bullock, R. M. Inorg. Chem. **2013**, *52*, 3823-3835.

(92) Kütt, A.; Leito, I.; Kaljurand, I.; Sooväli, L.; Vlasov, V. M.; Yagupolskii, L. M.; Koppel, I. A., *J. Org. Chem.* **2006,** *71* (7), 2829-2838.

(93) Kaljurand, I.; Kütt, A.; Sooväli, L.; Rodima, T.; Mäemets, V.; Leito, I.; Koppel, I. A., Extension of the Self-Consistent Spectrophotometric Basicity Scale in Acetonitrile to a Full Span of 28 pKa Units: Unification of Different Basicity Scales. *The Journal of Organic Chemistry* **2005,** *70* (3), 1019-1028.

(94) Schwesinger, R., *Nachrichten aus Chemie, Technik und Laboratorium* **1990,** *38* (10), 1214-1226.

(95) Costentin, C.; Robert, M.; Savéant, J.-M.; Tatin, A., *PNAS* **2015,** *112* (22), 6882-6886.

(96) Espenson, James H. Chemical Kinetics and Reaction Mechanisms / James H. Espenson. New York: McGraw-Hill, 1995.

(97) Matheu, R.; Neudeck, S.; Meyer, F.; Sala, X.; Llobet, A., *ChemSusChem* **2016,** *9* (23), 3361-3369.

(98) Zott, M. D.; Garrido-Barros, P.; Peters, J. C., *ACS Catal.* **2019,** *9* (11), 10101-10108.

(99) Ahmad, E.; Rai, S.; Padhi, S. K., *Int. J. Hydrog. Energy* **2019,** *44* (31), 16467-16477.

(100) Clark, M. L.; Cheung, P. L.; Lessio, M.; Carter, E. A.; Kubiak, C. P., *ACS Catal.* **2018,** *8* (3), 2021-2029.

(101) Liu, X.; Li, F.-F.; Peng, P.; Licht, G.; Licht, S., *Eur. J. Inorg. Chem.* **2020,** *2020* (15-16), 1428-1436.

(102) Crabtree, R. H., *Chem. Rev.* **2015,** *115* (1), 127-150.

(103) Whitesides, G. M.; Hackett, M.; Brainard, R. L.; Lavalleye, J. P. P. M.; Sowinski, A. F.; Izumi, A. N.; Moore, S. S.; Brown, D. W.; Staudt, E. M., *Organometallics* **1985,** *4* (10), 1819-1830.

(104) Sconyers, D. J.; Blakemore, J. D., *Chem. Commun.* **2017,** *53* (53), 7286-7289.

(105) Lin, Y.; Finke, R. G., *Inorg. Chem.* **1994,** *33* (22), 4891-4910.

(106) Sconyers, D. J.; Blakemore, J. D., *Analyst* **2020,** *145* (2), 466-477.

(107) Sconyers, D. J.; Blakemore, J. D., *Dalton Trans.* **2019,** *48* (19), 6372-6382.

(108) Nie, W.; Wang, Y.; Zheng, T.; Ibrahim, A.; Xu, Z.; McCrory, C. C. L., *ACS Catal.* **2020,** *10* (9), 4942-4959.

(109) This bulk electrolysis cell may be available for purchase at redox.me; item: bulk electrolysis basic cell – 50 mL. https://redox.me/products/bulk-electrolysis-basic-cell-50-ml. Accesses June 2021.

(110) Harris, D. C. Quantitative Chemical Analysis. New York, NY: W.H. Freeman and Co, 2007. Print.

(111) Eaton, G. R.; Eaton, S. S.; Barr, D. P.; Weber, R. T. Quantitative EPR; Springer-Verlag: Vienna, 2010.

(112) Dau, H.; Limberg, C.; Reier, T.; Risch, M.; Roggan, S.; Strasser, P., *ChemCatChem* **2010,** *2* (7), 724-761.

(113) Blakemore, J. D.; Crabtree, R. H.; Brudvig, G. W., *Chem. Rev.* **2015,** *115* (23), 12974-13005.

(114) Hunter, B. M.; Gray, H. B.; Müller, A. M., *Chem. Rev.* **2016,** *116* (22), 14120-14136.

(115) Yagi, M.; Kaneko, M., *Chem. Rev.* **2001,** *101* (1), 21-36.

(116) Meyer, T. J.; Huynh, M. H. V.; Thorp, H. H., *Angew. Chem. Int. Ed.* **2007,** *46* (28), 5284-5304.

(117) Armstrong, D. A.; Huie, R. E.; Koppenol, W. H.; Lymar, S. V.; Merényi, G.; Neta, P.; Ruscic, B.; Stanbury, D. M.; Steenken, S.; Wardman, P., *Pure Appl. Chem.* **2015,** *87* (11-12), 1139-1150.

(118) Harriman, A.; Richoux, M.-C.; Christensen, P. A.; Mosseri, S.; Neta, P., *J. Chemi. Soc., Faraday Trans.* **1987,** *83* (9), 3001-3014.

(119) Harriman, A.; Thomas, J. M.; Millward, G. R., *New J. Chem.* **1987**, *11*, 757−762.

(120) Najafpour, M. M.; Ehrenberg, T.; Wiechen, M.; Kurz, P., *Angew. Chem., Int. Ed.* **2010**, *49*, 2233− 2237.

(121) Gersten, S. W.; Samuels, G. J.; Meyer, T. J., *J. Am. Chem. Soc.* **1982,** *104* (14), 4029-4030.

(122) Duan, L.; Bozoglian, F.; Mandal, S.; Stewart, B.; Privalov, T.; Llobet, A.; Sun, L., *Nat. Chem.* **2012,** *4* (5), 418-423.

(123) M Schulze, M.; Kunz, V.; Frischmann, P. D.; Würthner, F., *Nat. Chem.* **2016,** *8* (6), 576-583.

(124) McDaniel, N. D.; Coughlin, F. J.; Tinker, L. L.; Bernhard, S., Cyclometalated Iridium(III) Aquo Complexes: Efficient and Tunable Catalysts for the Homogeneous Oxidation of Water. *J. Am. Chem. Soc.* **2008,** *130*, 210-217.

(125) Hull, J. F.; Balcells, D.; Blakemore, J. D.; Incarvito, C. D.; Eisenstein, O.; Brudvig, G. W.; Crabtree, R. H., *J. Am. Chem. Soc.* **2009,** *131* (25), 8730-8731.

(126) Zhao, Y.; Yang, K. R.; Wang, Z.; Yan, X.; Cao, S.; Ye, Y.; Dong, Q.; Zhang, X.; Thorne, J. E.; Jin, L.; Materna, K. L.; Trimpalis, A.; Bai, H.; Fakra, S. C.; Zhong, X.; Wang, P.; Pan, X.;

Guo, J.; Flytzani-Stephanopoulos, M.; Brudvig, G. W.; Batista, V. S.; Wang, D., *PNAS* **2018,** *115* (12), 2902-2907.

(127) Najafpour, M. M.; Renger, G.; Hołyńska, M.; Moghaddam, A. N.; Aro, E.-M.; Carpentier, R.; Nishihara, H.; Eaton-Rye, J. J.; Shen, J.-R.; Allakhverdiev, S. I., *Chem. Rev.* **2016,** *116* (5), 2886-2936.

(128) Singh, A.; Spiccia, L., *Coord. Chem. Rev.* **2013,** *257* (17), 2607-2622.

(129) Blakemore, J. D.; Schley, N. D.; Balcells, D.; Hull, J. F.; Olack, G. W.; Incarvito, C. D.; Eisenstein, O.; Brudvig, G. W.; Crabtree, R. H., *J. Am. Chem. Soc.* **2010,** *132* (45), 16017-16029.

(130) Savini, A.; Bellachioma, G.; Ciancaleoni, G.; Zuccaccia, C.; Zuccaccia, D.; Macchioni, A., *Chem. Commun.* **2010,** *46* (48), 9218-9219.

(131) Blakemore, J. D.; Schley, N. D.; Olack, G. W.; Incarvito, C. D.; Brudvig, G. W.; Crabtree, R. H., *Chem. Sci.* **2011,** *2* (1), 94-98.

(132) Schley, N. D.; Blakemore, J. D.; Subbaiyan, N. K.; Incarvito, C. D.; D'Souza, F.; Crabtree, R. H.; Brudvig, G. W. *J. Am. Chem. Soc.* **2011,** 133 (27), 10473-10481.

(133) Sconyers, D. J.; Blakemore, J. D. Distinguishing between homogeneous and heterogeneous hydrogen-evolution catalysis with molecular cobalt complexes. *Chem. Commun.* **2017,** *53*, 7286-7289.

(134) Sconyers, D. J.; Blakemore, J. D. Distinguishing deposition, corrosion, and stripping of transient heterogeneous materials during molecular electrocatalysis. *Dalton Trans.* **2019,** *48* (19), 6372-6382.

(135) Sconyers, D. J.; Blakemore, J. D. Electrodeposition behavior of homoleptic transition metal acetonitrile complexes interrogated with piezoelectric gravimetry. *Analyst* **2020,** *145* (2), 466-477.

(136) Adli, N. M.; Zhang, H.; Mukherjee, S.; Wu, G., *J. Electrochem. Soc.* **2018,** *165* (15), J3130-J3147.

(137) Dunn, P. L.; Cook, B. J.; Johnson, S. I.; Appel, A. M.; Bullock, R. M., *J. Am. Chem. Soc.* **2020,** *142* (42), 17845-17858.

(138) Habibzadeh, F.; Miller, S. L.; Hamann, T. W.; Smith, M. R., *PNAS.* **2019,** *116* (8), 2849-2853.

(139) Zott, M. D.; Peters, J. C., *J. Am. Chem. Soc.* **2021,** *143* (20), 7612-7616.

(140) McKone, J. R.; Marinescu, S. C.; Brunschwig, B. S.; Winkler, J. R.; Gray, H. B., *Chem. Sci.* **2014,** *5* (3), 865-878.

(141) Tong, L.; Duan, L.; Zhou, A.; Thummel, R. P., *Coord. Chem. Rev.* **2020,** *402*, 213079.

(142) McKone, J. R.; Marinescu, S. C.; Brunschwig, B. S.; Winkler, J. R.; Gray, H. B., *Chem. Sci.* **2014,** *5* (3), 865-878.

(143) Cheng, N.; Stambula, S.; Wang, D.; Banis, M. N.; Liu, J.; Riese, A.; Xiao, B.; Li, R.; Sham, T.-K.; Liu, L.-M.; Botton, G. A.; Sun, X., *Nat. Commun.* **2016,** *7* (1), 13638.

(144) Jaramillo, T. F.; Jørgensen, K. P.; Bonde, J.; Nielsen, J. H.; Horch, S.; Chorkendorff, I., *Science* **2007,** *317* (5834), 100-102.

(145) Valdez, C. N.; Dempsey, J. L.; Brunschwig, B. S.; Winkler, J. R.; Gray, H. B., *PNAS.* **2012,** *109* (39), 15589-15593.

(146) Michael Gratzel, U. K., *Chem. Ber.* **1989,** *122*, 1869-1880.

(147) Francke, R.; Schille, B.; Roemelt, M., *Chem. Rev.* **2018,** *118* (9), 4631-4701.

(148) Qiao, J.; Liu, Y.; Hong, F.; Zhang, J *Chem. Soc. Rev.* **2014,** *43* (2), 631-675.

(149) Frese, K. W. Electrochemical Reduction of carbon dioxide at solid electrodes. In Electrochemical and Electrocatalytic Reactions of Carbon Dioxide; Sullivan, B. P., Krist, K., Guard, H. E., Eds.; Elsevier: Amsterdam, 2012; pp 145−216.

(150) Bhugun, I.; Lexa, D.; Savéant, J.-M., *J. Am. Chem. Soc.* **1996,** *118* (7), 1769-1776.

(151) Hawecker, J.; Lehn, J.-M.; Ziessel, R., *J. Chem Soc. Chem commun.* **1984,** (6), 328-330.

(152) Sullivan, B. P.; Bolinger, C. M.; Conrad, D.; Vining, W. J.; Meyer, T. J., *J. Chem. Soc. Chem. Commun.* **1985,** (20), 1414-1416.

(153) Tignor, S. E.; Kuo, H.-Y.; Lee, T. S.; Scholes, G. D.; Bocarsly, A. B., *Organometallics* **2019,** *38* (6), 1292-1299.

(154) Henke, W. C.; Otolski, C. J.; Moore, W. N. G.; Elles, C. G.; Blakemore, J. D., *Inorg. Chem.* **2020,** *59* (4), 2178-2187.

(155) Machan, C. W.; Sampson, M. D.; Chabolla, S. A.; Dang, T.; Kubiak, C. P., *Organometallics* **2014,** *33* (18), 4550-4559.

(156) Sampson, M. D.; Nguyen, A. D.; Grice, K. A.; Moore, C. E.; Rheingold, A. L.; Kubiak, C. P., *J. Am. Chem. Soc.* **2014,** *136* (14), 5460-5471.

(157) Bazhenova, T. A.; Shilov, A. E., *Coord. Chem. Rev.* **1995,** *144*, 69-145.

(158) Nishibayashi, Y., *Inorg. Chem.* **2015,** *54*, 9234-9247.

(159) Fields, S., *Environ. Health Perspect.* **2004,** *112*, A556-A563.

(160) Please insert a cross reference to the chapter of COMC-IV from Holland and co-authors regarding nitrogenase chemistry.

(161) Chalkley, M. J.; Drover, M. W.; Peters, J. C., *Chem. Rev.* **2020,** *120* (12), 5582-5636.

(162) Del Castillo, T. J.; Thompson, N. B.; Peters, J. C., *J. Am. Chem. Soc.* **2016,** *138* (16), 5341-5350.

(163) Chalkley, M. J.; Garrido-Barros, P.; Peters, J. C., *Science* **2020,** *369* (6505), 850-854.

(164) Chalkley, M. J.; Del Castillo, T. J.; Matson, B. D.; Roddy, J. P.; Peters, J. C., *ACS Central Science* **2017,** *3* (3), 217-223.

(165) Horn, E. J.; Rosen, B. R.; Baran, P. S., *ACS Cent. Sci.* **2016,** *2* (5), 302-308.

(166) Francke, R.; Little, R. D., *Chem. Soc. Rev.* **2014,** *43* (8), 2492-2521.

(167) Siu, J. C.; Fu, N.; Lin, S., *Acc. Chem. Res.* **2020,** *53* (3), 547-560.

(168) Faraday, M., *Ann. Phys.* **1834,** *109* (23-30), 433-451.

(169) Kolbe, H., *J. Prakt. Chem.,***1847,** *41* (1), 137-139.

(170) Schöenbein, ChF. *Liebigs Ann. Chem.*, **1845**, *54*, 164.

(171) Yan, M.; Kawamata, Y.; Baran, P. S., *Chem. Rev.* **2017,** *117* (21), 13230-13319.

(172) Caix, C.; Chardon-Noblat, S.; Deronzier, A.; Moutet, J.-C.; Tingry, S., *J. Organomet. Chem.* **1997,** *540* (1), 105-111.

(173) Hou, Z.-W.; Mao, Z.-Y.; Zhao, H.-B.; Melcamu, Y. Y.; Lu, X.; Song, J.; Xu, H.-C., *Angew. Chem. Int. Ed.* **2016,** *55* (32), 9168-9172.

(174) Choi, G. J.; Zhu, Q.; Miller, D. C.; Gu, C. J.; Knowles, R. R., *Nature* **2016,** *539* (7628), 268-271.

(175) Tafel, J.; Zeit. *Physik. Chem.,* **1905**, *50A*, 641-712.

(176) Li, D.; Lin, C.; Batchelor-McAuley, C.; Chen, L.; Compton, R. G., *J. Electroanal. Chem.* **2018,** *826*, 117-124.

(177) Costentin, C.; Drouet, S.; Robert, M.; Savéant, J.-M., *J. Am. Chem. Soc.* **2012,** *134*, 11235-11242.

(178) Sconyers, D. J.; Shaughnessy, C. I.; Lee, H.-J.; Subramaniam, B.; Leonard, K. C.; Blakemore, J. D., *ChemSusChem* **2020,** *13*, 6338-6345.

(179) Roberts, J. A. S.; Bullock, R. M., *Inorg. Chem.* **2013,** *52* (7), 3823-3835.

(180) Pegis, M. L.; Roberts, J. A. S.; Wasylenko, D. J.; Mader, E. A.; Appel, A. M.; Mayer, J. M., *Inorg. Chem.* **2015,** *54* (24), 11883-11888.

Chapter 3

Evidence for Charge Delocalization in Diazafluorene Ligands Supporting Low-Valent [Cp*Rh] Complexes

This chapter is adapted from a published manuscript: Henke, W.C., Stiel, J.P., Day, V.W., and Blakemore, J.D.* Evidence for Charge Delocalization in Diazafluorene Ligands Supporting Low-Valent [Cp*Rh] Complexes, *Chem. Eur. J.* **2022**, *28*, e202103970, doi: 10.1002/chem.202103970

3.1 Introduction

Development of systems that can carry out difficult reduction reactions, like conversion of CO_2 and N_2 into fuels and chemicals, is an important goal of redox chemistry.[1,2] Redox non-innocent ligands can directly assist in these reaction sequences with redox load management.[3,4] Consequently, development of redox non-innocent and/or redox-active ligands is an active area, particularly due to the need for stability across oxidation states and under highly reducing conditions.[5]

One family of ligands that is well known for use in both redox and photoredox catalytic applications includes 2,2′-bipyridyl and its derivatives.[6] 2,2′-bipyridyl (bpy) was prepared very early by Blau,[7] and has since become one of the most popular supporting ligands in inorganic and organometallic chemistry.[8] Some features that enable 2,2′-bipyridyl to support catalysts include: (i) the presence of two nitrogen donor atoms that can bond effectively with most transition metals by forming a stable five-membered metallacycle, (ii) the presence of a conjugated 12π-electron system that can stabilize electron-rich intermediates through π-backbonding and charge delocalization, and (iii) a chemically robust structure lacking Brønsted-acidic or reactive moieties that could engage in deleterious side reactions. Widespread use of bpy has promoted significant creative work in the development of ligands that are adept at stabilizing metal complexes, but with tuneable properties.[6]

By comparison, 4,5-diazafluorene (daf) is a much newer ligand technology, with the first synthesis being reported in 1950 by Schmidt and co-workers.[9] The structures of daf-based ligands are reminiscent of bpy, but they are distinguished by the presence of an additional sp^3 hybridized carbon atom that ties the two pyridyl rings together; this establishes an additional five-membered

carbocycle, rigidifying the daf core (see Chart 3.1). The presence of this additional five-membered ring also "pulls back" the nitrogen donor atoms, increasing the bite angle.[10] Thus, unlike bpy, which typically and reliably binds transition metals in an [*N,N*]-bidentate (κ^2) fashion, daf-type ligands have demonstrated the ability to coordinate metals in pentahapto (η^5),[11] bridging (μ),[12,13] and monodentate (κ^1)[14] modes, as well as the more familiar κ^2 mode.

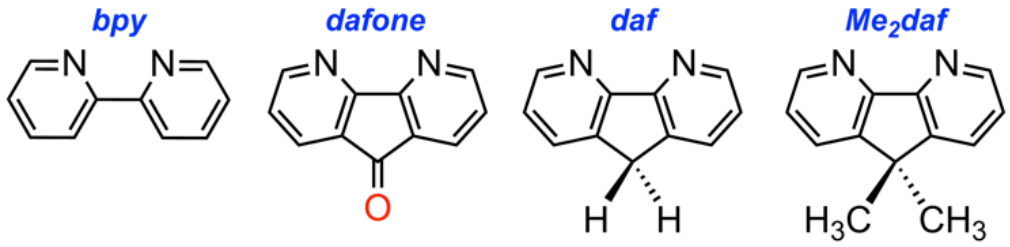

Chart 3.1: The structures of 2,2′-bipyridyl (bpy), 4,5-diazafluoren-9-one (dafone), 4,5-diazafluorene (daf), and 9,9′-dimethyl-4,5-diazafluroene (Me_2daf).

On the other hand, the structure of daf features Brønsted-acidic, doubly benzylic C–H bonds on the backbone of the ligand that can become directly involved in reactivity. For reference, cyclopentadiene, fluorene, and pentamethylcyclopentadiene have pK_a values of 18.0, 22.6, and 26.1 in dimethyl sulfoxide; the acidity of fluorene is consistent with the behavior of daf toward deprotonation in the presence of metals.[15] Indeed, Song and co- workers[16,17] have leveraged daf for use in heterolytic dihydrogen splitting [18] and olefin hydrogenation[19]. Complementing this work, Stahl and co-workers have recently shown that congeners of daf, especially 4,5-diazafluoren-9-one (dafone) and 9,9′-dimethyldiazafluorene (Me_2daf) impart significant advantages in Pd-catalyzed acetoxylation,[20] dehydrogenation,[21] and aerobic oxidation reactions.[14]

In view of these promising uses of daf-type ligands in redox chemistry and catalysis, we were surprised to find that little spectroscopic or structural evidence is available regarding the ability of the daf framework to delocalize electron density or form reduced species by charge transfer events. The latter behavior underpins the exemplary performance of $[Ru(bpy)_3]^{2+}$ in catalysis, wherein direct electron transfer or light-promoted metal-to-ligand charge transfer events drive important reactivity. The photochemically accessible states are not unlike bpy-centered radicals, in that the reducing electron density resides on the conjugated bpy framework.[22,23] In the former case, delocalization of electron density into the bpy framework occurs via π-backdonation from low-valent, reducing metal centers, for example in Cp*Rh(bpy) (where Cp* is pentamethylcyclopentadienyl).[24-27] In this situation, the formally Rh(I) center donates electron density into the lowest unoccupied molecular orbital (LUMO) of bpy, stabilizing the compound. This is observed in the solid-state structure of the reduced Cp*Rh(bpy), where the C–C bond interconnecting the two pyridyl rings is noticeably shorter in comparison to that in the Rh(III) analogue and free bpy (1.422(4), 1.49(2), and 1.488(1) Å, respectively), confirming π-backdonation into bpy.[28,29] Hoping to investigate the possibility that daf-based ligands could exhibit similar behaviors, we anticipated that the demonstrated Brønsted acid-base reactivity of daf would likely muddle studies of charge delocalization into the conjugated ligand framework. In such a scheme, we imagined that protective methylation of the 9 and 9′ positions could allow such studies by disfavoring acid-base reactivity, unlocking the ability to study reduced forms of the diazafluorene core.

Here, we report the synthesis, structural characterization, and electrochemical studies of a series of [Cp*Rh] complexes supported by dafone, daf, and Me_2daf. We find that the complexes bearing dafone and daf undergo reduction-induced chemical reactivity via pathways that are arrested when

using Me_2daf; methylation of daf prevents the harmful ligand-driven radical chemistry and undesired Brønsted acid/base reactivity observed in other congeners. Use of Me_2daf affords access to distinctive rhodium species in the formal +III, +II, and +I oxidation states and enables spectroscopic characterization, demonstrating that Me_2daf actively stabilizes the reduced species. Single-crystal X-ray diffraction analysis of Cp*Rh(Me_2daf) reveals the structural changes associated with delocalization of electron density into the Me_2daf framework for the first time. Our quantitative data show that the more constrained binding geometry of Me_2daf moderates its σ-donor and π- acceptor properties relative to bpy. Taken together, this study shows that Me_2daf is a promising supporting ligand for the development of redox chemistries and encourage utilization of the daf framework under reducing conditions.

3.2 Results and Discussion

Diazafluorene-type ligands[9,30-32] have not previously been used for preparation of [Cp*Rh] complexes. Based on the similarity of the daf framework to bpy, we selected synthetic procedures that have previously been useful for preparation of [Cp*Rh] complexes supported by bpy and other bidentate ligands.[2,33] We find that $[Cp^*RhCl_2]_2$ is readily cleaved by dafone, daf, and Me_2daf, [34,35] enabling us to access the new complexes [Cp*RhCl(dafone)]OTf, [Cp*RhCl(daf)]OTf, and [Cp*RhCl(Me_2daf)]OTf (**1**-**3**, see Scheme 3.1). Cleavage of $[Cp^*RhCl_2]_2$ was facilitated here through use of salt metathesis with AgOTf, favoring binding of the daf-based ligands. No unusual behaviors were encountered in these syntheses, and following generation of the desired complexes, they were fully characterized (see Appendix A, Figures A1-A9, A27-A29, and A31-A36).

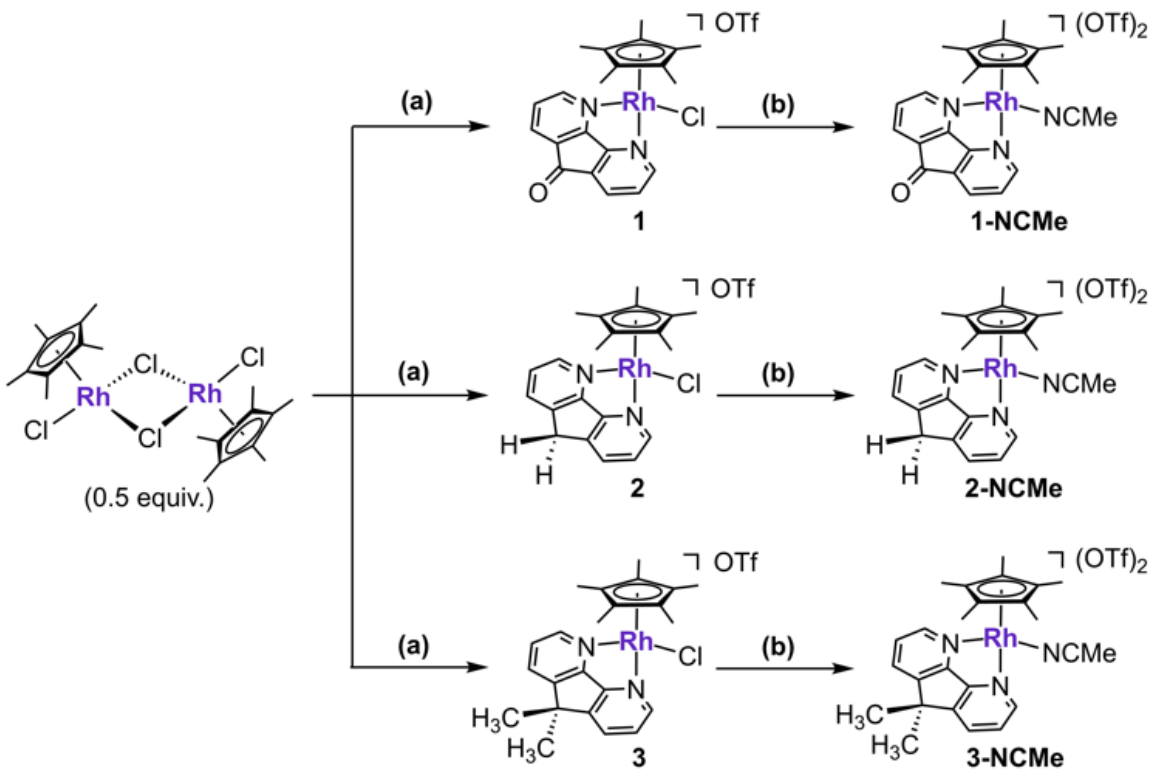

Scheme 3.1: Synthesis of **1**, **2**, **3**, **1-NCMe**, **2-NCMe**, and **3-NCMe**. **(a)** 1. AgOTf (1 equiv.) in MeCN; 2. Appropriate daf-based ligand (1 equiv.) in MeCN, **(b)** AgOTf (1 equiv.) in MeCN.

Nuclear magnetic resonance (NMR) spectroscopic studies revealed that **1**, **2**, and **3** each exhibit C_s symmetry in solution, consistent with κ^2-[*N*,*N*]-coordination of the bidentate ligands and free rotation of [η^5-Cp*]. The spectrum of **2** features a singlet at 4.32 ppm (integrating to 2H), which corresponds to the diastereotopic methylene protons in the daf backbone; the appearance of a singlet for these chemically inequivalent protons is attributable to coincidental magnetic equivalence of the two individual methylene protons. ^{1}H-NMR of **3** confirmed the presence of two diastereotopic methyl groups (both chemically and magnetically inequivalent) appearing as unique singlets that each integrate to 3H at 1.67 and 1.55 ppm. Taken together, these results confirm the expected connectivity of **1**, **2**, and **3** in solution.

In order to enable comprehensive electrochemical work (*vide infra*), acetonitrile-bound complexes **1**-**NCMe**, **2**-**NCMe**, and **3**-**NCMe** were also prepared by addition of 1 equiv. of AgOTf to **1**, **2**, and **3** (see Scheme 3.1 and Experimental Section for details). ^{1}H-NMR spectra confirmed clean generation of the desired solvento species in all cases (see Appendix A, Figures A10-A17). Contrasting with results for **2**, the ^{1}H-NMR spectrum of **2**-**NCMe** features a pair of doublets corresponding to the chemically and magnetically inequivalent diastereotopic methylene protons of the daf backbone. The resonances are reminiscent of those corresponding to the diastereotopic methylene protons of related daf complexes.[36] To confirm our assignment of these resonances, we carried out multifrequency NMR experiments at 400, 500, 600, and 800 MHz that confirm the involvement of second-order effects which are visible in the spectra as "roofing".[37,38] Digital simulations of the field-dependent spectra reproduced the experimental data, confirming our assignment (see Appendix A, Figure A26).

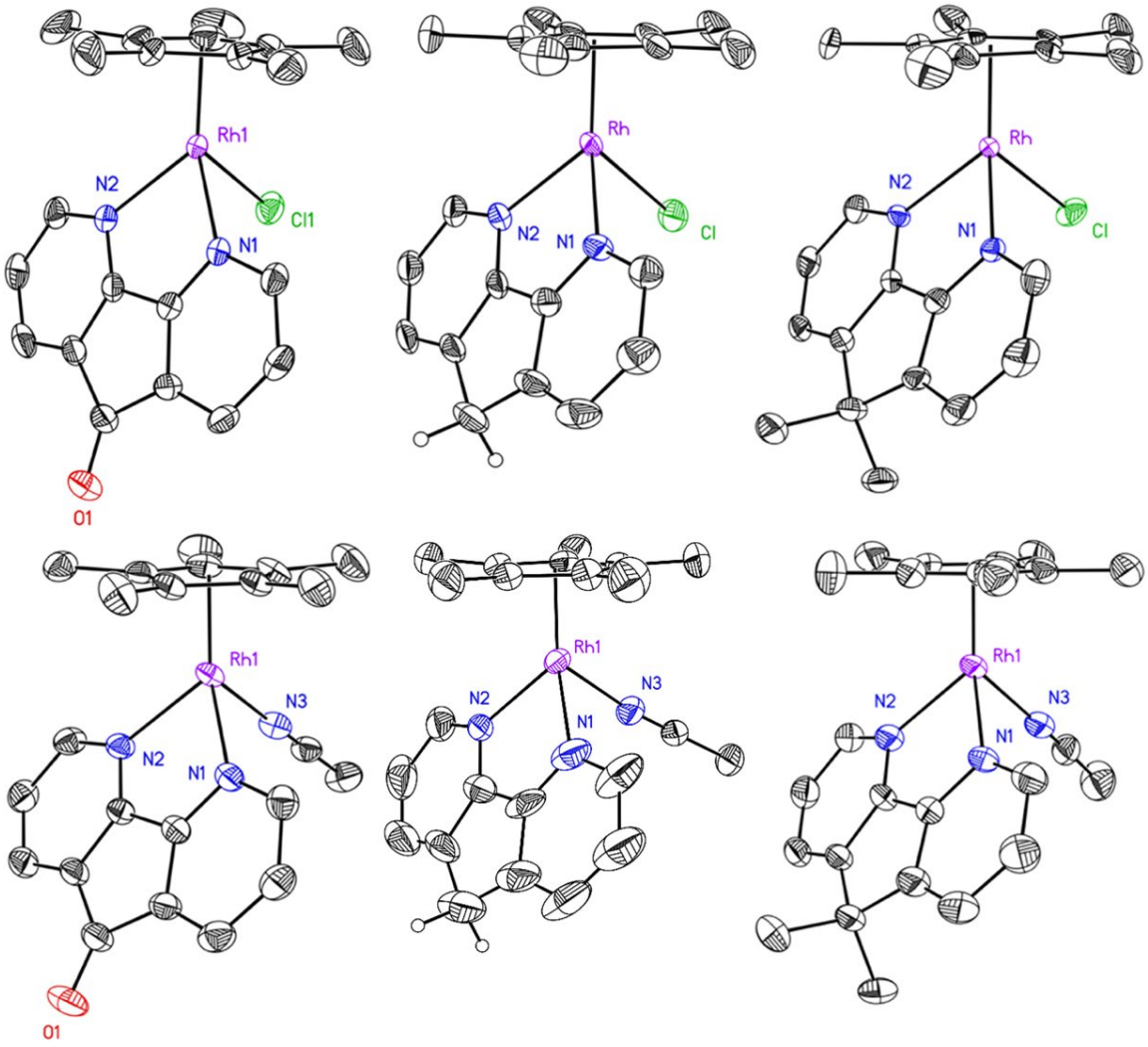

Figure 3.1: Molecular structures of **1** (upper left), **1-NCMe** (lower left), **2** (upper middle), **2-NCMe** (lower middle), **3** (upper right) and **3-NCMe** (lower right). Displacement ellipsoids are shown at the 50% probability level. Hydrogen atoms (except H11A and H11B for **2** and **2-NCMe**), outer sphere triflate counteranions, any co-crystallized solvent molecules, and secondary molecular cations present in the asymmetric units of **1**, **2-NCMe**, and **3-NCMe** are omitted for clarity.

Single crystals of **1**, **2**, **3**, **1-NCMe**, **2-NCMe**, and **3-NCMe** suitable for X-ray diffraction (XRD) analysis were obtained by vapor diffusion of diethyl ether into concentrated MeCN

solutions of the appropriate complex. The resulting structures are the first examples of [Cp*Rh] complexes ligated by dafone, daf, and Me_2daf, and these structures provide a comprehensive basis for the interpretation of the structural properties of the complexes. The coordination geometries about the Rh centers are *pseudo*-octahedral in each case, with η^5-Cp* and κ^2–[*N,N*]-daf-type ligands present in addition to bound chloride (**1**, **2**, and **3**) or acetonitrile (**1-NCMe, 2-NCMe,** and **3-NCMe**) (see Table 3.1, Figure 3.1, and Appendix A, Figures A64-A69). Overall, the Rh–L (where L = Cl or MeCN) and Rh–Cp^*_{cent} distances are similar across the series, consistent with the identical formal oxidation state (+III) of the rhodium centers. The angles formed between the Cp* centroids, the Rh centers, and the centroids of the two nitrogen atoms of the diimine ligands (Cp*–Rh–N*, see Table 3.1) lie in a narrow range of 147–151º for all of the compounds, consistent with the similar steric profiles of all three daf-type ligands studied here.[39]

Table 3.1: Selected bond lengths and angles in complexes **1**, **2**, **3**, **bpy^{Cl}**, **1-NCMe**, **2-NCMe**, **3-NCMe**, and **bpy^{NCMe}**.

Compound	Rh–N1 (Å)	Rh–N2 (Å)	Rh–L (Å)	d_{c-c} (Å) [b]	Rh–Cp^*_{cent} (Å)	∠ N–Rh–N (º)	∠ Cp^*_{cent}–Rh–N′ (º) [c]	Reference
1 [a]	2.202(3), 2.197(3)	2.199(3), 2.197(3)	2.399(1), 2.402(1)	1.445(5), 1.438(5)	1.765, 1.764	80.4(1), 80.2(1)	150.9, 151.5	*This Work*
2	2.185(4)	2.183(4)	2.384(1)	1.422(7)	1.770	80.1(1)	148.0	*This Work*
3	2.202(4)	2.184(4)	2.392(1)	1.424(7)	1.776	80.3(2)	146.0	*This Work*
bpy^{Cl}	2.140(7)	2.140(7)	2.379(3)	1.490(17)	1.774	75.3(4)	147.7	40
1–NCMe	2.200(3)	2.191(2)	2.098(3)	1.441(4)	1.774	80.28(9)	147.0	*This Work*
2–NCMe [a]	2.174(3), 2.184(3)	2.225(3), 2.171(3)	2.101(3), 2.088(3)	1.428(8), 1.416(6)	1.775, 1.778	80.2(1), 81.8(2)	149.9, 149.2	*This Work*
3–NCMe [a]	2.190(6), 2.204(6)	2.188(7), 2.191(6)	2.102(7), 2.088(7)	1.434(11), 1.445(10)	1.768, 1.767	81.2(2), 80.6(2)	150.9, 147.2	*This Work*
bpy^{NCMe} [a]	2.097(2), 2.109(2)	2.104(2), 2.112(2)	2.074(2), 2.066(2)	1.467(3), 1.466(3)	1.780, 1.783	77.09(6), 76.74(7)	146.1, 148.0	41

[a] Values for independent molecular cations in the asymmetric unit cells of the structures are listed. [b] Defined as the distance between the two central carbons interconnecting the two pyridyl-like rings. [c] Refers to the angle between the Cp* ring centroid, Rh center, and the centroid of N1 and N2 within the diimine ligand.

The strained geometries of the 5-membered metallacycles formed by coordination of the daf-type ligands in these complexes can be best understood by comparing the metallacycles present in the analogous structures [Cp*Rh(bpy)Cl]OTf (**bpy^{Cl}**) and [Cp*Rh(bpy)NCMe]PF_6 (**bpy^{NCMe}**).[40,41] In particular, the N1–Rh–N2 bite angles are ca. 5º wider for **1**, **2**, and **3** compared to **bpy^{Cl}** while the N1–Rh–N2 bite angles are ca. 4º wider for **1-NCMe**, **2-NCMe**, and **3-NCMe** compared to **bpy^{NCMe}**. This is attributable to the strained geometry induced by the fused five-membered carbocycles in all of the daf-type complexes. Confirming this situation, the Rh–N1 and Rh–N2 bond lengths are longer than those in the analogous bpy complexes by ca. 0.05–0.10 Å. This suggests an attenuation of the σ-donor power of the daf-type ligands, in that the more rigid structure constrains the flexibility of the ligands upon coordination and elongates the Rh–N distances in comparison to those found in the analogous bpy species.

The presence of the fused five-membered carbocycles in all the daf-type ligands impacts the intraligand bond distances. In particular, the C–C bonds that directly link the pyridyl-like rings of the free dafone, daf, and Me_2daf ligands (denoted as $d_{C–C}$) are similar to the corresponding C–C bonds in bpy (1.485(1), 1.467(2), 1.475(2), and 1.488(1) Å, respectively).[14,28,42,43] However, the $d_{C–C}$ values are smaller for dafone, daf, and Me_2daf upon coordination; as given in Table 3.1, the $d_{C–C}$ values are shorter by ca. 0.07 Å and ca. 0.03 Å for **3** and **3-NCMe**, respectively, in comparison to the analogous bpy complexes.

In order to understand the oxidation states accessible to [Cp*Rh] complexes with daf-type ligands, we carried out electrochemical studies. Initially, we examined the voltammetric properties of **1**, **2**, and **3**, but encountered quasireversible and irreversible reductive waves that are consistent with significant chemical reactivity upon reduction of the starting Rh(III) complexes (see Appendix A, Figures A38, A43, and A47). We hypothesize that the irreversible behaviors result,

in part, from the generation of Rh(II) species by initial electron transfer followed by loss of the daf-type ligands and formation of $[Cp^*RhCl]_2$.[44] Formation of $[Cp^*RhCl]_2$ under reductive conditions is supported by related chemical work with **3** and Cp_2Co. In this chemical work, the presence of $[Cp^*RhCl]_2$ was confirmed by i) ^{1}H-NMR spectra showing a singlet at 1.60 ppm (see Appendix A, Figure A25) and ii) visually with the appearance of a blue-colored solution. Notably, we have previously encountered the generation of $[Cp^*RhCl]_2$ in electrochemical work with chloride-bound complexes supported by dipyridylmethane (dpma) ligands.[45,46] Daf-type ligands resemble dpma ligands in that both feature strained metallacycles that could promote decoordination upon formation of the labile Rh(II) oxidation state in the presence of chloride. In order to avoid this complication driven by chloride ligands, we turned our focus to the electrochemical properties of the solvento complexes.

Electrochemical studies of **1-NCMe**, **2-NCMe**, and **3-NCMe** reveal the rich electrochemical properties of these systems in the absence of complications from chloride (see Figure 3.2, and Appendix A, Figures A39-A41, A44-A46, and A48-A50). Qualitatively, the voltammograms of all three complexes reveal two individual cathodic reduction events in each case, as well as two return anodic oxidation events. This suggests that formally Rh(III), Rh(II), and Rh(I) species are accessible with dafone, daf, and Me_2daf. However, the behavior of **1-NCMe** and **2-NCMe** can be described as quasireversible at best, considering the attenuated anodic currents associated with the re-oxidation of the products of reduction.[47] The diminished currents for the return oxidations indicate that follow-up chemical reactivity ensues after the initial reductions and that the reduced forms thus have limited stability. The instability implied by the voltammetry is consistent, however, with the presence of the ketone moiety in dafone and the methylene group in daf. In the case of dafone, the benzophenone-like core could undergo formation of radical species.[48]

Similarly, the doubly benzylic methylene group in daf is likely to be sufficiently acidic to undergo deprotonation by nascent Rh(I). Two lines of evidence support this reactivity: first, the cyclic voltammogram of **2-NCMe** features a first reduction wave that is significantly more reversible than the second (see Figure 3.2, middle panel and Appendix A, Figure A44-A46); second, chemical reduction experiments suggest that the Rh(I) form of **2-NCMe** is sufficiently basic to deprotonate the starting Rh(III) form (See Appendix A, Figure A71).[17,49]

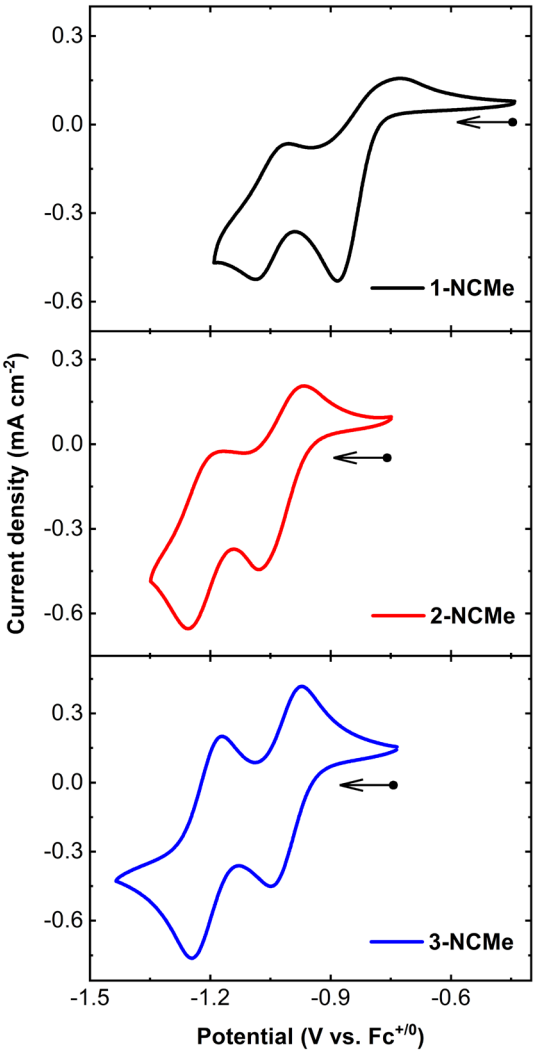

Figure 3.2: Cyclic voltammograms (MeCN, 0.1 M [nBu_4N][PF_6], 100 mV s^{-1}) of **1-NCMe** (upper panel), **2-NCMe** (middle panel), and **3-NCMe** (lower panel).

Contrasting with these results, the cyclic voltammogram of **3-NCMe** reveals that Me_2daf enables clean generation of both Rh(II) and Rh(I) forms of the complex under electrochemical conditions. This conclusion is supported by the chemically reversible nature of the two, sequential $1e^-$ reductions present in the voltammetry (see Figure 3.2, lower panel) as well as related chemical reduction experiments (*vide infra*). Studies at scan rates between 50 and 300 mV/s retain the chemically reversible appearance of the voltammetry, supporting both the stability of the reduced forms as well as the soluble, diffusional nature of all three accessible oxidation states of the compound (see Appendix, Figures A49-A50). Thus, we conclude that use of Me_2daf in place of daf protects the [Cp*Rh] complex from detrimental follow-up reactivity upon reduction.

Returning to the question of the role of chloride in these complexes, we carried out an electrochemical titration of **3-NCMe** with chloride (in the form of NBu_4Cl) in order to track the generation of **3** upon chloride binding. During the CV experiment, increasing equivalents of NBu_4Cl were added to **3-NCMe** resulting in the appearance of irreversible redox events (see Appendix A, Figure A52) that match those encountered in the voltammetry of **3** (see Appendix A, Figure A47). The similar appearance of the voltammetry after the addition of chloride confirms its involvement in promoting the irreversible behavior encountered in the electrochemical studies of **3**. In light of these experiments, **3** can be assigned to undergo a single, net $2e^-$ reduction event in contrast to the two sequential $1e^-$ events measured for **3-NCMe**. This profile is reminiscent of a [Cp*Rh] complex ligated by a hybrid phosphine-imine ligand that our group has studied; this compound displays a net $2e^-$ reduction wave with a chloride ligand present, but two $1e^-$ waves when isolated as a solvento complex.[50] Dipyridylmethane-ligated [Cp*Rh] systems also show net $2e^-$ vs. $1e^-$ chemistry when studied with or without chloride.[46] These findings are overall

consistent with the *in situ* production of **3** over the course of the chloride titration and underscore the broad importance of chloride in the redox chemistry of [Cp*Rh] complexes.

Summarizing, the electrochemical data for **3-NCMe** reveal sequential 1e$^-$ reductions at –1.04 V and –1.25 V vs. the ferrocenium/ferrocene couple (denoted hereafter as $Fc^{+/0}$). Similarly, the data for **2-NCMe** reveal reductions at –1.07 V and –1.25 V. In both cases, the more positive wave can be assigned to reduction of Rh(III) to Rh(II) and the more negative wave can be assigned to reduction of Rh(II) to Rh(I). However, the chemical reversibility of **3-NCMe** appears significantly better than that of **2-NCMe**.

Based on the greater chemical reversibility of electrochemical data for **3-NCMe**, we next moved to generate the Rh(II) and Rh(I) forms of the compound by chemical reduction. We selected cobaltocene (Cp_2Co) for this work based on its reduction potential ($E_{1/2} \approx$ –1.34 V vs. $Fc^{+/0}$),[51] which we anticipated is sufficiently negative to be effective for generation of first Rh(II) and then Rh(I). We performed a spectrochemical titration by treating **3-NCMe** with substoichiometic equivalents of Cp_2Co while monitoring the solution with UV-visible absorption (UV-vis) spectroscopy. The starting spectrum of **3-NCMe** is unremarkable and similar to other Rh(III) species that we have studied,[4,52] with an absorption centered at 373 nm (see Figure 3.3 and see Appendix A, Figures A53-A56). Upon addition of Cp_2Co up to 1 equiv. per Rh, the spectrum changes substantially, with the most obvious difference being the growth of a new band at 716 nm, which corresponds to the Rh^{II} form of **3**. We observe clean 1e$^-$ reduction of **3-NCMe** with isosbestic points at 223, 246, 320, and 349 nm. As the initial concentration of **3-NCMe** and the various concentrations of Cp_2Co were known, we determined the molar absorptivity of the new band at 716 nm to be 3200 M^{-1} cm^{-1} (see Appendix A, Figure A53).

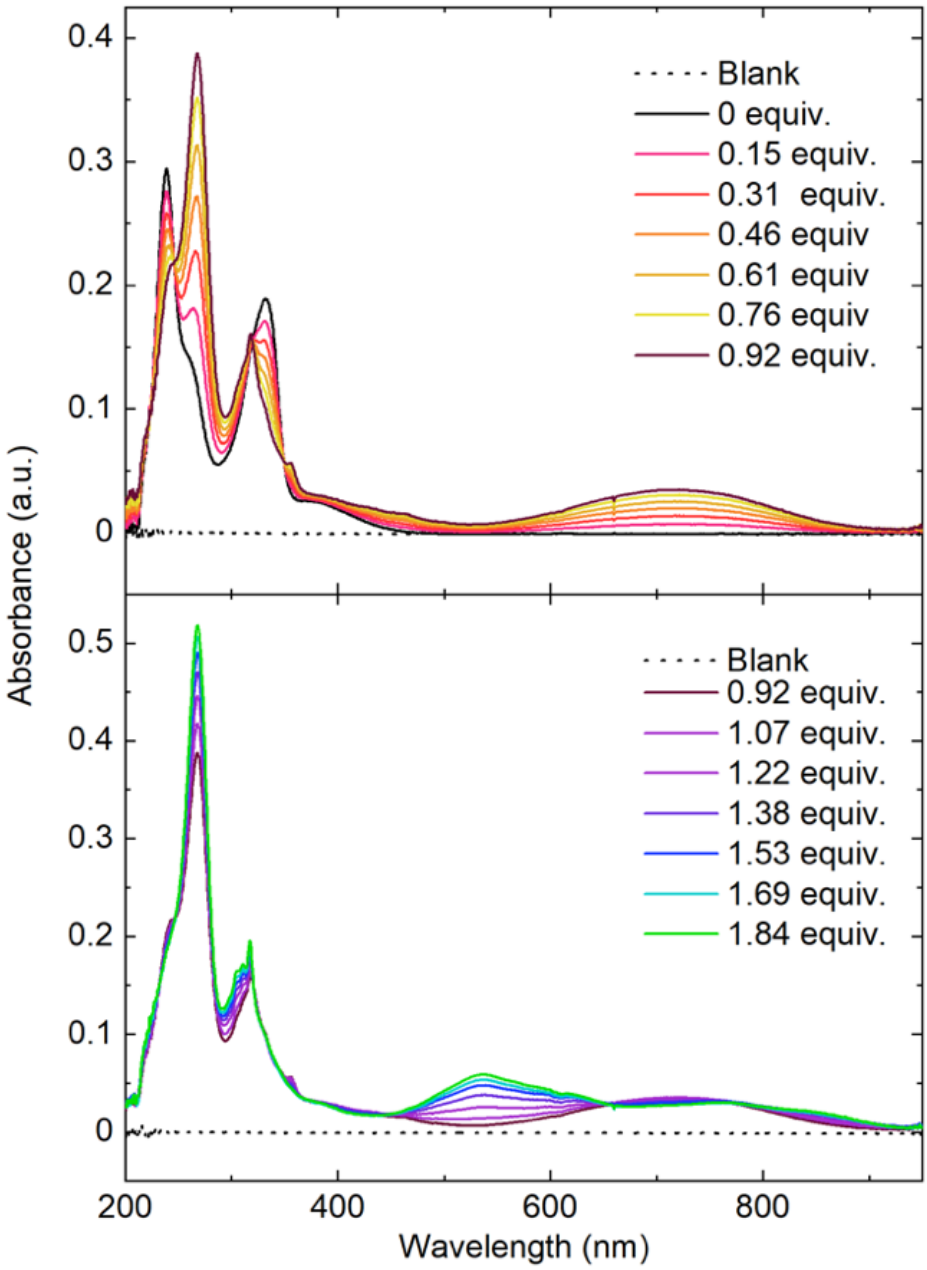

Figure 3.3: Spectrochemical titration of **3-NCMe** using Cp_2Co as a reductant in THF solution. Upper panel: data corresponding to generation of Rh^{II}. Lower panel: data corresponding to generation of Rh^{I}.

Continued additions of Cp_2Co up to 2 equiv. per 1 equiv. of **3-NCMe** resulted in growth of a new feature at 534 nm, as well as sharpening of both shorter and longer wavelength absorption features to reveal apparent vibronic structure. Vibronic bands were observed at 305, 310, and 317 nm in the UV region, similar to bands at 316, 324, and 332 that we observed for the $[Mn^I(CO)_3]$ complex of Me_2daf.[36] Longer wavelength vibronic bands were also observable at 697, 763, and 835 nm. Isosbestic points at 247, 320, and 660 nm in this data are consistent with clean generation of the Rh^I form of **3**, namely Cp*Rh(Me_2daf) (**4**, *vide infra*). This species represents a notable analogue of Cp*Rh(bpy), which features a very similar UV-visible absorption spectrum; Cp*Rh(bpy) displays an absorption at 515 nm as well as longer wavelength features with absorption maxima at ca. 684, 749, and 824 nm (see Appendix A, Figure A37).

Delocalization of electron density from Rh(I) into the bpy ligand in Cp*Rh(bpy) has been discussed in a significant body of prior work; this phenomenon gives rise to the long wavelength absorptions and apparent vibronic features, which are derived from intra-bpy vibrations.[22] Considering the striking similarity between the spectral profiles of Cp*Rh(bpy) and Cp*Rh(Me_2daf) (see Appendix A, Figure A37), significant charge delocalization from the electron-rich rhodium center into the Me_2daf ligand is implicated in the data. In particular, the long wavelength absorptions displaying vibronic structure that likely arises due to intra-Me_2daf vibrations that are not unlike those present in bpy, considering the similar conjugated frameworks of these ligands. Thus, in both these cases, the long wavelength absorption bands are attributable to excitation of electron density present in the ligand π-system into higher-lying ligand π* orbitals. The electron density in question, however, is originally derived from the formally Rh(I) center and is shared via backbonding.

A quantitative comparison of the molar absorptivity values for the [Cp*Rh^{I}] complexes of bpy and Me$_2$daf provides insight into their properties as ligands. The molar absorptivity values for Cp*Rh(Me$_2$daf) were found to be 6,200 M^{-1} cm^{-1} at λ_{max} = 534 nm and 3,100 M^{-1} cm^{-1} at λ_{max} = 763 nm. Cp*Rh(bpy), on the other hand, has corresponding molar absorptivity values of 14,900 M^{-1} cm^{-1} at λ_{max} = 515 nm and 4,400 M^{-1} cm^{-1} at λ_{max} = 749 nm. The more modest values for the Me$_2$daf complex can be attributed to more moderate delocalization of electron density from the formally Rh(I) center in Cp*Rh(Me$_2$daf) into the Me$_2$daf framework. The decreased population of the Me$_2$daf-centered π* orbitals would lead to diminished intensities for these longer wavelength features in the absorption spectrum. These findings suggest that Me$_2$daf is a weaker π-acceptor than bpy, and provide evidence for similar charge delocalization behaviors for both bpy and its less commonly studied analogue Me$_2$daf. Confirming this theory, the Rh^{III}/Rh^{I} reduction potential of **3** is –1.25 V, approximately, while the value for Cp*Rh(bpy) is –1.05 V.[53]

Characterization of the Rh^{II} form of **3-NCMe** by X-band electron paramagnetic resonance spectroscopy confirms the redox scheme described above. An *in situ* reduction experiment was carried out in which **3-NCMe** was treated with 1.0 equiv. of Cp$_2$Co in THF, resulting in a color change from yellow to green. The green solution was then loaded into a quartz EPR tube and frozen in liquid nitrogen for transport to the spectrometer. EPR at 7 K revealed a broad rhombic signal near g = 2 (see Appendix A, Figure A57) that lacks signals corresponding to Cp$_2$Co.[52] The EPR spectrum for the *in situ* reduced sample of **3-NCMe** could be satisfactorily modelled as a two-component mixture with the EasySpin simulation package.[54] The two components, labelled as **A** and **B** are present in an apparent ratio of 2:1, both display rhombic signals (**A:** g_x = 2.15, g_y = 2.03, g_z = 1.94; **B:** g_x = 2.08, g_y = 2.02, g_z = 2.00). These overlapping signals are consistent with Rh^{II} radicals in both cases, resembling prior EPR spectra that we have obtained for [Cp*Rh^{II}]

complexes. We anticipate that **A** and **B** correspond to the MeCN-bound (19e$^-$) and MeCN-free (17e$^-$) species, consistent with observations from prior work.[45,46]

To complement this characterization of the Rh(II) form of **3-NCMe**, we next pursued chemical reduction of **3-NCMe** by treatment with 10 equiv. of Na(Hg). This experiment enabled us to isolate the 2e$^-$ reduced form, Cp*Rh(Me$_2$daf) (**4**; see Experimental Section). Like its counterpart Cp*Rh(bpy), **4** is intensely colored and appears purple in THF solution. However, unlike Cp*Rh(bpy), **4** could only be isolated from this synthetic procedure with minor aromatic and aliphatic impurities (see Appendix A, Figure A18-A20). Despite these slight impurities, ^{1}H NMR reveals that **4** exhibits C_{2v} symmetry in solution, including two singlets in the aliphatic region at 2.00 and 1.16 ppm that integrate to 15H and 6H, respectively, and correspond to the 15 equivalent methyl protons of the Cp* ligand and 6 equivalent methyl protons of the κ^2-Me$_2$daf ligand. The magnetic equivalence of the methyl protons of Me$_2$daf in **4** suggests that this compound adopts a "T-shaped" geometry.

Single-crystal X-ray diffraction (XRD) analysis confirmed this expectation. Crystals suitable for XRD analysis were grown from a hexane solution of **4** cooled to –35 ºC. The solid-state structure (see Figure 3.4) reveals that **4** is rigorously C_{2v} symmetric, featuring the expected η^5-Cp* and κ^2-Me$_2$daf ligands around the metal center. **4** is much more electron-rich than **3-NCMe**, as observed by the elongated Rh–Cp*$_{cent}$ distance (1.829 Å in **4** vs. 1.768 Å in **3-NCMe**; see Tables 3.1 and 3.2). Consistent with the greater electron-richness of the metal center, the Rh–N distances are shorter in **4** compared to those in **3-NCMe** by approximately 0.13 Å, a finding that supports a role for π-backbonding into the Me$_2$daf ligand of this complex.

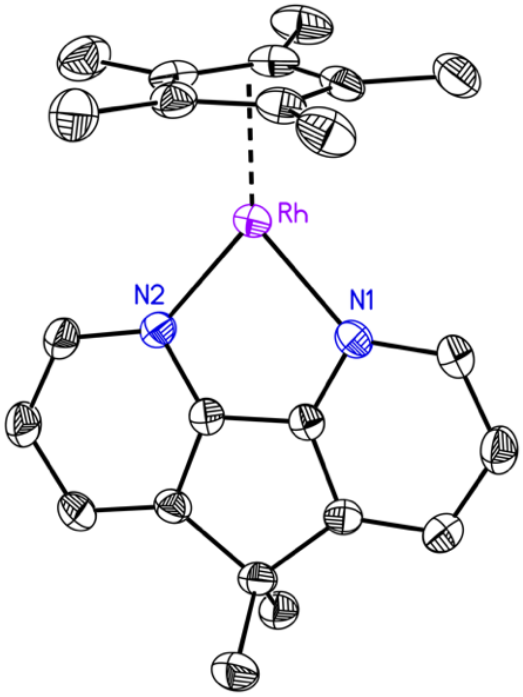

Figure 3.4: Solid-state structure of **4**. Displacement ellipsoids are shown at the 50% probability level. Hydrogen atoms are omitted for clarity.

Table 3.2: Selected bond lengths and angles in complexes **4,** Cp*Rh(bpy), and CpRh(bpy).

Bond Metrics	4	Cp*Rh(bpy)	CpRh(bpy)
Rh–N1 (Å)	2.064(2)	2.00(3)	1.993(2)
Rh–N2 (Å)	2.064(2)	2.005(2)	1.990(3)
d_{c-c} (Å) [a]	1.393(3)	1.422(4)	1.441(3)
Rh–Cp*$_{cent}$ (Å)	1.829	1.847	1.868 [b]
∠ N–Rh–N (°)	82.03(8)	78.2(1)	78.76(8)
∠ Cp*–Rh–N′ (°) [c]	176.4	177.3	177.1

[a] Defined as the distance between the two central carbons interconnecting the two pyridyl-like rings. [b] Note, this is for the cyclopentadienyl (Cp) complex and not for the Cp* analogue. [c] Refers to the angle between the Cp* or Cp ring centroid, Rh center, and the centroid of N1 and N2 within the diimine ligand.

Examination of the intraligand C–C bonds of the Me_2daf ligand in **4** provides evidence for charge delocalization. This conclusion can be drawn on the basis of similar prior findings for bpy-based ligands, in that both Cp*Rh(bpy)[40] and CpRh(bpy) (where Cp is cyclopentadienyl)[55] display partially reduced ligand character that can be inferred from changes in their intraligand C–C bonds. Table 3.2 provides selected bond lengths and angles, and Figure 3.5 provides a full comparison of the intraligand bond lengths in the diimine ligands in these complexes. In particular, reduced bpy character has been shown to result in a pronounced contraction of the C–C bond that links the two pyridyl rings of bpy (denoted here as $d_{C–C}$), a phenomenon attributable to occupation of the lowest-energy unoccupied π* orbital of bpy.[28] Occupation of the bpy LUMO contributes to the double bond character observed for $d_{C–C}$ and can be visualized with a combination of Hückel MO theory and solid-state structural data (see Table 3.2).[56] As the conjugated frameworks of Me_2daf and bpy are similar, Me_2daf can be seen on the basis of the structural data in Figure 3.5 to also be capable of stabilizing electron-rich Rh(I) centers via charge delocalization. **4** displays a marked contraction of the $d_{C–C}$ bond (1.393(3) Å) in comparison to that in **3-NCMe** (1.434(1)/1.445(10) Å), providing structural evidence that Me_2daf is able to stabilize low-valent metal centers via bonding motifs similar to those found in complexes supported by workhorse bipyridyl-type ligands. Notably, the value of $d_{C–C}$ is significantly shorter in **4** than in its bipyridyl analogues (see Table 3.2 and Figure 3.5); this is attributable to the simultaneous influence of π-backbonding from the electron-rich metal as well as the presence of the additional five-membered fused carbocycle resulting from inclusion of the dimethylmethylene group of Me_2daf.

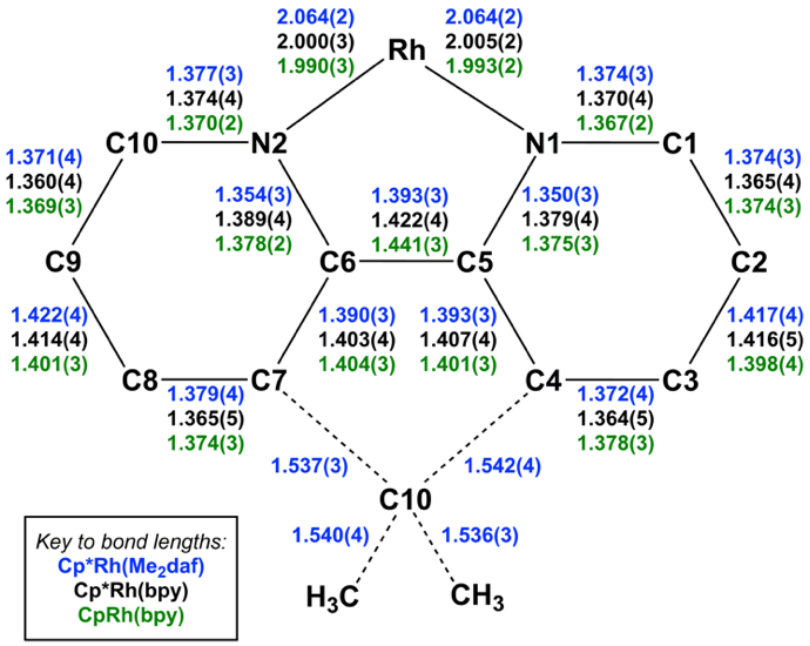

Figure 3.5: Comparison of intraligand bond lengths for Cp*Rh(Me$_2$daf) (**4**, blue), Cp*Rh(bpy) (black), and CpRh(bpy) (green).

Considering the established structural and electronic similarities between Me$_2$daf and bpy, we wondered if a monohydride complex or [η^4-Cp*H]-bound species would be preferred for the case of the Me$_2$daf system. Addition of weak acids to Cp*Rh(bpy) has recently been shown to result in generation of [η^4-Cp*H]-bound complexes rather than the expected analogous rhodium monohydrides.[53, 57, 58] To test this, **3** was exposed to 1.0 equiv. of sodium formate in d_3-MeCN, resulting in a gradual color change from orange to red-brown. ^{1}H NMR revealed a spectrum consistent with the generation of [(η^4-Cp*H)Rh(Me$_2$daf)]$^+$ (see Appendix A, Figures A21-A23), a species that displays the hallmark resonances indicating proton transfer to the η^5-Cp* ligand of **3**. In particular, a quartet at 2.44 ppm (1H, $^4J_{H,H}$ = 6.2 Hz) and a doublet at 0.55 ppm (3H, $^4J_{H,H}$ = 6.2 Hz) confirm the generation of the η^4-Cp*H ligand, which presumably forms through binding of formate to Rh(III), β-hydride elimination and extrusion of CO_2, and proton-hydride

tautomerization.[57] Me_2daf can thus be additionally concluded to engender similar reactivity to [Cp*Rh] complexes in comparison to those supported by bipyridyl-type ligands.

3.3 Conclusion

Here, we have described the synthesis and characterization of a new series of [Cp*Rh] complexes supported by diazafluorene-type ligands. On the basis of structural, spectroscopic, and electrochemical evidence, 9,9′-dimethyl-4,5-diazafluorene (Me_2daf) can be concluded to be able to stabilize low-valent complexes through charge delocalization and π-backbonding that is reminiscent of behavior more commonly encountered with complexes of 2,2′-bipyridyl and its analogues. In this work, a comprehensive set of solid-state structures from X-ray diffraction analysis has been used to highlight the bond lengths and angles that distinguish diazafluorene complexes from their more common analogues. On the basis of clean electrochemical behavior for the [Cp*Rh] species supported by Me_2daf, a spectrochemical titration was carried out with Cp_2Co that revealed the unique spectroscopic signatures of Rh(III), Rh(II), and Rh(I) supported by Me_2daf. The charge delocalization implied by the spectroscopic results for Cp*Rh(Me_2daf) was confirmed by related X-ray diffraction analysis for this compound, which showed changes in the intra-Me_2daf framework consistent with sharing of electron density from the [Cp^*Rh^I] core into the LUMO of Me_2daf via π-backbonding. Use of Me_2daf in place of dafone or daf avoids detrimental reactivity under highly reducing conditions and, thus, Me_2daf can be concluded to be a useful new ligand for use in reductive chemistry and electrochemistry.

3.4 Experimental Section

3.4.1 General considerations

All manipulations were carried out in dry N_2-filled gloveboxes (Vacuum Atmospheres Co., Hawthorne, CA, USA) or under an N_2 atmosphere using standard Schlenk techniques unless otherwise noted. All solvents were of commercial grade and dried over activated alumina using a PPT Glass Contour (Nashua, NH, USA) solvent purification system prior to use, and were stored over molecular sieves. All chemicals were obtained from major commercial suppliers and used as received after extensive drying. Rhodium chloride hydrate (Pressure Chemical Co.) and 1,10-phenanthroline (95%; Matrix Scientific) were used as received. $[Cp^*RhCl_2]_2$,[34,35] 4,5-diazafluorene-9-one,[9] 4,5-dizafluorene,[9] and 9,9′-dimethyldiazafluorene[31] were prepared according to literature methods with minor modifications. Detailed synthetic procedures for the preparation of dafone, daf, and Me_2daf are given in the Supporting Information (see Appendix A, Figures A78-A80). $[Cp^*RhCl_2]_2$, silver hexafluorophosphate (98%, Alfa Aesar), mercury, sodium, and cobaltocene were dried extensively at 1 mTorr (133 Pa) for 24 hours using standard Schlenk techniques before being brought into a dry N_2-filled glovebox.

3.4.2 Synthesis

General Procedure for the Synthesis of 1, 2, and 3: To a 20 mL scintillation vial equipped with a Teflon stir bar, 1 equiv. of $[Cp^*RhCl_2]_2$ was dissolved in MeCN (ca. 4mL) to give a deep red suspension. To this suspension, 2 equiv. of AgOTf in MeCN (ca. 2 mL) was added, resulting in a lightening of the red solution to orange, and formation of AgCl as a precipitate. The solution was allowed to stir for 10 min. Then 2.1 equiv. of the appropriate diazafluorene-based ligand was added to the orange solution and was allowed to stir for 20 minutes. The AgCl was then filtered off and the resulting yellow solution was placed in a beaker. Next, a large excess of diethyl ether (ca. 80 mL) was added, causing precipitation of the desired product. The yellow solid was then filtered

and washed with diethyl ether. The material was purified by recrystallization through vapor diffusion of diethyl ether into a concentrated solution of the compound in MeCN. The resulting red crystals were washed with diethyl ether to afford the title compound.

Synthesis of [(η^5-C_5Me_5)Rh(4,5-diazafluorene-9-one)Cl](OTf) (1): Yield: 0.3073 g (63 %). ^{1}H NMR (500 MHz, CD_3CN): δ = 8.83 (d, 2H, $^3J_{H,H}$ = 5.5 Hz), 8.26 (d, 2H, $^3J_{H,H}$ = 7.5 Hz), 7.82 (dd, 2H, $^3J_{H,H}$ = 7.5 Hz, $^4J_{H,H}$ = 5.5 Hz), 1.76 ppm (s, 15H). $^{13}C\{^1H\}$ NMR (126 MHz, CD3CN): δ = 186.69, 165.23, 154.14, 135.96, 130.96, 130.85, 97.77 (d, $^1J_{C,Rh}$ = 9.0 Hz, Cp*), 9.60 ppm. ^{19}F NMR (471 MHz, CD_3CN): δ = -80.19 ppm. Electronic absorption spectrum (MeCN): 247 (22000), 307 (7100), 313 (6700), 320 (8000), 382 nm (1969 M^{-1} cm^{-1}) ESI-MS (positive) found m/z: 455.0389 (100%) (**1** – OTf^-), 456.0459 (6%), 457.0396 (14%), 458.0471 (1%). Anal. Calcd. for $C_{22}H_{21}ClF_3N_2O_4RhS$: C, 43.69; H, 3.50; N, 4.63. Found: C, 43.69; H, 3.35; N, 4.87.

Synthesis of [(η^5-C_5Me_5)Rh(4,5-diazafluorene)Cl](OTf) (2): Yield: 0.3044 g (80%). ^{1}H NMR (500 MHz, CD_3CN): δ = 8.72 (d, 2H, $^3J_{H,H}$ = 5.4 Hz), 8.25 (d, 2H, $^3J_{H,H}$ = 7.7 Hz), 7.73 (dd, 2H, $^3J_{H,H}$ = 7.7 Hz, $^4J_{H,H}$ = 5.4 Hz), 4.32 (s, 2H) 1.74 ppm (s, 15H). $^{13}C\{^1H\}$ NMR (126 MHz, CD_3CN): δ = 161.48, 148.79, 138.61, 137.62, 127.98, 97.14 (d, $^1J_{C,Rh}$ = 9.0 Hz, Cp*), 37.51, 9.52 ppm. ^{19}F NMR (471 MHz, CD_3CN): δ = -80.19 ppm. Electronic absorption spectrum (MeCN): 242 (19000), 315 (17000), 325 (18000), 391 nm (1557 M^{-1} cm^{-1}. ESI-MS (positive) found m/z: 441.0605 (100%) (**2** – OTf^-), 442.0679 (9%), 443.0600 (12%), 444.0689 (2%). Anal. Calcd. for $C_{22}H_{23}ClF_3N_2O_3RhS$: C, 44.72; H, 3.92; N, 4.74. Found: C, 44.77; H, 3.86; N, 4.87.

Synthesis of [(η^5-C_5Me_5)Rh(9,9′-dimethyl-4,5-diazafluorene)Cl](OTf) (3): Yield: 0.6763 g (85 %). ^{1}H NMR(500 MHz, CD_3CN): δ = 8.68 (d, 2H, $^3J_{H,H}$ = 5.4 Hz), 8.20 (d, 2H, $^3J_{H,H}$ = 7.7 Hz), 7.72 (d, 2H, $^3J_{H,H}$ = 7.7 Hz $^4J_{H,H}$ = 5.4 Hz), 1.75 (s, 15H), 1.67 (s, 3H), 1.55 ppm (s, 3H). $^{13}C\{^1H\}$

NMR (126 MHz, CD_3CN): δ = 159.49, 149.01, 148.05, 135.18, 128.57, 97.17 (d, $^1J_{C,Rh}$ = 9.1 Hz, Cp*), 51.82, 24.94, 24.44, 9.54 ppm. ^{19}F NMR (471 MHz, CD_3CN): δ = -80.18 ppm. Electronic absorption spectrum (MeCN):241 (18000), 319 (17000), 328 (18000), 389 nm (1570 M^{-1} cm^{-1}). ESI-MS (positive) found m/z: 469.0911 (100%) (**3** – OTf^-), 470.0975 (10%), 471.1101 (25%), 472.1255 (3%). Anal. Calcd. for $C_{24}H_{27}ClF_3N_2O_3RhS$ + 0.5 H_2O: C, 45.91; H, 4.49; N, 4.46. Found: C, 45.77; H, 4.42; N, 4.63.

General Procedure for the Synthesis of 1-NCMe, 2-NCMe, and 3-NCMe: To a solution of 1 equiv. of **1**, **2** or **3** in MeCN (ca. 5 mL) was added 1.1 equiv. of AgOTf dissolved in MeCN. The 20 mL scintillation vial was then sealed, covered with aluminum foil, and allowed to stir for 48 hrs. in the dark. Following completion, the precipitated silver chloride is filtered off and the solution is pumped to dryness. The resulting solid is transferred to a frit and washed with THF (ca. 20 mL) to remove any excess AgOTf to obtain the title compound as a yellow powder.

Synthesis of [(η^5-C_5Me_5)Rh(4,5-diazafluorene-9-one)(NCMe)](OTf) (1-NCMe): Yield: 0.0548 g (47%). ^1H NMR (400 MHz, CD_3CN): δ = 8.90 (dd, 2H, $^3J_{H,H}$ = 5.6 Hz, $^4J_{H,H}$ = 1.0 Hz), 8.36 (dd, 2H, $^3J_{H,H}$ = 7.6 Hz, $^4J_{H,H}$ = 1.0 Hz), 7.92 (dd, 2H, $^3J_{H,H}$ = 7.6 Hz, $^4J_{H,H}$ = 5.6 Hz), 1.96 (s, 3H), 1.79 ppm (s, 15H). ^{19}F NMR (376 MHz, CD_3CN): δ = -80.19 ppm.

Synthesis of [(η^5-C_5Me_5)Rh(4,5-diazafluorene)(NCMe)](OTf) (2-NCMe): Yield: 0.1307 g (83%). ^1H NMR (400 MHz, CD_3CN): δ = 8.77 (dd, 2H, $^3J_{H,H}$ = 5.5 Hz, $^4J_{H,H}$ = 0.9 Hz), 8.35 (dd, 2H, $^3J_{H,H}$ = 7.7 Hz, $^4J_{H,H}$ = 0.9 Hz), 7.82 (dd, 2H, $^3J_{H,H}$ = 7.7 Hz, $^4J_{H,H}$ = 5.5 Hz), 4.40 (d, 1H, $^3J_{H,H}$ = 21.1 Hz), 4.33 (d, 1H, $^3J_{H,H}$ = 21.1 Hz), 1.96 (s, 3H), 1.77 ppm (s, 15H). $^{13}C\{^1H\}$ NMR (126 MHz, CD_3CN): δ = 162.05, 149.29, 139.23, 138.69, 128.61, 123.39, 120.84, 100.30 (d, $^1J_{C,Rh}$ = 8.9 Hz, Cp*), 37.89, 9.60 ppm. ^{19}F NMR (376 MHz, CD_3CN): δ = -80.20 ppm.

Synthesis of [(η^5-C_5Me_5)Rh(9,9′-dimethyl-4,5-diazafluorene)(NCMe)](OTf) (3-NCMe): Yield: 0.2475 g (66%). ^{1}H NMR (400 MHz, CD_3CN): δ = 8.73 ((dd, 2H, $^3J_{H,H}$ = 5.5 Hz, $^4J_{H,H}$ = 1.0 Hz), 8.30 (dd, 2H, $^3J_{H,H}$ = 7.7 Hz, $^4J_{H,H}$ = 1.0 Hz), 7.82 (dd, 2H, $^3J_{H,H}$ = 7.7 Hz, $^4J_{H,H}$ = 5.5 Hz), 1.96 (s, 3H), 1.77 (s, 15H), 1.69 (s, 3H), 1.62 (s, 3H). $^{13}C\{^1H\}$ NMR (126 MHz, CD_3CN): δ = 159.54, 149.21, 148.23, 136.05, 128.94, 123.04, 120.49, 99.99 (d, $^1J_{C,Rh}$ = 8.9 Hz, Cp*), 52.07, 24.11, 23.92, 9.26 ppm. ^{19}F NMR (376 MHz, CD_3CN): δ = -80.19 ppm.

Synthesis of (η^5-C_5Me_5)Rh(9,9′-dimethyl-4,5-diazafluorene) (4): A suspension of **3-NCMe** (0.0250 g, 0.032 mmol) in THF (ca. 2 mL) was added to a 20 mL scintillation vial containing 1% Na(Hg) (0.0074 g, 0.322 mmol Na, ca. 10 equiv.). The yellow suspension slowly darkened to an intense green color, which subsided to a dark purple color over a 24 h period while stirring. The reaction mixture was filtered to remove Hg and NaOTf. THF was then removed in vacuo and the resulting solid was extracted with hexanes (ca. 10 mL), followed by diethyl ether, to obtain the title product as a dark solid. Yield 0.0112 g (80%). ^{1}H NMR (500 MHz, C_6D_6): δ = 8.74 (d, 2H, $^3J_{H,H}$ = 6.1 Hz), 6.90 (d, 2H, $^3J_{H,H}$ = 6.6 Hz), 6.60 (t, 2H, $^3J_{H,H}$ = 6.3 Hz), 2.00 (s, 15H), 1.16 ppm (s, 6H). $^{13}C\{^1H\}$ NMR (126 MHz, C_6D_6): δ = 149.65, 147.84, 145.62, 118.74, 111.15, 87.10 (d, $^1J_{C,Rh}$ = 7.3 Hz, Cp*), 50.86, 24.85, 10.39 ppm.

3.4.4 Spectroscopy and Characterization

Deuterated solvents for NMR studies were purchased from Cambridge Isotope Laboratories (Tewksbury, MA, USA); CD_3CN was dried with CaH_2 and stored over molecular sieves and C_6D_6 was dried over sodium/benzophenone. ^{1}H, ^{13}C, and ^{19}F spectra were collected with 400, 500, 600, or 800 MHz Bruker spectrometers. Spectra were referenced to the residual protio-solvent signal[59] in the cases of ^{1}H and ^{13}C. Heteronuclear NMR spectra were referenced to the appropriate external

standard following the recommended scale based on ratios of absolute frequencies (Ξ).[60] ^{19}F NMR spectra are reported relative to CCl_3F. Chemical shifts (δ) and coupling constants (*J*) are reported in Hz. Simulations of NMR spectra were carried out using the Advanced Spin Simulation program in MestReNova (Mestrelab Research, chemistry software solutions).

Experimental mass spectrometry data was collected on a LCT Premier mass spectrometer equipped with a quadrupole, time-of-flight mass analyzer, and an electrospray ion source. Predicted mass spectrometry data was obtained from PerkinElmer Informatics' ChemDraw Professional Suite. Electronic absorption spectra were collected with an Ocean Optics Flame spectrometer equipped with a DH-Mini light source (Ocean Optics, Largo, FL, USA) using a quartz cuvette. Elemental analyses were performed by Midwest Microlab, Inc. (Indianapolis, IN). Elemental analysis could not be obtained for **1**-**NCMe**, **2**-**NCMe**, **3**-**NCMe**, and **4** because of their acute air sensitivity. Continuous-wave electron paramagnetic resonance spectra were collected at X-band with a Bruker EMX spectrometer using a high-sensitivity perpendicular-mode cavity (4119HS-W1). Temperature control was achieved with an Oxford ESR 900 flow-through cryostat. Simulation of continuous-wave electron paramagnetic spectra were carried out using the EasySpin[54] package in MATLAB.

3.4.5 X-ray Crystallography

Single crystals of complexes **1**, **2**, **3**, **1**-**NCMe**, **2**-**NCMe**, **3**-**NCMe**, **1**-**PF_6,** and **3**-**NCMePF_6** were obtained by vapor diffusion of diethyl ether into a concentrated acetonitrile solution of the appropriate complex. Single crystals of **4** were obtained by slow cooling a concentrated solution of the species in hexanes. Single crystals of **2**-**red** were obtained by vapor diffusion of pentane into a concentrated solution of the species in THF. Single crystals of **Bn_3daf** were obtained by

vapor diffusion of pentane into a concentrated solution of the species in $CHCl_3$. Single-crystal X-ray diffraction data were collected with a Bruker Proteum diffractometer equipped with two CCD detectors (Apex II and Platinum 135) sharing a common MicroStar microfocus Cu rotating anode generator running at 45 mA and 60 kV (Cu Kα = 1.54178 A).

3.4.6 Deposition Numbers

2038430 (for **Bn_3daf**), 2038431 (for **1-NCMe**), 2038432 (for **1**), 2038433 (for **3-NCMePF_6**), 2038434 (for **2**), 2038435 (for **2-red**), 2038436 (for **1-PF_6**), 2038437 (for **4**), 2038438 (for **2-NCMe**), 2038439 (for **3**), 2038440 (for **3-NCMe**) contain the supplementary crystallographic data for this paper. These data are provided free of charge by the joint Cambridge Crystallographic Data Centre and Fachinformationszentrum Karlsruhe Access Structures service.

3.4.7 Electrochemistry

Electrochemical experiments were carried out in a nitrogen-filled glove box. Tetra(n-butylammonium) hexafluorophosphate (0.10 M; Sigma-Aldrich; electrochemical grade) in acetonitrile served as the supporting electrolyte. Measurements were made with a Gamry Reference 600 Plus Potentiostat/ Galvanostat using a standard three-electrode configuration. The working electrode was the basal plane of highly oriented pyrolytic graphite (HOPG, GraphiteStore.com, Buffalo Grove, Ill.; surface area: 0.09 cm^2), the counter electrode was a platinum wire (Kurt J. Lesker, Jefferson Hills, PA; 99.99%, 0.5 mm diameter), and a silver wire immersed in electrolyte served as a pseudo-reference electrode (CH Instruments). The reference was separated from the working solution by a Vycor frit (Bioanalytical Systems, Inc.). Ferrocene (Sigma Aldrich; twice-sublimed) was added to the electrolyte solution at the conclusion of each

experiment (~1 mM); the midpoint potential of the ferrocenium/ferrocene couple (denoted as $Fc^{+/0}$) served as an external standard for comparison of the recorded potentials. Concentrations of analyte for cyclic voltammetry were typically 2 mM.

3.5 Acknowledgements

The authors thank Justin Douglas and Sarah Neuenswander for assistance with NMR and EPR spectroscopy. This work was supported by the US National Science Foundation through award OIA-1833087. W.C.H. was supported by the US National Institutes of Health Graduate Training Program in the Dynamic Aspects of Chemical Biology (T32 GM008545-25) as well as by a Graduate Student Research Grant from the Kansas Academy of Science. J.P.S. was supported by the Beckman Scholars Program at the University of Kansas, funded by the Arnold & Mabel Beckman Foundation. Support for NMR instrumentation was provided by the NIH (S10OD016360, S10RR024664) and NSF (CHE-1625923), and support for EPR instrumentation was provided by the NSF (CHE-0946883).

3.6 References

(1) a) T. R. O'Toole, L. D. Margerum, T. D. Westmoreland, W. J. Vining, R. W. Murray and T. J. Meyer, *J. Chem. Soc., Chem Commun.* **1985**, 1416-1417. b) B. P. Sullivan, C. M. Bolinger, D. Conrad, W. J. Vining and T. J. Meyer, *J. Chem. Soc., Chem Commun.***1985**, 1414-1416. c) D. V. Yandulov and R. R. Schrock, *Science* **2003**, *301*, 76. d) J. S. Anderson, J. Rittle and J. C. Peters, *Nature* **2013**, *501*, 84.

(2) a) U. Kölle, M. Grätzel, *Angew. Chem.* **1987**, *99*, 572-574; b) U. Kölle, M. Grätzel, *Angew. Chem. Int. Ed. Engl.* **1987**, *26*, 567-570.

(3) a) M. Bourrez, F. Molton, S. Chardon-Noblat and A. Deronzier, *Angew. Chem. Int. Ed.* **2011**, *50*, 9903-9906. b) M. L. Clark, P. L. Cheung, M. Lessio, E. A. Carter and C. P. Kubiak, *ACS Catal.* **2018**, *8*, 2021-2029.

(4) W. C. Henke, D. Lionetti, W. N. G. Moore, J. A. Hopkins, V. W. Day and J. D. Blakemore, *ChemSusChem* **2017**, *10*, 4589-4598.

(5) (a) W. Kaim and B. Schwederski, *Coord. Chem. Rev.* **2010**, *254*, 1580-1588. (b) V. Lyaskovskyy and B. de Bruin, *ACS Catal.* **2012**, *2*, 270-279.

(6) a) C. P. Anderson, D. J. Salmon, T. J. Meyer and R. C. Young, *J. Am. Chem. Soc.* **1977**, *99*, 1980-1982. b) G. F. Strouse, J. R. Schoonover, R. Duesing, S. Boyde, W. E. Jones, Jr., T. J. Meyer, *Inorg. Chem.* **1995**, *34*, 473-487. c) H. Takeda, K. Koike, H. Inoue and O. Ishitani, *J. Am. Chem. Soc.* **2008**, *130*, 2023-2031. d) H. Takeda, K. Koike, T. Morimoto, H. Inumaru and O. Ishitani in *Photochemistry and photocatalysis of rhenium(I) diimine complexes*, *Vol. 63* Eds.: R. v. Eldik and G. Stochel), Academic Press, **2011**, pp. 137-186. e) J. England, C. C.

Scarborough, T. Weyhermüller, S. Sproules and K. Wieghardt, *Eur. J. Inorg. Chem.* **2012**, *2012*, 4605-4621.

(7) F. Blau, *Monatsh. Chem.* **1889**, 10, 375-388.

(8) C. Kaes, A. Katz and M. W. Hosseini, *Chem. Rev.* **2000**, *100*, 3553-3590.

(9) J. Druey and P. Schmidt, *Helv. Chim. Acta* **1950**, *33*, 1080-1087.

(10) L. J. Henderson, F. R. Fronczek and W. R. Cherry, *J. Am. Chem. Soc.* **1984**, *106*, 5876-5879.

(11) V. T. Annibale, R. Batcup, T. Bai, S. J. Hughes and D. Song, *Organometallics* **2013**, *32*, 6511-6521.

(12) a) H.-j. Pang, J.-q. Sha, J. Peng, A.-x. Tian, C.-j. Zhang, P.-p. Zhang, Y. Chen, M. Zhu and Y.-h. Wang, *Inorg. Chem. Commun.* **2009**, *12*, 735-738. b) H.-j. Pang, C.-j. Zhang, J. Peng, Y.-h. Wang, J.-q. Sha, A.-x. Tian, P.-p. Zhang, Y. Chen, M. Zhu and Z.-m. Su, *Eur. J. Inorg. Chem.* **2009**, *2009*, 5175-5180.

(13) a) W. Wong, *Coord. Chem. Rev.,* 2005, *249*, 971–997. b) K. Ono and K. Saito, *Heterocycles*, **2008**, *75*, 2381–2413. c) V. T. Annibale and D. Song, *Dalton Trans.*, **2016**, *45*, 32-49.

(14) P. B. White, J. N. Jaworski, C. G. Fry, B. S. Dolinar, I. A. Guzei and S. S. Stahl, *J. Am. Chem. Soc.* **2016**, *138*, 4869-4880.

(15) F. G. Bordwell, *Acc. Chem. Res.* **1988**, *21*, 456-463.

(16) a) H. Jiang, E. Stepowska and D. Song, *Dalton Trans.* **2008**, 5879-5881. b) R. Tan, F. S. N. Chiu, A. Hadzovic and D. Song, *Organometallics* **2012**, *31*, 2184-2192. c) V. T. Annibale, R.

Batcup, T. Bai, S. J. Hughes and D. Song, *Organometallics* **2013**, *32*, 6511-6521. d) R. Batcup, V. T. Annibale and D. Song, *Dalton Trans.* **2014**, *43*, 8951-8958. e) V. T. Annibale and D. Song, *Organometallics* **2014**, *33*, 2776-2783. f) T. Janes, K. M. Osten, A. Pantaleo, E. Yan, Y. Yang and D. Song, *Chem. Commun.* **2016**, *52*, 4148-4151. g) T. Janes, V. T. Annibale and D. Song, *J. Organomet. Chem.* **2018**, *872*, 79-86.

(17) H. Jiang and D. Song, *Organometallics* **2008**, *27*, 3587-3592.

(18) E. Stepowska, H. Jiang and D. Song, *Chem. Commun.* **2010**, *46*, 556-558.

(19) H. Jiang, E. Stepowska and D. Song, *Eur. J. Inorg. Chem.* **2009**, *2009*, 2083-2089.

(20) A. N. Campbell, P. B. White, I. A. Guzei and S. S. Stahl, *J. Am. Chem. Soc.* **2010**, *132*, 15116-15119.

(21) a) T. Diao, T. J. Wadzinski and S. S. Stahl, *Chem. Sci.* **2012**, *3*, 887-891. b) W. Gao, Z. He, Y. Qian, J. Zhao and Y. Huang, *Chem. Sci.* **2012**, *3*, 883-886.

(22) C. Creutz, *Comments Inorg. Chem.* **1982**, *1*, 293-311.

(23) (a) W. Kaim, *Coord. Chem. Rev.* **1987**, *76*, 187-235. (b) W. Kaim, A. Klein and M. Glöckle, *Acc. Chem. Res.* **2000**, *33*, 755-763.

(24) a) M. Ladwig and W. Kaim, *J. Organomet. Chem.* **1992**, *439*, 79-90. b) W. Kaim, R. Reinhardt, E. Waldhoer and J. Fiedler, *J. Organomet. Chem.* **1996**, *524*, 195-202.

(25) a) J. O. Taylor, R. Culpeck, A. M. Chippindale, M. J. Calhorda and F. Hartl, *Organometallics* **2021**, *40*, 1598-1613. b) J. Tory, L. King, A. Maroulis, M. Haukka, M. J. Calhorda and F. Hartl, *Inorg. Chem.* **2014**, *53*, 1382-1396.

(26) M. A. Scharwitz, I. Ott, Y. Geldmacher, R. Gust and W. S. Sheldrick, *J. Organomet. Chem.* **2008**, *693*, 2299-2309.

(27) J. J. Soldevila-Barreda, A. Habtemariam, I. Romero-Canelón, and P.J. Sadler, *J. Inorg. Biochem.,* **2015**, *153*, 322-333.

(28) F. E. Kühn, M. Groarke, É. Bencze, E. Herdtweck, A. Prazeres, A. M. Santos, M. J. Calhorda, C. C. Romão, I. S. Gonçalves, A. D. Lopes, M. Pillinger, *Chem. – Eur. J.* **2002**, *8*, 2370-2383.

(29) E. Gore-Randall, M. Irwin, M. S. Denning, J. M. Goicoechea, *Inorg. Chem.* **2009**, *48*, 8304-8316.

(30) The ligands themselves were prepared from 1,10-phenanthroline (phen), which is readily oxidized by manganate to produce dafone. Wolff-Kishner reduction of dafone generates daf, and sequential deprotonation of daf with potassium *tert*-butoxide (tBuOK) followed by addition of iodomethane affords access to Me_2daf. See SI pp. S82-S87 for detailed information on these procedures.

(31) H. Ohrui, A. Senoo and T. Kosuge in *Preparation of diazafluorene compounds via palladium-catalyzed condensation reaction of diazafluorene dihalides with boronic acid derivatives*, Patent US20080161574A1, Canon Kabushiki Kaisha, Japan, **2008**, pp. 22.

(32) Considering the straightforward synthesis of Me_2daf using iodomethane as an electrophile, we anticipated other electrophiles might be useful for generation of daf-type ligands. Unfortunately, use of benzyl bromide (BnBr) as an electrophile in this reaction sequence results in the apparent preferential formation of 9,9′-dibenzyl-1-N-benzyl-4,5-diazafluorenium bromide (**Bn_3daf**), an off-target compound that is confirmed using ^{1}H-NMR, mass

spectrometry, and single crystal X-ray diffraction analysis (XRD, see Figures A24, A30, and A68). Thus, the use of BnBr here provides a contrasting result to what occurs when using iodomethane as the electrophile and was not pursued further.

(33) A. Nutton, P. M. Bailey, P. M. Maitlis, *J. Chem. Soc. Dalton Trans.* **1981**, 1997-2002.

(34) C. White, A. Yates, P. M. Maitlis and D. M. Heinekey, *Inorg. Synth.*, Vol. 29, Wiley- VCH, Weinheim, **1992**, 228-234.

(35) M. A. Mantell, J. W. Kampf and M. Sanford, *Organometallics*, **2018**, *37*, 3240-3242.

(36) W. C. Henke, J. A. Hopkins, M. L. Anderson, J. P. Stiel, V. W. Day, J. D. Blakemore, *Molecules* **2020**, *25*, 3189-3203.

(37) a) J. W. Akitt and B. E. Mann, *NMR and Chemistry: An Introduction to Modern NMR Spectroscopy*, CRC Press, **2000**, 4th edn., p. 69. b) R. K. Harris, in *Nuclear Magnetic Resonance Spectroscopy: A Physicochemical View*, Pearson Education, **1986**. p. 26.

(38) C. G. Comadoll, W. C. Henke, J. A. Hopkins Leseberg, J. T. Douglas, A. G. Oliver, V. W. Day, J. D. Blakemore, *Organometallics* **2021**, *40*, 3808-3818.

(39) The identity of the counteranion in the structures of the daf-type complexes was not found to significantly impact the structural properties of the [Cp*Rh] frameworks. In particular, the structure of **1** was compared here to the structure of [Cp*Rh(daf)Cl]PF_6 (denoted as **1-PF6**; see Appendix A, Figures A73-A75 and Table A2) and the structure of **3-NCMe** was compared to that of [Cp*Rh(Me_2daf)NCMe](PF_6)$_2$] (denoted as **3–NCMePF$_6$**; see Appendix A, Figures A76-A77 and Table S2). Considering this result, the structures of **1**-**NCMe**, **2**-**NCMe**, and **3**-

NCMe can be compared to that of [Cp*Rh(bpy)NCMe]$(PF_6)_2$ (**bpy^{NCMe}**), despite the presence of triflate counteranions in the solvento structures reported here.

(40) M. A. Scharwitz, I. Ott, Y. Geldmacher, R. Gust and W. S. Sheldrick, *J. Organomet. Chem.* **2008**, *693*, 2299-2309.

(41) J.D. Blakemore, E.S. Hernandez, W. Sattler, B.M. Hunter, L.M. Henling, B.S. Brunschwig, and H.B. Gray, *Polyhedron*, **2014**, *84*, 14-18.

(42) H.-K. Fun, K. Sivakumar, D.-R. Zhu, and X. -Z. You, *Acta. Cryst. C* **1995**, *51*, 2076-2078.

(43) M. Riklin, A. von Zelewsky, A. Bashall, M. McPartlin, A. Baysal, J. A. Connor, J. D. Wallis, *Helv. Chim. Acta* **1999**, *82*, 1666-1680.

(44) a) P. R. Sharp, D. W. Hoard and C. L. Barnes, *J. Am. Chem. Soc.*, **1990**, *112*, 2024-2026. b) D. W. Hoard and P. R. Sharp, *Inorg. Chem.*, **1993**, *32*, 612-620.

(45) D. Lionetti, V. W. Day, B. Lassalle-Kaiser and J. D. Blakemore, *Chem. Commun.* **2018**, *54*, 1694-1697.

(46) D. Lionetti, V. W. Day, J. D. Blakemore, *Dalton Trans*. **2019**, *48*, 12396-12406.

(47) R. S. Nicholson and I. Shain, *Anal. Chem.* **1964,** *36*, 706-723.

(48) M. K. Kalinowski, Z. R. Grabowski and B. Pakula, *Trans. Faraday Soc.* **1966**, *62*, 918-925.

(49) Chemical reduction of **2-NCMe** using 1% Na(Hg) resulted in the generation of Na_2(4,5-diazafluorene)$_2$(4,5-diazafluorenide)$_2$ (**2-red**), which was identified by X-ray crystallography (see Appendix A, Figure A71). This result highlights the deleterious Brønsted acid-base

reactivity that may occur without protective methylation of the doubly benzylic methylene protons of 4,5-diazafluorene.

(50) J. A. Hopkins, D. Lionetti, V. W. Day and J. D. Blakemore, *Organometallics* **2019**, *38*, 1300-1310.

(51) N. G. Connelly and W. E. Geiger, *Chem. Rev.* **1996**, *96*, 877-910.

(52) W. N. G. Moore, W. C. Henke, D. Lionetti, V. W. Day and J. D. Blakemore, *Molecules* **2018**, *23*, 2857-2873.

(53) Y. Peng, M. V. Ramos-Garcés, D. Lionetti and J. D. Blakemore, *Inorg. Chem.* **2017**, *56*, 10824-10831.

(54) S. Stoll and A. Schweiger, *J. Magn. Reson.*, **2006**, *178*, 42-55.

(55) D. Lionetti, V. W. Day and J. D. Blakemore, *Organometallics* **2017**, *36*, 1897-1905.

(56) a) J. P. Maier and D. W. Turner, *Faraday Disc. Chem. Soc.* **1972**, *54*, 149-167. b) P. S. Braterman and J. I. Song, *J. Org. Chem.* **1991**, *56*, 4678-4682.

(57) a) L. M. A. Quintana, S. I. Johnson, S. L. Corona, W. Villatoro, W. A. Goddard, M. K. Takase, D. G. VanderVelde, J. R. Winkler, H. B. Gray and J. D. Blakemore, *Proc. Nat. Acad. Sci. U.S.A.* **2016**, *113*, 6409-6414. b) C. L. Pitman, O. N. L. Finster and A. J. M. Miller, *Chem. Commun.* **2016**, *52*, 9105–9108.

(58) E. A. Boyd, D. Lionetti, W. C. Henke, V. W. Day and J. D. Blakemore, *Inorg. Chem.* **2019**, *58*, 3606-3615.

(59) G. R. Fulmer, A. J. M. Miller, N. H. Sherden, H. E. Gottlieb, A. Nudelman, B. M. Stoltz, J. E. Bercaw, K. I. Goldberg, *Organometallics* **2010**, *29*, 2176-2179.

(60) a) R. K. Harris, E. D. Becker, S. M. Cabral De Menezes, R. Goodfellow, P. Granger, *Pure Appl. Chem.* **2001**, *73*, 1795-1818; b) R. K. Harris, E. D. Becker, S. M. Cabral De Menezes, P. Granger, R. E. Hoffman, K. W. Zilm, *Pure Appl. Chem.* **2008**, *80*, 59-84.

Chapter 4

Mechanistic Roles of Metal- and Ligand-Protonated Species in Hydrogen Evolution with [Cp*Rh] Complexes

4.1 Introduction

Cyclopentadienyls are among the most common ligands in organometallic chemistry, capable of supporting metallocene and half-sandwich type complexes across a wide range of metals and oxidation states (1,2,3,4). Cyclopentadienyl-type ligands are distinguished by their planarity and aromaticity, as well as their tendency to "slip" with adopted hapticities of η^5, η^3, or η^1 (5,6,7,8). The accessibility of these various coordination modes contributes to the tremendous variety of reactions that can be catalyzed by complexes supported by this ligand type. With few exceptions (9,10), the aromatic [C_5H_5] core is maintained and non-interacting with substrates, leading to the usefulness of cyclopentadienyl as a flexible but commonly innocent ligand that reliably promotes metal-centered reactivity.

On the other hand, the pentamethylcyclopentadienyl (Cp*) ligand has recently been shown to undergo ligand-centered protonation in certain cases by direct proton transfer from acids or by tautomerization of transition metal hydrides resulting from metal-centered protonation reactions (see Figure 4.1) (11,12). These reactions result in the generation of isolable complexes bearing the uncommon η^4-pentamethylcyclopentadiene (Cp*H) ligand, a species that can serve as a net H-atom (H•) or hydride (H^-) donor via cleavage of the unique C–H bond on the Cp*H ring (13,14). The orientation of the proton on the Cp*H ligand can give rise to unique isomers; the *endo*-isomer has the proton facing toward the metal center, while the *exo*-isomer has the proton facing away from the metal center. Peters and co-workers showed that exposure of the unreactive hydride $[Cp^*Fe(dppe)H]^+$ (dppe = 1,2-bis(diphenylphosphino)ethane) (15) to CO results in the formation of $[(endo\text{-}Cp^*H)Fe(dppe)CO]^+$, a species with a weak C–H bond capable of H-atom transfer (16). Similarly, Chalkley, Peters, and co-workers showed that Cp^*_2Co serves as a catalytic PCET

mediator via the formation of [(*exo*-Cp*H)CoCp*]$^+$ in the presence of strong acid, enabling enhanced N_2 reduction to NH_3 (17). In these examples, the metal center and Cp*H ligand work in concert to provide H• or H^- equivalents to promote multi-proton and multi-electron reactivity.

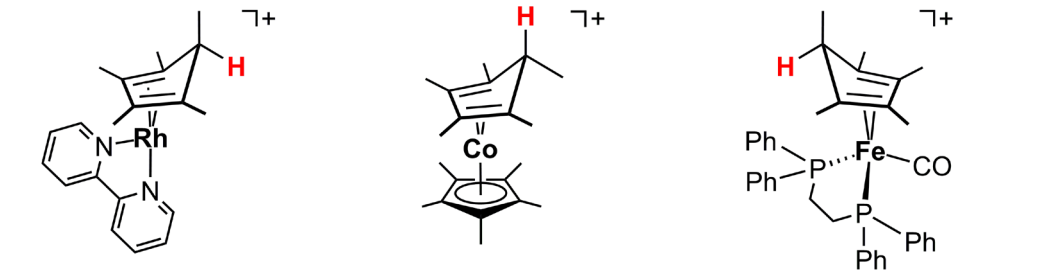

[(*endo*-η^4-Cp*H)**Rh**(bpy)]$^+$ *Blakemore 2016*

[(*exo*-η^4-Cp*H)**Co**Cp*]$^+$ *Peters 2019*

[(*endo*-η^4-Cp*H)**Fe**(dppe)(CO)]$^+$ *Peters 2020*

Figure 4.1. Notable complexes bearing the η^4-pentamethylcyclopentadiene (Cp*H) ligand.

In the course of investigating the mechanism of H_2 generation with Cp*Rh(bpy), we found that the addition of weak acids, such as triethylammonium ([$HNEt_3$]$^+$, pK_a = 18.8 in acetonitrile (MeCN)), to the complex results in the generation of an isolable Cp*H complex formulated as [(*endo*-Cp*H)Rh(bpy)]$^+$ (11,13,18). X-ray diffraction studies and spectroscopic evidence confirm the exclusive generation of [(*endo*-Cp*H)Rh(bpy)]$^+$ (hereafter denoted as [(Cp*H)Rh(bpy)]$^+$) when using weak acids. Catalytic proton reduction using Cp*Rh(bpy), a system notable for its ease of preparation and longevity, was first described by Grätzel and Kölle in 1987 (19,20). At that time, the mechanism of catalysis was proposed to involve a first protonation that leads to a [Cp*Rh–H] species that could undergo protonolysis to generate H_2. This elusive hydride has also been repeatedly proposed to be involved in the formation of NADH from NAD^+ in bioelectrochemical applications (21,22). However, despite attempts, the putative [Cp*Rh–H]

intermediate has only been observed in mixtures of products that were generated under stringent reaction conditions involving photochemical reactors, buffered solutions, or low temperatures (–40° C) and has not been fully characterized (12,23). Recently, our group has developed reliable synthetic procedures to access analogous phosphine-supported [Cp*Rh] monohydrides, but these species are remarkably resistant to protonolysis due to enhanced stabilization provided by the phosphine ligand (24,25,26). On the other hand, isolated $[(Cp^*H)Rh(bpy)]^+$ reacts with even moderate acids, such as anilinium ($[PhNH_3]^+$, p*Ka* = 10.6 in MeCN) to quantitatively yield H_2 and regenerate the starting Rh(III) complex (18).

More recently, Nozaki et al. and Ishitani et al. have utilized [Cp*Rh]-based complexes to promote catalytic dehydrogenation of dimethylamine-borane and photocatalytic reduction of CO_2 to formate, respectively (27,28). In these investigations, among others (29,30), the identity of the species driving the observed reactivity is proposed to be either [Cp*Rh–H] or [(Cp*H)Rh], and this lingering ambiguity in the literature continues to fuel the debate about the precise role of these protonated intermediates during catalytic turnover, meriting further investigation. In particular, the mechanistic details surrounding the conversion of the proposed metal hydride and observed Cp*H species via hydride-proton tautomerism is not yet clear, with respect to, for example, the involvement of the conjugate base in assisting with migration of the proton to the ring, or the kinetic details of the overall process, whether they are concerted or multi-step. In the case of the [Cp*Rh] systems, the ability to access [Cp*H]-type compounds appears to be essential for catalytic turnover, a finding in agreement with the apparent transient nature of the corresponding [Cp*Rh] monohydride. However, considering that reliable syntheses are now available for Cp*Rh(bpy) and $[(Cp^*H)Rh(bpy)]^+$, contrasting with the more reactive and temperature-sensitive nature of analogous first-row metals supporting Cp*H species, we anticipated that time-resolved

spectroscopic studies under conditions relevant to catalysis could be useful to investigate the elementary steps involved in hydrogen evolution using Cp*Rh(bpy).

Here, we report time-resolved pulse radiolysis and stopped-flow measurements that map the elementary electron- and proton-transfer steps leading to hydrogen evolution with Cp*Rh(bpy) in MeCN. In particular, stopped-flow measurements with UV-vis detection exhibit spectra with isosbestic behavior, indicating clean conversion from the starting complex to a new molecular species, and complementary stopped-flow IR measurements confirm that the sole product of initial protonation is $[Cp^*Rh(H)(bpy)]^+$ based on a characteristic hydride stretch at 1920 cm^{-1}. This is followed by a concomitant tautomerization to generate $[(Cp^*H)Rh(bpy)]^+$. Variable temperature kinetic measurements, as well as isotopic labeling experiments, confirm that the activation energy barriers involved are sufficiently modest to allow for the hydride to tautomerize to the Cp*H complex. Such involvement gives Cp* a possible role in catalytic applications that were not previously believed to be possible. Taken together, our results suggest that Cp* non-innocence can play a crucial role in catalytic applications and should be actively considered in mechanistic investigations.

4.2 Results

4.2.1 Synthesis of Isolable Intermediates

Long-standing work by Kölle and Grätzel, et al. describes a reliable synthetic procedure for the clean and facile generation of $[Cp^*Rh(OH_2)(bpy)]^{2+}$ (**1**) (see Figure 4.2, where L = H_2O); **1** is a well-known precatalyst for the chemical and electrochemical reduction of protons to dihydrogen (31). Using Na(Hg), **1** can be reduced by $2e^-$ to generate the electron-rich, neutral species,

Cp*Rh(bpy) (**3**) (32). Addition of 2 equiv. of a strong proton source, such as dimethylformamidinium ($[DMF{\cdot}H]^+$, $pK_a \approx 6.1$ in MeCN), to **3** results in the quantitative formation of dihydrogen and regeneration of **1** (33). However, more recently, we have shown that the addition of weak acids, such as $[HNEt_3]^+$, to **3** results in the unexpected generation of $[(Cp^*H)Rh(bpy)]^+$ (**5**) instead of the anticipated metal hydride complex (11,34). We have since developed a synthetic procedure that enables the clean isolation of **5** (13). With these reported procedures readily available, we took the opportunity to prepare **1**, **3**, and **5** (see Appendix B, Figures B1-B3), and with careful handling, use these complexes to map the sequential electron and proton transfer events leading to hydrogen evolution using time-resolved pulse radiolysis and stopped-flow experiments.

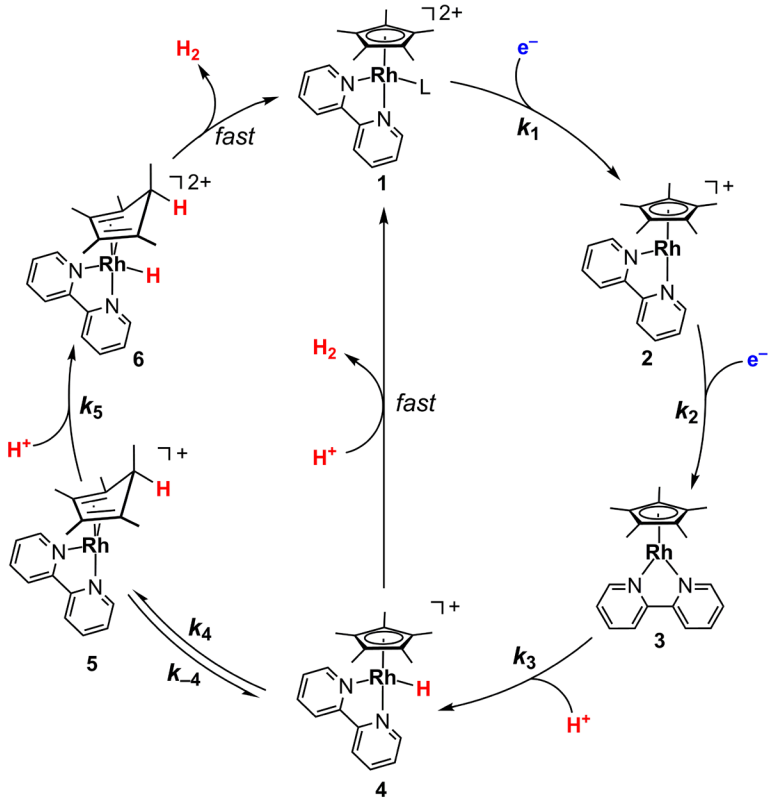

Figure 4.2. Proposed catalytic cycle for hydrogen evolution starting with **1**. **L** = H_2O, or MeCN.

4.2.2 Mapping the Initial Electron Transfer Events

Prior cyclic voltammetry (CV) data for **1** reveals a single, quasireversible $2e^-$ redox event centered at –1.05 V versus ferrocenium/ferrocene (31). This process can be confidently assigned as the Rh(III)/Rh(I) redox couple based on previous synthetic work and CV measurements of similar [Cp*Rh] complexes (14,32). Since the potential of the Rh(II)/Rh(I) couple is similar to or more positive than that of the Rh(III)/Rh(II) couple, isolation of the Rh(II) species cannot be achieved by electrochemical or chemical reduction. This prompted us to use the technique of pulse radiolysis (PR), which allows for the rapid generation of singly-reduced intermediates and their

characterization by time-resolved spectroscopic methods (35). In 1989, Kölle and Grätzel investigated the reduction events of **1** in aqueous solutions using PR (31). In their isolated study, absorbance vs time kinetic data were used to support a disproportionation mechanism that involves the generation of **1** and **3**, from **2** in aqueous solution. Building on this work, we performed PR in concert with time-resolved UV-vis detection, starting with **1** in MeCN. The excess energy deposited into acetonitrile solvent by high-energy electrons results in the rapid generation of solvated electrons (e^-_{solv}), $MeCN^{\bullet+}$, and solvent excited states. The latter two species are very unstable, leading to a cascade of fragmentations that include the generation of protons ($MeCNH^+$) and a variety of solvent-derived radicals (34). While the reduction of **1** by solvated electrons can promptly generate **2**, the stability of the radical product will be severely impacted by its reaction with the radiolytic solvent radicals. Fortunately, formate anion can be used to scavenge the radicals by H-atom transfer in PR experiments in MeCN, producing $CO_2^{\bullet-}$, which is a strong reductant ($E°(CO_2/CO_2^{\bullet-})$ = –2.21 V vs SCE in dimethylformamide) (36,37). Thus, under the experimental conditions used in this work, i.e., air-free MeCN solutions containing **1** (40 μM) and [n-Bu_4N][HCO_2] (50 mM), the radiolytically produced solvated electrons and $CO_2^{\bullet-}$ are the reducing species that react with **1**. The amount of reducing equivalents produced by a single electron pulse was determined in a dosimetry experiment, using the Co macrocycle, $[Co(HMD)]^{2+}$ (where HMD = 5,7,7,12,14,14-hexamethyl-1,4,8,11-tetraazacyclotetradeca-4,11-diene), as an efficient electron scavenger, and the known molar absorption coefficient of its reduced form, $[Co(HMD)]^+$ ($\varepsilon = 1.80 \times 10^4\ M^{-1}\ cm^{-1}$, see Appendix B, Figure B19) (38). After determining the proper dose, solutions of **1** and [n-Bu_4N][HCO_2] were mixed rapidly to produce the above-mentioned concentrations and delivered directly into a PR cell using a remote-controlled syringe pump. About 2-3 seconds after

mixing, an electron pulse was introduced into the sample using a 2 MeV Van de Graaff accelerator (39, 40).

The absorption spectrum of **1** is unremarkable, with a feature at approximately 370 nm that slightly tails into the visible region, and no absorption beyond 500 nm (see Figure 4.3). Following pulse radiolysis, a dramatic change in absorption occurs, with the observation of a UV-vis spectrum 1 ms after the electron pulse that is consistent with the generation of **3** (Figure 4.3, purple squares). Taking a cue from the known absorption profile of **3**, kinetic traces were monitored near the prominent absorption feature at 520 nm in an attempt to examine the rates of the two reduction events (see Figure 4.3, inlay). The resulting absorbance vs time data revealed two distinct processes; the first process is very rapid (occurring over a timescale of ~10 μs) and is assigned as the reduction of **1** to $[Cp^*Rh(bpy)]^+$ (**2**), while the second, comparatively slower, process (occurring over a timescale of ~1 ms) is assigned as the reduction of **2** to **3** (see Appendix B, Figures B20-B25). Examining the earliest absorbance vs wavelength data reveals a UV-vis spectrum 10 μs after the electron pulse that is unique from **1** and **3**. This spectrum is assigned to the $1e^-$ reduced species, **2**, and has absorbance features that span the range of the visible region, with prominent transitions at 474 (3100 M^{-1} cm^{-1}) and 723 nm (4900 M^{-1} cm^{-1}, *vide supra*). The spectrum of **2** is consistent with other [Cp*Rh(II)] complexes examined by us (41,42); in particular, the UV-vis spectrum of **2** obtained by PR is comparable to the Rh^{II} complex, $[Cp^*Rh(Me_2daf)]^+$, which exhibits similar, but less intense, transitions at 462 (1400 M^{-1} cm^{-1}) and

716 nm (3200 M^{-1} cm^{-1}). With the spectrum of **2** in hand, we then moved to examine the second reduction event.

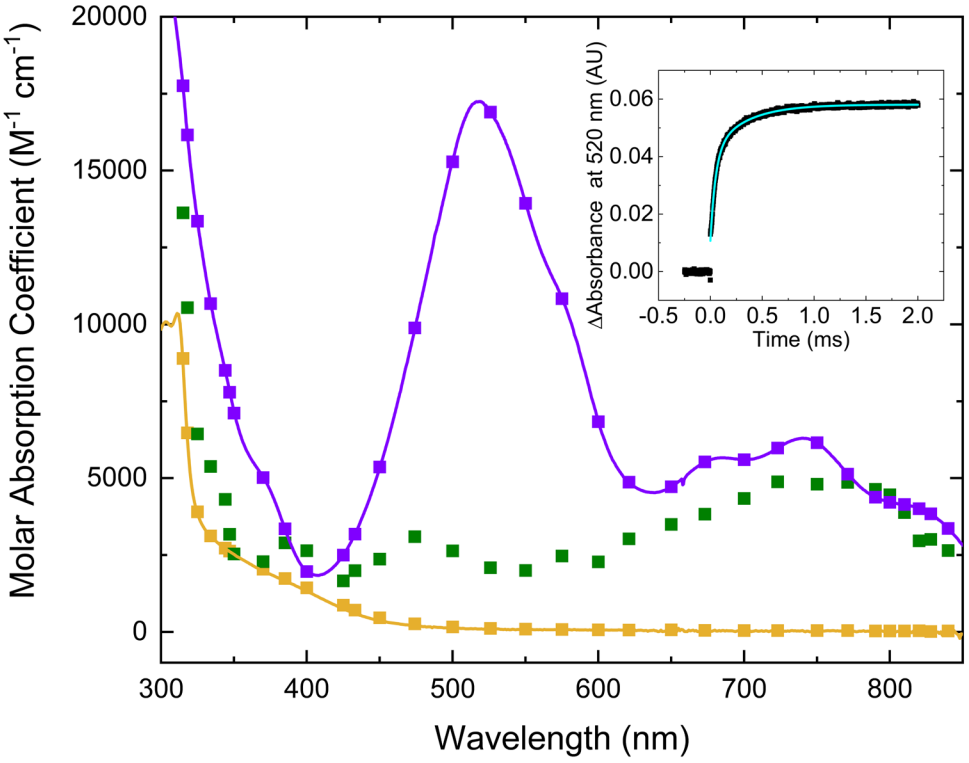

Figure 4.3. Absorption spectrum of **1** in MeCN before PR (gold squares). The spectrum of **2** obtained after 1e^- reduction of 40 mM **1** in MeCN in the presence of 50 mM formate is shown by green squares (measured at 10 ms after the e^- pulse). Further reduction of **2** then leads to the formation of **3** (purple squares, measured at 1 ms after the e^- pulse). The gold and purple lines are the UV-vis spectra of isolated **1** and **3**, respectively. Shown inset is a transient absorption kinetic trace measured at 520 nm after PR, with a biexponential fit overlaid in blue.

In foundational work performed by Kölle and Grätzel, PR was carried out with **1** under aqueous conditions where they observed the generation of **3**, which they attribute to a disproportionation

event involving 2 equiv. of **2** (31). However, our work in MeCN does not support a kinetic model involving disproportionation of **2** because when this is considered, the resulting extinction coefficients are too large for **3**. To further confirm this observation, initial rate analysis (43) was performed to determine the reaction order with respect to **2**. PR experiments were performed at time delays where **2** has already formed, and by controlling the dose, we can generate different concentrations of **2**. Plotting the logarithm of the initial rate of formation of **3** as a function of the logarithm of the concentration of generated **2** (log(dose) = log([**2**])), reveals a line with a slope of 1.03 ± 0.07, confirming a first-order dependence on **2** in the conversion of **2** to **3** (see Appendix B, Figure B25). Thus, a disproportionation mechanism can be ruled out here under our specific conditions. Instead, the reduction of **2** to **3** here most likely results from the reaction of **2** with formate. A biexponential fit of the kinetic trace at 520 nm (Figure 4.3, inlay) results in two observed rates of 2.6 x 10^4 s^{-1} and 3.2 x 10^3 s^{-1}, with the former being attributed to the reduction of **1** by $CO_2^{\bullet-}$ (since reduction of **1** by the solvated electron will occur on a much faster timescale that is not resolved in our data), and the latter corresponding to the conversion of **2** to **3** by formate anion; regarding the faster rate constant, reduction by $CO_2^{\bullet-}$ is expected to be much slower than by e^-_{solv}, meaning the reaction with $CO_2^{\bullet-}$ should be rate limiting. Lending support to this kinetic model, the extinction coefficients for **3** obtained during PR agree well with those obtained from isolated material (see Figure 4.3); the UV-vis spectrum of **3** exhibits absorption bands that span the visible region ($\varepsilon \approx$ 4-17 x 10^3 M^{-1} cm^{-1} in MeCN) and displays strong absorption features around 511 nm ($\varepsilon \approx 1.7 \times 10^4$ M^{-1} cm^{-1}) as well as longer wavelength transitions with vibronic structure between 650 and 850 nm, presumably arising from delocalization of electron density into

the bpy ligand (*vide infra*) (44). Following our interrogation of the reduction events leading to **3**, we then moved to explore the reactivity of **3** with protons.

4.2.3 Initial Proton Transfer and Tautomerization Steps.

Complex **3** reacts readily with weak acids, an observation established in prior work (11). With this in mind, we set out to determine the rate constant, the reaction order, and molecularity of this protonation reaction using stopped-flow equipped with UV-Vis or IR detection. Control reactions rapidly mixing **3** with pure MeCN did not show degradation over the duration of the experiment (see Appendix B, Figures B26-B29). Next, **3** was rapidly mixed with $[HNEt_3]^+$ at various concentrations under pseudo-first order conditions (see Appendix B, Figures B30-S40 and B46-B49). The prominent absorption feature at approximately 511 nm (*vide supra*) was used to monitor the consumption of **3** after rapid mixing with $[HNEt_3]^+$ (see Figure 4.4a). The spectral changes observed after the addition of acid illustrate the rapid decay of **3** with isosbestic behavior at 379 and 431 nm, indicating clean conversion to a new molecular species. The decay of the absorbance at 511 nm occurs monoexponentially, and the resulting observed rate constants (k_{obs}) are plotted as a function of acid concentration to extract the overall second-order rate constant, $k_3 = (6.4 \pm 0.2) \times 10^3\ M^{-1}\ s^{-1}$ (see Figure 4.4b) (43). Notably, after initial protonation (~100 ms), the resulting UV-vis spectrum did not resemble the experimental spectrum of $[(Cp^*H)Rh(bpy)]^+$ (see Figure 4.4c). Eager to further interrogate this species, we repeated this protonation experiment with IR monitoring, providing the first unequivocal evidence for the formation of $[Cp^*Rh(H)(bpy)]^+$ (**4**) based on a characteristic Rh–H stretch at 1920 cm^{-1} (Figure 4.5). Notably, this value is similar to other Rh–H stretches (1986–1936 cm^{-1}) previously reported for analogous [Cp*Rh] monohydride complexes ligated by bisphosphine ligands, albeit slightly lower in energy, and is in good

agreement with our DFT-calculated spectrum (1920 vs 1902 cm^{-1}, respectively, see Appendix B, Figure B32) (24,26).

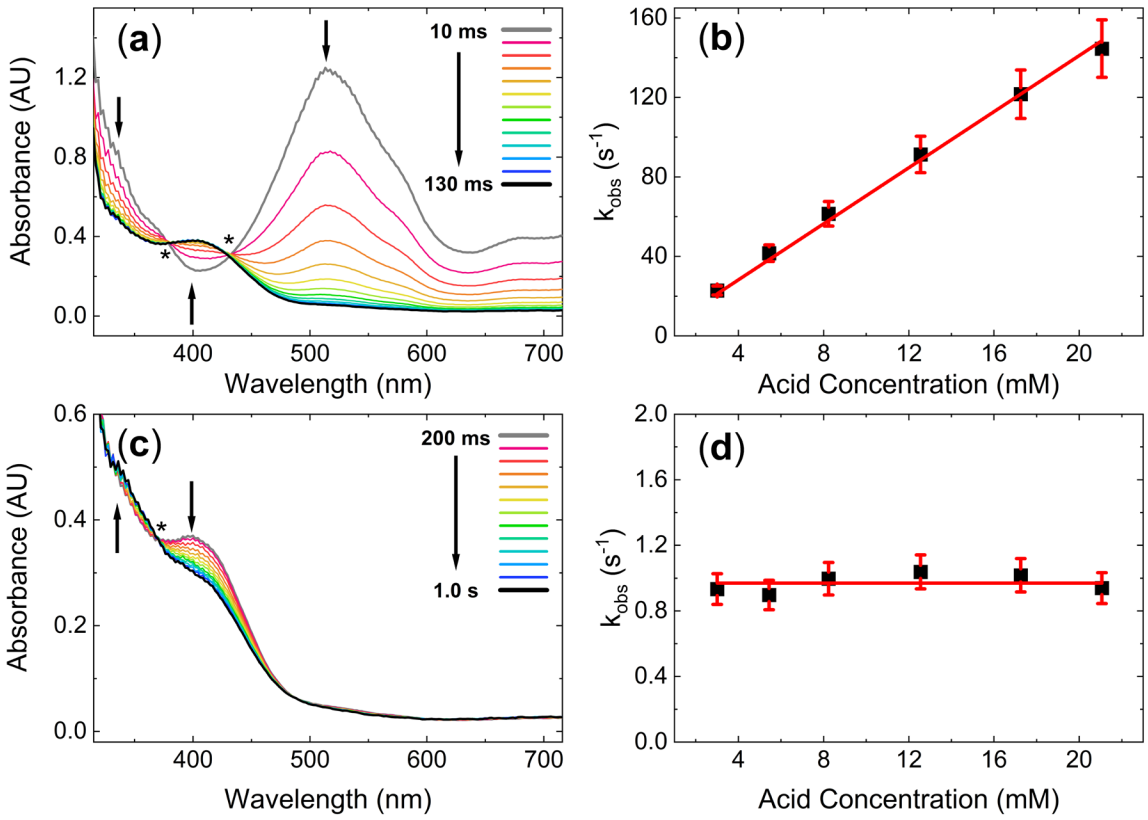

Figure 4.4. (a) Stopped-flow UV-vis spectra for the protonation of **3** with $[HNEt_3]^+$ to generate **4**. Isosbestic behavior at 379 and 431 nm is denoted by *. (**b**) Observed rate constants monitored at 511.1 nm as a function of $[HNEt_3]^+$ concentration. The linear dependence reveals a first-order dependence on $[HNEt_3]^+$ and the overall second-order rate constant. (**c**) Stopped-flow UV-vis spectra for the tautomerization of **4** to generate **5**. Isosbestic behavior at 370 nm is denoted by *. (**d**) Observed rate constants monitored at 399.8 nm as a function of $[HNEt_3]^+$ concentration. The slope of zero reveals a zero-order dependence on $[HNEt_3]^+$.

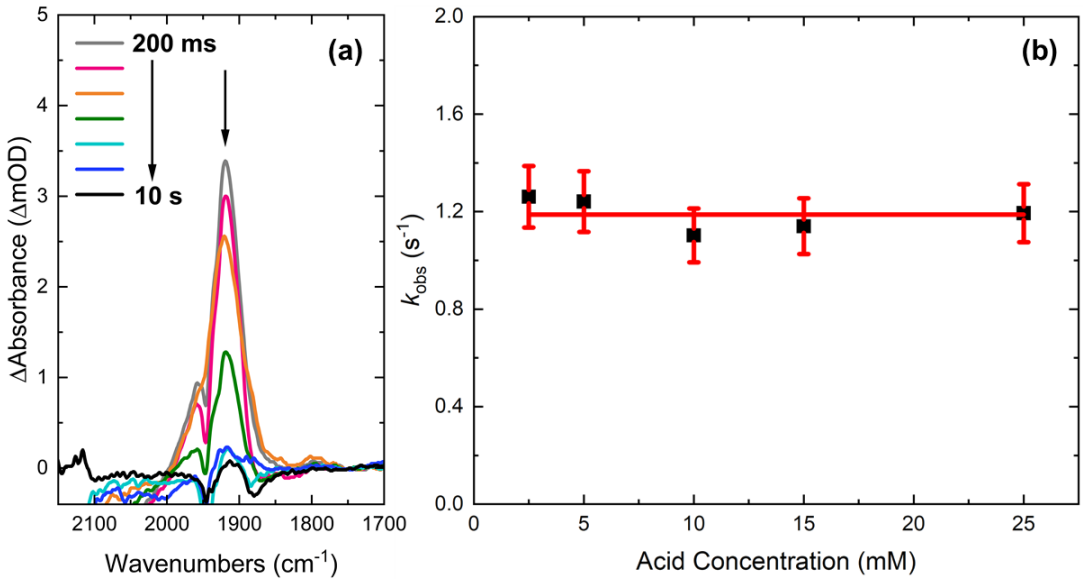

Figure 4.5. (a) Stopped-flow IR spectra for the tautomerization of 4 to generate 5. The signal at 1920 cm^{-1} is consistent with a Rh-H stretch. (**b**) Observed rate constants monitored at 1923 cm^{-1} as a function of $[HNEt_3]^+$ concentration. The slope of zero reveals a zero-order dependence on $[HNEt_3]^+$.

The UV-vis spectrum of **4** displays a prominent absorption at 400 nm and weaker features that tail into the visible region. As a result, the full reaction sequence can be monitored at 400 nm between 1-10 s following the rapid mixing of **3** with $[HNEt_3]^+$ (see Appendix B, Figures B36-B39) (45). The resulting absorbance vs time data reveal two distinct chemical steps, where the first step corresponds to the initial protonation of **3** to generate **4**. Following the generation of **4**, the evolution of the absorbance vs wavelength spectra results in a new isosbestic point at 370 nm, supporting the formation of a new species (see Figure 4.4c). The monoexponential decay of **4** is monitored as a function of time at 400 nm and the corresponding k_{obs} values are plotted as a

function of $[HNEt_3]^+$ concentration, revealing a second step that is zero-order in acid (k_4 = 870 ± 30 s^{-1}, see Figure 4.4d). This zero-order dependence is further confirmed by monitoring the decay of the Rh–H stretch at 1920 cm^{-1} during stopped-flow IR (See Appendix B, Figures B34-B35). These kinetic data are consistent with **4** undergoing hydride-proton tautomerization to generate $[(Cp^*H)Rh(bpy)]^+$ (**5**), and provide tantalizing kinetic and spectroscopic characterization of the species involved in these proton transfer reactions for the first time. Having identified the sequence of the elementary protonation and tautomerization reactions, we next set out to further characterize the steps leading to Cp*H formation using variable temperature kinetic experiments.

Variable temperature kinetic data were collected between 20–40 °C under pseudo first-order conditions following rapid mixing of **3** with either $[HNEt_3]^+$ or $[DNEt_3]^+$ (D incorporation >95%, see Appendix B, Figure B6). Eyring and Arrhenius plots of $\ln(k_{obs}/T)$ as a function of T^{-1} using **3** reveal the enthalpy of activation ($\Delta H^‡$), entropy of activation ($\Delta S^‡$), free energy of activation ($\Delta G^‡$), and activation energy (E_a), respectively, for the elementary protonation and tautomerization steps that convert **3** to **4(D)** (where **4(D)** refers to the protonated (**4**) or deuterated species (**4D**)), and **4(D)** to **5(D)** (see Table 4.1, and Appendix B, Figures B41-B45 and B50-B67) (46). Experimentally derived activation parameters for the protonation of **3** with $[HNEt_3]^+$ or $[DNEt_3]^+$ ($[H(D)–NEt_3]^+$) reveal values for $\Delta H^‡$ (H^+ = 8.8 kcal/mol, D^+ = 9.7 kcal/mol) and $\Delta S^‡$ (H^+ = –22.3 cal mol^{-1} K^{-1}, D^+ = –21.0 cal mol^{-1} K^{-1}) at 25 °C that are in good agreement with activation parameters observed for other proton transfer reactions (47), and with prior calculations for the protonation of **3** with $[HNEt_3]^+$ (34). Our experimentally determined $\Delta H^‡$ and $\Delta S^‡$ parameters support the swift protonation of **3** in an associative bimolecular fashion (see Table 4.1). The separation between the lines in the Eyring plots (see Appendix B, Figure B74) here demonstrate the attenuation of the reaction rate when using $[DNEt_3]^+$, supporting the larger $\Delta H^‡$. The kinetic

isotope effect (KIE = k_{obs}^{H}/k_{obs}^{D}) measured for the protonation of **3** is 2.2 ± 0.2 at 298 K, a value that corresponds to a normal primary KIE. Taken together, our activation entropy and KIE data support a three centered transition state involving the cleavage of the $[H(D)–NEt_3]^+$ bond and formation of the new [Rh–H(D)] bond in a concerted fashion, enabling handoff of the proton (or deuteron) to the electron-rich Rh(I) during the generation of **4(D)**.

Table 4.1. Experimentally determined rate constants and activation parameters for $k_{3(D)}$ and $k_{4(D)}$.

Reaction	Rate Constant[(d)]	$\Delta G^{\ddagger}$ [(c,d)] (kcal mol^{-1})	$\Delta H^{\ddagger}$ [(c)] (kcal mol^{-1})	$\Delta S^{\ddagger}$ [(c)] (cal mol^{-1} K^{-1})
3→4	6400 ± 200[a]	14.9 ± 0.9	8.2 ± 0.3	–22.3 ± 0.8
3→4D	2900 ± 100[a]	15.3 ± 0.4	9.1 ± 0.1	–21.0 ± 0.3
4→5	870 ± 30[b]	17.7 ± 0.7	14.0 ± 0.5	–12.2 ± 0.5
4D→5D	1000 ± 30[b]	18 ± 1	12.0 ± 0.4	–19 ± 1

(**a**) units are M^{-1} s^{-1}. (**b**) Units are s^{-1} (**c**) Errors on the activation energy and activation parameters were derived from the uncertainty of the linear fit of the corresponding Arrhenius and Eyring Plots, respectively. (**d**)Values are for T = 298 K.

Perhaps more interesting, however, are the Eyring plots describing the tautomerization process of **4(D)** to **5(D)**. To further examine the tautomerization event, the $\Delta H^{\ddagger}$ for the conversion of **4** to **5** was determined experimentally to be approximately 2 kcal/mol higher than the corresponding transformation involving deuterons (**4D** to **5D**, see Table 4.1). Remarkably, the $\Delta S^{\ddagger}$ for the tautomerization of **4** to **5** is 10 cal mol^{-1} K^{-1} more positive in comparison to the initial protonation step. The large negative $\Delta S^{\ddagger}$ values suggests that the transition state leading to tautomerization involves associative behavior (43,[48]). However, we note that this is only one plausible explanation

and that there are multiple contributions to the activation entropy that must be considered, including solvation and translational, rotational, and vibrational degrees of freedom ([49],[50]). Under these considerations, the transition state describing the migration of the hydride (deuteride) to the Cp* ring during tautomerization may be less symmetrical ([51]). Thus, this would lead to less rotational and vibrational degrees of freedom and would also be consistent with the negative $\Delta S^{\ddagger}$ values measured. However, to provide further support for the proposed bimolecular behavior during the tautomerization step, we performed a KIE analysis.

Superficially, the tautomerization of **4(D)** to **5(D)** involves hydride (deuteride) migration, dearomatization of the Cp* ligand, and the formation of a new sp^3-hybridized C–H(D) bond. The measured KIE, which was determined from the activation parameters measured for the tautomerization of **4(D)** to **5(D),** is 0.87 ± 0.09 at 298 K. Intriguingly, inverse KIEs of 0.8–0.9 have been measured for reactions in which a carbon atom undergoes a hybridization change from sp^2- to sp^3-hybridized, much like the situation encountered in this work when η^5-Cp* is transformed to η^4-Cp*H (52,53,54,55,56). Our measured inverse KIE, in combination with the experimentally determined $\Delta S^{\ddagger}$, is consistent with a plausible mechanism involving NEt_3 playing the role of a proton shuttle, effectively facilitating tautomerization of the [Rh–H] to form (Cp*H) (57). Within this proposed mechanism, the atomistic picture for the hand-off of the proton from the metal center to the Cp* ring includes a role for exogenous conjugate base, resembling traditional tautomerization reactions in organic chemistry ([58],[59]).

4.2.4 Roles of Intermediates in Hydrogen Evolution

In prior work, *in situ* nuclear magnetic resonance (NMR) studies demonstrated that addition of excess $[HNEt_3]^+$ to **3** results in the generation of **5**, with no observable hydrogen evolution (11). On the other hand, addition of 2 equiv. of dimethylformamidinium ($[DMF{\cdot}H]^+$, pK_a = 6.1) results in quantitative dihydrogen formation and regeneration of **1**. Previously, we have also shown that $[PhNH_3]^+$ reacts with **5** to readily generate dihydrogen (14). Here, to confirm dihydrogen evolution using **5** and $[DMF{\cdot}H]^+$, 1 equiv. of $[DMF{\cdot}H]^+$ was added to **5** in MeCN solution, and after 10 min, the headspace of the reaction was injected into a gas chromatograph. The resulting chromatogram confirms quantitative generation of dihydrogen, closing the catalytic cycle, and poising the system for further turnover (see Appendix B, Figure B78-B79).

To more closely examine the role of **5** in hydrogen evolution, **5** was rapidly mixed with either anilinium ($[PhNH_3]^+$) or $[DMF{\cdot}H]^+$ at various concentrations under pseudo first-order conditions using a stopped-flow apparatus equipped with a UV-Vis detector (see Appendix B, Figures B68-B73, and Table B3). When using $[PhNH_3]^+$ as the proton source, consumption of **5** was monitored at 400 nm following rapid mixing with $[PhNH_3]^+$. The spectral changes observed after the addition of $[PhNH_3]^+$ illustrate a monoexponential decay of **5** with isosbestic behavior at 325 nm, which ultimately results in a UV-vis spectrum consistent with **1** (see Figure 4.6, panels (**a**) and (**b**)). In a similar fashion, when $[DMF{\cdot}H]^+$ is rapidly mixed with **5**, isosbestic behavior is observed at 326 nm, and the absorbance at 400 nm decays monoexponentially, resulting in a UV-vis spectrum consistent with **1** (see Figure 4.6). The resemblance of the spectra and isosbestic points when using either $[PhNH_3]^+$ or $[DMF{\cdot}H]^+$ suggests the final product(s) absorbing in this region are presumably the same in both instances.

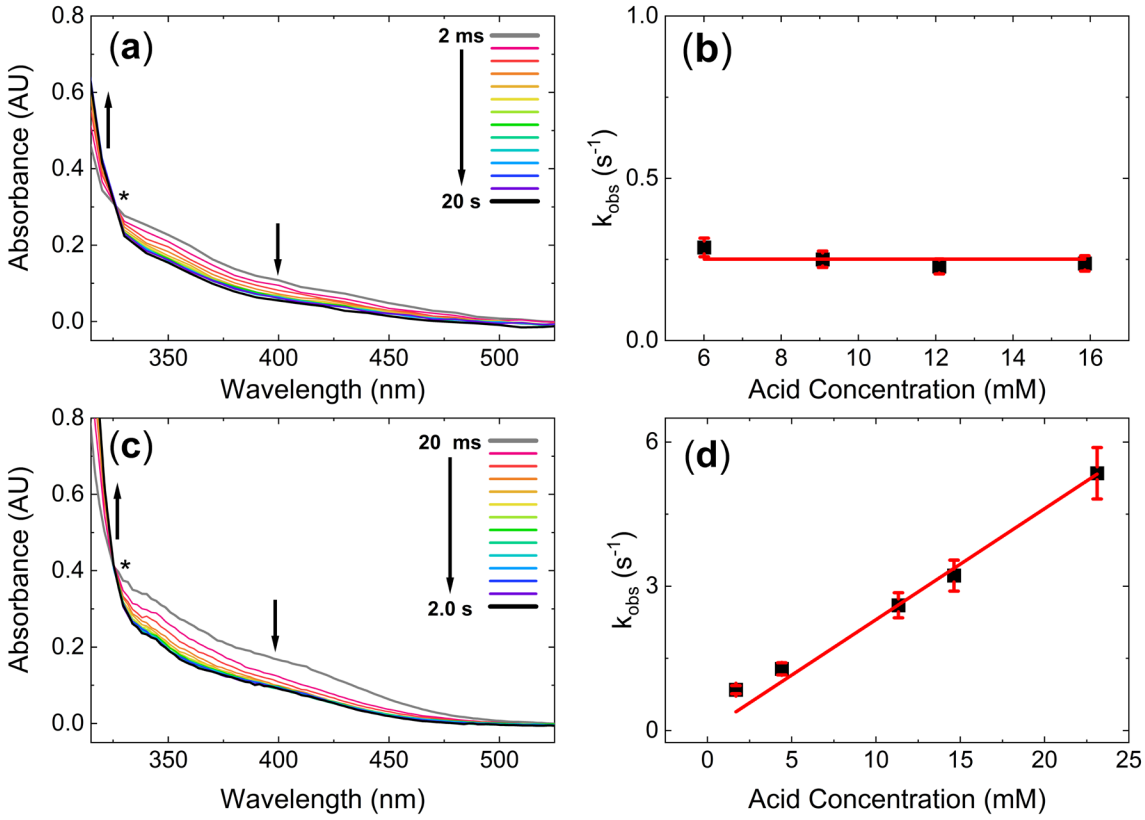

Figure 4.6. (**a**) Stopped-flow UV-vis spectra for the reaction between **5** and $[PhNH_3]^+$, assigned to back-tautomerization (k_{-4}) of **5** to generate **4**, followed by fast protonation of **4** to regenerate **1** and dihydrogen. Isosbestic behavior at 326 nm is denoted by *. (**b**) Observed rate of disappearance of **5** monitored at 399.8 nm as a function of $[PhNH_3]^+$ concentration. The slope of zero reveals a zero-order dependence on $[PhNH_3]^+$. (**c**) Stopped-flow UV-vis spectra for the proposed protonation of **5** by $[DMFH]^+$ to generate **6**, followed by the fast elimination of dihydrogen to generate **1**. Isosbestic behavior at 325 nm is denoted by *. (**d**) Observed rate constant monitored at 399.8 nm as a function of $[DMFH]^+$ concentration. The linear dependence reveals a first-order dependence on $[DMFH]^+$ and the overall second-order rate constant $k_5 = 230 \pm 10\ M^{-1}\ s^{-1}$

While hydrogen evolution and the regeneration of **1** is observed following addition of $[PhNH_3]^+$ or $[DMF{\cdot}H]^+$ to **5**, when the k_{obs} values are plotted as a function of acid concentration, two pathways to dihydrogen evolution are apparent. When the respective k_{obs} values are plotted as a function of $[PhNH_3]^+$ concentration, a zero-order acid dependence (k_{-4} = 260 ± 10 s^{-1}, see Figure 4.1) on $[PhNH_3]^+$ is observed. On the other hand, plotting the resulting k_{obs} values as a function of $[DMF{\cdot}H]^+$ reveal a first-order dependence on acid (k_5 = 230 ± 10 M^{-1} s^{-1}, see Figure 4.1). Taking into account the use of a much weaker acid ($[HNEt_3]^+$) when determining the rates for the initial protonation and tautomerization events (*vide supra*), the second protonation event(s) are comparatively slower, suggesting that either step k_{-4} or k_5 could represent the rate-determining step in dihydrogen evolution when using $[PhNH_3]^+$ or $[DMF{\cdot}H]^+$ with this system.

The defining characteristic distinguishing the reactivity of the second protonation event is the observed zero-order and first-order dependences on $[PhNH_3]^+$ and $[DMF{\cdot}H]^+$, respectively, implicating the involvement of two pathways with different intermediates leading to dihydrogen evolution. When using $[PhNH_3]^+$ to protonate **5**, the observed zero-order dependence is consistent with a reaction sequence involving relatively slow back tautomerization of **5** to the more reactive hydride species, **4**, followed by comparatively fast reactivity with $[PhNH_3]^+$ to generate **1** and dihydrogen. Whereas, when $[DMF{\cdot}H]^+$ is used, our kinetic data are consistent with protonation of **5** at the relatively electron-rich Rh(I) center to generate the plausible, and presumably highly reactive, $[(Cp^*H)Rh(H)(bpy)]^{2+}$ (**6**). This species could then undergo relatively fast intramolecular reactivity to generate dihydrogen and **1**. Notably, prior computational work regarding the protonation of **5** with $[DMF{\cdot}H]^+$ postulated the accessibility of this pathway (34); the experimentally determined first-order dependence of H_2 generation on $[DMF{\cdot}H]^+$ concentration

shows that **5** is indeed not an off-cycle intermediate, but instead can play a direct role in opening an additional pathway to dihydrogen evolution.

4.3 Discussion

Our work here has elucidated and clarified the mechanistic details underpinning the elementary electron- and proton-transfer steps involved in the generation of dihydrogen using the model system Cp*Rh(bpy). Variable temperature experiments examining the crucial proton-transfer steps have provided insight into the atomistic details involved in the initial handoff of the proton to the metal center, followed by the migration of the proton to the Cp* ring. In particular, the experimentally determined KIEs and activation parameters describing the tautomerization event provide direct evidence for the involvement of a proton shuttle, despite the fact that the Cp* ligand is closely associated with the metal center. Based on the known geometry of **5** from X-ray crystallography (11), and the computed structure of **4** (34), the distance (ca. 1.57 Å) between the hydride and a sp^2-hybridized carbon in the ring would likely be too great for an unassisted proton transfer, highlighting the necessity of the proton shuttle (57). Notably, the requirement of a proton shuttle is not problematic because the typical synthetic or bioelectrochemical conditions used to access **4** or **5** generally involve organic acids and conjugate base pairs, or water, respectively (11,14, 22, 23,31).

Beyond the initial protonation and tautomerization, the mechanistic path of the second protonation event is governed by the strength of the acid. Specifically, we have experimental kinetic evidence that the identity of the acid determines the role of the hydride and Cp*H species, the intermediates that form, and the rate of dihydrogen evolution. In particular, the hydride complex, **4**, has perhaps been among the most elusive, but hotly pursued, intermediates in

organometallic rhodium chemistry. In a sense, identification of the hydride here as an intermediate in dihydrogen evolution confirms the intuition of the field over the past 35 years. However, our work has provided among the first evidence that the hydride is but one possible protonated intermediate in this system. More broadly, our work suggests the Cp*H moiety should be actively considered in mechanistic investigations when both hydride and Cp* ligands are possibly involved in reactivity. Indeed, Kölle and Grätzel previously investigated the protonation of **3** with electrochemical measurements in aqueous phosphate buffer (31); following electrolysis, spectrophotometric data revealed an absorption spectrum that was not consistent with **1**, **2**, or **3**, and instead proposed **4** as a plausible intermediate. Upon reflection, the observation of the Cp*H complex, **5**, was likely missed in the early work because we now see that the colors of **4** and **5** are very similar. The fact that these species are similarly colored can be attributed to the non-innocence of the bpy π-system, which is intimately involved in management of redox load in these compounds. To this point, **3** exhibits vivid pigmentation, attributable to delocalization of electron density by π-backbonding into the bpy π-system (44). The properties of bpy thus strongly influence the catalytic reactivity paradigm observed, reactivity that is not echoed in systems with bidentate bisphosphine ligands (24,26) or even the closely related 9,9′-dimethyl-4,5-diazafluorene ligand (42), as well as impart spectral uniqueness to the [Cp*Rh] system.

The Cp*Rh(bpy) system represents one of the sole examples of a case where a metal-bound protonated Cp-type ligand can be isolated and studied at room temperature. Cp* is not merely a spectator ligand, and seems to be quite special, particularly in light of the reactivity observed by Peters and co-workers (16,17). The five methyl groups of Cp* appear to play a key role, imparting stability in the sense that clean reactivity is observed with this system through all the various protonations. In the Cp*Rh(bpy) system, the involvement of both initial metal-centered

protonation as well as the requirement of a proton shuttle in hydride-to-proton tautomerization appear to engender exclusively endo-protonation, a point of difference from related iron and cobalt systems (16,17). For robust catalysis to occur with this system, the endo-protonated species is presumably required for both of the H–H bond forming reaction channels proposed here; if $[PhNH_3]^+$ is utilized, back tautomerization is needed, and if $[DMF{\cdot}H]^+$ is used to form a second hydride with adjacent Cp*H, an acidified C–H bond pointing downward toward the hydride to promote intramolecular reactivity. On the other hand, since both *endo*- and *exo*-species are active in work with cobalt for H-atom transfer, Cp* ligand-centered H-management could find further applications and appears worthy of further study.

4.4 Conclusion

In summary, we have described the elementary steps leading to dihydrogen evolution using Cp*Rh(bpy) as a molecular model. Using PR, we confirmed a first-order dependence on **2**, when **3** is generated in MeCN in the presence of excess formate, excluding the plausible disproportionation mechanism initially proposed for this system in aqueous solution. Following the reaction of **3** with weak acids, we provide strong kinetic and spectroscopic evidence that confirms the initial site of protonation is metal centered, forming **4**, followed by subsequent tautomerization to generate **5**. To further support our assignments, variable temperature kinetic data using isotopically labeled acid suggest that NEt_3 plays an essential role as a proton shuttle, facilitating tautomerization of the proton (in the hydride ligand) to form the unusual η^4-Cp*H moiety. **5** reacts further with stronger acids, demonstrating that Cp*H can be an active participant in dihydrogen evolution, opening viable reaction pathways that depend on the strength of the acid. Our findings provide key insight into the rates and elementary reduction and protonation steps that

promote dihydrogen evolution with this system; taken together with the experimental activation parameters and mechanistic insights gleaned into metal-mediated hydride-proton tautomerism, these findings provide a springboard for further investigations involving the uncommon but apparently quite catalytically promiscuous η^4-Cp*H moiety.

4.5 Acknowledgments

This research at the University of Kansas, and travel to carry out experiments at Brookhaven National laboratory (BNL), was supported by the US National Science Foundation through award OIA-1833087. W.C.H. was also supported by the US National Institutes of Health Graduate Training Program in the Dynamic Aspects of Chemical Biology (T32 GM008545-25) as well as by a Graduate Student Research Grant from the Kansas Academy of Science. The work at BNL including the use of the Van de Graaff accelerator of the Accelerator Center for Energy Research, was supported by the U.S. Department of Energy, Office of Science, Office of Basic Energy Sciences, Chemical Sciences, Geosciences, and Biosciences Division, under contract DE-SC0012704.

4.6 References:

(1). G. Wilkinson, M. Rosenblum, M. C. Whiting, R. B. Woodward, The structure of iron bis-cyclopentadienyl. *J. Am. Chem. Soc.* **74**, 2125-2126 (1952).

(2). T. S. Piper, G. Wilkinson, Alkyl and aryl derivatives of π-cyclopentadienyl compounds of chromium, molybdenum, tungsten, and iron. *J. Inorg. Nucl. Chem.* **3**, 104-124 (1956).

(3). J. W. Lauher, R. Hoffmann, Structure and chemistry of bis(cyclopentadienyl)-MLn complexes. *J. Am. Chem. Soc.* **98**, 1729-1742 (1976).

(4). T. Kuwana, D. E. Bublitz, G. Hoh, Chronopotentiometric studies on the oxidation of ferrocene, ruthenocene, osmocene and some of their derivatives. *J. Am. Chem. Soc.* **82**, 5811-5817 (1960).

(5). A. Pedersen, M. Tilset, Solvent-induced reductive elimination of pentamethylcyclopentadiene from a (pentamethylcyclopentadienyl)metal hydride. *Organometallics* **12**, 3064-3068 (1993).

(6). F. A. Cotton, J. L. Calderon, J. Takats, Stereochemically nonrigid organometallic molecules. XXVII. Fluxional behavior of tetra(cyclopentadienyl)titanium. *J. Am. Chem. Soc.* **93**, 3587-3591 (1971).

(7). H. G. Alt, E. Samuel, Fluorenyl complexes of zirconium and hafnium as catalysts for olefin Polymerization. *Chem. Soc. Rev.* **27**, 323-329 (1998).

(8). M. J. Calhorda, C. C. Romão, L. F. Veiros, The nature of the indenyl effect. *Chem. Eur. J.* **8**, 868-875 (2002).

(9). U. Köelle, P. P. Infelta, M. Grätzel, Kinetics and mechanism of the reduction of protons to hydrogen by cobaltocene. *Inorg. Chem.* **27**, 879-883 (1988).

(10). T. J. Curphey, J. O. Santer, M. Rosenblum, J. H. Richards, Protonation of metallocenes by strong acids. Structure of the cation. *J. Am. Chem. Soc.* **82**, 5249-5250 (1960).

(11). L. M. A. Quintana *et al.*, Proton–hydride tautomerism in hydrogen evolution catalysis. *PNAS* **113**, 6409-6414 (2016).

(12). C. L. Pitman, O. N. L. Finster, A. J. M. Miller, Cyclopentadiene-mediated hydride transfer from rhodium complexes. *Chem. Commun.* **52**, 9105-9108 (2016).

(13). Y. Peng, M. V. Ramos-Garcés, D. Lionetti, J. D. Blakemore, Structural and electrochemical consequences of [Cp*] ligand protonation. *Inorg. Chem.* **56**, 10824-10831 (2017).

(14). W. C. Henke *et al.*, Ligand substituents govern the efficiency and mechanistic path of hydrogen production with [Cp*Rh] Catalysts. *ChemSusChem* **10**, 4589-4598 (2017).

(15). P. Hamon, L. Toupet, J. R. Hamon, C. Lapinte, Novel diamagnetic and paramagnetic iron(II), iron(III), and iron(IV) classical and nonclassical hyrides. X-ray crystal structure of $[Fe(C_5Me_5)(dppe)D]PF_6$. *Organometallics* **11**, 1429-1431 (1992).

(16). D. J. Schild, M. W. Drover, P. H. Oyala, J. C. Peters, Generating potent C–H PCET donors: ligand-Induced Fe-to-ring proton migration from a Cp^*Fe^{III}–H complex demonstrates a promising strategy. *J. Am. Chem. Soc.* **142**, 18963-18970 (2020).

(17). M. J. Chalkley, P. H. Oyala, J. C. Peters, Cp* Noninnocence leads to a remarkably weak C–H bond via metallocene protonation. *J. Am. Chem. Soc.* **141**, 4721-4729 (2019).

(18). I. Kaljurand *et al.*, Extension of the Self-Consistent Spectrophotometric Basicity Scale in Acetonitrile to a Full Span of 28 pKa Units: Unification of Different Basicity Scales. *J. Org. Chem.* **70**, 1019-1028 (2005).

(19). U. Kölle, M. Grätzel, Organometallic rhodium(III) complexes as catalysts for the photoreduction of protons to hydrogen on colloidal TiO_2. *Angew. Chem. Int. Ed.* **26**, 567-570 (1987).

(20). U. Kölle, M. Grätzel, Metallorganische rhodium(III)-komplexe als homogenkatalysatoren für die photoreduktion von protonen zu wasserstoff an kolloidalem TiO_2. *Angew. Chem.* **99**, 572-574 (1987).

(21). E. Steckhan *et al.*, Analytical study of a series of substituted (2,2'-bipyridyl)(pentamethylcyclopentadienyl)rhodium and -iridium complexes with regard to their effectiveness as redox catalysts for the indirect electrochemical and chemical reduction of $NAD(P)^+$. *Organometallics* **10**, 1568-1577 (1991).

(22). R. Ruppert, S. Herrmann, E. Steckhan, Efficient indirect electrochemical in-situ regeneration of NADH: electrochemically driven enzymatic reduction of pyruvate catalyzed by d-ldh. *Tetrahedron Lett.* **28**, 6583-6586 (1987).

(23). D. H. Nam, C. B. Park, Visible light-driven NADH regeneration sensitized by proflavine for biocatalysis. *ChemBioChem* **13**, 1278-1282 (2012).

(24). E. A. Boyd, D. Lionetti, W. C. Henke, V. W. Day, J. D. Blakemore, Preparation, characterization, and electrochemical activation of a model [Cp*Rh] hydride. *Inorg. Chem.* **58**, 3606-3615 (2019).

(25). J. A. Hopkins, D. Lionetti, V. W. Day, J. D. Blakemore, Synthesis and reactivity studies of a [Cp*Rh] complex supported by a methylene-bridged hybrid phosphine-imine ligand. *J. Organomet. Chem.* **921**, 121294 (2020).

(26). C. G. Comadoll *et al.*, Examining the modular synthesis of [Cp*Rh] monohydrides supported by chelating diphosphine ligands. *Organometallics* **40**, 3808-3818 (2021).

(27). S. Pal, S. Kusumoto, K. Nozaki, Dehydrogenation of dimethylamine–borane catalyzed by half-sandwich Ir and Rh complexes: mechanism and the role of Cp* noninnocence. *Organometallics* **37**, 906-914 (2018).

(28). D. Ghosh, H. Takeda, D. C. Fabry, Y. Tamaki, O. Ishitani, Supramolecular photocatalyst with a Rh(III)-complex catalyst unit for CO_2 reduction. *ACS Sustain. Chem. Eng.* **7**, 2648-2657 (2019).

(29). S. Banerjee *et al.*, New activation mechanism for half-sandwich organometallic anticancer complexes. *Chem. Sci.* **9**, 3177-3185 (2018).

(30). T. K. Todorova, T. N. Huan, X. Wang, H. Agarwala, M. Fontecave, Controlling Hydrogen evolution during photoreduction of CO_2 to formic acid using $[Rh(R\text{-}bpy)(Cp^*)Cl]^+$ catalysts: a structure–activity study. *Inorg. Chem.* **58**, 6893-6903 (2019).

(31). U. Kölle, B.-S. Kang, P. Infelta, P. Comte, M. Grätzel, Elektrochemische und pulsradiolytische reduktion von (pentamethylcyclopentadienyl)(polypyridyl)rhodium-complexen. *Chem. Ber.* **122**, 1869-1880 (1989).

(32). H. Nakai, K. Jeong, T. Matsumoto, S. Ogo, Catalytic C–F bond hydrogenolysis of fluoroaromatics by [(η^5-C_5Me_5)RhI(2,2′-bipyridine)]. *Organometallics* **33**, 4349-4352 (2014).

(33). A. M. Appel, M. L. Helm, Determining the Overpotential for a Molecular Electrocatalyst. *ACS Catalysis* **4**, 630-633 (2014).

(34). S. I. Johnson, H. B. Gray, J. D. Blakemore, W. A. Goddard, Role of ligand protonation in dihydrogen evolution from a pentamethylcyclopentadienyl rhodium catalyst. *Inorg. Chem.* **56**, 11375-11386 (2017).

(35). D. C. Grills, D. E. Polyansky, E. Fujita, Application of Pulse Radiolysis to Mechanistic Investigations of Catalysis Relevant to Artificial Photosynthesis. *ChemSusChem* **10**, 4359-4373 (2017).

(36). D. C. Grills, S. V. Lymar, Radiolytic formation of the carbon dioxide radical anion in acetonitrile revealed by transient IR spectroscopy. *Phys. Chem. Chem. Phys.* **20**, 10011-10017 (2018).

(37). E. Lamy, L. Nadjo, J. M. Saveant, Standard potential and kinetic parameters of the electrochemical reduction of carbon dioxide in dimethylformamide. *J. Electroanal. Chem. Interf. Electrochem.* **78**, 403-407 (1977).

(38). D. C. Grills, S. V. Lymar, Solvated Electron in Acetonitrile: Radiation Yield, Absorption Spectrum, and Equilibrium between Cavity- and Solvent-Localized States. *The J. Phys. Chem. B* **126**, 262-269 (2022).

(39). The pre-mixing of **1** and formate was necessary due to slow reduction of **1** by [n-Bu_4N][HCO_2] on timescales > 20 s.

([40]). E. Fujita, D. J. Szalda, C. Creutz, N. Sutin, Carbon dioxide activation: thermodynamics of carbon dioxide binding and the involvement of two cobalt centers in the reduction of carbon dioxide by a cobalt(I) macrocycle. *J. Am. Chem. Soc.* **110**, 4870-4871 (1988).

(41). W. N. G. Moore, W. C. Henke, D. Lionetti, V. W. Day, J. D. Blakemore, Single-electron redox chemistry on the [Cp*Rh] platform enabled by a nitrated bipyridyl ligand. *Molecules* **23**, 2857 (2018).

(42). W. Henke, J. Stiel, V. Day, J. Blakemore, Evidence for Charge Delocalization in Diazafluorene Ligands Supporting Low-Valent [Cp*Rh] Complexes. *Chem. Eur. J.*, **in press** (2022).

(43). J. H. Espenson, *Chemical kinetics and reaction mechanisms* (McGraw-Hill : Primis Custom, New York, 2002).

(44). C. Creutz, Bipyridine Radical Ions. *Comments Inorg. Chem.* **1**, 293-311 (1982).

(45). The zero-order rate constant determined for the tautomerization reaction was identical within error when monitoring the observed rate of tautomerization to 1 s or 10 s (See Appendix B, Figures B44-B49).

(46). As an alternative way to analyze this reactivity, we included data for both [$HNEt_3$]OTf and [$HNEt_3$]BF_4 to see if the counteranion of the acid impacts reactivity. The data for [$HNEt_3$]BF_4 were collected under the same conditions as the data using [$HNEt_3$]OTf and [$DNEt_3$]OTf (20–

40 °C under pseudo first-order conditions). The resulting data confirm that these counteranions do not affect the rate of protonation or tautomerization and merely behave as spectator ions. The similarity of the resulting rate constants, activation energies, and activation parameters among the respective protonation and tautomerization events is unsurprising due to the similar non-coordinating triflate and tetrafluoroborate counteranions.

(47). K. T. Leffek, P. Pruszynski, Proton transfer reactions between ortho-methyl substituted derivatives of 4-nitrophenylphenylcyanomethane and nitrogen bases in acetonitrile solvent. *Can. J. Chem.* **66**, 1454-1458 (1988).

(48). A. L. Casado, P. Espinet, On the Configuration Resulting from Oxidative Addition of RX to $Pd(PPh_3)_4$ and the Mechanism of the cis-to-trans Isomerization of $[PdRX(PPh_3)_2]$ Complexes (R = Aryl, X = Halide). *Organometallics* **17**, 954-959 (1998).

(49). D. W. Flaherty, E. Iglesia, Transition-State Enthalpy and Entropy Effects on Reactivity and Selectivity in Hydrogenolysis of n-Alkanes. *J. Am. Chem. Soc.* **135**, 18586-18599 (2013).

(50). S. C. L. Kamerlin, J. Florián, A. Warshel, Associative Versus Dissociative Mechanisms of Phosphate Monoester Hydrolysis: On the Interpretation of Activation Entropies. *ChemPhysChem* **9**, 1767-1773 (2008).

(51). J. W. McIver, Structure of transition states. Are they symmetric. *Acc. Chem. Res.* **7**, 72-77 (1974).

(52). T.-Y. Cheng, R. M. Bullock, Isotope Effects on Hydride Transfer Reactions from Transition Metal Hydrides to Trityl Cation. An Inverse Isotope Effect for a Hydride Transfer. *J. Am.Chem. Soc.* **121**, 3150-3155 (1999).

(53). C. P. Park, A. Nagle, C. H. Yoon, C. Chen, K. W. Jung, Formal aromatic C−H insertion for stereoselective isoquinolinone synthesis and studies on mechanistic insights into the C−C bond formation. *J. Org. Chem.* **74**, 6231-6236 (2009).

(54). M. Gómez-Gallego, M. A. Sierra, Kinetic Isotope effects in the study of organometallic reaction mechanisms. *Chem. Rev.* **111**, 4857-4963 (2011).

(55). D. G. Churchill, K. E. Janak, J. S. Wittenberg, G. Parkin, Normal and inverse primary kinetic deuterium isotope effects for C−H bond reductive elimination and oxidative addition reactions of molybdenocene and tungstenocene complexes: evidence for benzene σ-complex intermediates. *J. Am. Chem. Soc.* **125**, 1403-1420 (2003).

(56). M. Wolfsberg, Theoretical evaluation of experimentally observed isotope effects. *Acc. Chem. Res.* **5**, 225-233 (1972).

(57). H. Xu, S. S. Alguindigue, A. H. West, P. F. Cook, A Proposed Proton Shuttle Mechanism for Saccharopine Dehydrogenase from Saccharomyces cerevisiae. *Biochemistry* **46**, 871-882 (2007).

(58). E. V. Anslyn and D. A. Dougherty, *Modern physical organic chemistry*. (2006).

(59). D. R. Klein, Organic Chemistry, 3rd Edition. (2016).

Part II

Chapter 5

Ultrafast Spectroscopy of [$Mn(CO)_3$] Complexes: Tuning the Kinetics of Light-Driven CO Release and Solvent Binding

This chapter is adapted from a published manuscript: Henke, W.C.,[#] Otolski, C.J.,[#] Moore, W.N.G., Elles, C.G.,* and Blakemore, J.D.* Ultrafast Spectroscopy of [$Mn(CO)_3$] Complexes: Tuning the Kinetics of Light-Driven CO Release and Solvent Binding, *Inorg. Chem.* **2020**, *59*, 2178-2187. [#] Equal contributions

5.1 Introduction

Manganese tricarbonyl complexes of the form $Mn(CO)_3(^{R}bpy)Br$ (^{R}bpy = 4,4′-disubstituted–2,2′-bipyridyl) are promising catalysts for conversion of carbon dioxide (CO_2) into carbon monoxide and/or formate, valuable precursors to chemical feedstocks and commodity chemicals.[1,2] The synthetic chemistry for the Mn complexes was developed by Wilkinson and co-workers,[3] and later extended by Wrighton, Meyer, and others.[4] These complexes are remarkable for their ease of preparation and can be synthesized from commercially available or readily prepared ligands, ^{R}bpy, and the synthon $Mn(CO)_5Br$. Similar synthetic chemistry and catalytic properties have been demonstrated with analogous rhenium tricarbonyl complexes, $Re(CO)_3(^{R}bpy)Br$, which were investigated for catalysis much earlier by Lehn[5] and Meyer[6], and popularized by Fujita[7], Kubiak[8], Ishitani[9], and others.[10] However, considering the significantly greater abundance of manganese, many research groups have continued to develop new $[Mn(CO)_3]$-based catalysts. These efforts have led to a remarkable flourishing of reports showing that a variety of bidentate ligands can support and/or tune the electronic, photo-physical, and catalytic properties of $[Mn(CO)_3]$ complexes.[11,12,13]

A defining feature that distinguishes the rhenium complexes from their manganese analogues is markedly better stability upon irradiation with visible light.[14] Importantly, many $[Mn(CO)_3]$ complexes are susceptible to speciation[15] and/or degradation[16] upon exposure to visible light. For example, our preliminary investigations in organic solvents revealed that $Mn(CO)_3(^{R}bpy)Br$ complexes begin to decompose within minutes under ambient fluorescent lighting, as evident from peak broadening in the ^{1}H nuclear magnetic resonance (NMR) spectra. A review describing the photochemistry of a variety of metal carbonyl species provides context to the light sensitivity of

$Mn(CO)_3(^{R}bpy)Br$ in solution.[17] Specifically, the light sensitivity of many first-row transition metal complexes is often a consequence of the inherent excited-state electronic structure of the compounds. However, as the light sensitivity of the $Mn(CO)_3(^{R}bpy)Br$ complexes presents a potential challenge to their use in electrochemical or, especially, photoelectrochemical systems for CO_2 conversion, we became interested in the underlying processes that contribute to speciation and/or degradation.

Separate from their role as catalysts, the light-induced reactivity of manganese complexes makes the $[Mn(CO)_3]$ moiety a promising motif for developing a relatively new class of putative therapeutics known as photo-induced carbon monoxide releasing molecules (photo-CORMs).[18] Classic work on the photochemical properties of dimanganese decacarbonyl ($[Mn(CO)_5]_2$) revealed the susceptibility of low-valent manganese complexes to release CO under irradiation with visible light.[19,20] However, $[Mn(CO)_5]_2$ absorbs only very weakly in the visible region, which is problematic from the standpoint of therapeutic development because UV light does not readily penetrate the skin.[21] The need for efficient activation of photo-CORMs at longer wavelengths has motivated the development of novel $[Mn(CO)_3]$-based compounds that absorb light in the visible region. Toward this goal, Schatzschneider and co-workers developed the first $[Mn(CO)_3]$-based photo-CORMs supported by various tripodal ligands.[22] Further work by several research groups has led to numerous platforms and ligand systems in this family that allow effective photo-induced CO release.[23] Notably, Mascharak and co-workers highlighted the light sensitivity of $Mn(CO)_3(^{R}bpy)Br$ complexes, demonstrating that $Mn(CO)_3(^{H}bpy)Br$ is capable of visible light induced CO release at 420 nm.[24]

Despite the potential role of $Mn(CO)_3(^{R}bpy)Br$ complexes in diverse applications ranging from catalysis to phototherapeutics, the photophysical properties of these compounds have received

surprisingly little attention. The analogous [$Re(CO)_3$] complexes have been studied with nanosecond and femtosecond transient absorption spectroscopy, as well as time-resolved infrared absorption measurements.[25,26] Vlček and co-workers in particular have examined various aspects of the ligand-dependent excited state behavior of [$Re(CO)_3$] complexes bearing diimine-type ligands, providing important insights into electron transfer behavior and the resulting chemical reactivity.[27,28] However, to the best of our knowledge, no femtosecond or picosecond pump-probe experiments have examined the fundamental photochemistry of [$Mn(CO)_3$] complexes bearing diimine ligands. Only steady-state experiments involving spectroscopic characterization of the products following bulk photolysis,[15] and a nanosecond pulse radiolysis study of the reduction-induced reactivity of $Mn(CO)_3(^{tBu}bpy)Br$ have been reported.[29]

In this contribution, we examine the fundamental photochemistry of $Mn(CO)_3(^{R}bpy)Br$ complexes with disubstituted ligands bearing *tert*-butyl (**1**), hydryl (**2**), trifluoromethyl (**3**), and nitro (**4**) groups (Chart 5.1) following exposure to visible light. Ultrafast transient absorption (TA) spectroscopy reveals the loss of a CO ligand on the femtosecond timescale, followed by solvent coordination on the picosecond timescale for **1**, **2**, and **3** in acetonitrile. The kinetics of these reactions depend on the identity of the substituents at the 4 and 4′ positions of the ^{R}bpy ligand and correlate well with the Hammett parameters associated with the substituent groups. In contrast with the results for **1**, **2**, and **3**, TA spectroscopy and gas chromatography (GC) measurements indicate that **4** does not undergo CO release. Taken together, these observations implicate metal-to-ligand charge transfer (MLCT) and dissociative ligand field (LF) states in driving the photoinduced reactivity, and suggest that the relative energies of these electronic states are tuned through the modification of the supporting ligand. Our results are discussed in the context of

developing new design principles that could be used to selectively control light-driven CO release from $[Mn(CO)_3]$ complexes.

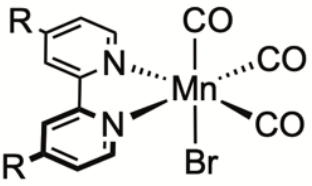

R = –^{t}Bu (**1**), –H (**2**), –CF_3 (**3**), –NO_2 (**4**)

Chart 5.1: $Mn(CO)_3(^R bpy)Br$ complexes **1**-**4**.

5.2 Results and Discussion

5.2.1 Synthesis and Characterization

In order to study $[Mn(CO)_3]$ complexes with uniformly tuned properties, we prepared compounds that differ only in the electron donating/withdrawing nature of the substituents in the 4 and 4′ positions of the supporting 2,2′-bipyridyl ligand. Complexes **1** and **2** were prepared according to prior reports[1,2] and new derivatives **3** and **4** were synthesized and isolated using methods similar to those of Wrighton and co-workers (see Experimental Section for details).[4] Overall, no unusual features were encountered for the synthesized complexes. All of the formally manganese(I) complexes were prepared from $Mn(CO)_5Br$ and isolated with inner-sphere bromide ligands. The compounds have C_s symmetry, and are soluble in common organic solvents (e.g., acetonitrile, chloroform) (see Figures C1-C5).

The $Mn(CO)_3(^R bpy)Br$ complexes have a variety of useful signatures that can be readily interrogated using NMR, IR, and electronic absorption spectroscopies. Trends in the spectra can

be correlated with the ^{R}bpy substituents using Hammett parameters.[30] However, the traditional Hammett parameter (σ) does not consider stabilization of partial or full charges in reference to inductive and resonance effects of the conjugated ligand. These limitations are accounted for in Brown's sigma plus parameter (σ^+) and Kubota's sigma minus parameter (σ^-), which stabilize partial or full positive and negative charges, respectively.[31,32] To determine which parameter is most appropriate for a given system or spectroscopic signature, a series of Hammett plots are constructed to compare goodness-of-fit with σ^+, σ, and σ^-. For example, the ^{1}H-NMR chemical shifts for the *ortho*-pyridyl protons of each complex correlate best with Brown's σ^+ parameter (see Figures C6-C7), in agreement with prior literature.[33] The correlation with σ^+ indicates an inductive ground-state interaction between the ligand framework and the substituents.

Infrared absorption spectroscopy confirms the presence of the *fac*-tricarbonyl geometry for each of the complexes **1**-**4** in solution (see Figure C8), and demonstrates that the samples are free of $Mn(CO)_5Br$ starting material (associated with absorption bands at 2004 cm^{-1}, 2046 cm^{-1}, and 2083 cm^{-1}). Our results from IR spectroscopy are consistent with previous observations of heteroleptic carbonyl complexes, as we observe a systematic increase of the C–O stretching frequencies upon changing the character of the 4,4′-substituents of ^{R}bpy from electron donating to electron withdrawing.[34] Hammett plots of the A′′-symmetry C–O stretching frequency[35] as a function of ligand substituent are best fit by the σ parameter (R^2 = 0.993), although the correlations with σ^+ (R^2 = 0.989) and σ^- (R^2 = 0.945) are not vastly different from the correlation with σ (see Figure C9). This observed correlation of C–O stretching frequencies is in agreement with previous work on *para*-substituted isocyanide complexes $CpFe(CO)_2(CN^RPh)$ and $CpMn(CO)_2(CN^RPh)$, where Cp is cyclopentadienyl.[36,37] However, as C–O stretching modes are affected principally by π-

bonding effects, the measured range of 15 cm^{-1} for the bipyridyl complexes under investigation here is consistent with the expected distal influence of the bipyridyl ligand substituents on the Mn metal center and the CO ligands.

Complexes **1**-**4** give vividly colored solutions when dissolved in common organic solvents like MeCN (see Figure C10). Figure 5.1 shows the electronic absorption spectra for all four complexes, and Table 5.1 lists the transition energies and molar absorptivities for each of the lowest-energy absorption bands. Plotting the energies of the first absorption band for **1**-**4** as a function of σ^- parameter gives an excellent correlation ($R^2 = 0.998$; see Figures C11-C15). On the basis of the molar absorptivity and comparison with related compounds, the lowest-energy absorption bands for **1**-**4** can all be confidently assigned as having significant MLCT character (See Table 5.1). These findings agree with prior work on $Mn(CO)_3$(diimine)Br complexes showing that the highest occupied molecular orbital is primarily localized on the Mn center, while the lowest unoccupied molecular orbital has significantly more ligand character, suggesting that the visible transitions are primarily MLCT in nature.[38] Plotting the molar absorptivity of the lowest-energy absorption bands of **1**-**4** as a function of the Hammett parameter also reveals a linear correlation with σ^-, where the transition strength increases for more electron-donating substituents (see Figure C16). Thus, the trend in transition strength across all four compounds is roughly linear with σ^-, consistent with previous studies of transition metal complexes featuring MLCT behavior.[39] A likely explanation for the decreasing transition strength with increasing electron-withdrawing character of the ligand substituents is reduced overlap of the HOMO and LUMO due to increased localization of the LUMO on the electron-withdrawing substituents. The electron-donating groups, in contrast, localize the LUMO closer to the Mn metal center, leading to better overlap with the HOMO and therefore a stronger MLCT transition. Based on this reasoning, the relatively weak transition for **4**

follows the trend in MLCT transition strengths set by the other three compounds, even though the lower absorption strength for **4** would typically be associated with a d-d transition. Although we cannot rule out the possibility of some d-d character in the lowest-energy transition for **4**, the strong correlation of both the transition energies and strengths with σ^- reinforces our assignment of the lowest-energy absorption bands as primarily MLCT in nature for all four compounds.

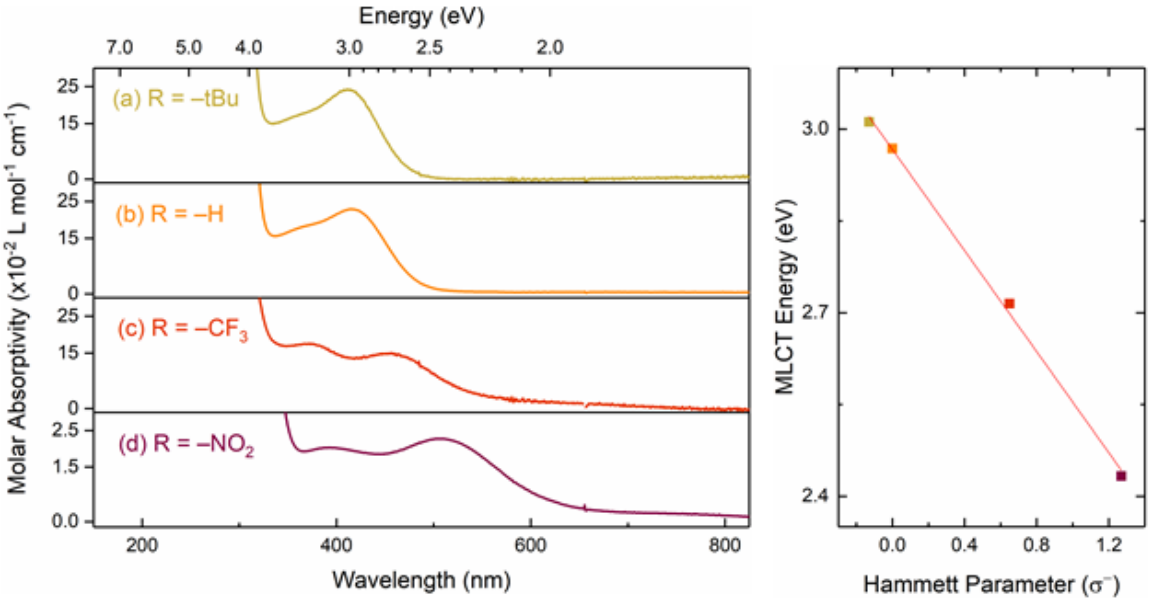

Figure 5.1: Electronic absorption spectra of **1**, **2**, **3**, and **4** in MeCN (left). Hammett plot of MLCT energy in eV as a function of the σ^- parameter (right). The best fit line in the Hammett plot reveals a correlation with $R^2 = 0.998$, and a slope of -0.41 ± 0.01.

Table 5.1: Hammett parameters of the ligand substituents and selected spectral parameters for complexes **1**–**4**.

Compound	Hammett parameter (σ^-)	λ (nm, eV)	ε (M^{-1} cm^{-1})
1	–0.13	412, 3.00	2426
2	0.0	415, 2.99	2288
3	0.65	457, 2.71	1502
4	1.27	510, 2.43	228

5.2.2 Transient absorption spectroscopy

Ultrafast transient absorption (TA) spectroscopy probes the reaction dynamics following MLCT excitation of the [$Mn(CO)_3$] complexes. Based on the shift of the MLCT bands with ligand substitution, we used excitation pulses at 420 nm for **1** and **2**, 470 nm for **3**, and 510 nm for **4**. Figure 5.2 shows the evolution of the TA spectra for **1-4** in MeCN. The initial excited-state absorption bands for compounds **1**-**3** are double-peaked and partially decay in ≤1 ps, followed by the delayed appearance of a narrower absorption band at slightly longer wavelength within ~100 ps. The transient spectra are similar for all three compounds at longer time delays as well, except for a red-shift of the TA bands that is similar to the shift of the ground-state MLCT bands across the three compounds. Notably, both the initial excited-state absorption bands and the new features that appear within ~100 ps follow the same trend as the ground-state MLCT bands of **1**-**3**, indicating that the ^{R}bpy ligand remains bound to the Mn center for each of the transient species (see Figure C17).

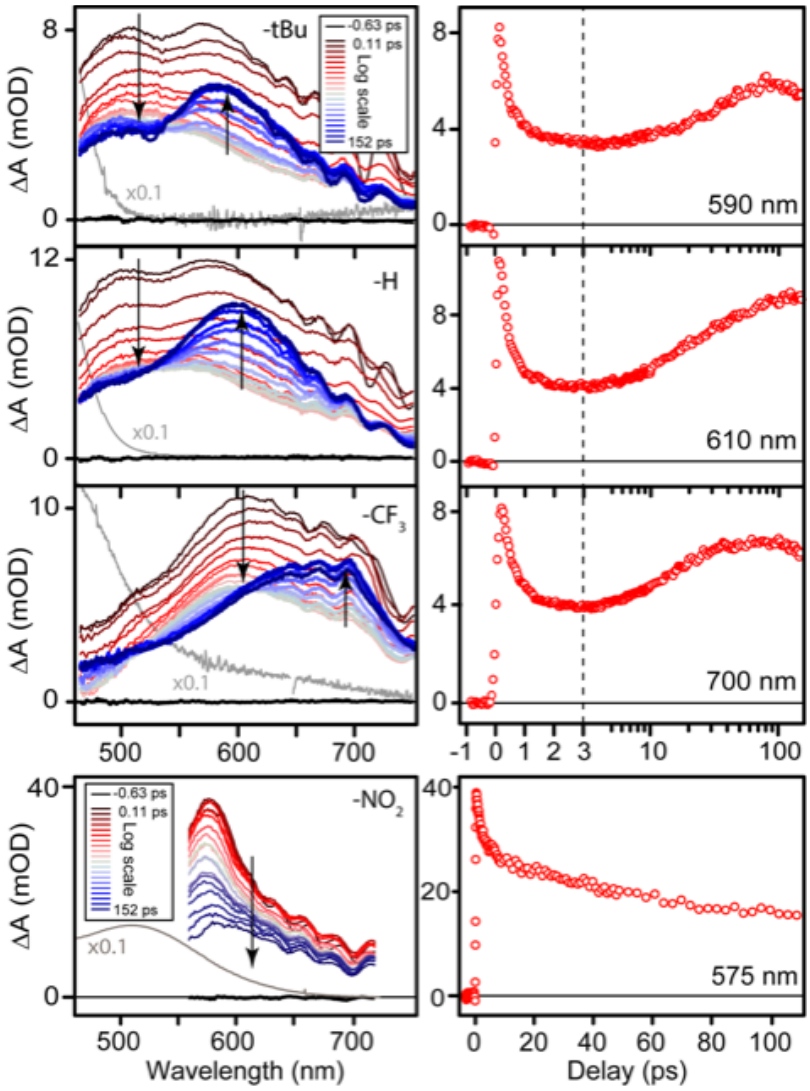

Figure 5.2: Transient absorption spectra of **1**, **2**, **3,** and **4** (top to bottom) in MeCN. Left panel shows spectral evolution, right panel shows the absorption change at a single wavelength. For reference, the ground-state absorption spectra are scaled by 1/10 and shown as grey lines.

The evolution of the TA spectrum for the nitro disubstituted compound (**4**), also shown in Figure 5.2, is noticeably different from the other complexes. The initial excited-state absorption band is stronger, narrower, and decays more slowly than in the other compounds. Furthermore, there is not a secondary absorption feature that appears on the ~100 ps timescale in the transient spectrum

of compound **4**. Unlike **1**-**3**, the shift in wavelength of the initial TA band of **4** also does not follow the same trend as the ground-state MLCT bands. The strongly electron withdrawing nitro groups likely localize the charge in the MLCT state, resulting in a more stable and longer-lived excited state for **4**.

Based on the TA spectroscopy and kinetics, as well as the observation of CO in the headspace of irradiated samples using GC analysis (see Figures C18-C19), we propose a pathway for the early speciation process of complexes **1**-**3** that involves rapid CO loss followed by solvent coordination, as shown in Scheme 5.1. Optical excitation initially promotes an electron from a metal d-orbital to the π* orbital of the bpy ligand. The MLCT state is likely to be close in energy to a ligand field (LF) state with d-d excitation on the metal that has significant antibonding (σ*) character in the equatorial manganese-carbon bonds.[40] The anti-bonding ligand field state is stabilized by increasing the Mn-CO bond length, which results in a curve crossing that allows adiabatic population transfer from the MLCT state to the directly dissociative LF state (Figure 5.3). Impulsive release of a CO ligand via the LF state generates an electron-deficient (16 e^-), five-coordinate intermediate, $Mn(CO)_2(^{R}bpy)Br$. In acetonitrile, such an intermediate species is likely to bind a solvent ligand in order to recover a more stable 18 e^- configuration. Thus, we attribute the new signal that rises on the tens of picoseconds timescale to the formation of a solvent-coordinated complex. Reduced electron back-bonding by the newly associated MeCN ligand compared with the CO that it replaces explains the red-shift of the MLCT absorption bands of the solvent-coordinated complexes compared with the initial compounds.

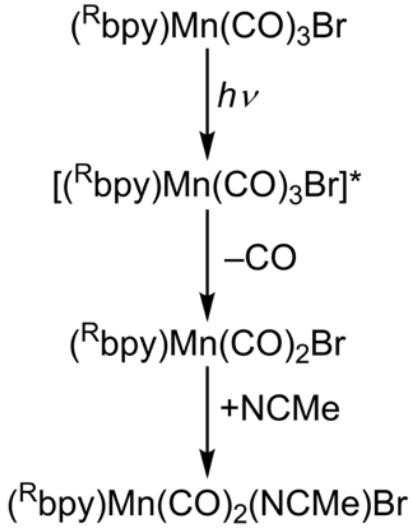

Scheme 5.1: Proposed mechanism for the initial pathway leading to speciation for complexes **1-3**.

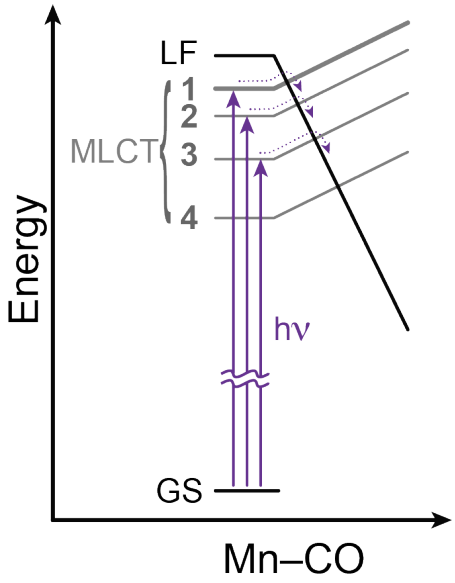

Figure 5.3: Schematic energy-level diagram illustrating how the change in Mn-CO bond length affects the curve crossing between MLCT and LF states. The barrier for adiabatic population transfer increases with decreasing MLCT energy across the series **1-4** (R = ^{t}Bu, H, CF_3, NO_2).

A global fit to the TA spectrum of each compound using a bi-exponential function reveals the time constants for CO loss (τ_1) and solvent coordination (τ_2). The global fits give the time constants

in Table 5.2 and the decay-associated spectra (DAS) in Figures C20-C22 of Appendix C.[41] The time-constants indicate a slightly longer timescale for CO release and a shorter timescale for solvent coordination as the ligand becomes more electron withdrawing. The trend in τ_2 is consistent with formation of a relatively more electron-poor 16 e^- complex in the case of the more electron-withdrawing ligand for **3**, compared with **2** and **1**.

In the proposed mechanism, the rate of CO loss is dependent on how quickly the MLCT state converts to the d-d dissociative LF state. Therefore, the observed rate of CO loss during photolysis likely depends on the initial relative energies of the MLCT and dissociative LF states. Changing the substituents on the 4 and 4′ positions of the bpy ligand should leave the metal d-orbitals relatively unaffected while tuning the ligand π* orbitals to a larger extent. The MLCT energy depends on π* of the ligand, but the LF energy should be relatively insensitive to substitution, as illustrated in Figure 5.3. This picture is consistent with the trend that we observe in the timescales for CO loss in Table 5.2. Changing the substituents on the bpy ligand from electron-donating to electron-withdrawing stabilizes the MLCT state and therefore increases the barrier to reach the LF state (Figure 5.3). Accordingly, the increasing electron-withdrawing character of ^{R}bpy from **1** to **3** is associated with a corresponding decrease in the rate for CO loss (*i.e.* increase of τ_1) due to stabilization of the MLCT state and, therefore, larger barrier to charge recombination by accessing the dissociative LF state.

Table 5.2: Time constants for CO release (τ_1) and solvent coordination (τ_2)[a]

Compound	τ_1 (ps)	τ_2 (ps)
1	0.50 ± 0.10	39 ± 4
2	0.46 ± 0.10	30 ± 4
3	0.68 ± 0.20	18 ± 3

[a] From global fits to the TA spectra for ~2 mM solutions of **1-3** in MeCN.

As the substituents become even more electron withdrawing, the π* level of the bpy ligand is pushed substantially lower in energy compared with the occupied metal d-orbitals. In the limiting case of the ^{NO2}bpy complex (**4**), the MLCT band is > 0.5 eV below that of the prototypical ^{H}bpy complex (**2**) due to charge stabilization and localization of electron density on the nitro groups. Thus the MLCT state of **4** is much lower than the dissociative LF state, significantly increasing the barrier for charge recombination and strongly disfavoring CO loss (see Figure C23 in Appendix C). Instead, the MLCT state of **4** probably relaxes through a competing mechanism, possibly intersystem crossing (ISC) to a triplet state that is relatively long lived and persists beyond the time resolution of our experiment.

5.2.3 Measurement of CO release by infrared spectroscopy

To confirm that the [$Mn(CO)_3$] complexes undergo CO loss followed by subsequent chemical reactivity in MeCN solvent, a series of photolysis experiments were carried out with infrared spectroscopic monitoring to interrogate the generation of new species by irradiation of **2** with visible light. Following 2 min. of irradiation with 415 nm light (at a total lamp power of 175 W),

unique CO stretches appear in the IR spectrum, including stretches associated with Mn complexes between 2050–1825 cm^{-1} as well as the diagnostic stretch corresponding to free CO gas dissolved in MeCN near 2143 cm^{-1} (see Figure C24 for all spectra). Over time, the bands associated with **2** at 1924, 1934, and 2028 cm^{-1} decrease in intensity, and C–O stretches presumably associated with Mn-containing photoproducts grow in at 1883, 1961, and 1976 cm^{-1}; two less intense features also appear at 1856 cm^{-1} and 2050 cm^{-1}, but these features show minor variations in intensity over the 15 min. irradiation time, suggesting they may be associated with metastable intermediates. The presence of the $[Mn(CO)_3(bpy)]_2$ dimer can be inferred from related work examining electrochemical generation of the analogous $[Mn(CO)_3(^{tBu}bpy)]_2$ dimer by Kubiak and co-workers.[42] As the speciation processes occurring at longer times are likely complex and multistep in nature, a portion of our future work will be devoted to further exploration by both time-resolved spectroscopies and more detailed steady-state photolysis experiments.

5.2.4 Involvement of MLCT vs. LF states

Although the changing energy of the MLCT state with ligand substituents is evident from the shifting of the ground-state absorption bands of **1**-**4**, we have been unable to directly observe the relative energies of the LF states. The weak d-d transitions are not evident in the absorption spectra, due to the stronger overlapping MLCT bands. We also attempted to measure the d-d transition for the analogous bis-pyridine complex, $Mn(CO)_3Br(py)_2$ (**5**), in an effort to determine the relative energy of the LF state in $[Mn(CO)_3]$ complexes (see Figure C25).

Although the synthesis of **5** has been previously reported, the molecular structure of the complex was not reported. To obtain the structure, we grew single crystals of **5** suitable for X-ray diffraction (XRD) analysis by vapor diffusion of diethyl ether into a concentrated MeCN solution (see Figures

C26-C27). Single crystals of the new complexes **3** and **4** suitable for XRD analysis were obtained with similar conditions (see Figures C28-C30). The expected atomic connectivity and *fac*-tricarbonyl geometry were confirmed in each case. While the donor strengths of py and bpy are similar (both molecules are conjugated imines with roughly the same electronic character), the average Mn–N bond distance in **5** (2.096(8) Å) is significantly longer than that found in the bipyridyl complexes **3** or **4** (2.051(4) and 2.039(6) Å, respectively), indicating a weaker interaction of the independent pyridyl rings in the $(py)_2$ complex compared with bpy. Eliminating conjugation between the rings also pushes the π^* orbital of py to higher energy and shifts the MLCT band of **5** to shorter wavelength. However, even with the simultaneous blue shift of the MLCT band and weaker donation by pyridine, we do not observe a distinct d-d transition in the absorption spectrum of **5**. On the other hand, it is interesting to note the presence of a shoulder band near 390 nm in the absorption spectra of all four diimine complexes (Figure 5.1), as well as **5**; this band could be consistent with the presence of an overlapping d-d feature at higher energy than the observed lowest-energy MLCT bands.

Considering all of these features, the ultrafast TA results show that we can selectively control the sensitivity of the initial CO release by tuning the orbital energy levels of the $[Mn(CO)_3Br(^{R}bpy)]$ complexes based on ligand substitution. Selectively controlling the loss of a CO ligand at the femtosecond timescale can lead to improved catalysts and more efficient photo-CORMs. On one hand, preventing CO release would give more stable catalysts, and on the other hand, complexes with tunable reactivity could serve as model compounds for regulating the therapeutic release of CO.

5.2.5 Secondary reactivity following CO loss

The CO release step is only the beginning of a more complex speciation process for these Mn complexes. After CO release in MeCN, the resulting electron deficient five-coordinate species [(^{R}bpy)Mn(CO)$_2$Br] quickly binds a ligand to regain a full 18 e$^-$ valence. Table 5.2 shows that the time constants for solvent coordination (τ_2) decrease markedly as the ligand becomes more electron withdrawing. Complexes with a more electron deficient Mn center due to the electron-withdrawing ^{CF3}bpy ligand (**3**) bind an acetonitrile more quickly than the complexes bearing electron-donating ^{tBu}bpy (**1**) or ^{H}bpy ligands (**2**).

In order to test the solvent dependence of the secondary reactivity occurring upon CO loss, we also measured the evolution of the TA spectrum of **2** in chloroform ($CHCl_3$). Unlike MeCN, $CHCl_3$ is not generally considered to be a coordinating solvent.[43] Figure 5.4 shows that the evolution of the TA spectrum following MLCT excitation of **2** is very different in the two solvents. Specifically, the spectroscopic feature that appears on a picosecond timescale and is assigned as solvent-coordination in MeCN is completely attenuated in $CHCl_3$, resulting in a broad and featureless spectrum that persists beyond the duration of our experiment.

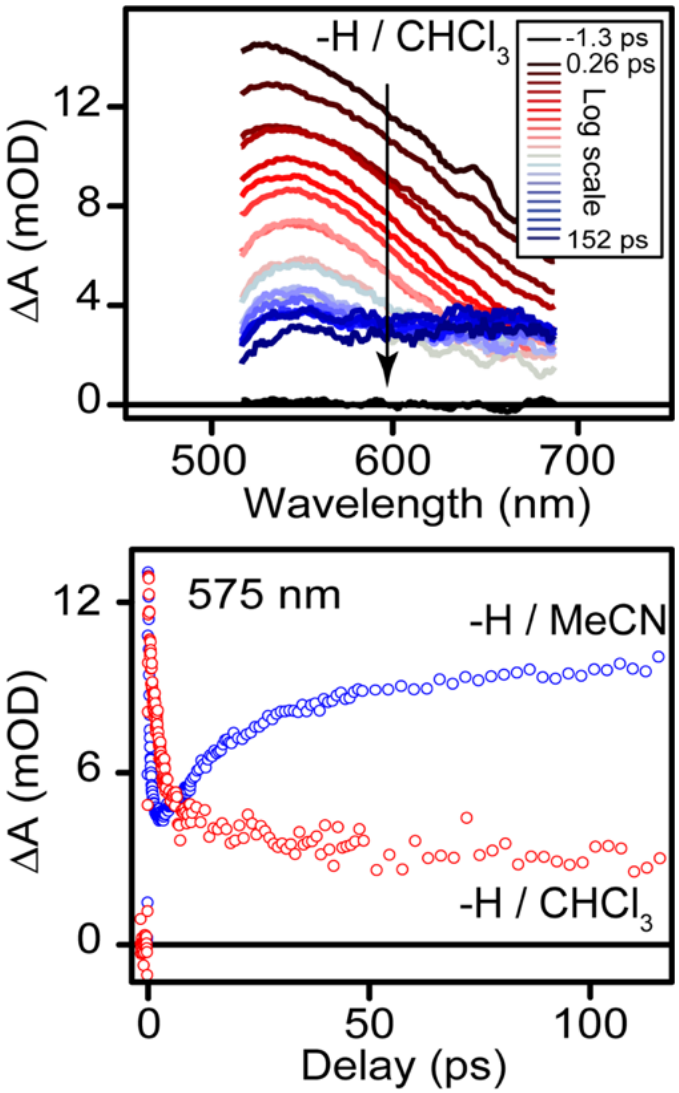

Figure 5.4: Transient absorption spectrum of **2** in $CHCl_3$ (upper panel), and comparison of the kinetics at 575 nm for **2** in the coordinating solvent MeCN (blue markers) and in the noncoordinating solvent $CHCl_3$ (red markers).

In both the cases of MeCN and $CHCl_3$ as solvent, CO release exposes the coordinatively unsaturated, 16 e^- metal center to the solvent. Although direct solvent coordination is suppressed in $CHCl_3$, the electron-deficient, 5-coordinate complex is likely to be susceptible to other bimolecular reactions, possibly including oxidative addition of $CHCl_3$ or hydrogen atom transfer from the solvent. The products from any of these reactions, or a combination of them, could be

responsible for the broad, featureless TA spectrum that develops following excitation of **2** in $CHCl_3$. Indeed, the reactivity of this complex in $CHCl_3$ is consistent with recently reported transient absorption measurements for Mn tetracarbonyl complexes supported by anionic chelating ligands.[44] However, regardless of the subsequent reactivity following solvent coordination, our results suggest that the feature that grows in at 100 ps in MeCN is likely a solvent coordinated species, and this event can be controlled based on the choice of solvent.

5.3 Conclusions

$Mn(CO)_3(^{R}bpy)Br$ complexes are stable in the absence of light, which allowed us to extensively characterize them using a variety of techniques. Transitions in the NMR, IR, and electronic absorption spectra are linearly correlated with the Brown (σ^+), Hammett (σ), and Kubota (σ^-) parameters, respectively, providing insight into how ligand substituents govern electronic properties at the metal center. In the presence of light, $Mn(CO)_3(^{R}bpy)Br$ complexes **1**, **2**, and **3** decompose via CO loss, with subsequent solvent coordination in MeCN or other reactions in $CHCl_3$. Ultrafast TA spectroscopy revealed the previously unknown 5-coordinate and solvento intermediates in the photo-speciation process. Complex **4** follows a different reaction path that is likely the result of a long-lived triplet excited state that does not undergo decay to a dissociative LF (d-d) state. The different behavior of **1**-**4** illustrates how the reactivity and speciation of these complexes can be tuned by changing the electronic properties of the bidentate diimine ligand. Notably, as only limited computational modeling has examined the excited state electronic structure of $Mn(CO)_3Br$(diimine) complexes,[38,45] further experimental work combined with computational modeling would be useful in providing new insights into the speciation mechanisms operative during irradiation. Our ongoing experimental work aims to analyze the structure and

electronics of the transient species generated upon irradiation using time resolved X-ray absorption and IR spectroscopies.

5.4 Experimental Section

5.4.1 Potential Hazards:

Working with carbonyl complexes poses a potential hazard of generating the colorless, odorless, tasteless, and acutely toxic gas carbon monoxide (CO). Work with carbonyl complexes should be carried out in a well ventilated fume hood and with use of a sensitive CO monitor. The synthesis of complexes **1-5** involves the displacement of two CO ligands, resulting in generation of a significant amount of CO during the reaction; this is especially true when working on larger scales, as has been done in the course of this work (hundreds of milligrams). Additionally, when complexes **1-5** are exposed to even low-intensity ambient visible light, they readily undergo photolysis to release CO. Caution should always be exercised when working with metal-carbonyl complexes.

5.4.2 General Considerations:

Manganese pentacarbonyl bromide (98%, Beantown Chemical Co.), 2,2′-bipyrdiyl (bpy) (98%; Alfa Aesar), 4,4′-bis(*tert*-butyl)-bipyridine (tBu-bpy) (98%, Sigma Aldrich), 2-chloro-4-trifluoromethyl-pyridine (98%; Oakwood Chemical), fuming nitric acid (90%, Alfa Aesar), and PCl_3 (98%, Alfa Aesar) were used as received. 2,2′-bipyridyl-N,N′-dioxide[46], 4,4′-dinitro-2,2′-bipyridyl-N,N′-dioxide[46], 4,4′-dinitro-2,2′-bipyridyl[46] (dnbpy), 4,4′-bis(trifluoromethyl)-2,2′-bipyridyl (CF_3-bpy)[47], $Mn(CO)_3Br(pyridine)_2$[48], $Mn(CO)_3Br(2,2'\text{-bipyridyl})$[1], and

$Mn(CO)_3Br$(4,4′-bis(*tert*-butyl)-2,2′-bipyridyl)[2] were prepared according to literature methods with minor modifications. If necessary, the ligands 2,2′-bipyridyl, 4,4′-bis(*tert*-butyl)-2,2′-bipyridyl, and 4,4′-bis(trifluoromethyl)-2,2′-bipyridyl can be sublimed (at ca. 80°C and 1 mTorr) if pre-purification is necessary.

Deuterated NMR solvents were purchased from Cambridge Isotope Laboratories; CD_3CN was dried over molecular sieves. ^1H, ^{13}C, and ^{19}F NMR spectra were collected with 400 or 500 MHz Bruker spectrometers. Spectra were referenced to the residual protio-solvent signal in the cases of ^1H and ^{13}C.[49] Heteronuclear NMR spectra were referenced to the appropriate external standard following the recommended scale based on ratios of absolute frequencies (Ξ).[50] ^{19}F NMR spectra are reported relative to CCl_3F. Chemical shifts (δ) are reported in units of ppm, and coupling constants (*J*) are reported in Hz.

All manipulations were done in dry N_2-filled gloveboxes (Vacuum Atmospheres Co. Hawthorne, CA) or under a N_2 atmosphere using standard Schlenk techniques unless otherwise noted. All solvents were of commercial grade and dried over activated alumina using a Pure Process Technology (PPT; Nashua, NH) solvent purification system prior to use and were stored over molecular sieves. All chemicals were from major commercial suppliers and used as received after extensive drying.

IR spectra were collected on a PerkinElmer Spectrum 100 FTIR spectrometer. UV-visible spectra were collected with an Ocean Optics FLAME-S spectrometer equipped with a DH-Mini light source. Steady-state photolysis experiments were carried out using an Oriel HgXe arc lamp operating at 175 W and equipped with an Oriel Cornerstone 130 1/8 m monochromator accessory. For the experiments in which IR spectroscopic monitoring was used to examine the products of

photolysis, an appropriate KBr-plate cell was charged with a 17 mM solution of **2** in MeCN under inert atmosphere, and an initial IR spectrum was collected prior to irradiation. Subsequent short periods of irradiation (totaling 2, 5, 10, and 15 min) with 415 nm light generated by the HgXe arc lamp operating at 175 W were followed in each case by collection of a new spectrum in order to examine evolution of the system over time. These spectra are given in Figure C24.

Elemental analyses were performed by Midwest Microlab, Inc. (Indianapolis, IN).

Single-crystal diffraction data were collected with a Bruker KAPPA APEX/II X-ray diffractometer. CCDC entries 1922040, 1922041, and 1922042 contain the supplementary crystallographic data for this paper. These data can be obtained free of charge from The Cambridge Crystallographic Data Centre via http://www.ccdc.cam.ac.uk/data_request/cif.

The transient absorption measurements used pump and probe pulses derived from the 800 nm output of a 1 kHz regeneratively amplified Ti:sapphire laser (Legend Elite, Coherent). A portion of the laser fundamental pumped an optical parametric amplifier with two stages of nonlinear frequency conversion (TOPAS) to generate the visible pump pulses. The beam diameter at the sample was 160 μm with an energy of 800 nJ per pulse. The relative polarization was set to magic angle by rotating the pump pulses with a zero-order λ/2 wave-plate. We used active background subtraction by passing the pump beam though a synchronized chopper wheel running at 500 Hz to block every other pump pulse. Broadband probe pulses with the desired wavelength range were generated by focusing a small fraction of the fundamental 800 nm laser light into a mechanically rotating CaF_2 crystal. The sample is cycled through a flow cell with a path length of 0.5 mm. After passing through the sample the probe pulse is dispersed using a prism onto a 2069-element CCD array. Each TA spectrum is an average of 10^3 laser pulses per time delay.

Synthesis of $Mn(CO)_3$(4,4′-bis(trifluoromethyl)-2,2′-bipyridine)Br (3): To a 50 mL Schlenk flask equipped with a stir bar was added 4,4′-bis(trifluoromethyl)-2,2′-bipyridine (0.0998 g, .342 mmol) in 50 mL of pentane. Then $Mn(CO)_5Br$ (0.0890 g, .324 mmol) was added and the reaction was brought to reflux under an argon atmosphere. The reaction was monitored by ^1H NMR until consumption of the starting material was observed (~ 6 hours). Once the reaction had reached completion the Schlenk flask was placed into a refrigerator at –20°C for 30 minutes. The resulting solid is then filtered off with a fritted glass funnel and washed with cold pentane to afford the title compound as an orange-red solid. Yield: 0.0801 g (48%). ^1H NMR (400 MHz, CD_3CN): δ 9.48 (d, 2H, $^3J_{H,H}$ = 5.8 Hz), 8.77 (s, 2H), 7.91 (dd, 2H, $^3J_{H,H}$ = 5.8 Hz, $^4J_{H,H}$ = 1.8 Hz) ppm. $^{13}C\{^1H\}$ NMR (176 MHz, CD_3CN): δ 185.5, 157.5, 156.4, 141.2 (q, $^1J_{C,F}$ = 35.3 Hz), 124.8, 123.9 (q, $^4J_{C,F}$ = 3.5 Hz), 122.6, 121.4 (q, $^4J_{C,F}$ = 3.5 Hz) ppm. ^{19}F NMR (376 MHz, CD_3CN) δ 65.4 ppm. Electronic absorption spectrum (MeCN): 208 (32000), 224 (33000), 293 (10000), 374 (1800), 454 nm (1500 $M^{-1}cm^{-1}$). IR (THF): $\nu_{C=O}$ 2027 (m) (A′), and $\nu_{C=O}$ 1944 (m) (A″), $\nu_{C=O}$ 1923 (m) (A′) cm^{-1}. ESI-MS (positive) m/z: 471.9 (100%) (**3**-Br^-+NCMe), 472.9 (23%), 474.0 (11%); 430.9 (87%) (**3**-Br^-), 431.9 (16%), 432.9 (2%); 429.0 (23%) (**3**-Br^--3CO+2NCMe), 430.0 (4%); 402.9 (17%) (**3**-Br^--CO), 403.9 (3%); 388.0 (20%) (**3**-Br^--3CO+NCMe), 389.0 (4%); 374.9 (22%) (**3**-Br^--2CO), 375.9 (4%); 346.9 (11%) ((**3**-Br^--3CO), 347.9 (2%) (see Figure C15). Anal. Calcd. for $MnC_{15}H_6BrF_6N_2O_3$: C, 35.25; H, 1.18; N, 5.48. Found: C, 35.20; H, 1.24; N, 5.46.

Synthesis of $Mn(CO)_3$(4,4′-dinitro-2,2′-bipyridyl)Br (4): To a Schlenk flask equipped with a stir bar was added 4,4′-dinitro-2,2′-bipyridine (0.3761 g, 1.53 mmol) and 50 mL of Et_2O. Then $Mn(CO)_5Br$ (0.4005 g, 1.46 mmol) was added and the reaction was brought to reflux under an argon atmosphere. The reaction was monitored by ^1H NMR until consumption of the starting material was observed (~ 12 hours). Once the reaction had reached completion the Schlenk flask

was placed into a -20°C refrigerator for 30 minutes. The resulting solid is then filtered off with a fritted glass funnel and washed with cold Et_2O to afford the title compound as a purple solid. Yield: 0.6409 g (95 %). ^{1}H NMR (400 MHz, CD_3CN): δ 9.58 (d, 2H, $^3J_{H,H}$ = 6.0 Hz), 9.21 (s, 2H), 8.29 (dd, 2H, $^4J_{H,H}$ = 6.0 Hz) ppm. $^{13}C\{^1H\}$ NMR (176 MHz, CD_3CN): δ 158.1, 157.1, 156.3, 120.5, 118.2 ppm. Electronic absorption spectrum (MeCN): 223 (1800), 245 (1400), 325 (800), 393 (200), 510 nm (230 M^{-1} cm^{-1}). IR (THF): $\nu_{C=O}$ 2027 (m) (A′), $\nu_{C=O}$ 1945 (m) (A″), $\nu_{C=O}$ 1927 (m) (A′) cm^{-1}. ESI-MS (positive) m/z: 425.9 (100%) (**4**-Br^-+NCMe), 426.9 (17%), 427.9 (3%); 411.0 (31%) (**4**-Br^--2CO+2NCMe), 412.0 (6%) 413.0 (1%); 384.9 (9%) (**4**-Br^-), 385.9 (1%), 386.9 (1%); 383.0 (51%) (**4**-Br^--3CO+2NCMe), 384.0 (9%); 369.9 (7%) (**4**-Br^--2CO+NCMe), 370.9 (1%), 372.0 (1%); 368.0 (20%) (**4**-Br^--CO-2O+2H+NCMe), 369.0 (3%) (see Figure C16). Anal. Calcd. for $MnC_{13}H_6BrN_4O_7$ (+1H_2O): C, 32.32; H, 1.67; N, 11.60. Found: C, 32.52; H, 1.41; N, 11.67.

5.5 Acknowledgements

The authors thank Dr. Davide Lionetti for numerous helpful discussions, Dr. Victor Day for assistance with X-ray crystallography, Keaton Prather for assistance with preparation of 4,4′-dinitro-2,2′-bipyridine, and Prof. Misha Barybin for generous access to a benchtop infrared spectrometer. This work was supported by the Hall Chemical Research Fund at the University of Kansas (to J.D.B. and C.G.E.) and a grant from the U.S. National Science Foundation (CHE-1151555; to C.G.E.). WCH was supported by the U.S. National Institutes of Health Graduate Training Program in the Dynamic Aspects of Chemical Biology (T32 GM008545-25).

5.6 References

(1) Bourrez, M.; Molton, F.; Chardon-Noblat, S.; Deronzier, A., [Mn(bipyridyl)$(CO)_3$Br]: An Abundant Metal Carbonyl Complex as Efficient Electrocatalyst for CO_2 Reduction. *Angew. Chem. Int. Ed.* **2011,** *50*, 9903-9906.

(2) Smieja, J. M.; Sampson, M. D.; Grice, K. A.; Benson, E. E.; Froehlich, J. D.; Kubiak, C. P., Manganese as a Substitute for Rhenium in CO2 Reduction Catalysts: The Importance of Acids. *Inorg. Chem.* **2013,** *52*, 2484-2491.

(3) Abel, E. W.; Bennett, M. A.; Wilkinson, G., Substituted carbonyl compounds of chromium, molybdenum, tungsten, and manganese. *J. Chem. Soc.* **1959**, 2323-2327.

(4) (a) Luong, J. C.; Faltynek, R. A.; Wrighton, M. S., Ground- and excited-state oxidation-reduction chemistry of (triphenyltin)- and (triphenylgermanium)tricarbonyl(1,10-phenanthroline)rhenium and related compounds. *J. Am. Chem. Soc.* **1980,** *102*, 7892-7900. (b) Caspar, J. V.; Meyer, T. J., Application of the energy gap law to nonradiative, excited-state decay. *J. Phys. Chem.* **1983,** *87*, 952-957. (c) Miguel, D.; Riera, V., Synthesis of manganese(I) carbonyls with σ-bonded alkynyl ligands. *J. Organomet. Chem.* **1985,** *293*, 379-390.

(5) (a) Hawecker, J.; Lehn, J. M.; Ziessel, R., Efficient photochemical reduction of CO_2 to CO by visible light irradiation of systems containing Re(bipy)$(CO)_3$X or $Ru(bipy)_3^{2+}$–Co^{2+} combinations as homogeneous catalysts. *J. Chem. Soc., Chem. Commun.* **1983**, 536-538. (b) Hawecker, J.; Lehn, J. M.; Ziessel, R., Electrocatalytic reduction of carbon dioxide mediated by Re(bipy)$(CO)_3$Cl (bipy = 2,2′-bipyridine). *J. Chem. Soc., Chem. Commun.* **1984**, 328-330.

(6) (a) Sullivan, B. P.; Bolinger, C. M.; Conrad, D.; Vining, W. J.; Meyer, T. J., One- and two-electron pathways in the electrocatalytic reduction of CO_2 by fac-Re(bpy)$(CO)_3$Cl (bpy = 2,2′-bipyridine). *J. Chem. Soc., Chem. Commun.* **1985**, 1414-1416. (b) O'Toole, T. R.; Margerum, L. D.; Westmoreland, T. D.; Vining, W. J.; Murray, R. W.; Meyer, T. J., Electrocatalytic reduction of CO_2 at a chemically modified electrode. *J. Chem. Soc., Chem. Commun.* **1985,** 1416-1417.

(7) Fujita, E.; Hayashi, Y.; Kita, S.; Brunschwig, B. S., Spectroscopic characterization of intermediates in CO_2 reduction with rhenium photocatalysts. Vol. 153, pp 271-276, Elsevier, Amsterdam, 2004.

(8) (a) Smieja, J. M.; Kubiak, C. P., Re(bipy-tBu)$(CO)_3$Cl−improved Catalytic Activity for Reduction of Carbon Dioxide: IR-Spectroelectrochemical and Mechanistic Studies. *Inorg. Chem.* **2010,** *49*, 9283-9289. (b) Clark, M. L.; Cheung, P. L.; Lessio, M.; Carter, E. A.; Kubiak, C. P., Kinetic and Mechanistic Effects of Bipyridine (bpy) Substituent, Labile Ligand, and Brønsted Acid on Electrocatalytic CO_2 Reduction by Re(bpy) Complexes. *ACS Catal.* **2018,** *8*, 2021-2029.

(9) Takeda, H.; Koike, K.; Morimoto, T.; Inumaru, H.; Ishitani, O., Photochemistry and photocatalysis of rhenium(I) diimine complexes. *Adv. Inorg. Chem.*, **2011**; *63*, 137-186.

(10) El Nahhas, A.; van der Veen, R. M.; Penfold, T. J.; Pham, V. T.; Lima, F. A.; Abela, R.; Blanco-Rodriguez, A. M.; Záliš, S.; Vlček, A.; Tavernelli, I.; Rothlisberger, U.; Milne, C. J.; Chergui, M., X-ray Absorption Spectroscopy of Ground and Excited Rhenium–Carbonyl–Diimine Complexes: Evidence for a Two-Center Electron Transfer. *J. Phys. Chem. A,* **2013,** *117*, 361-369.

(11) (a) Blakemore, J. D.; Gupta, A.; Warren, J. J.; Brunschwig, B. S.; Gray, H. B., Noncovalent Immobilization of Electrocatalysts on Carbon Electrodes for Fuel Production. *J. Am. Chem. Soc.* **2013,** *135*, 18288-18291. (b) Agarwal, J.; Shaw, T. W.; Stanton, C. J.; Majetich, G. F.; Bocarsly, A. B.; Schaefer, H. F., NHC-containing manganese(I) electrocatalysts for the two-electron reduction of CO_2. *Angew. Chem., Int. Ed.* **2014,** *53*, 5152-5155. (c) Grice, K. A.; Kubiak, C. P., Recent studies of rhenium and manganese bipyridine carbonyl catalysts for the electrochemical reduction of CO_2. *Adv. Inorg. Chem.* **2014,** *66*, 163-188. (d) Grills, D. C.; Farrington, J. A.; Layne, B. H.; Lymar, S. V.; Mello, B. A.; Preses, J. M.; Wishart, J. F., Mechanism of the Formation of a Mn-Based CO_2 Reduction Catalyst Revealed by Pulse Radiolysis with Time-Resolved Infrared Detection. *J. Am. Chem. Soc.* **2014,** *136*, 5563-5566. (e) Sampson, M. D.; Nguyen, A. D.; Grice, K. A.; Moore, C. E.; Rheingold, A. L.; Kubiak, C. P., Manganese catalysts with bulky bipyridine ligands for the electrocatalytic reduction of carbon dioxide: Eliminating dimerization and altering catalysis. *J. Am. Chem. Soc.* **2014,** *136*, 5460-5471. (f) Walsh, J. J.; Neri, G.; Smith, C. L.; Cowan, A. J., Electrocatalytic CO_2 reduction with a membrane supported manganese catalyst in aqueous solution. *Chem. Commun.* **2014,** *50*, 12698-12701. (g) Zeng, Q.; Tory, J.; Hartl, F., Electrocatalytic Reduction of Carbon Dioxide with a Manganese(I) Tricarbonyl Complex Containing a Nonaromatic α-Diimine Ligand. *Organometallics* **2014,** *33*, 5002-5008.

(12) (a) Agarwal, J.; Shaw, T. W.; Schaefer, H. F., III; Bocarsly, A. B., Design of a Catalytic Active Site for Electrochemical CO_2 Reduction with Mn(I)-Tricarbonyl Species. *Inorg. Chem.* **2015,** *54*, 5285-5294. (b) Fei, H.; Sampson, M. D.; Lee, Y.; Kubiak, C. P.; Cohen, S. M., Photocatalytic CO_2 Reduction to Formate Using a Mn(I) Molecular Catalyst in a Robust Metal-Organic Framework. *Inorg. Chem.* **2015,** *54*, 6821-6828. (c) Machan, C. W.; Stanton, C. J., III;

Vandezande, J. E.; Majetich, G. F.; Schaefer, H. F., III; Kubiak, C. P.; Agarwal, J., Electrocatalytic Reduction of Carbon Dioxide by Mn(CN)(2,2'-bipyridine)$(CO)_3$: CN Coordination Alters Mechanism. *Inorg. Chem.* **2015,** *54*, 8849-8856. (d) Riplinger, C.; Carter, E. A., Influence of Weak Bronsted Acids on Electrocatalytic CO_2 Reduction by Manganese and Rhenium Bipyridine Catalysts. *ACS Catal.* **2015,** *5*, 900-908. (e) Walsh, J. J.; Smith, C. L.; Neri, G.; Whitehead, G. F. S.; Robertson, C. M.; Cowan, A. J., Improving the efficiency of electrochemical CO_2 reduction using immobilized manganese complexes. *Faraday Discuss.* **2015,** *183*, 147-160. (f) Agnew, D. W.; Sampson, M. D.; Moore, C. E.; Rheingold, A. L.; Kubiak, C. P.; Figueroa, J. S., Electrochemical Properties and CO_2-Reduction Ability of m-Terphenyl Isocyanide Supported Manganese Tricarbonyl Complexes. *Inorg. Chem.* **2016,** *55*, 12400-12408. (g) Rawat, K. S.; Mahata, A.; Choudhuri, I.; Pathak, B., N-Heterocylic Carbene-Based Mn Electrocatalyst for Two-Electron CO_2 Reduction over Proton Reduction. *J. Phys. Chem. C* **2016,** *120*, 8821-8831.

(13) (a) Sampson, M. D.; Kubiak, C. P., Manganese Electrocatalysts with Bulky Bipyridine Ligands: Utilizing Lewis Acids To Promote Carbon Dioxide Reduction at Low Overpotentials. *J. Am. Chem. Soc.* **2016,** *138*, 1386-1393. (b) Spall, S. J. P.; Keane, T.; Tory, J.; Cocker, D. C.; Adams, H.; Fowler, H.; Meijer, A. J. H. M.; Hartl, F.; Weinstein, J. A., Manganese Tricarbonyl Complexes with Asymmetric 2-Iminopyridine Ligands: Toward Decoupling Steric and Electronic Factors in Electrocatalytic CO_2 Reduction. *Inorg. Chem.* **2016,** *55*, 12568-12582. (c) Stanton, C. J.; Vandezande, J. E.; Majetich, G. F.; Schaefer, H. F.; Agarwal, J., Mn-NHC Electrocatalysts: Increasing π Acidity Lowers the Reduction Potential and Increases the Turnover Frequency for CO_2 Reduction. *Inorg. Chem.* **2016,** *55*, 9509-9512. (d) Ngo, K. T.; McKinnon, M.; Mahanti, B.; Narayanan, R.; Grills, D. C.; Ertem, M. Z.; Rochford, J., Turning

on the Protonation-First Pathway for Electrocatalytic CO2 Reduction by Manganese Bipyridyl Tricarbonyl Complexes. *J. Am. Chem. Soc.* **2017,** *139*, 2604-2618. (e) Reuillard, B.; Ly, K. H.; Rosser, T. E.; Kuehnel, M. F.; Zebger, I.; Reisner, E., Tuning Product Selectivity for Aqueous CO_2 Reduction with a Mn(bipyridine)-pyrene Catalyst Immobilized on a Carbon Nanotube Electrode. *J. Am. Chem. Soc.* **2017,** *139*, 14425-14435. (f) Franco, F.; Pinto, M. F.; Royo, B.; Lloret-Fillol, J., A Highly Active N-Heterocyclic Carbene Manganese(I) Complex for Selective Electrocatalytic CO_2 Reduction to CO. *Angew. Chem., Int. Ed.* **2018,** *57*, 4603-4606. (g) Myren, T. H. T.; Lilio, A. M.; Huntzinger, C. G.; Horstman, J. W.; Stinson, T. A.; Donadt, T. B.; Moore, C.; Lama, B.; Funke, H. H.; Luca, O. R., Manganese N-Heterocyclic Carbene Pincers for the Electrocatalytic Reduction of Carbon Dioxide. *Organometallics* **2019,** *38*, 1248-1253. (h) Takeda, H.; Kamiyama, H.; Okamoto, K.; Irimajiri, M.; Mizutani, T.; Koike, K.; Sekine, A.; Ishitani, O., Highly Efficient and Robust Photocatalytic Systems for CO_2 Reduction Consisting of a Cu(I) Photosensitizer and Mn(I) Catalysts. *J. Am. Chem. Soc.* **2018,** *140*, 17241-17254. (i) Tignor, S. E.; Kuo, H.-Y.; Lee, T. S.; Scholes, G. D.; Bocarsly, A. B., Manganese-Based Catalysts with Varying Ligand Substituents for the Electrochemical Reduction of CO_2 to CO. *Organometallics* **2019,** *38*, 1292-1299, (j) Walsh, J. J.; Neri, G.; Smith, C. L.; Cowan, A. J., Water-Soluble Manganese Complex for Selective Electrocatalytic CO_2 Reduction to CO. *Organometallics* **2019,** *38*, 1224-1229.

(14) Vollmer, M. V.; Machan, C. W.; Clark, M. L.; Antholine, W. E.; Agarwal, J.; Schaefer, H. F.; Kubiak, C. P.; Walensky, J. R., Synthesis, Spectroscopy, and Electrochemistry of (α-Diimine)$M(CO)_3Br$, M = Mn, Re, Complexes: Ligands Isoelectronic to Bipyridyl Show Differences in CO_2 Reduction. *Organometallics* **2015,** *34*, 3-12.

(15) Takeda, H.; Koizumi, H.; Okamoto, K.; Ishitani, O., Photocatalytic CO_2 reduction using a Mn complex as a catalyst. *Chem. Commun.* **2014,** *50*, 1491-1493.

(16) Agarwal, J.; Stanton Iii, C. J.; Shaw, T. W.; Vandezande, J. E.; Majetich, G. F.; Bocarsly, A. B.; Schaefer III, H. F., Exploring the effect of axial ligand substitution (X = Br, NCS, CN) on the photodecomposition and electrochemical activity of $[MnX(N–C)(CO)_3]$ complexes. *Dalton Trans.* **2015,** *44*, 2122-2131.

(17) Perutz, R. N.; Torres, O.; Vlček, A., "Photochemistry of Metal Carbonyls," in *Comprehensive Inorganic Chemistry II*, Reedijk, J., Poeppelmeier, K., Eds., 2nd Ed., **2013**, *Vol. 8*.

(18) (a) Schatzschneider, U., PhotoCORMs: Light-triggered release of carbon monoxide from the coordination sphere of transition metal complexes for biological applications. *Inorg. Chim. Acta* **2011,** *374*, 19-23. (b) Kottelat, E., Fabio, Z., Visible Light Activated PhotoCORMs. *Inorganics* **2017**, *5*, 24. (c) Ling, K.; Men, F.; Wang, W.-C.; Zhou, Y.-Q.; Zhang, H.-W.; Ye, D.-W., Carbon Monoxide and Its Controlled Release: Therapeutic Application, Detection, and Development of Carbon Monoxide Releasing Molecules (CORMs). *J. Med. Chem.* **2018,** *61*, 2611-2635.

(19) (a) Hughey, J. L.; Anderson, C. P.; Meyer, T. J., Photochemistry of $Mn_2(CO)_{10}$. *J. Organomet. Chem.* **1977,** *125*, C49-C52. (b) Meyer, T. J.; Caspar, J. V., Photochemistry of metal-metal bonds. *Chem. Rev.* **1985,** *85*, 187-218.

(20) Motterlini, R. C., James E.; Foresti, Roberta; Sarathchandra, Padmini; Mann, Brian E.; Green, Colin J., Carbon Monoxide-Releasing Molecules: Characterization of Biochemical and Vascular Activities. *J. Am. Heart Assoc.* **2002,** *90*, e17-e24.

(21) Bolze, F.; Jenni, S.; Sour, A.; Heitz, V. Molecular photosensitisers for two-photon photodynamic therapy. *Chem. Commun.* **2017,** *53*, 12857-12877.

(22) Niesel, J.; Pinto, A.; N'Dongo, H. W. P.; Merz, K.; Ott, I.; Gust, R.; Schatzschneider, U., Photoinduced CO release, cellular uptake and cytotoxicity of a tris(pyrazolyl)methane (tpm) manganese tricarbonyl complex. *Chem. Commun.* **2008**, 1798-1800.

(23) (a) He, Q.; Kiesewetter, D. O.; Qu, Y.; Fu, X.; Fan, J.; Huang, P.; Liu, Y.; Zhu, G.; Liu, Y.; Qian, Z.; Chen, X., NIR-Responsive On-Demand Release of CO from Metal Carbonyl-Caged Graphene Oxide Nanomedicine. *Adv. Mater.* **2015,** *27*, 6741-6746. (b) Ruggi, A.; Zobi, F., Quantum-CORMs: quantum dot sensitized CO releasing molecules. *Dalton Trans.* **2015,** *44*, 10928-31. (c) Aucott, B. J.; Ward, J. S.; Andrew, S. G.; Milani, J.; Whitwood, A. C.; Lynam, J. M.; Parkin, A.; Fairlamb, I. J. S., Redox-tagged carbon monoxide-releasing molecules (CORMs): ferrocene-containing [Mn(C-N)$(CO)_4$] complexes as a promising new CORM class. *Inorg. Chem.* **2017,** *56*, 5431-5440. (d) Carmona, F. J.; Jimenez-Amezcua, I.; Rojas, S.; Romao, C. C.; Navarro, J. A. R.; Maldonado, C. R.; Barea, E., Aluminum Doped MCM-41 Nanoparticles as Platforms for the Dual Encapsulation of a CO-Releasing Molecule and Cisplatin. *Inorg. Chem.* **2017,** *56*, 10474-10480. (e) Li, Z.; Pierri, A. E.; Huang, P.-J.; Wu, G.; Iretskii, A. V.; Ford, P. C., Dinuclear PhotoCORMs: Dioxygen-Assisted Carbon Monoxide Uncaging from Long-Wavelength-Absorbing Metal–Metal-Bonded Carbonyl Complexes. *Inorg. Chem.* **2017,** *56*, 6094-6104. (f) Mansour, A. M., Rapid green and blue light-induced CO release from bromazepam Mn(I) and Ru(II) carbonyls: synthesis, density functional theory and biological activity evaluation. *Appl. Organomet. Chem.* **2017,** *31*, e3564. (g) Mede, R.; Hoffmann, P.; Klein, M.; Goerls, H.; Schmitt, M.; Neugebauer, U.; Gessner, G.; Heinemann, S. H.; Popp, J.; Westerhausen, M., Water-Soluble Mn$(CO)_3$-Based and Non-Toxic

PhotoCORM for Administration of Carbon Monoxide Inside of Cells. *Anorg. Allg. Chem.* **2017,** *643*, 2057-2062. (h) Reddy, G. U.; Liu, J.; Gorls, H.; Askes, S. H. C.; Schiller, A.; Hoffmann, P.; Neugebauer, U.; Hoffmann, P.; Neugebauer, U.; Steinmetzer, J.; Kupfer, S.; Grafe, S., Light-responsive paper strips as CO-releasing material with a colourimetric response. *Chem. Sci.* **2017,** *8*, 6555-6560. (i) Mansour, A. M.; Shehab, O. R., Reactivity of visible-light induced CO releasing thiourea-based Mn(I) tricarbonyl bromide (CORM-NS1) towards lysozyme. *Inorg. Chim. Acta* **2018,** *480*, 159-165.

(24) Carrington, S. J.; Chakraborty, I.; Mascharak, P. K., Exceptionally rapid CO release from a manganese(I) tricarbonyl complex derived from bis(4-chloro-phenylimino)acenaphthene upon exposure to visible light. *Dalton Trans.* **2015,** *44*, 13828-13834.

(25) Glyn, P.; George, M. W.; Hodges, P. M.; Turner, J. J., Fast time-resolved IR studies of the excited states of co-ordination compound: direct observation of intramolecular charge transfer. *Chem. Commun.* **1989**, 1655-1657.

(26) Sato, S.; Matubara, Y.; Koike, K.; Falkenström, M.; Katayama, T.; Ishibashi, Y.; Miyasaka, H.; Taniguchi, S.; Chosrowjan, H.; Mataga, N.; Fukazawa, N.; Koshihara, S.; Onda, K.; Ishitani, O., Photochemistry of fac-[Re(bpy)$(CO)_3$Cl]. *Chem.: Eur. J.* **2012,** *18*, 15722-15734.

(27) Stufkens, D. J.; Vlček, A. Ligand-dependent excited state behaviour of Re(I) and Ru(II) carbonyl–diimine complexes. *Coord. Chem. Rev.* **1998**, *177*, 127-179.

(28) (a) Cannizzo, A.; Blanco-Rodriguez, A. M.; El Nahhas, A.; Sebera, J.; Zalis, S.; Vlček, A.; Chergui, M. Femtosecond Fluorescence and Intersystem Crossing in Rhenium(I) Carbonyl−Bipyridine Complexes. *J. Am. Chem. Soc.* **2008,** *130*, 8967-8974. (b) El Nahhas, A.;

Consani, C.; Blanco-Rodriguez, A. M.; Lancaster, K. M.; Braem, O.; Cannizzo, A.; Towrie, M.; Clark, I. P.; Zalis, S.; Chergui, M.; Vlcek, A. Ultrafast Excited-State Dynamics of Rhenium(I) Photosensitizers [Re(Cl)$(CO)_3$(N,N)] and [Re(imidazole)$(CO)_3$(N,N)]$^+$: Diimine Effects. *Inorg. Chem.* **2011,** *50*, 2932-2943.

(29) Grills, D. C.; Farrington, J. A.; Layne, B. H.; Lymar, S. V.; Mello, B. A.; Preses, J. M.; Wishart, J. F., Mechanism of the Formation of a Mn-Based CO_2 Reduction Catalyst Revealed by Pulse Radiolysis with Time-Resolved Infrared Detection. *J. Am. Chem. Soc.* **2014,** *136*, 5563-5566.

(30) Hammett, L. P., The Effect of Structure upon the Reactions of Organic Compounds. Benzene Derivatives. *J. Am. Chem. Soc.* **1937,** *59*, 96-103.

(31) Brown, H. C.; Okamoto, Y., Electrophilic Substituent Constants. *J. Am. Chem. Soc.* **1958,** *80*, 4979-4987.

(32) Yoshioka, M.; K. H., and Kubota, T.; Relationship between Acid and Dissociation Constants of N1-Aryl-sulfanilamides and the Hammett Equation. *Bull. Chem. Soc. Japan* **1962,** *35*, 1723-1728.

(33) von Philipsborn, W., Probing organometallic structure and reactivity by transition metal NMR spectroscopy. *Chem. Soc. Rev.* **1999,** *28*, 95-105.

(34) Hoye, T. R.; Rehberg, G. M., Reactions of $(CO)_5$Cr:C(Me)N$(CH_2CH_2)_2$ with enynes: mechanistic insight and synthetic value of changing a carbene donor group from alkoxy to dialkylamino. *Organometallics* **1989,** *8*, 2070-2071.

(35) Stor, G. J.; Morrison, S. L.; Stufkens, D. J.; Oskam, A., The Remarkable Photochemistry of *fac*-XMn(CO)$_3$(α-diimine) (X = Halide): Formation of Mn$_2$(CO)$_6$(α-diimine)$_2$ via the mer Isomer and Photocatalytic Substitution of X- in the Presence of PR$_3$. *Organometallics* **1994,** *13*, 2641-2650.

(36) Zimmer, P.; Sun, Y.; Thiel, W. R., Cationic isonitrile complexes of the CpFe(CO)$_2$ fragment. *J. Organomet. Chem.* **2014,** *774*, 12-18.

(37) Herberhold, M.; Brabetz, H., Übergangsmetallkomplexe mit N-haltigen Liganden, III. Donator-Akzeptor-Eigenschaften organischer Nitrile im System C$_5$H$_5$Mn(CO)$_2$L. *Chem. Ber.* **1970,** *103*, 3909-3917,

(38) Jiang, Q.; Xia, Y.; Barrett, J.; Mikhailovsky, A.; Wu, G.; Wang, D.; Shi, P.; Ford, P. C., Near-Infrared and Visible Photoactivation to Uncage Carbon Monoxide from an Aqueous-Soluble PhotoCORM. *Inorg. Chem.* **2019,** *58*, 11066-11075,

(39) Papadakis, R.; Tsolomitis, A., Study of the correlations of the MLCT Vis absorption maxima of 4-pentacyanoferrate- 4′-arylsubstituted bispyridinium complexes with the Hammett substituent parameters and the solvent polarity parameters E and AN. *J. Phys. Org. Chem.* **2009,** *22*, 515-521.

(40) Hummel, P.; Oxgaard, J.; Goddard, W. A.; Gray, H. B. Ligand-Field Excited States of Metal Hexacarbonyls. *Inorg. Chem.* **2005,** *44*, 2454-2458.

(41) van Stokkum, I. H. M.; Larsen, D. S.; van Grondelle, R. Global and target analysis of time-resolved spectra. *Biochem. Biophys. Acta – Bioenerg.* **2004,** *1657*, 82-104.

(42) Machan, C. W.; Sampson, M. D.; Chabolla, S. A.; Dang, T.; Kubiak, C. P., developing a mechanistic understanding of molecular electrocatalysts for CO_2 reduction using infrared spectroelectrochemistry. *Organometallics* **2014,** *33*, 4550-4559.

(43) Díaz-Torres, R.; Alvarez, S. Coordinating ability of anions and solvents towards transition metals and lanthanides. *Dalton Trans.* **2011,** *40*, 10742-10750.

(44) Hammarback, L. A.; Clark, I. P.; Sazanovich, I. V.; Towrie, M.; Robinson, A.; Clarke, F.; Meyer, S.; Fairlamb, I. J. S.; Lynam, J. M. Mapping out the key carbon–carbon bond-forming steps in Mn-catalysed C–H functionalization. *Nature Catalysis* **2018**, *1*, 830-840.

(45) Mansour, A. M.; Ragab, M. S., Spectroscopic and DFT studies of photoactivatable Mn(I) tricarbonyl complexes. *Appl. Organomet. Chem.* **2019,** *33*, e4944.

(46) Maerker, G.; Case, F. H., The Synthesis of Some 4,4'-Disubstituted 2,2'-Bipyridines. *J. Am. Chem. Soc.* **1958,** *80*, 2745-2748.

(47) Li, H.; Oppenheimer, J.; Smith III, M. R.; Maleczka Jr, R. E., Improved synthesis of electron deficient bipyridines. *Tet. Lett.* **2016,** *57*, 2231-2232.

(48) Pons, M.; Herberich, G., Bromotricarbonyldi(pyridine)manganese(I). *Inorg. Synth*. **2014**, *36*, 148-149.

(49) G. R. Fulmer, A. J. M. Miller, N. H. Sherden, H. E. Gottlieb, A. Nudelman, B. M. Stoltz, J. E. Bercaw, K. I. Goldberg, NMR Chemical Shifts of Trace Impurities: Common Laboratory Solvents, Organics, and Gases in Deuterated Solvents Relevant to the Organometallic Chemist. *Organometallics* **2010**, *29*, 2176-2179.

(50) (a) R. K. Harris, E. D. Becker, S. M. Cabral De Menezes, R. Goodfellow, P. Granger, NMR nomenclature. Nuclear spin properties and conventions for chemical shifts (IUPAC Recommendations 2001). *Pure Appl. Chem.* **2001**, *73*, 1795-1818. (b) R. K. Harris, E. D. Becker, S. M. Cabral De Menezes, P. Granger, R. E. Hoffman, K. W. Zilm, Further Conventions for NMR Shielding and Chemical Shifts (IUPAC Recommendations 2008). *Pure Appl. Chem.* **2008**, *80*, 59-84.

Chapter 6

4,5-Diazafluorene and 9,9'-Dimethyl-4,5-Diazafluorene as Ligands Supporting Redox-Active Mn and Ru Complexes

This chapter is adapted from a published manuscript: Henke, W.C., Hopkins, J.A., Anderson, M.L., Stiel, J.P., Day, V.W., and Blakemore, J.D.* 4,5-Diazafluorene and 9,9′-Dimethyl-4,5-Diazafluorene as Ligands Supporting Redox-Active Mn and Ru Complexes, *Molecules* **2020**, *25*, 3189.

6.1 Introduction

2,2′-bipyridyl (bpy) is among the most ubiquitous ligands in inorganic and organometallic chemistry. As a chelating ligand, bpy often binds to transition metals in a bidentate (κ^2) mode and can support a variety of compounds with useful photophysical, redox, and/or catalytic properties [1,2,3,4,5,6,7]. Metal complexes and catalysts bearing bpy-type ligands can be tuned by appending electron-donating groups (EDG) and electron-withdrawing groups (EWG) to the bpy ligand; such groups primarily modulate the π-accepting ability of the conjugated framework and, to a lesser extent, the σ-donating ability of the nitrogen donor atoms. For example, we have recently used 4,4′-disubstituted-2,2′-bipyridyl (^{R}bpy) ligands to tune the photophysical properties and light-induced reactivity of $Mn(CO)_3X(^{R}bpy)$ complexes [8] as well as to modulate the accessible pathways and efficiency of dihydrogen production by [Cp*Rh] complexes bearing ^{R}bpy ligands [9]. Such modifications have also been used to tune catalysis of carbon dioxide (CO_2) reduction to carbon monoxide (CO) by $[Re(CO)_3]$ and $[Mn(CO)_3]$ complexes [10,11]. With these observations and many others from the field, ^{R}bpy ligands have been found to be uniquely suited to systematic investigation of transition metal complexes. Furthermore, the wide range of accessible ^{R}bpy ligands makes them attractive for efforts in rational design of new metal complexes and molecular catalysts.

Ligands based upon 4,5-diazafluorene (daf) have several features in common with the workhorse ^{R}bpy ligands, and thus offer a notable alternative for development of new metal complexes and catalysts [12]. In particular, both daf and bpy have $12e^{-}$ π systems and both commonly bind to metals in a κ^2 fashion. However, daf is distinguished from bpy by its more rigid structure, attributed to the linking inter-ring sp^3-hybridized carbon present in the fused five-

membered ring. Photochemical studies of metal complexes supported by daf and bpy have mapped the importance of these features, including involvement of the daf π-system in metal-to-ligand charge transfer behavior [12,13]. Furthermore, the constrained chelate angle of daf has been implicated in giving rise to more significant excited-state reactivity than that encountered for bpy [14].

Unfunctionalized daf features two doubly benzylic C–H bonds at the 9-position, opening further possibilities for ligand-centered acid/base reactivity that cannot occur with simple 2,2′-bipyridyl derivatives. Along these lines, Song and co-workers have explored the coordination chemistry of daf and substituted diazafluorenes, including significant work aimed at leveraging this unique acid/base chemistry [15]. In their work, Song and co-workers have found that the acidic C–H bonds of daf can undergo deprotonation that results in follow-up reactivity [16,17,18,19,20]. More broadly, Stahl [21,22,23] and several other groups [24,25,26] have developed a number of catalyst systems supported by diazafluorene ligands. In all these cases, daf and its derivatives seem to play a decisive role in enabling unique chemistry, confirming the usefulness of the ligands as a counterpoint to the more common ^{R}bpy family.

As we have found in our own work that redox-active compounds and catalysts can be readily tuned by substituent effects with ^{R}bpy ligands [8,9], 4,5-diazafluorene-based ligands could be useful in modulating the structural, electronic, and electrochemical properties of redox-active compounds more commonly supported by ^{R}bpy derivatives. In particular, the coordination chemistry of the ligand 9,9′-dimethyl-4,5-diazafluorene (Me_2daf) has received less attention than it deserves [23], as this ligand avoids the acidic C–H bonds present in daf that can readily engage in non-innocent behavior. Furthermore, reliable methods from Schmidt and co-workers [27] and

Tetsuya and co-workers [28] are available for preparation of Me_2daf, encouraging further exploration of its chemistry.

Here, we now report the synthesis, characterization, and electrochemical properties of $Mn(CO)_3Br$(daf) (**2**), $Mn(CO)_3Br(Me_2daf)$ (**3**), and $[Ru(Me_2daf)_3](PF_6)_2$ (**5**), and compare their properties to the more common analogues $Mn(CO)_3$(bpy)Br (**1**) and $[Ru(bpy)_3]^{2+}$ (**4**), respectively (see Chart 6.1 for structures of all compounds). We find that the use of daf and Me_2daf ligands in the complexes leads to unique spectroscopic features in the NMR and electronic absorption spectra, as well as a characteristic shift in the C–O vibrational frequencies found in the infrared (IR) spectra of **2** and **3** compared to that of **1**. Consistent with these spectroscopic observations, results from single-crystal X-ray diffraction analysis of **2**, **3**, and **5** reveal wider chelate angles and elongated M-N bond lengths in comparison with the analogous bpy complexes. The new complexes exhibit electrochemical profiles that are akin to those of their bpy analogues, confirming the similar redox-active natures of bpy, daf, and Me_2daf. However, related tests shows that complexes **2** and **3** are not catalysts for the reduction of CO_2 to CO, contrasting with the robust catalytic behavior of **1** [4]. Taken together, these results suggest that Me_2daf is an attractive ligand for development of new coordination compounds for use in studies of redox chemistry and catalysis.

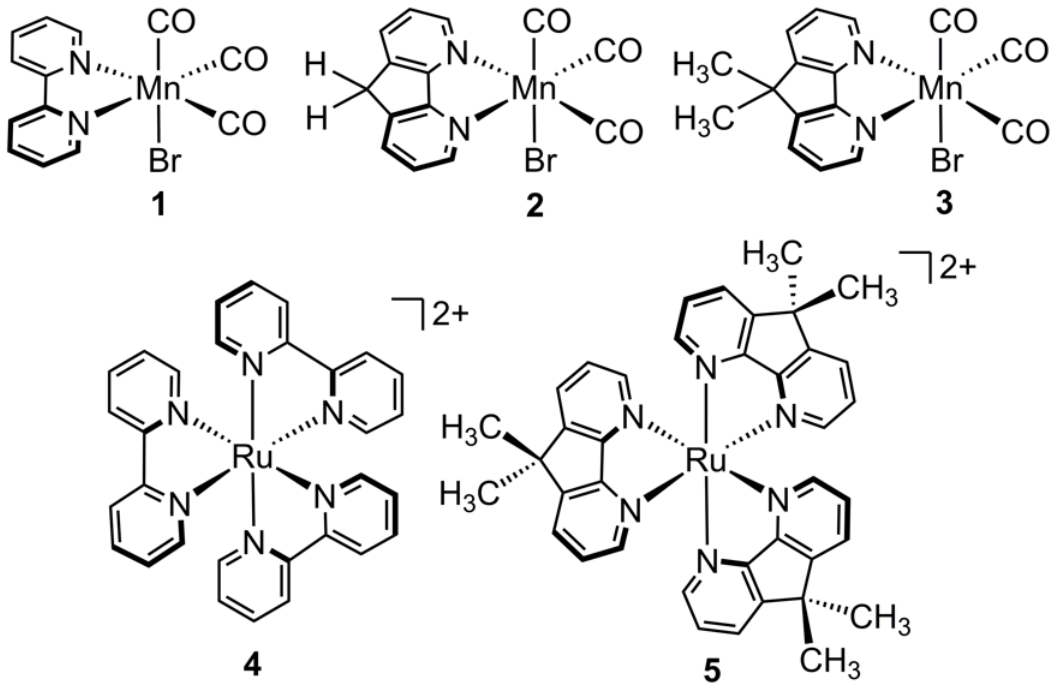

Chart 6.1. Manganese tricarbonyl and ruthenium complexes supported by bpy, daf, and Me_2daf discussed in this study.

6.2. Results and Discussion

6.2.1. Synthesis and NMR characterization of complexes 2, 3, and 5

In order to synthesize the new compounds **2**, **3**, and **5**, we first prepared the daf and Me_2daf ligands according to literature procedures starting from 1,10-phenanthroline (phen) (see Scheme 6.1). Oxidation of the unique olefinic functionality within phen results in the production of 4,5-diazafluoren-9-one (dafone); Wolf-Kishner reduction of dafone with hydrazine hydrate results in the generation of the desired daf [27]. To generate Me_2daf, we initially attempted deprotonation of the daf methylene protons using *n*–butyllithium, but in our hands this resulted in decomposition. Instead, we utilized a milder, sterically hindered base, potassium *tert*-butoxide (tBuOK), to

deprotonate daf, followed by the addition of iodomethane, to generate the anticipated Me_2daf ligand [28].

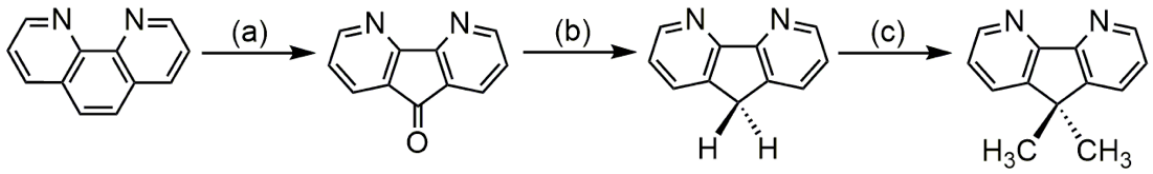

Scheme 6.1. The synthetic pathway for the generation of daf and Me_2daf. (**a**) 1. KOH, $KMNO_4$; H_2O, 16 h, 100 °C (**b**) $NH_2NH_2{\cdot}H_2O$; diethylene glycol, 170 °C, (**c**) 1. tBuOK 2. MeI; THF, –10 °C to rt.

With the desired ligands in hand, we next moved to prepare **2** and **3** with synthetic chemistry developed earlier by Wrighton, Meyer, and others for related bpy and phen derivatives [29,30,31]. Suspension of the appropriate ligand with $Mn(CO)_5Br$ in diethyl ether at 38 °C results in the generation of complexes **2** and **3** in moderate yields, 62% and 73%, respectively. Previously, Cherry and co-workers have reported the synthesis of the complex $[Ru(daf)_3](PF_6)_2$ to examine its structural properties and photophysical properties [12]. By adapting this literature procedure, the Me_2daf analogue of $[Ru(bpy)_3]^{2+}$ could be prepared in a relatively low yield of ca. 17%. As an aside, we anticipate that the modest yield is likely due to differences in solubility between $[Ru(daf)_3](PF_6)_2$ and **5** engendered by the methyl groups of Me_2daf. Notably, all the compounds in this study were found to be acutely light sensitive and were handled in the dark or under red light to the extent possible. Following successful generation of the complexes they were each fully characterized (see Experimental Section and Figures D1-D9).

To begin characterization of the newly synthesized complexes, we turned to nuclear magnetic resonance (NMR) spectroscopy. Complexes **2**, **3**, and **5** each exhibit three resonances in the

aromatic region of their ^{1}H-NMR spectra with splitting patterns arising from $^{3}J_{H–H}$ and $^{4}J_{H–H}$ coupling; these signals correspond to the hydrogen atoms on the pyridyl rings of the daf and Me_2daf ligands coordinated to their respective Mn and Ru centers (see Figure 6.1). Notably, complexes **2**, **3**, and **5** exhibit unique resonances for their daf-methylene and Me_2daf-methyl protons. While complexes **2** and **3** exhibit C_s symmetry in solution, complex **5** shows D_3 symmetry. Correspondingly, the six methyl groups belonging to the three Me_2daf ligands coordinated to the Ru center give rise to a singlet at 1.68 ppm (integrating to 18 H) confirming the successful preparation of complex **5**. The assignment of D_3 symmetry suggests that complex **5** is chiral and thus should be present as a 50:50 racemic mixture (of Δ and Λ isomers; *vide infra*). However, enantiomers have identical chemical and physical properties and thus we observe no additional resonances in the NMR spectra for the material isolated here.

Considering the change in symmetry from D_3 for **5** to C_s symmetry for **2** and **3**, unique NMR resonance in the latter two cases can be readily interpreted. Complex **2** possesses C_s symmetry in solution and, as a result, the chemical environment of the two protons on the methylene bridge (9-position) become chemically distinct from each other and are diastereotopic. This results in a distinctive signal centered at 4.29 ppm. The geminal coupling between the two methylene protons on daf might be anticipated to give rise to two unique doublets. However, when the frequency of the coupling constant (^{2}J = 22.6 Hz) is on the same order of magnitude as the chemical shift difference (25 Hz) between the two expected resonances, the usual one-to-one value for the resonance intensities is not observed [32,33]. Instead, a multiplet with intense inner peaks and weaker outer peaks is obtained, providing a diagnostic signal for the generation of complex **2** (in general, a phenomenon known in the field as ‘roofing’). The identity of this signal is further confirmed by ^{13}C-distortionless enhancement polarization transfer (DEPT-135) and 2D ^{1}H-^{13}C

heteronuclear single quantum coherence (HSQC) NMR techniques (see Figures D10-D11). Similarly, complex **3** exhibits C_s symmetry in solution; the methyl groups on the apical carbon are diastereotopic, with one methyl oriented toward the axial CO ligand and the other oriented toward the bromide ligand. The difference in the chemical environment between the methyl group protons gives rise the anticipated diastereotopic resonances; these were observed using ^{1}H and ^{13}C NMR, providing two signals for the protons (δ 1.58 and 1.66 ppm, each integrating to 3 H) and two signals for the carbons (δ 24.4 and 25.3 ppm), confirming the expected structure of **3** in solution.

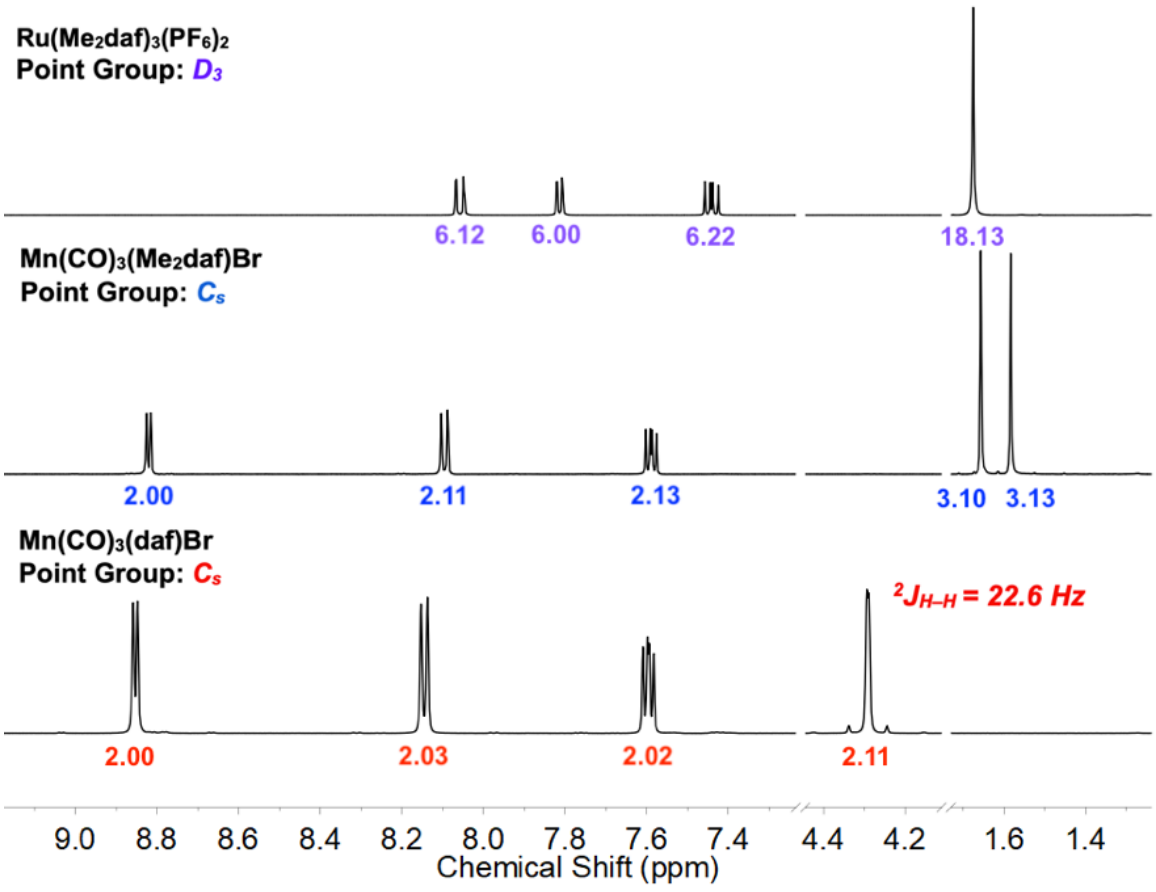

Figure 6.1. Partial ^{1}H NMR spectra of **2** (bottom), **3** (middle), and **5** (top) in CD_3CN. Peak integrations are given beneath each resonance or multiplet in colored text.

6.2.2. Electronic Absorption, IR, and X-ray Diffraction Studies

Complexes **1**–**5** are all highly colored and thus we next turned to electronic absorption (EA) spectroscopy. The EA spectrum for complex **5** exhibits a strong transition at 445 nm with a molar absorptivity of 13,000 $M^{-1}cm^{-1}$ (see Figures D17-D25). The value of the molar absorptivity and the remarkable similarity of the spectrum to that of complex **4** enables assignment of this transition as a metal-to-ligand charge transfer (MLCT) [34,35]. This assignment is also consistent with known ability of daf ligands to enable visible-light induced charge transfer transitions at transition metal centers, similar to what is observed for complexes bearing bpy [12,13]. The observation of an MLCT transition for **5** supported by Me_2daf is also reasonable, since the two methyl groups installed at the 9 position of daf do not perturb the conjugated system of the two aromatic rings. The EA spectra for complexes **2** and **3** reveal transitions in the visible region at 410 nm and 411 nm with molar absorptivities of 2,200 $M^{-1}cm^{-1}$ and 3,300 $M^{-1}cm^{-1}$, respectively (see Figure 6.2). Notably, these EA spectra are very similar to complex **1** [8], and based on this similarity, we are confident that these transitions can also be attributed to MLCT events.

However, a distinguishing feature of the EA spectra of complexes **2** and **3** compared to that of complex **1** is the presence of four, relatively narrow absorptions in the UV region between 250 and 350 nm. Based on their wavelengths and molar absorptivities, these absorptions can be assigned as π-π^* excitations displaying marked vibronic structure. Such vibronic structure has previously been observed for titanium complexes bearing diazafluorenide ligands [36], suggesting that vibronic coupling may be a common feature of the spectral profiles ligated by daf or substituted diazfluorenes. As expected, the spacing between the sharp transitions is uniform in a progression from approximately 700 cm^{-1} to 900 cm^{-1}. This common observation for **2** and **3**

suggests that the vibronic structure engendered by daf and Me_2daf are similar in these compounds. Based on this rich spectroscopic profile, we anticipate that **2** and **3** may behave differently in the presence of light than the bpy analogue **1**, encouraging further work in the future to gain insight into how these complexes behave following exposure to visible and/or UV light [8].

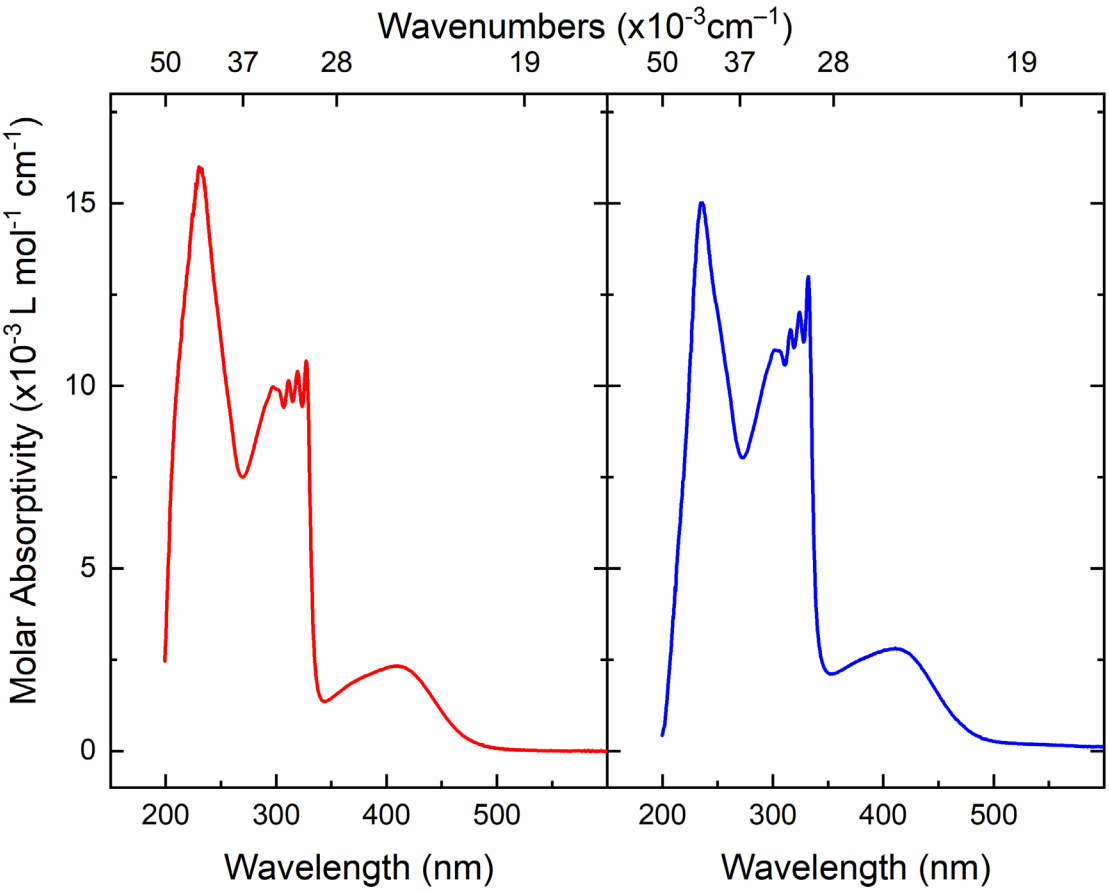

Figure 6.2. Electronic absorption spectra for **2** (left panel) and **3** (right panel) in MeCN.

The IR spectra of complexes **1**, **2**, and **3** confirm that the starting material, $Mn(CO)_5Br$ (associated with absorption bands at 2004 cm^{-1}, 2046 cm^{-1}, and 2083 cm^{-1}) was consumed during the synthetic reactions and is not present in the products. The C_s symmetry of a *fac*-tricarbonyl complex is expected to give rise to three distinct C–O stretches in IR spectra based on group theory

analysis. Upon examination of the experimental data, a three-band spectrum is observed and confirms the expected *fac*-tricarbonyl geometry for the complexes in THF solution (see Figure 6.3). The complexes have rather similar C–O stretching, likely a consequence of the similar environment at Mn in all three cases. In particular, C–O stretching frequencies are primarily affected by π-bonding effects, and as the π-character of bpy, daf, and Me_2daf are not significantly different, a large shift in the vibrational frequencies for the CO ligands among **1**, **2**, and **3** is not expected. On the other hand, the modest shifts that are observable likely arise from the increased chelate bite angle of daf (**2**, 82.14(10)°) and Me_2daf (**3**, 82.2(3)°) compared to bpy (78.80(7)°, *vide infra*) [37]. As a result of the increased bite angle, the σ-donor power of the nitrogen donor atoms to the manganese center should be decreased, resulting in a correspond increase in the C–O stretching frequency due to decreased Mn-to-CO backbonding. In accord with this model, the vibrational frequencies for **2** and **3** are virtually identical, confirming that the addition of distal methyl groups at the ligand 9 position does not substantially perturb the structure of Me_2daf in comparison with daf. To gain further structural insights into the properties of the new compounds, we next turned to X-ray diffraction analysis (XRD).

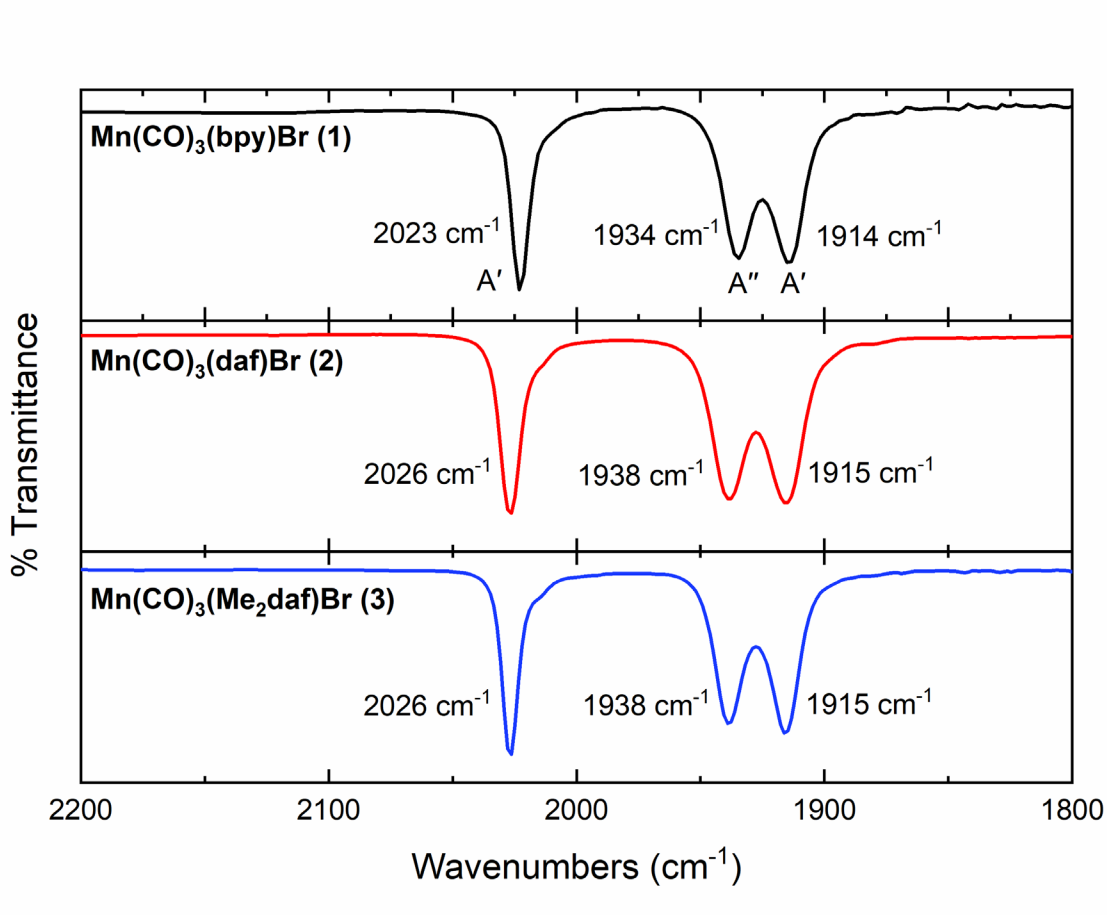

Figure 6.3. FTIR spectra of **1**–**3** in THF solution.

Vapor diffusion of diethyl ether into a concentrated THF solution of **2**, or vapor diffusion of diethyl ether into a concentrated acetonitrile (MeCN) solution of **3**, results in yellow crystals suitable for single crystal X-ray diffraction studies (see Figure 6.4). The results confirm the expected *fac*-geometry of the complexes with two equatorial CO ligands, an axial CO ligand, an axial bromide, and a κ^2-daf ligand surrounding the manganese center. Although this is the first example of a formally Mn(I) complex chelated by daf or Me_2daf, the octahedral geometries of **2** and **3** resemble those of the analogous $Mn(CO)_3(^{R}bpy)Br$ complexes [8,37]. However, there is a significant increase in the diimine ligand bite angle for complexes **2** (82.14(10)°) and **3** (82.2(3)°) compared to **1** (78.80(7)°, *vide supra*). Additionally, the average Mn–N distances for **2** and **3** are

significantly longer than those of complex **1** (2.118(4) Å and 2.109(5) Å vs. 2.047(3) Å, respectively) [37]. This is attributable to the rigid polycyclic structure of the daf framework, enforced by the inter-ring methylene group at the 9 position, which presumably drives poorer orbital overlap between the metal center and the ligand in the cases of **2** and **3**, and results in an overall increase in the M–N bond distances.

Complex **5** is chiral and possesses D_3 symmetry in solution, on the basis of NMR spectra (*vide supra*). No measures were taken to obtain enantiomerically pure material, and thus we isolated **5** as the 50:50 racemic mixture of delta (Δ) and lambda (Λ) isomers. Vapor diffusion of pentane into a concentrated acetone solution, or vapor diffusion of pentane into a concentrated 50:50 acetone/THF solution resulted in two separate sets of orange crystals of **5** that were suitable for single-crystal XRD studies (see Figure 6.4). These two structures, named v74e and q36k respectively, both provide data confirming the successful synthesis of the $[Ru(Me_2daf)_3]^{2+}$ core and reveal bond distances and angles that are within error of each other (see the Supporting Information, Table D3 and D4 for comparisons. On the other hand, q36k represents a higher quality structure and will be discussed here. As expected, the average chelate angle (N-Ru-N) and corresponding average Ru–N distances for complex **5** (data from q36k) are larger than in the case of the famous $[Ru(bpy)_3]^{2+}$ (82.9(3)° vs. 78.9(2)°; 2.117(13) Å vs. 2.063(6) Å) [38,39,40]. Gratifyingly, these values align with structural data previously available for $[Ru(daf)_3]^{2+}$, confirming that use of daf or Me_2daf to form homoleptic Ru(II) complexes results in wider chelate angles and longer Ru–N distances in both cases [41].

Overall, observing the increased bite angles of the daf and Me_2daf ligands in complexes **2**, **3**, and **5** was gratifying, since these changes should influence the electronic properties and reactivity at the metal centers in comparison with their bpy-supported analogues. Therefore, we next turned

to electrochemical methods to probe the redox properties of these systems, with a particular focus on identifying features that distinguish the daf and Me_2daf compounds from their bpy-supported analogues.

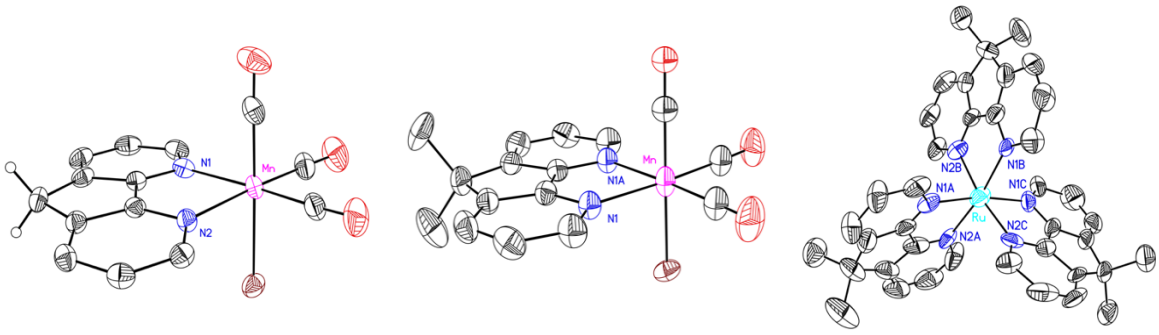

Figure 6.4. Solid-state structures of **2** (left), **3** (middle), and **5** (right, from structure v74e). Displacement ellipsoids are shown at 50% probability level. Hydrogen atoms (except H14A and H14B for **2**) and outer sphere hexafluorophosphate counteranions and disordered co-crystallized solvent (for **5**, from structure v74e) are omitted for clarity.

6.2.3. Electrochemical Studies

Initial cyclic voltammetry experiments were performed with **4** and **5** to interrogate how Me_2daf behaves under electrochemical conditions in comparison to bpy (see Figure 6.5). As one scans cathodically, the cyclic voltammetry of the parent bpy-complex **4** exhibits three quasi-reversible reductions centered at –1.73 V, –1.92 V, and –2.17 V respectively (all potentials are quoted versus ferrocenium/ferrocene, denoted $Fc^{+/0}$). Based on previous electrochemical studies, these reductive features can be confidently assigned to ligand-centered events; the complex is progressively reduced from $[Ru^{II}(bpy)_3]^{2+}$, to $[Ru^{II}(bpy)_2(bpy^{\cdot-})]^{+}$, to $[Ru^{II}(bpy)(bpy^{\cdot-})_2]$, and

finally to $[Ru^{II}(bpy^{\cdot-})_3]^-$ [42,43,44]. This rich manifold of accessible ground-state reductions for **4** highlights the redox non-innocence of the bpy ligand; redox non-innocent ligands continue to grow in popularity [1,4Error! Bookmark not defined.,45,46] because of their wide-ranging applications in redox chemistry and small-molecule activation.

We were excited to find that the cyclic voltammetric profile of **5** is remarkably similar to that of **4**. As scanning cathodically with **5** reveals three quasi-reversible reductions at –1.79 V, –1.99 V, and –2.24 V, respectively; each is centered at a slightly more negative potential than the corresponding event associated with bpy-complex **4**. The more negative reduction potentials likely arise from the inductive effect of the additional fused five-membered ring and methyl groups of Me_2daf, resulting in a structure that is overall more electron-rich and slightly increasing the reduction potentials associated with Me_2daf-centered reductions of **5**. Based on the electronic similarities of bpy and Me_2daf, we can reliably implicate redox non-innocence of the Me_2daf ligand as giving rise to the manifold of reductions observed for **5**, similar to the case of bpy in **4**. Considering this situation, we anticipate that **5** may have significant photochemical reactivity, and might serve as a useful photosensitizer in future work.

Consistent with the ligand-centered nature of the reductive events measured for **4** and **5**, the difference in the bite angle between Me_2daf and bpy does not strongly affect the reductive cyclic voltammetry of these compounds. However, confirmation that that Me_2daf behave as a redox-active ligand suggests that similar processes may be accessible in the tricarbonyl compounds **2** and **3**.

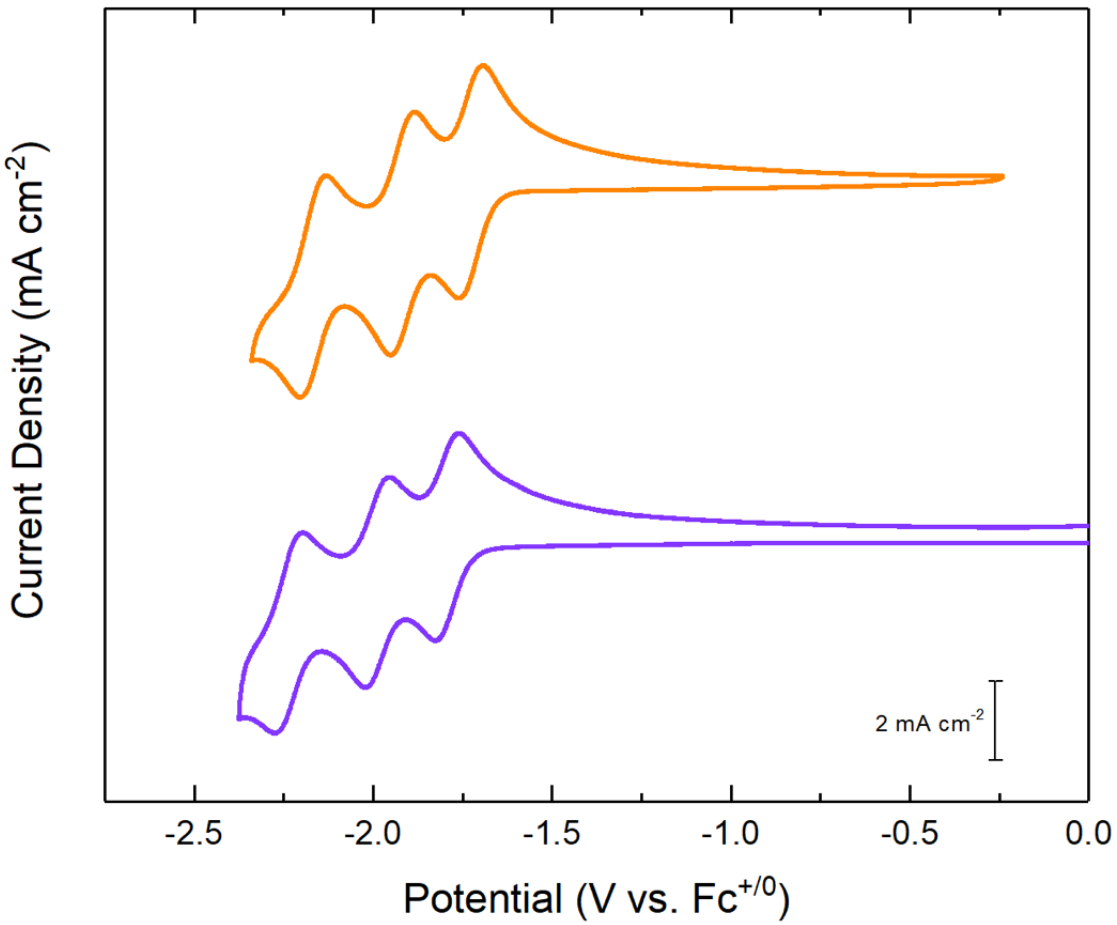

Figure 6.5. Cyclic voltammetry of **4** (orange) and **5** (purple) in MeCN solution with 0.1 M $TBAPF_6$ supporting electrolyte (working electrode: highly-oriented pyrolytic graphite; pseudo-reference electrode: $Ag^{+/0}$; counter electrode: Pt wire). Ferrocene was used as an internal potential reference.

The electrochemical behavior of **1** was previously established by Deronzier, Chardon-Noblat and co-workers [4]. We have confirmed their findings here for comparison purposes (see Figure 6.6); scanning cathodically with **1** in solution, we observe two irreversible reductions with cathodic peak potentials ($E_{p,c}$) at –1.61 V and –1.83 V, followed by an oxidation at a more positive potential ($E_{p,a}$ = –0.61 V). Based upon extensive mechanistic work from prior studies, the first reduction of **1** is associated with formation of a 19 e^- complex (an electron transfer or E process) which is

coupled to the loss of bromide that generates a 17 e^- species (a chemical reaction or C process). This 17 e^- complex then dimerizes with itself (C process), forming $[Mn(CO)_3(bpy)]_2$ in an overall ECC-type process. $[Mn(CO)_3(bpy)]_2$ itself can then undergo reduction at the more negative potential, breaking the dimer to form $[Mn(CO)_3(bpy)]^-$ in an EC-type process. Finally, scanning anodically, oxidation of $[Mn(CO)_3(bpy)]_2$ can regenerate the starting material **1**.

The cyclic voltammetric profiles of **2** and **3** are very similar to that associated with **1** (See Figure 6.6). Scanning cathodically with **2** or **3**, two irreversible reductions and followed by an oxidation at more positive potentials during the paired anodic sweep (for **2**, $E^1_{p,c} = -1.75$ V, $E^2_{p,c} = -2.04$ V, $E_{p,a} = -0.62$ V; for **3**, $E^1_{p,c} = -1.71$ V, $E^2_{p,c} = -2.02$ V, $E_{p,a} = -0.67$ V). Qualitatively, these results suggest that the irreversible reductions corresponding to the ECC and EC processes exhibited by **1** also occur with **2** and **3**. Notably, however, the reduction events associated with **2** and **3** appear significantly broader than those associated with **1**, suggesting that heterogeneous electron transfer is slower with the diazafluorene derivatives. Furthermore, as $E^1_{p,c}$ and $E^2_{p,c}$ are both more negative for **2** than **3**, we anticipate that electron transfer kinetics dominate the potentials measured for these reductions; Me_2daf might have been expected to engender a more negative reduction potential for **3** over the case of daf in **2**, but the opposite is in fact observed here; this may be attributable to the influence of the disparate electron-transfer kinetics, which push the reduction potential ($E^1_{p,c}$) of **2** to a more negative potential than **3**, contrary to the thermodynamic trend that would be predicted on the basis of the inductive effect of the methyl groups of Me_2daf.

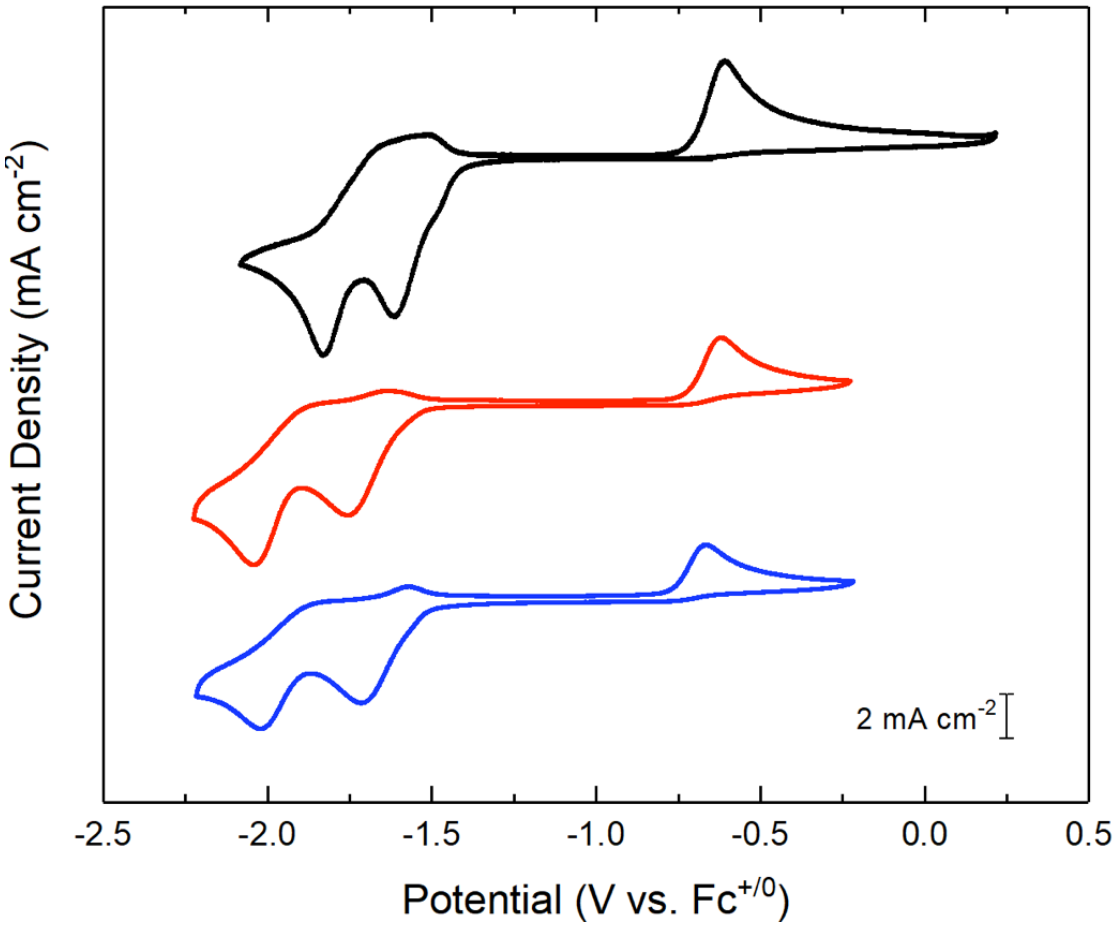

Figure 6.6. Cyclic voltammogram of complexes **1** (black), **2** (red), and **3** (blue) in MeCN solution with 0.1 M $TBAPF_6$ electrolyte (WE: HOPG, Psuedo Ref: $Ag^{+/0}$, CE: Pt, internal Ref: $Fc^{+/0}$).

Encouraged by the similar cyclic voltammetry (CV) behavior displayed by **1**, **2**, and **3**, we also tested the new compounds for activity towards CO_2 reduction (see Figures D34–D39) since the known **1** has been demonstrated to be a robust catalyst for CO generation from CO_2 [4]. For this testing, water was added as a proton source (similar to the prior work with **1** described in reference 4) and CO_2 was sparged through the working solution and electrochemical cell to fully saturate the atmosphere and solution. Voltammograms collected immediately following these additions reveal enhancements in the current flowing at both the first and second irreversible reductions

associated with **2** and **3**. The observed current enhancement suggests that significant reduction-induced reactivity is taking place at the electrode surface. Notably, the overall catalytic enhancement encountered with **2** is significantly greater than that with **3**, suggesting a unique role of the acidic protons on the methylene bridge of daf in promoting reactivity.

However, controlled potential electrolysis (CPE) coupled to product detection does not suggest effective catalytic reduction of CO_2 is taking place with **2** and **3**. Results from controlled potential electrolyses at –2.05 V vs $Fc^{+/0}$ for 90 min (see Figures D40 and D41) in a custom two-compartment electrochemical cell do show that experiments with **2** and **3** produce less H_2 and more CO during the 90 min electrolysis (see Table D1). However, **2** and **3** give low Faradic efficiencies (27% and 34%) and sub-stoichiometric yields (turnovers of 0.82 and 0.62, respectively) of CO, on the basis of total charge passed and initial loading of **2** or **3**, respectively. As analysis of working solutions with NMR spectroscopy following electrolysis did not reveal the presence of alternative products, including formate, we conclude that electrochemical reduction of **2** or **3** in the presence of H_2O and CO_2 leads primarily to decomposition.

On a final note, we wish to note that the chronoamperogram associated with electrolysis of **2** is considerably different than that of **3**. The current passed as a function of time widely fluctuated during the course of the electrolysis (see Figure D40). In particular, the initial current is rather large but becomes attenuated over the course of the experiment, suggesting undesirable chemical reactivity may be taking place with the daf ligand. These results suggest that further work is needed to reveal the precise role of the acidic methylene protons in the daf framework during conditions of redox catalysis, like those explored here. It should also be noted that both metal- and bpy-centered reductions have been implicated in effective catalysis of CO_2 reduction with **1** [47]. As incoming CO_2 might therefore be required to interact with both the metal and the ligand, the

enhanced steric profile of Me_2daf ligand in **3** could negatively impact the approach of CO_2 and deactivate the catalyst. Consequently, our future work will include a focus on revealing the influence of the functionalization pattern of the 9-position of daf on redox chemistry and catalysis.

6.3. Conclusions

We have described the synthesis, characterization, and electrochemical properties of the new daf- or Me_2daf-supported complexes **2**, **3**, and **5** and compared the properties of these compounds to their bpy-supported analogues **1** and **4**. When daf and Me_2daf are bound to Mn or Ru centers, we observe characteristic spectra that confirm the formation and symmetry of the desired complexes. In particular, comparisons of bond lengths and geometric parameters confirm that daf and Me_2daf enforce wider chelate angles and offer weaker σ-donation than bpy. Electrochemical studies of **5** reveal that Me_2daf is a non-innocent redox active ligand at modestly reducing potentials, and related electrochemical work with **2** and **3** shows that this ligand-centered reduction behavior is also accessible in **2** and **3**, albeit with apparently slower heterogeneous electron transfer kinetics that those encountered with analogous **1**. Taken together, these studies demonstrate daf and Me_2daf could be useful for preparation of a variety of new redox-active compounds, building on the significant body of findings for the workhorse bpy and ^{R}bpy ligands

6.4. Materials and Methods

6.4.1. General Considerations

All manipulations were carried out in dry N_2-filled gloveboxes (Vacuum Atmospheres Co., Hawthorne, CA, USA) or under an N_2 atmosphere using standard Schlenk techniques unless otherwise noted. All solvents were of commercial grade and dried over activated alumina using a

PPT Glass Contour (Nashua, NH, USA) solvent purification system prior to use, and were stored over molecular sieves. All chemicals were obtained from major commercial suppliers. Manganese pentacarbonyl bromide (98%, Strem Chemical Co.), ruthenium chloride hydrate (Pressure Chemical Co.), and 1,10-phenantrholine (95%, Matrix Scientific) were used as received. The ligands, 4,5-diazafluorene and 9,9-dimethyldiazafluorene were prepared according to literature methods with minor modifications [27,28]. 4,5-diazafluorene can be sublimed at ca. 80 ºC and 1 mTorr if pre-purification is necessary. Deuterated solvents for NMR studies were purchased from Cambridge Isotope Laboratories (Tewksbury, MA, USA); CD_3CN was dried over molecular sieves. ^{1}H-, ^{13}C-, ^{19}F-, and ^{31}P-NMR spectra were collected on 400 or 500 MHz Bruker spectrometers (Bruker, Billerica, MA, USA) and referenced to the residual protio-solvent signal in the case of ^{1}H and ^{13}C [48]. Heteronuclear NMR spectra were referenced to the appropriate external standard following the recommended scale based on ratios of absolute frequencies (Ξ) [49,50]. 19F NMR spectra are reported relative to CCl_3F, and ^{31}P NMR spectra are reported relative to H_3PO_4. Chemical shifts (δ) are reported in units of ppm and coupling constants (J) are reported in Hz. Elemental analyses were performed by Midwest Microlab, Inc. (Indianapolis, IN, USA).

Electronic absorption spectra were collected with an Ocean Optics Flame spectrometer equipped with a DH-Mini light source (Ocean Optics, Largo, FL, USA).

IR spectra were collected using a Shimadzu IRSpirit Fourier Transform Infrared Spectrometer in transmission mode using a 0.1 cm liquid IR cell with KBr windows.

6.4.2. X-ray Crystallography

Single-crystal diffraction data were collected with a Bruker APEX-II CCD diffractometer. The Cambridge Crystallographic Data Centre (CCDC) entries 1977431, 1994285, 1982214, and 2013030 contain the supplementary crystallographic data for complexes **2**, **3**, and **5** (v74e and q36k), respectively. These data can be obtained free of charge via www.ccdc.cam.ac.uk/data_request/cif, or by emailing data_request@ccdc.cam.ac.uk, or by contacting The Cambridge Crystallographic Data Centre, 12, Union Road, Cambridge CB2 1EZ, UK; fax: +44 1223 336033.

6.4.3.Electrochemistry

Electrochemical experiments were performed in a N_2-filled glovebox, or outside of the box in an argon flushed electrochemical cell. Dry, degassed MeCN and 0.1 M tetra(*n-butyl*)ammonium hexafluorophosphate ($[^nBu_4N]^+[PF_6]^-$ (Sigma-Aldrich, electrochemical grade) were used as the solvent and supporting electrolyte; Measurements were carried out with Reference 600+ Potentiostat/Galvanostat (Gamry Instruments, Warminster, PA, USA), or an Electrochemical Analyzer potentiostat (CH Instruments), using a standard three-electrode configuration. For CV experiments: the working electrode was the basal plane of highly oriented pyrolytic graphite (HOPG) (GraphiteStore.com, Buffalo Grove, IL, USA; surface area: 0.09 cm^2), the counter electrode was a platinum wire (Kurt J. Lesker, Jefferson Hills, PA, USA; 99.99%, 0.5 mm diameter), and a silver wire immersed in electrolyte solution served as a pseudo-reference electrode (CH instruments). The reference was separated from the working solution by a Vycor frit (Bioanalytical Systems, Inc., West Lafayette, IN, USA). For CV acid addition experiments: the working electrode was the basal plane of HOPG (surface area: 0.09 cm^2), the counter and

reference electrodes were platinum wires (99.99%, 0.5 mm diameter). Ferrocene (Sigma-Aldrich, St. Louis, MO, USA; twice-sublimed) was added to the electrolyte solution at the end of each experiment; the midpoint potential of the ferrocenium/ferrocene couple (denoted as $Fc^{+/0}$) was used as an external standard for comparison of the recorded potentials. Concentrations of the analytes for cyclic voltammetry were typically 1 mM. Experiments were typically conducted by first scanning cathodically, then anodically on the return sweep.

Bulk electrolysis experiments were performed in a custom two-chamber electrochemical cell equipped with connections to achieve gas-tight operation. The working electrode was the basal plane of HOPG ((Graphitestore.com, Buffalo Grove, IL, USA; surface area: 10 cm^2), the counter electrode was a platinum wire (99.99%, 0.5 mm diameter), and a silver wire immersed in electrolyte solution served as a pseudo-reference electrode. The volume of solution held by the cell in total was 60 mL, with about 105 mL of total head-space volume.

6.4.4. Gas Chromatography

Gas chromatography were collected with a Shimadzu GC-2014 Custom-GC gas chromatograph with a thermal conductivity detector and dual flame-ionization detectors. A custom set of 8 columns and timed valves enable quantitative analysis of the following gases: hydrogen, nitrogen, oxygen, carbon dioxide, carbon monoxide, methane, ethane, ethylene, and ethyne. Argon serves as the carrier gas. The instrument was calibrated with a standard checkout gas mixture (Agilent 5190-0519, Santa Clara, CA, USA) prior to experimental runs to obtain quantitative data for CO and other gases. Calibration curves over a range of 100–35,000 ppm were constructed with prepared mixture of CO and N_2 to enable CO quantification.

6.4.5 Synthesis

Preparation of $Mn(CO)_3$(4,5-diazafluorene)Br (2). In the dark, to a 50 mL Schlenk flask equipped with a stir bar, was added 4,5-diazafluorene (0.0644 g, 0.383 mmol) in 50 mL of diethyl ether. Then $Mn(CO)_5Br$ (0.0998 g, 0.363 mmol) was added and the reaction was brought to reflux. The reaction was monitored by ^1H NMR until consumption of the starting material was observed to be complete, after approximately 3 hours. Once the reaction had reached completion, the Schlenk flask was placed into a refrigerator at –20 °C for 30 minutes. The resulting solid was then filtered off with a fritted glass funnel and washed with cold pentane to afford the title compound as a yellow solid. Yield: 0.088 g (62%). ^1H-NMR (CD_3CN, 500 MHz) δ 8.85 (d, $^3J_{H–H}$ = 5.3 Hz, 2H), 8.14 (d, $^3J_{H–H}$ = 7.6 Hz, 2H), 7.61-7.58 (dd, $^3J_{H–H}$ = 7.6 Hz, $^4J_{H–H}$ = 5.6 Hz, 2H), 4.29 (d, $^2J_{H–H}$ = 22.6 Hz, 2H) ppm. $^{13}C\{^1H\}$ NMR (176 MHz, CD3CN): δ 162.3, 151.3, 137.7, 136.5, 126.9, 37.6 ppm. $^{13}C\{^1H\}$-DEPT-135 NMR δ 151.2, 136.4, 126.9, 37.5 ppm. Electronic absorption spectrum (MeCN): 230 (16000), 297 (9970), 301 (9910), 311 (10100), 320 (10400), 327 (10700), 410 nm (2200 M^{-1} cm^{-1}). IR (THF)): $\nu_{C=O}$ 2026 (m) (A'), $\nu_{C=O}$ 1938 (m) (A''), and $\nu_{C=O}$ 1917 (m) (A') cm^{-1}. ESI-MS (positive) m/z: 348.0 (98%)(**1**–Br^-+NCMe), 349.0 (18%), 350.0 (2%); 306.9 (29%) (**1**–Br^-), 307.9 (5%), 308.9 (0.5%); 305.0 (96%) (**1**–Br^-–3CO+2NCMe), 306.0 (18%); 264.0 (45%) (**1**–Br^-–3CO+NCMe), 265.0 (7%); 223.0 (100%) (**1**–Br^-–3CO), 224.0 (13%). Anal. Calcd. for $MnC_{14}H_8BrN_2O_3$: C, 43.44; H, 2.08; N, 7.24. Found: C, 43.38; H, 2.08; N, 7.14.

Preparation of $Mn(CO)_3$(9,9′-dimethyl-4,5-diazafluorene)Br (**3**). In the dark, to a Schlenk flask equipped with a stir bar was added 9,9′-dimethyl-4,5-diazafluorene (0.0749 g, 0.364 mmol) and 50 mL of diethyl ether. Then $Mn(CO)_5Br$ (0.1000g, 0.382 mmol) was added and the reaction was brought to reflux. The reaction was monitored by ^1H NMR until consumption of the starting

material was observed to be complete, after approximately 3 hours. Once the reaction had reached completion the Schlenk flask was placed into a –20 °C refrigerator for 30 minutes. The resulting solid was then filtered off with a fritted glass funnel and washed with cold Et_2O to afford the title compound as a yellow solid. Yield: 0.1098 g (73%). ^{1}H-NMR (CD_3CN, 500 MHz) δ 8.82 (d, $^3J_{H–H}$ = 5.3 Hz, 2H), 8.10 (d, $^3J_{H–H}$ = 7.7 Hz, 2H), 7.59 (dd, $^3J_{H–H}$ = 7.7 Hz, $^4J_{H–H}$ = 5.3 Hz, 2H), 1.66 (s, 3H), 1.58 (s, 3H) ppm. $^{13}C\{^1H\}$ NMR (176 MHz, CD_3CN): δ 160.3, 151.5, 147.2, 134.0, 127.5, 52.1, 25.3, 24.4 ppm. Electronic absorption spectrum (MeCN): 236 (15000), 301 (11000), 306 (11000), 316 (11600), 324 (12000), 332 (13000), 411 nm (3300 M^{-1} cm^{-1}). IR (THF): $\nu_{C=O}$ 2026 (m) (A'), $\nu_{C=O}$ 1938 (m) (A''), and $\nu_{C=O}$ 1915 (m) (A') cm^{-1}. ESI-MS (positive) m/z: 251.0 (100%)(**1**–Br^-–3CO), 252.0 (15%), 253.0 (1%). Anal. Calcd. for $MnC_{16}H_{12}BrN_2O_3$: C, 46.29; H, 2.91; N, 6.75. Found: C, 46.35; H, 3.03; N, 6.97.

Preparation of [Tris(9,9′-dimethyl-4,5-diazafluorene)Ruthenium](PF$_6$)$_2$ (5). In the dark, to a three-neck round bottom flask equipped with a stir bar was added 9,9′-dimethyl-4,5-diazafluorene (0.1000 g, 0.509 mmol), $RuCl_3$ xH_2O (0.0266 g, 0.128 mmol), and Zn^0 powder (0.0420 g, 0.642 mmol). A 2:1 ethanol:water mixture was used as a solvent to suspend the material, the reaction mixture was brough to reflux, and was allowed to stir overnight. The resulting bright-orange solution was then filtered into a flask containing ammonium hexafluorophosphate (0.0438 g, 0.269 mmol), which resulted in immediate precipitation of the desired product. The precipitate was filtered, and then washed progressively with cold water and diethyl ether. The desired complex was purified by recrystallization from boiling methanol to afford an orange solid. Yield (0.0210 g, 17%). ^{1}H-NMR (CD_3CN, 400 MHz) δ 8.06 (dd, $^3J_{H–H}$ = 7.8 Hz, $^4J_{H–H}$ = 0.9 Hz, 6H), 7.81 (dd, $^3J_{H–H}$ = 5.5 Hz, $^4J_{H–H}$ = 0.9 Hz, 6H), 7.44 (dd, $^3J_{H–H}$ = 7.8 Hz, $^4J_{H–H}$ = 5.5 Hz, 6H), 1.68 (s, 18H) ppm.$^{13}C\{^1H\}$ NMR (176 MHz, CD3CN): δ 162.8, 152.9, 147.4, 133.4, 127.9, 53.2, 24.5 ppm. ^{19}F

NMR (276 MHz, CD_3CN): δ -72.9 (d, 706.4 Hz) ppm.^{31}P NMR (162 MHz, CD_3CN): δ -144.7 (m, 706.4 Hz) ppm. Electronic absorption spectrum (MeCN): 231 (27000), 249 (14400), 256 (13500), 295 (75000), 445 nm (17000 M^{-1} cm^{-1}). Anal. Calcd. for $RuC_{29}H_{36}N_6F_{12}P_2$: C, 47.81; H, 3.70; N, 8.58. Found: C, 47.62; H, 3.70; N, 8.30.

6.5 Acknowledgments

The authors thank Javier Concepcion (Brookhaven National Laboratory) for helpful discussions regarding the synthesis of **5**, and Justin Douglas and Sarah Neuenswander for assistance with NMR spectroscopy. This work was supported by the US National Science Foundation through award OIA-1833087. Synthesis and preliminary characterization of **5** was supported by the US National Science Foundation through the NSF REU Program in Chemistry at the University of Kansas (CHE-1560279). W.C.H. was supported by the US National Institutes of Health Graduate Training Program in the Dynamic Aspects of Chemical Biology (T32 GM008545-25). Support for the NMR instrumentation was provided by NIH Shared Instrumentation Grants (S10OD016360, S10RR024664) and NSF MRI funding (CHE-1625923).

6.6 References

(1) English, A. M.; DeLaive, P. J.; Gray, H. B.; Lum, V. R., Metalloprotein electron-transfer mechanisms. Quenching of electronically excited tris(2,2'-bipyridine)ruthenium(II) by reduced blue copper proteins. *J. Am. Chem. Soc.* **1982,** *104*, 870-871.

(2) Brunschwig, B. S.; DeLaive, P. J.; English, A. M.; Goldberg, M.; Gray, H. B.; Mayo, S. L.; Sutin, N., Kinetics and mechanisms of electron transfer between blue copper proteins and electronically excited chromium and ruthenium polypyridine complexes. *Inorg. Chem.* **1985,** *24*, 3743-3749.

(3) Sullivan, B. P.; Bolinger, C. M.; Conrad, D.; Vining, W. J.; Meyer, T. J., One- and two-electron pathways in the electrocatalytic reduction of CO_2 by fac-Re(bpy)$(CO)_3$Cl (bpy = 2,2′-bipyridine). *J. the Chem. Soc., Chem. Commun.* **1985**, 1414-1416.

(4) Bourrez, M.; Molton, F.; Chardon-Noblat, S.; Deronzier, A., [Mn(bipyridyl)$(CO)_3$Br]: An abundant metal carbonyl complex as efficient electrocatalyst for CO_2 reduction. *Angew. Chem. Int. Ed.* **2011,** *50*, 9903-9906.

(5) Meyer, T. J., Electron Transfer Reactions Induced by Excited State Quenching. *Isr. J. Chem.* **1976,** *15*, 200-205.

(6) Moyer, B. A.; Meyer, T. J., Properties of the oxo/aqua system $(bpy)_2(py)RuO^{2+}/(bpy)_2(py)Ru(OH_2)^{2+}$. *Inorg. Chem.* **1981,** *20*, 436-444.

(7) Imayoshi, R.; Tanaka, H.; Matsuo, Y.; Yuki, M.; Nakajima, K.; Yoshizawa, K.; Nishibayashi, Y., Cobalt-catalyzed transformation of molecular dinitrogen into silylamine under ambient reaction conditions. *Chem–Eur. J.* **2015,** *21*, 8905-8909.

(8) Henke, W. C.; Otolski, C. J.; Moore, W. N. G.; Elles, C. G.; Blakemore, J. D., Ultrafast spectroscopy of [$Mn(CO)_3$] complexes: tuning the kinetics of light-driven CO release and solvent binding. *Inorg. Chem.* **2020**, *59*, 2178-2187.

(9) Henke, W. C.; Lionetti, D.; Moore, W. N. G.; Hopkins, J. A.; Day, V. W.; Blakemore, J. D., Ligand substituents govern the efficiency and mechanistic path of hydrogen production with [Cp*Rh] catalysts. *ChemSusChem* **2017,** *10*, 4589-4598.

(10) Clark, M. L.; Cheung, P. L.; Lessio, M.; Carter, E. A.; Kubiak, C. P., Kinetic and mechanistic effects of bipyridine (bpy) substituent, labile ligand, and brønsted acid on electrocatalytic CO_2 reduction by Re(bpy) complexes. *ACS Catal.* **2018,** *8*, 2021-2029.

(11) Tignor, S. E.; Kuo, H.-Y.; Lee, T. S.; Scholes, G. D.; Bocarsly, A. B., Manganese-based catalysts with varying ligand substituents for the electrochemical reduction of CO_2 to CO. *Organometallics* **2019,** *38*, 1292-1299.

(12) Henderson, L. J.; Fronczek, F. R.; Cherry, W. R., Selective perturbation of ligand field excited states in polypyridine ruthenium(II) complexes *J. Am. Chem. Soc.* **1984,** *106*, 5876-5879.

(13) Yam, V. W.-W.; Wang, K.-Z.; Wang, C.-R.; Yang, Y.; Cheung, K.-K., Synthesis, Characterization, and Second-Harmonic Generation Studies of Surfactant Rhenium(I)

Diimine Complexes in Langmuir−Blodgett Films. X-ray Crystal Structure of fac-$ClRe(CO)_3L$ (L = 9-Heptylamino-4,5-diazafluorene). *Organometallics* **1998,** *17*, 2440-2446.

(14) Sykora, M.; Kincaid, J. R., Synthetic Manipulation of Excited State Decay Pathways in a Series of Ruthenium(II) Complexes Containing Bipyrazine and Substituted Bipyridine Ligands. *Inorg. Chem.* **1995,** *34*, 5852-5856.

(15) Annibale, V. T.; Song, D., Coordination chemistry and applications of versatile 4,5-diazafluorene derivatives. *Dalton Trans.* **2016,** *45*, 32-49.

(16) Jiang, H.; Song, D., Syntheses, characterizations, and reactivities of 4,5-diazafluorenide complexes of palladium(II) and rhodium(I). *Organometallics* **2008,** *27*, 3587-3592.

(17) Jiang, H.; Stepowska, E.; Song, D., Syntheses, structures and reactivities of rhodium 4,5-diazafluorene derivatives. *Eur. J. Inorg. Chem.* **2009,** 2083-2089.

(18) Stepowska, E.; Jiang, H.; Song, D., Reversible H_2 splitting between Ru(ii) and a remote carbanion in a zwitterionic compound. *Chem. Commun.* **2010,** *46*, 556-558.

(19) Annibale, V. T.; Batcup, R.; Bai, T.; Hughes, S. J.; Song, D., RuCp* Complexes of ambidentate 4,5-diazafluorene derivatives: from linkage isomers to coordination-driven self-assembly. *Organometallics* **2013,** *32*, 6511-6521.

(20) Batcup, R.; Chiu, F. S. N.; Annibale, V. T.; Huh, J.-e. U.; Tan, R.; Song, D., Selective one-pot syntheses of Pt II Cu I heterobimetallic complexes of 4,5-diazafluorenide derivatives. *Dalton Trans.* **2013,** *42*, 16343-16350.

(21) Campbell, A. N.; White, P. B.; Guzei, I. A.; Stahl, S. S., Allylic C−H acetoxylation with a 4,5-diazafluorenone-ligated palladium catalyst: a ligand-based strategy to achieve aerobic catalytic turnover. *J. Am. Chem. Soc.* **2010,** *132*, 15116-15119.

(22) Campbell, A. N.; Meyer, E. B.; Stahl, S. S., Regiocontrolled aerobic oxidative coupling of indoles and benzene using Pd catalysts with 4,5-diazafluorene ligands. *Chem. Commun.* **2011,** *47*, 10257-10259.

(23) White, P. B.; Jaworski, J. N.; Fry, C. G.; Dolinar, B. S.; Guzei, I. A.; Stahl, S. S., Structurally diverse diazafluorene-ligated palladium(II) complexes and their implications for aerobic oxidation reactions. *J. Am. Chem. Soc.* **2016,** *138*, 4869-4880.

(24) Elsevier, C. J., Catalytic and stoichiometric C–C bond formation employing palladium compounds with nitrogen ligands. *Coord. Chem. Rev.* **1999,** *185-186*, 809-822.

(25) Baran, M. F.; Durap, F.; Aydemir, M.; Baysal, A., Transfer hydrogenation of aryl ketones with homogeneous ruthenium catalysts containing diazafluorene ligands. *Appl. Organomet. Chem.* **2016,** *30*, 1030-1035.

(26) Klein, R. A.; Witte, P.; van Belzen, R.; Fraanje, J.; Goubitz, K.; Numan, M.; Schenk, H.; Ernsting, J. M.; Elsevier, C. J., Monodentate and bridging coordination of 3,3′-Annelated 2,2′-Bipyridines in zerovalent palladium- and platinum-p-quinone complexes. *Eur. J. Inorg. Chem.* **1998,** *1998*, 319-330.

(27) Druey, J.; Schmidt, P., Phenanthrolinchinone und diazafluorene. *Helv. Chim. Acta* **1950,** *33*, 1080-1087.

(28) H. Ohrui, A. Senoo, K. Tetsuya, U.S. Pat. Appl. 0161574, **2008**.

(29) Luong, J. C.; Faltynek, R. A.; Wrighton, M. S. Ground- and excited-state oxidation-reduction chemistry of (triphenyltin)- and (triphenylgermanium)tricarbonyl(1,10-phenanthroline)rhenium and related compounds. *J. Am. Chem. Soc.* **1980**, 102, 7892−7900.

(30) Caspar, J. V.; Meyer, T. J. Application of the energy gap law to nonradiative, excited-state decay. *J. Phys. Chem.* **1983**, 87, 952−957.

(31) Miguel, D.; Riera, V. Synthesis of manganese(I) carbonyls with σ- bonded alkynyl ligands. *J. Organomet. Chem.* **1985**, 293, 379−390.

(32) H. Günther, NMR spectroscopy, John Wiley & Sons, New York, **1980**.

(33) Türschmann, P.; Colell, J.; Theis, T.; Blümich, B.; Appelt, S., Analysis of parahydrogen polarized spin system in low magnetic fields. *Phys. Chem. Chem. Phys.* **2014,** *16*, 15411-15421.

(34) Meyer, T.J., Pure Appl. Chem., **1986**, *58*, 1193-1206.

(35) Kalyanasundaram, K., Photophysics, photochemistry and solar energy conversion with tris(bipyridyl)ruthenium(II) and its analogues. *Coord. Chem. Rev.* **1982,** *46*, 159-244.

(36) Witte, P. T.; Klein, R.; Kooijman, H.; Spek, A. L.; Polášek, M.; Varga, V.; Mach, K., Electron transfer in the reactions of titanocene-bis(trimethylsilyl) acetylene complexes with 2,2'-bipyridine and 4,5-diazafluorene. The crystal structure of (4,5-diazafluorenyl) bis(pentamethylcyclopentadienyl) titanium(III). *J. Organomet. Chem.* **1996,** *519*, 195-204.

(37) Machan, C. W.; Sampson, M. D.; Chabolla, S. A.; Dang, T.; Kubiak, C. P., Developing a mechanistic understanding of molecular electrocatalysts for CO_2 reduction using infrared spectroelectrochemistry. *Organometallics* **2014,** *33*, 4550-4559,

(38) Rillema, D. P.; Jones, D. S.; Levy, H. A., Structure of tris(2,2'-bipyridyl)ruthenium(II) hexafluorophosphate, $[Ru(bipy)_3][PF_6]_2$; x-ray crystallographic determination. *J. Chem. Soc., Chem. Commun.* **1979**, 849-851.

(39) Rillema, D. P.; Jones, D. S.; Woods, C.; Levy, H. A., Comparison of the crystal structures of tris heterocyclic ligand complexes of ruthenium(II). *Inorg. Chem.* **1992,** *31*, 2935-2938.

(40) Breu, J.; Domel, H.; Stoll, A., Racemic compound formation versus conglomerate formation with $[M(bpy)_3](PF_6)_2$ (M = Ni, Zn, Ru); molecular and crystal structures. *Eur. J. Inorg. Chem.* **2000,** 2401-2408.

(41) Fronczek, F. R., CCDC 287572: Experimental Crystal Structure Determination, 2006, DOI: 10.5517/cc9n7jp

(42) Constable, E. C., Homoleptic complexes of 2,2′-bipyridine. *Adv. Inorg. Chem.*, Sykes, A. G., Ed. Academic Press: 1989; Vol. 34, pp 1-63.

(43) Kaim, W., The transition metal coordination chemistry of anion radicals. *Coord. Chem. Rev.* **1987,** *76*, 187-235.

(44) England, J.; Scarborough, C. C.; Weyhermüller, T.; Sproules, S.; Wieghardt, K., Electronic Structures of the Electron Transfer Series $[M(bpy)_3]^n$, $[M(tpy)_2]^n$, and $[Fe(tbpy)_3]^n$ (M = Fe,

Ru; n = 3+, 2+, 1+, 0, 1–): A Mössbauer Spectroscopic and DFT Study. *Eur. J. Inorg. Chem.* **2012,** 4605-4621.

(45) Lyaskovskyy, V.; de Bruin, B., Redox non-Innocent ligands: versatile new tools to control catalytic reactions. *ACS Catal.* **2012,** *2*, 270-279.

(46) Corcos, A. R.; Villanueva, O.; Walroth, R. C.; Sharma, S. K.; Bacsa, J.; Lancaster, K. M.; MacBeth, C. E.; Berry, J. F., Oxygen activation by Co(II) and a redox non-innocent ligand: spectroscopic characterization of a radical–Co(II)–superoxide complex with divergent catalytic reactivity. *J. Am. Chem. Soc.* **2016,** *138*, 1796-1799.

(47) Riplinger, C.; Sampson, M. D.; Ritzmann, A. M.; Kubiak, C. P.; Carter, E. A., Mechanistic contrasts between manganese and rhenium bipyridine electrocatalysts for the reduction of carbon dioxide. *J. Am. Chem. Soc.* **2014,** *136*, 16285-16298.

(48) Fulmer, G.R.; Miller, A.J.M.; Sherden, N.H.; Gottlieb, H.E.; Nudelman, A.; Stoltz, B.M.; Bercaw, J.E.; Goldberg, K.I. NMR Chemical Shifts of Trace Impurities: Common Laboratory Solvents, Organics, and Gases in Deuterated Solvents Relevant to the Organometallic Chemist. *Organometallics* **2010,** *29*, 2176–2179.

(49) Harris, R.K.; Becker, E.D.; Cabral De Menezes, S.M.; Goodfellow, R.; Granger, P. NMR nomenclature. Nuclear spin properties and conventions for chemical shifts (IUPAC recommendations 2001). *Pure Appl. Chem.* **2001,** *73*, 1795–1818.

(50) Harris, R.K.; Becker, E.D.; Cabral De Menezes, S.M.; Granger, P.; Hoffman, R.E.; Zilm, K.W. Further conventions for NMR shielding and chemical shifts: (IUPAC recommendations 2008). *Pure Appl. Chem.* **2008,** *80*, 59–84.

Chapter 7

Synthesis, structural studies, and redox chemistry of bimetallic [$Mn(CO)_3$] and [$Re(CO)_3$] complexes

This chapter is adapted from a published manuscript: Henke, W.C., Kerr, T.A., Sheridan, T.R., Henling, L.M., Takase, M.K., Day, V.W., Gray, H.B., and Blakemore, J.D.* Synthesis, structural studies, and redox chemistry of bimetallic [$Mn(CO)_3$] and [$Re(CO)_3$] complexes, *Dalton Trans.* **2021**, *50*, 2746-2756.

7.1 Introduction

Tricarbonyl complexes of the Group 7 transition metals (manganese, technetium, and rhenium) represent a privileged class of complexes that show remarkable versatility in studies of energy science,[1,2,3] therapeutics,[4,5] and electrocatalysis.[6,7] The facile syntheses and numerous spectroscopic handles presented by these compounds have enabled fundamental insights to be gained over the years into how their structures give rise to useful properties as photosensitizers, carbon monoxide releasing molecules (CORMs), and electrocatalysts. The synthetic chemistry for the tricarbonyl complexes, which was developed early by Wrighton,[8] Meyer,[9] and Miguel,[10] has led to explosive growth in research on $[Re(CO)_3]$[11,12,13,14,15] and $[Mn(CO)_3]$[16,17,18,19,20] chemistry.

In particular, diimine ligands are often used to support these tricarbonyl complexes; these ligands are attractive because they are readily prepared, easily derivatized, and make stable chelate complexes. Notably, 2,2′-bipyridyl (bpy) and 4,4′-disubstituted-2,2′-bipyridyl (^{R}bpy) ligands have been frequently used in this area; installation of electron-donating or electron-withdrawing groups on the bpy ligand can readily tune the chemical, photophysical, and redox properties of the resulting complexes.[21] In one study, Kubiak and co-workers utilized a range of electron-donating and electron-withdrawing ^{R}bpy ligands to generate a series of $[Re(CO)_3]$ complexes that revealed ligand influences on the production of carbon monoxide (CO) from carbon dioxide (CO_2).[22] Bocarsly and co-workers carried out related work with the $[Mn(CO)_3]$ unit; the electron-donating and electron-withdrawing ^{R}bpy ligands were shown to modulate the electrocatalytic properties of these complexes in a similar fashion.[23] More recently, some of us have been exploring the related coordination chemistry of $[Mn(CO)_3]$ complexes bearing 4,5-diazafluorene (daf) ligands.[24] In comparison to $Mn(CO)_3Br(bpy)$, $Mn(CO)_3(daf)Br$ displays an increased bite angle which

moderates the σ-donating and π-accepting abilities of daf, resulting in a unique electrochemical profile. Use of daf thus represents a complementary method for tuning often accomplished via traditional inductive effects. Considered together, these cases provide an appealing snapshot of the influence that diimine-type ligands can have on the properties of Group 7 tricarbonyl complexes.

An alternative strategy for tuning the properties of metal complexes involves development of heteromultimetallic systems.[25,26] In such structures, the influence of one metal upon a second can be leveraged to engender new properties that are inaccessible with a single metal center alone. To accomplish work in this area, ditopic ligands are needed which can bring two metals into close proximity.[27,28,29,30] In part thanks to their stability, [$Mn(CO)_3$] and [$Re(CO)_3$] moieties can be brought into close proximity. Several approaches have been employed for this purpose, including tethering alkyl groups,[31] metal organic frameworks (MOFs),[32] and multidentate ligands.[33] In particular, the chelating ligand 2,2′-bipyrimidine (bpm) is attractive for this purpose, as it offers direct synthetic access to both monometallic and bimetallic complexes. Superficially, bpm and bpy are similar ligands; however, the additional N-atoms in the bpm framework result in modulated donor properties compared to bpy. Synthetically, bpm is perhaps best known for effectively bridging Ru centers,[34,35] but it has also been successfully deployed to bridge between [$Re(CO)_3$] motifs.[36,37]

In the 1980s, Vogler and co-workers first prepared the monometallic complex $Re(CO)_3Cl(bpm)$ (**1**).[36] Taking advantage of the additional bis-chelate site contained within **1**, they also synthesized the homobimetallic complex $[Re(CO)_3Cl]_2(bpm)$.[36] This species was also explored by Juris and co-workers[38] as well as Kaim and Kohlman.[39] In their report, elemental analysis data and emission spectroscopic properties were described for the characterization of $[Re(CO)_3Cl]_2(bpm)$. However, considering the structure of $[Re(CO)_3Cl]_2(bpm)$, there are two possible isomers, a situation

recognized early by the others working in this arena.[38,39] A syn isomer is possible which orients the halide ligands in the same direction (**2-syn**), as well as an anti isomer that orients the halides in opposite directions (**2-anti**).[40,41] Vogler and co-workers did not explicitly state whether they were working with isomerically pure complexes, but based on previous studies[37,38,39,40] and our work here (*vide infra*), we conclude that they were indeed studying a mixture of the **2-syn** and **2-anti** isomers (see Chart 7.1). More recently, Bocarsly and co-workers[23] and Jain and co-workers[42] showed that the related monometallic Mn complexes $Mn(CO)_3Br(bpz)$ (**3**) and $Mn(CO)_3Br(bpm)$ (**4**) can be prepared. In light of the considerable interest in $[Mn(CO)_3]$ complexes as catalysts and photoactive compounds,[7,21] we were surprised to see that bimetallic complexes containing $[Mn(CO)_3]$ moieties bridged by the bpm ligand have not been reported. Furthermore, there have been no prior crystallographic studies of either mono- or bimetallic $[Mn(CO)_3]$ bpm complexes, motivating structural work to complement findings available regarding the structures of $[Re(CO)_3]$ complexes with bpm.[40,43,44,45,46,47]

Here, we report the syntheses, solid-state structures, and electrochemical properties of a family of $[Re(CO)_3]$ and $[Mn(CO)_3]$ complexes, including compounds $[Mn(CO)_3Br]_2(bpm)$ (isolable as a mixture of **5-syn** and **5-anti**) and $[Re(CO)_3Br(bpm)Mn(CO)_3Br]$ (also isolable as a mixture of **6-syn** + **6-anti**, see Chart 7.1). Consistent with prior work on homo-bimetallic Re compounds of bpm, both the syn and anti isomers of $[Mn(CO)_3Br]_2(bpm)$ and $[Re(CO)_3Br(bpm)Mn(CO)_3Br]$ are accessible based on NMR spectroscopy; the isomers are confirmed here by crystallographic studies of **5-syn**, **5-anti,** and **6-syn**. New solid-state structures of **1**,[36,] **2-anti**,[36,] **3**,[23] and **4**[42] have also been collected for comparison to these new bimetallic compounds. In agreement with prior findings on $[Mn(CO)_3(diimine)]$ complexes,[21,48] all of the $[Mn(CO)_3]$-containing compounds reported here are acutely light-sensitive. We find that the homo- and hetero-bimetallic Mn

complexes undergo reduction at more positive potentials compared to their monometallic counterparts. Related electron paramagnetic resonance (EPR) studies reveal that chemical reduction of $[Re(CO)_3Cl]_2(bpm)$, which displays similar electrochemical properties to our new Mn compounds, involves a first ligand-centered reduction.[49,50] Taken together, our studies suggest that the presence of a second tricarbonyl unit leads to a strong inductive effect that shifts the ligand-centred reduction process to more positive potentials in the cases of all the bimetallic compounds.

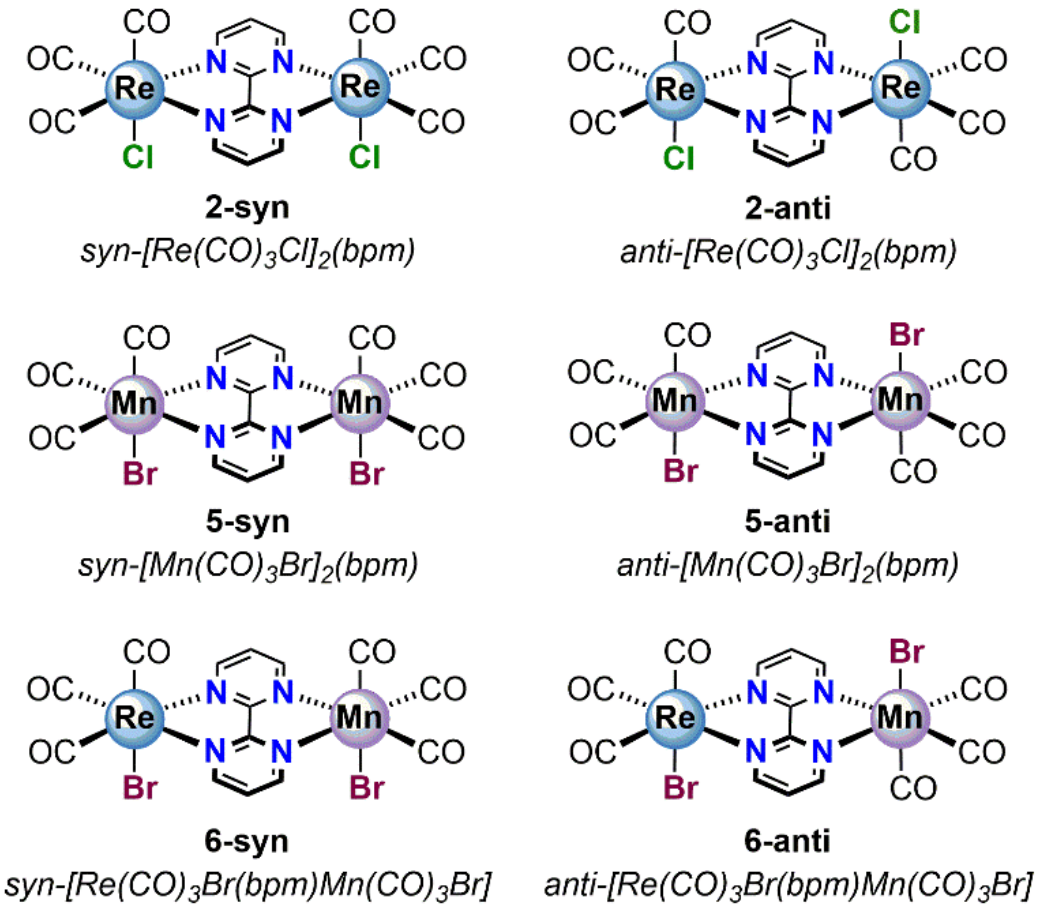

Chart 7.1: $[Re_2]$, $[Mn_2]$, and [ReMn] bimetallic complexes described in this study. The dirhenium compounds were prepared according to Vogler and co-workers.[36]

7.2 Results and Discussion

7.2.1 Synthesis and spectroscopic characterization

The synthons $Re(CO)_5Cl$, $Re(CO)_5Br$, and $Mn(CO)_5Br$ were obtained from commercial suppliers, and monometallic 1, 3, and 4 were prepared according to the literature.[23,36,42] Of particular interest to our group was the work carried out by Vogler and co-workers,[36] who reported the synthesis of the bimetallic complex, $[Re(CO)_3Cl]_2(bpm)$. Following their reported synthetic procedure, we isolated $[Re(CO)_3Cl]_2(bpm)$ as a mixture of 2-syn and 2-anti isomers; the appearance of the ^1H nuclear magnetic resonance (NMR) spectrum of the isolated material (see Figure E7) and the solid state structural data (see Figures E35-E36) confirm the presence of both the expected isomers.[37] Encouraged by these previous reports and keeping in mind that $[Re(CO)_3Cl]_2(bpm)$ can be isolated as a mixture of syn and anti isomers, our group pursued the synthesis of new homo- and heterobimetallic complexes bearing the $[Mn(CO)_3]$ moiety using the bpm framework (see Scheme 7.1).

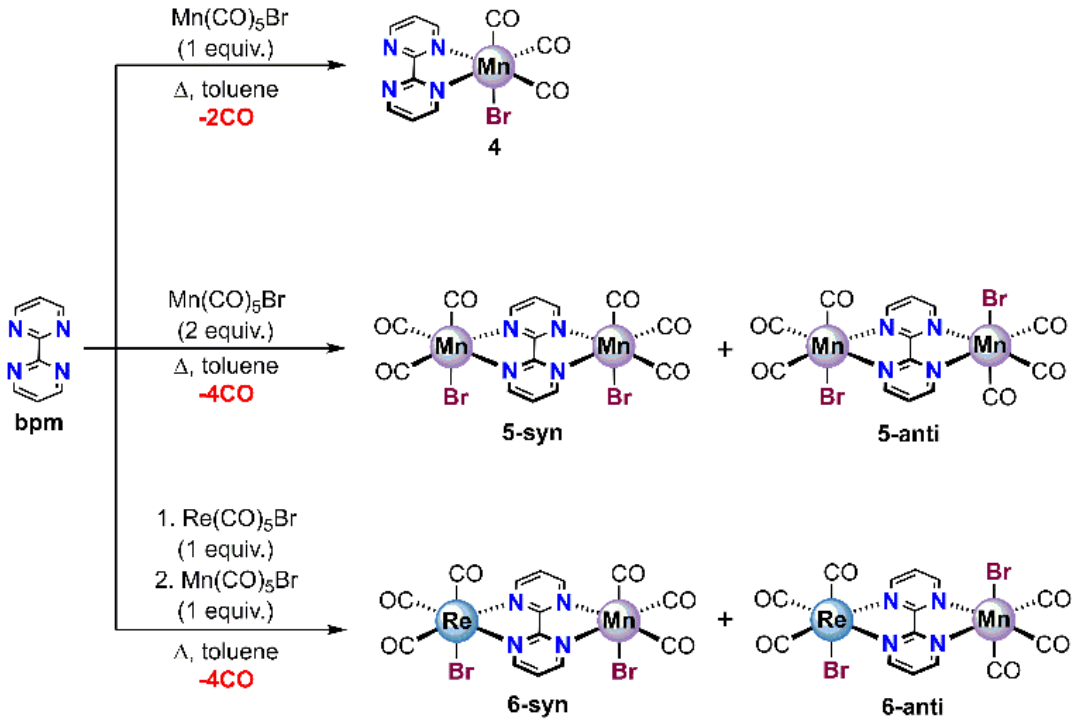

Scheme 7.1: Synthetic pathway for the generation of homo- and hetero-bimetallic complexes.

Due to the light sensitivity of these complexes, all reactions containing Mn were performed in the dark. In a refluxing suspension of toluene, $Mn(CO)_5Br$ and bpm were combined in the appropriate stoichiometry (2 equiv. to 1 equiv., respectively) to generate $[Mn(CO)_3Br]_2(bpm)$, resulting in the formation of a mixture of the syn and anti isomers (**5-syn** and **5-anti**) in a good yield of 91%. The synthesis of the syn and anti isomers that are contained in the analogous $[Re(CO)_3Br(bpm)Mn(CO)_3Br]$ (**6-syn** and **6-anti**) was accomplished by first generating the light-stable monometallic complex **1-Br** ($Re(CO)_3Br(bpm)$); $Re(CO)_5Br$ was selected as the transition metal precursor to ensure that there would be no halide scrambling in solution upon formation of the bimetallic complex. Following the generation of **1-Br**, 1 equiv. of $Mn(CO)_5Br$ was added to the solution to generate $[Re(CO)_3Br(bpm)Mn(CO)_3Br]$, also as a mixture of **6-syn** and **6-anti**

isomers in a good yield of 89%. Following successful generation of the mixtures of the desired complexes, they were each fully characterized (see Experimental Section and Supporting Information). Separation of the isomers of these new compounds was not pursued, although it may be possible based on our crystallographic studies (*vide infra*).

To begin characterization of the newly synthesized bimetallic complexes, we turned to ^{1}H NMR spectroscopy (see Figures E1-E7). In solution, complexes $[Mn(CO)_3Br]_2(bpm)$ and $[Re(CO)_3Br(bpm)Mn(CO)_3Br]$ exist as a mixture of isomers with resonance splitting patterns arising from the $^{3}J_{H,H}$ and $^{4}J_{H,H}$ coupling in the aromatic region of their ^{1}H-NMR spectra. These signals correspond to the hydrogen atoms on the bpm ligands coordinated to their corresponding Mn and Re centers. The isomers **5-syn**, **5-anti, 6-syn** and **6-anti** exhibit C_{2v}, $C_{2h,}$ $C_{s,}$ and C_s symmetry in solution, respectively, and this results in resonances that clearly distinguish the isomers of the homobimetallics **5-syn** and **5-anti** from the heterobimetallics **6-syn** and **6-anti**. The ^{1}H-NMR spectrum of the mixture containing **5-syn** and **5-anti** exhibits four unique protons in total which confirms that both the isomers are present. The different isomers of $[Mn(CO)_3Br]_2(bpm)$ are discernible from one another based on their different signal intensities; each isomer has a corresponding triplet at d 7.85 or 7.88 ppm (integrating to 2H) and doublet at d 9.43 or 9.46 ppm (integrating to 4H) in the aromatic region. The isomers of $[Mn(CO)_3Br]_2(bpm)$ are present in an approximately 3:1 ratio based on the relative integration of the separated resonances at d 9.43 and 9.46 ppm. Identifying which pair of resonances belongs to the **5-syn** or **5-anti** isomers based on the ^{1}H-NMR spectrum alone was not pursued here. Nonetheless, the expected connectivity of both isomers in solution is confirmed.

Considering the change in symmetry from C_{2v} and C_{2h} for **5-syn** and **5-anti** to C_s symmetry for **6-syn** or **6-anti**, we observed a significant change in the number of unique protons in the aromatic

region of the ^{1}H-NMR spectrum. The decrease in the symmetry for **6-syn** and **6-anti** of $[Re(CO)_3Br(bpm)Mn(CO)_3Br]$ in comparison to the **5-syn** and **5-anti** isomers of $[Mn(CO)_3Br]_2(bpm)$ results in a ^{1}H-NMR spectrum with peak groupings at 9.52, 9.27, and 7.86 ppm (integrating to 2H, 2H, 2H, respectively). Additionally, there is another resolved isomer with peak groupings at 9.55, 9.30, and 7.89 ppm (integrating to 2H, 2H, 2H). The isomers are present in an approximately 2:1 ratio based on the integration of the separated resonances at d 9.52 and 9.55 ppm. ^{1}H-NMR alone did not identify which set of resonances belongs to **6-syn** or **6-anti**, but did confirm the expected connectivity in solution.

The bimetallic complexes $[Mn(CO)_3Br]_2(bpm)$ and $[Re(CO)_3Br(bpm)Mn(CO)_3Br]$ have carbonyl ligands and are vividly colored in solution and thus we next turned to investigate their vibrational and absorption characteristics using infrared (IR) and electronic absorption (EA) spectroscopy (see Figure 7.1, and Figures E9 and E10-E13). The IR spectrum of **5-syn** and **5-anti** exhibits CO vibrational bands at 2031, 1952, and 1936 cm^{-1}, while the spectrum for **6-syn** and **6-anti** displays bands at 2028, 1951, 1935, and 1914 cm^{-1}. The observation of the additional band in the analysis of **6-syn** and **6-anti** compared to **5-syn** and **5-anti** is consistent with the decrease in symmetry for the heterobimetallic compounds (C_{2v} and C_{2h} for **5-syn** and **5-anti** to C_s for **6-syn** and **6-anti**).

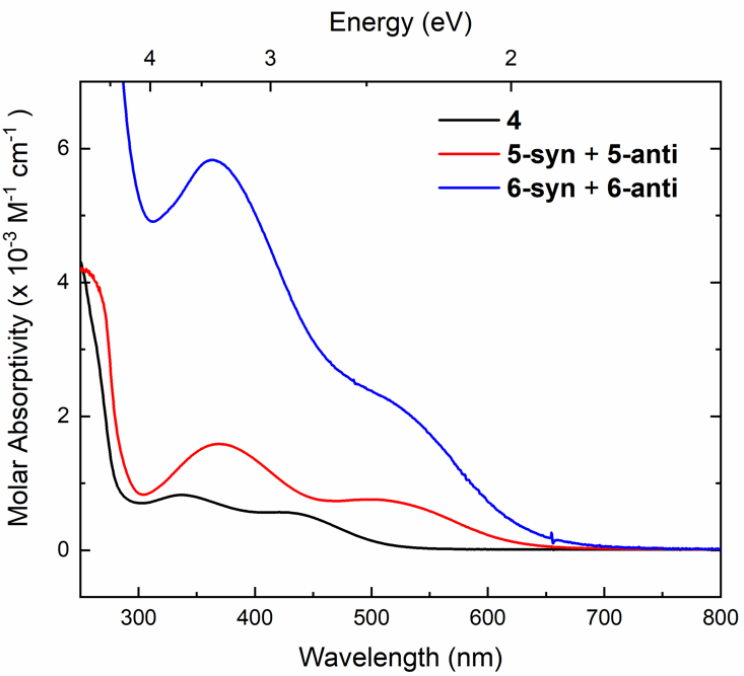

Figure 7.1: Electronic absorption spectra for **4**, **5-syn** + **5-anti**, and **6-syn** + **6-anti** in MeCN solution.

The EA spectrum of the mixture of **5-syn** and **5-anti** isomers of $[Mn(CO)_3Br]_2(bpm)$ exhibits two transitions in the visible region at 369 nm and 510 nm with molar absorptivities of 1600 M^{-1} cm^{-1} and 800 M^{-1} cm^{-1}, respectively. The values of the molar absorptivities and the similarity of the spectrum to those of $Mn(CO)_3Br(bpy)$ and **4** (337 nm, 800 M^{-1} cm^{-1}; 430 nm, 600 M^{-1} cm^{-1}) enables their assignment as metal-to-ligand charge transfer (MLCT) transitions.[51] Notably, the molar absorptivities associated with the charge transfer transitions in the syn and anti isomers of $[Mn(CO)_3Br]_2(bpm)$ are greater than those observed for the analogous monometallic **4**, which confirmed that the presence of the additional $[Mn(CO)_3]$ unit plays a role in the light absorption properties of these complexes. We also investigated the EA properties of the mixture of **6-syn** and **6-anti** in the heterobimetallic compound $[Re(CO)_3Br(bpm)Mn(CO)_3Br]$; the spectrum displays a similar absorption profile to **4** and the isomers of $[Mn(CO)_3Br]_2(bpm)$, with features at 364 nm

(5800 M^{-1} cm^{-1}) and 515 nm (2300 M^{-1} cm^{-1}). The molar absorptivities of the electronic transitions associated with the syn and anti isomers of $[Re(CO)_3Br(bpm)Mn(CO)_3Br]$ are three times greater than the comparable peaks in $[Mn(CO)_3Br]_2(bpm)$, and seven times greater than those associated with the monometallic complex **4**. These results suggest that the presence of a second tricarbonyl moiety increases the EA intensity, and suggest a distinct role for the heavier metal rhenium in engendering efficient light absorption.[52]

7.2.2 X-ray diffraction studies

The syntheses of the monometallics **1**, **3**, and **4,** and the bimetallic complex $[Re(CO)_3Cl]_2(bpm)$ (**2-syn** and **2-anti**) have been previously described, but their solid-state structures have not been reported to the Cambridge Structural Database (CSD).[53] To gain further insight into the properties of both the newly prepared and previously reported complexes, we turned to single crystal X-ray diffraction (XRD) analysis and report here seven new solid-state structures (see Figures 7.2 and E33-E43). The results confirm the expected *fac*-geometry of **1**, **3** and **4** with two equatorial CO ligands, an axial CO ligand, an axial halide, and the associated k^2-diimine ligand surrounding the rhenium or manganese center in each case. Based on the previous NMR analyses of $[Re(CO)_3Cl]_2(bpm)$, $[Mn(CO)_3Br]_2(bpm)$, and $[Re(CO)_3Br(bpm)Mn(CO)_3Br]$, we anticipated that either or both of the syn and anti isomers could in principle be present in the solid-state. The results here confirm the presence of **2-syn**, **2-anti**, **5-syn**, **5-anti**, and **6-syn** in our solid-state samples; the syn isomers feature halides oriented in the same direction, and the anti isomers feature halides oriented in opposite directions. The structure for **2-anti**, in particular, reveals packing disorder (apparent in the axial chloride and CO ligands) driven by the presence of both **2-anti** and **2-syn** in the crystal unit cell; **2-anti** and **2-syn** are present in an 80:20 ratio. As **2-**

anti predominates in the structure, we will refer to the structure here as being associated with the **2-anti** isomer. On the other hand, the packing disorder encountered for **2-anti** was not present in the data for **5-syn**, **5-anti**, or **6-syn** (see Figures E39-E43). Indeed, we were pleased to find that the individual crystals of **5-syn** and **5-anti** were visually distinguishable from one another in the vial; careful crystal harvesting ultimately led to their separate and unique solid-state structures. In the case of the heterobimetallic complex, only crystals of **6-syn** could be obtained.

The structures of the monometallic complexes **1, 3,** and **4** closely resemble the well-known bpy-based complexes $Re(CO)_3X(bpy)$ (X = Cl, Br) and $Mn(CO)_3Br(bpy)$.[54,55,56] A comparison of relevant bond lengths and angles of the monometallic Re complex **1** from this study with the structurally analogous complexes $Re(CO)_3X(bpy)$ (X = **Cl**, **Br**) revealed very similar average Re–N distances of 2.172(4) Å (**1**) , 2.175(7) Å (**Cl**), and 2.166(16) Å (**Br**) with N–Re–N bite angles of 74.85(9)° (**1**), 74.9(2)° (**Cl**), and 74.7(4)° (**Br**), respectively. Comparing the monometallic Mn-based complex **4** with the structurally similar complex Mn(CO)Br(bpy) revealed average Mn–N distances of 2.046(2) and 2.043(6) Å, and N–Mn–N bite angles of 79.5(3)° and 78.9(15)°, respectively. For both Re and Mn, we thus found that the presence of the additional nitrogen atoms on the bpm ligand does not induce significant structural changes in comparison to the complexes ligated with bpy. However, the bpm ligand has the attractive ability to chelate an additional tricarbonyl moiety to generate homo- and hetero-bimetallic complexes (see Table 7.1 and Figure 7.2).

Table 7.1: Selected bond lengths and distances in complexes **1**, **2-anti**, **3**, **4**, **5-syn**, **5-anti**, and **6-syn**.

Compound	Re-CO_{AX} (Å)	Re-CO_{EQ} (Å)	Re-N (Å)	Re-Halide (Å)	Mn-CO_{AX} (Å)	Mn-CO_{EQ} (Å)	Mn-N (Å)	Mn-Halide (Å)	BPM_{C-C} (Å)
1	1.894(6)	1.920(3), 1.926(3)	2.171(2), 2.172(3)	2.484(1), 2.31(3)	----------	----------	----------	----------	1.484(4)
2-anti	1.894(15), 1.96(4)	1.934(7), 1.911(7)	2.192(5), 2.189(5)	2.455(3), 2.43(2)	----------	----------	----------	----------	1.46(1)
3	----------	----------	----------	----------	1.813(1)	1.825(1), 1.827(1)	2.028(1), 2.038(1)	2.5255(2)	1.460(2)
4	----------	----------	----------	----------	1.8257(17)	1.812(2), 1.820(2)	2.045(1), 2.048(1)	2.5332(3)	1.481(2)
5-syn	----------	----------	----------	----------	1.805(14)	1.806(9), 1.806(9)	2.062(6), 2.062(6)	2.521(2)	1.46(2)
5-anti	----------	----------	----------	----------	1.843(10)	1.81(1), 1.82(1)	2.061(7), 2.061(7)	2.503(2)	1.44(2)
6-syn	1.933(14)	1.921(12), 1.921(12)	2.161(3), 2.161(3)	2.614(2)	1.825(16)	1.82(2, 1.82(2)	2.092(8), 2.092(8)	2.497(9)	1.451(7)

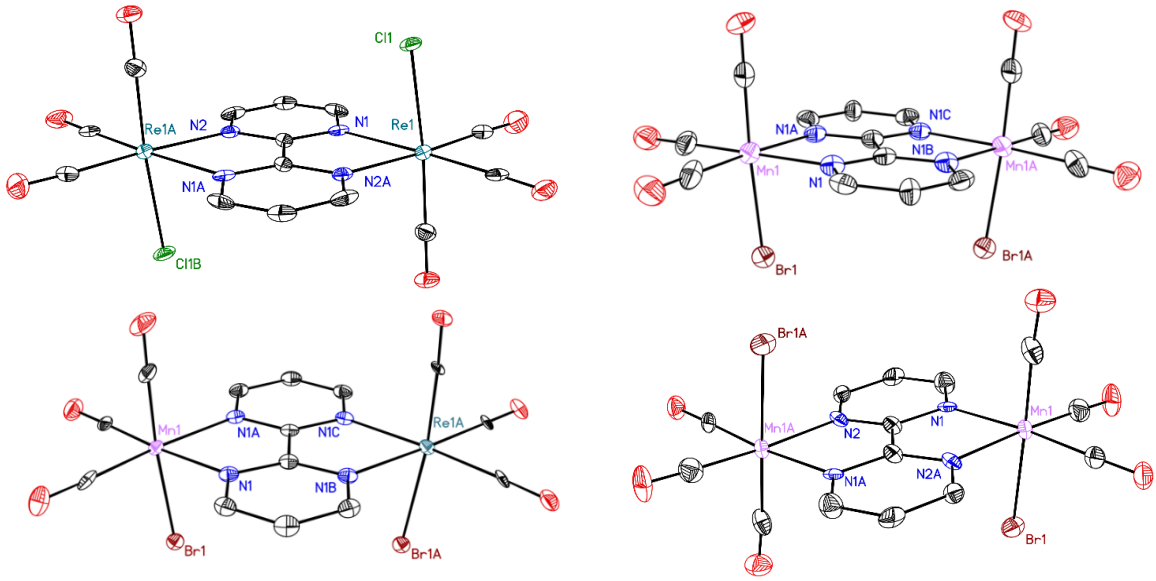

Figure 7.2: Solid-state structures of **2-anti** (upper-left), **5-syn** (upper-right), **5-anti** (lower-right), **6-syn** (lower-left). Displacement ellipsoids are shown at 50% probability level. Hydrogens and co-crystallized solvents are omitted for clarity.

Comparison of **1** with the homobimetallic **2-anti** revealed similar Re–CO_{AX} and Re–CO_{EQ} bond distances between the two complexes. A similar evaluation of the Mn-based monometallic complex **4** with the bimetallic complexes **5-syn** and **5-anti** showed that the Mn–CO_{AX} and Mn–CO_{EQ} bond distances remain indistinguishable within error as well. Thus, although the introduction of a second tricarbonyl moiety has a large effect on the electronics of the bimetallic complexes, this does not appear to correlate to significant structural changes when comparing the [$M(CO)_3$] units within **1**, **2-anti**, **4**, **5-syn** and **5-anti.** On the other hand, there is a slight contraction in the metal-halide distances between the monometallic and homobimetallic complexes bearing the same transition metals, suggesting modulation of the donor power of the bpm ligand upon coordination of a second tricarbonyl unit. Furthermore, there are changes associated with the M–N bond distances, N–M–N bond angles, and $d_{C–C}$ bond distances ($d_{C–C}$ refers to the distance between the two central carbons connecting the individual pyrimidine rings) that result from the introduction of the second tricarbonyl unit.

In accord with these findings, comparison of **1** with **2-anti**, and **4** with **5-syn** and **5-anti** revealed elongation of the M–N bond lengths upon introduction of the second tricarbonyl unit. This likely occurs because initial introduction of a transition metal causes the bpm bite angle to narrow in an effort to facilitate metal binding. However, when a second metal tricarbonyl unit is introduced into the open site of a monometallic bpm complex, the nitrogen atoms are pulled back so that the optimal bite angle for both metal centers is established. Consistent with this proposal, we see a small increase in the bite angle upon generation of the homobimetallic complexes (see Table 7.2).

Table 7.2: Selected bond angles in complexes **1**, **2-anti**, **3**, **4**, **5-syn**, **5-anti**, and **6-syn**.

Compound	N_1-Re-N_2	N_1-Mn-N_2
1	74.85(9)°	----------
2-anti	75.15(19)°	----------
3	----------	79.04(4)°
4	----------	78.68(5)°
5-syn	----------	79.5(3)°
5-anti	----------	79.7(3)°
6-syn	75.94(14)°	78.9(4)°

Further examination of the bond lengths around the bpm ligand for our series of complexes revealed a trend in the $d_{C–C}$ bond distances; a slight contraction was observed when comparing the monometallic complexes to the bimetallic complexes. The solid-state structure of free bpm showed that the $d_{C–C}$ bond length is 1.497(4) Å.[57] When we introduce Re or Mn to form a monometallic complex, we observed a small initial contraction of $d_{C–C}$, which is exacerbated further with the addition of a second metal to form the bimetallic complexes. This indicates that there is active backdonation from the transition metal to bpm and suggests that backbonding is further increased when a second metal is present. This trend was exciting to see since the C–C bond that binds the two pyridyl rings of bpy has also been observed to contract when [Cp*Rh(bpy)Cl]PF_6 is reduced to Cp*Rh(bpy).[58,59] Thus, some degree of backdonation from the electron-rich Re(I) and Mn(I) metal centers into the π* orbitals of bpm may be present in these systems.

Overall, there are similar trends in the metrical parameters for both the manganese- and rhenium-containing species characterized here. This speaks to the modularity of the [$M(CO)_3$] units (M = Mn, Re) as judged by this structural work on the bpm framework. The inductive

presence of an additional metal tricarbonyl unit, although giving rise to subtle changes to the solid-state structures, provides more pronounced effects on the electronic structure, as assessed by the EA spectroscopy. Consequently, we turned to cyclic voltammetry to identify further features that could distinguish the monometallic and bimetallic complexes

7.2.3 Electrochemistry

The electrochemical properties of **1**, **3** and **4** have been previously described and were reconfirmed here for comparison to results on our new compounds (see Figures E17-E31).[23,49] Cyclic voltammetry (CV) experiments using the monometallic complexes **1** and **4** were conducted with specific interest in determining the impact the additional nitrogen atoms on the bpm ligand could have on their electrochemical behavior with respect to the well-known analogues, $Re(CO)_3Cl(bpy)$[6,22] and $Mn(CO)_3Br(bpy)$.[7,24] Based on prior studies, the electrochemical profile of $Re(CO)_3Cl(bpy)$ exhibited an initial quasi-reversible ligand-centered reduction at –1.78 V followed by an irreversible metal-centered reduction at –2.16 V (all potentials are quoted versus ferrocenium/ferrocene, denoted $Fc^{+/0}$).[22] As expected, the CVs of **1** are strikingly similar to $Re(CO)_3Cl(bpy)$; an initial quasi-reversible reduction centered at –1.42 V was followed by an irreversible reduction at –1.91 V. These results indicate that $Re(CO)_3Cl(bpy)$ and **1** behave in a similar fashion.

$Mn(CO)_3Br(bpy)$ and **4** exhibit comparable CVs. Based on previous reports regarding $Mn(CO)_3Br(bpy)$, the CV of this compound exhibits two irreversible reductions at –1.61 V and –1.83 V, coupled with an oxidation at –0.61 V.[7,24] The presence of two irreversible reductions, while a more challenging case, can be readily explained and is consistent with a previously proposed mechanism.[7,60] For the purpose of subsequent comparisons, the first irreversible wave

can be attributed to a Mn-centred reduction that results in a $19e^-$ complex that loses the bound halide ligand, generating a transient $17e^-$ complex that dimerizes to form the $18e^-$ complex, $[Mn(CO)_3(bpy)]_2$. $[Mn(CO)_3(bpy)]_2$ can then be reduced at the more negative potential, a process that results in cleavage of the dimer to generate the formally $18e^-$ complex $[Mn(CO)_3(bpy)]^-$. Scanning anodically, the oxidation of $[Mn(CO)_3(bpy)]_2$ can also be observed at a more positive potential. **4** thus behaves similarly to $Mn(CO)_3Br(bpy)$, showing two irreversible reductions at –1.37 V and –1.58 V, and two irreversible oxidations at –1.36 and –0.42 V. Notably, in comparison to $Mn(CO)_3Br(bpy)$, complex **4** shows an additional oxidative feature at –1.36 V, suggesting that the electron-withdrawing ability of the additional nitrogen atoms present on bpm stabilizes one of the reduced forms. Nonetheless, these findings suggest that the presence of the additional nitrogen atoms on bpm do not significantly impact the electrochemical profile, in terms of the number of the observable reduction events. However, the presence of the nitrogen atoms on the bpm ligand results in a noticeable inductive effect that shifts the reduction potentials of complexes **1** and **4** by *ca.* 250 mV in comparison to their corresponding bpy-based complexes.

With these results in hand, we investigated the cyclic voltammetry of the synthesized homo- and hetero-bimetallic complexes (see Figure 7.3). In each instance, $[Re(CO)_3Cl]_2(bpm)$, $[Mn(CO)_3Br]_2(bpm)$, and $[Re(CO)_3Br(bpm)Mn(CO)_3Br]$ were interrogated as the mixture of their corresponding syn and anti isomers. These bimetallic compounds exhibit distinct electrochemical profiles in comparison to their monometallic analogues **1** and **4** (see Figure E24). In particular, the initial reduction for each of the bimetallic systems is quasi-reversible and at much more positive potentials than their comparable monometallic complexes (see Figure 7.3). The observation of an initial, quasi-reversible reduction is common for monometallic $[Re(CO)_3]$-based diimine systems, but is not observed for most $[Mn(CO)_3]$-based diimine systems. This suggests that the presence of

an additional tricarbonyl moiety results in an inductive effect that shifts the initial reduction to much more positive potentials, significantly moderating the potential needed to introduce an electron into these systems. As a result, the first reduction for the isomers of $[Re(CO)_3Cl]_2(bpm)$ is shifted by +600 mV and the first reduction for the isomers of $[Mn(CO)_3Br]_2(bpm)$ is shifted by +380 mV in comparison to **1** and **4**, respectively. Intriguingly, the first reduction of the mixture of syn and anti isomers of $[Re(CO)_3Br(bpm)Mn(CO)_3Br]$ falls in between the two homo-bimetallic complexes, further signifying that the electronic characteristics of this system are averaged between the two homobimetallics.

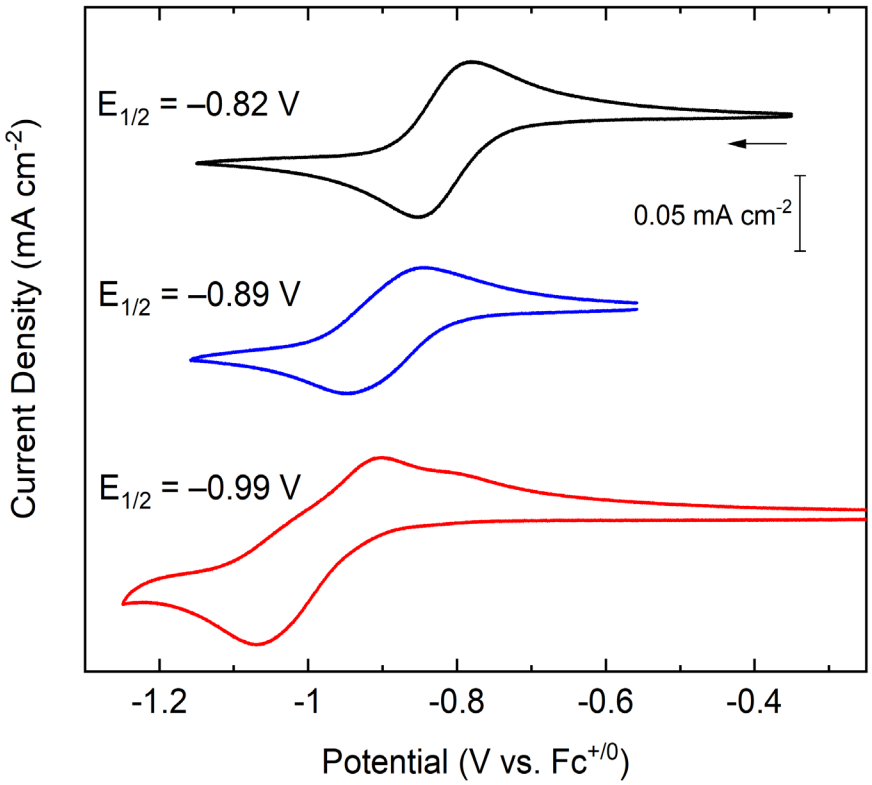

Figure 7.3: Cyclic voltammetry of $[Re(CO)_3Cl]_2(bpm)$ (**2-syn** and **2-anti**, black), $[Re(CO)_3Br(bpm)Mn(CO)_3Br]$ (**6-syn** and **6-anti**, blue), and $[Mn(CO)_3Br]_2(bpm)$ (**5-syn** and **5-anti**, red), in MeCN solution with 0.1 M $TBAPF_6$ supporting electrolyte (working electrode:

highly oriented pyrolytic graphite; pseudo reference electrode: $Ag^{+/0}$; counter electrode: Pt wire). Ferrocene was used as an internal potential reference.

More negative cathodic scans with each bimetallic complex led to further unique electrochemical reductions; these are mostly irreversible and can tentatively be assigned to metal-centered events (see Figures E22-E23). In particular, after the initial quasi-reversible reduction, the isomers of $[Re(CO)_3Cl]_2(bpm)$ undergo a further quasi-reversible reduction at –1.46 V followed by an irreversible reduction at –2.37 V. CVs of the homobimetallic Mn species are more complex; the mixture of isomers displayed irreversible reductions at –1.49 V and –2.14 V, as well as several oxidations, suggesting that there are coupled chemical reactions that result in formation of multiple new species. For the mixture of syn and anti isomers of $[Re(CO)_3Br(bpm)Mn(CO)_3Br]$, three additional irreversible reductions are observed at –1.40 V, –1.93 V, and –2.27 V, as well as several oxidations, implying that this complex also undergoes reduction-induced chemical reactivity, the products of which have not been investigated here. However, the value of the comproportionation constant K_C for the singly reduced, paramagnetic intermediate (*vide infra*) can be computed for $[Re(CO)_3Cl]_2(bpm)$ based upon the difference between the first and second reduction potentials.[61] This value is estimated to be $10^{10.8}$, a high value consistent with the large separation (640 mv) between the first and second reductions of $[Re(CO)_3Cl]_2(bpm)$ that indicates strong coupling between the redox-active centers here.

7.2.4 Electron paramagnetic resonance studies

Based on the electrochemical profile of the mixture of syn and anti isomers of $[Re(CO)_3Cl]_2(bpm)$, we next set out to study the chemical reduction of these complexes in order to provide evidence for the assignment of the initial reductions as either ligand- or metal-based.

Specifically, we targeted the 1e$^-$ chemical reduction of the mixture of syn and anti isomers of $[Re(CO)_3Cl]_2$(bpm) to complement previously reported spectroelectrochemical (SE) electron paramagnetic resonance (EPR) results of **1** and $[Re(CO)_3Cl]_2$(bpm).[39,49,50,62] In an *in situ* reduction experiment, treatment of the mixture of syn and anti isomers of $[Re(CO)_3Cl]_2$(bpm) with 1.0 equiv. of cobaltocene (Cp_2Co, $E_{1/2}$ = –1.34 V vs. $Fc^{+/0}$)[63] in CD_3CN resulted in a rapid color change; analysis by ^{1}H NMR revealed the presence of cobaltocenium ($[Cp_2Co]^+$ at 5.66 ppm, see Figures E8 and E32) as the primary diamagnetic product.[64] Simultaneously, the disappearance of the signals associated with the mixture of syn and anti isomers of $[Re(CO)_3Cl]_2$(bpm) confirmed conversion of the diamagnetic starting materials into paramagnetic products. Although these products could not be isolated cleanly due to similar solubility profiles with $[Cp_2Co]^+$, EPR was used to interrogate the mixture further. For the EPR analysis, the syn and anti isomers of $[Re(CO)_3Cl]_2$(bpm) were dissolved in toluene, frozen in a quartz EPR tube held at 78 K, and an equimolar solution of Cp_2Co was layered on top; the entire sample was then refrozen. The air-sensitive sample was then brought out of the glovebox, frozen in liquid nitrogen, and transported to the EPR spectrometer. When the sample was ready for measurement, it was briefly thawed to allow the two layers to mix and then quickly refrozen before interrogation by EPR spectroscopy.

EPR data for the sample revealed an isotropic signal at g = 2 (see Figure 7.4), consistent with formation of a bpm ligand-centered radical. This result mirrors findings from the prior work based upon spectroelectrochemical methods carried out by Kaim and Kohlmann.[39] Our experimental data was modelled using the Easyspin[65] package in MATLAB; a satisfactory match between the experimental data and the simulated data was obtained with a single-component system centered at g = 1.999, consistent with the expected similarity of the singly reduced forms of the syn and anti isomers of $[Re(CO)_3Cl]_2$(bpm). Thus, the EPR signal observed upon the first electrochemical

reduction can be assigned to a ligand-centered radical. Based on the similar voltammetric properties among all the bimetallic species, we anticipate that the first reductions of $[Mn(CO)_3Br]_2(bpm)$ and $[Re(CO)_3Br(bpm)Mn(CO)_3Br]$ are also ligand centered.

7.3 Conclusions

The novel bimetallic complexes $[Mn(CO)_3Br]_2(bpm)$ and $[Re(CO)_3Br(bpm)Mn(CO)_3Br]$ were synthesized as an inseparable mixture of syn and anti isomers in solution; the compounds displayed characteristic spectra that confirm their expected symmetry characteristics. The solid-state structures of **1**, **2-anti**, **3**, **4**, **5-syn**, **5-anti**, and **6-syn** provided data for comparison of metrical parameters that differentiate the monometallic and bimetallic complexes. In particular, the data suggest that an inductive effect arises from incorporation of an additional tricarbonyl unit in the bimetallic compounds. The inductive effect was confirmed using cyclic voltammetry; shifts of greater than 380 mV were measured for the initial reductions of the bimetallic species in comparison to their monometallic analogues. Experimental EPR data and simulations for one derivative suggest that these initial reductions are ligand centered. Taken together, these studies confirm that 2,2′-bipyrimidine is a useful ligand for formation of modular bimetallic metal tricarbonyl complexes.

7.4 Experimental Section

7.4.1 General considerations

All manipulations were carried out in dry N_2-filled gloveboxes (Vacuum Atmospheres Co., Hawthorne, CA, USA) or under an N_2 atmosphere using standard Schlenk techniques unless otherwise noted. All solvents were of commercial grade and dried over activated alumina using a

PPT Glass Contour (Nashua, NH, USA) solvent purification system prior to use, and were stored over molecular sieves. All chemicals were obtained from major commercial suppliers. Manganese pentacarbonyl bromide (98%, Strem Chemical Co.) rhenium pentacarbonyl bromide (98%, Strem Chemical Co.), rhenium pentacarbonyl chloride (98%, Strem Chemical Co.), 2,2′-bipyrimidine (95%, Sigma Aldrich), and 2,2′-bipyrazine (97%, TCI Chemicals) were used as received. $Re(CO)_3Cl(bpm)$,[36] $[Re(CO)_3Cl]_2(bpm)$,[36] $Mn(CO)_3Br(bpz)$,[23] and $Mn(CO)_3Br(bpm)$[42] were prepared according to previously reported literature procedures. Deuterated solvents for NMR studies were purchased from Cambridge Isotope Laboratories (Tewksbury, MA, USA); CD_3CN was dried and stored over 3 Å molecular sieves.

^1H NMR spectra were collected on 400 MHz Bruker spectrometers (Bruker, Billerica, MA, USA) and referenced to the residual protio-solvent signal. Infrared spectra were collected on a PerkinElmer Spectrum 100 Fourier transform infrared spectrometer. Electronic absorption spectra were collected with an Ocean Optics Flame spectrometer equipped with a DH-Mini light source (Ocean Optics, Largo, FL, USA) using a quartz cuvette. Experimental high resolution mass spectrometry data were collected on a LCT Premier mass spectrometer equipped with a quadrupole, time-of-flight mass analyzer, and an electrospray ion source, or with a PE SCIEX API 365 triple quadrupole spectrometer. Predicted mass spectrometry data were obtained from PerkinElmer Informatics' ChemDraw Professional Suite. Continuous-wave electron paramagnetic resonance spectra were collected at X-band with a Bruker EMX spectrometer using a high-sensitivity perpendicular-mode cavity (4119HS-W1). Temperature control was achieved with an Oxford ESR 900 flow-through cryostat. Elemental analyses were performed by Midwest Microlab, Inc. (Indianapolis, IN, USA).

7.4.2 X-Ray diffraction procedures

Crystals were mounted on polyimide MiTeGen loops with STP Oil Treatment and placed under a nitrogen stream. Low temperature (100 K) X-ray data were collected on a Bruker AXS D8 KAPPA diffractometer with an APEX II CCD detector and TRIUMPH graphite monochromator running at 50 kV and 30 mA with Mo radiation (K_α = 0.71073 Å) for **1** and on a Bruker AXS D8 VENTURE KAPPA diffractometer with PHOTON 100 CMOS detector and Helios focusing multilayer mirror optics running at 50 kV and 1 mA using Cu radiation (K_α = 1.54178 Å) for **5-syn** and **5-anti** and using Mo radiation (K_α = 0.71073 Å) for **2-anti**, **3**, **4**, and **6-syn.** Totals of 2374 (**1**), 2053 (**2-anti**), 2444 (**3**), 1206 (**4**), 1338 (**5-syn**), 2013 (**5-anti**), 884 (**6-syn**), 0.5° or 1.0° -wide ω- *or* ϕ-scan frames were collected with counting times of 10-20 seconds (**1**), 4-30 seconds (**2**), 1-10 seconds (**3**), 1-20 seconds (**4**), 5-60 seconds (**5-syn**), 1-15 seconds (**5-anti**), and 2-60 seconds (**6-syn**). Preliminary lattice constants were obtained with the Bruker Apex2 Software Suite.[66] Integrated reflection intensities for all compounds were produced using SAINT in the Bruker Apex2 Software Suite. Each data set was corrected empirically for variable absorption effects with SADABS[67] using equivalent reflections. The Bruker software package SHELXTL was used to solve each structure using intrinsic direct methods phasing. Final stages of weighted full-matrix least-squares refinement were conducted using F_o^2 data with SHELXTL[68] or the Olex2 software package equipped with XL[69]. All non-hydrogen atoms were refined anisotropically. All hydrogen atoms were included into the model at geometrically calculated positions and refined using a riding model. The isotropic displacement parameters of all hydrogen atoms were fixed to 1.2 times the *U* value of the atoms they are linked to. The relevant crystallographic and structure refinement data for all seven structures are given in Table E1.

7.4.3 Electrochemistry

Electrochemical experiments were carried out in a nitrogen- filled glove box (in the dark for Mn-containing samples). 0.10 M tetra(n-butylammonium) hexafluorophosphate (Sigma-Aldrich; electrochemical grade) in acetonitrile served as the supporting electrolyte. Measurements were made with a Gamry Reference 600 Plus Potentiostat/ Galvanostat using a standard three-electrode configuration. The working electrode was the basal plane of highly oriented pyrolytic graphite (HOPG, GraphiteStore.com, Buffalo Grove, Ill.; surface area: 0.09 cm^2), the counter electrode was a platinum wire (Kurt J. Lesker, Jefferson Hills, PA; 99.99%, 0.5 mm diameter), and a silver wire immersed in electrolyte served as a pseudo-reference electrode (CH Instruments). The reference was separated from the working solution by a Vycor frit (Bioanalytical Systems, Inc.). Ferrocene (Sigma Aldrich; twice-sublimed) was added to the electrolyte solution at the conclusion of each experiment (~1 mM); the midpoint potential of the ferrocenium/ferrocene couple (denoted as $Fc^{+/0}$) served as an external standard for comparison of the recorded potentials. Concentrations of analyte for cyclic voltammetry were typically 1 mM.

7.4.4 Synthetic procedures

Synthesis of $[Mn(CO)_3Br]_2(bpm)]$ (5). In the dark, 2,2′-bipyrimidine (0.0996 g, 0.630 mmol) was dissolved in toluene (35 mL). $Mn(CO)_5Br$ was added (0.3563 g, 1.30 mmol) and the solution refluxed under N_2 for 4 hours. The solution was then allowed to cool, the precipitate collected by vacuum filtration, and washed with diethyl ether. The pure solid was then dried under vacuum before storing in the dark (0.3408 g, 91% yield). ^{1}H NMR (400 MHz, CD_3CN) δ 9.43 (d, $^3J_{H,H}$ = 5.5 Hz, 4H), 7.85 (t, $^3J_{H,H}$ = 5.5 Hz, 2H). Resolved isomer: δ 9.46 (d, $^3J_{H,H}$ = 5.5 Hz, 4H), 7.88 (t, $^3J_{H,H}$ = 5.5 Hz, 2H). A comparison of the resolved doublet peaks near δ 9.45 ppm revealed that the

desired product was present in two isomeric forms in the ratio 3.14 to 1. High Resolution ESI-MS (positive) m/z: expected 555.8497; found 555.8495 (**5** – Br^- + NCMe). Electronic absorption spectrum (MeCN): 250 (4200), 369 (1600), 510 nm (750 M^{-1} cm^{-1}). IR (THF): $\nu_{C=O}$ 2031 (m), $\nu_{C=O}$ 1952 (m), and $\nu_{C=O}$ 1936 (m) cm^{-1}. Anal. Calcd. for $Mn_2C_{14}H_6Br_2N_4O_6$: C, 28.22; H, 1.01; N, 9.40. Found: C, 28.00; H, 1.11; N, 9.21.

Synthesis of [Re(CO)$_3$Br(bpm)Mn(CO)$_3$Br] (6). 2,2′-bipyrimidine (0.1516 g, 0.959 mmol) was dissolved in toluene (35 mL). $Re(CO)_5Br$ was added (0.3478 g, 0.856 mmol) and the solution refluxed under N_2 for 22 hours. The solution was then allowed to cool and the resulting precipitate collected by vacuum filtration and washed with diethyl ether. The pure solid was then dried under vacuum. In the absence of light, a portion of pure product (0.0996 g, 0.245 mmol) was dissolved in toluene (35 mL). Then $Mn(CO)_5Br$ was added (0.0557 g, 0.203 mmol) and the solution refluxed under N_2 for 12 hours. The solution was then allowed to cool and the resulting precipitate collected by vacuum filtration and washed with diethyl ether. The pure solid was then dried under vacuum before storing in the dark (0.1313g, 89% yield). ^{1}H NMR (400 MHz, CD_3CN) δ 9.52 (dd, $^3J_{H,H}$ = 5.6 Hz, $^4J_{H,H}$ = 1.7 Hz, 2H), 9.27 (dd, $^3J_{H,H}$ = 5.6 Hz, $^4J_{H,H}$ = 1.7 Hz, 2H), 7.86 (t, $^3J_{H,H}$ = 5.6 Hz, 2H) ppm. Resolved isomer: δ 9.55 (dd, $^3J_{H,H}$ = 5.6 Hz, $^4J_{H,H}$ = 1.7 Hz, 2H), 9.30 (dd, $^3J_{H,H}$ = 5.6 Hz, $^4J_{H,H}$ = 1.7 Hz, 2H), 7.89 (t, $^3J_{H,H}$ = 5.6 Hz, 2H) ppm. A comparison of the resolved doublet peaks near δ 9.54 ppm revealed that the desired product was present in two isomeric forms in the ratio 1.80 to 1. High Resolution ESI-MS (positive) m/z: expected: 687.8674; found: 687.8672 (**6** – Br^- + NCMe). Electronic absorption spectrum (MeCN): 243 (28000); 365 (5800); 515 nm (2200 M^{-1} cm^{-1}). IR (THF): $\nu_{C=O}$ 2028 (m), $\nu_{C=O}$ 1951 (m), and $\nu_{C=O}$ 1935 (m), 1914 (m) cm^{-1}. Anal. Calcd. for $MnReC_{14}H_6Br_2N_4O_6$: C, 23.12; H, 0.83; N, 7.70. Found: C, 23.14; H, 0.85; N, 7.61.

7.5 Acknowledgements

The authors thank Dr. Justin Douglas and Sarah Neuenswander for assistance with NMR and EPR spectroscopy. This work was supported by the U.S. National Science Foundation through awards OIA-1833087 and CHE-1305124. W.C.H. was supported by the U.S. National Institutes of Health Graduate Training Program in the Dynamic Aspects of Chemical Biology (T32 GM008545-25).

The authors also acknowledge the U.S. National Science Foundation and U.S. National Institutes of Health for support of the EPR instrumentation (CHE-0946883) and NMR instrumentation (S10OD016360, S10RR024664, and CHE-0320648) used in this study. The Bruker D8 Kappa X-ray diffractometer used for **1** was purchased via an NSF CRIF:MU award to the California Institute of Technology (CHE-0639094). A Dow Next Generation Instrumentation Grant supported the work on **2-anti**, **3**, **4**, **5-syn**, **5-anti,** and **6-syn**.

7.6 References

(1) (a) D. J. Stufkens and A. Vlcek, *Coord. Chem. Rev.*, 1998, **177**, 127-179. (b) A. El Nahhas, C. Consani, A. M. Blanco-Rodriguez, K. M. Lancaster, O. Braem, A. Cannizzo, M. Towrie, I. P. Clark, S. Zalis, M. Chergui and A. Vlcek, *Inorg. Chem.*, 2011, **50**, 2932-2943.

(2) (a) L. Wallace and D. P. Rillema, *Inorg. Chem.*, 1993, **32**, 3836-3843. (b) R. J. Shaver, M. W. Perkovic, D. P. Rillema and C. Woods, *Inorg. Chem.*, 1995, **34**, 5446-5454.

(3) A. Léval, H. Junge, and M. Beller, *Catal. Sci.,* 2020**, 10**, 3931-3937.

(4) (a) U. Schatzschneider, *Inorg. Chim. Acta,* 2011, **374**, 19-23. (b) R. Alberto, R. Schibli, A. Egli, A. P. Schubiger, U. Abram, and T. A. Kaden, *J. Am. Chem. Soc.,* 1998, **120**, 7987-7988.

(5) M. N. Pinto, I. Chakraborty, C. Sandoval and P. K. Mascharak, *J. Controlled Release*, 2017, **264**, 192-202.

(6) (a) J. Hawecker, J. M. Lehn and R. Ziessel, *J. Chem. Soc., Chem. Commun.*, 1984, 328-330. (b) B. P. Sullivan, C. M. Bolinger, D. Conrad, W. J. Vining, T. J. Meyer, *J. Chem. Soc. Chem. Commun.,* 1985, 1414-1416.

(7) M. Bourrez, F. Molton, S. Chardon-Noblat, and A. Deronzier, *Angew. Chem. Int. Ed.,* 2011, **50**, 9903-9906.

(8) J. C. Luong, R. A. Faltynek, and M. S. Wrighton, *J. Am. Chem. Soc.,* 1980, **102**, 7892-7900.

(9) J. V. Caspar and T. J. Meyer, *J. Phys. Chem.*, 1983, **87**, 952−957.

(10) D. Miguel and V. Riera, *J. Organomet. Chem.*, 1985, **293**, 379−390.

(11) H. Takeda, K. Koike, H. Inoue, and O. Ishitani, *J. Am. Chem. Soc.,* 2008, **130**, 2023-2031.

(12) J.M. Smieja and C.P. Kubiak, *Inorg. Chem.,* 2010, **49**, 9283-9289.

(13) B. Gholamkhass, H. Mametsuka, K. Koike, T. Tanabe M. Furue and O. Ishitani, *Inorg. Chem.,* 2005, **44**, 2326-2336.

(14) P. Kurz, B. Probst, B. Spingler, and R. Alberto, *Eur. J. Inorg. Chem.,* 2006**, 2006**, 2966-2974.

(15) J. Ettedgui, Y. Diskin-Posner, L. Weiner, and R. Neumann, *J. Am. Chem. Soc.,* 2011, **133**, 188-190.

(16) J. M. Smieja, M. D. Sampson, K. A. Grice, E. E. Benson, J. D. Froehlich, and C. P. Kubiak, *Inorg. Chem.,* 2013, **52**, 2484-2491.

(17) H. Fei, M. D. Sampson, Y. Lee, C. P. Kubiak, and S. M. Cohen, *Inorg. Chem.,* 2015, **54**, 6821-6828.

(18) K. T. Ngo, M. McKinnon, B. Mahanti, R. Narayanan, D. C. Grills, M. Z. Ertem, and J. Rochford, *J. Am. Chem. Soc.,* 2017, **139**, 2604-2618.

(19) J. Agarwal, T. W. Shaw, H. F. Schaefer, and A. B. Bocarsly, *Inorg. Chem.,* 2015, **54**, 5285-5294.

(20) (a) K. J. Kadassery, S. N. MacMillan, and D. C. Lacy, *Dalton Trans.,* 2018, **47**, 12652-12655. (b) K. J. Kadassery and D. C. Lacy, *Dalton Trans.*, 2019, **48**, 4467-4470.

(21) W. C. Henke, C. J. Otolski, W. N. G. Moore, C. G. Elles, and J. D. Blakemore, *Inorg. Chem.* 2020**, 59**, 2178-2187.

(22) M. L. Clark, P. L. Cheung, M. Lessio, E. A. Carter, and C. P. Kubiak, *ACS Catal.,* 2018, **8**, 2021-2029.

(23) S. E. Tignor, H.-Y. Kuo, T. S. Lee, G. D. Scholes, and A. B. Bocarsly, *Organometallics,* 2019, **38**, 1292-1299.

(24) W.C. Henke, J.A. Hopkins, M.L. Anderson, J.P. Stiel, V.W. Day, and J.D. Blakemore, *Molecules,* 2020, **25**, 3189-3203.

(25) (a) J. S. Kanady, E. Y. Tsui, M. W. Day, T. Agapie, *Science,* 2011, **333**, 733−736. (b) E. Y. Tsui, R. Tran, J. Yano, T. Agapie, *Nat. Chem.,* 2013, **5**, 293-299.

(26) J. P. Krogman, B. M. Foxman and C. M. Thomas, *J. Am. Chem. Soc.*, 2011, **133**, 14582-14585.

(27) A. H. Reath, J. W. Ziller, C. Tsay, A. J. Ryan, J.Y. Yang, *Inorg. Chem.*, 2017, **56**, 3713−3718.

(28) A. Kumar, D. Lionetti, V. W. Day, and J. D. Blakemore, *Chem. Eur. J.,* 2018, **24**, 141-149.

(29) P. Sharma, D. R. Pahls, B. L. Ramirez, C. C. Lu and L. Gagliardi, *Inorg. Chem.* 2019, **58**, 10139-10147.

(30) A. Kumar, D. Lionetti, V. W. Day, and J. D. Blakemore, *J. Am. Chem. Soc.,* 2020, **142**, 3032-3041.

(31) Y. Tamaki, D. Imori, T. Morimoto, K. Koike, and O. Ishitani, *Dalton Trans.*, 2016, **45**, 14668-14677.

(32) D.A. Popov, J.M. Luna, N.M. Orchanian, R. Haiges, C.A. Downes, S.C. Marinescu, *Dalton Trans.*, 2018, **47**, 17450-17460.

(33) (a) W. Yang, S. Sinha Roy, W. C. Pitts, R. L. Nelson, F. R. Fronczek and J. W. Jurss, *Inorg. Chem.*, 2018, **57**, 9564-9575. (b) N. P. Liyanage, W. Yang, S. Guertin, S. S. Roy, C. A. Carpenter, R. E. Adams, R. H. Schmehl, J. H. Delcamp, and J. W. Jurss, *Chem. Commun.*, 2019, **55**, 993-996.

(34) (a) M. Hunziker and A. Ludi, *J. Am. Chem. Soc.*, 1977, **99**, 7370-7371. (b) R. R. Ruminski and J. D. Petersen, *Inorg. Chem.*, 1982, **21**, 3706-3708. (c) K. J. Brewer, W. R. Murphy and J. D. Petersen, *Inorg. Chem.*, 1987, **26**, 3376-3379. (d) W. Kaim, A. Klein and M. Glöckle, *Acc. Chem. Res.*, 2000, **33**, 755-763.

(35) J. J. Concepcion, J. W. Jurss, P. G. Hoertz, T. J. Meyer, *Angew. Chem. Int. Ed.,* 2009, **48**, 9473-9476.

(36) A. Vogler, and J. Kisslinger, *Inorganica Chim. Acta,* 1986, **115**, 193-196.

(37) K. D. Benkstein, J. T. Hupp, and C. L. Stern, *J. Am. Chem. Soc.,* 1998, **120**, 12982-12983.

(38) A. Juris, S. Campagna, I. Bidd, J. M. Lehn and R. Ziessel, *Inorg. Chem.*, 1988, **27**, 4007-4011.

(39) (a) W. Kaim and S. Kohlmann, *Chem. Phys. Lett.*, 1987, **139**, 365-369. (b) W. Kaim and S. Kohlmann, *Inorg. Chem.*, 1990, **29**, 2909-2914.

(40) K. Pollborn, B. Aechter, and W. Beck, *Z. Kristallogr. – New Cryst. Struct.,* 2001, **216**, 407-408.

(41) Syn and anti is the preferred IUPAC nomenclature for the isomers of the compounds. IUPAC. Compendium of Chemical Terminology, 2nd ed. (the "Gold Book"). Compiled by A. D. McNaught and A. Wilkinson. Blackwell Scientific Publications, Oxford (1997). Online version (2019-) created by S. J. Chalk. ISBN 0-9678550-9-8. https://doi.org/10.1351/goldbook

(42) P. Kumar, C. Joshi, A. K. Srivastava, P. Gupta, R. Boukherroub, and S. L. Jain, *ACS Sustain. Chem. Eng.,* 2016, **4**, 69-75.

(43) J. W. M. van Outersterp, D. J. Stufkens, J. Fraanje, K. Goubitz, and A. Vlcek, *Inorg. Chem.,* 1995, **34**, 4756-4766.

(44) K. Polborn, B. Aechter, W. Beck, *Z. Kristallog.-New Cryst. Struct.,* 2001, **216**, 407-408.

(45) N. M. Shavaleev, Z. R. Bell, and M. D. Ward, *J. Chem. Soc., Dalton Trans.,* 2002, 3925-3927.

(46) N. M. Shavaleev, G. Accorsi, D. Virgili, Z. R. Bell, T. Lazarides, G. Calogero, N. Armaroli, and M. D. Ward, *Inorg. Chem.,* 2005, **44**, 61-72.

(47) B. Aechter, J. Knizek, H. Noth, W. Beck, *Z. Kristallog.-New Cryst. Struct.,* 2005, **220**, 110.

(48) H. Takeda, H. Koizumi, K. Okamoto, and O. Ishitani, *Chem. Commun.,* 2014, **50**, 1491-1493.

(49) A. Klein, C. Vogler, and W. Kaim, *Organometallics,* 1996, **15**, 236-244.

(50) W. Kaim, T. Scheiring, M. Weber, J. Fiedler, *Z. Anorg. Allg. Chem.*, 2004, **630**, 1883-1893.

(51) T. J. Meyer, *Pure Appl. Chem.,* 1986, **58**, 1193–1206.

(52) R. Heydová, E. Gindensperger, R. Romano, J. Sýkora, A. Vlček, S. Záliš and C. Daniel, *J. Phys. Chem. A*, 2012, **116**, 11319-11329.

(53) C. R. Groom, I. J. Bruno, M. P. Lightfoot, S. C. Ward, The Cambridge Structural Database. *Acta Cryst. Sec. B,* 2016, **72**, 171--179.

(54) P. Kurz, B. Probst, B. Spingler, and R. Alberto, *Eur. J. Inorg. Chem.*, 2006, **15**, 2966-2974.

(55) R. Kia and F. Safari, *Inorg. Chim. Acta*, 2016, **453**, 357-368.

(56) I. Chakraborty, S. J. Carrington, and P. K. Mascharak, *ChemMedChem*, 2014, **9**, 1266-1274.

(57) L. Fernoholt, C. Rømming, and S. Samdal, *Acta. Chem. Scand.* 1981, **35a**, 707-715.

(58) (a) J. J. Soldevila-Barreda, A. Habtemariam, I. Romero-Canelón, and P.J. Sadler, *J. Inorg. Biochem.,* 2015, **153**, 322-333. (b) J.D. Blakemore, E.S. Hernandez, W. Sattler, B.M. Hunter, L.M. Henling, B.S. Brunschwig, H.B. Gray, *Polyhedron*, 2014, **84**, 14-18.

(59) C. Creutz, *Comments Inorg. Chem.*, 1982, **1**, 293-311.

(60) F. Hartl, B. D. Rossenaar, G. J. Stor and D. J. Stufkens, *Recl. Trav. Chim. Pays-Bas*, 1995, **114**, 565-570.

(61) (a) H. Hartmann, W. Kaim, M. Wanner, A. Klein, S. Frantz, C. Duboc-Toia, J. Fiedler and S. Záliš, *Inorg. Chem.*, 2003, **42**, 7018-7025. (b) P. J. Ball, T. R. Shtoyko, J. A. Krause Bauer, W. J. Oldham and W. B. Connick, *Inorg. Chem.*, 2004, **43**, 622-632.

(62) W. Kaim, H. E. A. Kramer, C. Vogler, and J. Rieker, *J. Organomet. Chem.* 1989, **367**, 107-115.

(63) N. G. Connelly and W. E. Geiger, *Chem. Rev.,* 1996, **96**, 877-910.

(64) S. Vanicek, H. Kopacka, K. Wurst, T. Müller, H. Schottenberger and B. Bildstein, *Organometallics*, 2014, **33**, 1152–1156.

(65) S. Stoll and A. Schweiger, *J. Magn. Res.*, 2006, **178**, 42-55.

(66) APEX2, Version 2 User Manual, M86-E01078,; Bruker Analytical X-ray Systems: Madison, WI, June 2006.

(67) G. M. Sheldrick, SADABS (version 2008/1): Program for Absorption Correction for Data from Area Detector Frames, University of Göttingen, 2008.

(68) G. M. Sheldrick, Crystal structure refinement with SHELXL. *Acta Crystallogr., Sect. A: Found. Crystallogr.* 2015, **71**, 3-8.

(69) O. V. Dolomanov, L. J. Bourhis, R. J. Gildea, J. A. K. Howard, H. J. Puschmann, *Appl. Crystallogr.* 2009, **42**, 339-341.

Chapter 8

Summary and Future Outlook

8.1 Summary and Future Outlook

The results described in Parts I and II of this dissertation characterize the intermediates involved in catalytic dihydrogen evolution with [Cp*Rh] and carbon monoxide release from [$Mn(CO)_3$] complexes using synthesis, electrochemistry, single-crystal X-ray diffraction, and time-resolved spectroscopy. We have utilized model [Cp*Rh] and [$Mn(CO)_3$] complexes which can readily be supported by a variety of bidentate chelating ligands including ^{R}bpy (R = tBu, H, CF_3, or NO_2) derivatives, bpm, daf, and Me_2daf. Electrochemical measurements were used to establish the formal oxidation states accessible to these systems and have provided insight into redox-induced follow-up chemical reactivity. Exquisite single-crystal X-ray diffraction measurements performed by Victor W. Day provided the key bond lengths and angles for many of the synthesized complexes described in this dissertation. Lastly, we have shown that time-resolved spectroscopic measurements, including approaches that combine pulse radiolysis, stopped-flow, and transient absorption techniques are well-suited to mapping the sequential elementary steps that lead to H_2 evolution or CO release using [Cp*Rh] or [$Mn(CO)_3$] model systems, respectively.

In Chapter 2, we discussed the widespread adoption of electrochemical measurements in organometallic chemistry. The availability of these sensitive and robust techniques has been made possible by the potentiostat. The extensive adoption of the potentiostat in many laboratories has led to substantial growth in the electrochemical investigation of redox processes in diverse compounds that are of interest to organometallic chemists. Modern electrochemical materials, methods, and techniques have assisted in interpreting chemical reactivity that can be promoted at electrode surfaces. Cyclic voltammetry and controlled potential electrolysis experiments have provided important insights and continue to provide a window into numerous applications in the fields of redox chemistry and catalysis. Voltammetry experiments can reveal the reduction

potential(s) associated with redox events; the exact nature of the products from these redox events can then be probed with stoichiometric redox reagents in chemical syntheses. The thermodynamic, kinetic, and mechanistic data provided by the cyclic voltammetric experiment informs design principles that can be used to generate organometallic complexes and catalysts with tailored properties. Further, the shapes of redox waves in cyclic voltammetry can provide crucial information about the nature of electron transfer events and chemical reactions that precede or follow them, offering insights difficult to obtain with other techniques. This is particularly important in the field of electrocatalysis, in which the efficiency and selectivity of a given catalyst can be investigated by coupling electrolysis methods to product analysis. Considering all the useful opportunities afforded by electrochemical methods, the future of electrochemistry is bright and will continue to expand to future organic, inorganic, and organometallic systems.

In Chapter 3, we described the synthesis and characterization of a new series of [Cp*Rh] complexes supported by diazafluorene-type ligands. On the basis of structural, spectroscopic, and electrochemical evidence, 9,9′-dimethyl-4,5-diazafluorene (Me_2daf) can be concluded to be capable of stabilizing low-valent complexes through charge delocalization and π-backbonding that is reminiscent of behavior more commonly encountered with complexes of 2,2′-bipyridyl and its analogues. In this work, a comprehensive set of solid-state structures from X-ray diffraction analysis was used to highlight the bond lengths and angles that distinguish diazafluorene complexes from analogues bearing more common ligands. On the basis of clean electrochemical behavior for the [Cp*Rh] species supported by Me_2daf, a spectrochemical titration was carried out with Cp_2Co that revealed the unique spectroscopic signatures of Rh(III), Rh(II), and Rh(I) supported by Me_2daf. The charge delocalization implied by the spectroscopic results for Cp*Rh(Me_2daf) was confirmed by related X-ray diffraction analysis for this compound, which

showed bond length changes in the intra-Me_2daf framework consistent with sharing of electron density from the formally [Cp*Rh^I] core into the LUMO of Me_2daf via π-backbonding. From this work, we can conclude that use of Me_2daf in place of dafone or daf avoids detrimental reactivity under highly reducing conditions and, thus, Me_2daf represents a useful new ligand for use in reductive chemistry and electrochemistry.

In a similar fashion, in Chapter 6, we described the synthesis, characterization, and electrochemical properties of the new daf- or Me_2daf-supported complexes $Mn(CO)_3Br$(daf), $Mn(CO)_3Br$(Me_2daf), and $[Ru(Me_2daf)_3]^{2+}$ and compared the properties of these compounds to their bpy-supported analogues $Mn(CO)_3Br$(bpy) and $[Ru(bpy)_3]^{2+}$. When daf and Me_2daf are bound to Mn or Ru centers, we observed characteristic spectra that confirmed the formation and symmetry of the desired complexes. In particular, comparisons of bond lengths and geometric parameters confirm that daf and Me_2daf enforce wider chelate angles and offer weaker σ-donation than bpy. Electrochemical studies of $[Ru(Me_2daf)_3]^{2+}$ reveal that Me_2daf is a non-innocent redox-active ligand at modestly reducing potentials, and related electrochemical work with $Mn(CO)_3Br$(daf) and $Mn(CO)_3Br$(Me_2daf) shows that this ligand-centered reduction behavior is also accessible in $Mn(CO)_3Br$(daf) and $Mn(CO)_3Br$(Me_2daf), albeit with apparently slower heterogeneous electron transfer kinetics than those encountered with analogous $Mn(CO)_3Br$(bpy). Taken together, these studies demonstrate daf and Me_2daf could be useful for the preparation of a variety of new redox-active compounds, building on the significant body of findings for the workhorse bpy and ^{R}bpy ligands. Future work involving the use of diazafluorene ligands could examine the use of the redox-active ligand Me_2daf in place of bpy in reductive catalytic applications. This possibility is also supported by the results from Chapter 3, making Me_2daf an especially attractive target for future developments.

In Chapter 4, we described the elementary steps leading to dihydrogen evolution using Cp*Rh(bpy) as a molecular model complex. Using pulse radiolysis (PR), we confirmed a first-order dependence on $[Cp^*Rh(L)(bpy)]^+$ during the generation of Cp*Rh(bpy) in MeCN. In prior work, disproportionation was postulated to lead to the reduction of $[Cp^*Rh(L)(bpy)]^+$ under aqueous conditions. However, under our specific conditions here in MeCN solvent, this disproportionation mechanism does not appear to be operative based on initial rate analysis and the known molar absorptivity of the final reduced metal-containing product, Cp*Rh(bpy). Instead, the available data suggest that formate ($HCOO^-$) could serve as a one-electron reductant in our system, converting $[Cp^*Rh(L)(bpy)]^+$ to Cp*Rh(bpy). Alternatively, carbon dioxide anion radical ($CO_2^{\bullet-}$) could serve as the reducing agent to generate Cp*Rh(bpy), as this species could be present under the conditions of pulse radiolysis as well. Following reaction of Cp*Rh(bpy) with weak acid, kinetic and spectroscopic evidence confirmed that the initial site of protonation is the Rh metal center, leading to formation of $[Cp^*Rh(H)(bpy)]^+$; this hydride generation is followed by a tautomerization step to generate $[(Cp^*H)Rh(bpy)]^+$.

To provide greater detail regarding these assignments, variable temperature kinetic data were collected using isotopically labeled acids. The results suggest that $NEt_3/HNEt_3^+$ plays an essential role as a proton shuttle, facilitating tautomerization of the hydride ligand to form the uncommon η^4-Cp*H moiety. Moreover, we showed that $[(Cp^*H)Rh(bpy)]^+$ reacts further with stronger acids, demonstrating that η^4-Cp*H is not an off-cycle intermediate, but instead is an active participant in dihydrogen evolution, contributing to a viable pathway that depends on the strength of the acid. Our experiments enabled direct quantification of the reaction rates associated with the individual elementary reduction and protonation steps that lead to dihydrogen evolution. Thus, taken together, our work provides an unprecedented level of atomistic detail regarding the mechanisms underlying

both metal-mediated proton-hydride tautomerization as well as catalytic H_2 evolution with this system; the data could serve as a springboard for further investigations involving the unique η^4-Cp*H moiety. Future work in this area could explore the linear free energy relationships underlying individual elementary steps leading to hydrogen evolution using substituted bpy ligands, as in Cp*Rh(^{R}bpy) (R = OMe, tBu, and CF_3). In particular, the linear free energy relationship underlying the hydride-to-proton tautomerization involved in the formation of the uncommon η^4-Cp*H moiety could provide insight into the role of the diimine ligands in promoting this reactivity. Such an effort could address the lingering, deeper questions regarding i) the origin of the phenomenon of η^4-Cp*H formation, and ii) the role of this reaction in enabling H_2 evolution with [Cp*Rh] complexes.

In Chapter 5, we discussed the light sensitivity of $Mn(CO)_3(^R$bpy)Br (R = tBu, H, CF_3, or NO_2) complexes in the context of CO release and catalytic CO_2 reduction. $Mn(CO)_3(^R$bpy)Br complexes are stable in the absence of light, which allowed us to extensively characterize them using a variety of techniques. Transitions in the NMR, IR, and electronic absorption spectra are linearly correlated with the Brown (σ^+), Hammett (σ), and Kubota (σ^-) parameters, respectively, providing insight into how ligand substituents govern electronic properties at the metal center. In the presence of light, $Mn(CO)_3(^R$bpy)Br complexes **1**, **2**, and **3** decompose via CO loss, with subsequent solvent coordination in MeCN or other reactions in $CHCl_3$. Ultrafast TA spectroscopy revealed the previously unknown five-coordinate and solvento intermediates in the photo-speciation process. Complex **4** follows a different reaction path that is likely the result of a long-lived triplet MLCT excited state that does not undergo decay to a dissociative ligand field (d-d) state. The unique behaviors of **1**-**4** illustrate how the reactivity and speciation of these complexes can be tuned by changing the electronic properties of the bidentate diimine ligand. Notably, as only limited

computational modeling has examined the excited-state electronic structure of $Mn(CO)_3Br$(diimine) complexes, further experimental work combined with computational modeling would be useful in providing new insights into the speciation mechanisms operative during irradiation. Experimental work that may continue in the years ahead will aim to better further characterize the structure and electronics of the transient species generated upon irradiation using time-resolved X-ray absorption and IR spectroscopies. Given the ultrafast nature of the initial CO loss for most of these systems, the $[Mn(CO)_3]$ platform is an excellent model for X-ray free electron laser (XFEL) studies. XFEL work with these systems would provide detailed structural and electronic information about the earliest species generated following exposure to light and understanding the properties of these species could form the basis of accessing ground rules for the design of more light-stable systems.

In Chapter 7, we described the synthesis of two new homo- and hetero-bimetallic complexes, $[Mn(CO)_3Br]_2$(bpm) and $[Re(CO)_3Br(bpm)Mn(CO)_3Br]$, which were synthesized as inseparable mixtures of *syn* and *anti* isomers in solution; these compounds displayed characteristic spectra that confirmed their expected symmetry characteristics. The solid state structures of $Re(CO)_3Cl$(bpm), *anti*-$[\{Re(CO_3)Cl\}_2(bpm)]$, $Mn(CO)_3Br$(bpz) (bpz = 2,2′-bipyrazine), $Mn(CO)_3Br$(bpm), *syn*- and *anti*-$[\{Mn(CO_3)Br\}_2(bpm)]$, and *syn*-$[Mn(CO_3)Br(bpm)Re(CO)_3Br]$) provided data for comparison of metrical parameters that differentiate the monometallic and bimetallic complexes. In particular, the data suggest that an inductive effect arises from incorporation of an additional tricarbonyl unit in the bimetallic compounds. The inductive effect was confirmed using cyclic voltammetry; shifts of greater than 380 mV were measured for the initial reductions of the bimetallic species in comparison to their monometallic analogues. Experimental EPR data and simulations for one derivative suggest that these initial reductions are ligand centered. Taken

together, these studies confirm that 2,2′-bipyrimidine is a useful ligand for formation of modular bimetallic metal tricarbonyl complexes. In future work, these systems could serve as a particularly useful models for high-energy X-ray scattering and pair distribution function analysis (HEXS/PDF); these techniques are used to reveal the structure of complexes in homogeneous solution and can distinguish differences between structures in solution- and the solid state. The homo- and hetero-bimetallic complexes discussed in Chapter 7, would be particularly useful for HEXS/PDF due to the presence of two transition metal centers, which would lead to useful scattering signatures. Additionally, these data in homogenous solution could be readily compared to the solid state data that is already available. And finally, an attractive further avenue for research could focus on testing these complexes as potential CO_2 reduction catalysts. This work could leverage the potential catalytic benefits of having two metal centers in close proximity during CO_2 reduction, a situation that could promote multielectron catalysis by enabling redox load management across the closely spaced metal centers.

Moving forward, it is becoming clear that renewable resources, such as wind and solar energy, have the potential to power the world. However, because the wind is not always blowing and the sun is not always shining, humanity stands before a great challenge: learning how to store energy from renewable resources—both at fundamental and practical levels. If we are ambitious, we will continue to confront this problem head-on with basic research aimed at understanding how molecular reactivity, structure, and function can be leveraged for storage of energy in the form of chemical bonds. In this dissertation, particular attention was focused on development of such chemistry with complexes that utilize the third-row transition metal rhodium and the first-row transition metal manganese. In Chapter 4 of this dissertation, time-resolved spectroscopic experiments provided a window into fundamental energy storage using Cp*Rh(bpy). Cp*Rh(bpy)

is an efficient and selective catalyst for H_2 evolution, and at room temperature we can watch the elementary reduction and protonation steps involved in this catalysis unfold as Cp*Rh(bpy) facilitates the coupling of two electrons and two protons to form H_2. Unfortunately, Cp*Rh(bpy) likely does not represent a practical solution for energy storage in the form of H_2, due to a scalability challenge; the cost of rhodium as well as its overall scarcity would become prohibitive when considering H_2 evolution with this system in an industrial setting and at scales large enough to impact the energy use in society. Thus, future studies of fundamental energy storage should likely focus on work with Earth-abundant elements, such as first-row transition metals. On the other hand, noble metals like rhodium are highly recyclable, form complexes with high stability, and reliably undergo attractive two-electron reactivity; we anticipate that these positive features will keep rhodium and other less-abundant metals competitive, particularly in the realm of model chemistry, for many years to come.

Making the general statement, "We should utilize Earth-abundant elements in catalytic systems," is straightforward to articulate, but many challenges will need to be addressed to make this guiding concept a reality. Earth-abundant first-row transition metal complexes tend to be more reactive and difficult to study than their analogous based on second and third row metals. As an example, $Mn(CO)_3(bpy)Br$ is a catalyst that utilizes the Earth-abundant metal manganese for the reduction of CO_2 to CO. However, as we discussed in Chapter 5 of this dissertation, $Mn(CO)_3(^{R}bpy)Br$ complexes (where R = tBu, H, CF_3, and NO_2) are inherently sensitive to visible light; this is a characteristic that is not shared by the analogous third-row transition metal complex $Re(CO)_3(bpy)Cl$. Thus, as we showed with rhodium in Chapters 3 and 4, third-row transition metal complexes can be used as valuable model systems to learn more about reactivity that might also be harnessed in first-row transition metal systems. In Chapter 5, we discussed the photo-driven

speciation pathway of $Mn(CO)_3(bpy)Br$ complexes (particularly at early times in the pathway) in an effort to elucidate design principles that could be used to develop more light-stable catalysts in the future. Moving forward, it seems that we will need to learn to work with abundant transition metal complexes, harness their reactivity, and generate efficient catalysts that utilize abundant feedstocks (H_2O, N_2, O_2 CO_2, etc.). Understanding the inherent reactivity of Earth-abundant metals will be crucial for the development of large-scale chemical energy storage solutions and these efforts appear to be essential for securing a clean and sustainable future.

Appendices for Chapters in Part I

Appendix A

Supplementary Information for Chapter 3

NMR Spectra

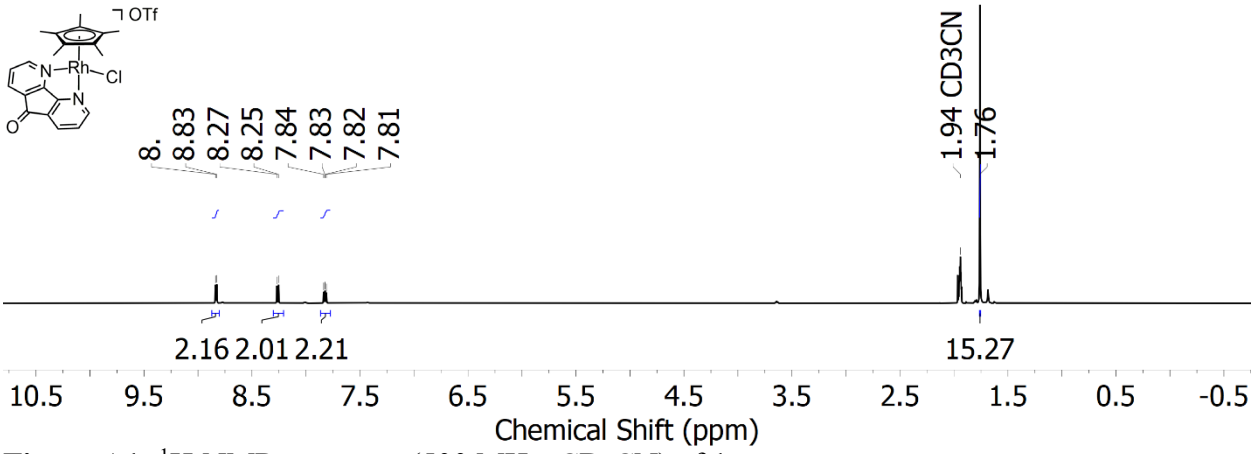

Figure A1: ^{1}H-NMR spectrum (500 MHz, CD_3CN) of **1**.

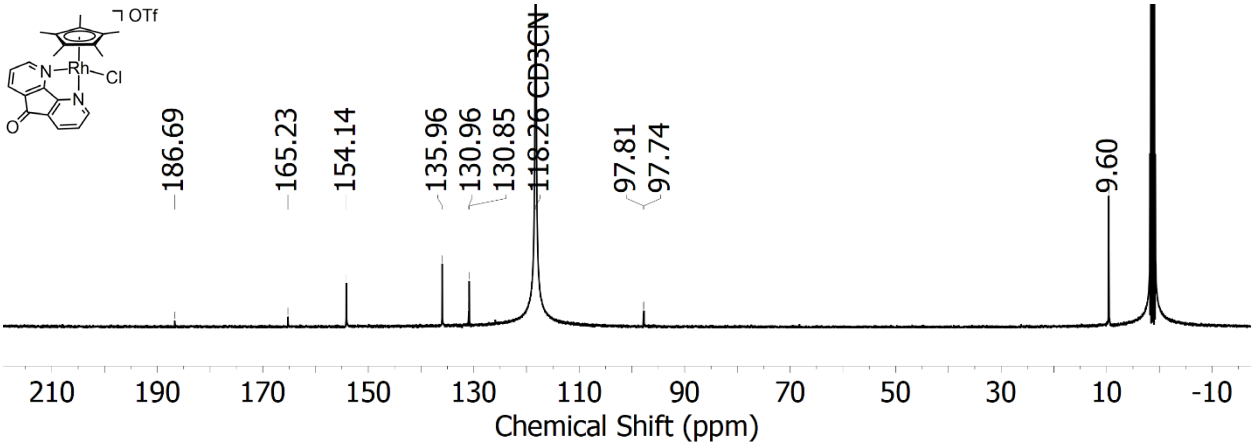

Figure A2: ^{13}C{^{1}H}-NMR spectrum (126 MHz, CD_3CN) of **1**.

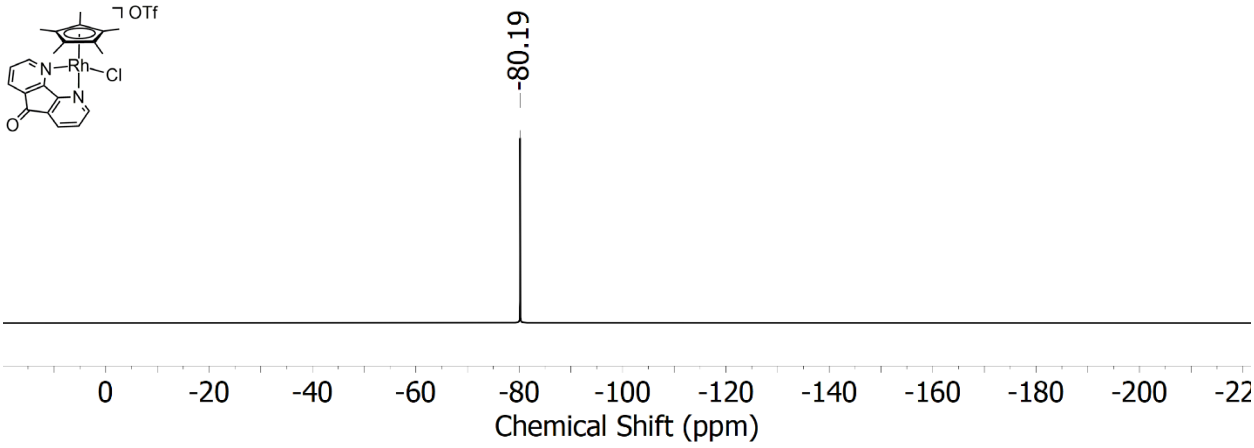

Figure A3: ^{19}F-NMR spectrum (471 MHz, CD_3CN) of **1**.

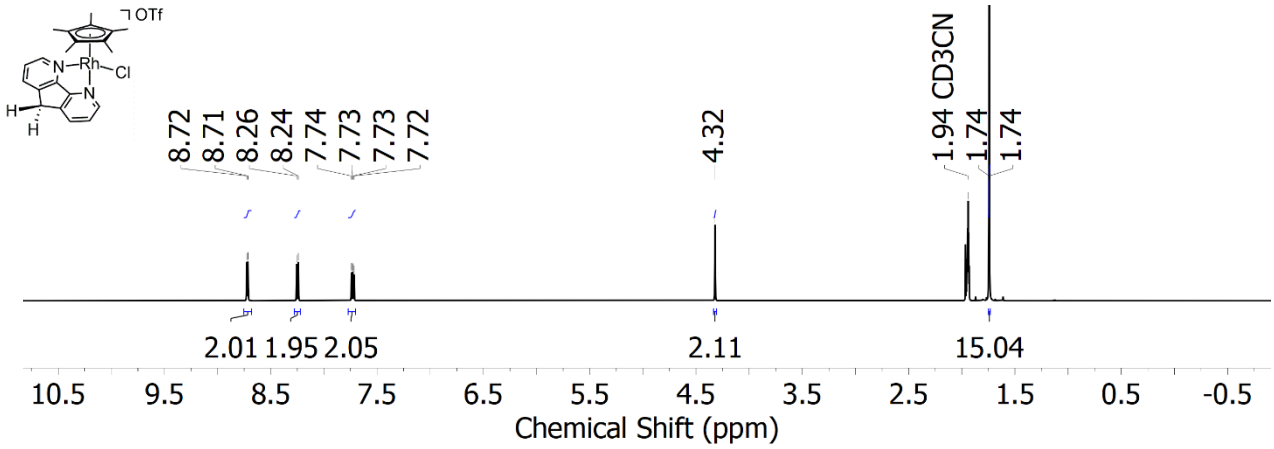

Figure A4: ^{1}H-NMR spectrum (500 MHz, CD_3CN) of **2**.

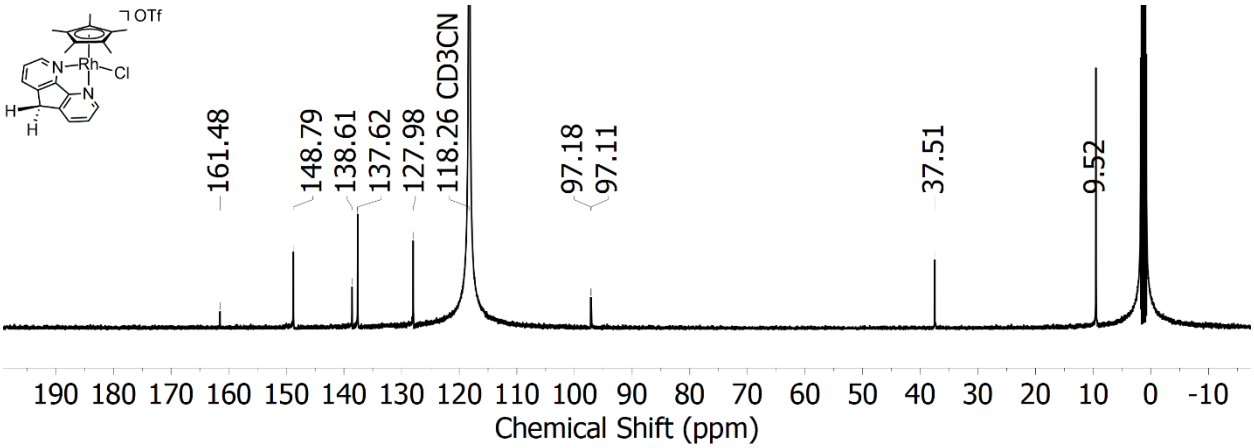

Figure A5: ^{13}C{^{1}H}-NMR spectrum (126 MHz, CD_3CN) of **2**.

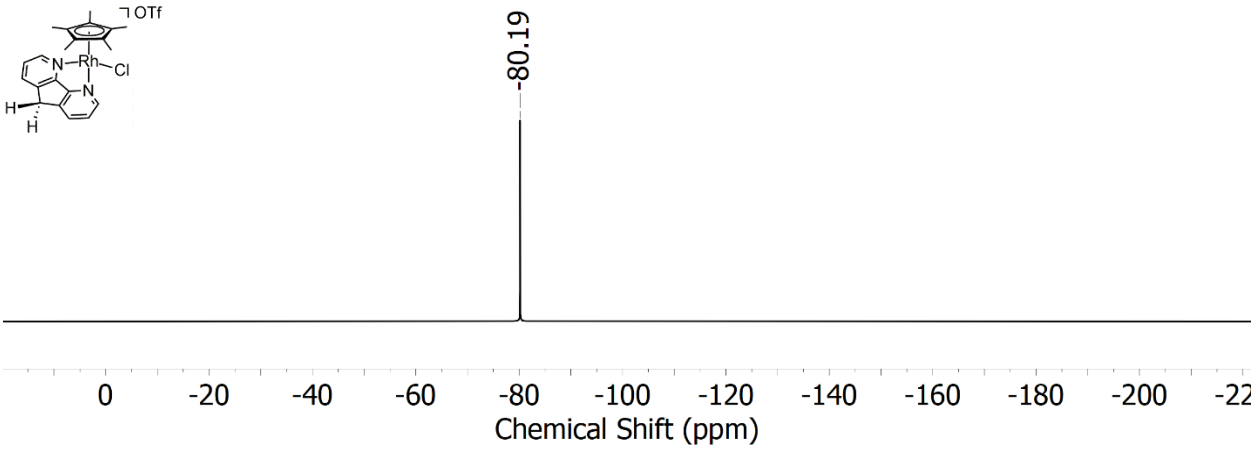

Figure A6: ^{19}F-NMR spectrum (471 MHz, CD_3CN) of **2**.

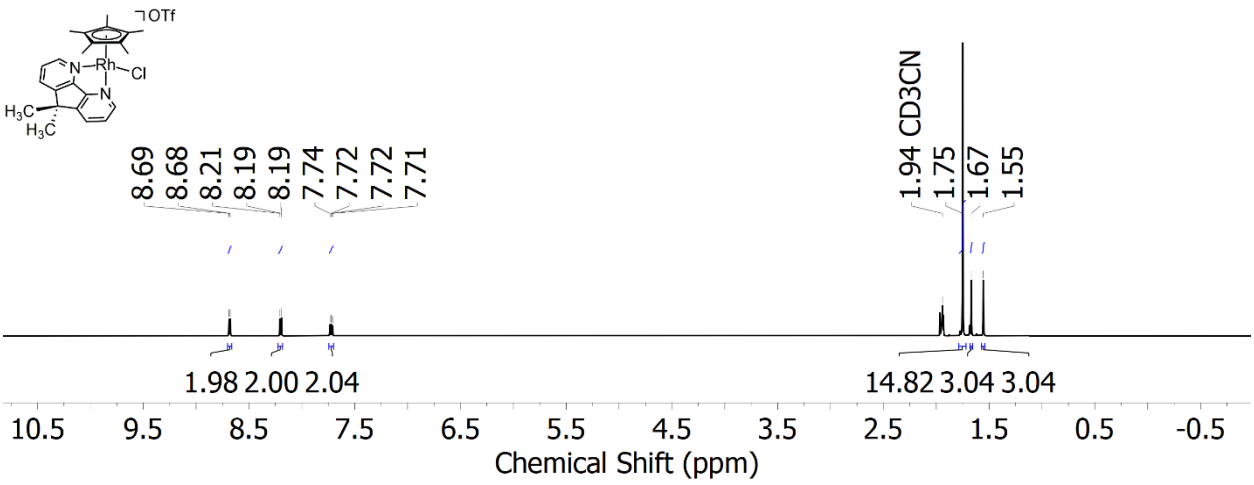

Figure A7: ^{1}H-NMR spectrum (500 MHz, CD_3CN) of **3**.

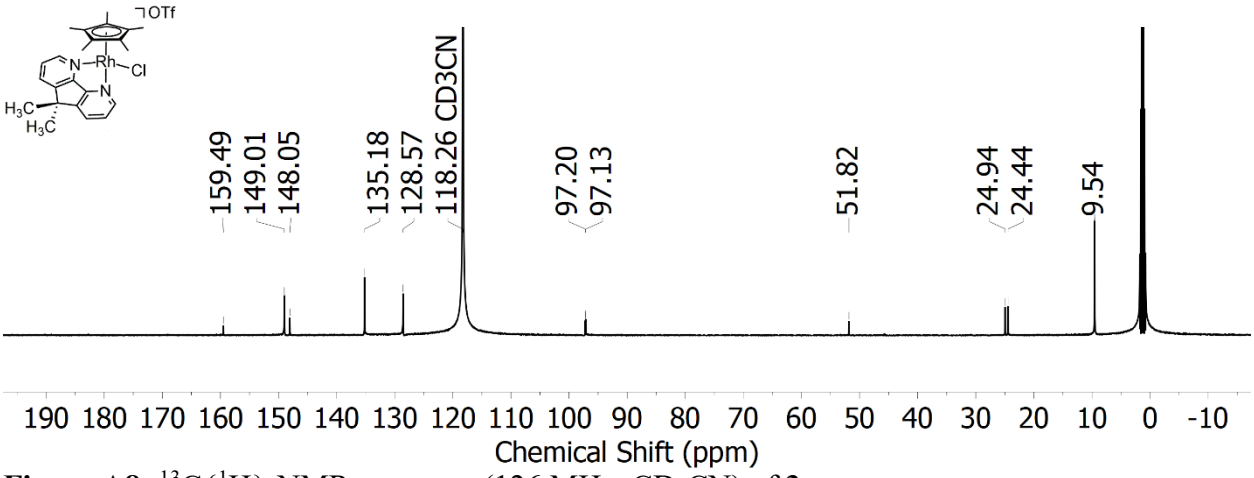

Figure A8: ^{13}C{^{1}H}-NMR spectrum (126 MHz, CD_3CN) of **3**.

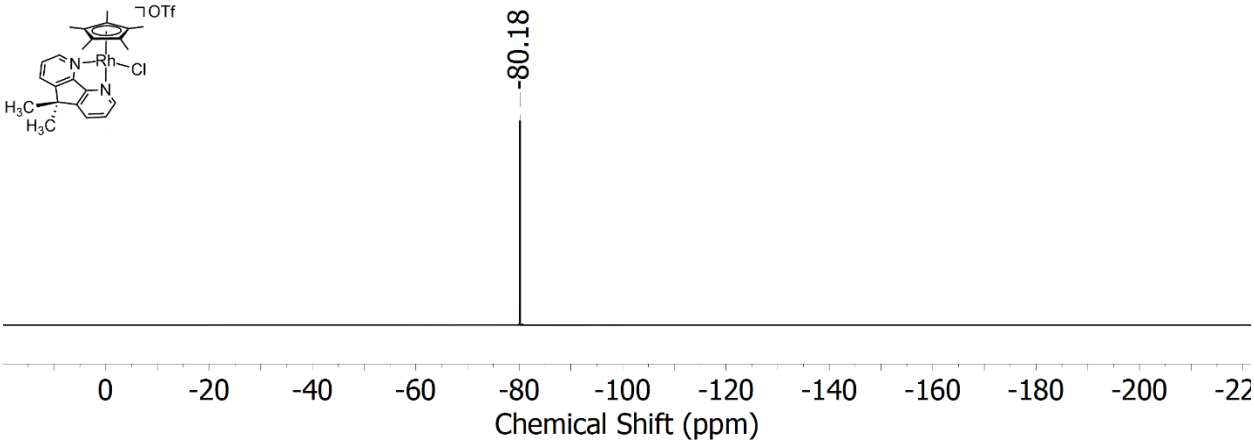

Figure A9: ^{19}F-NMR spectrum (471 MHz, CD_3CN) of **3**.

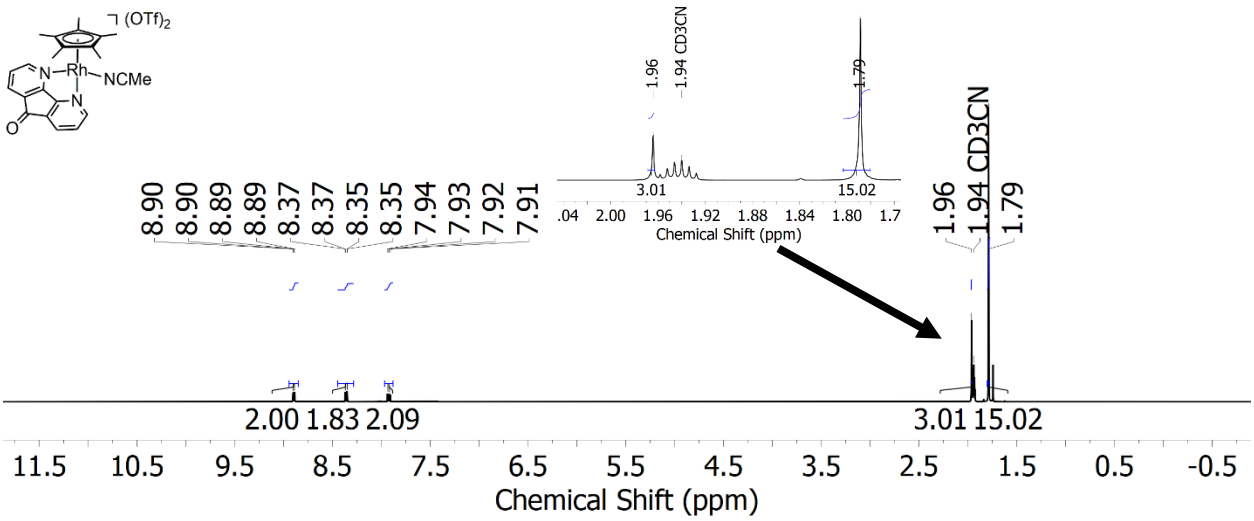

Figure A10: ^{1}H-NMR spectrum (400 MHz, CD_3CN) of **1-NCMe**.

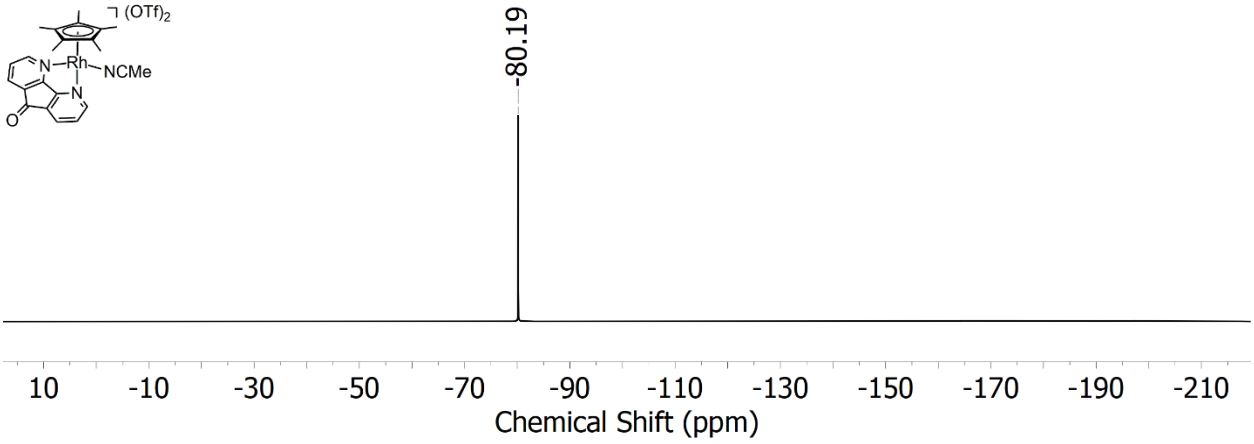

Figure A11: ^{19}F-NMR spectrum (376 MHz, CD_3CN) of **1-NCMe**.

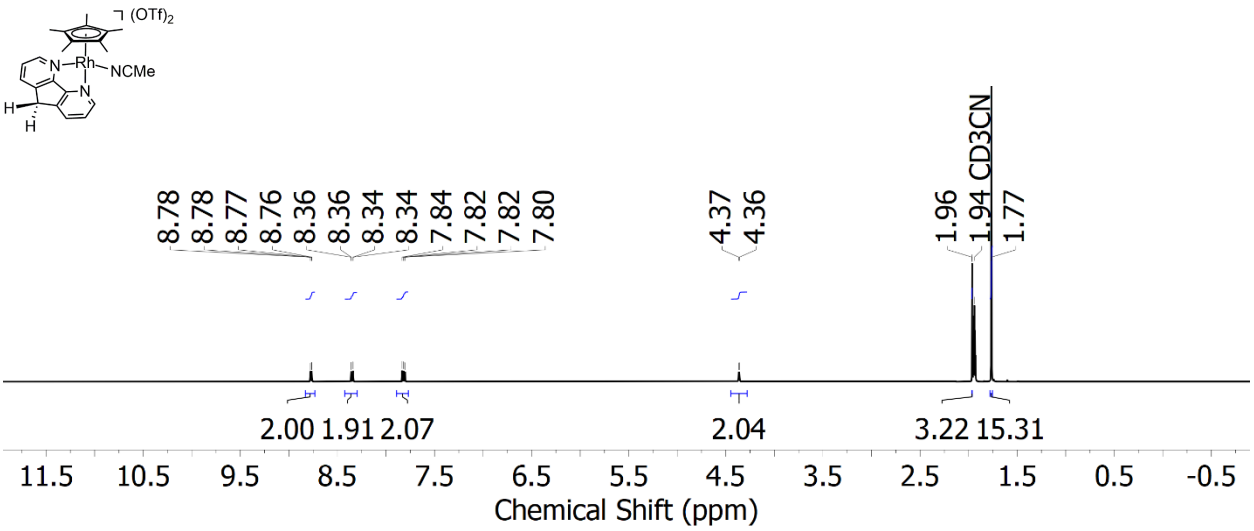

Figure A12: ^{1}H-NMR spectrum (400 MHz, CD_3CN) of **2-NCMe**.

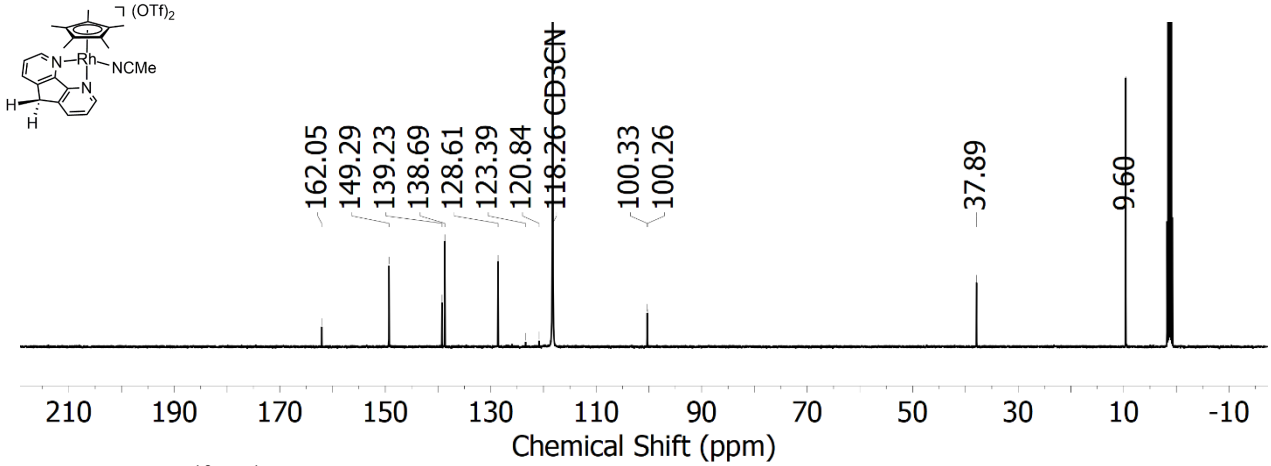

Figure A13: ^{13}C{^{1}H}-NMR spectrum (126 MHz, CD_3CN) of **2-NCMe**.

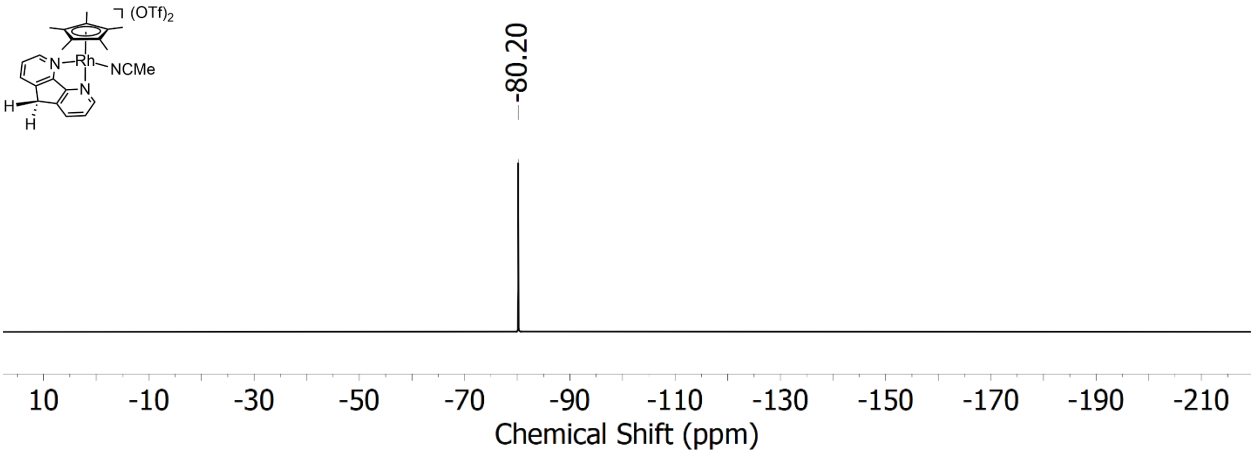

Figure A14: ^{19}F-NMR spectrum (376 MHz, CD_3CN) of **2-NCMe**.

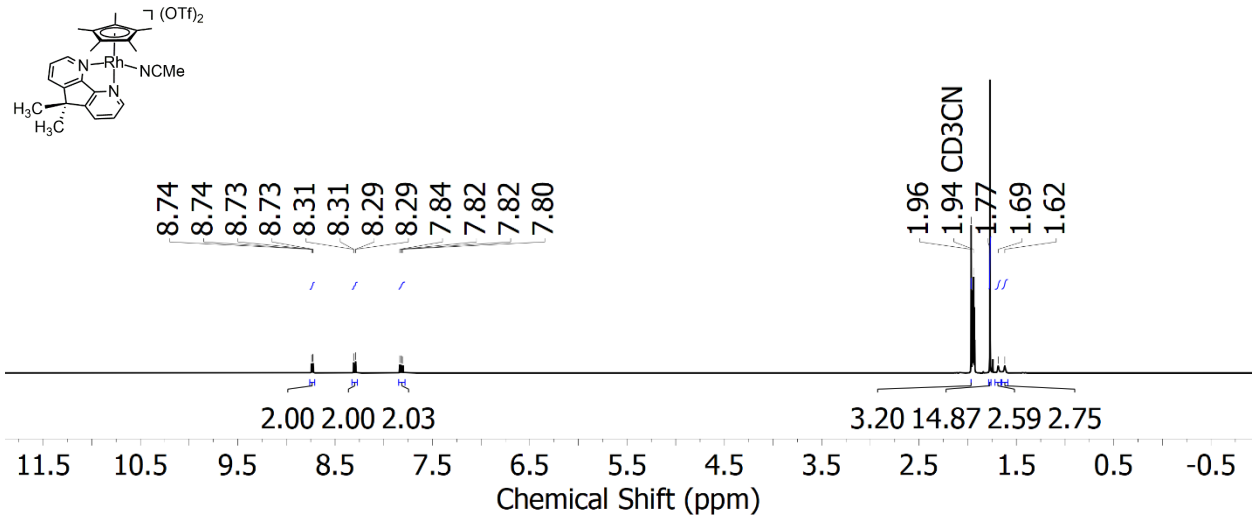

Figure A15: ^{1}H-NMR spectrum (400 MHz, CD_3CN) of **3-NCMe**.

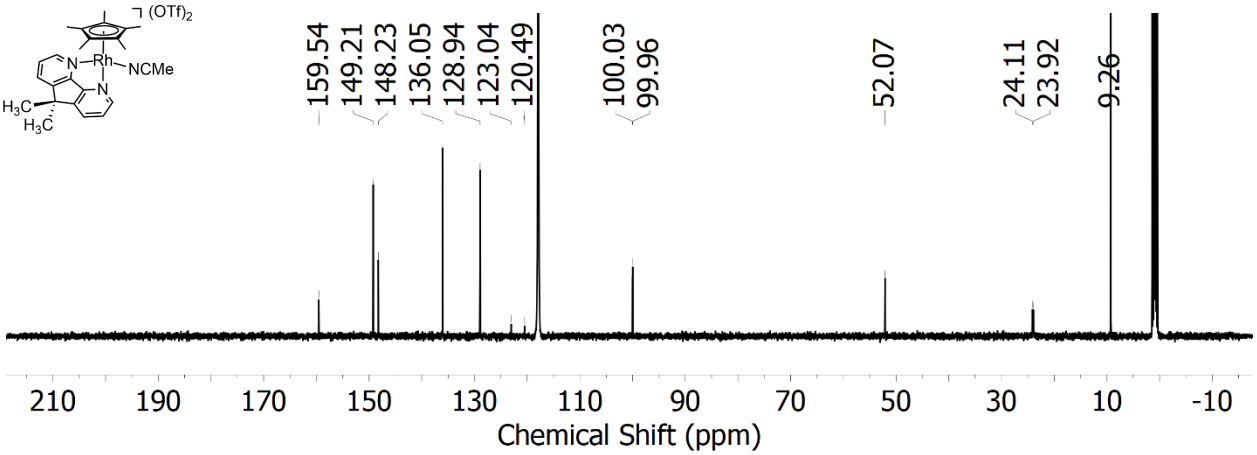

Figure A16: ^{13}C{^{1}H}-NMR spectrum (126 MHz, CD_3CN) of **3-NCMe**.

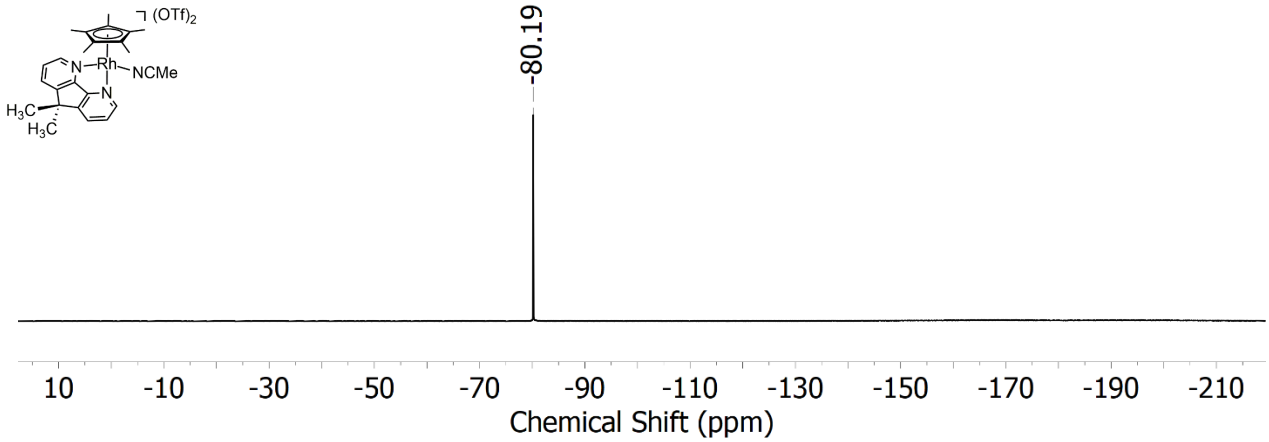

Figure A17: ^{19}F-NMR spectrum (376 MHz, CD_3CN) of **3-NCMe**

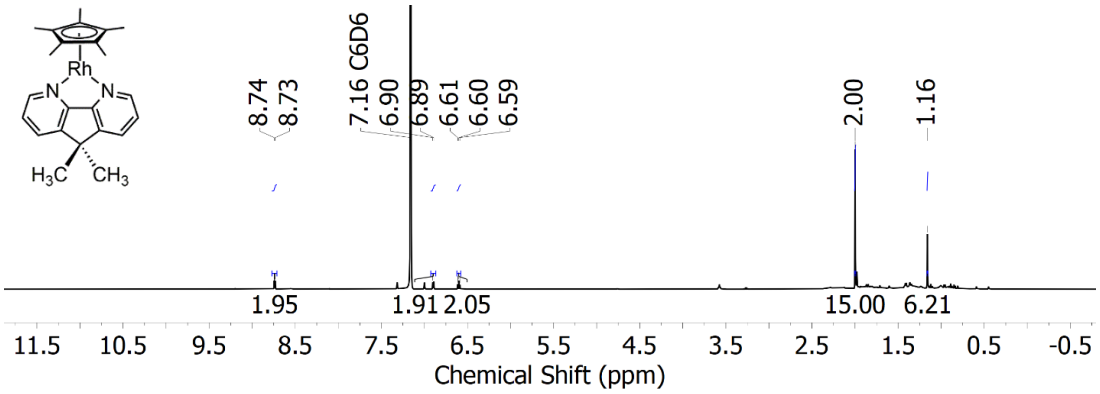

Figure A18: ^{1}H-NMR spectrum (500 MHz, C_6D_6) of **4**.

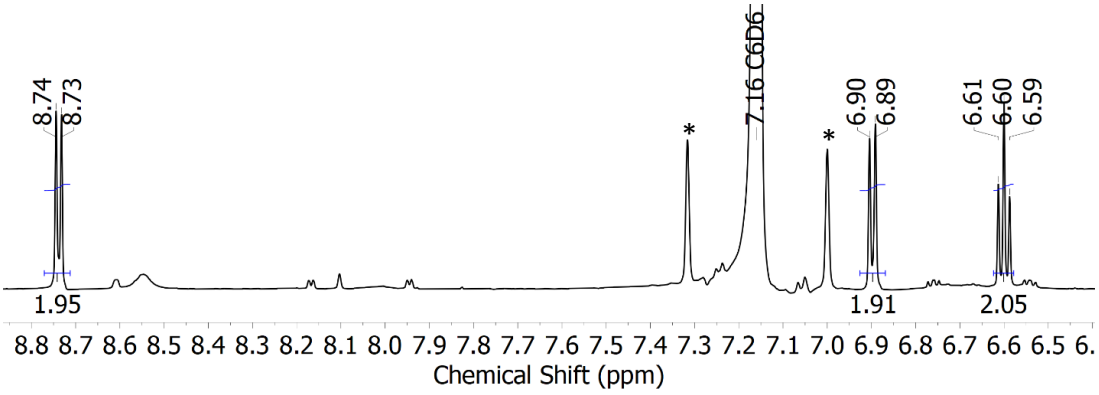

Figure A19: Zoomed in ^{1}H-NMR spectrum (500 MHz, C_6D_6) of **4** highlighting the aromatic region. Satellite signals from ^{13}C in C_6D_6 solvent residual are denoted by *.

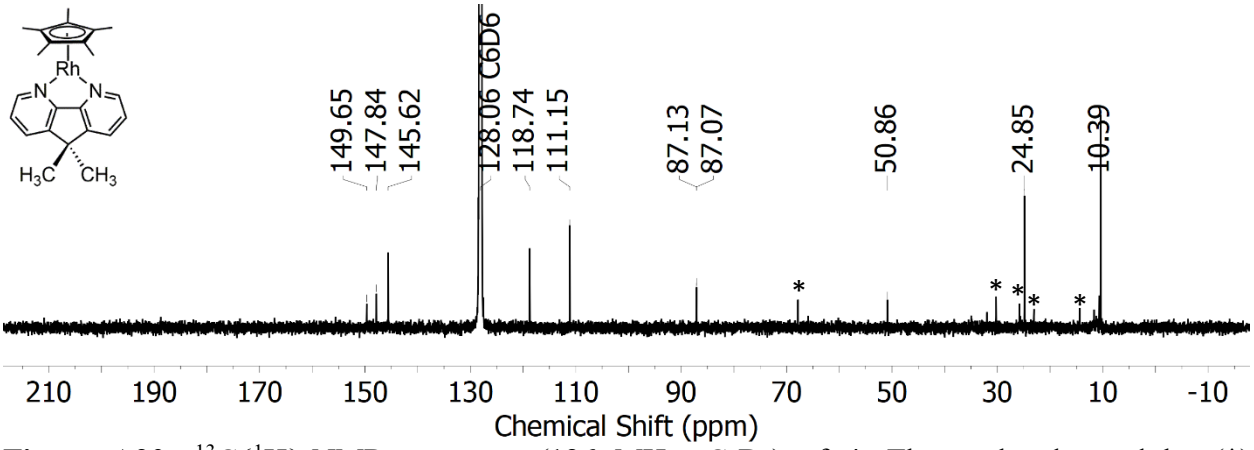

Figure A20: ^{13}C{^{1}H}-NMR spectrum (126 MHz, C_6D_6) of **4**. The peaks denoted by (*) correspond to H-grease (30.21 ppm), hexanes (14.32 ppm and 23.04 ppm) and adventitious tetrahydrofuran (25.72 ppm and 67.80 ppm).

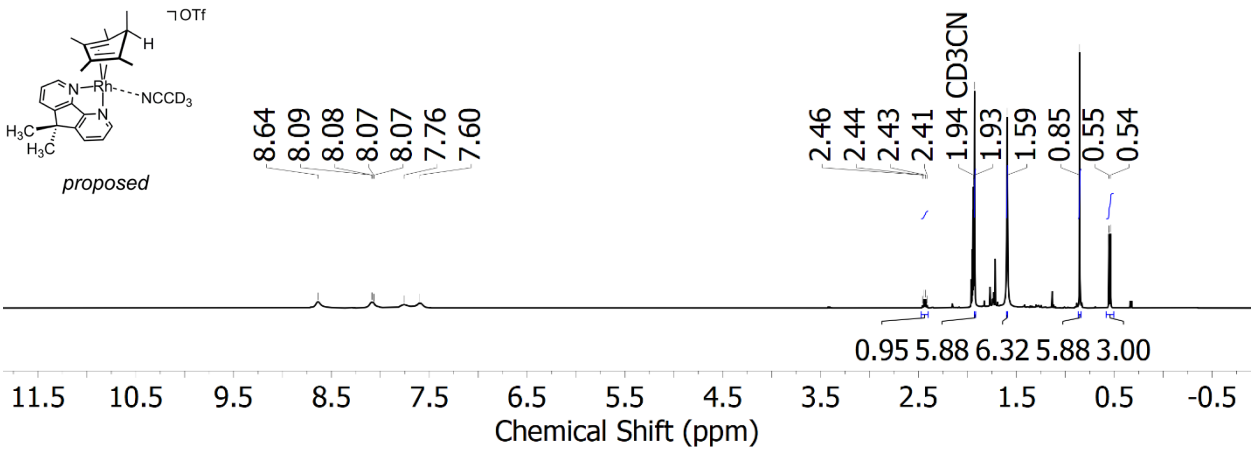

Figure A21: The ^{1}H-NMR spectrum (400 MHz, CD_3CN) collected following reaction of **3** with Na[HCO_2].

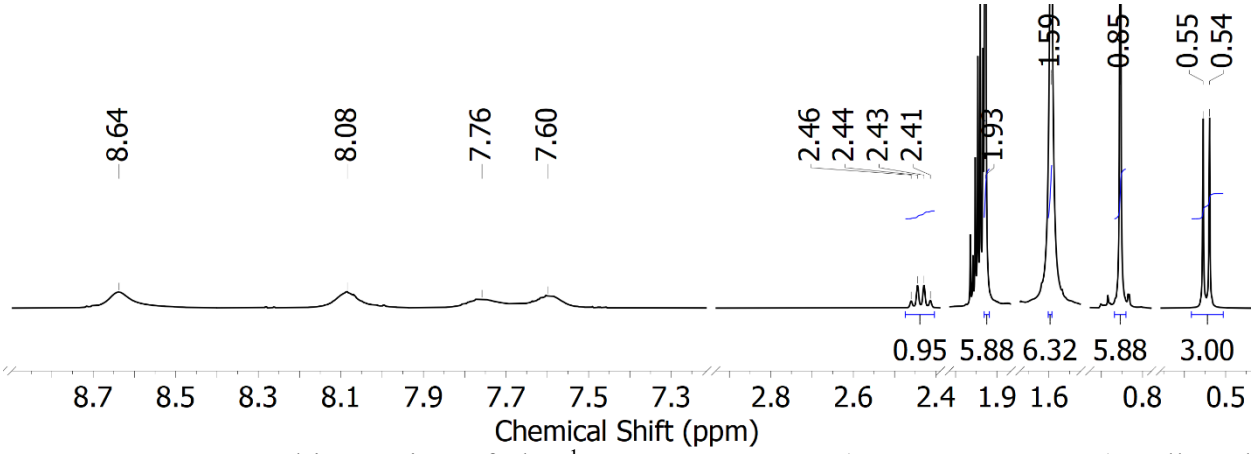

Figure A22: Zoomed-in version of the ^{1}H-NMR spectrum (400 MHz, CD_3CN) collected following reaction of **3** with Na[HCO_2].

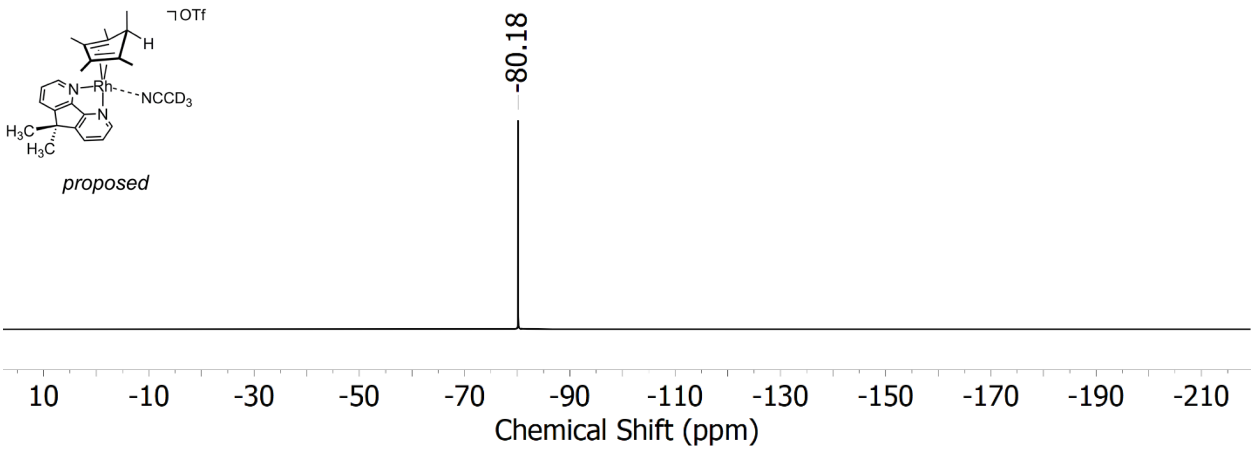

Figure A23: The ^{19}F-NMR spectrum (376 MHz, CD_3CN) collected following reaction of **3** with Na[HCO_2].

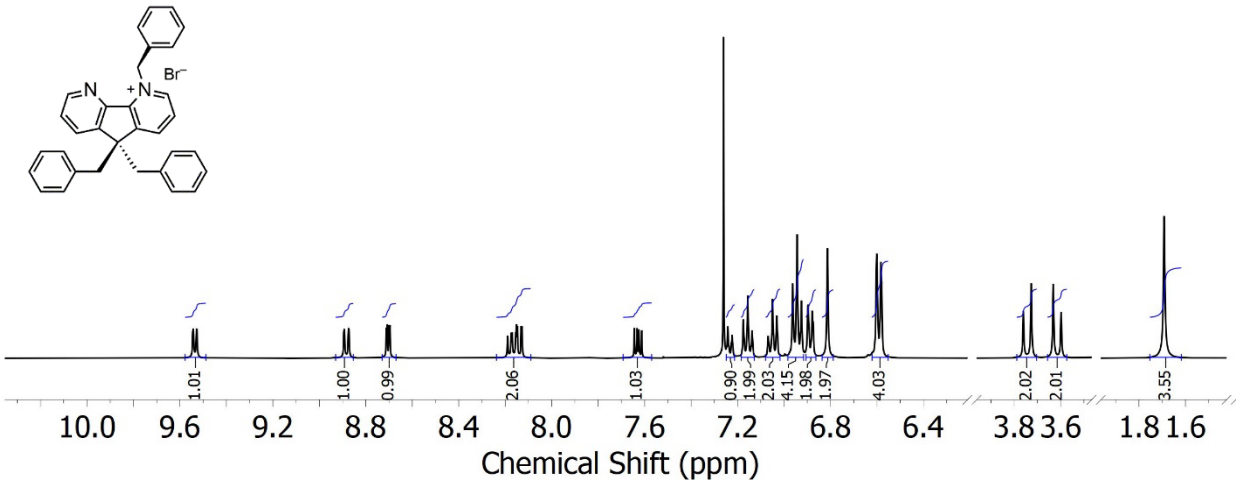

Figure A24: ^{1}H-NMR spectrum (400 MHz, $CDCl_3$) of **Bn$_3$daf**.

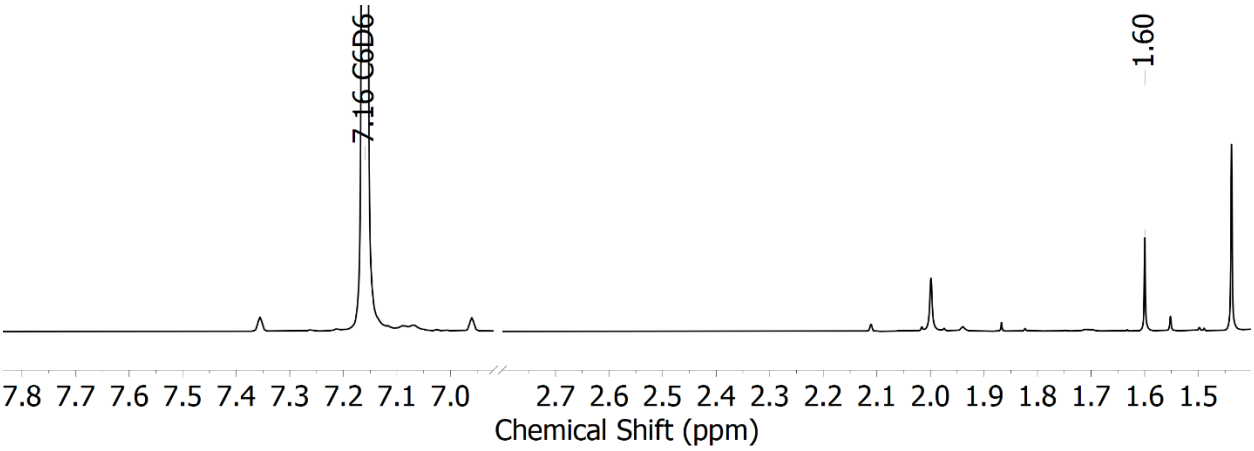

Figure A25: ^{1}H-NMR spectrum (400 MHz, C_6D_6) from the Et_2O fraction of the reduction of **3** with Cp_2Co. The peak at 1.60 ppm is consistent with $[Cp^*RhCl]_2$. (See Results and Discussion in main text.)

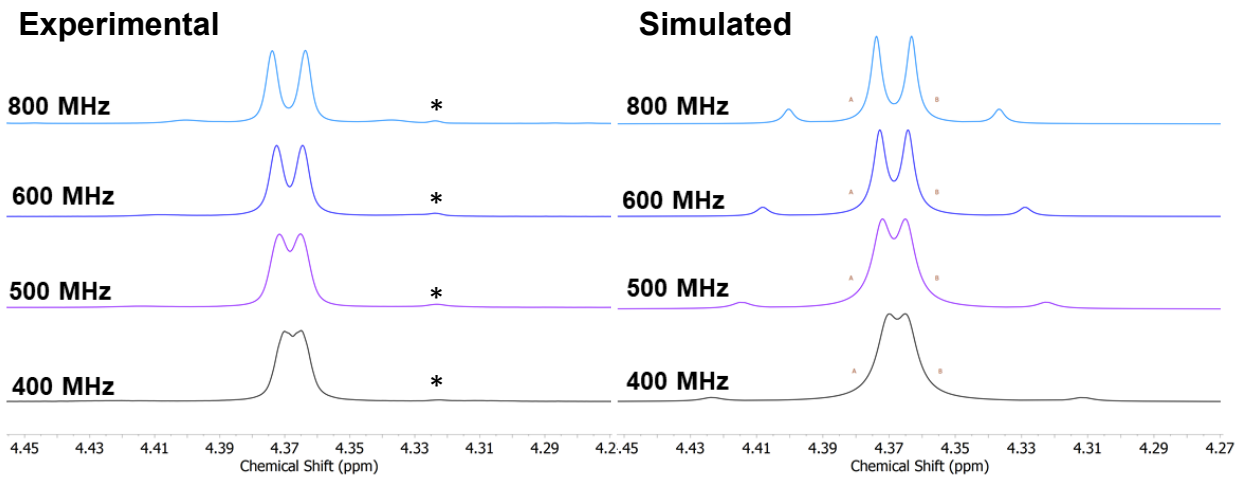

Figure A26: Experimental and simulated field-dependence study of **2-NCMe**. As the strength of the magnetic field increases, the resonances that arise from the geminal coupling of the diastereotopic protons become better resolved. The simulated spectra were generated using the spin simulation functionality within MestReNova. The diastereotopic protons of **2-NCMe** were modeled as an AB spin system, with a coupling constant of 21.2 Hz and the appropriate spectrometer operating frequency. A slight impurity, denoted by *, is present in the experimental spectrum.

Mass Spectra

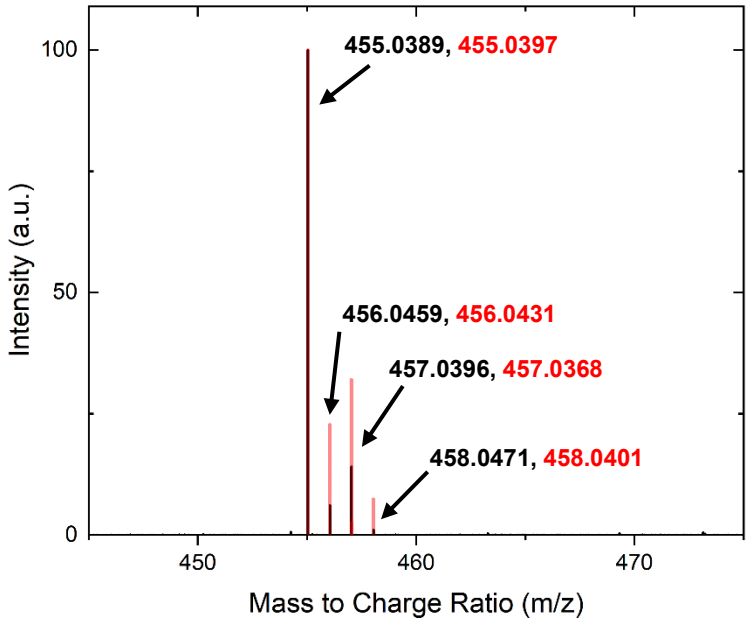

Figure A27: ESI-mass spectrum of **1.** The experimental data is shown in **black** and the predicted data is shown in **red**. The expected parent peak represents **1** – OTf.

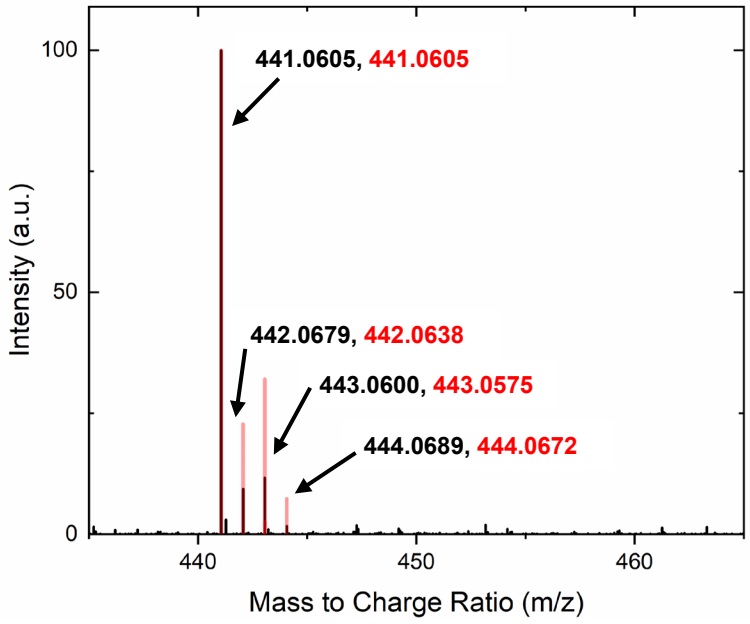

Figure A28: ESI-mass spectrum of **2.** The experimental data is shown in **black** and the predicted data is shown in **red**. The expected parent peak represents **2** – OTf.

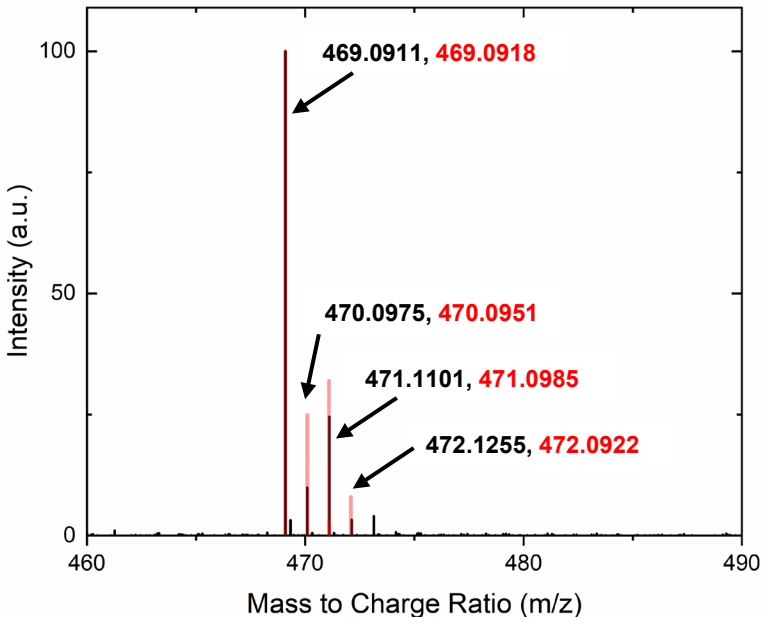

Figure A29: ESI-mass spectrum of **3.** The experimental data is shown in **black** and the predicted data is shown in **red**. The expected parent peak represents **3** – OTf.

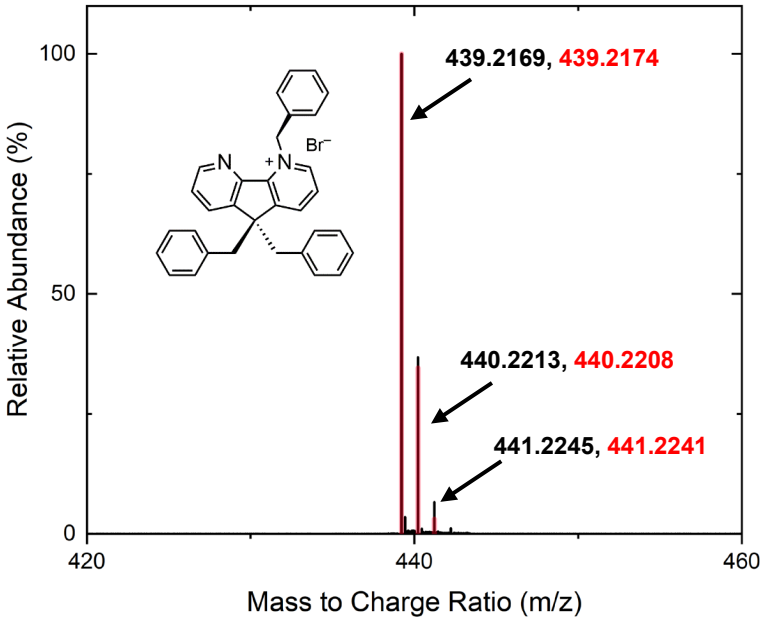

Figure A30: ESI-mass spectrum of **Bn$_3$daf**. The experimental data is shown in black and the predicted data is shown in red. The expected parent peak represents **Bn$_3$daf** –Br.

Electronic Absorption Spectra

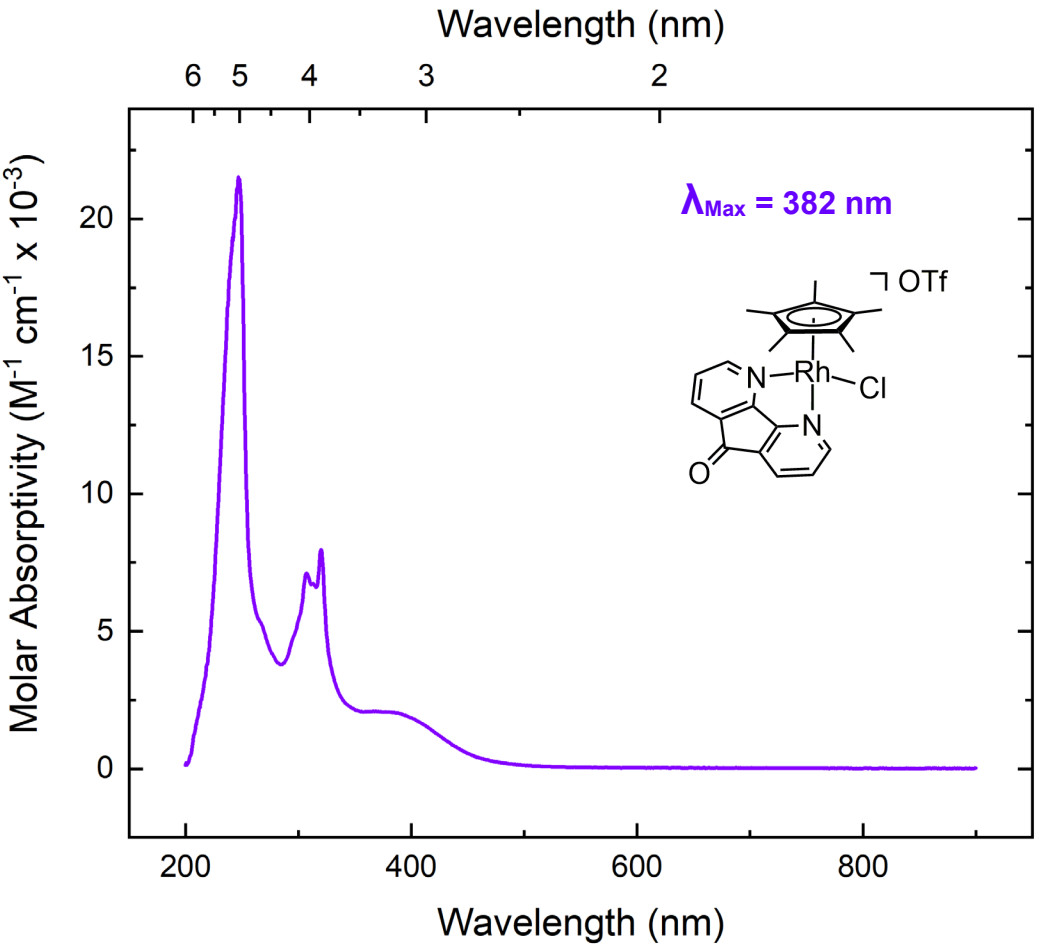

Figure A31: Electronic absorption spectrum of **1** in MeCN

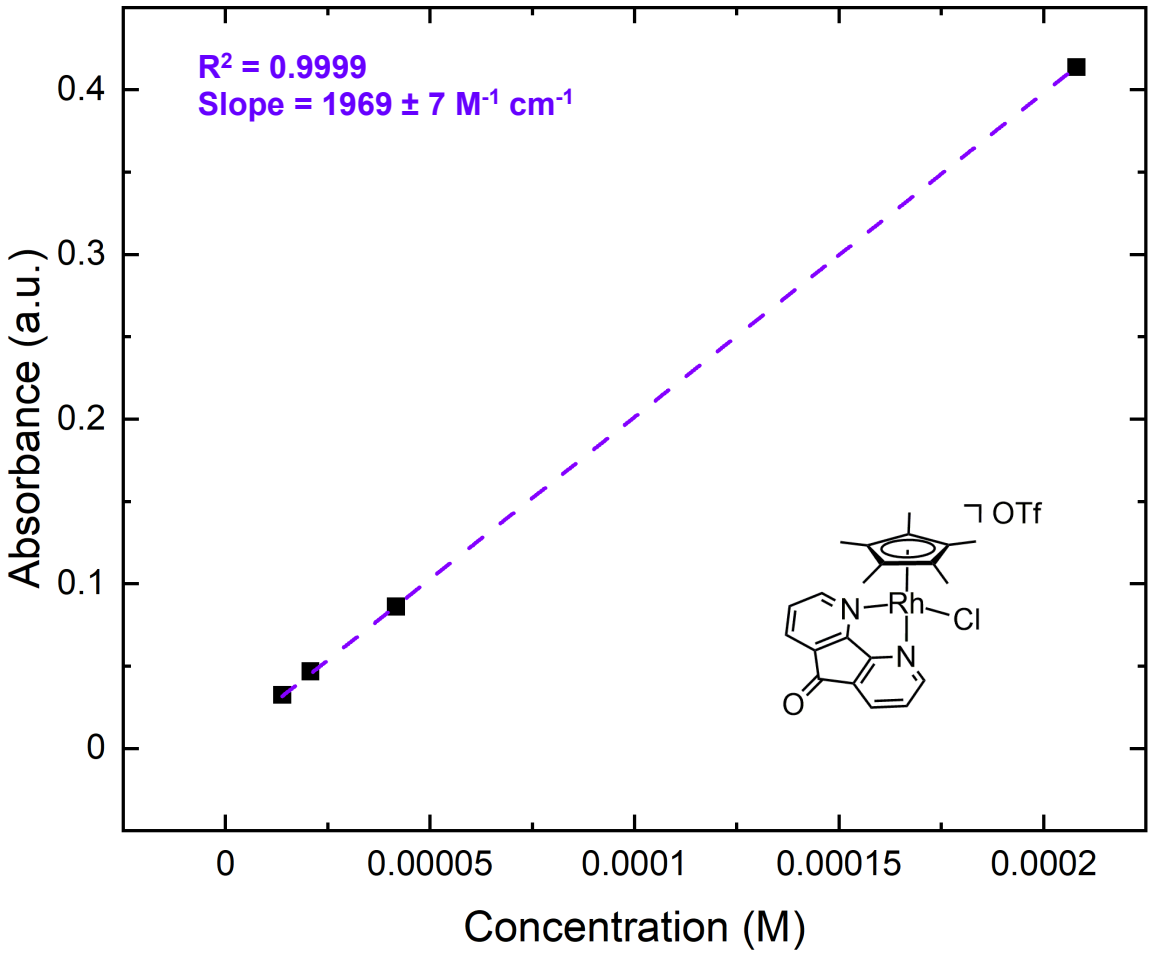

Figure A32: Absorbance vs concentration plot of **1** in MeCN monitored at 382 nm.

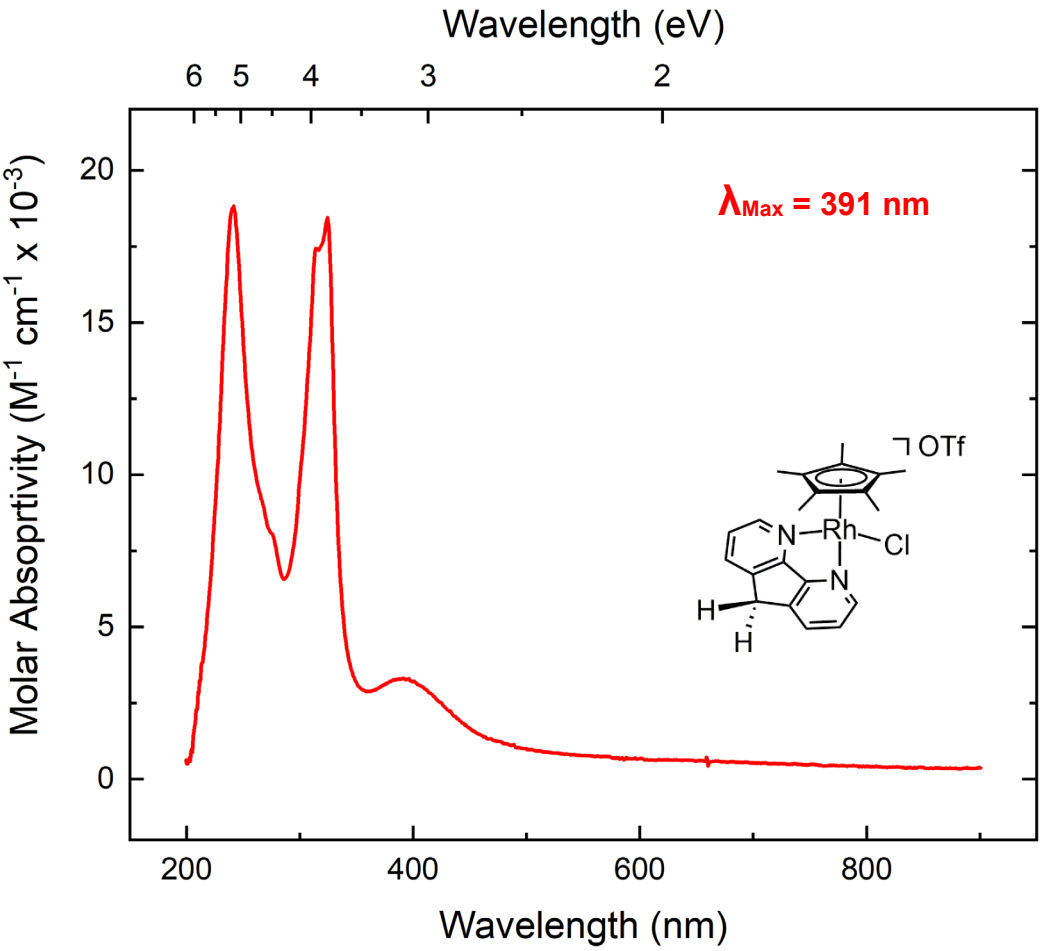

Figure A33: Electronic absorption spectrum of **2** in MeCN.

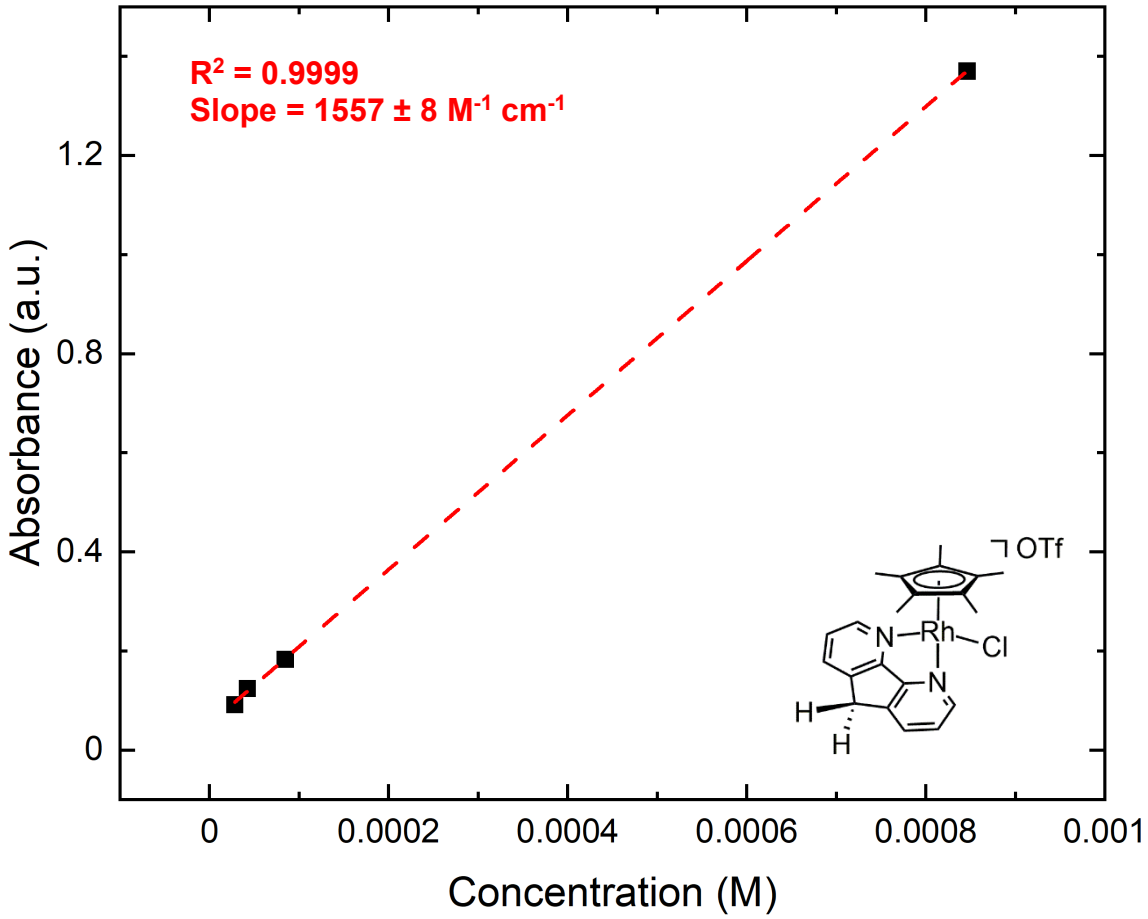

Figure A34: Absorbance vs concentration plot of **2** in MeCN monitored at 391 nm.

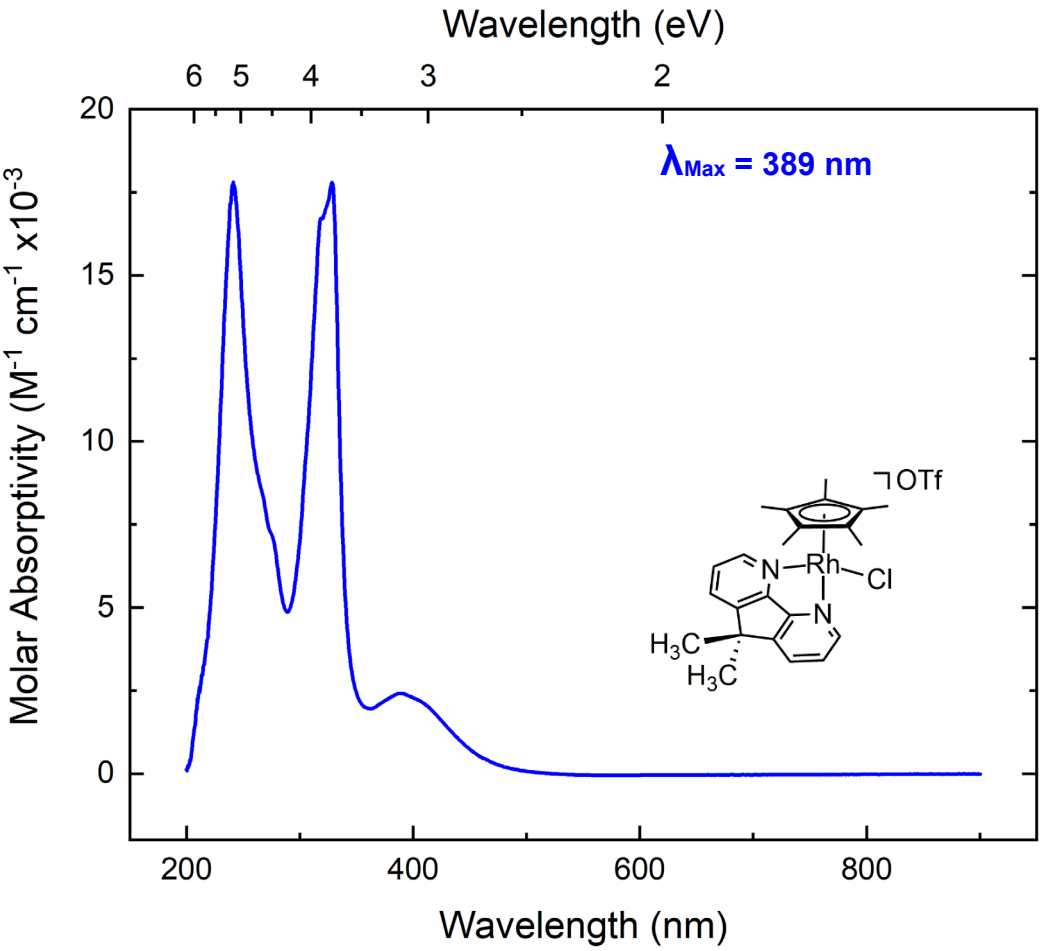

Figure A35: Electronic absorption spectrum of **3** in MeCN.

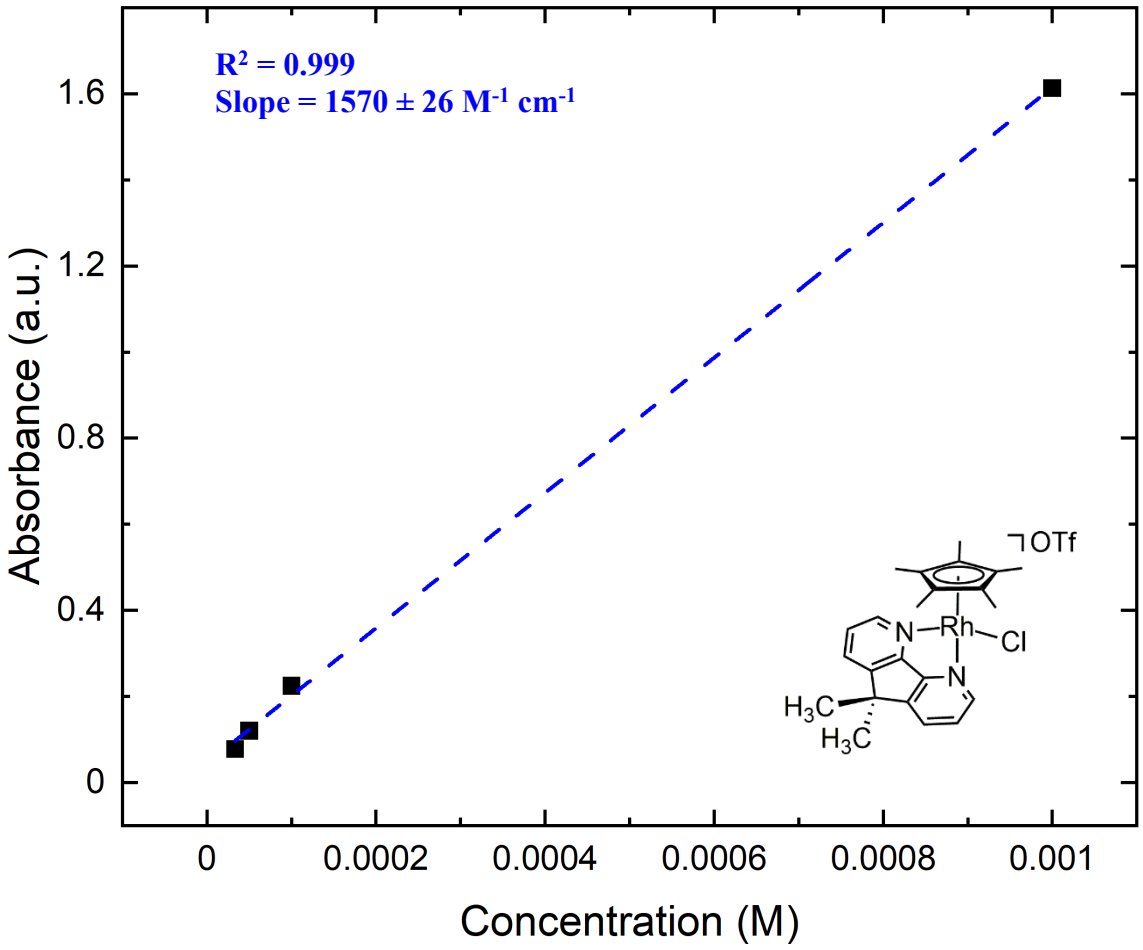

Figure A36: Absorbance vs concentration plot of **3** in MeCN monitored at 389 nm.

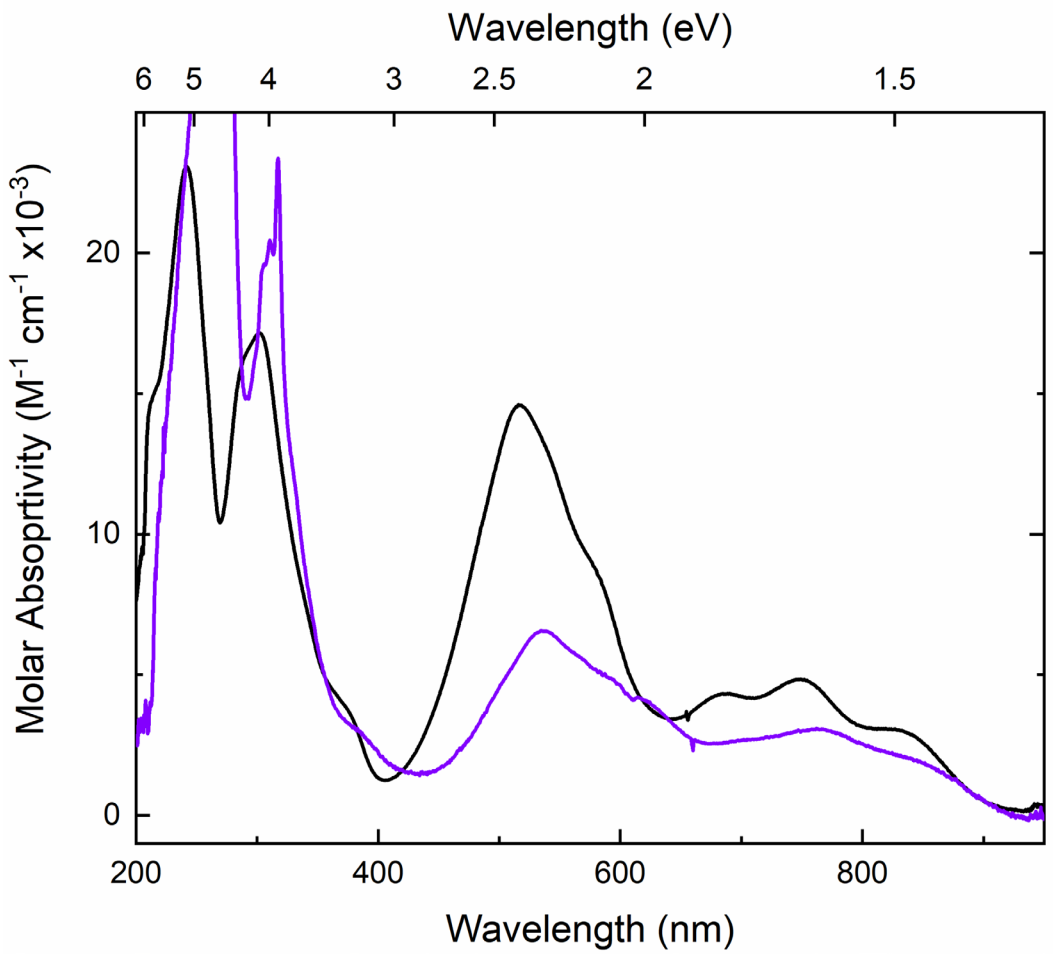

Figure A37: Comparison of the electronic absorption spectra of **3** (purple) and Cp*Rh(bpy) (black) in THF solution. The spectrum of **3** shown here was derived from a spectrochemical titration with $CoCp_2$ in THF.

Electrochemical Data

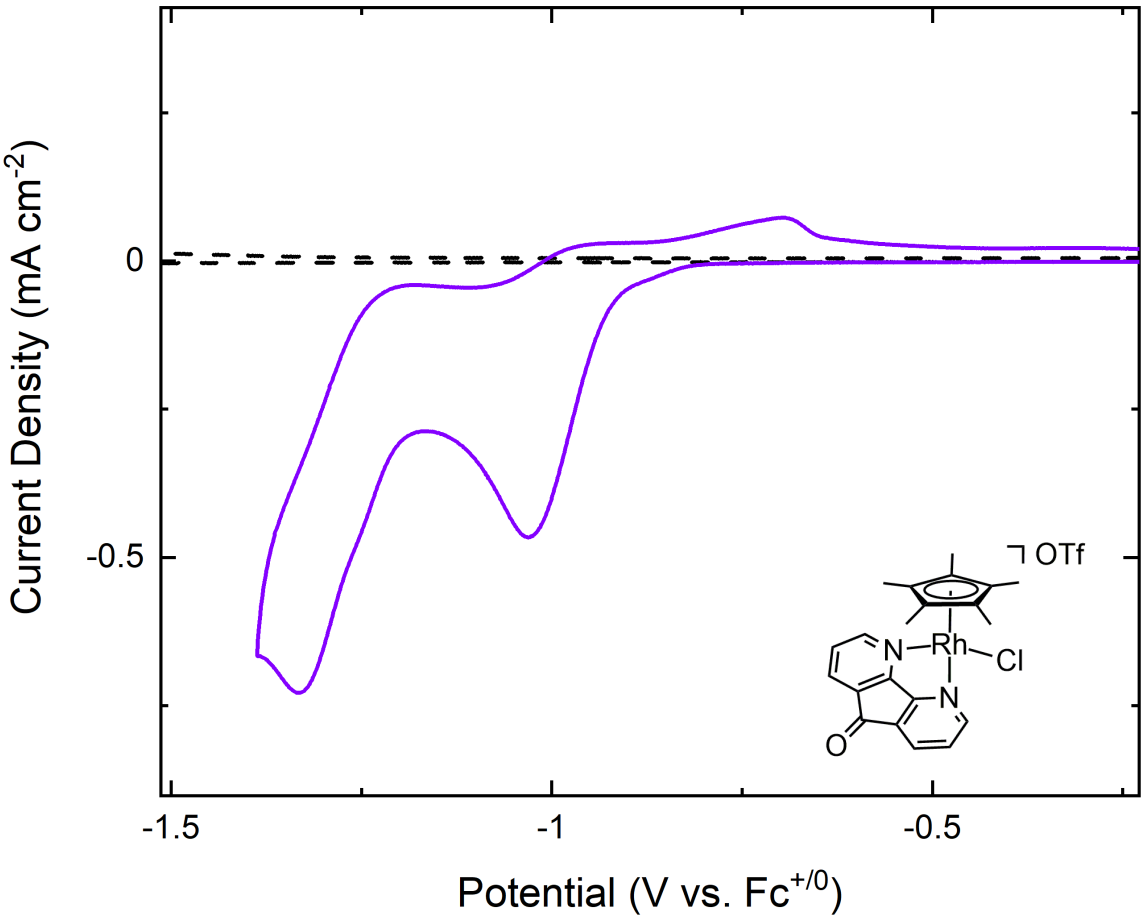

Figure A38: Cyclic Voltammetry of **1** (**purple**) in 0.1 M $TBAPF_6$/MeCN solution. The **black** trace is the blank taken prior to the beginning of the experiment.

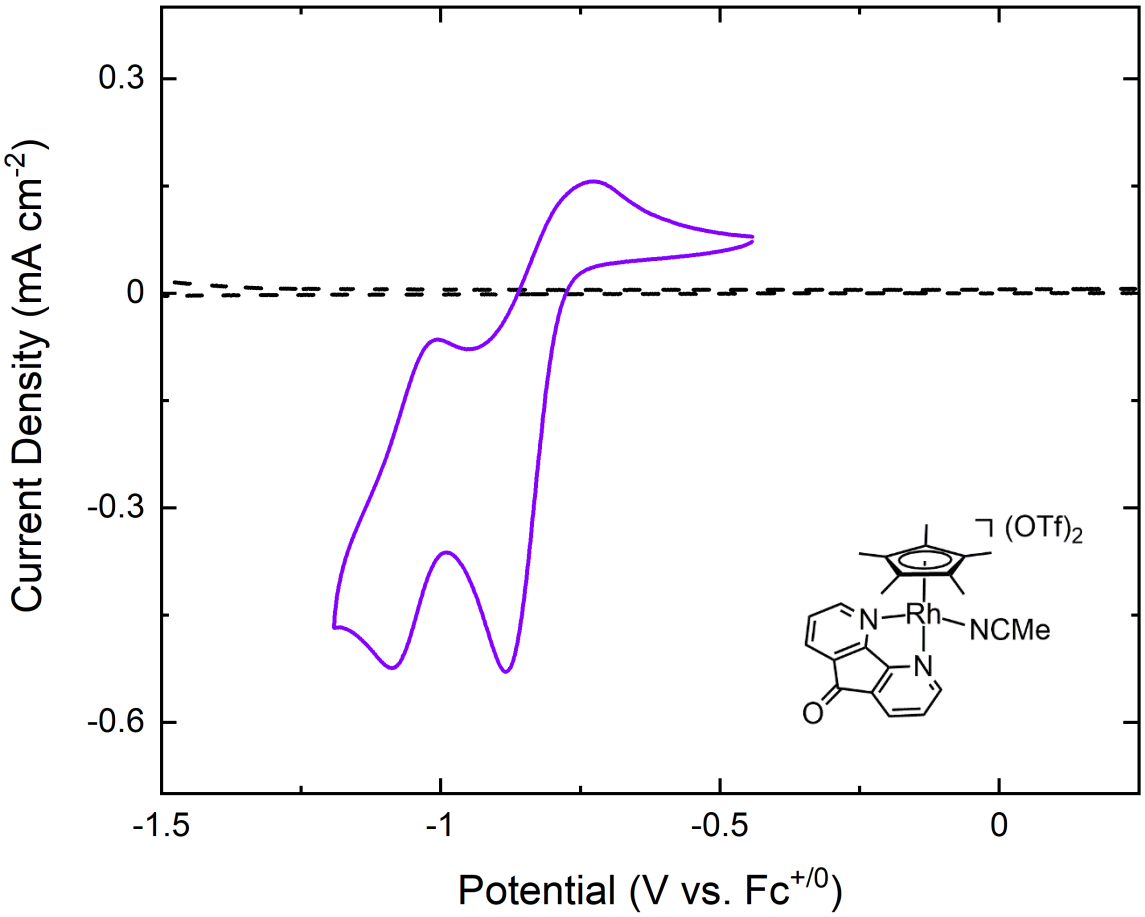

Figure A39: Cyclic Voltammetry of **1-NCMe** (**purple**) in 0.1 M $TBAPF_6$/MeCN solution. The **black** trace is the blank taken prior to the beginning of the experiment.

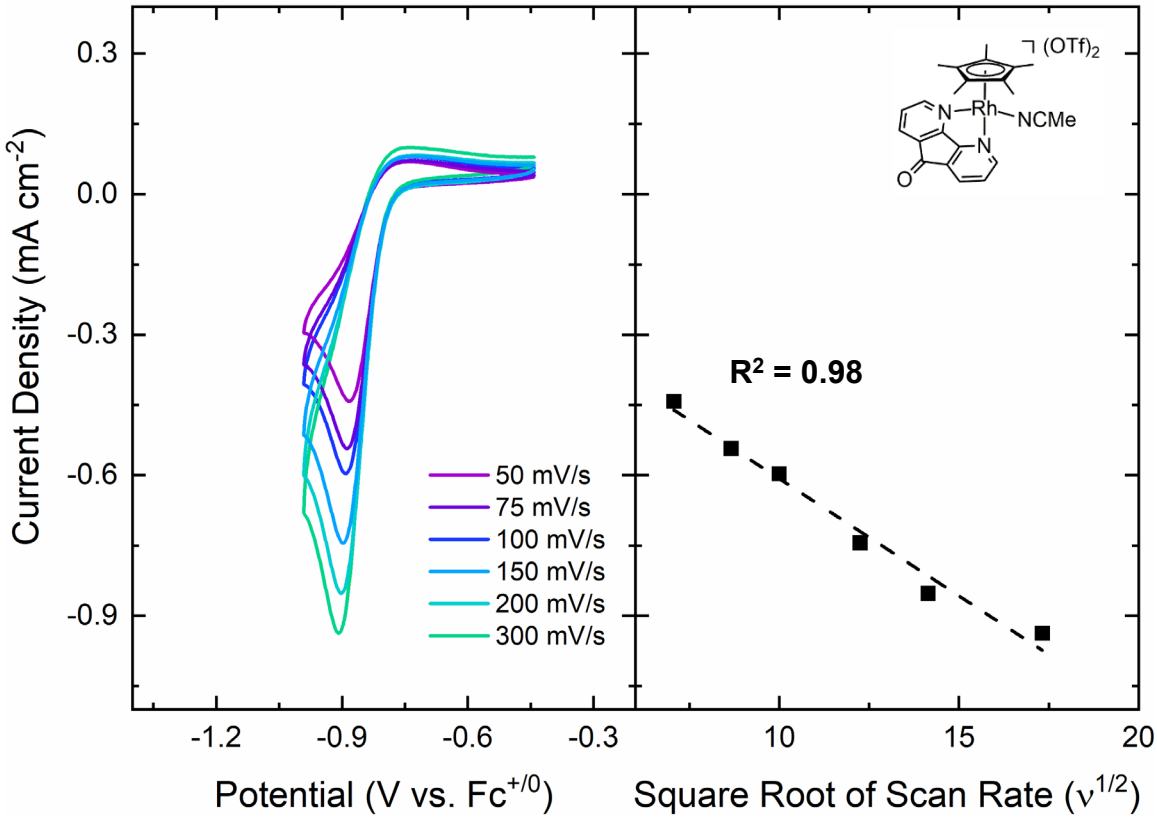

Figure A40: Scan rate dependence studies (left) and peak cathodic current density of the first electron transfer event as a function of the square root of scan rate (right) for complex **1-NCMe**.

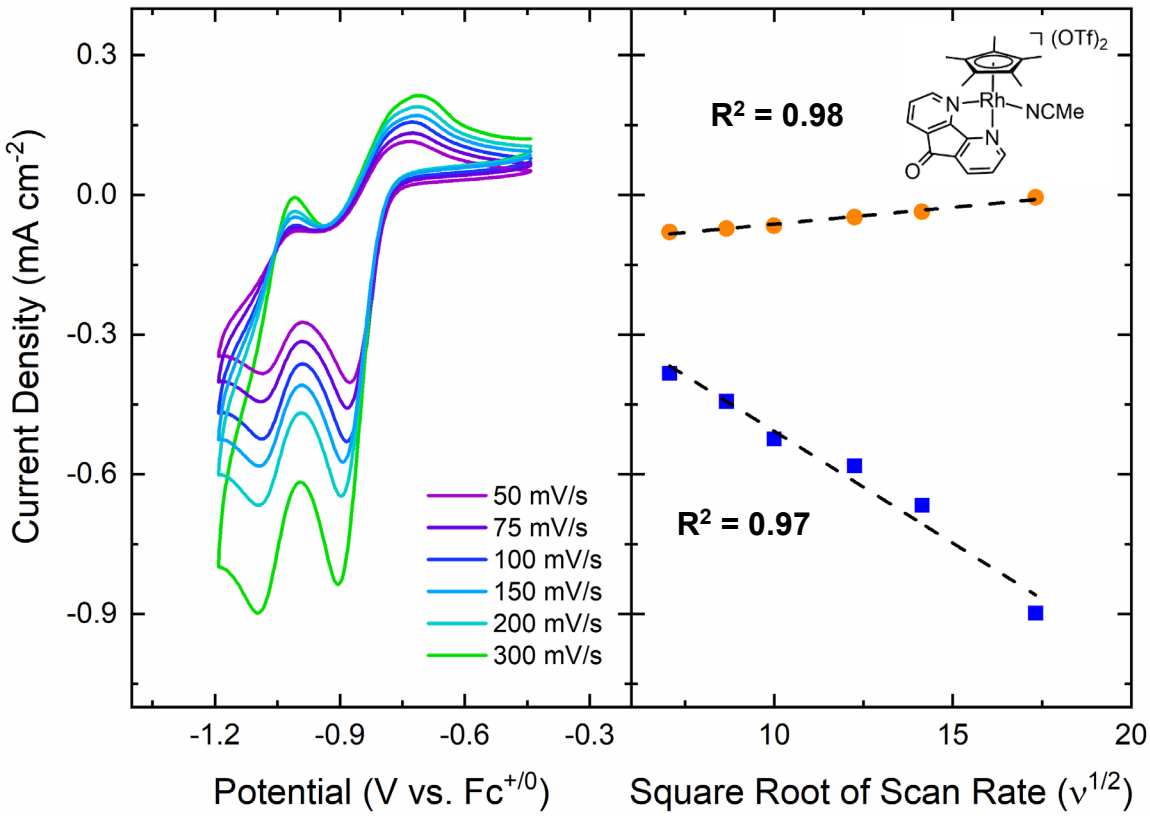

Figure A41: Scan rate dependence studies (left) and peak anodic and cathodic current density of the second electron transfer event as a function of the square root of scan rate (right) for complex **1-NCMe**.

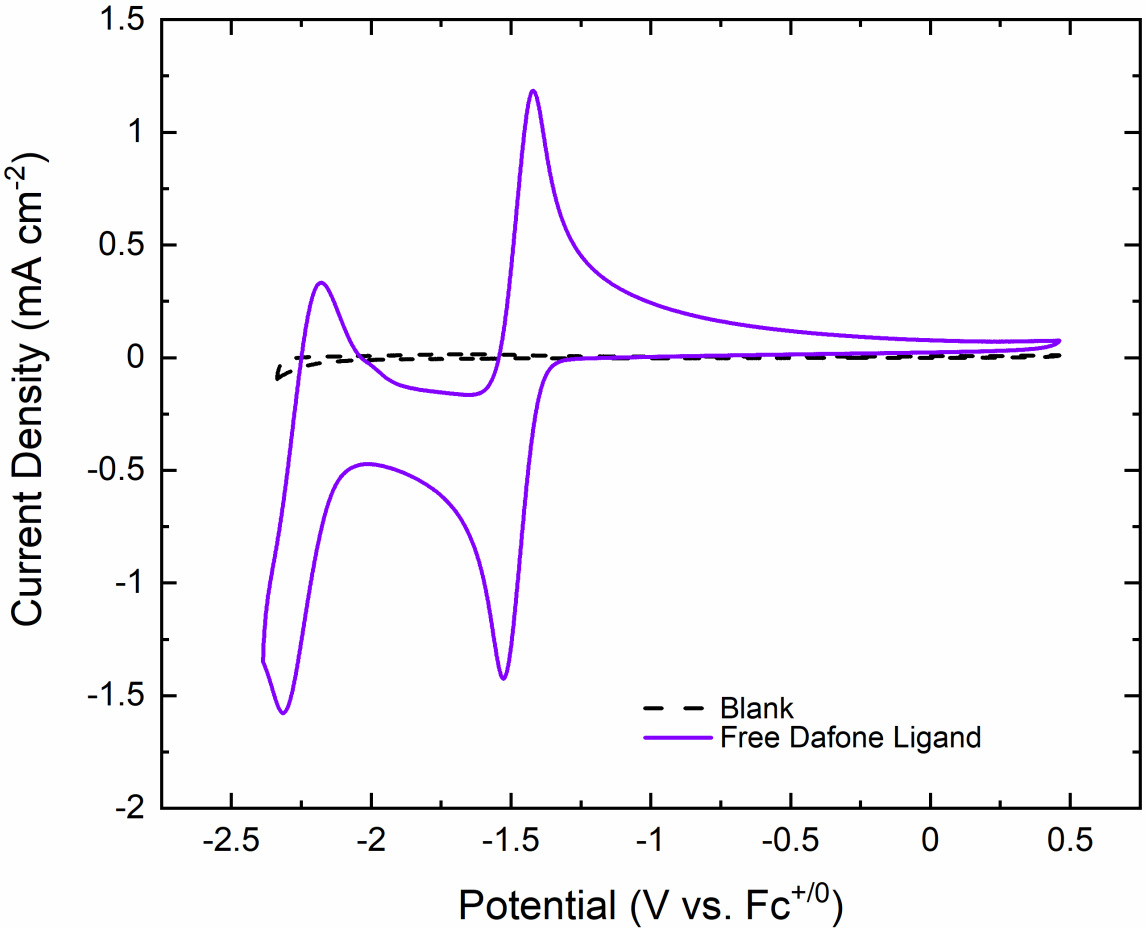

Figure A42: Cyclic voltammetry of free **dafone** ligand (**purple**) in 0.1 M $TBAPF_6$/MeCN solution. The black dashed line is the blank taken prior to addition of dafone to the electrochemical cell.

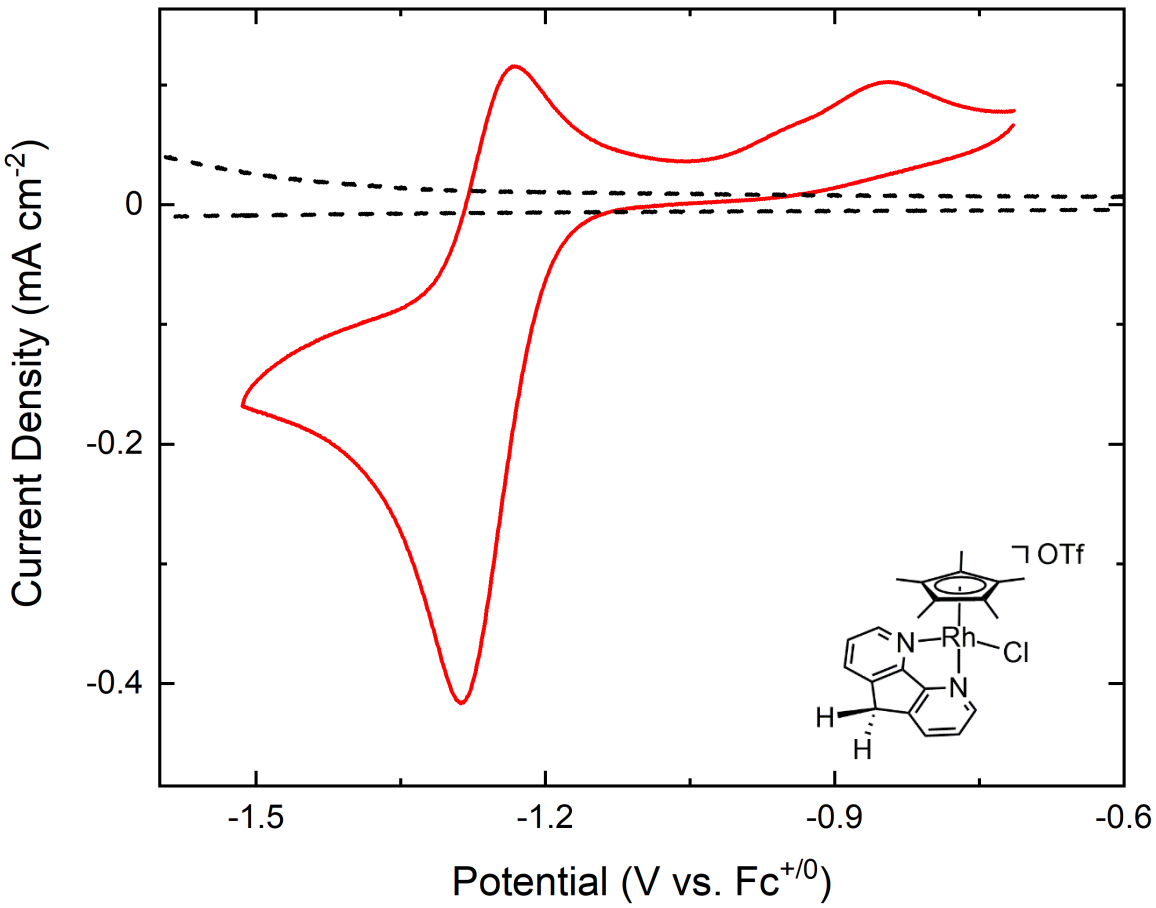

Figure A43: Cyclic voltammetry of **2** (**red**) in 0.1 M $TBAPF_6$/MeCN solution. The black dashed line is the blank taken prior to the beginning of the experiment.

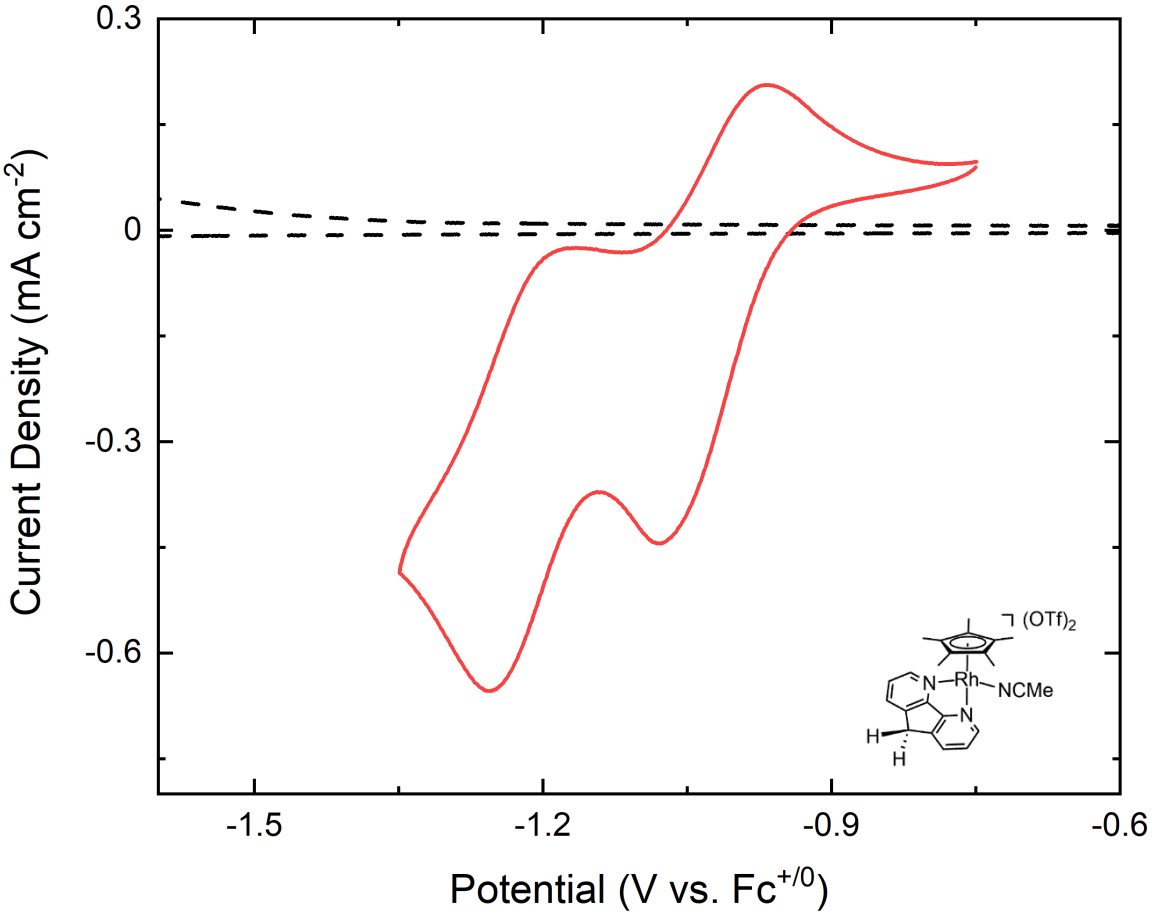

Figure A44: Cyclic Voltammetry of **2-NCMe** (**red**) in 0.1 M $TBAPF_6$/MeCN solution. The black dashed line is the blank taken prior to the beginning of the experiment.

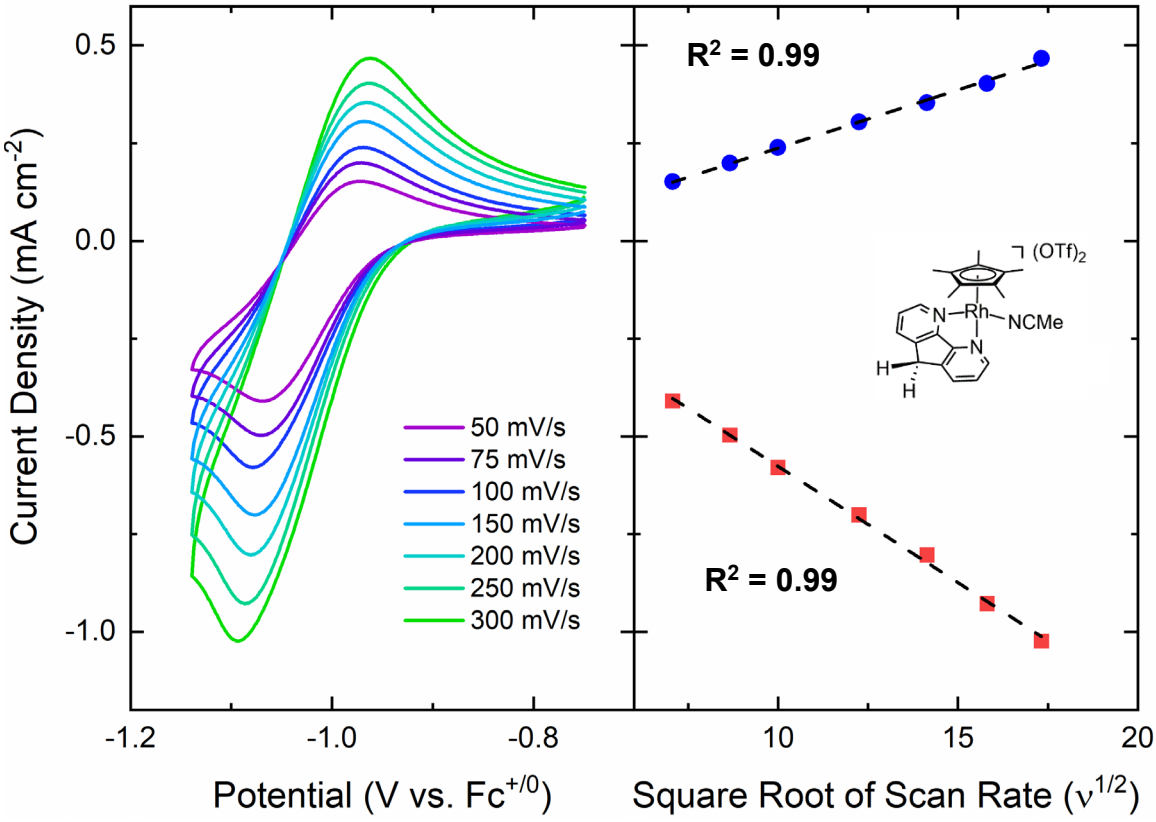

Figure A45: Scan rate dependence studies (left) and peak anodic and cathodic current density of the first electron transfer event as a function of the square root of scan rate (right) for complex **2-NCMe**.

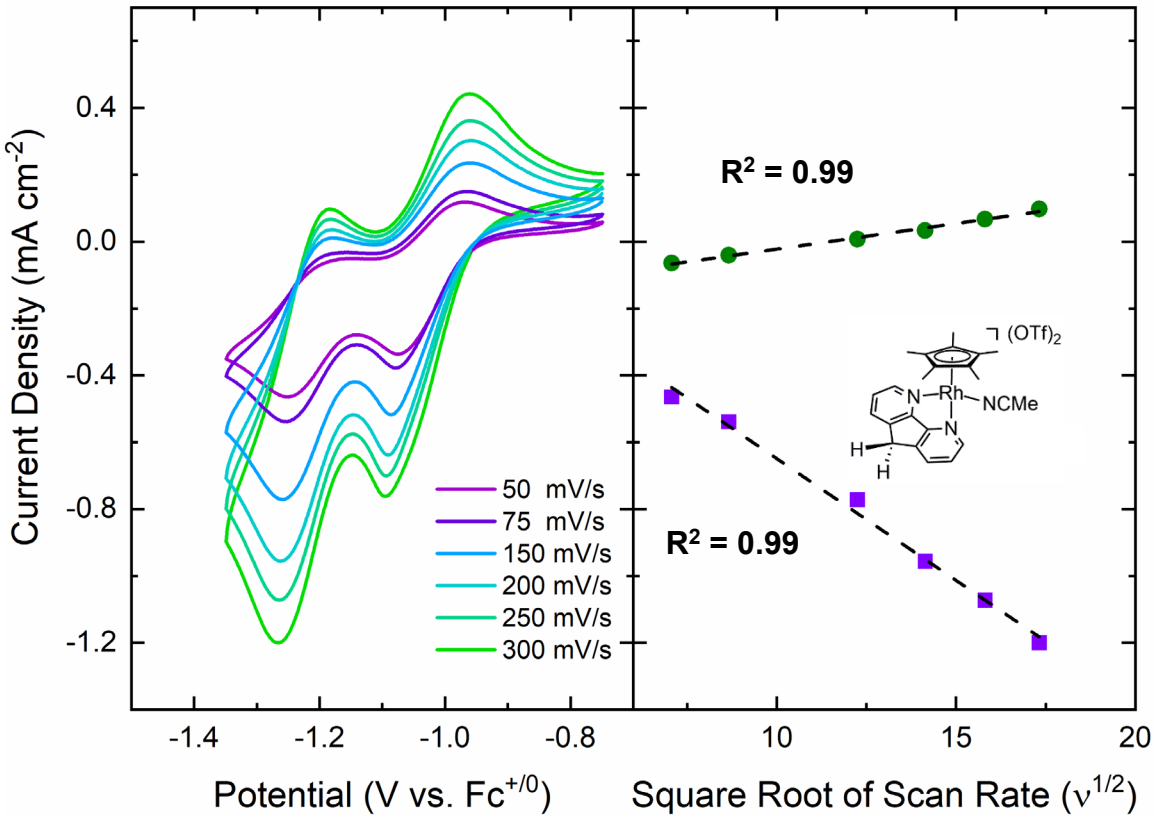

Figure A46: Scan rate dependence studies (left) and peak anodic and cathodic current density of the second electron transfer event as a function of the square root of scan rate (right) for complex **2-NCMe**.

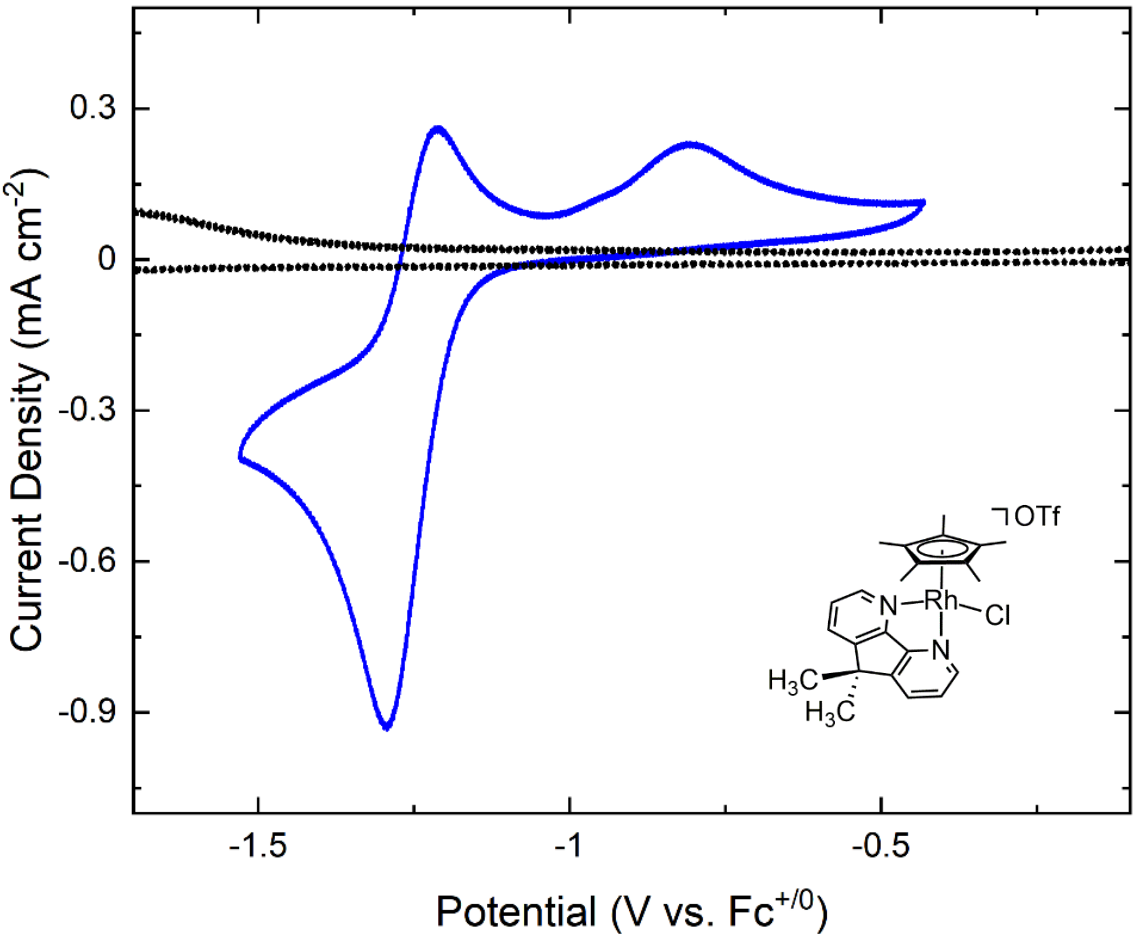

Figure A47: Cyclic Voltammetry of **3** (**blue**) in 0.1 M $TBAPF_6$/MeCN solution. The black dotted line is the blank taken prior to the beginning of the experiment.

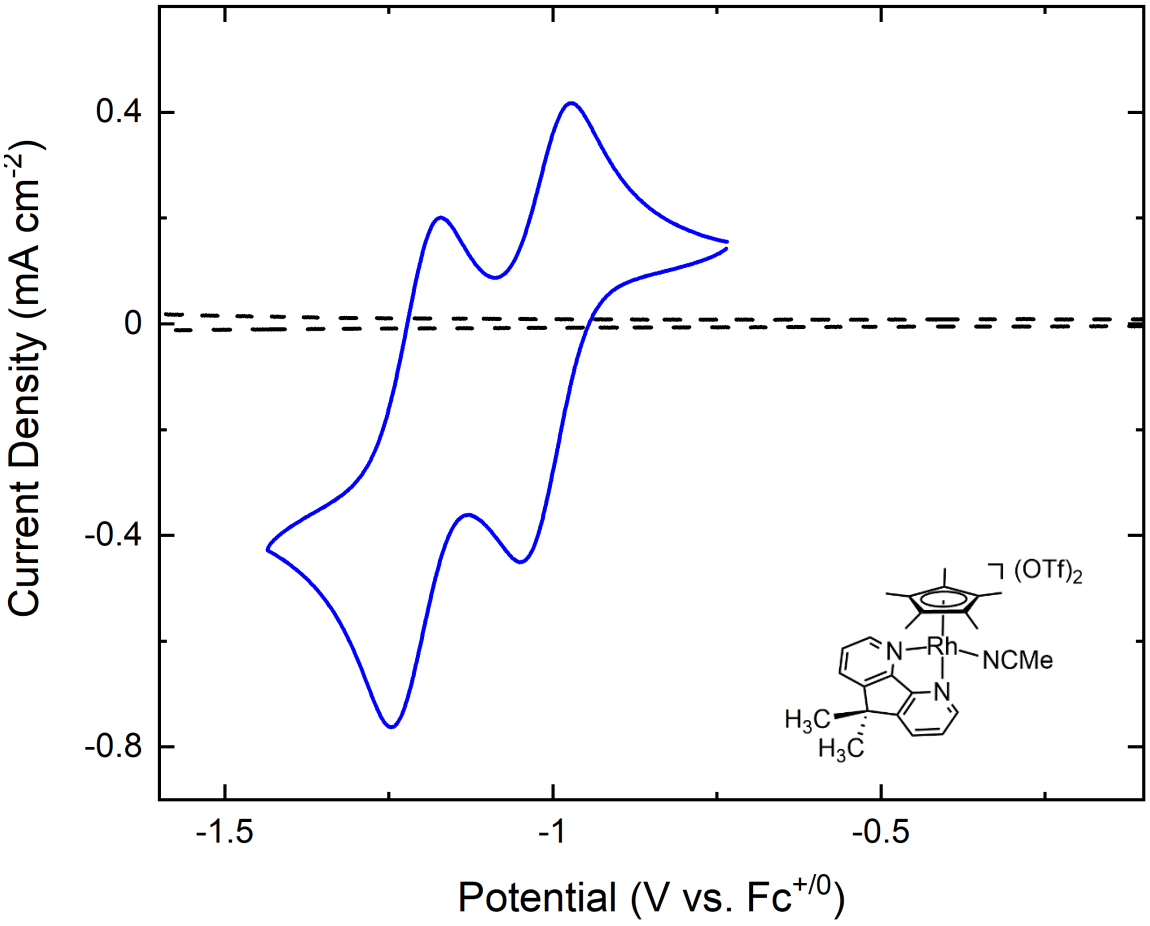

Figure A48: Cyclic Voltammetry of **3-NCMe** (**blue**) in 0.1 M $TBAPF_6$/MeCN solution. The black dashed line is the blank taken prior to the beginning of the experiment.

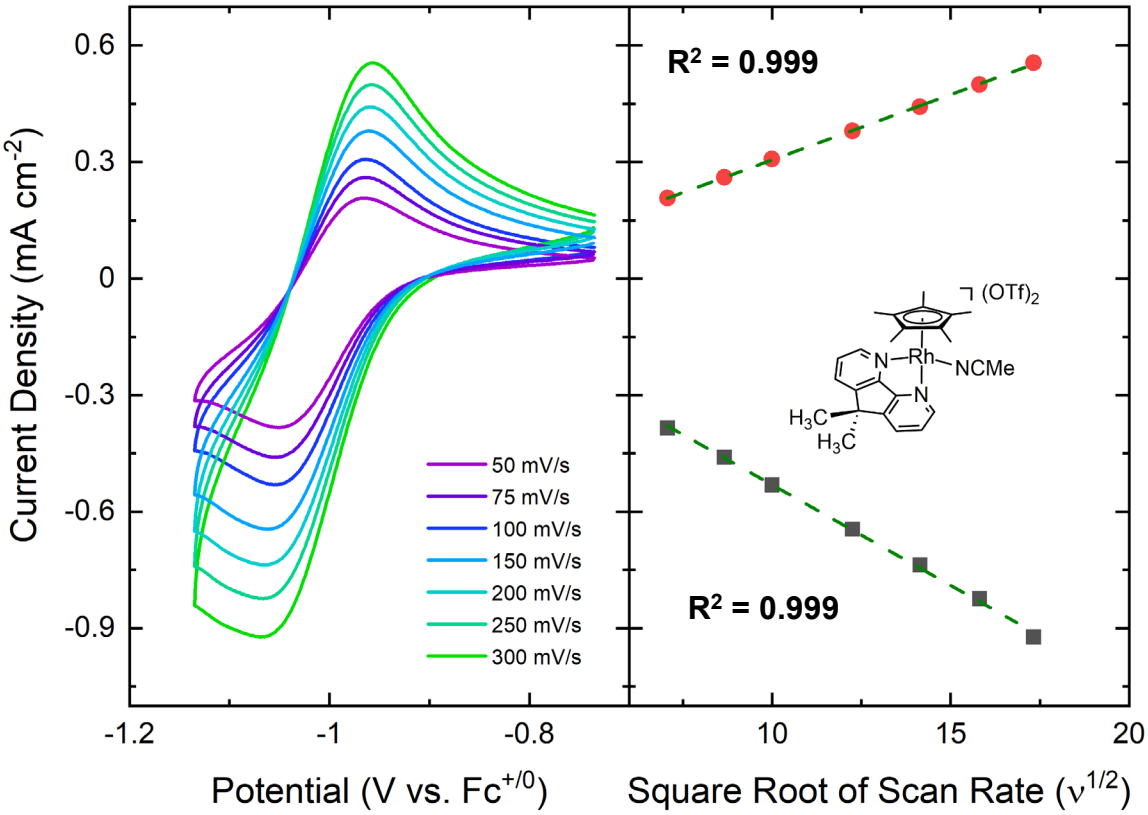

Figure A49: Scan rate dependence studies (left) and peak anodic and cathodic current density of the first electron transfer event as a function of the square root of scan rate (right) for complex **3-NCMe**.

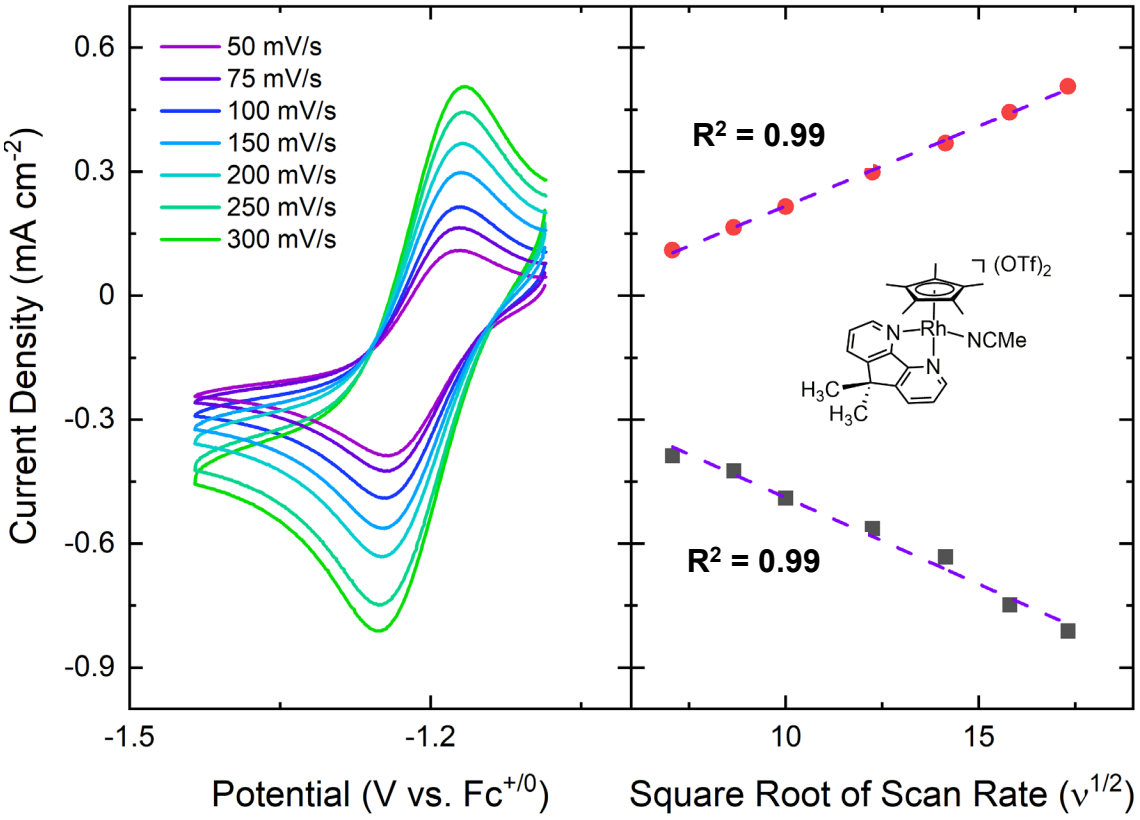

Figure A50: Scan rate dependence studies (left) and peak anodic and cathodic current density of the second electron transfer event as a function of the square root of scan rate (right) for complex **3-NCMe**.

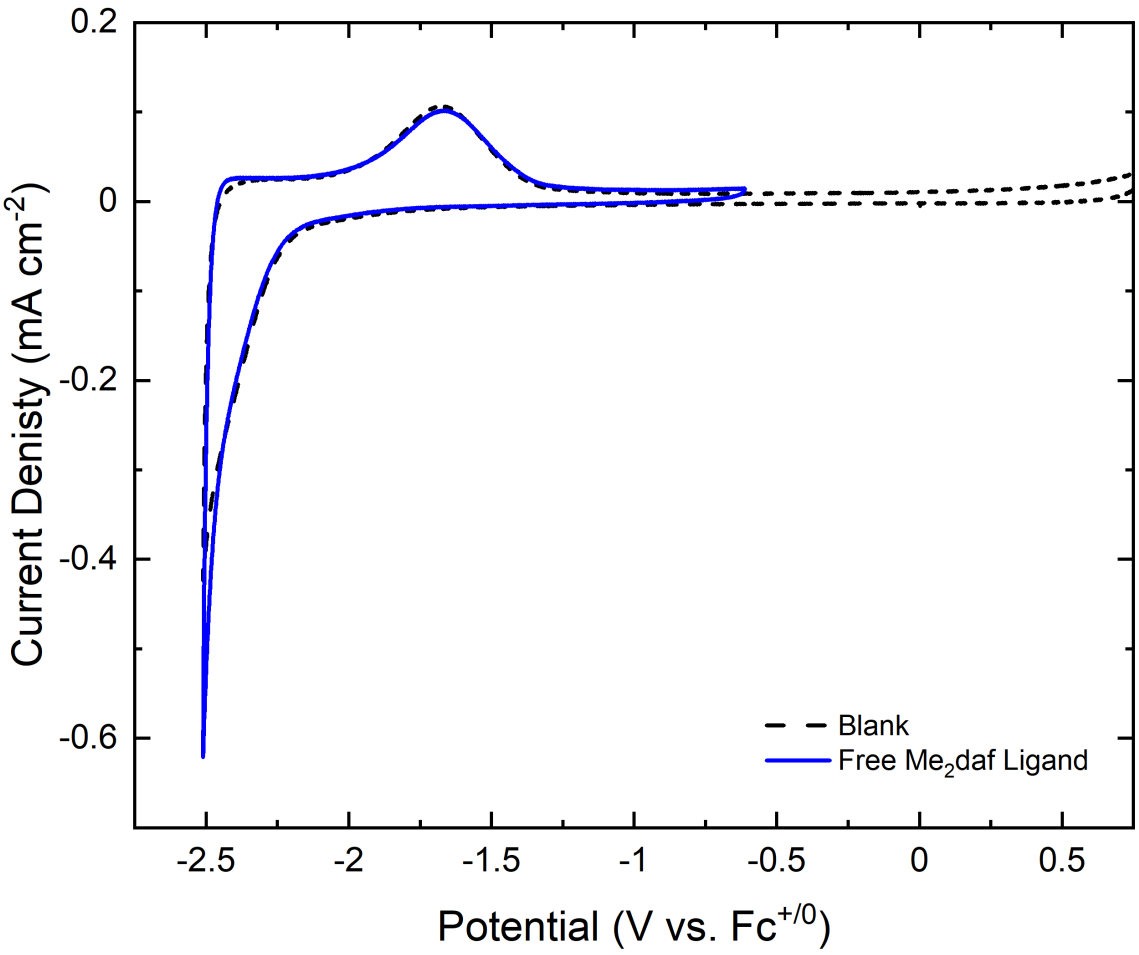

Figure A51: Cyclic Voltammetry of free **Me₂daf** ligand (**blue**) in 0.1 M $TBAPF_6$/MeCN solution. The black dashed line is the blank taken prior to the beginning of the experiment. The irreversible reduction and corresponding oxidation are a result of reducing the solvent; these features are present in both the blank and in the examination of free **Me₂daf** ligand.

Electrochemical Chloride Titration

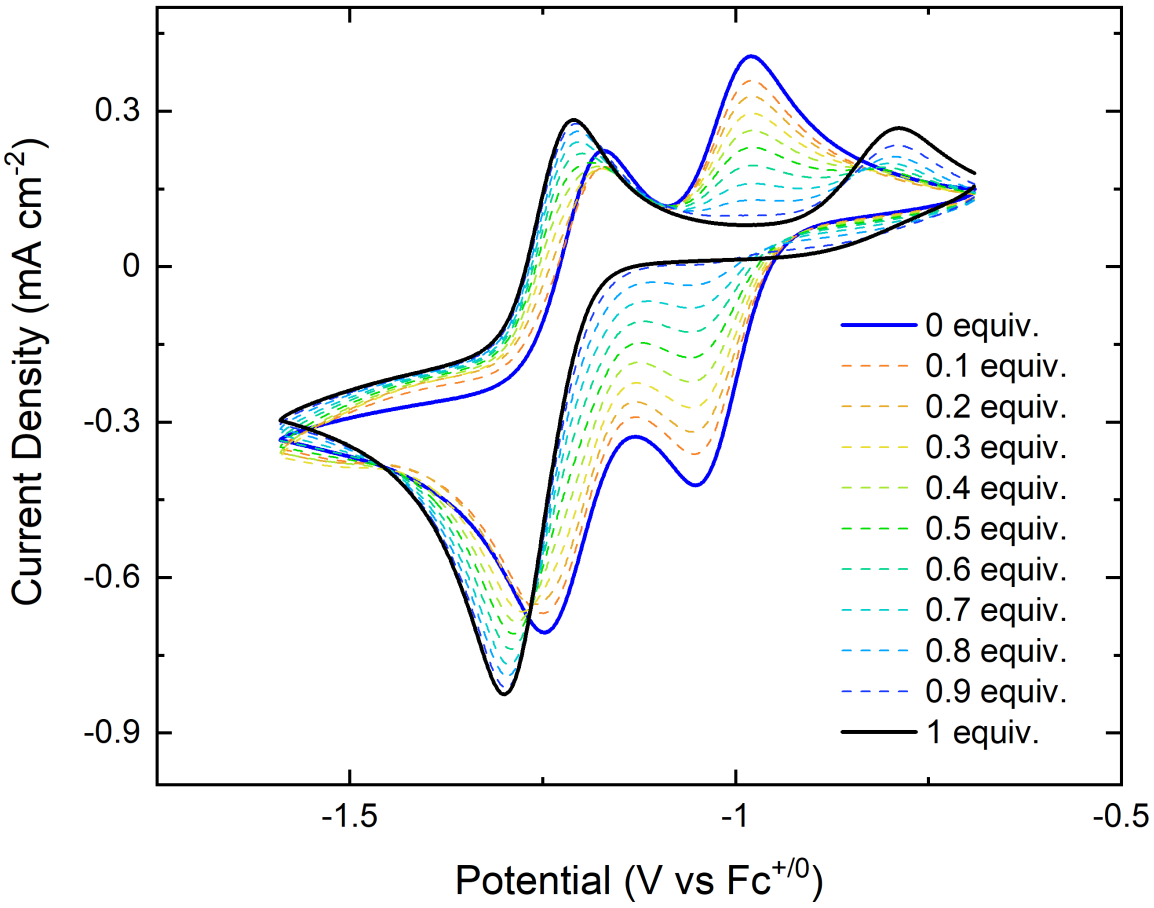

Figure A52: Electrochemical chloride titration of **3-NCMe** using increasing equivalents of tetrabutylammonium chloride to generate **3** in 0.1 M $TBAPF_6$/MeCN solution.

Spectrochemical Redox Titration

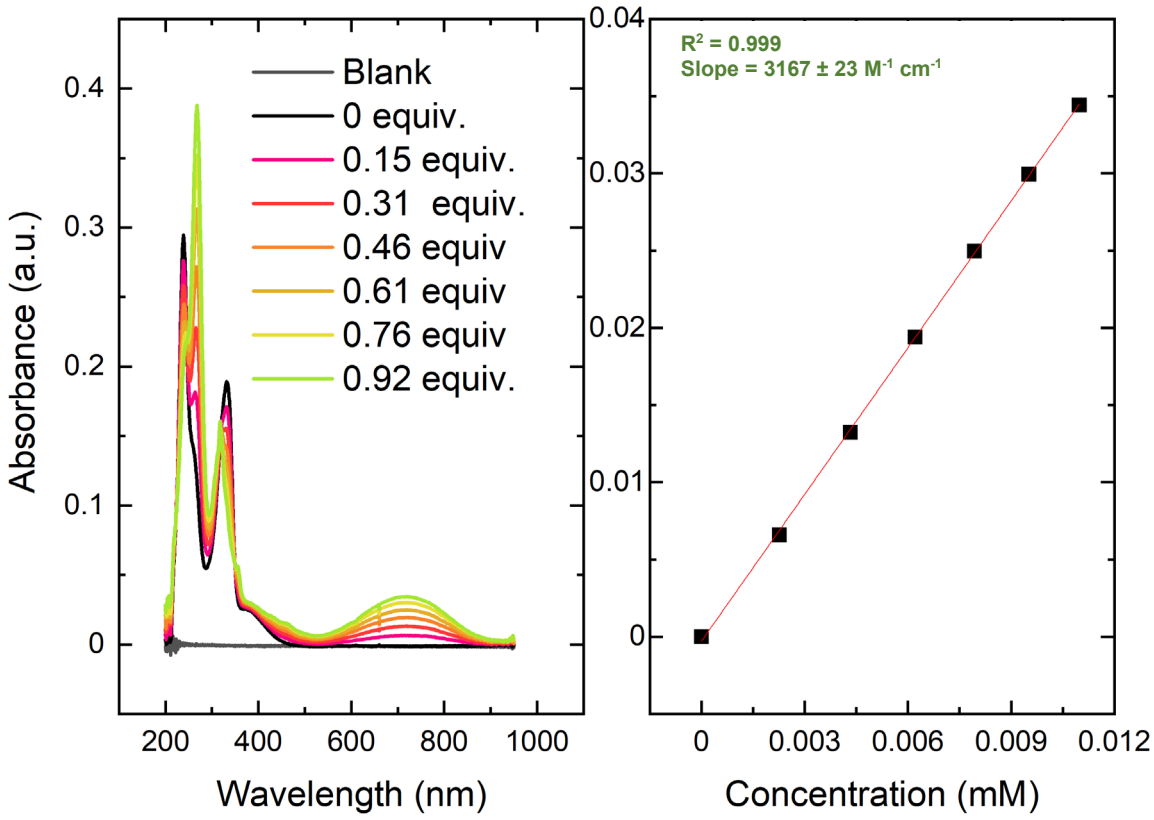

Figure A53: Spectrochemical redox titration of **3-NCMe** (Rh(III)) using increasing equivalents of cobaltocene in THF. UV-Vis of the generated Rh(II) species starting from **3-NCMe** and the resulting absorbance vs. concentration plot when monitoring at 716 nm. Isosbestic points located at 349, 320, 246, and 223 nm.

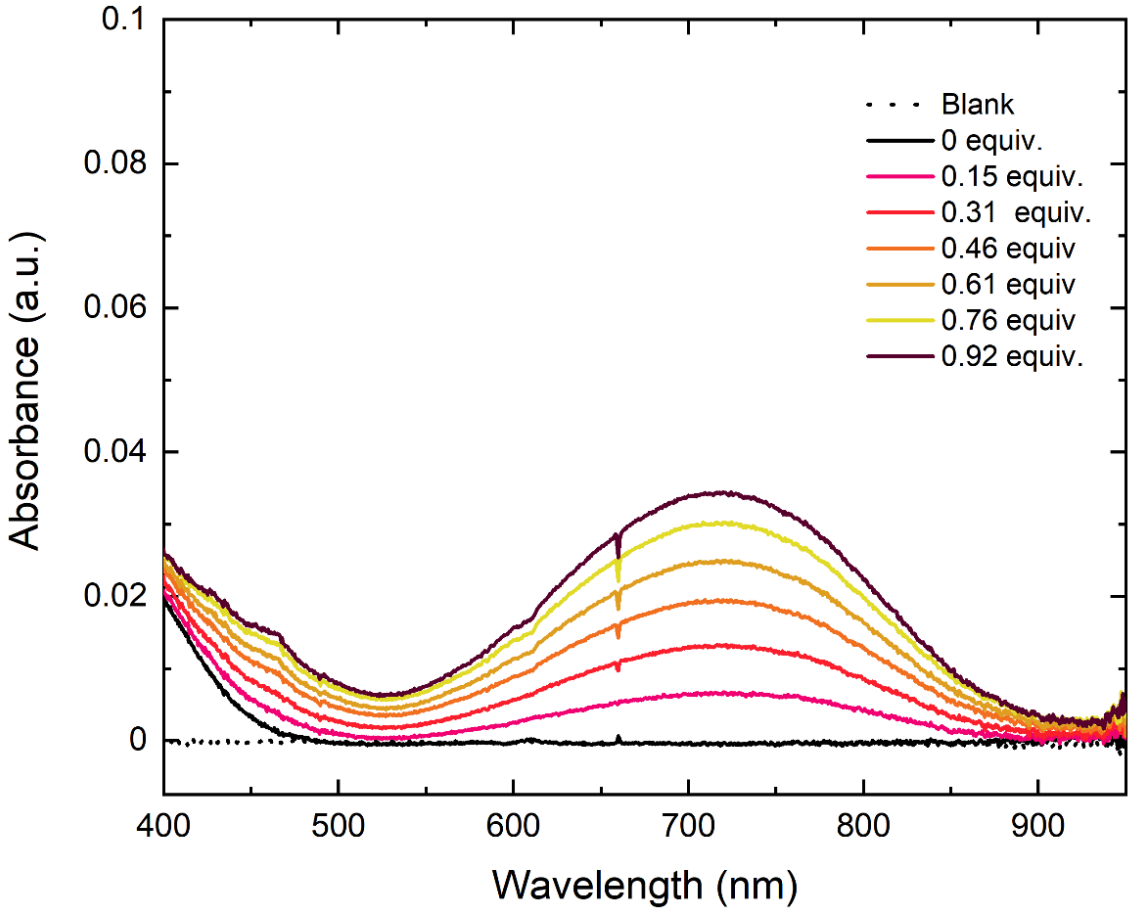

Figure A54: Zoomed-in look of the visible-region during spectrochemical redox titration of **3-NCMe** to generate a Rh(II) species.

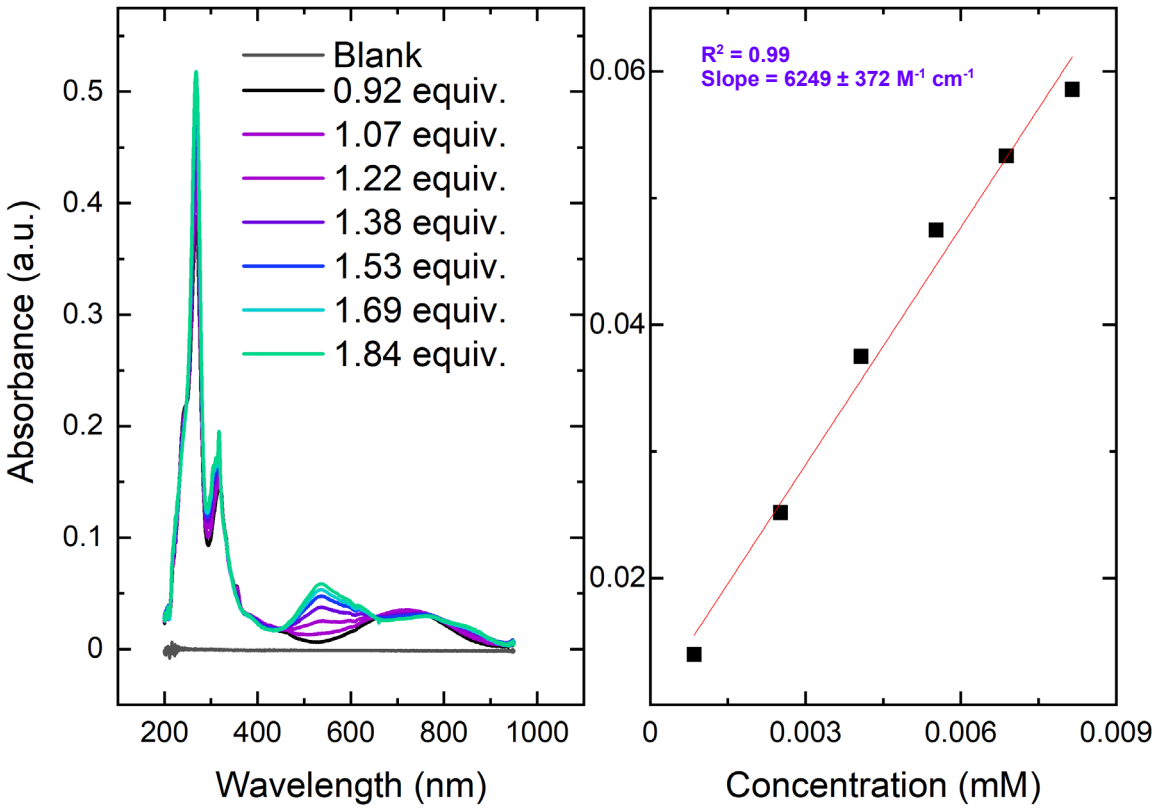

Figure A55: Continuation of the spectrochemical redox titration of **3-NCMe** (Rh(III)) using increasing equivalents of cobaltocene in THF. UV-Vis of the generated Rh(I) species starting from the generated Rh(II) species and the resulting absorbance vs. concentration plot monitored at 534 nm. Isosbestic points located at 660, 320, and 247 nm.

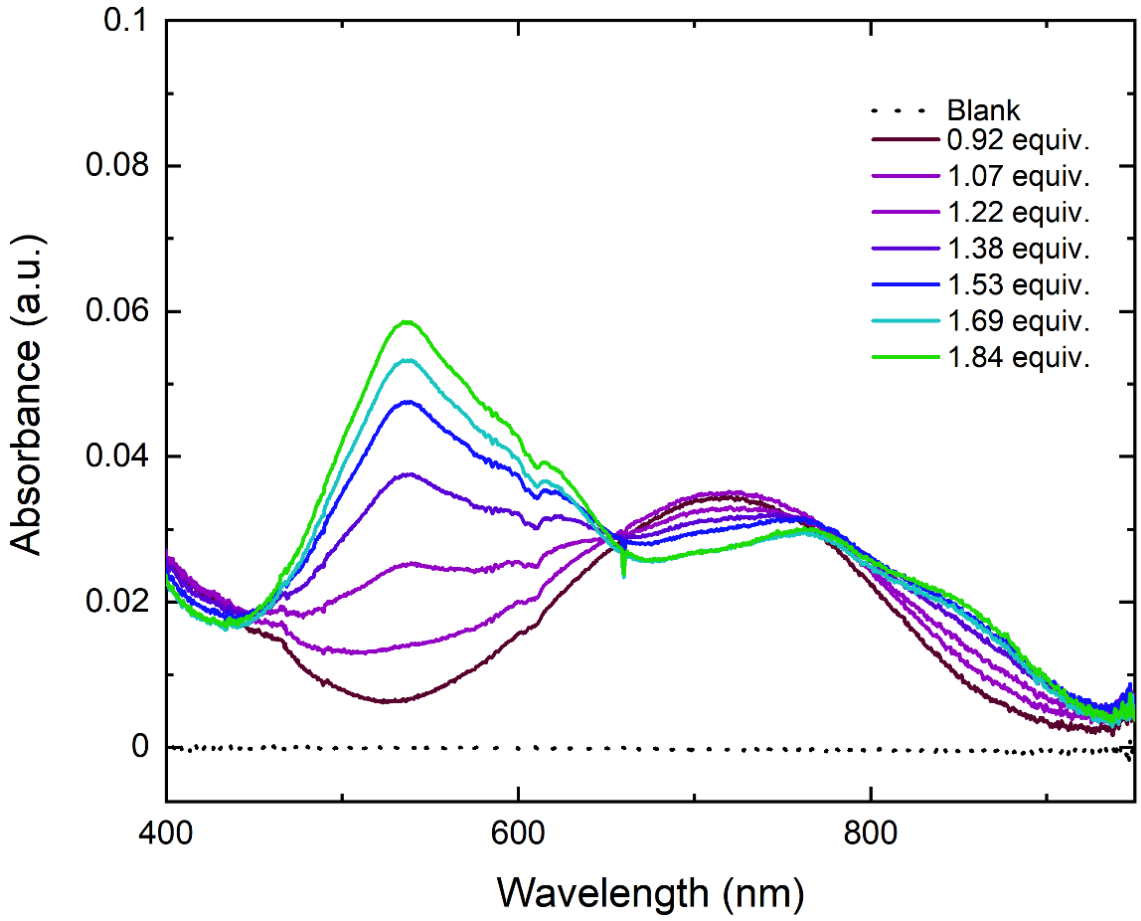

Figure A56: Zoomed-in look of the visible-region during spectrochemical redox titration of **3-NCMe** to generate a Rh(I) species.

Electron Paramagnetic Resonance

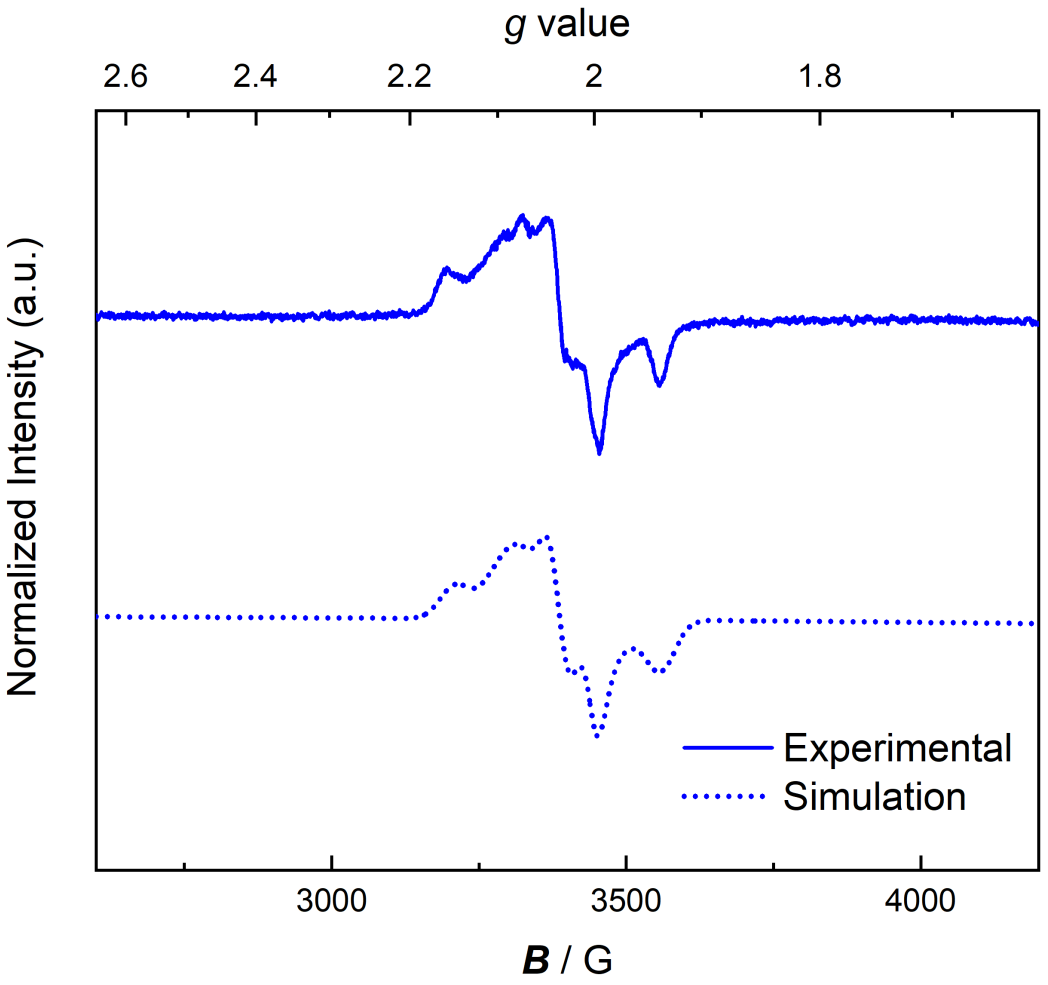

Figure A57: Experimental spectrum (solid-blue): perpendicular-mode, X-band EPR spectrum of the product of reduction of **3-NCMe** with $CoCp_2$ (MeCN, 7 K, frequency = 9.641497 GHz, power = 2 mW). Simulated spectrum (dashed-blue): Easyspin simulation of EPR data; simulations parameters for component **A**: g_x =2.15, g_y = 2.03, g_z = 1.94, A_x = 34 MHz, A_y = 72 MHz, A_z = 20 MHz, HStrain(x) = 141 MHz, HStrain(y) = 43 MHz, HStrain(z) = 125, linewidth = 2.76, weight = 1 ; component **B**: g_x = 2.08, g_y = 2.02, g_z = 2.00, A_x = 24 MHz, A_y = 14 MHz, A_z = 143 MHz, HStrain(x) = 160 MHz, HStrain(y) = 416 MHz, HStrain(z) = 64 MHz, linewidth = 0.082, weight = 0.47.

Crystallographic Information

Refinement Details

X-ray Crystallographic Studies for 1 (q10k), 2 (q84i), 3 (q71j), 1-NCMe (q20k), 2-NCMe (q21k), 3-NCMe (q54k), 4 (v46f), 2-red (q52k), Bn_3daf (v89e), 1-PF_6 (v46e), and 3-NCMePF_6 (q89h).

Crystals of **1** (q10k), **2** (q84i), **3** (q71j), **1-NCMe** (q20k), **2-NCMe** (q21k), **3-NCMe** (q54k), **4** (v46f), **2-red** (q52k), **Bn_3daf** (v89e), **1-PF_6** (v46e), and **3-NCMePF_6** (q89h) were mounted with Paratone N oil in MiTeGen nylon loops and placed in a cold nitrogen stream on a Bruker Proteum diffractometer equipped with two CCD detectors (Apex2 and Platinum 135) sharing a common MicroStar microfocus Cu rotating anode generator running at 45 mA and 60 kV (Cu Kα = 1.54178 Å). Complete sets of low temperature (200 K) X-ray diffraction data were obtained for all eleven compounds using monochromated Cu radiation with the Apex II detector (**1**, **2**, **3**, **1-NCMe**, **2-NCMe**, **3-NCMe**, **2-red**, and **3-NCMePF_6**) positioned at 50.0 mm and equipped with Helios multilayer mirror optics or the Platinum 135 detector (**4, Bn_3daf, 1-PF_6**) positioned at 80.0 mm and equipped with Helios high-brilliance multilayer mirror optics. Totals of 3930 (**1**), 1700 (**2**), 1638 (**3**), 3874 (**1-NCMe**), 4429 (**2-NCMe**), 2292 (**3-NCMe**), 1972 (**4**), 2191 (**2-red**), 1662 (**Bn_3daf**), 2091 (**1-PF_6**), and 2782 (**3-NCMePF_6**) 1.0°-wide ω- or ϕ-scan frames were collected with counting times of 4-6 seconds (**1, 2, 3, 1-NCMe, 2-NCMe and 1-PF_6**), 5-8 seconds (**3-NCMe**), 12-60 seconds (**4**), 10-30 seconds (**2-red**), 8-12 seconds (**Bn_3daf**), and 10-60 seconds (**3-NCMePF_6**).

Preliminary lattice constants for all crystals were obtained with SMART in the Bruker Apex2 Software Suite.[1] Integrated reflection intensities for all eleven crystals were produced using

SAINT in the Bruker Apex2 Software Suite.[1] Data sets were corrected for variable absorption effects with SADABS.[2] Numerical face-indexed absorption corrections were used for **1-NCMe** (q20k) and **2-NCMe** (q21k). The remaining data sets were corrected empirically using equivalent reflections. The Bruker software package SHELXTL[3] was used to generate the initial instruction file; then OLEX2[4] was used to solve each structure using intrinsic phasing. Final stages of weighted full-matrix least-squares refinement were conducted using F_o^2 data with SHELXTL[3] or the OLEX2[4] software package equipped with XL.[4] The relevant crystallographic and structure refinement data for all eleven structures are given in Table S1. The final structural model for each structure incorporated anisotropic thermal parameters for all full-occupancy nonhydrogen atoms. Isotropic thermal parameters were used for all included hydrogen atoms. Unless stated otherwise for a specific structure, non-methyl hydrogen atoms were fixed at idealized riding model sp^2- or sp^3-hybridized positions with C–H bond lengths of 0.95 – 0.99 Å. Methyl groups for the Cp* ligands, ordered acetonitrile moieties and Me_2daf ligands were incorporated into the structural model as idealized sp^3-hybridized riding model rigid rotors with C-H bond lengths of 0.98 Å that were allowed to rotate about their C–C bonds in least-squares refinement cycles. Whenever possible, methylene hydrogen atoms for diazafluorene ligands were located from difference Fouriers and initially included in the structural model as independent isotropic atoms whose parameters were allowed to vary in least-squares refinement cycles.

Table A1: Crystal Refinement Data.

	1 (q10k)	2 (q84i)	3 (q71j)
CCDC accession code	2038432	2038434	2038439
Empirical formula	$C_{22}H_{21}ClF_3N_2O_4RhS$	$C_{22}H_{23}ClF_3N_2O_3RhS$	$C_{24}H_{27}ClF_3N_2O_3RhS$
Formula weight	604.83	590.84	618.89
Temperature	200 K	200 K	200 K
Wavelength	1.54178 Å	1.54178 Å	1.54178 Å
Crystal system	triclinic	orthorhombic	orthorhombic
Space group	P-1 – C_i^1 (No. 2)	$P2_12_12_1 – D_2^4$ (No.19)	$P2_12_12_1 – D_2^4$ (No.19)
a	8.1461(3) Å	8.1232(9) Å	8.0252(2) Å
b	16.4108(5) Å	12.6604(15) Å	13.7687(3) Å
c	18.4277(5) Å	22.685(3) Å	23.2386(6) Å
α	73.257(1)°	90°	90°
β	89.324(1)°	90°	90°
γ	89.447(1)°	90°	90°
Volume	2358.84(13) $Å^3$	2333.0(5) $Å^3$	2567.79(11) $Å^3$
Z	4	4	4
Density (calculated)	1.703 g/cm^3	1.682 g/cm^3	1.601 g/cm^3
Absorption coefficient	8.234 mm^{-1}	8.273 mm^{-1}	7.545 mm^{-1}
F(000)	1216	1192	1256
Crystal size	0.105 × 0.09 × 0.055 mm^3	0.15 × 0.14 × 0.135 mm^3	0.2 × 0.18 × 0.14 mm^3
Number of data frames/time	3930 / 4-6 seconds	1700 / 4-6 seconds	1638 / 4-6 seconds
2-Theta range	5.008 to 140.51°	7.794 to 139.47°	7.462 to 140.46°
Index ranges	$-9 \le h \le 8$, $-19 \le k \le 19$, $-21 \le l \le 22$	$-9 \le h \le 9$, $-14 \le k \le 11$, $-25 \le l \le 27$	$-9 \le h \le 9$, $-16 \le k \le 15$, $-17 \le l \le 27$
Reflections collected	30235	15077	10490
Independent reflections	8270 [R_{int} = 0.044]	4067 [R_{int}= 0.039]	4264 [R_{int} = 0.046]
Completeness/θ_{max}	96.0% / 66.00°	99.5% / 66.00°	99.8% / 66.00°
Absorption correction	Multi-Scan	Multi-Scan	Multi-Scan
Max. and min. transmission	1.000 and 0.636	1.000 and 0.742	1.000 and 0.452
Refinement method	Full-matrix least-squares on F^2	Full-matrix least-squares on F^2	Full-matrix least-squares on F^2
Data / restraints / parameters	8270/0/642	4067/0/305	4264/0/324
Goodness-of-fit on F^2	1.052	1.164	1.100
Final R indices [I>2σ(I)]	R_1= 0.049, wR_2= 0.124	R_1= 0.035, wR_2= 0.073	R_1 = 0.039, wR_2 = 0.099
R indices (all data)	R_1= 0.050, wR_2= 0.126	R_1= 0.035, wR_2= 0.073	R_1 = 0.039, wR_2 = 0.100
Largest diff. peak and hole	1.49 and -1.47 $e^-/Å^3$	1.78 and -0.92 $e^-/Å^3$	1.41 and -1.43 $e^-/Å^3$

	1-NCMe (q20k)	2-NCMe (q21k)	3-NCMe (q54k)
CCDC accession code	2038431	2038438	2038440
Empirical formula	$C_{25}H_{24}F_6N_3O_7RhS_2$	$C_{27}H_{29}F_6N_4O_6RhS_2$	$C_{28}H_{31.5}F_6N_{3.5}O_6RhS_2$
Formula weight	759.50	786.57	794.10
Temperature	200 K	200K	200K
Wavelength	1.54178 Å	1.54178 Å	1.54178 Å
Crystal system	triclinic	triclinic	monoclinic
Space group	P-1 – C_i^1 (No. 2)	P-1– C_i^1 (No. 2)	$P2_1/n$ – C_{2h}^5 (No .14)
a	8.6396(3) Å	14.1667(6) Å	9.2985(4) Å
b	13.2145(4) Å	14.3906(6) Å	28.4503(13) Å
c	13.9275(4) Å	18.5208(7) Å	26.0122(12) Å
α	91.267(1)°	112.197(2)°	90°
β	104.718(1)°	107.740(2)°	99.981(3)°
γ	106.629(1)°	95.324(2)°	90°
Volume	1465.85(8) $Å^3$	3235.9(2) $Å^3$	6777.3(5) $Å^3$
Z	2	4	8
Density (calculated)	1.721 g/cm^3	1.615 g/cm^3	1.557 g/cm^3
Absorption coefficient	6.841 mm^{-1}	6.204 mm^{-1}	5.925 mm^{-1}
F(000)	764	1592	3224
Crystal size	0.11 × 0.08 × 0.07 mm^3	0.26 × 0.138 × 0.04 mm^3	0.21 × 0.02 × 0.02 mm^3
Number of data frames/time	3874 / 4-6 seconds	4429 / 4-6 seconds	2292 / 5-8 seconds
2-Theta range	6.60 to 140.13°	5.54 to 140.43°	3.11 to 140.83°
Index ranges	$-10 \le h \le 10$, $-13 \le k \le 16$, $-16 \le l \le 16$	$-17 \le h \le 16$, $-16 \le k \le 17$, $-22 \le l \le 22$	$-11 \le h \le 11$, $-33 \le k \le 29$, $-23 \le l \le 31$
Reflections collected	18471	45238	49617
Independent reflections	5138 [R_{int}= 0.047]	11367 [R_{int}= 0.052]	12671 [R_{int} = 0.085]
Completeness/θ_{max}	96.0% / 66.00°	96.1% / 66.00°	99.9%, 66.00°
Absorption correction	Numerical face-indexed	Numerical face-indexed	Multi-Scan
Max. and min. transmission	1.000 and 0.598	1.000 and 0.174	1.000 amd 0.636
Refinement method	Full-matrix least-squares on F^2	Full-matrix least-squares on F^2	Full-matrix least-squares on F^2
Data / restraints / parameters	5138/0/403	11367/4/843	12671/0/845
Goodness-of-fit on F^2	1.125	1.042	1.068
Final R indices [I>2σ(I)]	R_1= 0.042, wR_2= 0.105	R_1= 0.051, wR_2= 0.135	R_1 = 0.086, wR_2 = 0.227
R indices (all data)	R_1= 0.042, wR_2= 0.106	R_1= 0.055, wR_2= 0.142	R_1 = 0.091, wR_2 = 0.234
Largest diff. peak and hole	1.60 and -0.88 $e^-/Å^3$	1.62 and -1.21 $e^-/Å^3$	2.25 and -1.85 $e^-/Å^3$

	4 (v46f)	2-red (q52k)	Bn_3daf (v89e)
CCDC accession code	2038437	2038435	2038430
Empirical formula	$C_{23}H_{27}N_2Rh$	$C_{44}H_{30}N_8Na_2$	$C_{32}H_{27}BrN_2$
Formula weight	434.37	716.74	519.46
Temperature	200K	200K	200K
Wavelength	1.54178 Å	1.54178 Å	1.54178 Å
Crystal system	Monoclinic	Monoclinic	Monoclinic
Space group	$P2_1/c$ – C_{2h}^5 (No. 14)	$P2_1/n$ – C_{2h}^5 (No .14)	$P2_1/n$ – C_{2h}^5 (No .14)
a	8.8025(5) Å	14.4691(9) Å	9.6389(4) Å
b	22.5873(11) Å	15.3457(9) Å	11.8332(5) Å
c	10.8088(6) Å	16.7761(10) Å	22.4161(10) Å
α	90°	90°	90°
β	112.828(2)°	109.262(5)°	90.890(2)°
γ	90°	90°	90°
Volume	1980.73(19) $Å^3$	3516.4(4) $Å^3$	2556.45(19) $Å^3$
Z	4	4	4
Density (calculated)	1.457 g/cm^3	1.354 g/cm^3	1.350 g/cm^3
Absorption coefficient	7.014 mm^{-1}	0.869 mm^{-1}	2.353 mm^{-1}
F(000)	896	1488	1072
Crystal size	0.1 × 0.065 × 0.04 mm^3	0.03 × 0.02 × 0.02 mm^3	0.175 × 0.11 × 0.025 mm^3
Number of data frames/time	1972 / 12-60 seconds	2191 / 10-30 seconds	1662 / 8-12 seconds
2-Theta range	7.83 to 136.88°	7.01 to 140.57°	7.89 to 136.32°
Index ranges	$-10 \le h \le 10$, $-26 \le k \le 22$, $-12 \le l \le 12$	$-17 \le h \le 17$, $-18 \le k \le 13$, $-18 \le l \le 19$	$-11 \le h \le 10$, $-12 \le k \le 14$, $-23 \le l \le 26$
Reflections collected	10660	26048	11575
Independent reflections	3427 [R_{int} = 0.036]	6488 [R_{int} = 0.090]	4503 [R_{int}= 0.030]
Completeness/θ_{max}	97.0% / 66.00°	99.5% / 66.00°	98.5% / 66.00°
Absorption correction	Multi-Scan	Multi-Scan	Multi-Scan
Max. and min. transmission	1.000 and 0.859	1.000 and 0.766	1.000 and 0.793
Refinement method	Full-matrix least-squares on F^2	Full-matrix least-squares on F^2	Full-matrix least-squares on F^2
Data / restraints / parameters	3427/0/242	6488/0/607	4503/1/408
Goodness-of-fit on F^2	1.064	1.022	1.055
Final R indices [I>2σ(I)]	R_1 = 0.026, wR_2 = 0.067	R_1 = 0.055, wR_2 = 0.129	R_1= 0.038, wR_2= 0.096
R indices (all data)	R_1 = 0.029, wR_2 = 0.069	R_1 = 0.094, wR_2 = 0.152	R_1= 0.045, wR_2= 0.101
Largest diff. peak and hole	0.35 and -0.47 $e^-/Å^3$	0.17 and -0.20 $e^-/Å^3$	0.57 and -0.27 $e^-/Å^3$

	1-PF_6 (v46e)	**3-NCMePF_6 (q89h)**
CCDC accession code	2038436	2038433
Empirical formula	$C_{23}H_{21}ClF_6N_3O1.5PRh$	$C_{29}H_{39}F_{12}N_3OP_2Rh$
Formula weight	646.76	828.37
Temperature	200K	200K
Wavelength	1.54178 Å	1.54178 Å
Crystal system	monoclinic	monoclinic
Space group	$P2_1/m - C_{2h}^2$ (No. 11)	$C2/c - C_{2h}^6$ (No. 15)
a	8.8528(3) Å	38.928(2) Å
b	12.6964(5) Å	13.5456(9) Å
c	11.7024(4) Å	13.9185(10) Å
α	90°	90°
β	102.3654(9)°	102.269(4)°
γ	90°	90°
Volume	1284.82(8) $Å^3$	7171.6(8) $Å^3$
Z	2	8
Density (calculated)	1.672 g/cm^3	1.534 g/cm^3
Absorption coefficient	7.544 mm^{-1}	5.510 mm^{-1}
F(000)	646	3358
Crystal size	0.165 × 0.14 × 0.065 mm^3	0.17 × 0.04 × 0.02 mm^3
Number of data frames/time	2091 / 4-6 seconds	2782 / 10-60 seconds
2-Theta range	7.73 to 136.54°	4.64 to 142.06°
Index ranges	$-10 \le h \le 8$, $-15 \le k \le 10$, $-13 \le l \le 12$	$-45 \le h \le 46$, $-16 \le k \le 16$, $-14 \le l \le 16$
Reflections collected	7249	33274
Independent reflections	2361 [$R_{int} = 0.035$]	6491 [$R_{int} = 0.112$]
Completeness/θ_{max}	97.9% / 66.00°	96.9% / 66.00°
Absorption correction	Multi-Scan	Multi-Scan
Max. and min. transmission	1.000 and 0.630	1.000 and 0.683
Refinement method	Full-matrix least-squares on F^2	Full-matrix least-squares on F^2
Data / restraints / parameters	2361/0/188	6491/0/441
Goodness-of-fit on F^2	1.073	1.068
Final R indices [I>2σ(I)]	$R_1 = 0.041$, $wR_2 = 0.107$	$R_1 = 0.091$, $wR_2 = 0.235$
R indices (all data)	$R_1 = 0.041$, $wR_2 = 0.107$	$R_1 = 0.133$, $wR_2 = 0.268$
Largest diff. peak and hole	0.76 and -0.98 $e^-/Å^3$	2.38 and -0.80 $e^-/Å^3$

Special Refinement Details for 1

No special refinement was required.

Solid-State Structure of 1

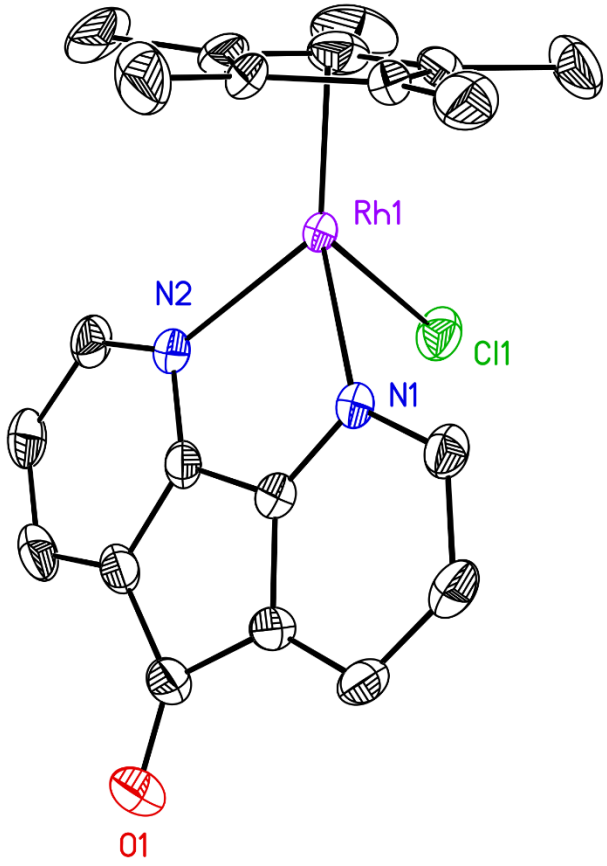

Figure A58: Solid-state structure for the first crystallographically-independent monocation of salt **1**. The second monocation of **1,** hydrogen atoms and the respective outer sphere triflate counteranions are omitted for clarity. Displacement ellipsoids are shown at the 50% probability level.

Full Solid-State Structure of 1

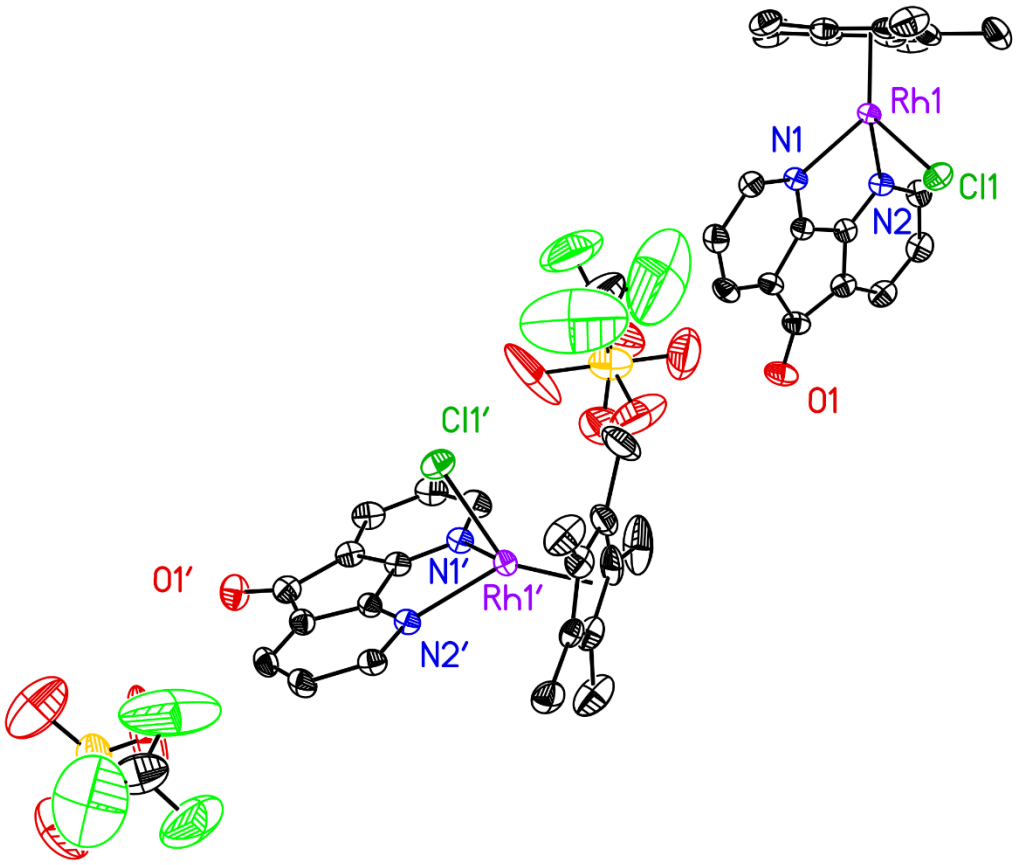

Figure A59: Full solid-state structure of the asymmetric unit for salt **1**. Hydrogen atoms are omitted for clarity. Displacement ellipsoids are shown at the 50% probability level.

Special Refinement Details for 2

Complex **2** crystallizes in the orthorhombic space group $P2_12_12_1$ and the structure was refined as a two-component 97/3 inversion twin.

Solid-State Structure of 2

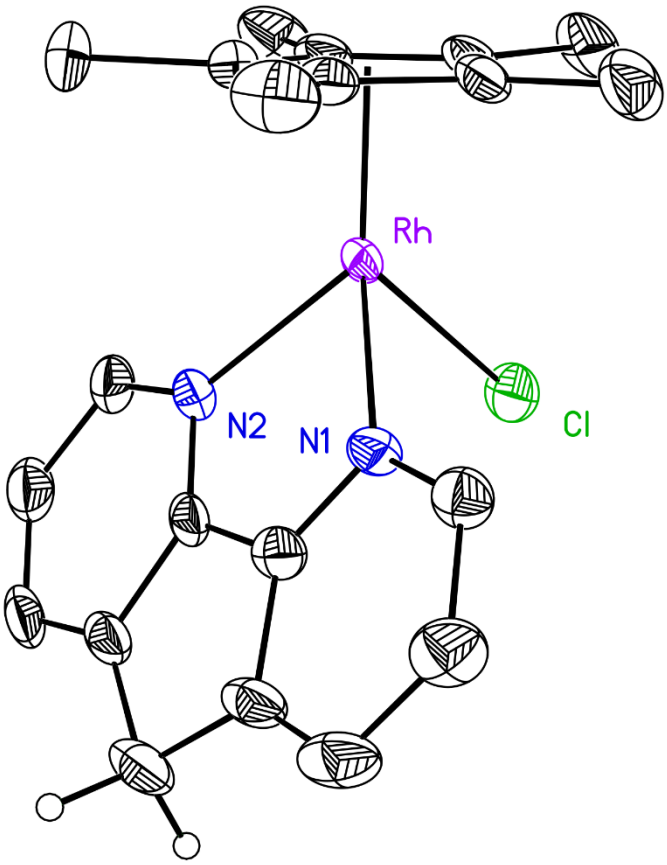

Figure A60: Solid-state structure for the monocation of salt **2**. The outer sphere triflate counteranion is omitted for clarity. Hydrogen atoms except for H11A and H11B are omitted for clarity. Displacement ellipsoids are shown at the 50% probability level.

Full Solid-State Structure of 2

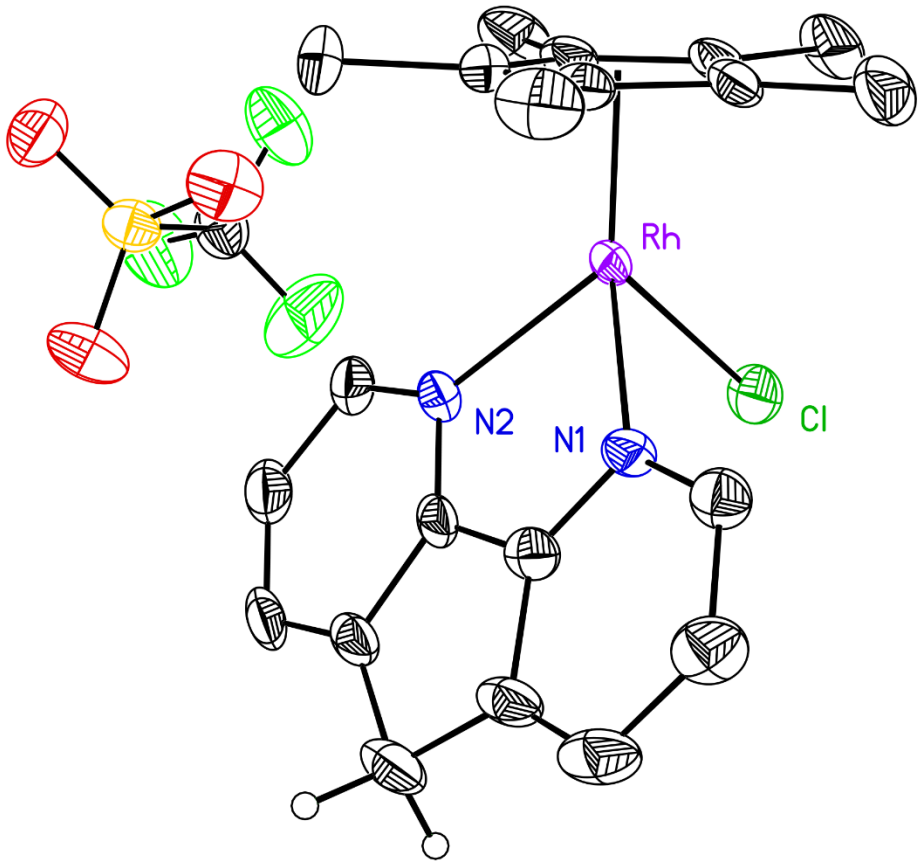

Figure A61: Solid-state structure for the asymmetric unit of salt **2**. Hydrogen atoms, except for H11A and H11B, are omitted for clarity. Displacement ellipsoids are shown at the 50% probability level.

Special Refinement Details for 3

Complex **3** crystallizes in the orthorhombic space group $P2_12_12_1$ and the structure was refined as a two-component 91/9 inversion twin.

Solid-State Structure of 3

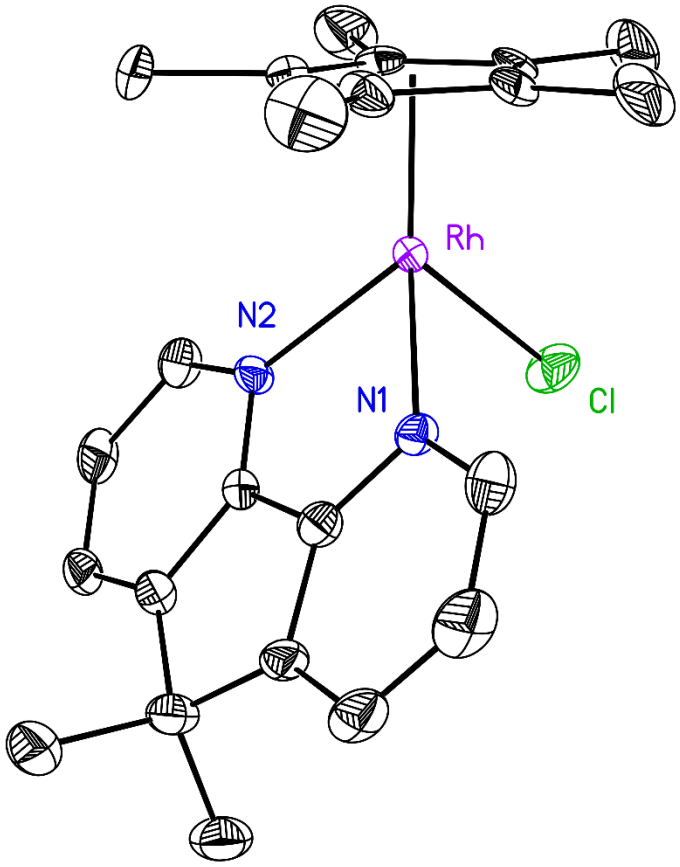

Figure A62: Solid-state structure for the monocation of salt **3**. The outer sphere triflate counteranion and all hydrogen atoms are omitted for clarity. Displacement ellipsoids are shown at the 50% probability level.

Full Solid-State Structure of 3

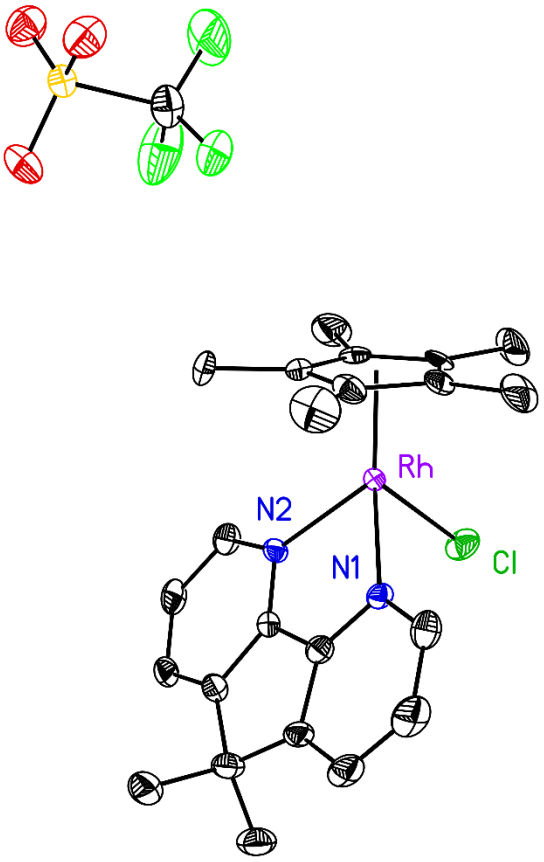

Figure A63: Full solid-state structure for the asymmetric unit of salt **3**. Hydrogen atoms are omitted for clarity. Displacement ellipsoids are shown at the 50% probability level.

Special Refinement Details for 1-NCMe

No special refinement was required.

Solid-State Structure of 1-NCMe

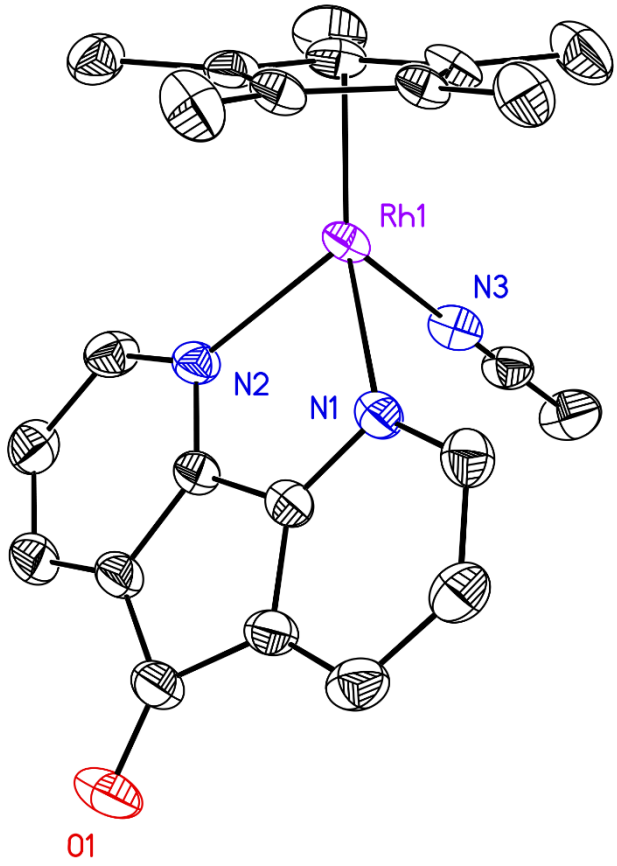

Figure A64: Solid-state structure for the dication in the asymmetric unit of salt **1-NCMe**. Hydrogen atoms and the outer sphere triflate counteranions are omitted for clarity. Displacement ellipsoids are shown at the 50% probability level.

Full Solid-State Structure of 1-NCMe

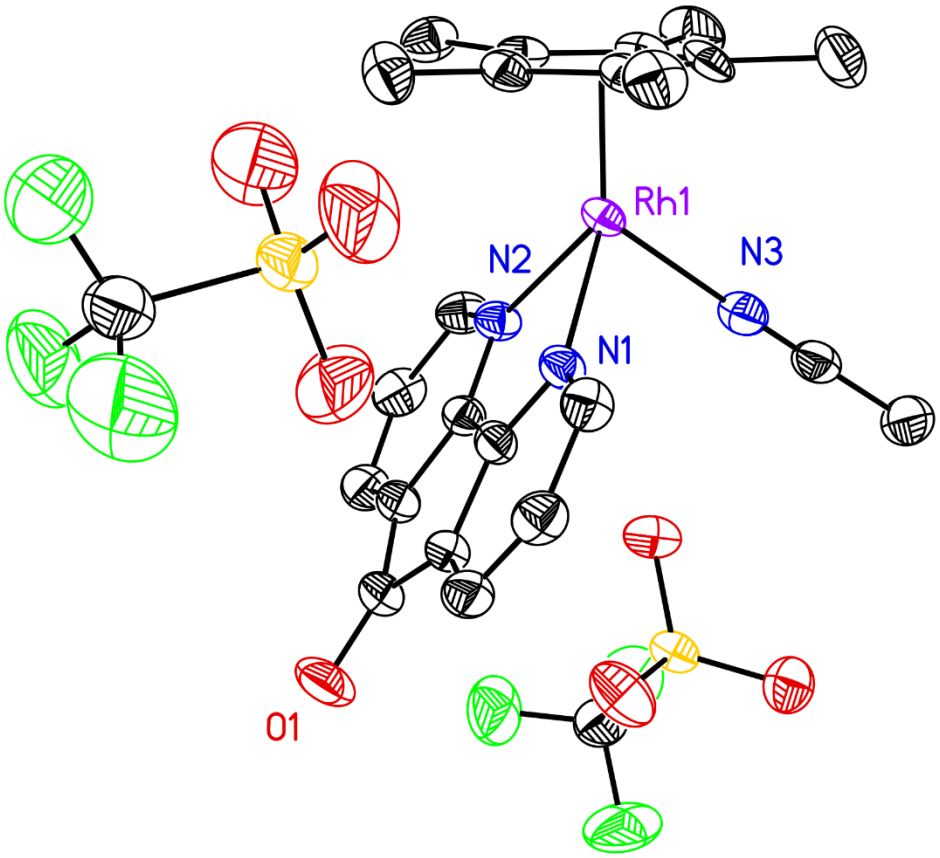

Figure A65: Full solid-state structure of the asymmetric unit for **1-NCMe**. Hydrogen atoms are omitted for clarity. Displacement ellipsoids are shown at the 50% probability level.

Special Refinement Details for 2-NCMe

No special refinement was required.

Solid-State Structure of 2-NCMe

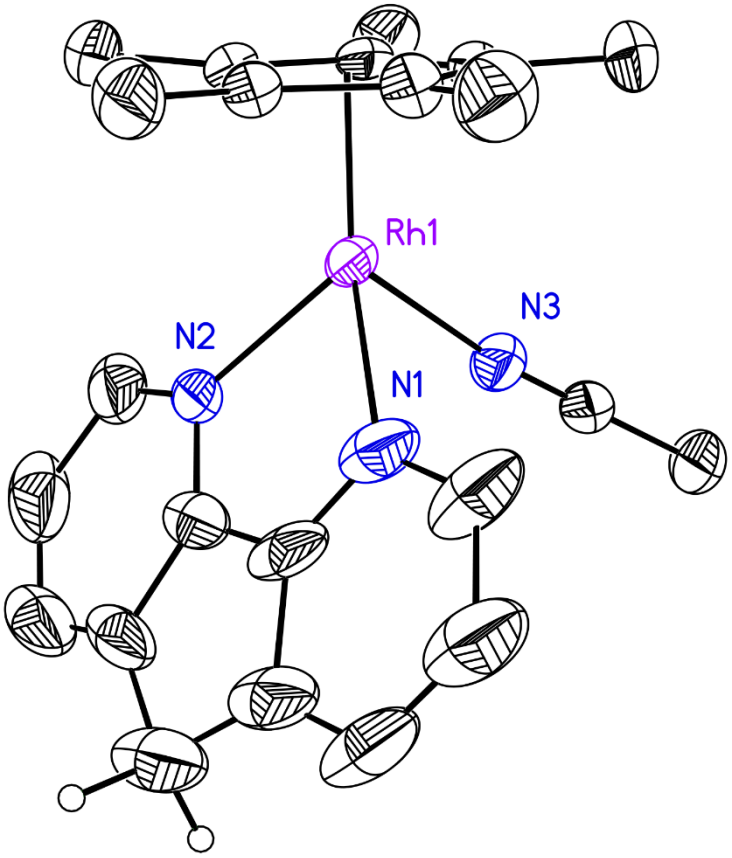

Figure A66: Solid-state structure for the first crystallographically-independent monocation in the asymmetric unit of salt **2-NCMe**. The second monocation of **2-NCMe**, their corresponding outer sphere triflate counteranions, and two co-crystallized acetonitrile molecules are omitted for clarity. Hydrogen atoms, except for H11A and H11B, are omitted for clarity. Displacement ellipsoids are shown at the 50% probability level.

Full Solid-State Structure of 2-NCMe

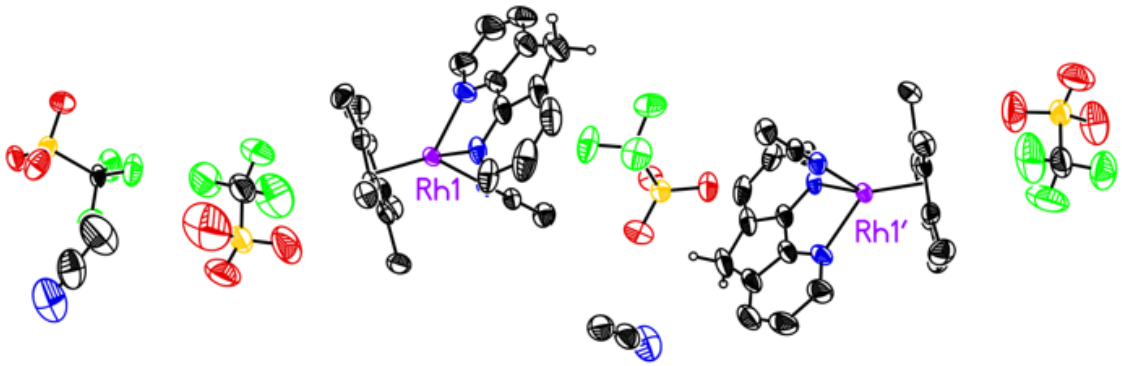

Figure A67: Solid-state structure of asymmetric unit for **2-NCMe**. Hydrogen atoms, except for H11A, H11B, H11C and H11D, are omitted for clarity. Displacement ellipsoids are shown at the 50% probability level.

Special Refinement Details for 3-NCMe

Salt **3-NCMe** crystallizes in the monoclinic space group $P2_1/n$ and the crystal was refined as a 86/14 two-component twin.

Solid-State Structure of 3-NCMe

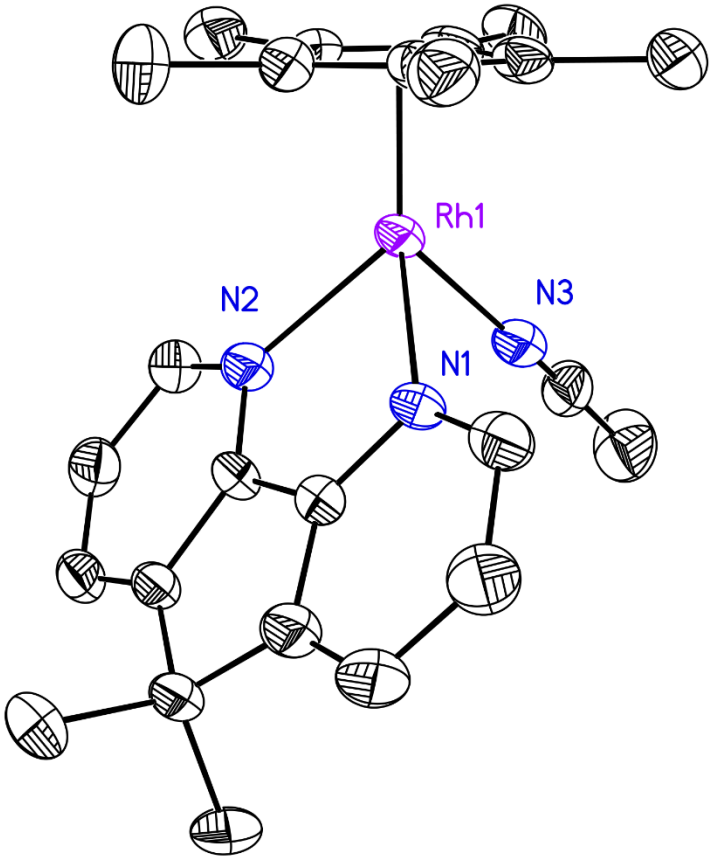

Figure A68: Solid-state structure for the first crystallographically-independent dication in the asymmetric unit of salt **3-NCMe**. The second dication of **3-NCMe**, the outer sphere triflate counteranions, a co-crystallized acetonitrile solvent molecule, and all hydrogen atoms are omitted for clarity. Displacement ellipsoids are shown at the 50% probability level.

Full Solid-State Structure of 3-NCMe

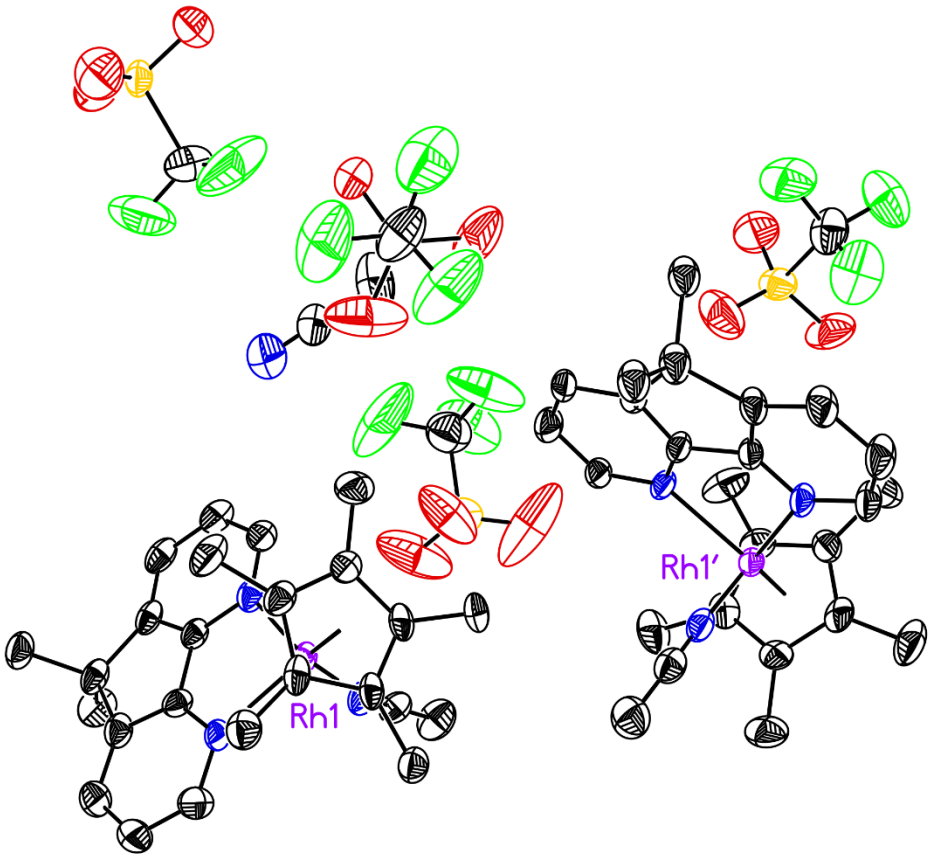

Figure A69: Full solid-state structure of the asymmetric unit for **3-NCMe**. Hydrogen atoms are omitted for clarity. Displacement ellipsoids are shown at the 50% probability level.

Special Refinement Details for 4

No special refinement was required.

Full Solid-State Structure of 4

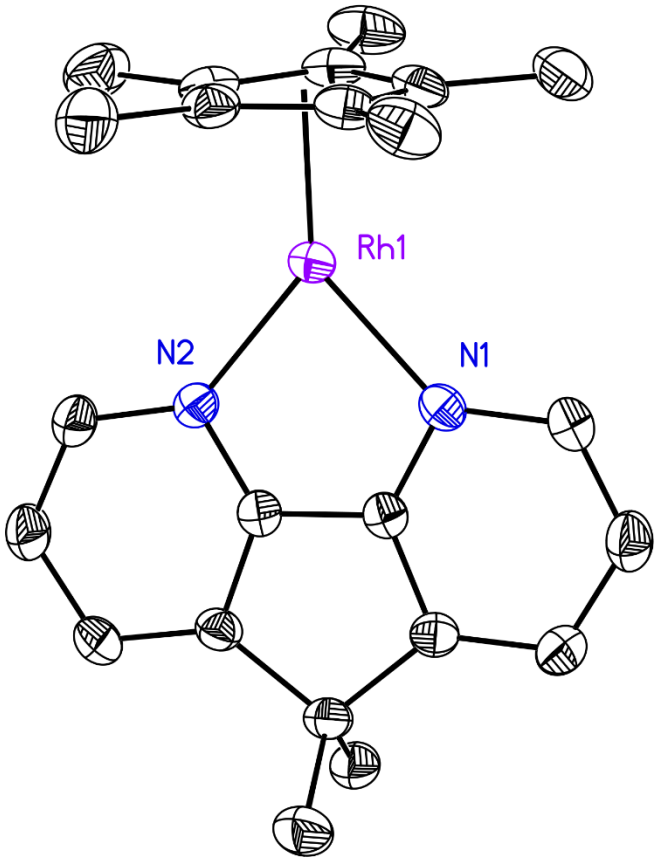

Figure A70: Full solid-state structure of the asymmetric unit for **4**. Hydrogen atoms are omitted for clarity. Displacement ellipsoids are shown at the 50% probability level.

Special Refinement Details for 2-red

All hydrogen atoms were located from a difference Fourier and included in the structural model as isotropic atoms whose parameters were allowed to vary in least-squares refinement cycles.

Synthesis and Isolation Details for 2-red

Reduction of a THF solution containing **2-NCMe** using 10 equiv. of 1% Na(Hg) results in a distinct color change from yellow to dark red. After 24 h, the solution was pumped down to dryness. The product complex could be extracted into THF; removal of the THF solvent enabled isolation of the material as a dark red solid. Crystals suitable for X-ray diffraction were obtained by vapor diffusion of pentane into a concentrated THF solution of the complex.

Thus, a product of reduction of **2-NCMe** characterized here, as observed by crystallography, is a five-coordinate dimeric structure (denoted as **2-red**) containing two sodium cations, two 4,5-diazafluorenide ligands, and two 4,5-diazafluorene ligands. This unusual structure has previously been obtained by Song and co-workers; in their work, deprotonation of daf could be accomplished with sodium hydride.[5] In our work, the structure of **2-red** highlights the off-target chemical reactivity induced by the reactive methylene protons of daf under reducing conditions.

The structure for **2-red** (**q52k**) reported here is quite comparable to the previous determination from Song and co-workers[5,6] even though the previous crystal was 320 times larger ($0.20 \times 0.16 \times 0.12$ mm^3) than the one used in the present study ($0.03 \times 0.02 \times 0.02$ mm^3). The similar final quality of the structures is attributable to the collection of data for **q52k** with an instrument featuring a Cu rotating anode generator equipped with optical mirrors.

Full Solid-State Structure of 2-red

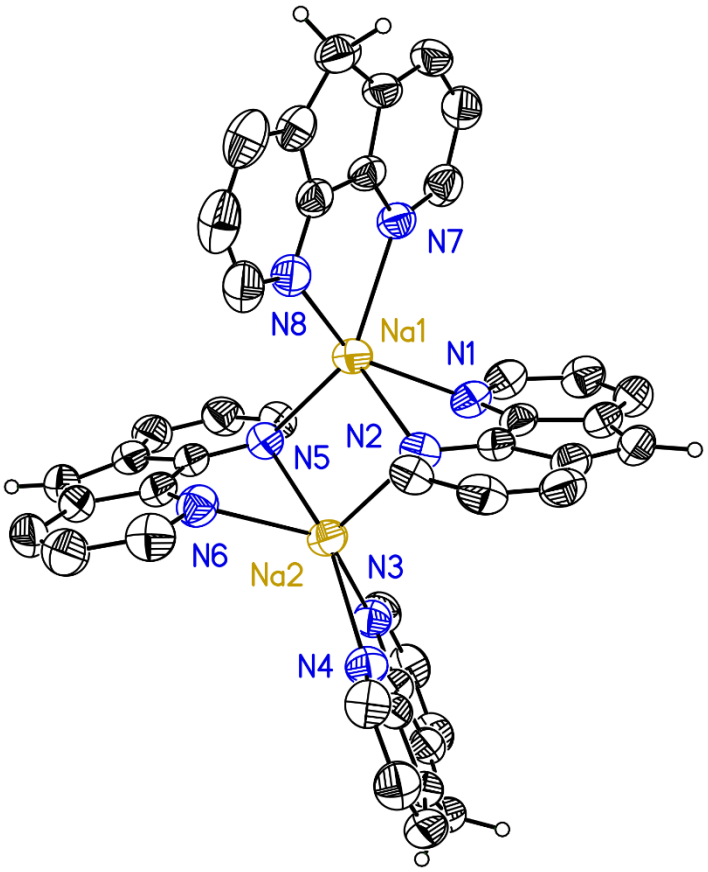

Figure A71: Solid-state structure of the asymmetric unit for complex **2-red**. Hydrogen atoms, except for H11, H22A, H22B, H33, H44A, and H44B, are omitted for clarity. Displacement ellipsoids are shown at the 50% probability level.

Special Refinement Details for Bn$_3$daf

All hydrogen atoms were located in a difference Fourier and initially refined as independent isotropic atoms in least-squares refinement cycles. Hydrogen atoms H17, H29, H31 and H32 were placed at idealized positions in the final refinement cycles with isotropic thermal parameters fixed at 1.2 times the equivalent isotropic thermal parameter of the carbon atom to which they are covalently bonded.

Full Solid-State Structure of Bn$_3$daf

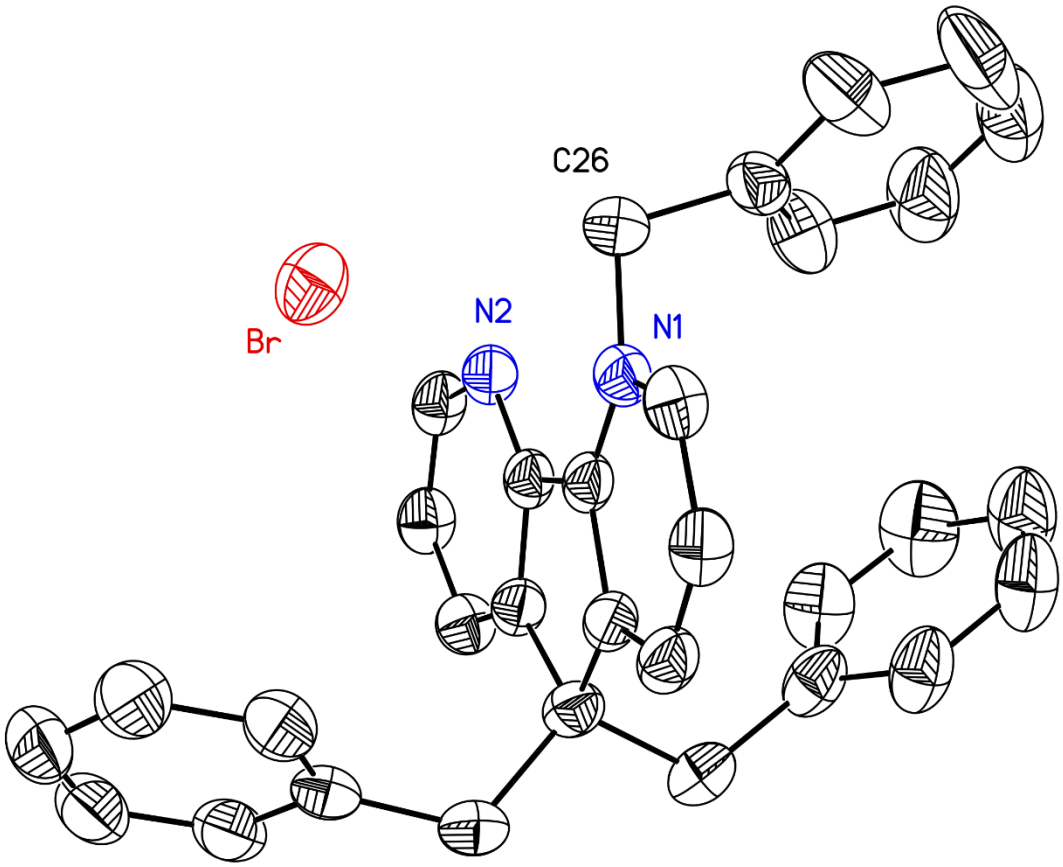

Figure A72: Full solid-state structure of the **Bn$_3$daf** asymmetric unit. Hydrogen atoms are omitted for clarity. Displacement ellipsoids are shown at the 50% probability level.

Special Refinement Details for 1-PF_6

Electron density corresponding to disordered solvent was modeled with an acetonitrile/water pair (N1S, C1S and C2S with O1WA at the mirror-related C2S position) being present in the asymmetric unit with occupancy factors of 0.25 and an additional single acetonitrile molecule (with the central C1S′ carbon in the mirror plane at 0.75) also being included with occupancy factors of 0.25. This yielded a normal full occupancy of 0.50 for the mirror plane site jointly occupied by N1S and C1S′.

Solid-State Structure of 1-PF_6.

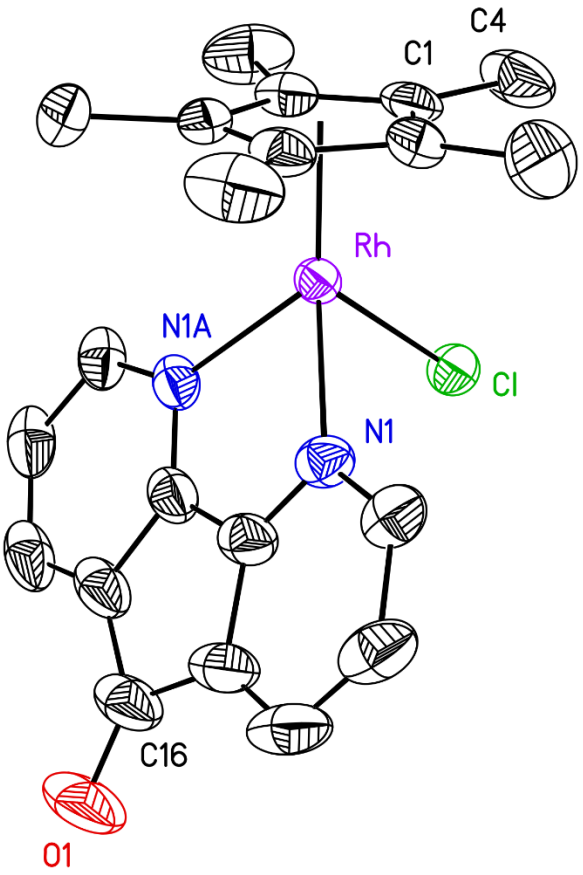

Figure A73: Solid-state structure of the monocation included in two asymmetric units for **1-PF_6**. The monocation utilizes a crystallographic mirror plane at y = 0.75 which contains Rh, Cl, O1, C1, C4, H4A and C16. Disordered acetonitrile and water solvent molecules of crystallization, hydrogen atoms and the outer sphere hexafluorophosphate counteranion are omitted for clarity. Displacement ellipsoids are shown at the 50% probability level.

Full-Solid State Structure of 1-PF_6

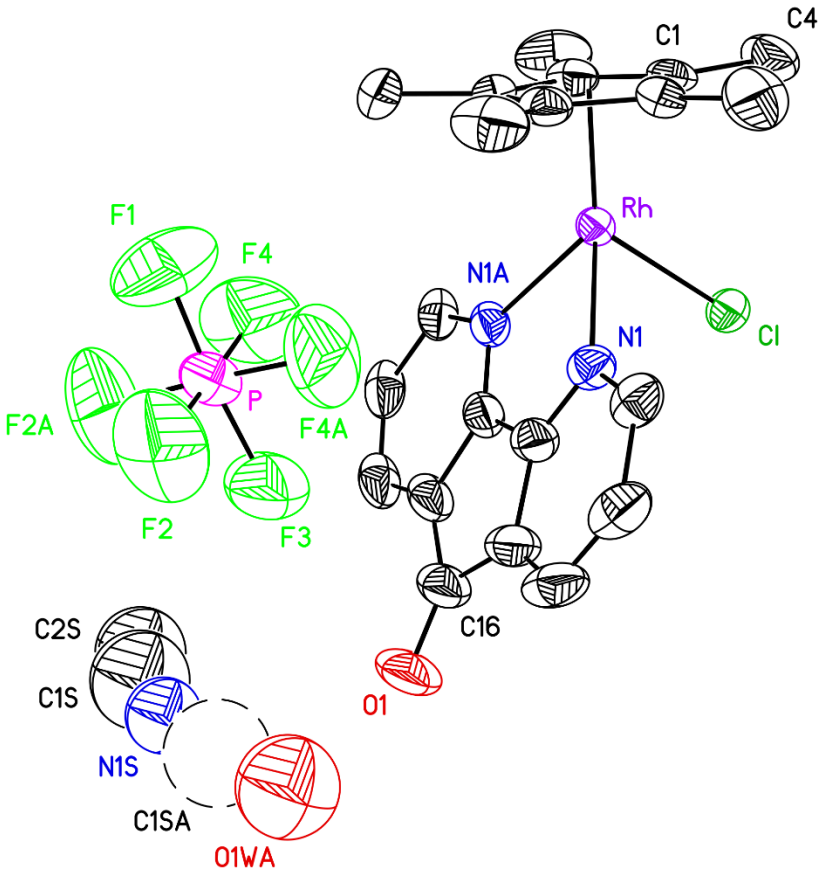

Figure A74: Full solid-state structure of two asymmetric units for **1-PF_6**. Hydrogen atoms are omitted for clarity. Displacement ellipsoids are shown at the 50 % probability level. Electron density corresponding to disordered solvent was modeled with an acetonitrile/water pair (N1S, C1S and C2S with O1WA) being present in the asymmetric unit part of the time and a second single acetonitrile molecule (N1SA–C1S′–C2S′ with the central C1S′ carbon in the mirror plane at 0.75) being present part of the time. O1WA and N1SA are symmetry-equivalent (related by the mirror plane at y = 0.75) O1W and N1S′ atoms, respectively. N1S and C1S′ have the same coordinates in the coordinate file as do the C2S and O1W pair. N/methyl orientational disorder

for the second acetonitrile is taken into account by having N1S′ and C2S′ occupy the same site as carbon atom C1S for the first acetonitrile shown in this Figure. The P, F1 and F3 atoms of the anion and the N1S/C1S′ atoms of the solvent lie in the crystallographic mirror plane at y = 0.75 along with the Rh, Cl, O1, C1, C4, H4A and C16 atoms of the monocation. The C1SA atom shown as a dashed sphere is not present for this acetonitrile/water pair.

Solvent Disorder in Solid-State Structure of 1-PF_6

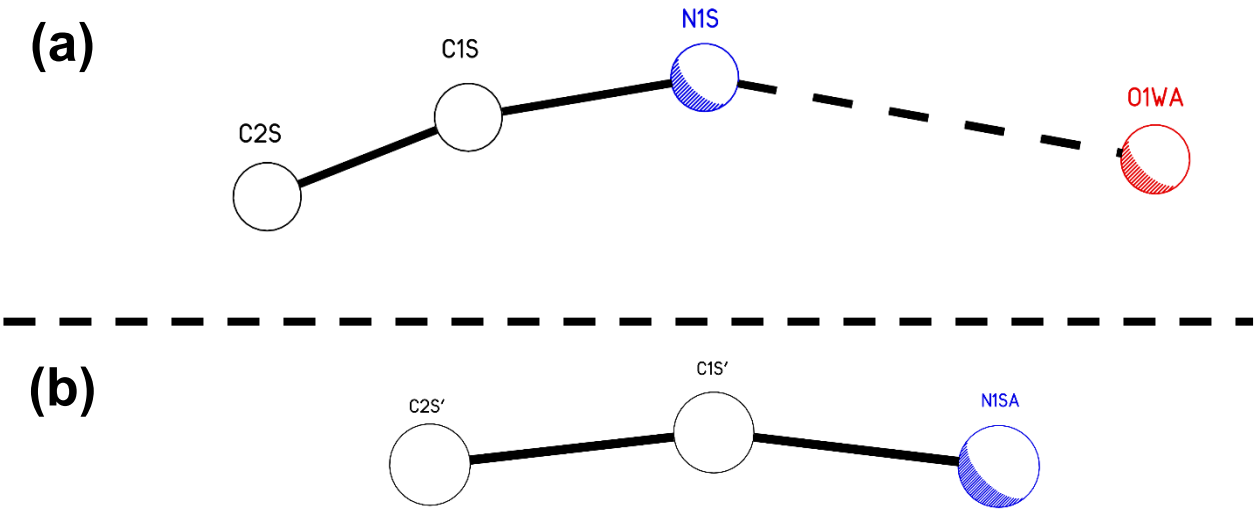

Figure A75: Electron density corresponding to disordered solvent was modeled with an acetonitrile/water pair (N1S, C1S and C2S with O1WA) being present in the asymmetric unit part of the time and a second single acetonitrile molecule (N1SA–C1S′–C2S′ with the central C1S′ carbon in the mirror plane at 0.75) being present part of the time. O1WA and N1SA are symmetry-equivalent (related by the mirror plane at y = 0.75) O1W and N1S′ atoms, respectively. N1S and C1S′ are both in the mirror plane at y = 0.75 and have the same coordinates in the coordinate file. C2S and O1W also jointly occupy another single site. N/methyl orientational disorder for the second acetonitrile is taken into account by having N1S′ and C2S′ both occupy the same site as carbon atom C1S for the first acetonitrile. Since each of these individual atoms (N1S, C1S, C2S, O1W, N1S′, C1S′ and C2S′) are included in the structural model with an occupancy of 0.25, the total combined occupancies for the three unique positions are: 0.50, N1S; 0.75, C1S; and 0.50, C2S. The normal value for full occupancy at the N1S position is also 0.50 and the other two (C1S and C2S) are 1.00. Interestingly, there appears

to be a 2.669 Å O1WA---N1S hydrogen bonding interaction (panel **(a)**) and the ***symmetry-imposed*** 166º bond angle for the second acetonitrile (panel **(b)**) reassuringly deviates only slightly from the expected linear value. Additional modeling is also possible for the solvent peaks that only involves the presence of water.

Special Refinement Details for 3NCMePF_6

The diethyl ether solvent molecule appears to have partially left the lattice and was included in the structural model with an occupancy factor of 0.85.

Solid-State Structure of 3NCMePF$_6$

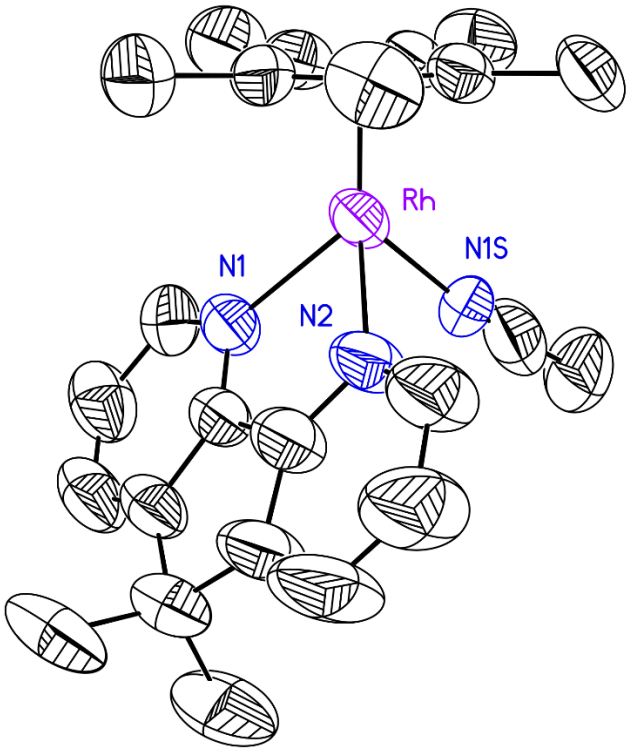

Figure A76: Solid-state structure for the dication present in the asymmetric unit of salt **3NCMePF$_6$**. A diethyl ether solvent molecule, outer sphere hexafluorophosphate counteranions and hydrogen atoms are omitted for clarity. Displacement ellipsoids are shown at the 50% probability level.

Full Solid-State Structure of 3NCMePF$_6$

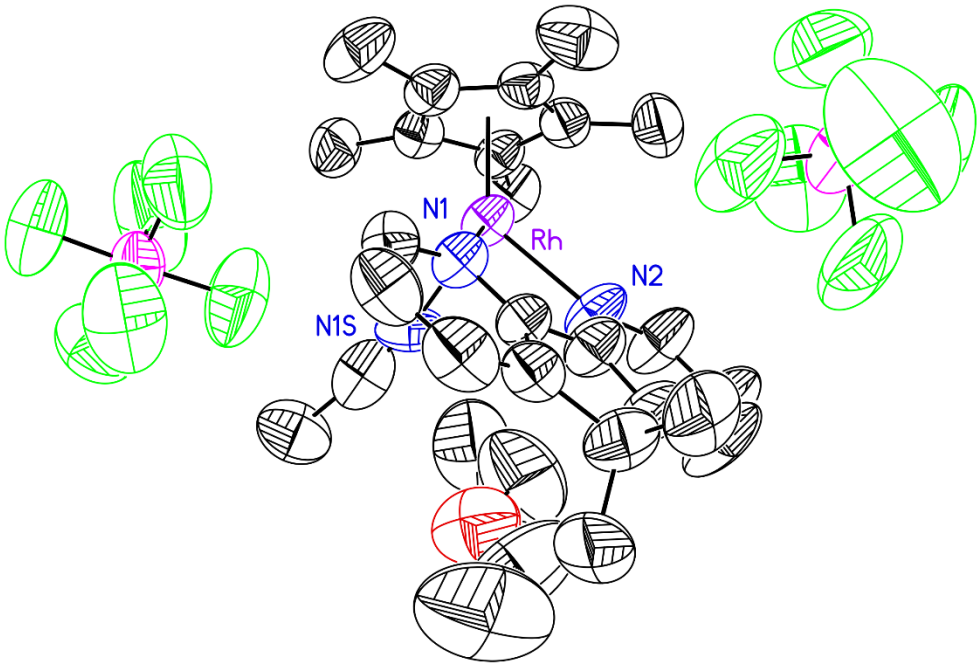

Figure A77: Solid-state structure of the asymmetric unit for **3NCMePF$_6$**. Hydrogen atoms are omitted for clarity. Displacement ellipsoids are shown at the 50% probability level.

Table A2: Selected bond lengths and angles in complexes **1**, **1-PF$_6$**, **3-NCMe**, and **3-NCMePF$_6$**.

Compound	Rh–N1 (Å)	Rh–N2 (Å)	Rh–L (Å)	d_{c-c} [b] (Å)	Rh–Cp*$_{cent}$ (Å)	∠ N–Rh–N (°)	∠ Cp*$_{cent}$–Rh–N*[c] (°)
1 [a]	2.202(3), 2.197(3)	2.199(3), 2.197(3)	2.399(1), 2.402(1)	1.445(5), 1.438(5)	1.765, 1.764	80.4(1), 80.2(1)	150.9, 151.5
1-PF$_6$	2.193(3)	2.193(3)	2.3955(11)	1.448(8)	1.765	79.7(2)	147.4
3-NCMe [a]	2.190(6), 2.204(6)	2.188(7), 2.191(6)	2.102(7), 2.088(7)	1.434(11), 1.445(10)	1.768, 1.767	81.2(2), 80.6(2)	150.9, 147.2
3-NCMePF$_6$	2.187(8)	2.156(8)	2.112(12)	1.428(16)	1.774	79.6(3)	146.9

[a] Values for the independent molecules in the asymmetric unit cell are listed.

[b] Refers to the bond between the two central carbons interconnecting the two pyridyl-like rings.

[c] Defined as the angle between the Cp* centroid, Rh center, and centroid of N1 and N2.

Full Synthetic Procedures for Preparation of dafone, daf, and Me_2daf

Synthesis of 4,5-diazafluorene-9-one (dafone)

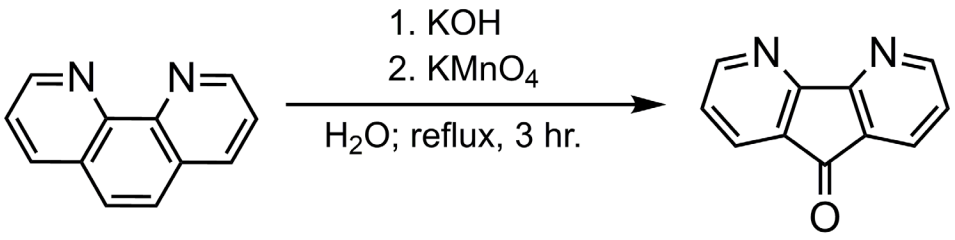

To a 3-neck round bottom flask equipped with a rubber septum, a reflux condenser, a glass stopper, and a stir bar was added 1,10-phenantrholine (phen, 10.0 g, 55.5 mmol), potassium hydroxide (KOH, 10.2 g, 181.5 mol), and water (625 mL). This solution was heated to reflux. Next, to a separate 3-neck round bottom flask equipped with an air inlet, a glass stopper, a rubber septum, and a stir bar was added potassium permanganate (25.5 g, 161.5 mmol) and water (375 mL). This mixture was heated to just below reflux. The hot permanganate solution was then transferred via cannula to the phen solution in a dropwise fashion over the course of an hour. The resulting mixture was then allowed to reflux for 3 hours. The initial emerald-green solution (attributable to the generation of the active oxidant, manganate) quickly subsides to a brown suspension with hints of orange. Upon completion, the solution was filtered hot into a medium porosity frit to remove the brown manganese dioxide solid. The resulting red-orange filtrate was then exhaustively extracted with chloroform, dried with magnesium sulfate, and filtered. The solvent was then removed under reduced pressure to obtain the crude material (a mixture of dafone and phen). The crude material may be purified by recrystallization from acetone, followed by washing with pentane, or by silica gel column chromatography (gravity) using ethyl acetate as the eluent. Attempts to purify the crude material by sublimation or by using a short silica column were not successful. The product was obtained as a pale-yellow solid. Yield: 3.77 g (40%). ^{1}H NMR (400 MHz, CD_3CN): δ = 8.76 (dd, 2H, $^3J_{H,H}$ = 5.0 Hz, $^4J_{H-H}$ = 1.6 Hz), 8.00 (dd,

2H, $^{3}J_{H,H}$ = 7.6 Hz, $^{4}J_{H–H}$ = 1.6 Hz), 7.42 ppm (dd, 2H, $^{3}J_{H,H}$ = 7.6 Hz, $^{4}J_{H,H}$ = 5.0 Hz). This method is based on the original reported in reference S7.

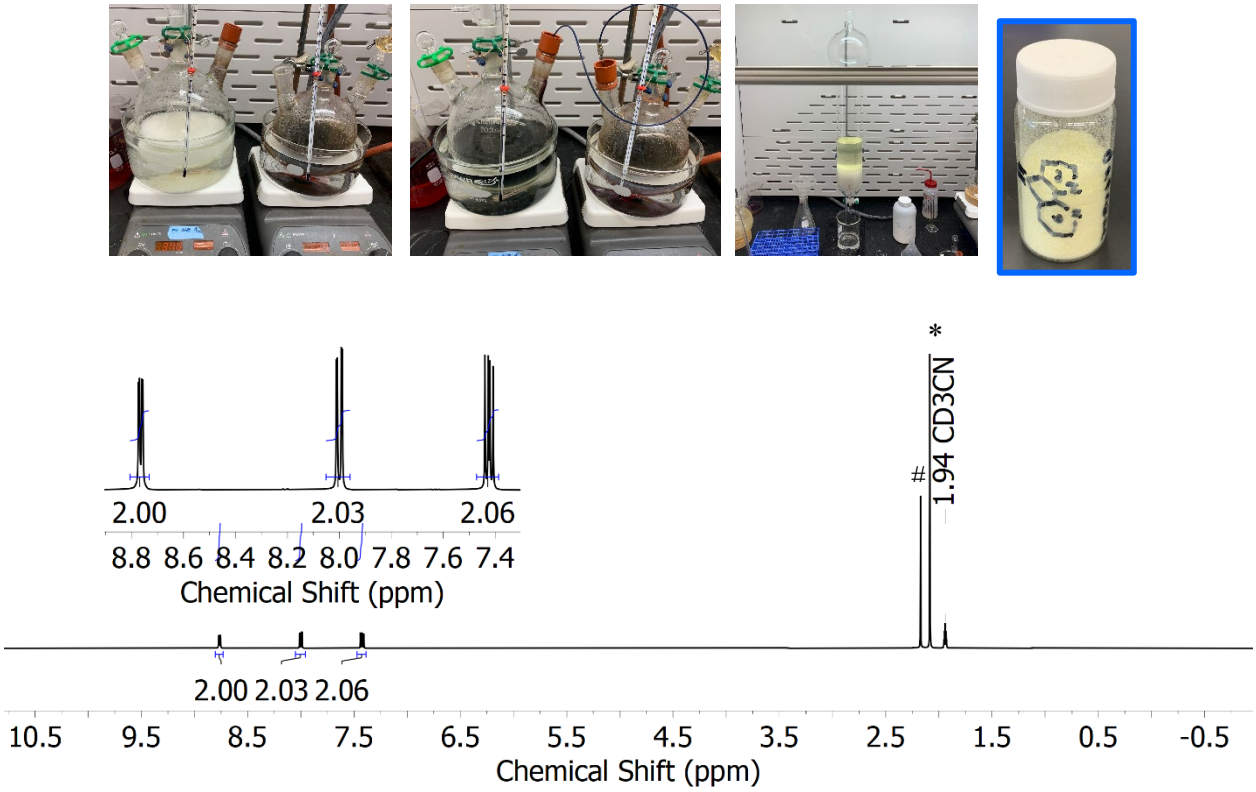

Figure A78: ^{1}H-NMR spectrum (400 MHz, CD_3CN) of **dafone**. Signals for water (*) and acetone (#) are present.

Synthesis of 4,5-diazafluorene (daf)

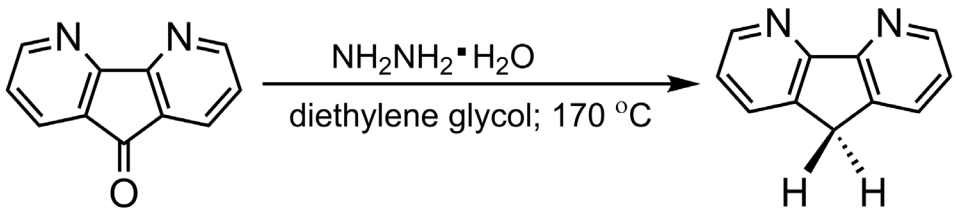

To a 3-neck round bottom flask equipped with a glass stopper, a reflux condenser connected to a bubbler, a rubber septum, and a stir bar was added dafone (3.85 g, 21.1 mmol) and diethylene glycol (35 mL). The flask was then purged with N_2 for 20 minutes to exclude oxygen from the reaction vessel. Hydrazine hydrate (5.7 mL, 117.5 mmol) was then added dropwise over the course of 5 min. Due to the potentially explosive nature of hydrazine, a blast shield was installed, and the reaction flask was brought to 170°C and allowed to stir for 3 hours. Upon completion, the reaction mixture was extracted with dichloromethane, dried with magnesium sulfate, and filtered. The solvent was then removed under reduced pressure to obtain an oil. The oil was then dissolved in dichloromethane and run through a short neutral alumina column. The volume of the resulting eluent was then concentrated under reduced pressure. Addition of pentane to the resulting oily residue resulted in the precipitation of the desired product as an off-white-to-colorless solid. In some instances, an extra extraction step involving the addition of water, followed by extraction with dichloromethane was needed to obtain pure product. Yield: 2.82 g (79%). ^{1}H NMR (400 MHz, CD_3CN): δ = 8.67 (d, 2H, $^3J_{H,H}$ = 4.8 Hz), 7.99 (d, 2H, $^3J_{H,H}$ = 7.6 Hz), 7.36 (dd, 2H, $^3J_{H,H}$ = 7.6 Hz, $^4J_{H,H}$ = 4.8 Hz), 3.91 ppm (s, 2H). This method is based on the original reported in reference S7.

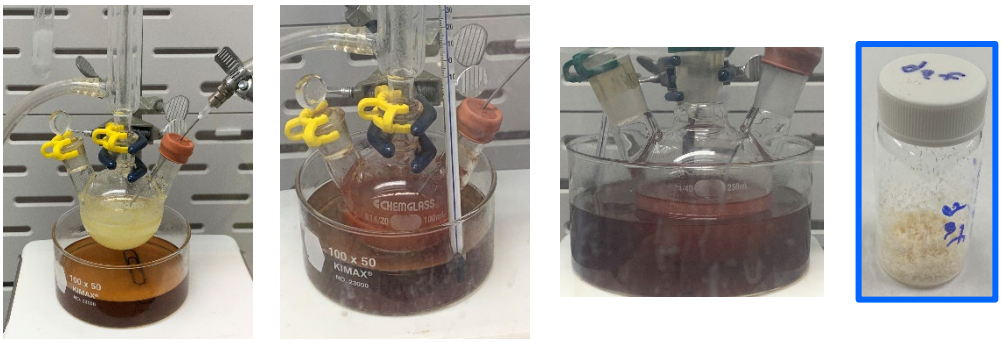

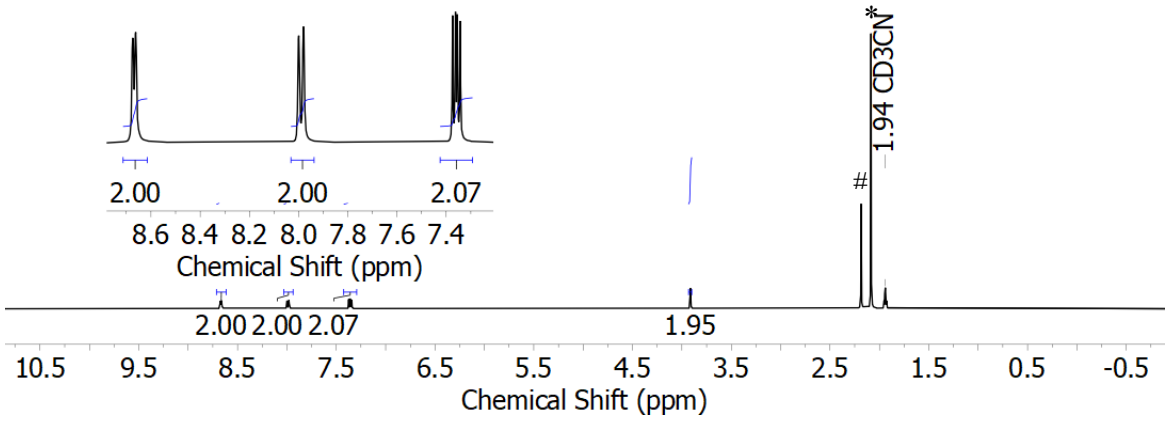

Figure A79: ^{1}H-NMR spectrum (400 MHz, CD_3CN) of **daf**. Signals for water (*) and acetone (#) are present.

Synthesis of 9,9'-dimethyl-4,5-diazafluorene (Me_2daf)

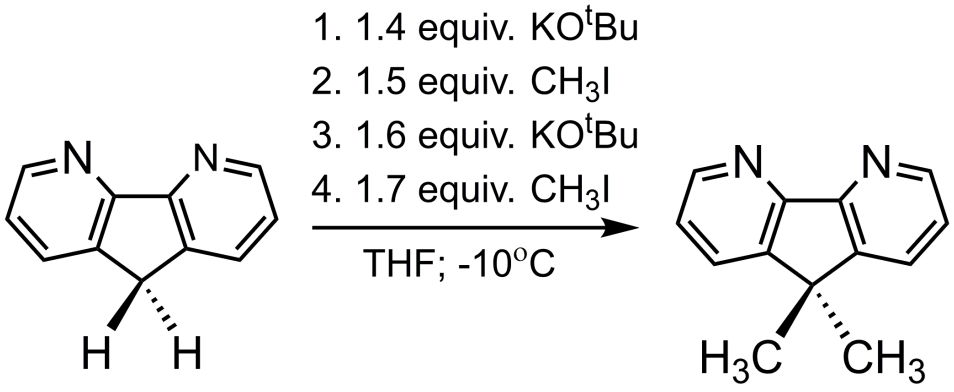

To a flame-dried Schlenk flask equipped with a stir bar was added daf (1.0014 g, 5.95 mmol) under an N_2 atmosphere. Dry THF (30 mL) was then cannula transferred into the Schlenk flask while maintaining the N_2 atmosphere and the solution was cooled to –10 °C (ice/acetone). Meanwhile, potassium tert-butoxide was dissolved in dry THF and taken up into two syringes inside an inert-atmosphere glovebox. Next, sequential additions of potassium tert-butoxide and methyl iodide were performed. Potassium tert-butoxide (0.9376 g, 8.36 mmol) was added dropwise over 5 min, resulting in a brilliant purple red solution that was allowed to stir for 30 min. Next, methyl iodide (1.2676 g, 8.93 mmol) was added. Over time, the purple-red color faded, and the solution was allowed to stir for 1 hr. Then, potassium tert-butoxide (1.0600 g, 9.45 mmol) was again added dropwise over 5 min. and allowed to stir for 30 min. Finally, methyl iodide (1.4366 g, 10.12 mmol) was added again, and the solution was allowed to stir for 1 hr. The resulting solution was then pumped down to dryness. The resulting dark brown solid was extracted with dichloromethane/water and placed into a separatory funnel containing water. The aqueous solution was then extracted with dichloromethane two more times. The resulting extracts were combined, and the solvent was removed under reduced pressure. The resulting solid was finally dissolved in a minimal amount of dichloromethane; addition of pentane resulted in precipitation of the desired product as a beige solid. Yield: 0.57 g (49%). ^{1}H NMR (400 MHz,

CD_3CN): δ = 8.63 (dd, 2H, $^3J_{H,H}$ = 4.8 Hz, $^4J_{H,H}$ = 1.5 Hz), 7.95 (dd, 2H, $^3J_{H,H}$ = 7.7 Hz, $^4J_{H,H}$ = 1.5 Hz), 7.36 (dd, 2H, $^3J_{H,H}$ = 7.7 Hz, $^4J_{H,H}$ = 4.8 Hz), 1.52 ppm (s, 6H). This method is based on the original reported in reference S8.

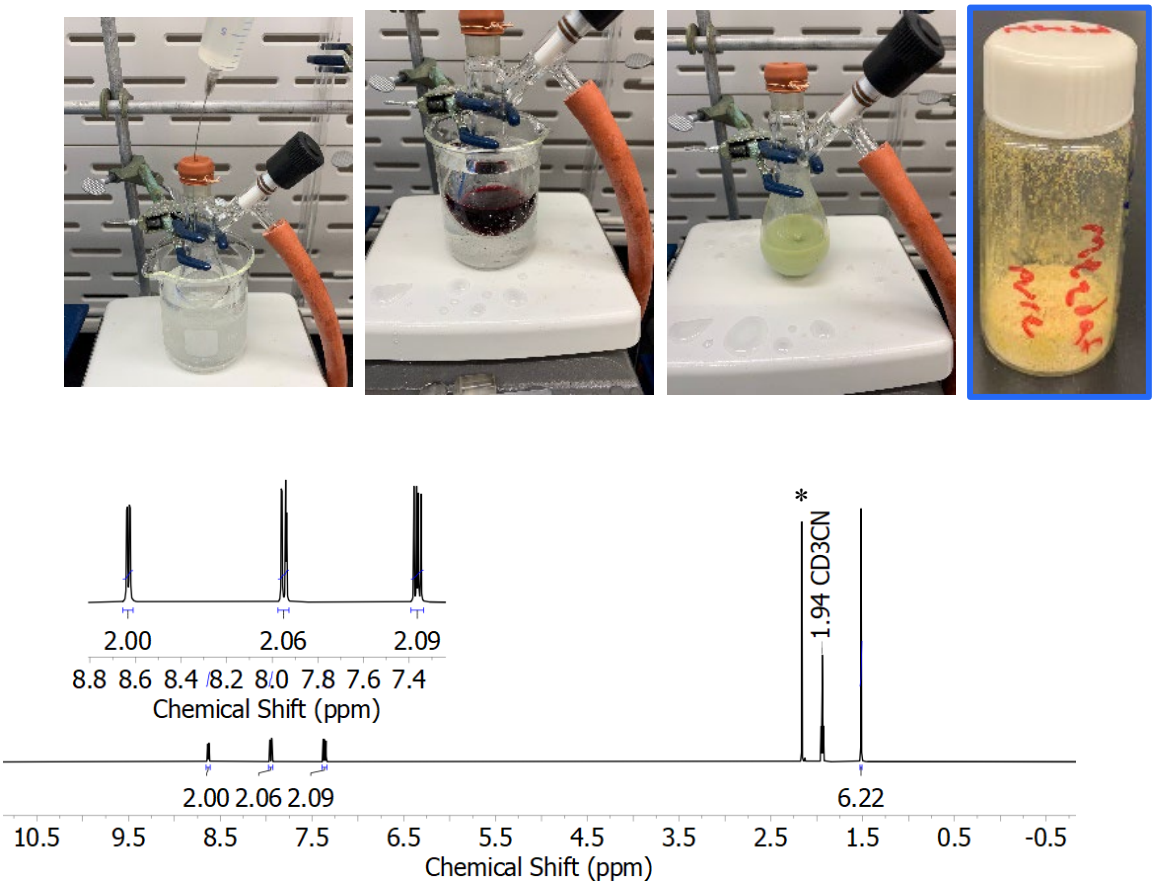

Figure A80: ^{1}H-NMR spectrum (400 MHz, CD_3CN) of **Me$_2$daf**. Signal for water (*) is present.

References

(1) APEX2, Version 2 User Manual, M86-E01078, Bruker Analytical X-ray Systems: Madison, WI, June 2006.

(2) G. M. Sheldrick, SADABS (version 2008/1): Program for Absorption Correction for Data from Area Detector Frames, University of Göttingen, 2008.

(3) G. Sheldrick, Crystal structure refinement with SHELXL. *Acta Cryst. A: Found. Crystallogr.* **2015**, *71*, 3-8.

(4) O. V. Dolomanov, L. J. Bourhis, R. J. Gildea, J. A. K. Howard, H. J. Puschmann, *Appl. Crystallogr.* **2009**, *42*, 339-341.

(5) H. Jiang and D. Song, *Organometallics* **2008**, *27*, 3587-3592.

(6) H. Jiang and D. Song, CCDC 701345: Experimental Crystal Structure Determination, **2009**; doi: 10.5517/ccrjt13

(7) J. Druey and P. Schmidt, *Helv. Chim. Acta* **1950**, *33*, 1080-1087.

(8) H. Ohrui, A. Senoo and T. Kosuge in *Preparation of diazafluorene compounds via palladium-catalyzed condensation reaction of diazafluorene dihalides with boronic acid derivatives*, Patent US20080161574A1, Canon Kabushiki Kaisha, Japan, **2008**, pp. 22.

Appendix B

Supplementary Information for Chapter 4

Materials and Methods

All manipulations were carried out in dry N_2-filled gloveboxes (Vacuum Atmospheres Co., Hawthorne, CA, USA) or under an N_2 atmosphere using standard Schlenk techniques unless otherwise noted. All solvents were of commercial grade and dried over activated alumina using a PPT Glass Contour (Nashua, NH, USA) solvent purification system prior to use, and were stored over molecular sieves in an N_2-filled glovebox. All chemicals were obtained from major commercial suppliers and used as received after extensive drying unless otherwise noted. Rhodium chloride hydrate (Pressure Chemical Co.), 1,2,3,4,5-pentamethylcyclopentadiene (93%; TCI), trifluoromethane sulfonic acid (>99%; Sigma Aldrich), deuterated trifluoromethane sulfonic acid (98 atom % D; Sigma Aldrich), and tetrafluoroboric acid (48% w/w; Alfa Aesar) were all used as received. 2,2′-bipyridyl (98%; Alfa Aesar) was purified by sublimation before use. Aniline (99.5%; Acros) and triethylamine (98%; J.T. Baker) were each dried and distilled from potassium hydroxide prior to use. $[Cp^*RhCl_2]_2$ ([1],[2]), $[Cp^*Rh(OH_2)(bpy)]SO_4$ ([3]), $[Cp^*Rh(bpy)]$ ([4]), $[(\eta^4\text{-}Cp^*H)Rh(bpy)]^+$ ([5]), triethylammonium triflate ([6]), deuterated triethylammonium triflate ([7]), triethylammonium tetrafluoroborate ([8]), anilinium triflate ([9]), and dimethylformamidinium triflate ([10]) were prepared according to literature methods and dried extensively at 1 mTorr (133 mPa) for 24 hours using standard Schlenk techniques before being brought into a dry N_2-filled glovebox.

Deuterated solvents for NMR and deuterium enrichment were purchased from Cambridge Isotope Laboratories (Tewksbury, MA, USA); CD_3CN was dried with CaH_2 and stored over molecular sieves, C_6D_6 was dried over sodium/benzophenone, and MeOD was used as received. ^{1}H-NMR spectra were collected with a 400 MHz Bruker spectrometer and referenced to the residual protio-solvent signal ([11]) to support the generation of pure material (see Appendix B,

Figures B1-B13). IR spectra were collected using a Shimadzu IRSpirit Fourier Transform Infrared Spectrometer in transmission mode using a high throughput diamond QATR-S single reflection attenuated total reflectance attachment at an incident angle of 45 degrees to support the generation of pure material (see SI, Figures B14-B18).

Pulse Radiolysis. Samples for PR were prepared in a dry N_2-filled glovebox and transferred to the instrument air-free in Hamilton air-tight syringes. Before initiating the experiment, the samples were rapidly mixed anaerobically and delivered directly to the PR cell using New Era syringe pumps (NE-100). Following 2-3 seconds of mixing, samples were immediately irradiated using the Brookhaven National Laboratory 2 MeV van de Graaf accelerator using electron pulses (pulse width of 40-500 ns) that led to irradiation doses of 200-800 rad (ca. 0.5-2.5 μM primary radicals) generated in solution. The yield of reducing equivalents was measured using the known extinction coefficient for $[Co(HMD)]^+$ (see Appendix B, Figure B19) The optical path of the cell was 2 cm. All measurements were carried out in MeCN solvent, with 40 μM of **1** and 50 mM $[n\text{-}Bu_4N]CO_2H$ at 25 °C. Under these conditions the reducing equivalents were a combination of solvated electrons and carbon dioxide anion radical. Quoted rate constants have an error of ca. 10%. All rates measured in PR here are averages of at least 3 measurements.

Stopped Flow and Data Analysis. Measurements were performed using an Applied Photophysics SX. 18MV-R Stopped-flow Reaction Analyzer equipped with a 150 W Xenon arc lamp, SpectraKinetic monochromator, a 1 cm path length mixing chamber, and an Applied Photophysics PhotoDiode array detector (280-750 nm scan range) (Need IR Detector info.) Temperature control was achieved using a Thermo Scientific NESLAB RTE-7 Circulating Bath; variations over the course of the kinetic experiments were ±0.1 °C. Samples were prepared in an N_2-filled glovebox and were transported to the stopped flow instrument in Hamilton gas tight syringes. The

concentrations of **3** and **5** were typically 0.20 mM before mixing and the concentrations of the acids used exceeded 10 equiv. in all instances to ensure pseudo-first order kinetics were operative. Observed rate constants (k_{obs}) were calculated using non-linear regression analysis (OriginPro 2021) and the residuals from the fits were determined to lie randomly about zero. Errors for k_{obs}, are reported as the calculated error from the direct non-linear fit of the decaying signals, or as a flat 10%, whichever is larger, unless otherwise noted. Variable temperature kinetic data were used to construct Arrhenius and Eyring plots. The resulting activation parameters were calculated using the method of least squares. Errors for Eyring and Arrhenius data are reported as the calculated error from the direct linear fitting of the k_{obs} data.

GC. Determination of gas evolution was performed with a Shimadzu 2014 Custom-GC gas chromatograph with a thermal conductivity detector and dual flame-ionization detectors. A custom set of 8 columns and timed valves enable quantitative analysis of the following gases: hydrogen, nitrogen, oxygen, carbon dioxide, carbon monoxide, methane, ethane, ethylene, and ethyne. Argon serves as the carrier gas. The instrument was calibrated prior to experimental runs with a standard gas mixture (Agilent 5190-0519), and a calibration curve was established to quantify H_2 evolution.

For the hydrogen detection experiment, 15 mg of **5** was loaded into an N_2-filled round bottom flask and dissolved in MeCN. Before beginning the experiment two background experiments confirmed only dinitrogen and nominal oxygen in the atmosphere of the glovebox. After addition of 1 equiv. of [DMFH]OTf, the headspace gas was taken and injected into the GC using a gas tight syringe.

Computational Details. All geometries were fully optimized at the M06 level of density functional theory ([12]) in conjunction with the SMD continuum solvation model ([13]) for acetonitrile

using def2-TZVP basis set ([14]) on Rh and the def2-SVP basis set (14) on all other atoms. Non-analytical integrals were evaluated using the integral=grid=ultrafine option as implemented in the Gaussian 16 software package. ([15]) The nature of all stationary points was verified by analytic computation of vibrational frequencies which were in turn used to obtain IR vibrational spectra.

NMR Spectra

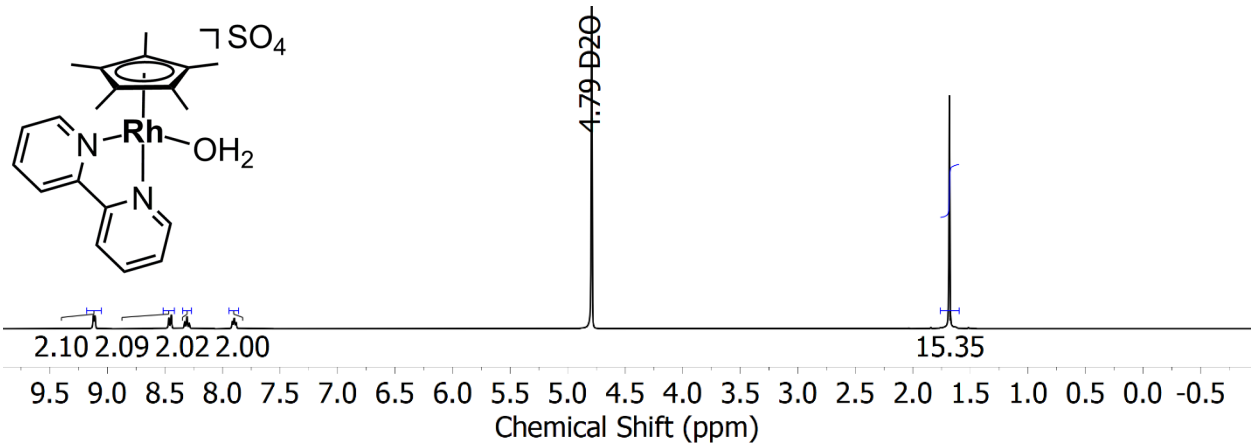

Figure B1: ^{1}H-NMR spectrum (400 MHz, D_2O) of **1**; this is a previously reported complex, but the NMR is shown here to support the generation of pure material.

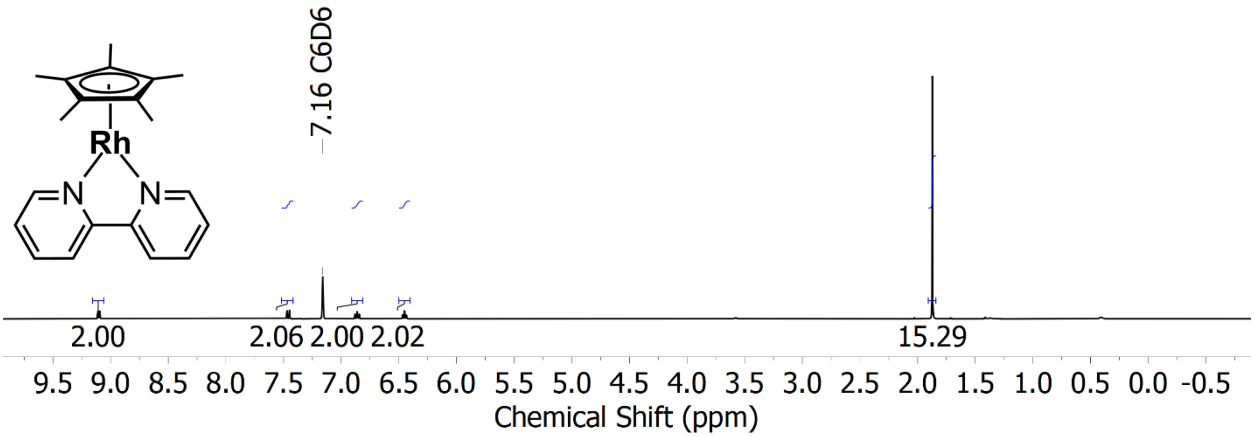

Figure B2: ^{1}H-NMR spectrum (400 MHz, C_6D_6) of **3**; this is a previously reported complex, but the NMR is shown here to support the generation of pure material.

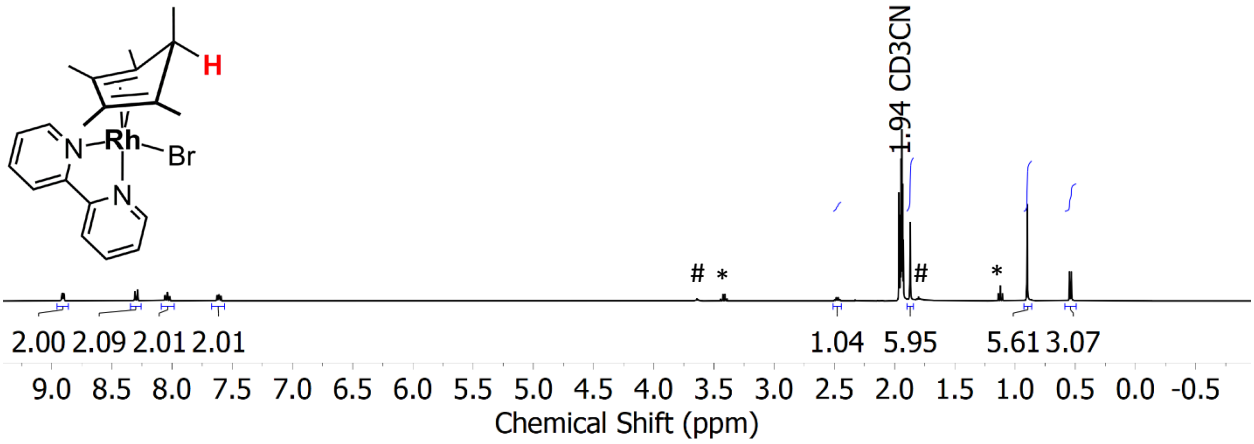

Figure B3: ^{1}H-NMR spectrum (400 MHz, CD_3CN) of **5**. Adventitious diethyl ether (*) and THF (#) are present. This is a previously reported complex, but the NMR is shown here to support the generation of pure material.

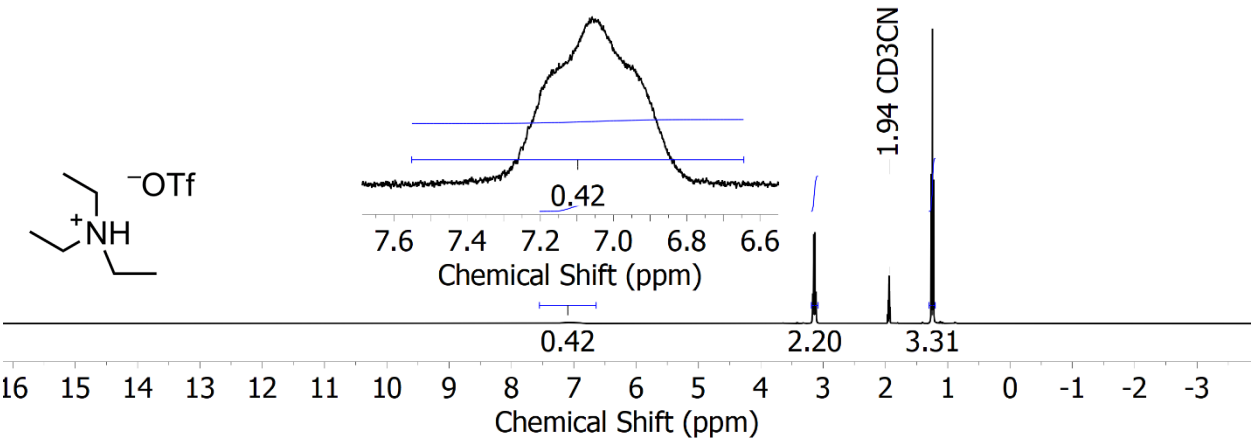

Figure B4: ^{1}H-NMR spectrum (400 MHz, CD_3CN) of [$HNEt_3$]OTf.

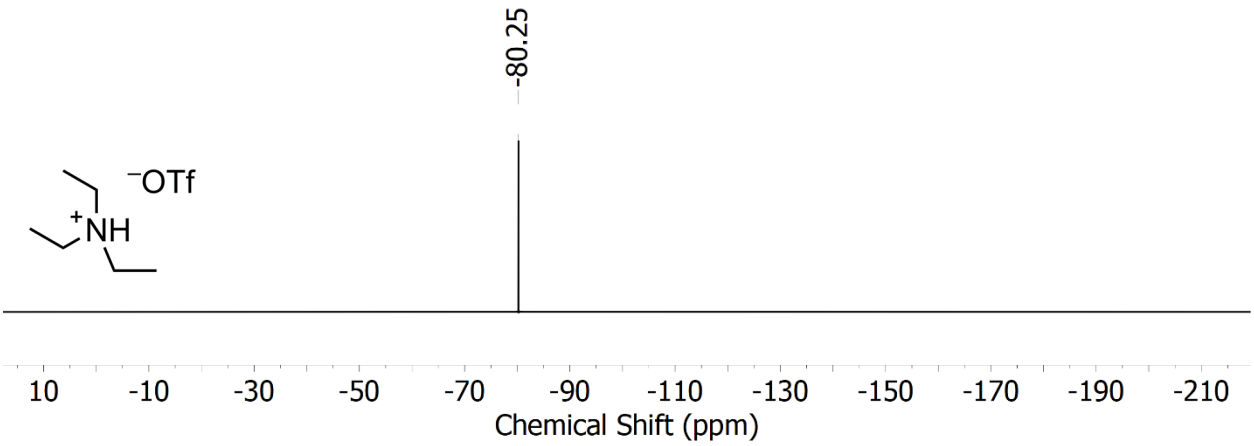

Figure B5: ^{19}F-NMR spectrum (376 MHz, CD_3CN) of $[HNEt_3]OTf$.

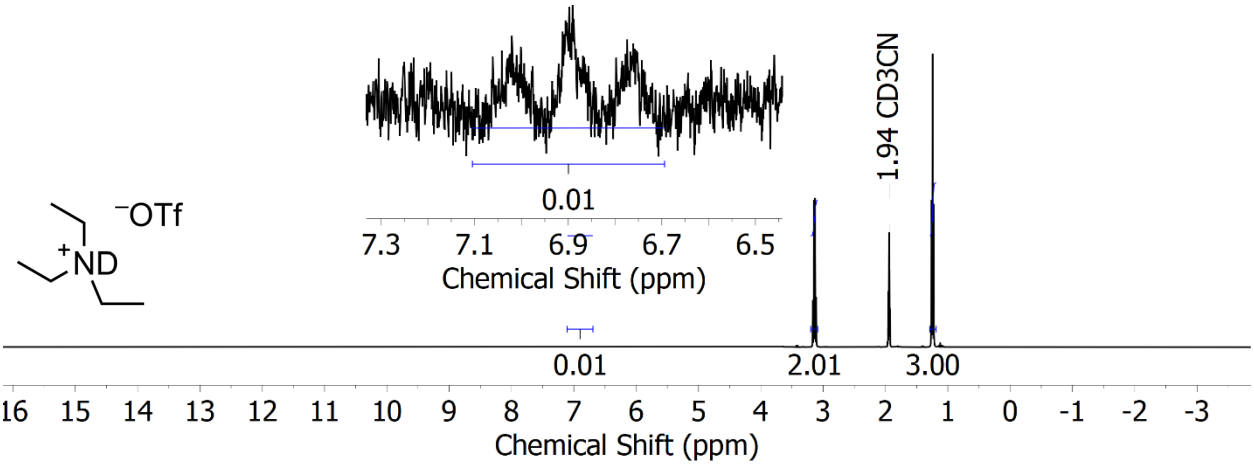

Figure B6: ^{1}H-NMR spectrum (400 MHz, CD_3CN) of [$DNEt_3$]OTf. Deuterium incorporation is >95% based on integration.

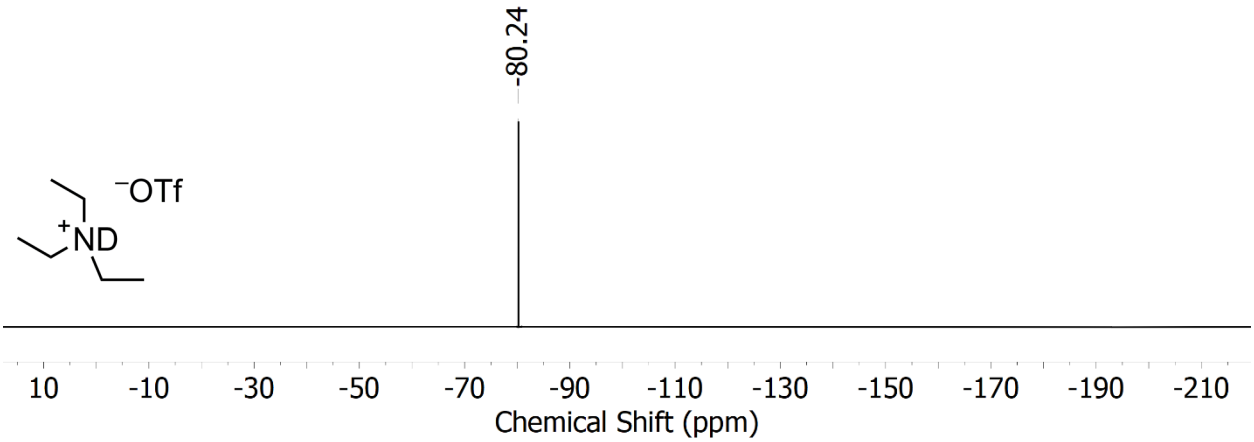

Figure B7: ^{19}F-NMR spectrum (376 MHz, CD_3CN) of [$DNEt_3$]OTf.

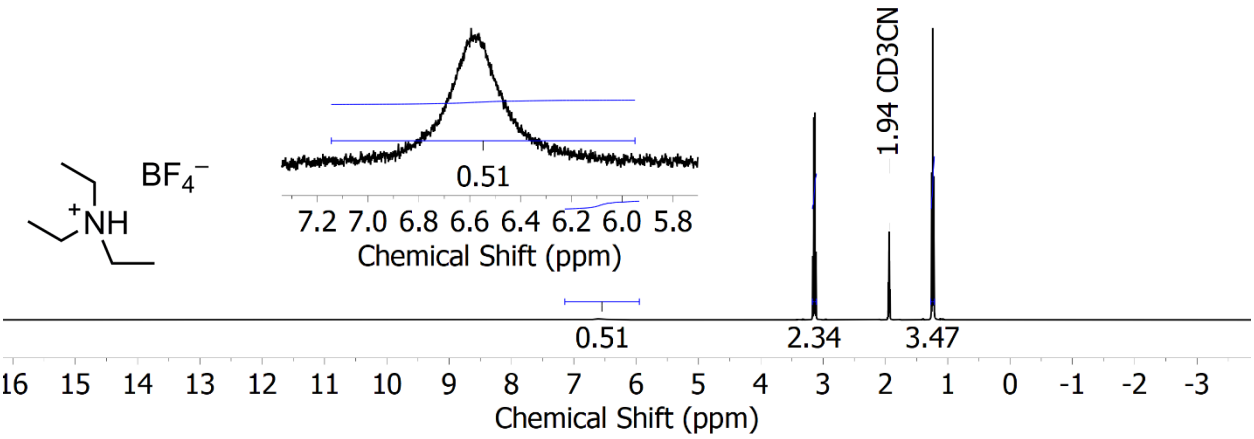

Figure B8: ^{1}H-NMR spectrum (400 MHz, CD_3CN) of $[HNEt_3]BF_4$.

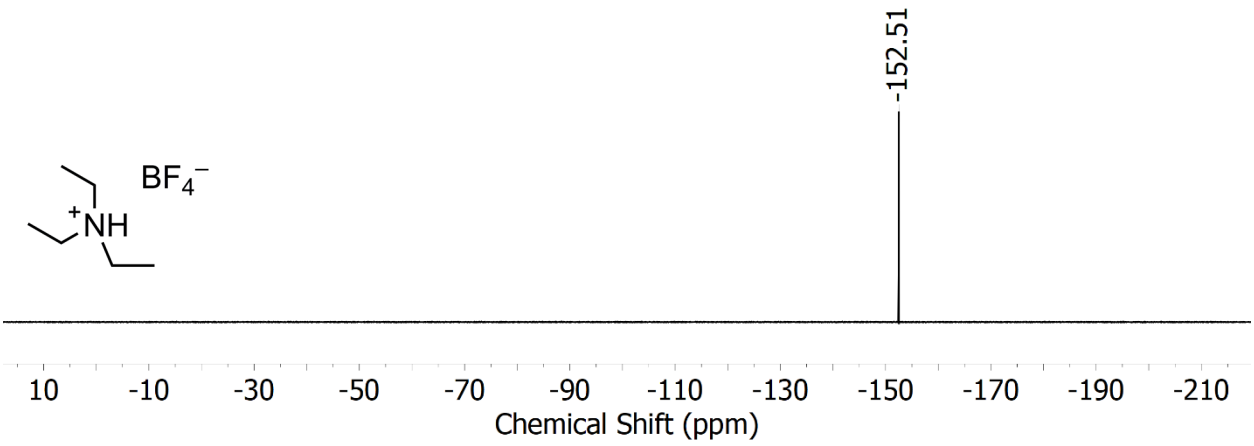

Figure B9: ^{19}F-NMR spectrum (376 MHz, CD_3CN) of $[HNEt_3]BF_4$.

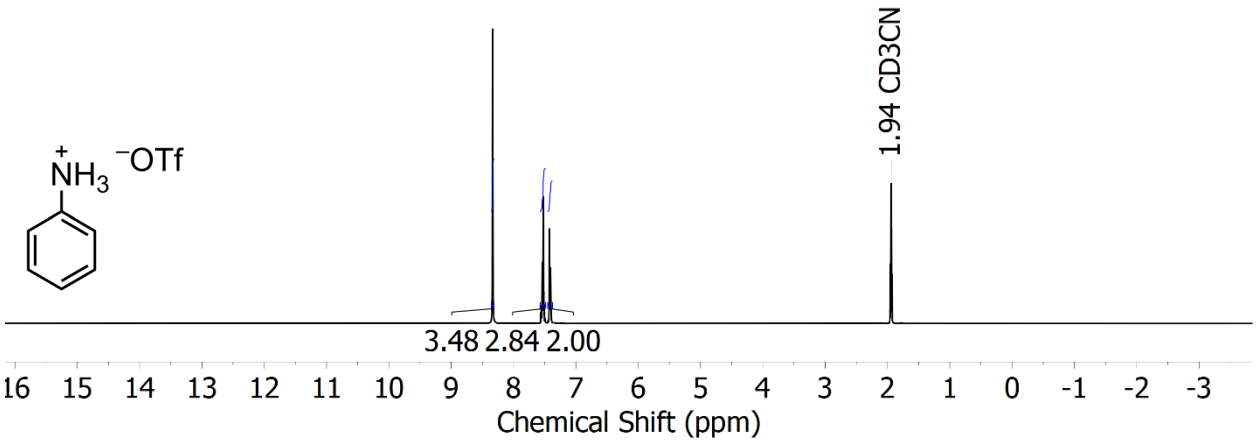

Figure B10: ^{1}H-NMR spectrum (400 MHz, CD_3CN) of $[PhNH_3]OTf$.

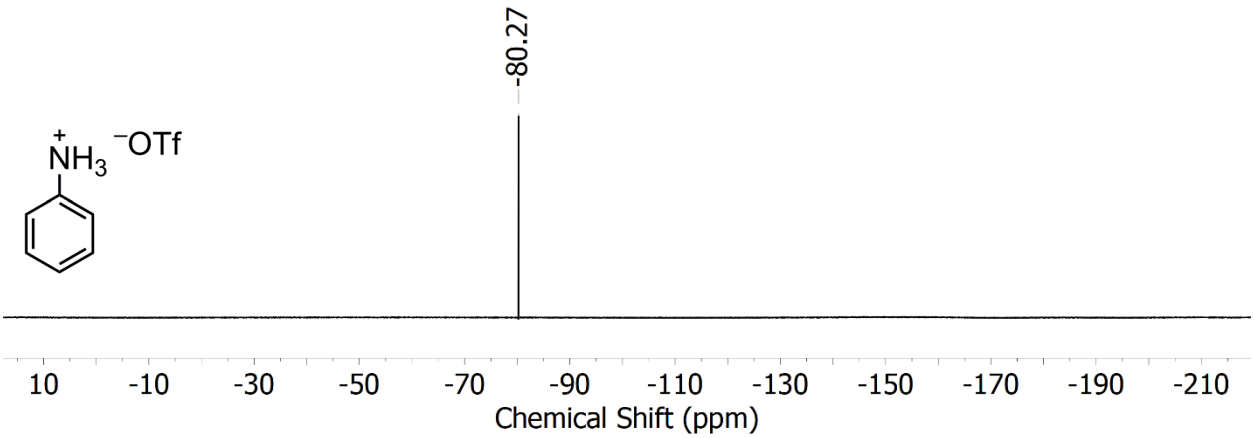

Figure B11: ^{19}H-NMR spectrum (376 MHz, CD_3CN) of $[PhNH_3]OTf$.

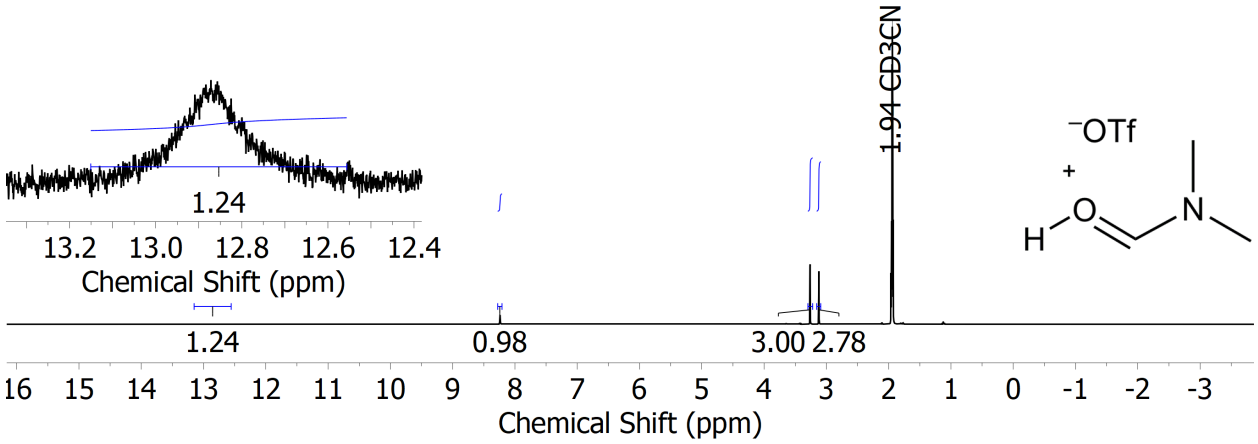

Figure B12: ^{1}H-NMR spectrum (400 MHz, CD_3CN) of [DMFH]OTf.

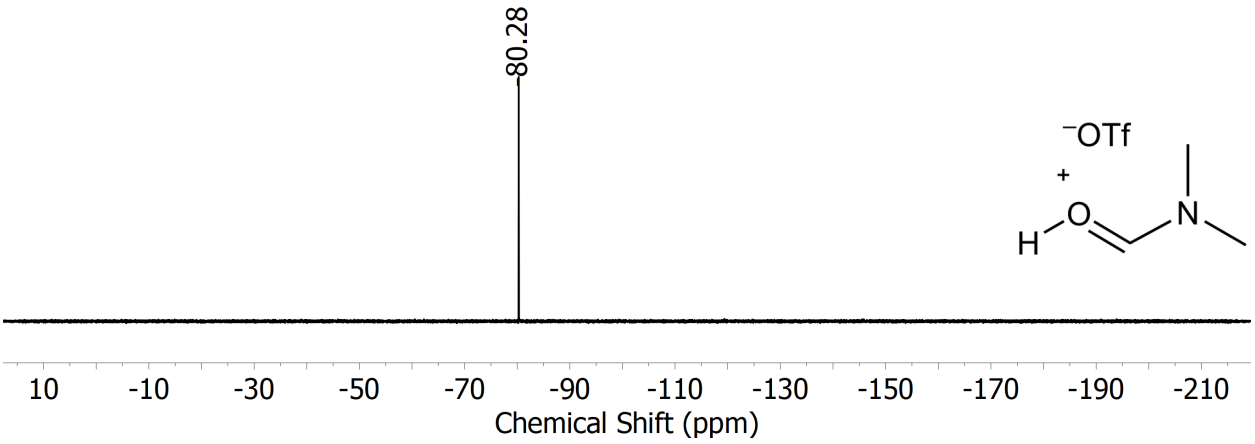

Figure B13: ^{19}F-NMR spectrum (376 MHz, CD_3CN) of [DMFH]OTf.

IR Spectra

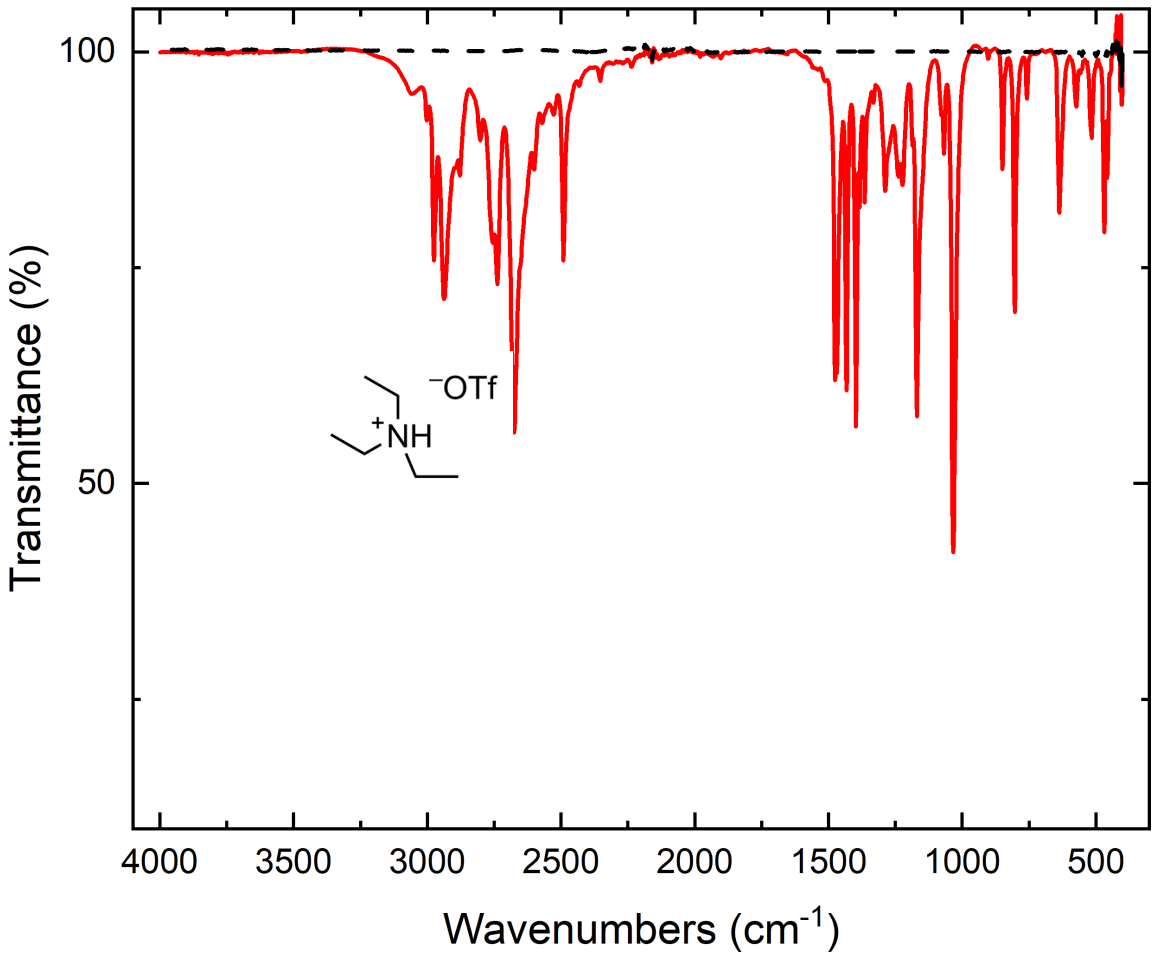

Figure B14: IR Spectrum (solid, diamond plate ATR) of [$HNEt_3$]OTf.

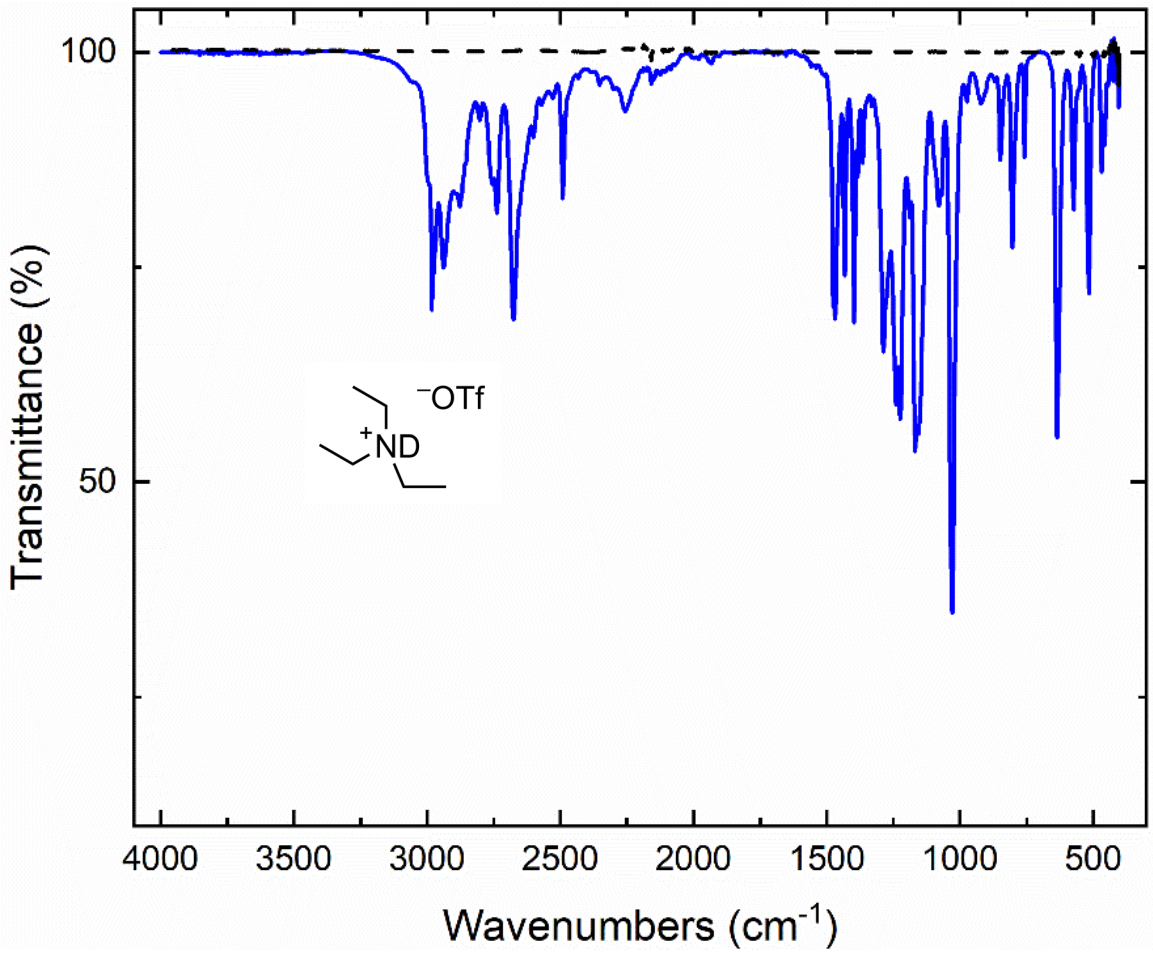

Figure B15: IR Spectrum (solid, diamond plate ATR) of [DNEt$_3$]OTf.

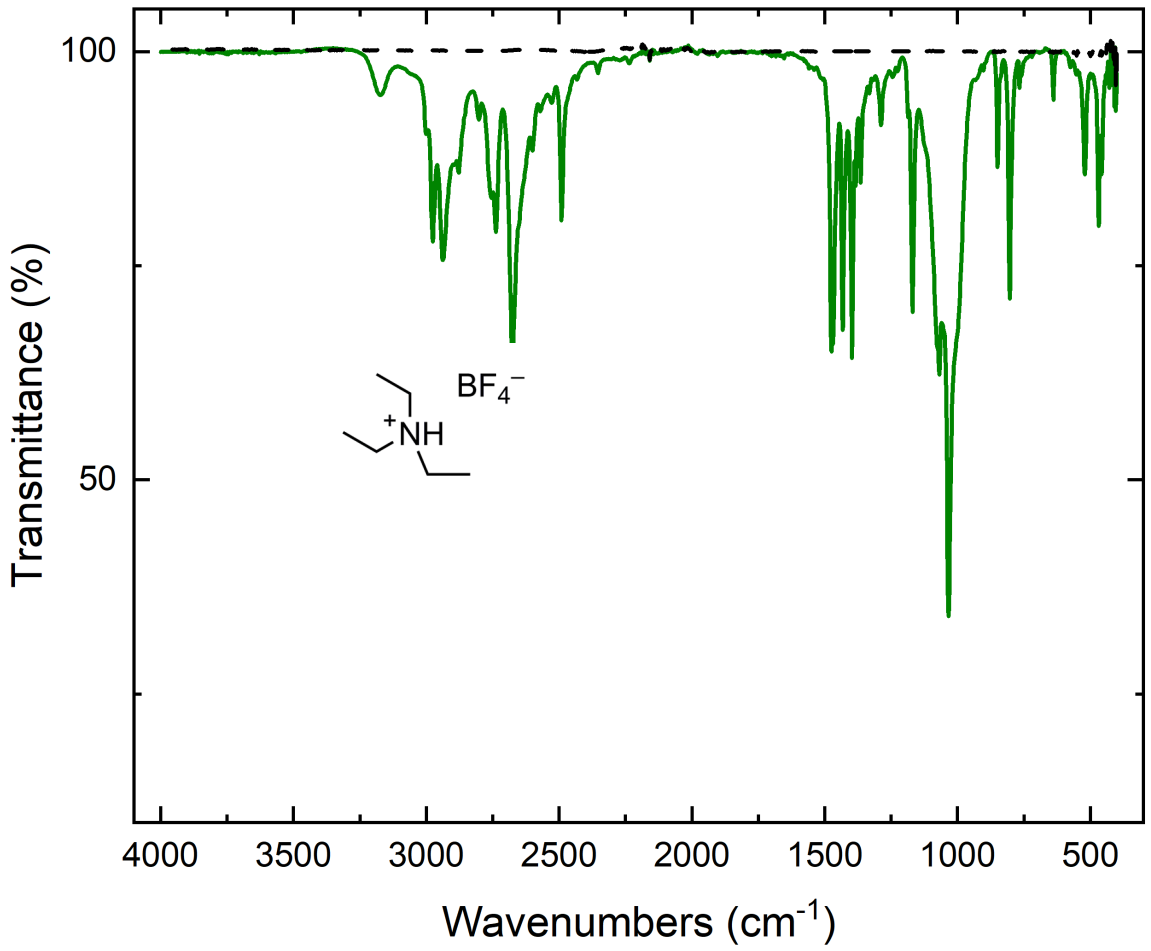

Figure B16: IR Spectrum (solid, diamond plate ATR) of $[HNEt_3]BF_4$.

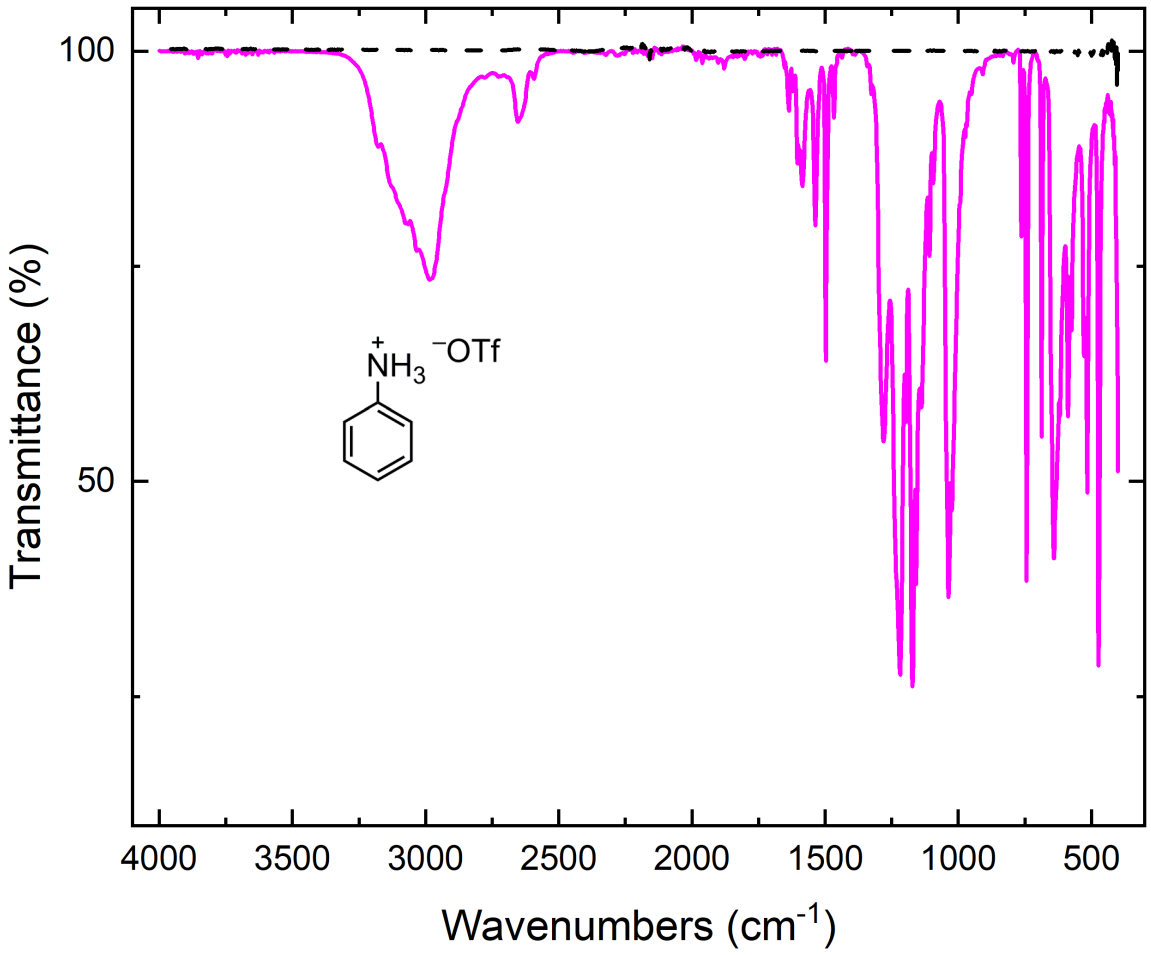

Figure B17: IR Spectrum (solid, diamond plate ATR) of [$PhNH_3$]OTf.

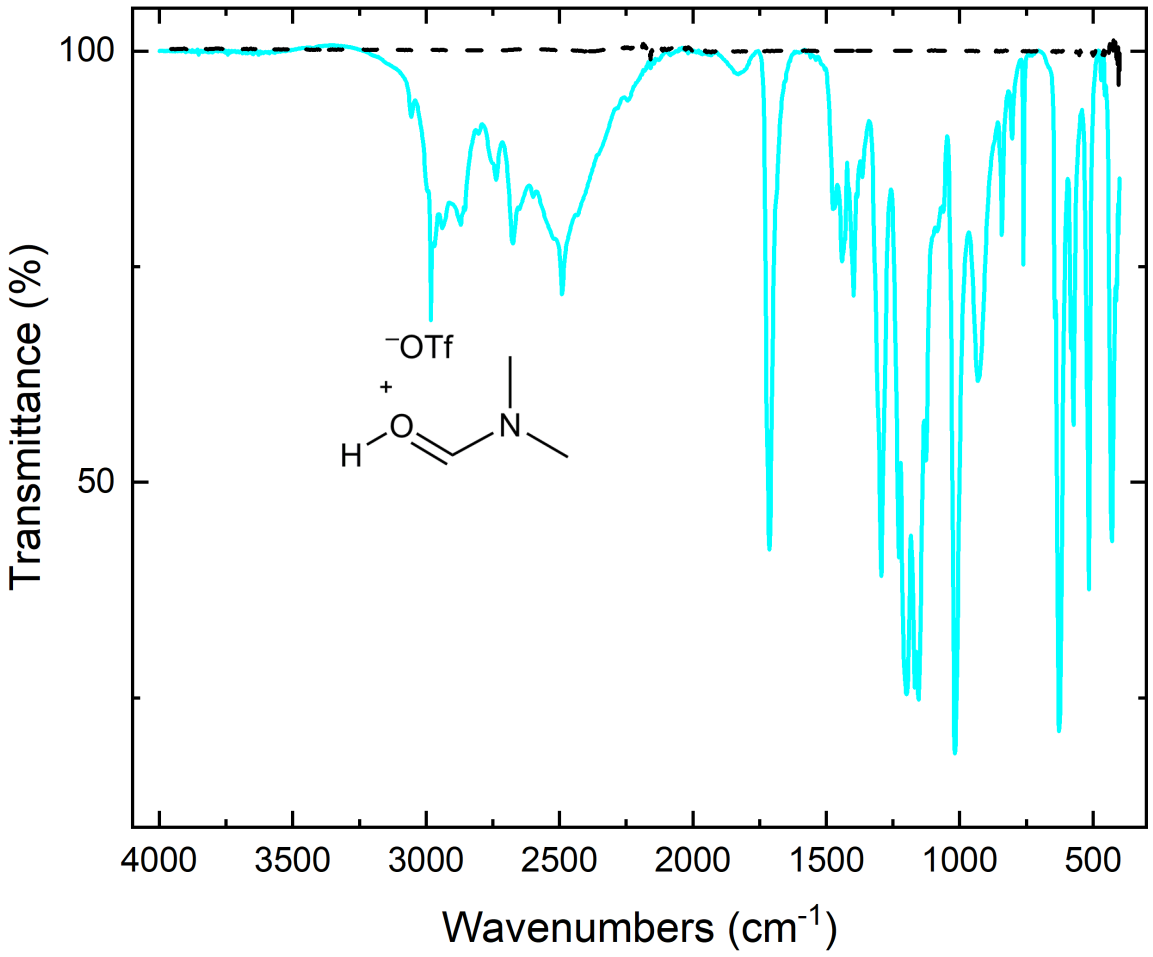

Figure B**18:** IR Spectrum (solid, diamond plate ATR) of [DMFH]OTf.

Pulse Radiolysis Data

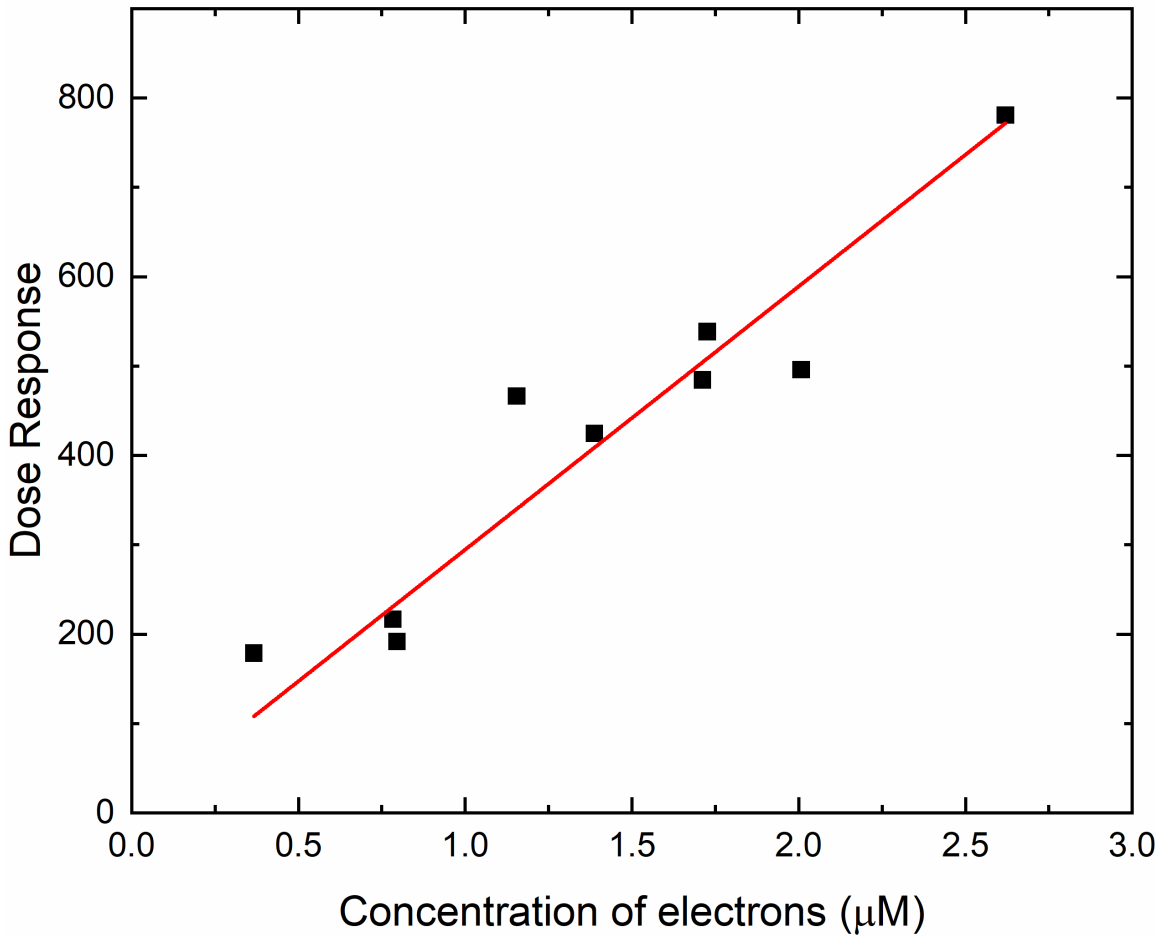

Figure B19: The concentration of reducing equivalents used for calculating the extinction coefficient is determined using calibrated dosimetry. The dose during pulse radiolysis is determined and calibrated by measuring the dose response as a function of electron concentration using $[Co(HMD)]^{+}$.

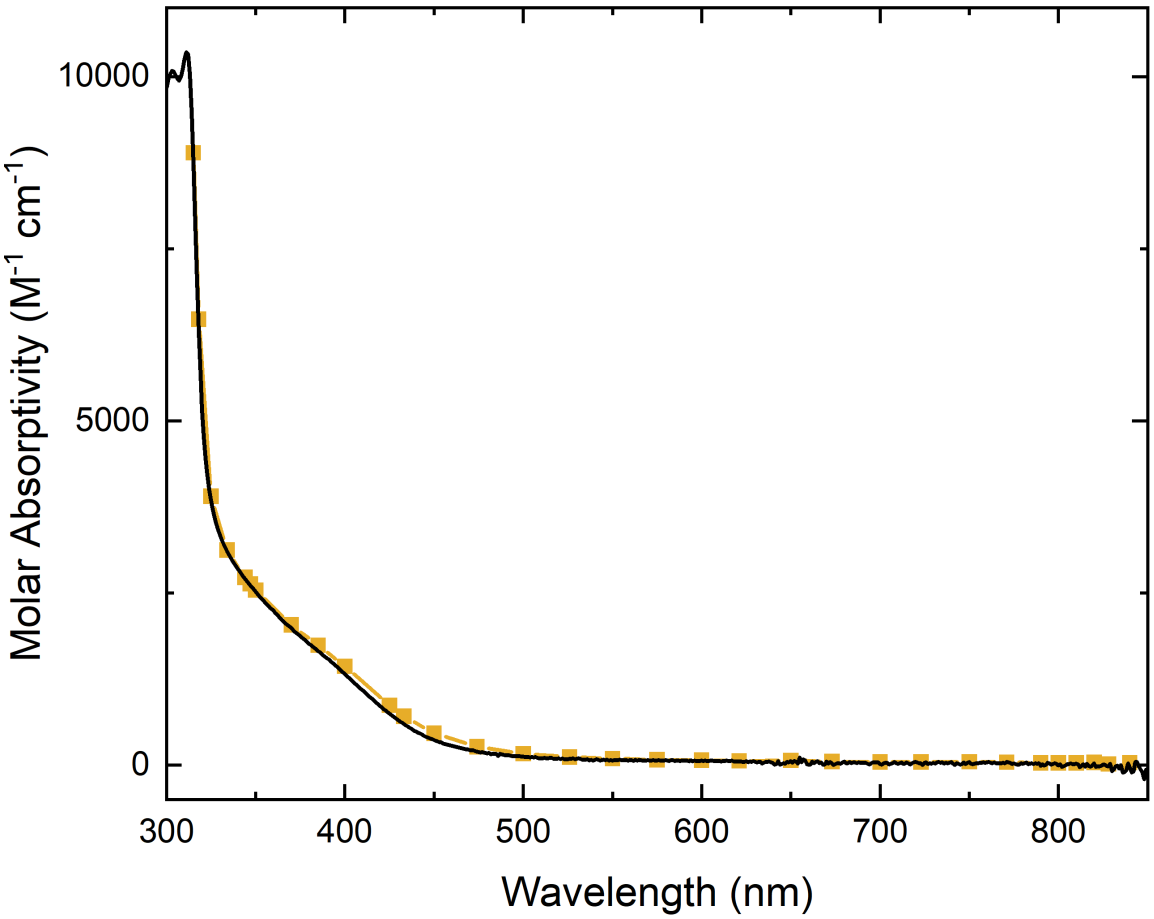

Figure B20: Absorption spectrum of **1** before pulse radiolysis is performed. The spectrum collected in the pulse radiolysis experiment (gold) matches the spectrum obtained from an isolated sample of **1** (black line).

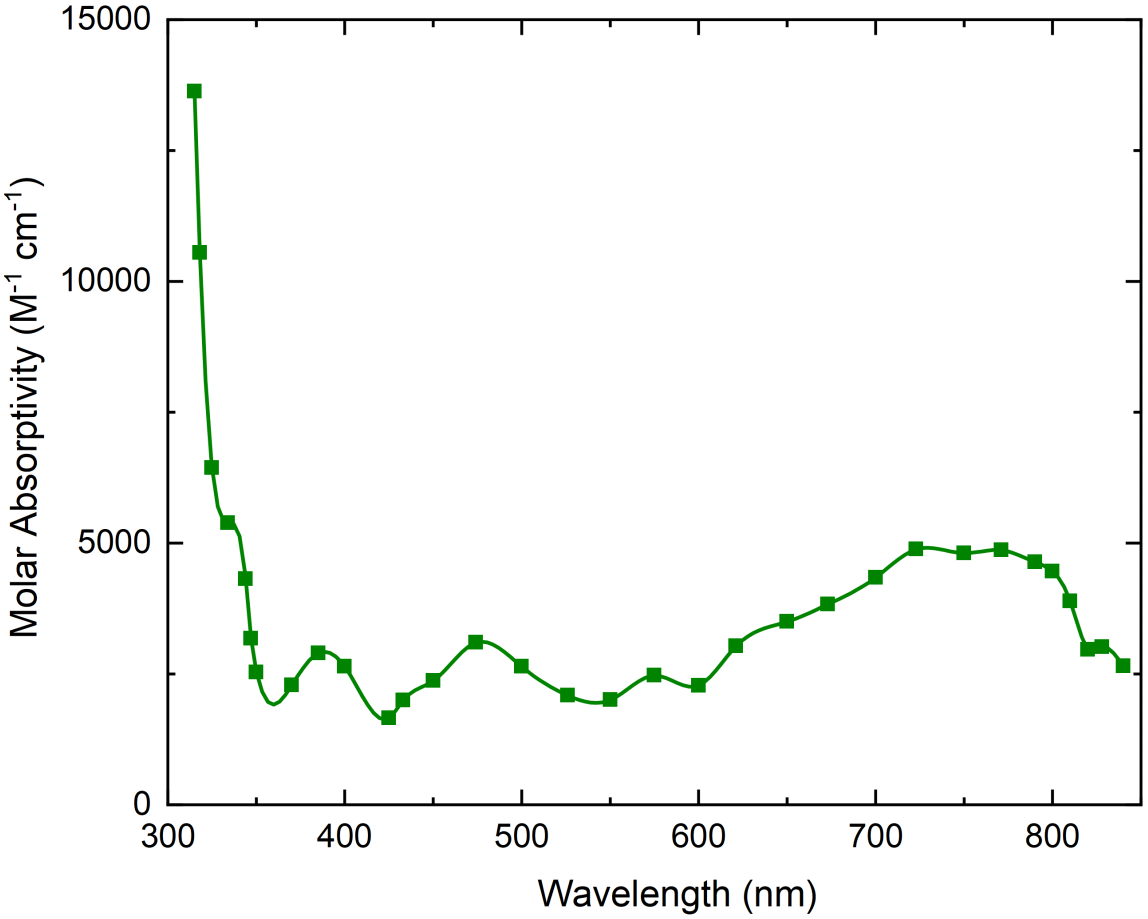

Figure B21: Absorption spectrum of **2** (green) measured after 1e⁻ reduction of **1** by pulse radiolysis in MeCN.

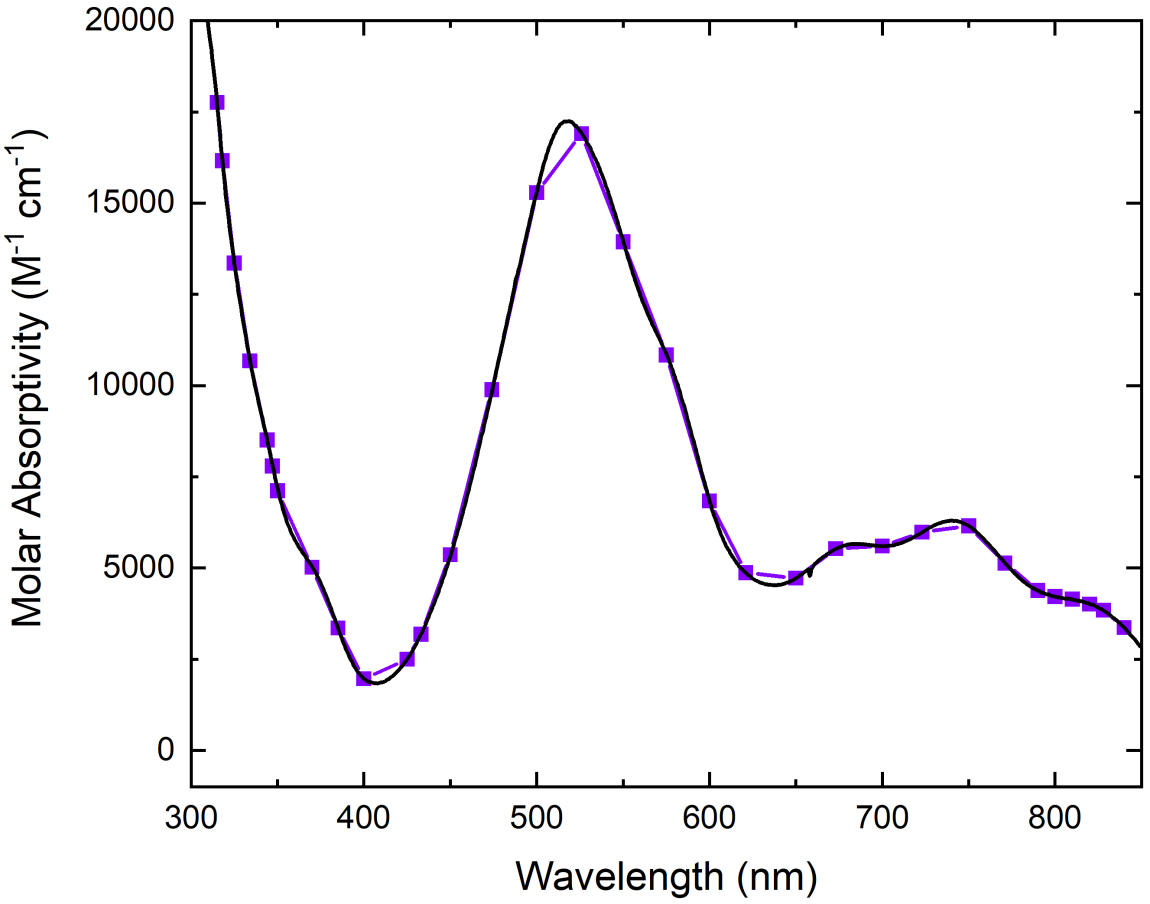

Figure B22: Absorption spectrum of **3** (purple) measured after $2e^-$ reduction of **1** by pulse radiolysis in MeCN. The spectrum collected in the pulse radiolysis experiment (purple) matches the spectrum obtained from an isolated sample of **3** (black).

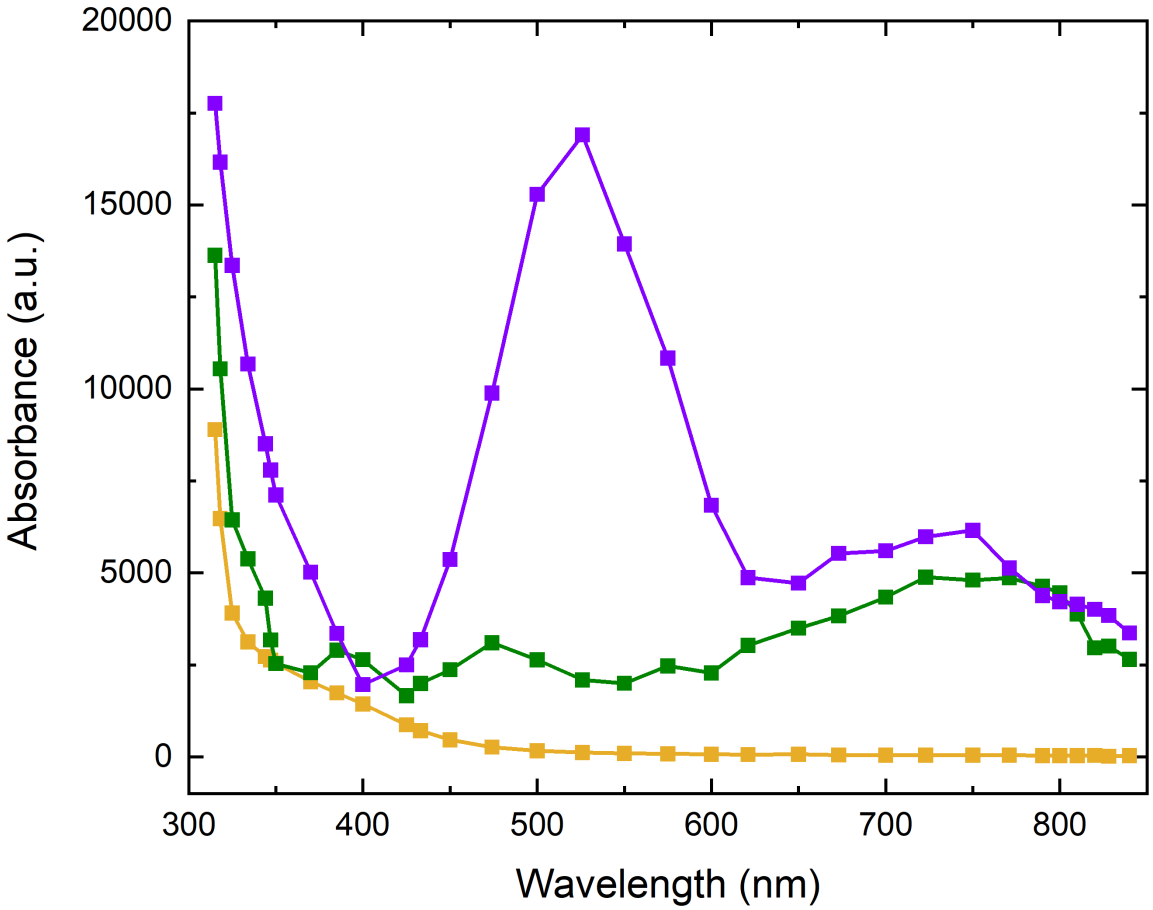

Figure B23: Overlay of absorption spectra measured after $1e^-$ (**2**, green) and $2e^-$ (**3**, purple) reduction of **1** (yellow) by pulse radiolysis in MeCN.

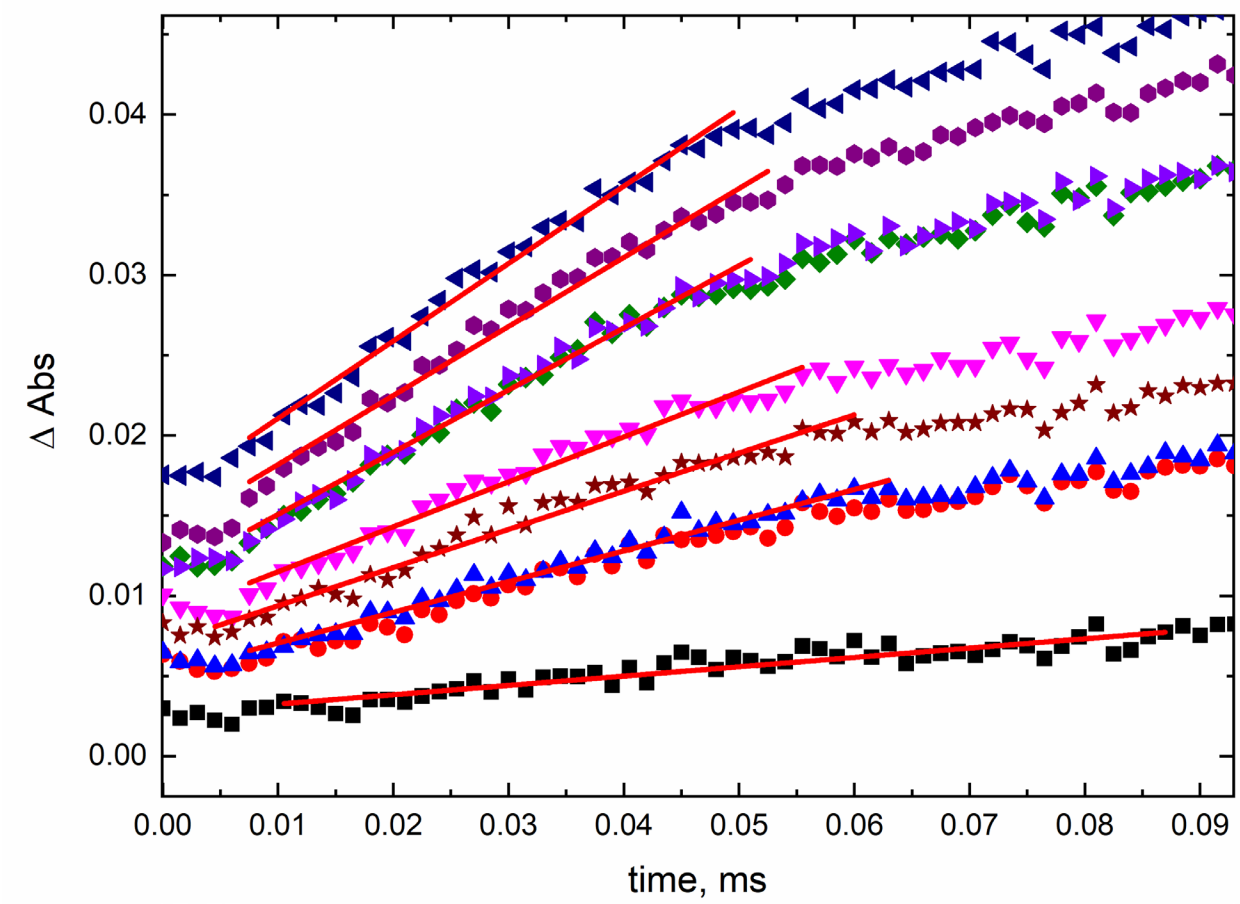

Figure B24: The plot of absorbance at 520 nm vs. time for pulse radiolysis of **1** in MeCN in the presence of 50 mM formate at different doses of an electron pulse. Red lines represent a linear fit through the linear region of the exponential signal growth near time zero. The slope of the fit provides an initial rate of the reaction at a given electron dose.

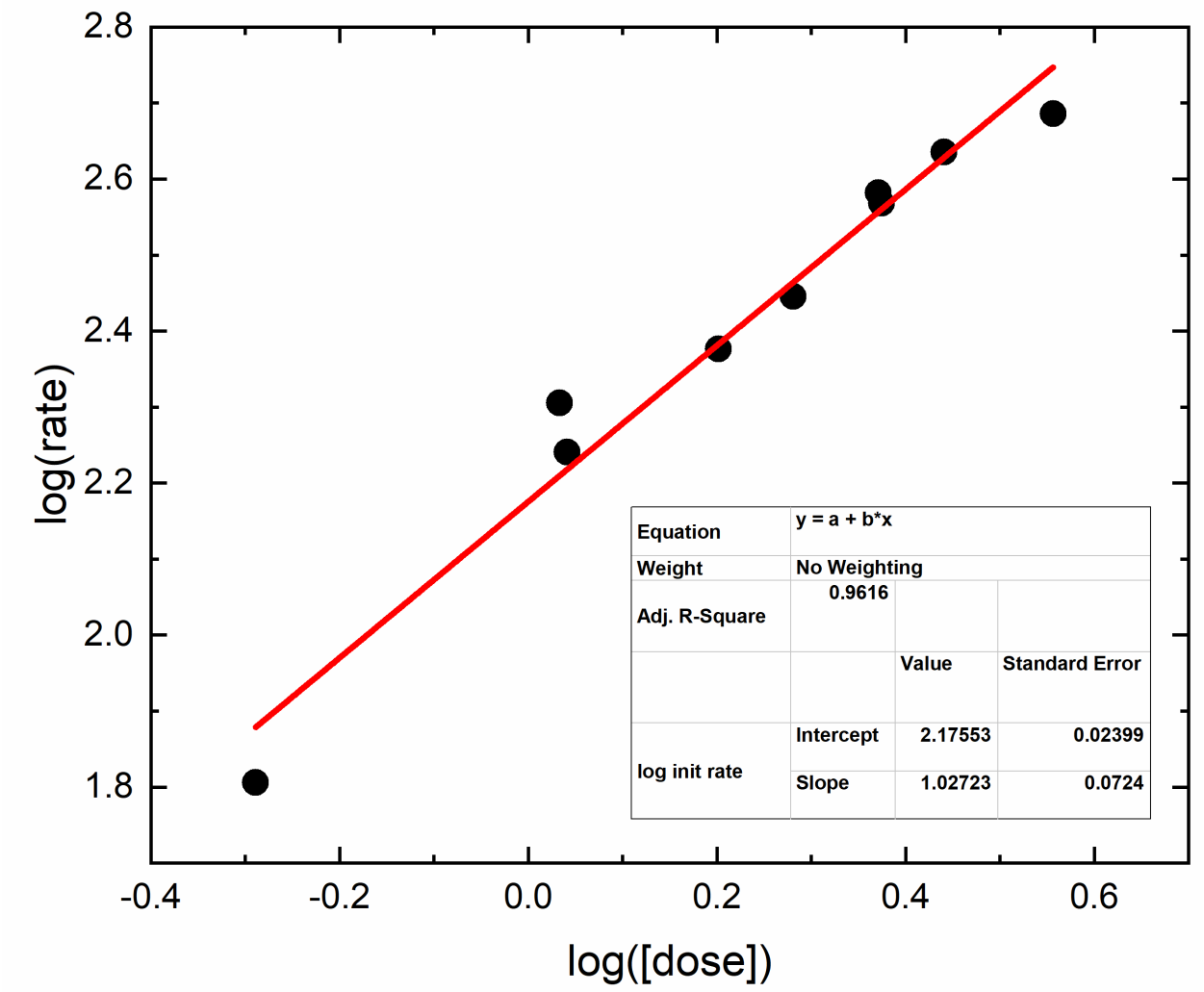

Figure B25: The log(rate) as a function of log([**dose**]) obtained from fits shown in Figure B29. The dose is defined as a duration of an electron pulse (in ns) and is directly proportional to the concentration of transient reducing radicals. The fit (red line) results in a slope of 1.03 ± 0.07, confirming a first-order dependence on **2** during generation of **3**.

Stopped-Flow Kinetic Data for Protonation and Tautomerization: Order and Rate Constant Determination

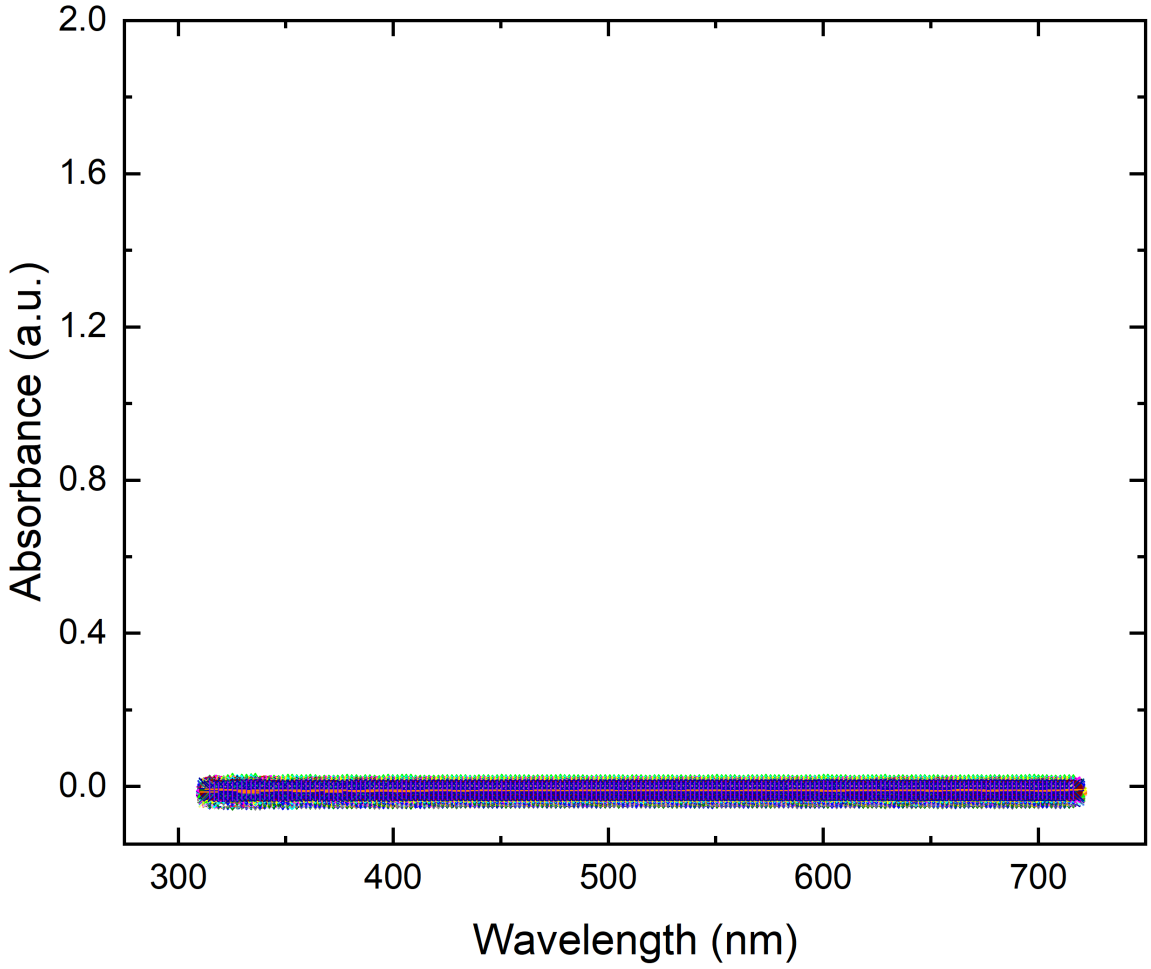

Figure B26: Stopped-flow absorbance vs wavelength plot of MeCN solvent (400 spectra).

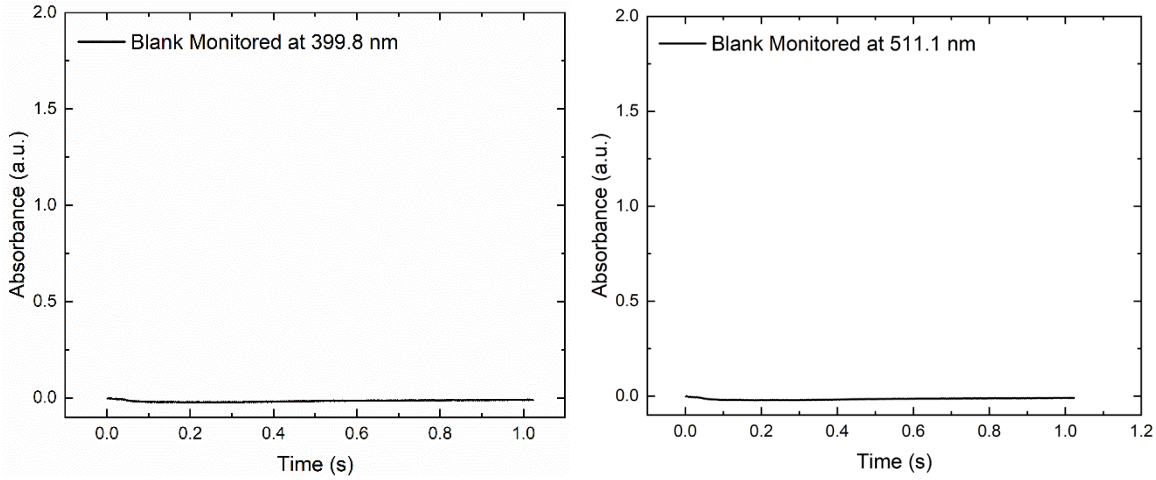

Figure B27: Stopped-flow absorbance vs time plots of MeCN solvent monitored at 399.8 nm and 511.1 nm.

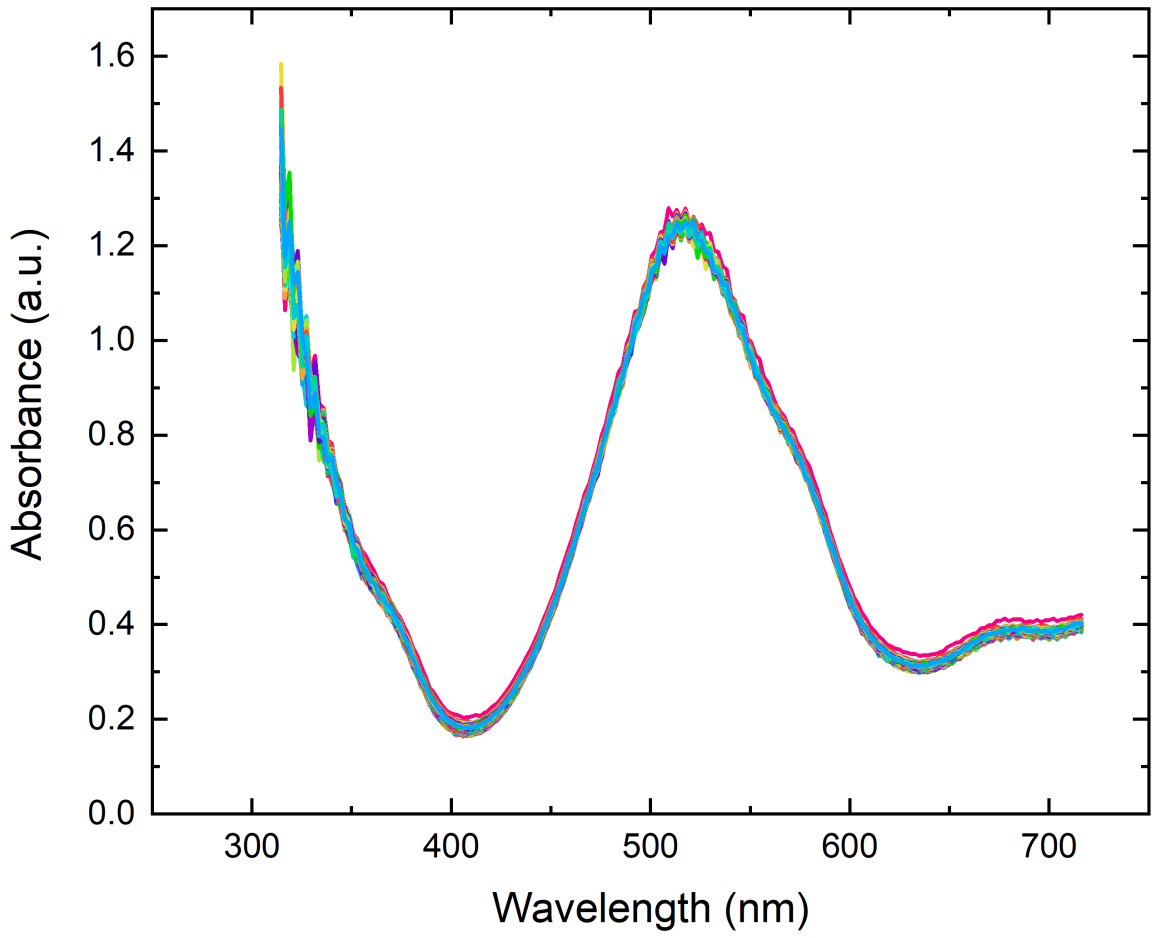

Figure B28: Stopped-flow absorbance vs wavelength plot following the rapid mixing of **3** with MeCN solvent.

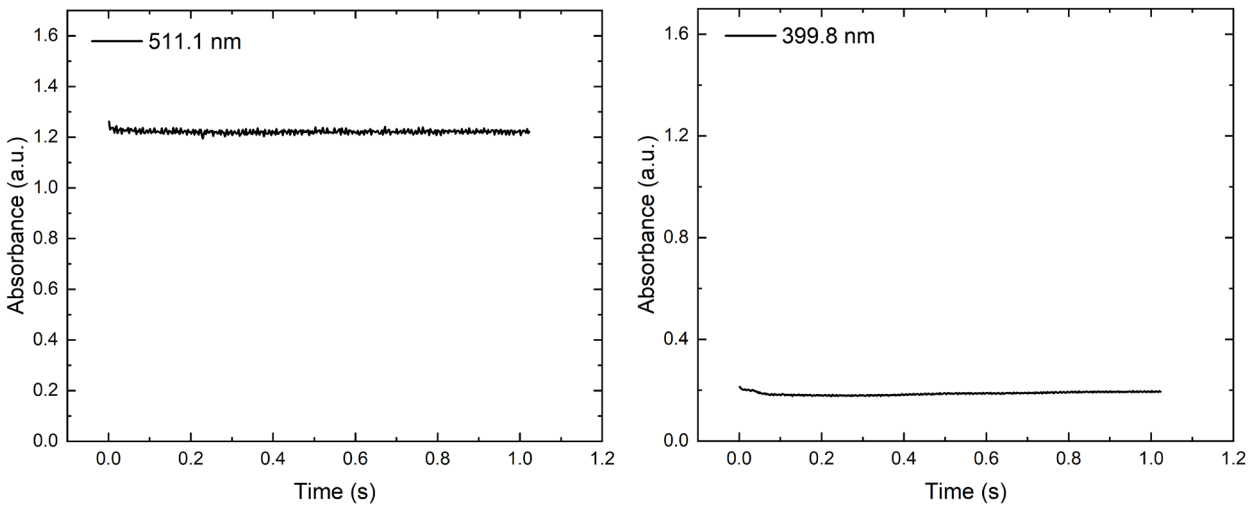

Figure B29: Stopped-flow absorbance vs time plots of **3** and MeCN solvent monitored at 399.8 nm (right) and 511.1 nm (left) illustrating no significant change in absorbance over the time course of the experiment.

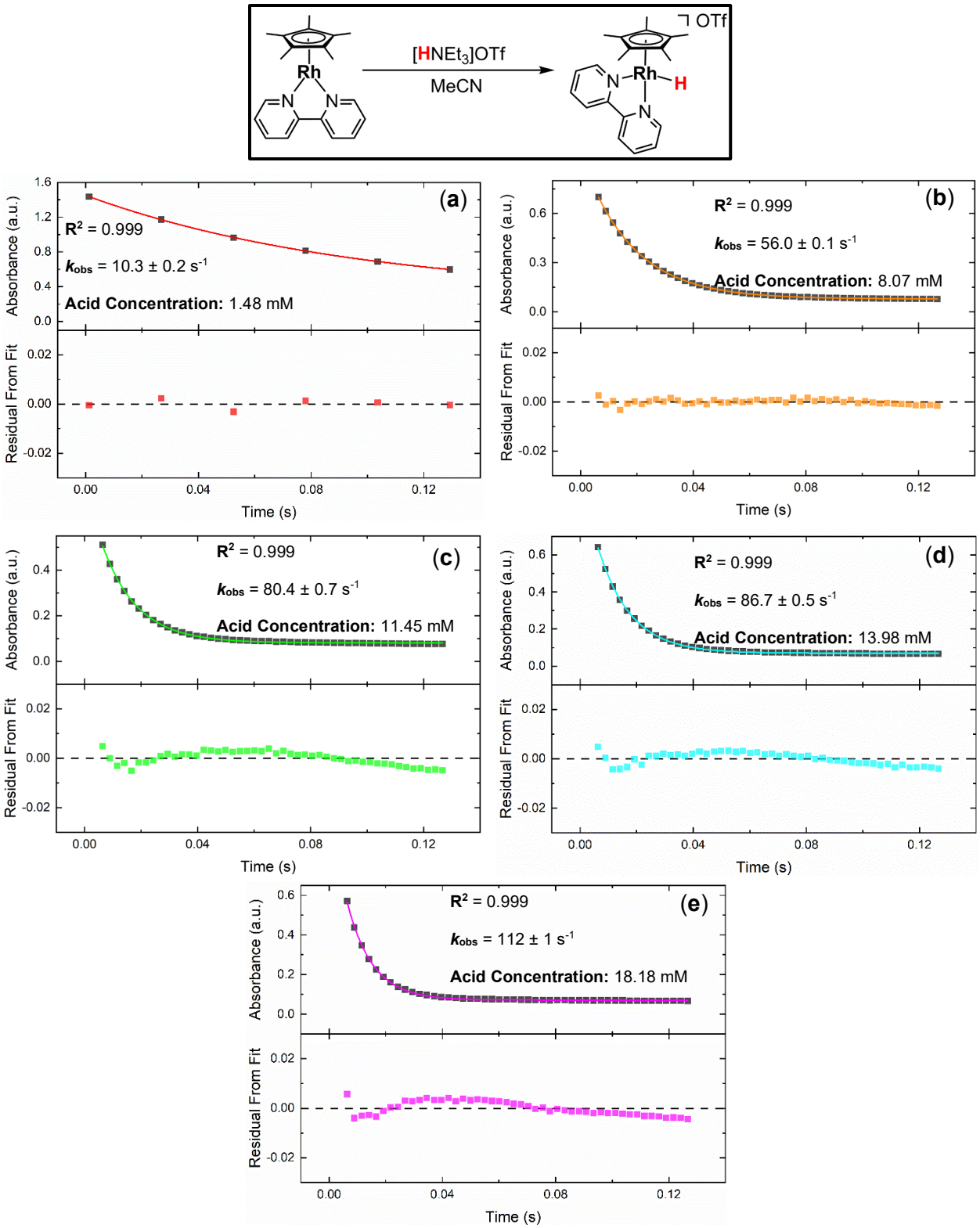

Figure B30: (**a-e**) Monitoring absorbance vs time at 511.1 nm for the initial protonation of **3** with [HNEt$_3$]OTf under pseudo-first order conditions. The decay of the signal at 511.1 nm is fit with a monoexponential function to extract the observed rate constant (k_{obs}). The residual from the fit monitored as a function of time rationalizes the use of a monoexponential fit here.

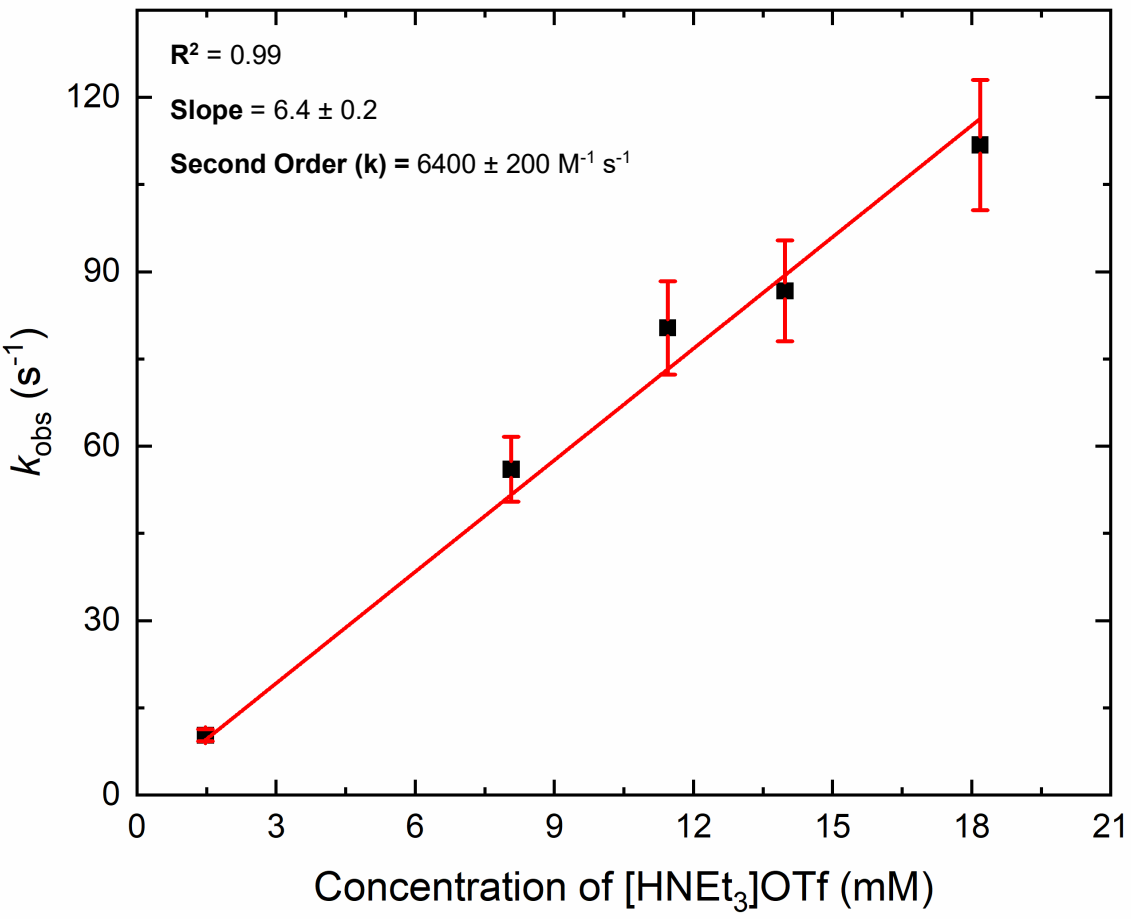

Figure B31: k_{obs} values (black squares) were obtained from the monoexponential fit of the decay signal at 511.1 nm in Figure B30 and are plotted here as a function of acid concentration. The k_{obs} values were measured at room temperature (298 K). The resulting plot is fit as a line (red) through the origin to extract the second order rate constant for the initial protonation of **3** with [$HNEt_3$]OTf to generate **4**.

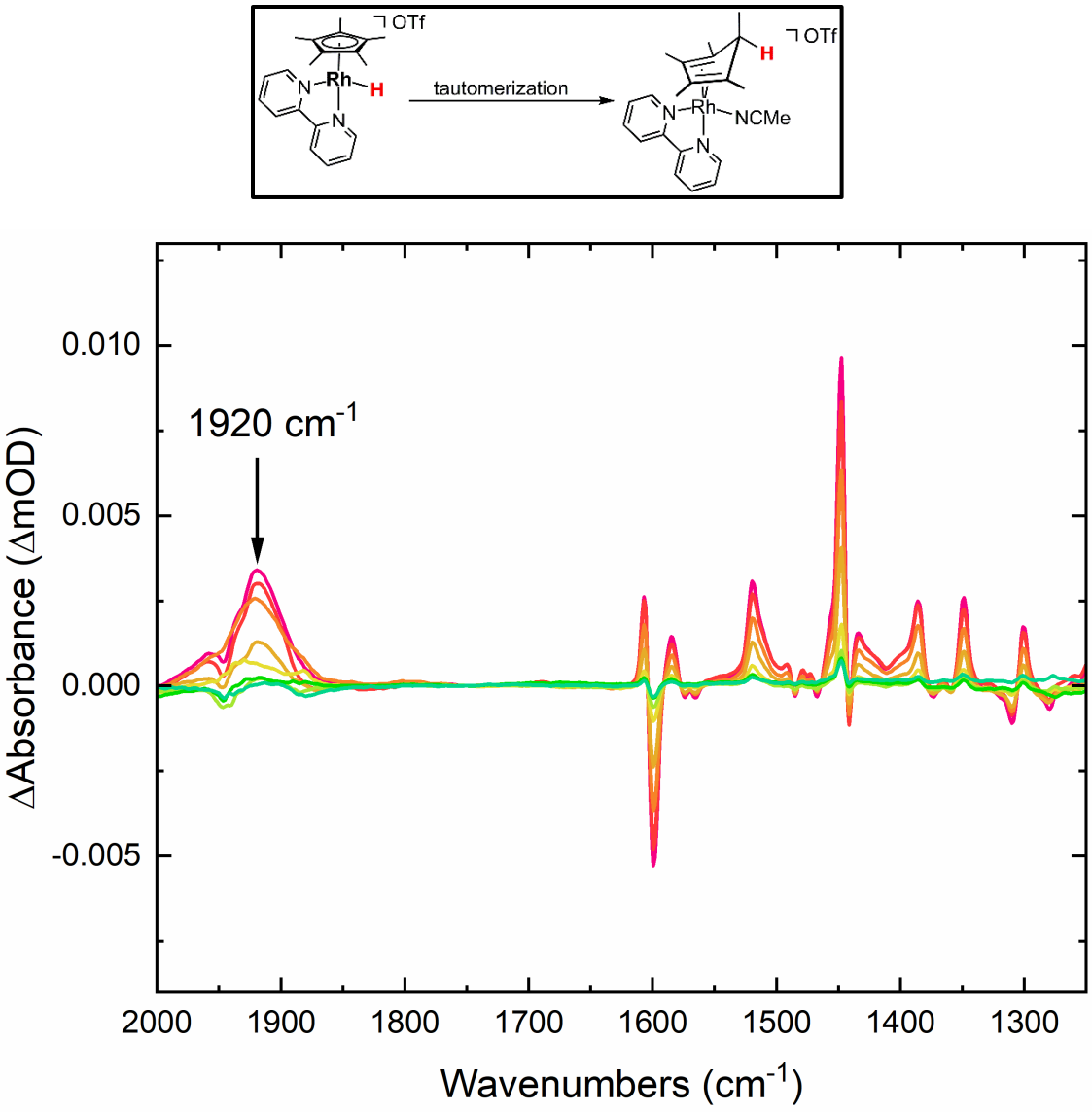

Figure B32: Stopped-flow IR monitoring the ΔAbsorbance vs wavenumbers for the tautomerization of **4** to generate **5** under pseudo-first order conditions. The signal at 1920 cm^{-1} is attributed to the Rh–H stretch.

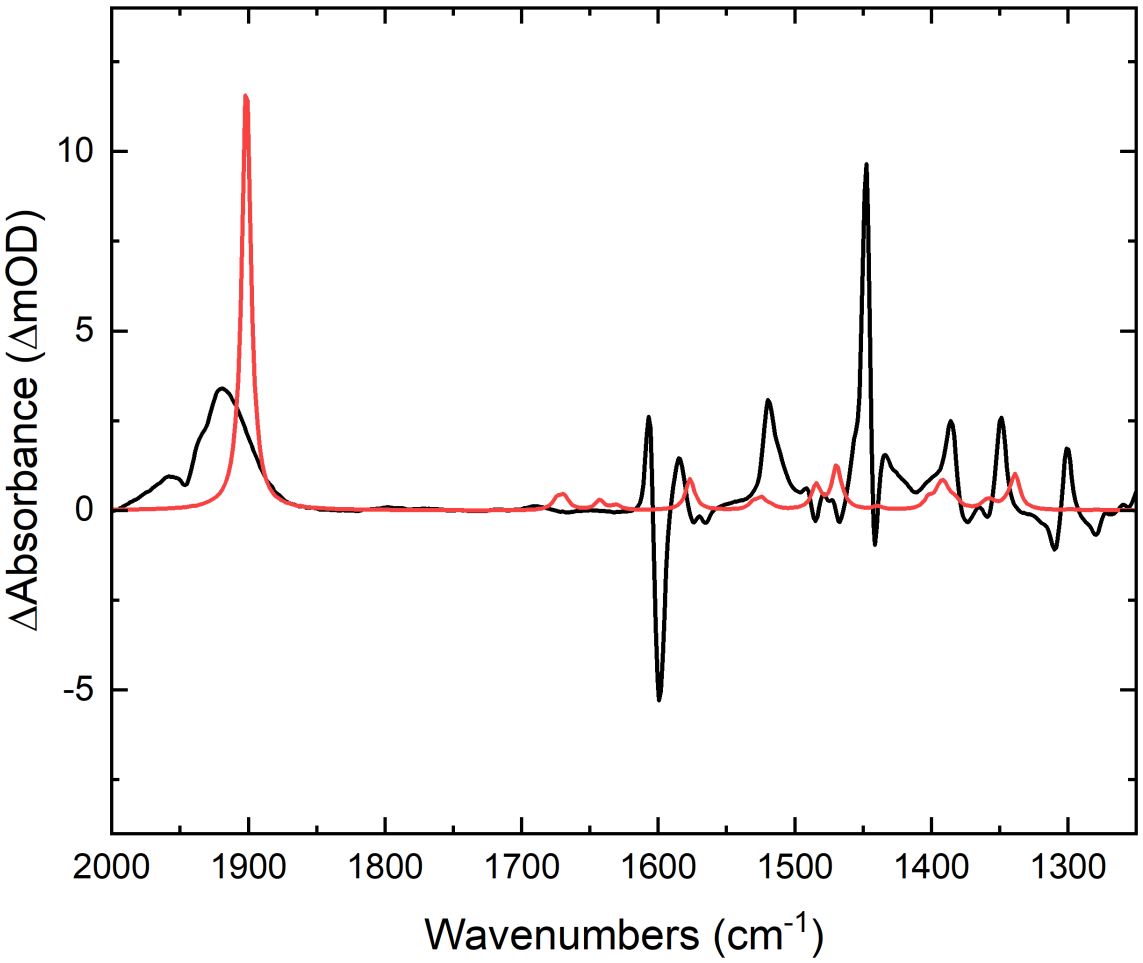

Figure B33: Experimental stopped-flow FTIR monitoring of the ΔAbsorbance vs wavenumbers for the tautomerization of **4** (**black**). The signal at 1920 cm^{-1} corresponds to the Rh–H stretch, and this observation is supported by the DFT calculated FTIR spectrum of **4** (**red**).

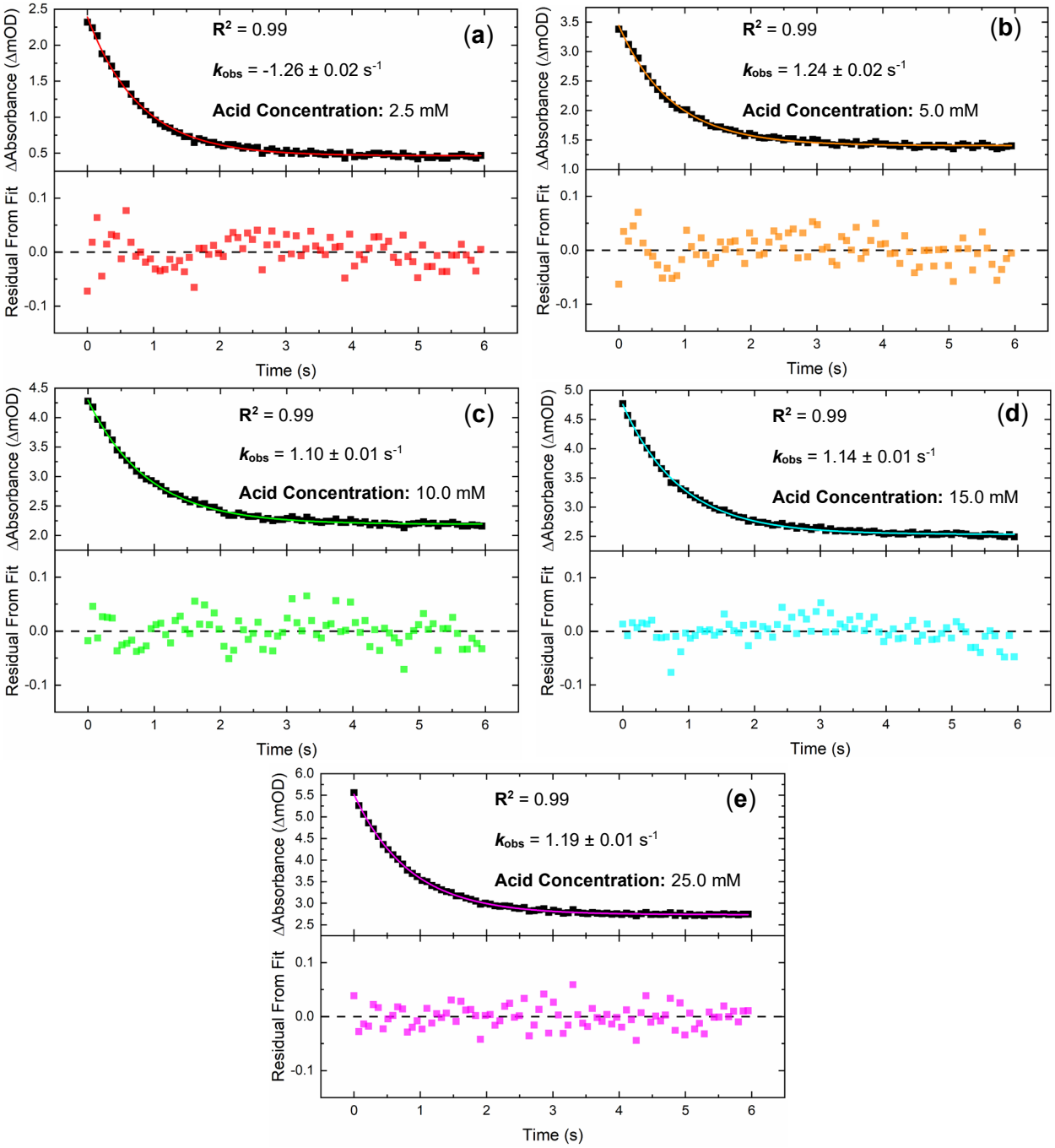

Figure B34: (**a-e**) Monitoring ΔAbsorbance vs wavenumbers at 1920 cm^{-1} for the tautomerization of **4** to generate **5** under pseudo-first order conditions. The decay of the signal at 399.8 nm is fit with a monoexponential function to extract the observed rate constant (k_{obs}). The residual from the fit monitored as a function of time rationalizes the use of a monoexponential fit here.

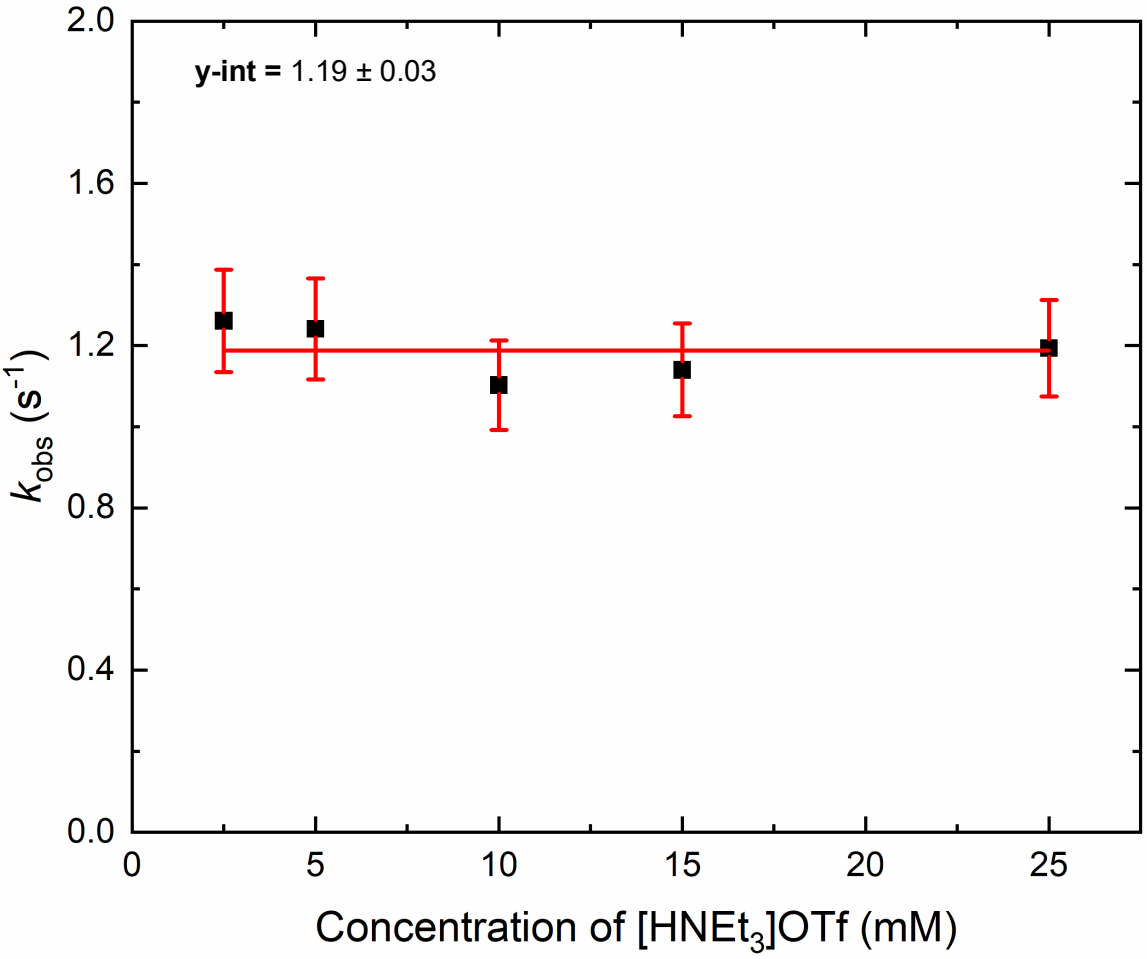

Figure B35: k_{obs} values (black squares) were obtained from the monoexponential fit of the decay signal at 1920 cm^{-1} in Figure B34 and are plotted here as a function of acid concentration. The k_{obs} values were measured at room temperature (298 K). The resulting plot is fit as a line with a fixed slope = 0 to extract the zero-order rate constant for the tautomerization of **4** to generate **5**.

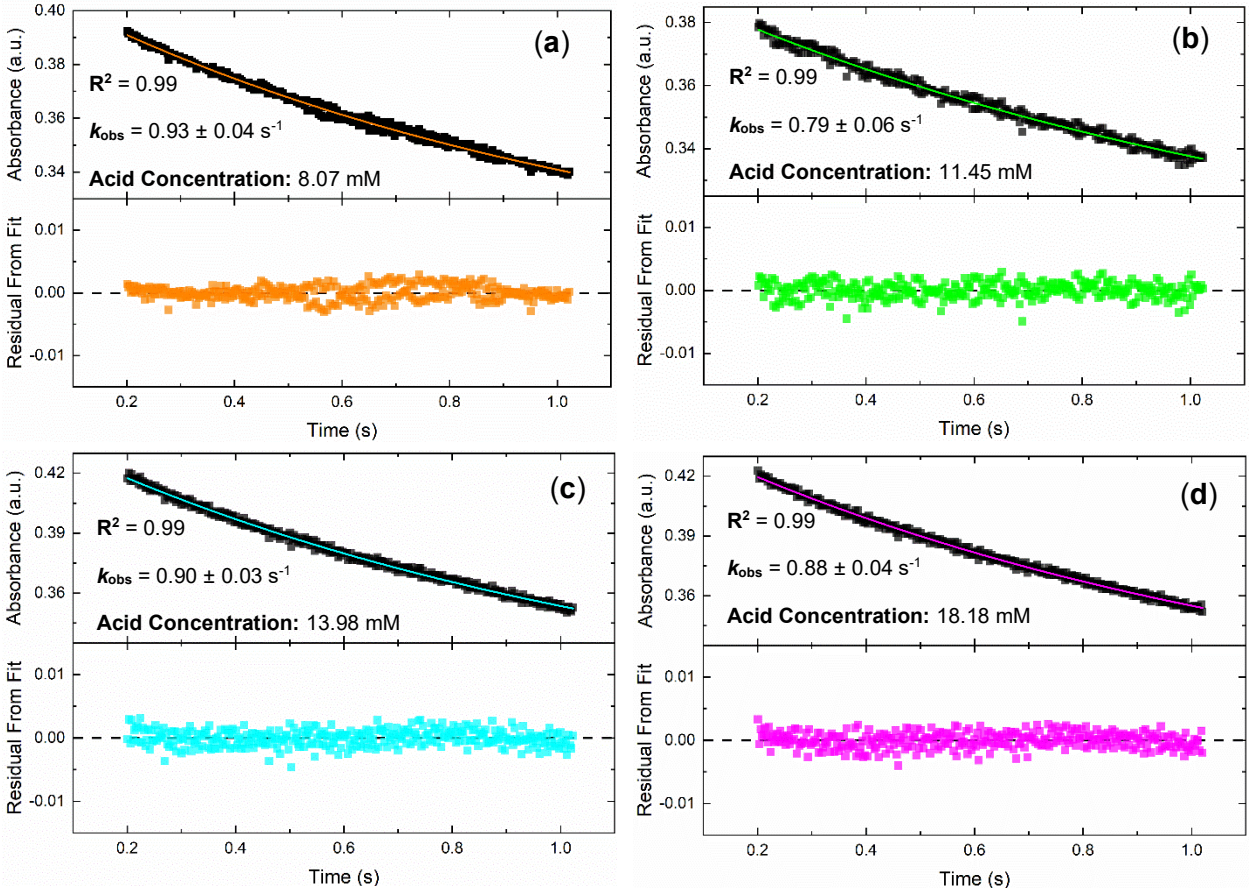

Figure B36: (**a-d**) Monitoring absorbance vs time at 399.8 nm out to 1 s for the tautomerization of **4** to generate **5** under pseudo-first order conditions. The decay of the signal at 399.8 nm is fit with a monoexponential function to extract the observed rate constant (k_{obs}). The residual from the fit monitored as a function of time rationalizes the use of a monoexponential fit here.

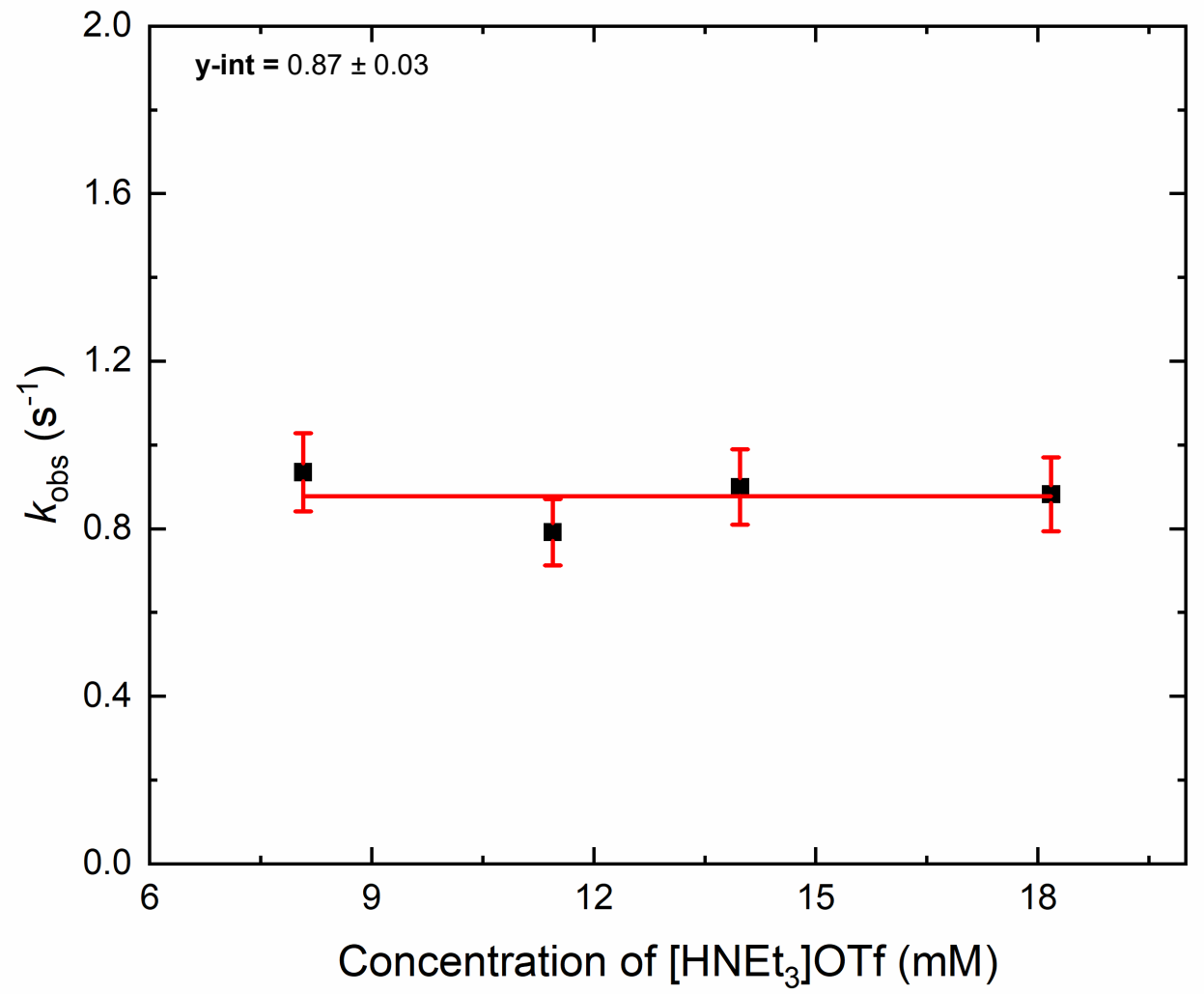

Figure B37: k_{obs} values (black squares) were obtained from the monoexponential fit of the decay signal at 399.8 nm in Figure B36 and are plotted here as a function of acid concentration. The k_{obs} values were measured at room temperature (298 K). The resulting plot is fit as a line with a fixed slope = 0 to extract the zero-order rate constant for the tautomerization of **4** to generate **5**.

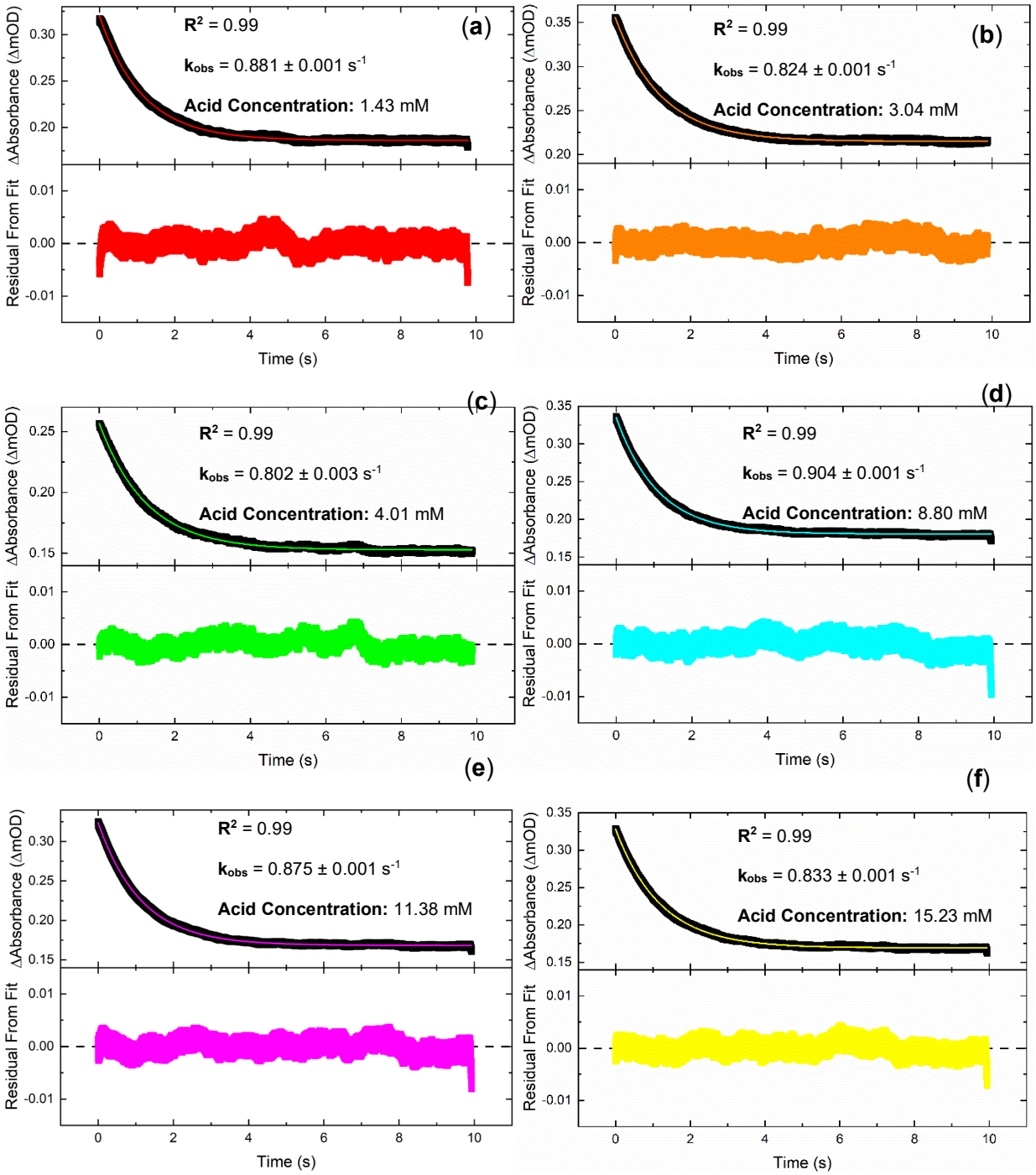

Figure B38: (**a-f**) Monitoring absorbance vs time at 399.8 nm out to 10 s for the tautomerization of **4** to generate **5** under pseudo-first order conditions. The decay of the signal at 399.8 nm is fit with a monoexponential function to extract the observed rate constant (k_{obs}). The residual from the fit monitored as a function of time rationalizes the use of a monoexponential fit here.

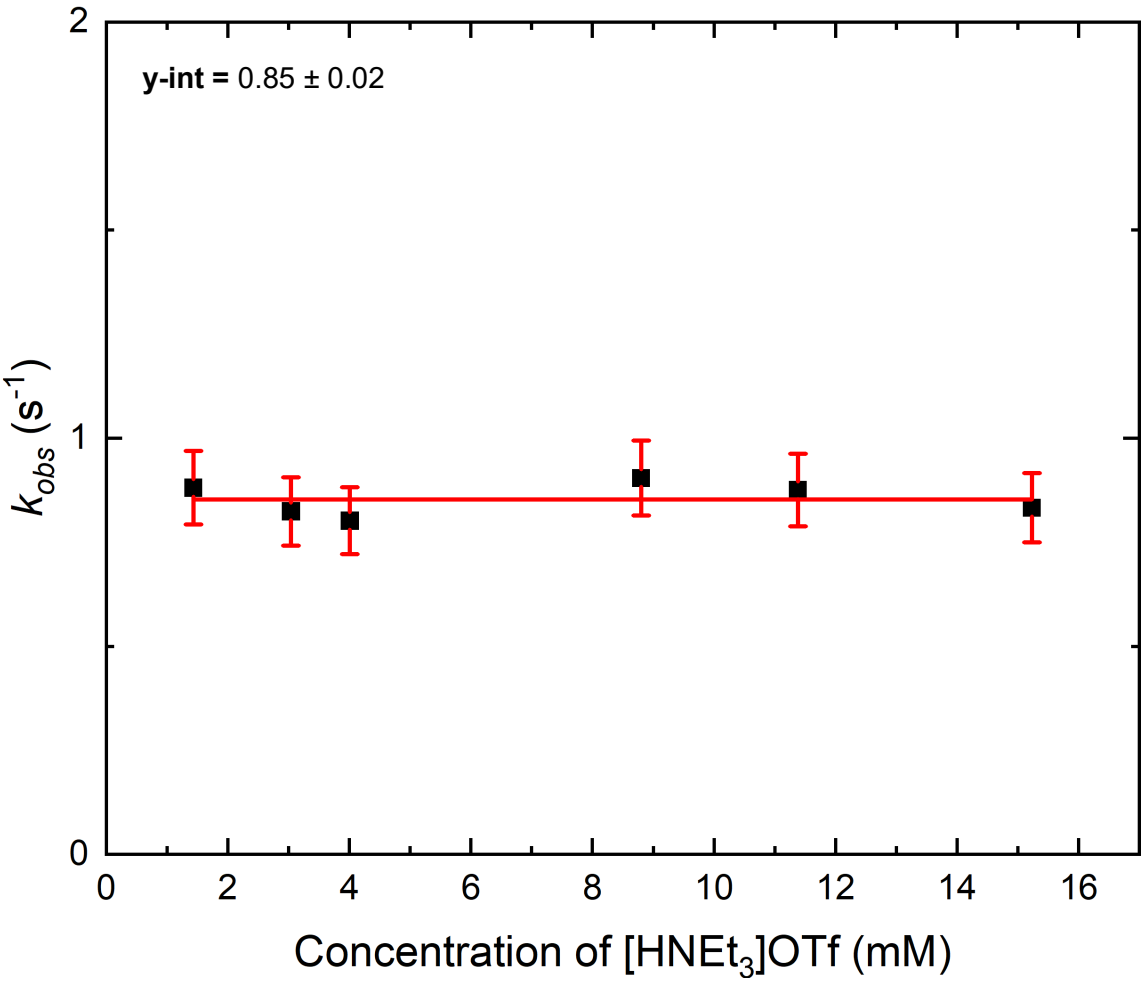

Figure B39: k_{obs} values (black squares) were obtained from the monoexponential fit of the decay signal at 399.8 nm over 10 s in Figure B38 and are plotted here as a function of acid concentration. The k_{obs} values were measured at room temperature (298 K). The resulting plot is fit as a line with a fixed slope = 0 to extract the zero-order rate constant for the tautomerization of **4** to generate **5**.

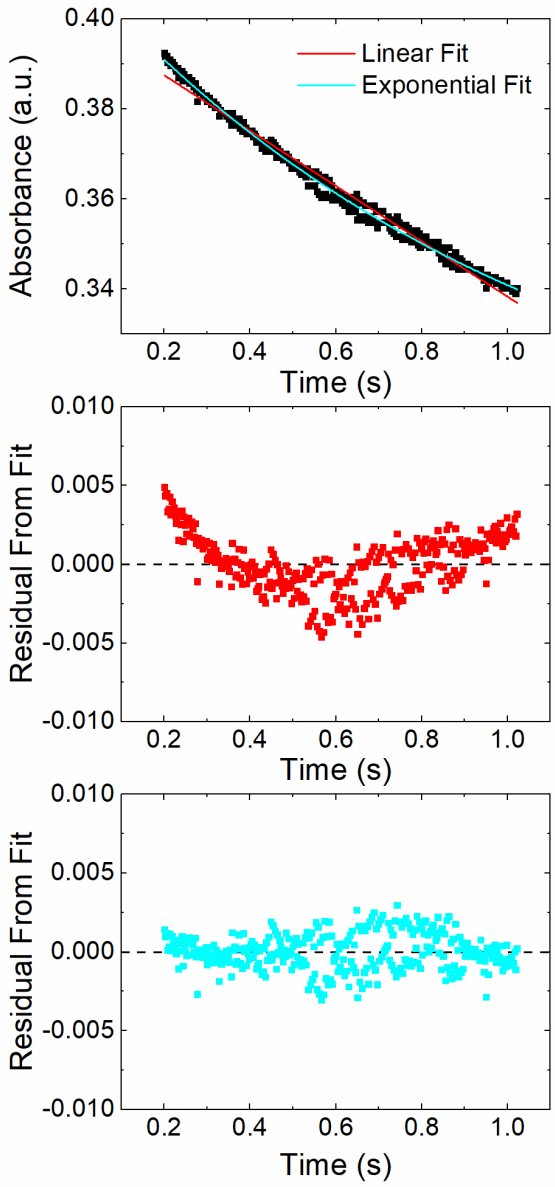

Figure B40: Residual analysis comparing linear vs monoexponential fits for the data in Figure B36. When the data are fit with a linear function the data show systematic deviations about zero. However, when the data are fit with a monoexponential function the data lie randomly about zero, confirming that a monoexponential fit is more suitable for this data than a linear function.

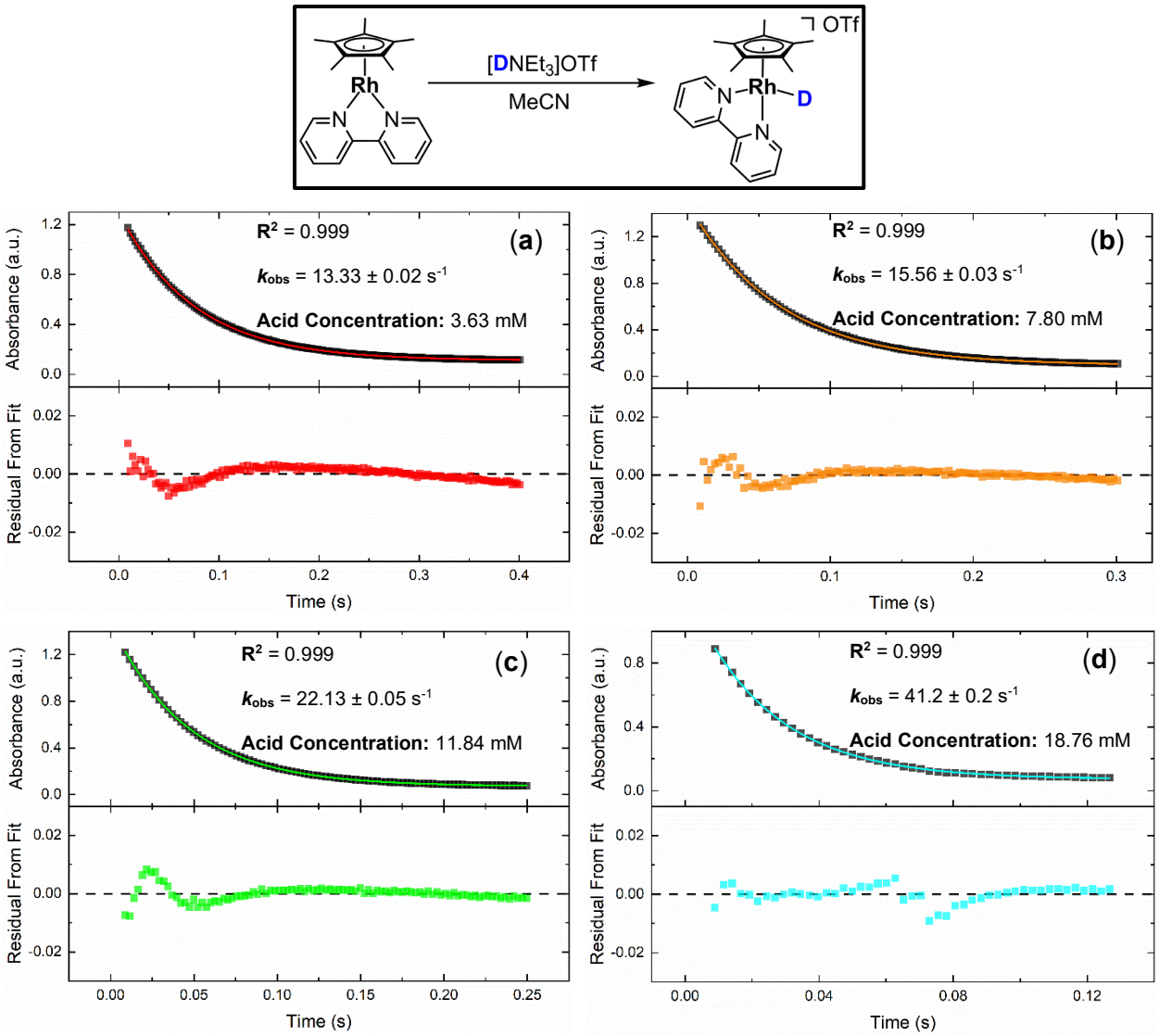

Figure B41: (**a-d**) Monitoring absorbance vs time at 511.1 nm for the initial deuteration of **3** with [DNEt$_3$]OTf under pseudo-first order conditions. The decay of the signal at 511.1 nm is fit with a monoexponential function to extract the observed rate constant (k_{obs}). The residual from the fit monitored as a function of time rationalizes the use of a monoexponential fit here.

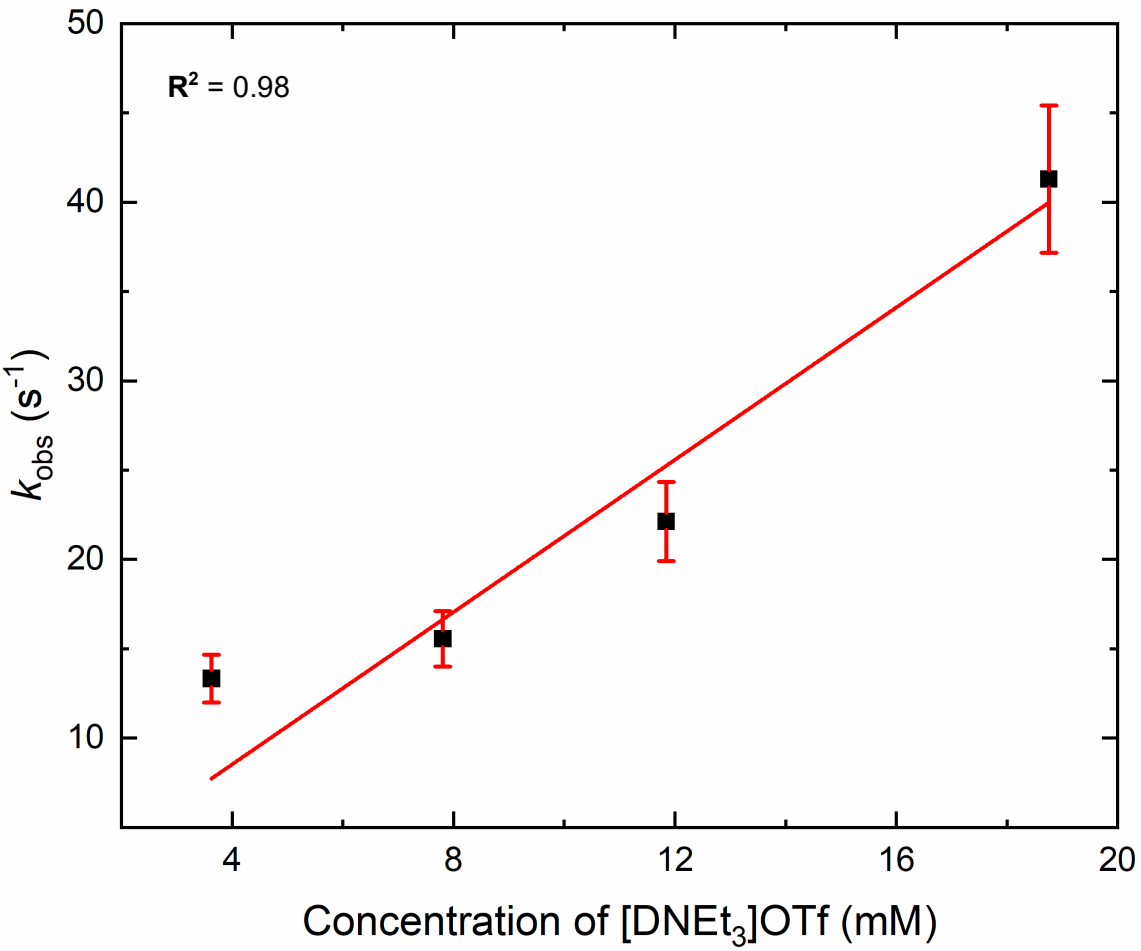

Figure B42: k_{obs} values (black squares) were obtained from the monoexponential fit of the decay signal at 511.1 nm and are plotted here as a function of acid concentration. The k_{obs} values were measured at room temperature (298 K). The resulting plot is fit as a line (red) through the origin to extract the second order rate constant for the initial protonation of **3** with [$DNEt_3$]OTf to generate **4D**.

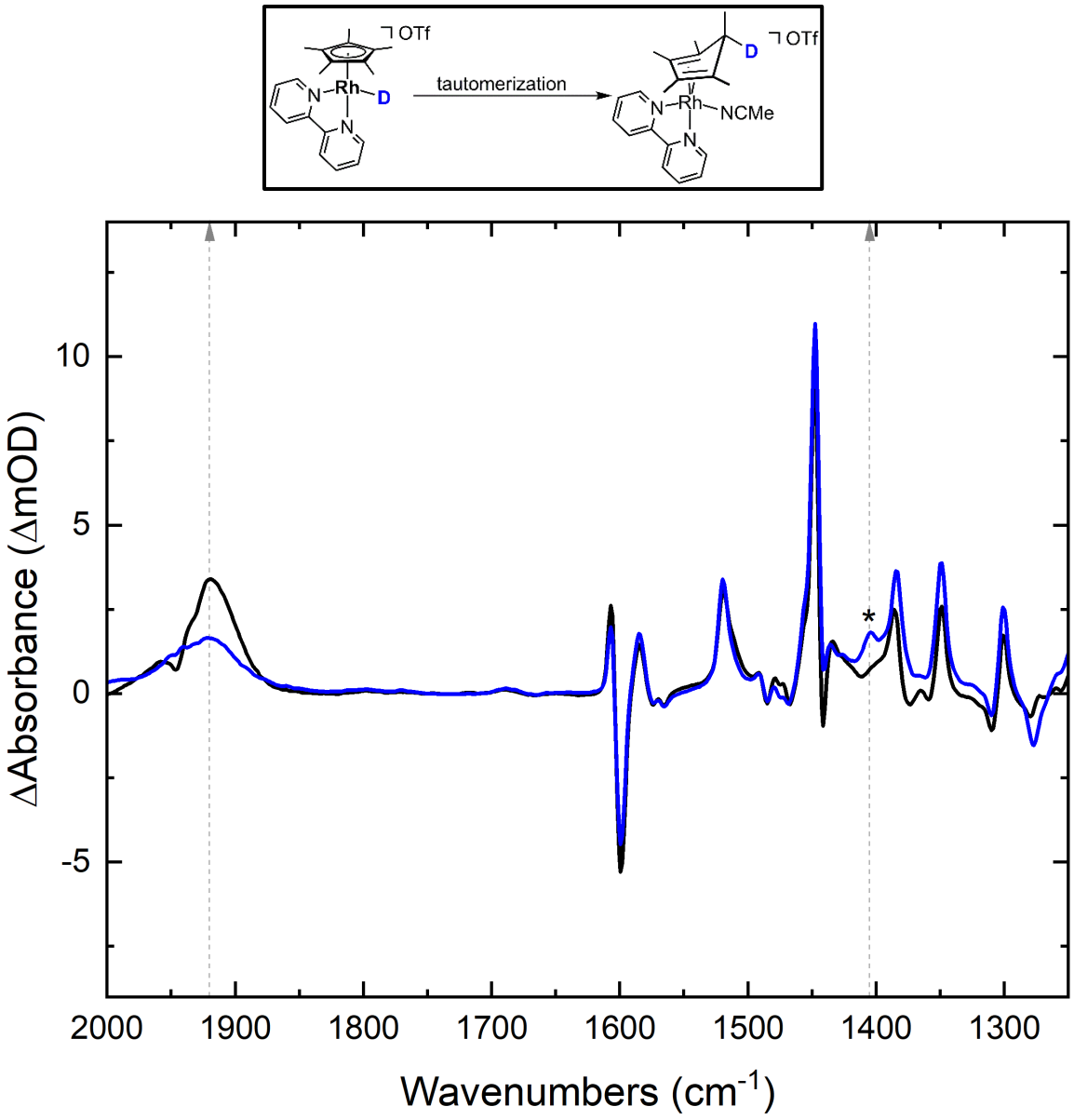

Figure B43: ΔAbsorbance vs wavenumbers comparing the Rh–H stretch for **4** (black) at 1920 cm^{-1} and the Rh–D stretch for **4D** at 1405 cm^{-1}(blue, *).

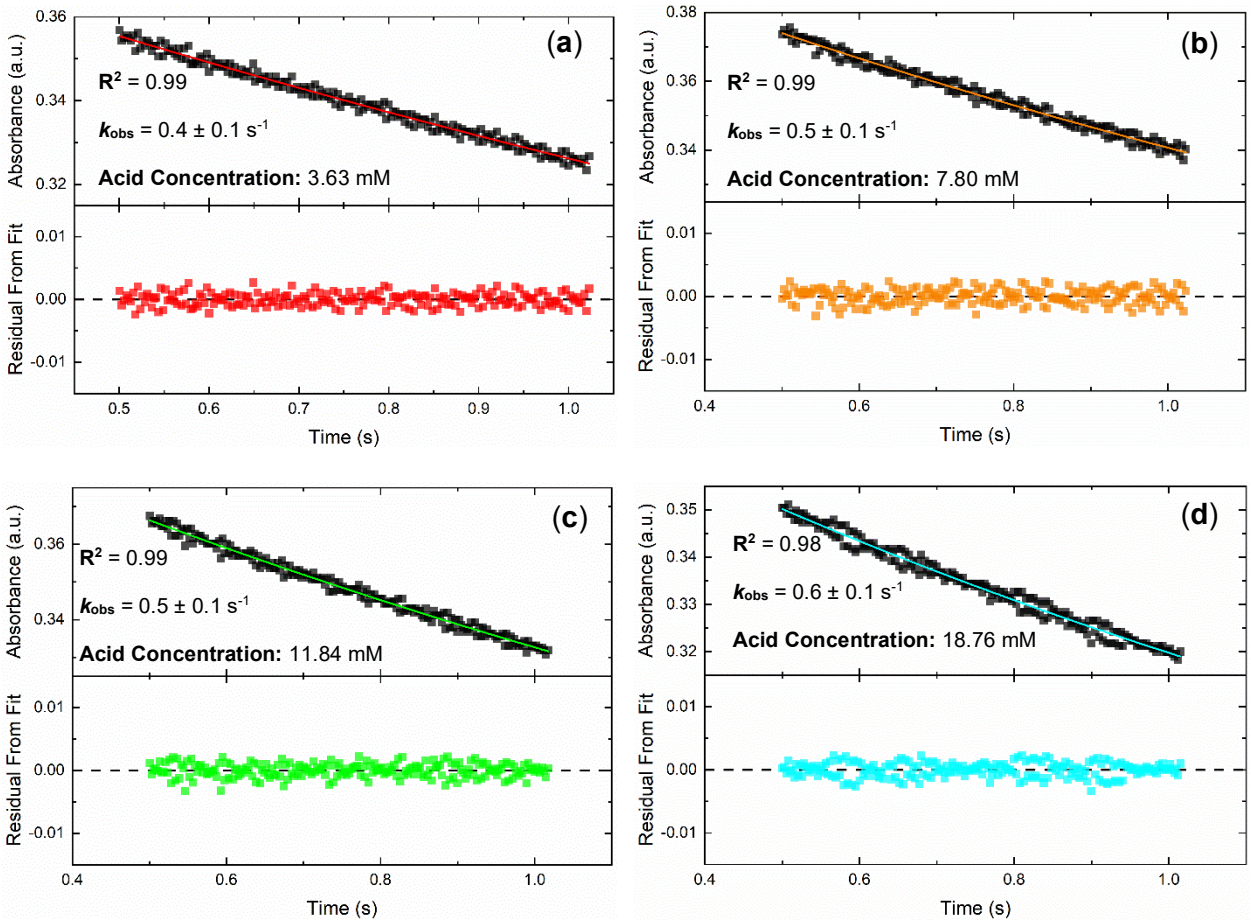

Figure B44: (**a-d**) Monitoring absorbance vs time at 399.8 nm for the tautomerization of **4D** to generate **5D** under pseudo-first order conditions. The decay of the signal at 399.8 nm is fit with a monoexponential function to extract the observed rate constant (k_{obs}). The residual from the fit monitored as a function of time rationalizes the use of a monoexponential fit here.

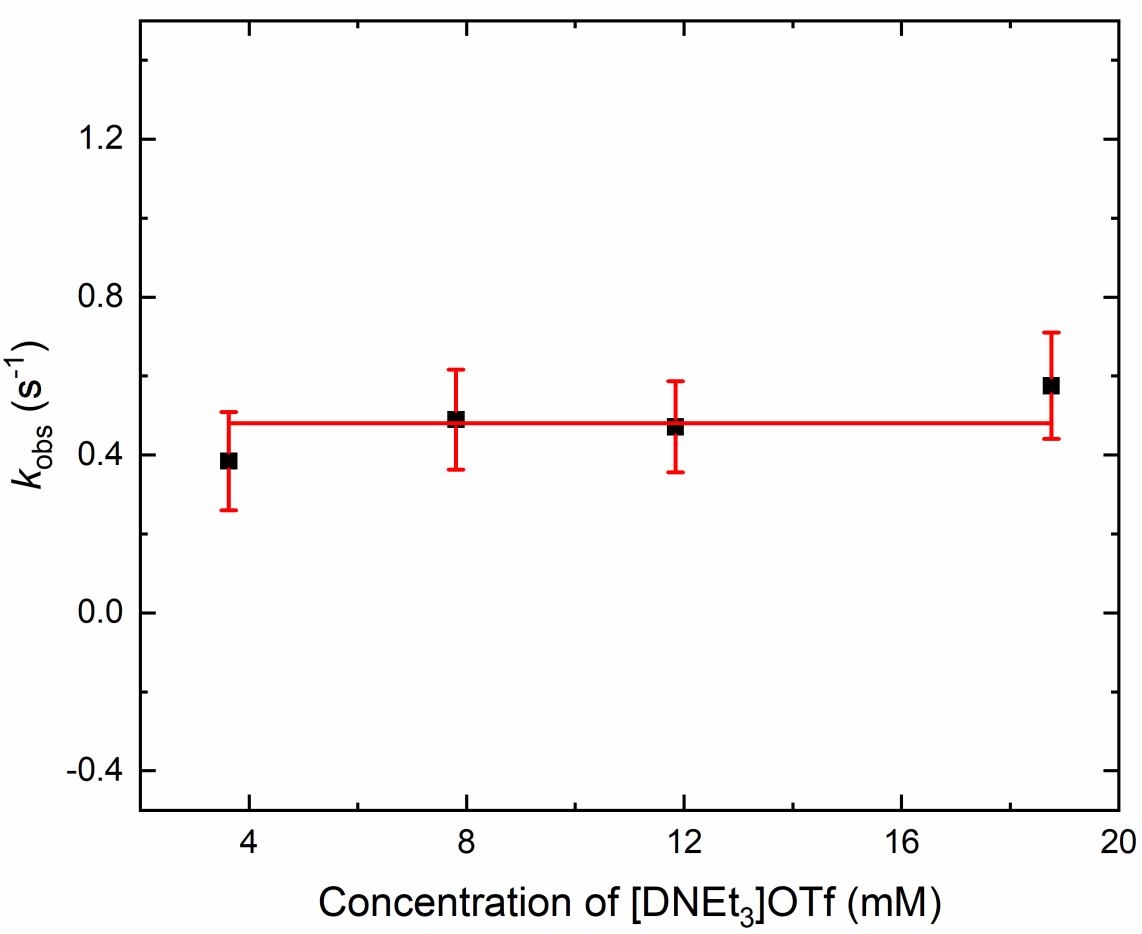

Figure B45: k_{obs} values (black squares) were obtained from the monoexponential fit of the decay signal at 399.8 nm in Figure B44 and are plotted here as a function of acid concentration. The k_{obs} values were measured at room temperature (298 K). The resulting plot is fit as a line with a fixed slope = 0 to extract the zero-order rate constant for the tautomerization of **4D** to generate **5D**.

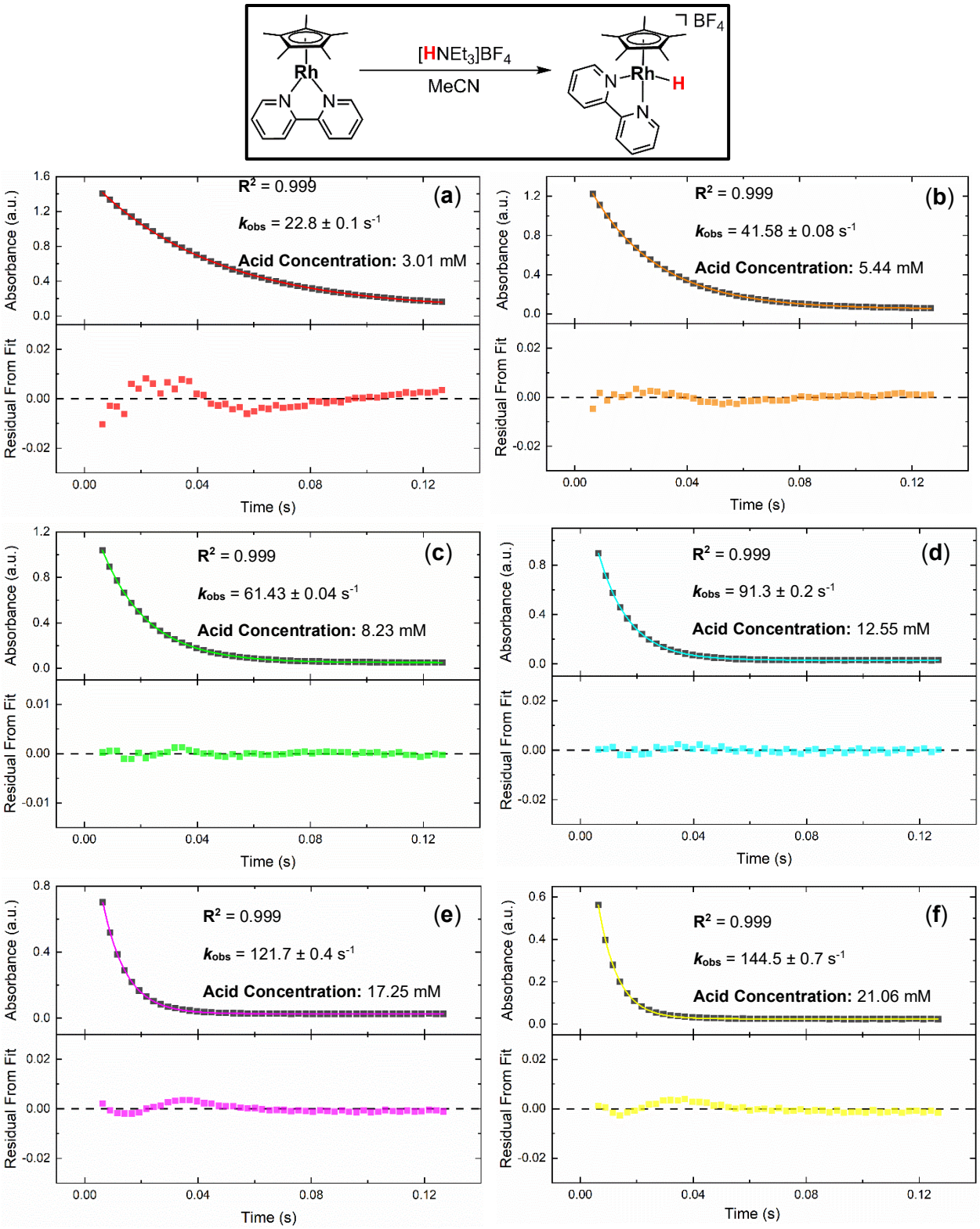

Figure B46: (a-f) Monitoring absorbance vs time at 511.1 nm for the initial protonation of **3** with $[HNEt_3]BF_4$ under pseudo-first order conditions. The decay of the signal at 511.1 nm is fit with a monoexponential function to extract the observed rate constant (k_{obs}). The residual from the fit monitored as a function of time rationalizes the use of a monoexponential fit here.

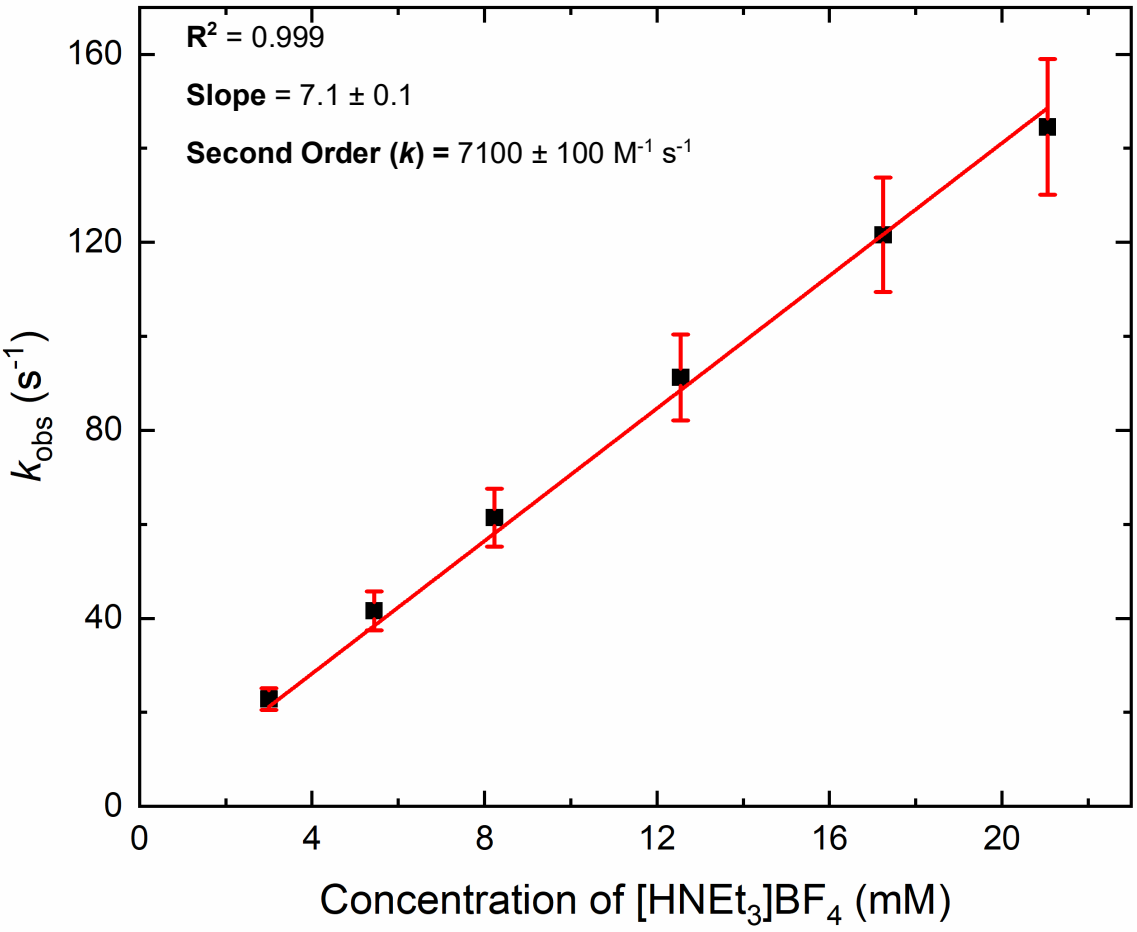

Figure B47: k_{obs} values (black squares) were obtained from the monoexponential fit of the decay signal at 511.1 nm in Figure B46 and are plotted here as a function of acid concentration. The k_{obs} values were measured at room temperature (298 K). The resulting plot is fit as a line (red) through the origin to extract the second order rate constant for the initial protonation of **3** with $[HNEt_3]BF_4$ to generate **4-BF$_4$**.

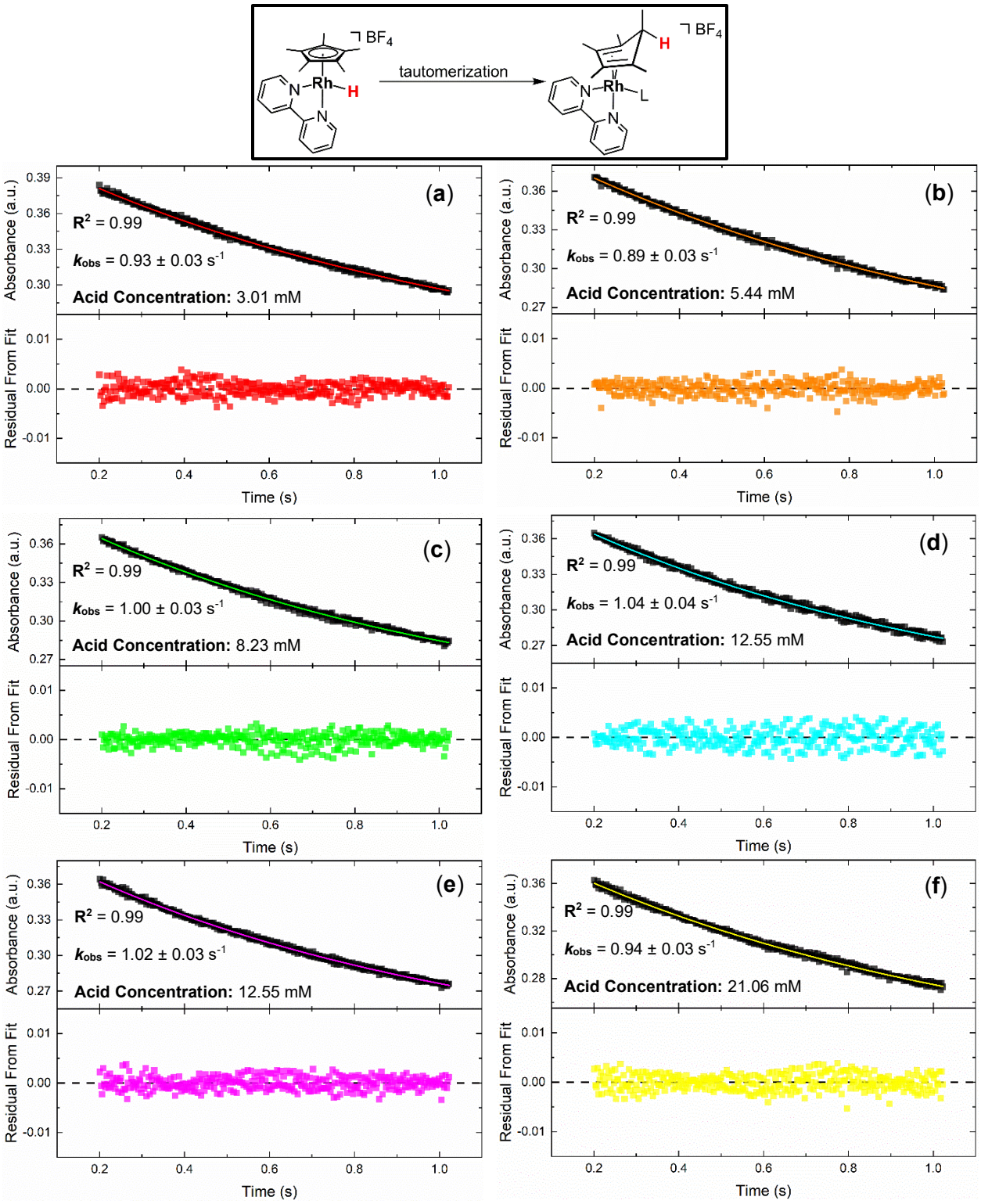

Figure B48: (**a-f**) Monitoring absorbance vs time at 399.8 nm for the tautomerization of **4-BF$_4$** to generate **5-BF$_4$** under pseudo-first order conditions. The decay of the signal at 399.8 nm is fit with a monoexponential function to extract the observed rate constant (k_{obs}). The residual from the fit monitored as a function of time rationalizes the use of a monoexponential fit here.

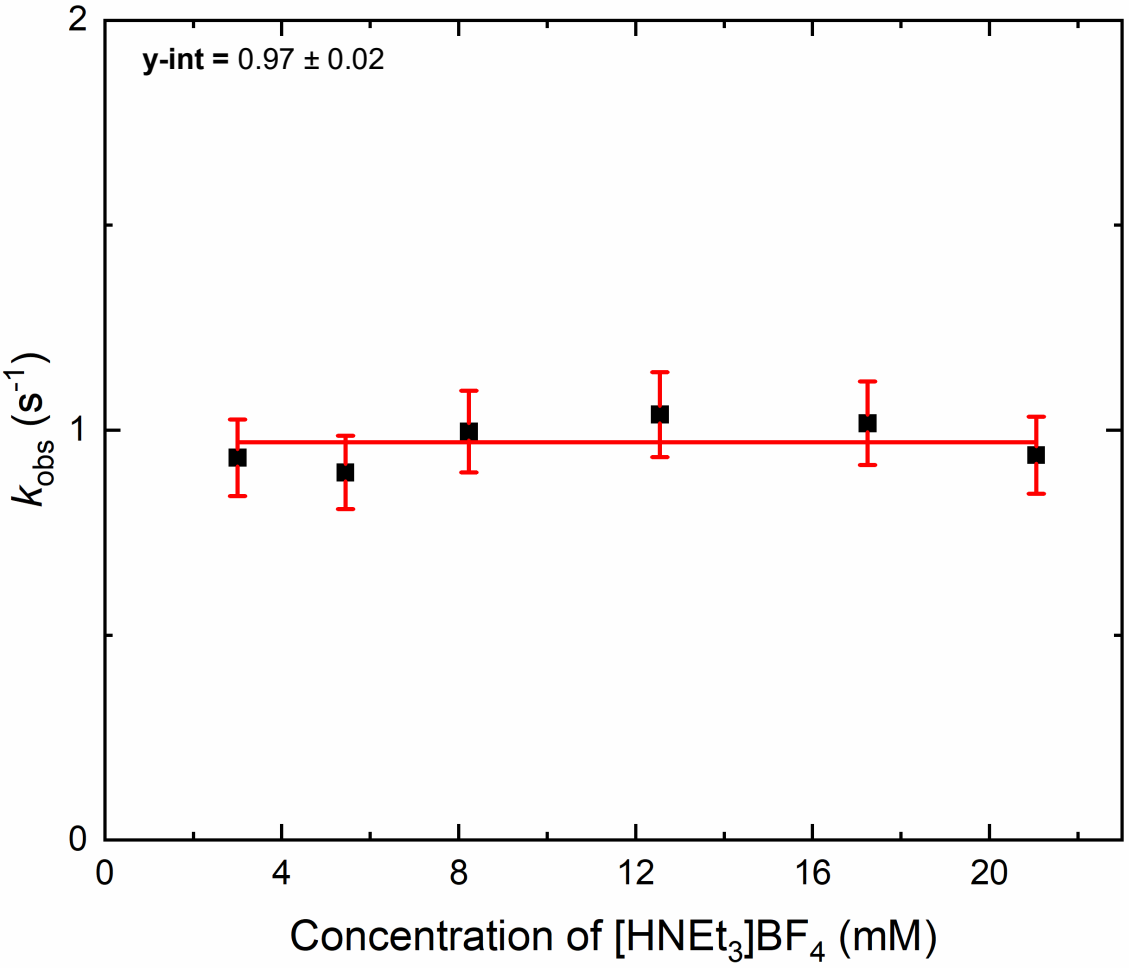

Figure B49: k_{obs} values (black squares) were obtained from the monoexponential fit of the decay signal at 399.8 nm in Figure B48 and are plotted here as a function of acid concentration. The k_{obs} values were measured at room temperature (298 K). The resulting plot is fit as a line with a fixed slope = 0 to extract the zero-order rate constant for the tautomerization of **4-BF$_4$** to generate **5-BF$_4$**.

Variable Temperature Data for Initial Protonation and Tautomerization

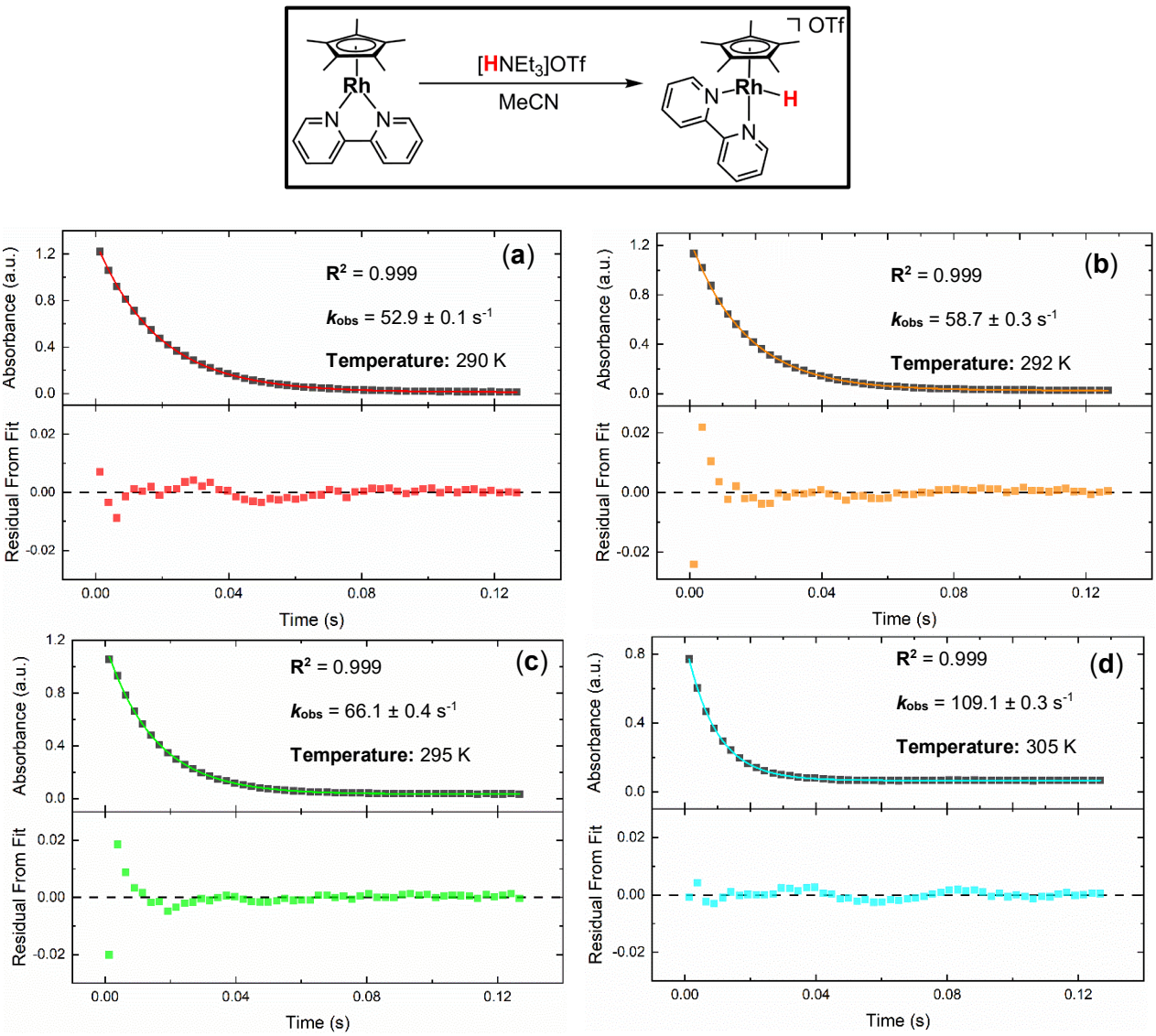

Figure B50: (a-d) Monitoring absorbance vs time at 511.1 nm for the initial protonation of **3** to generate **4** with [HNEt$_3$]OTf under pseudo-first order conditions while varying the temperature. The decay of the signal at 511.1 nm is fit with a monoexponential function to extract the observed rate constant for the initial protonation (k_{obs}) at different temperatures. The residual from the fit monitored as a function of time rationalizes the use of a monoexponential fit here.

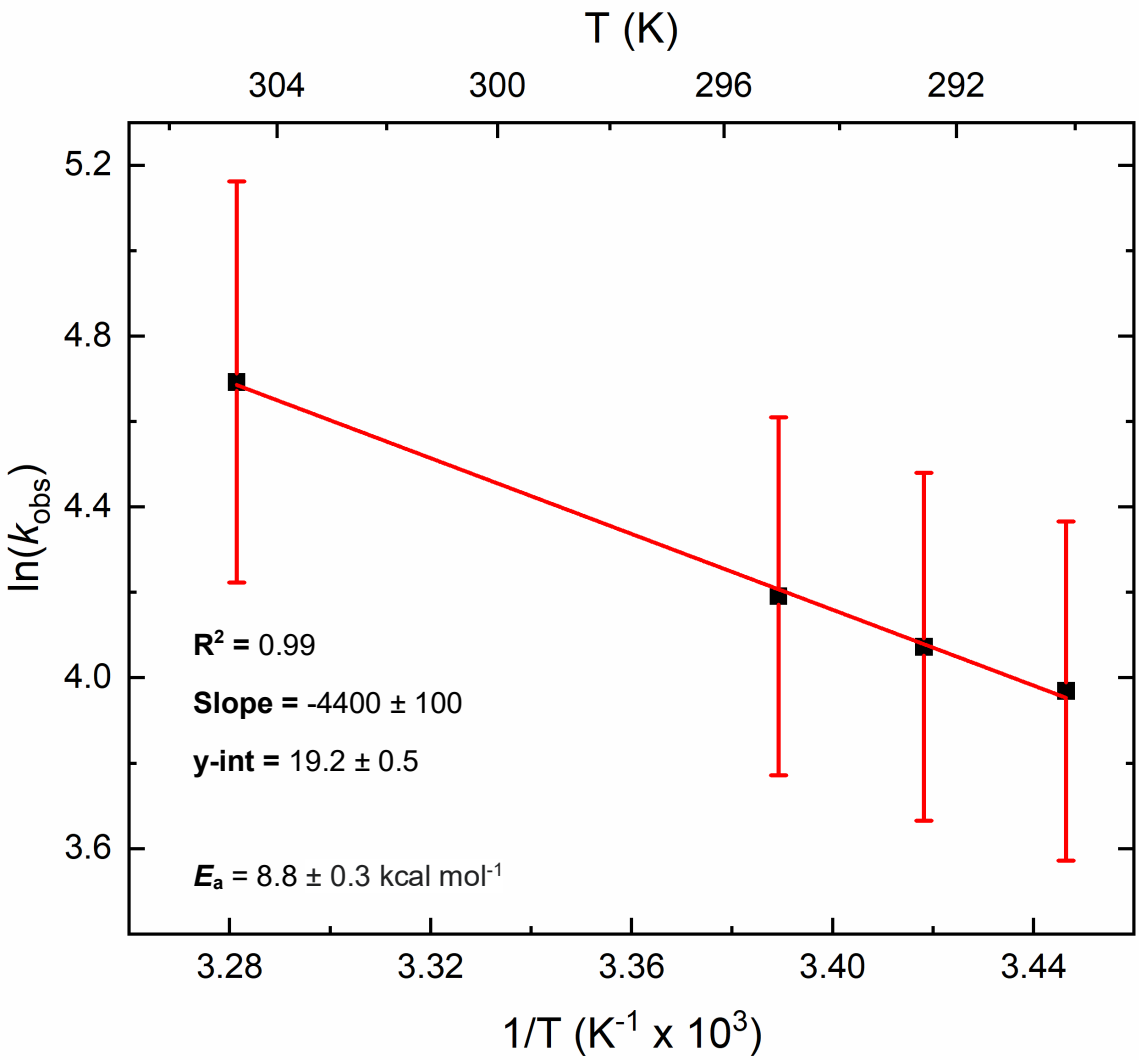

Figure B51: Arrhenius plot of variable temperature kinetic data to extract the activation energy (E_a) for the protonation of **3** to generate **4** using [$HNEt_3$]OTf monitored at 511.1 nm.

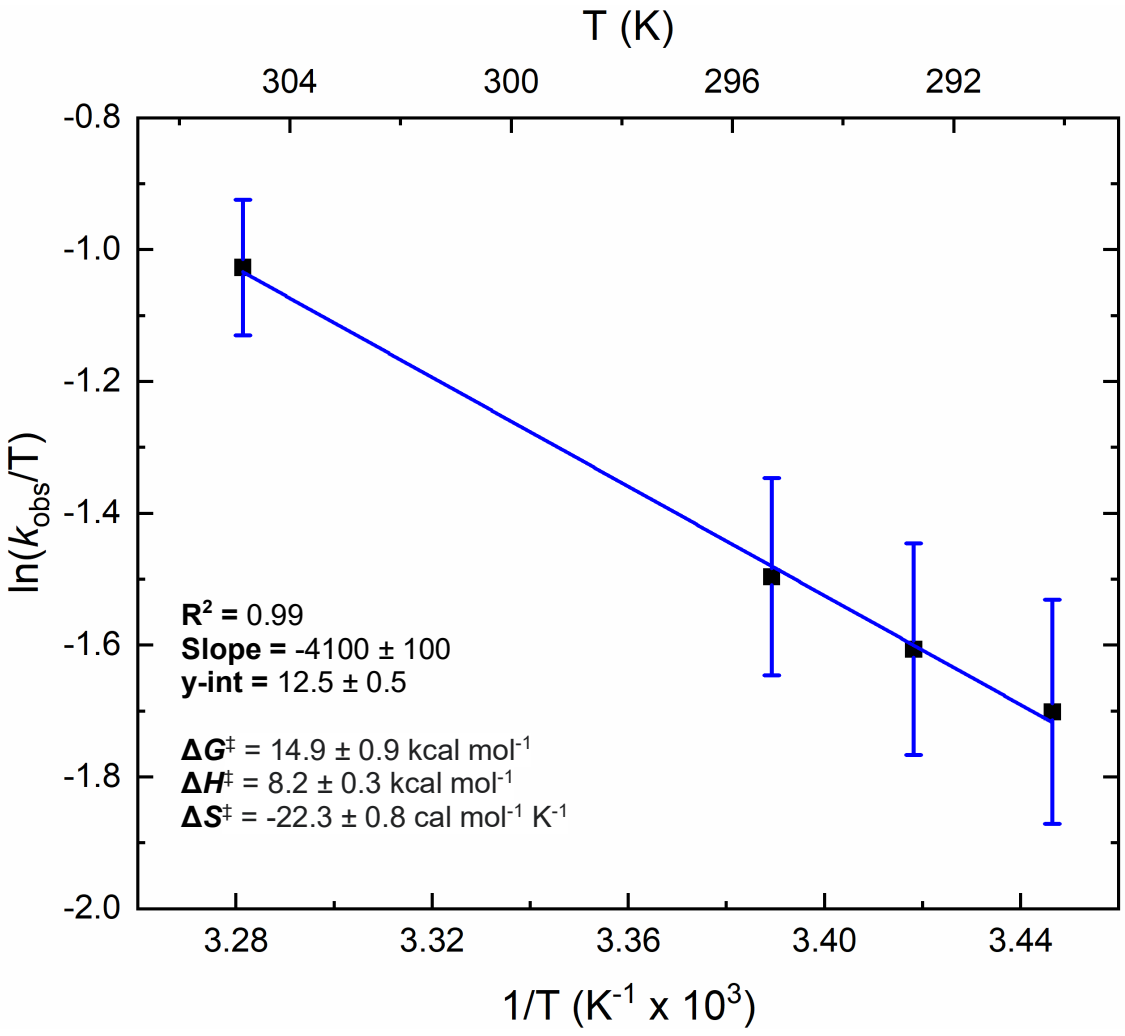

Figure B52: Eyring plot of variable temperature kinetic data to extract the activation enthalpy ($\Delta H^{\ddagger}$), entropy ($\Delta S^{\ddagger}$), and free energy ($\Delta G^{\ddagger}$) parameters, for the protonation of **3** to generate **4** using [$HNEt_3$]OTf monitored at 511.1 nm.

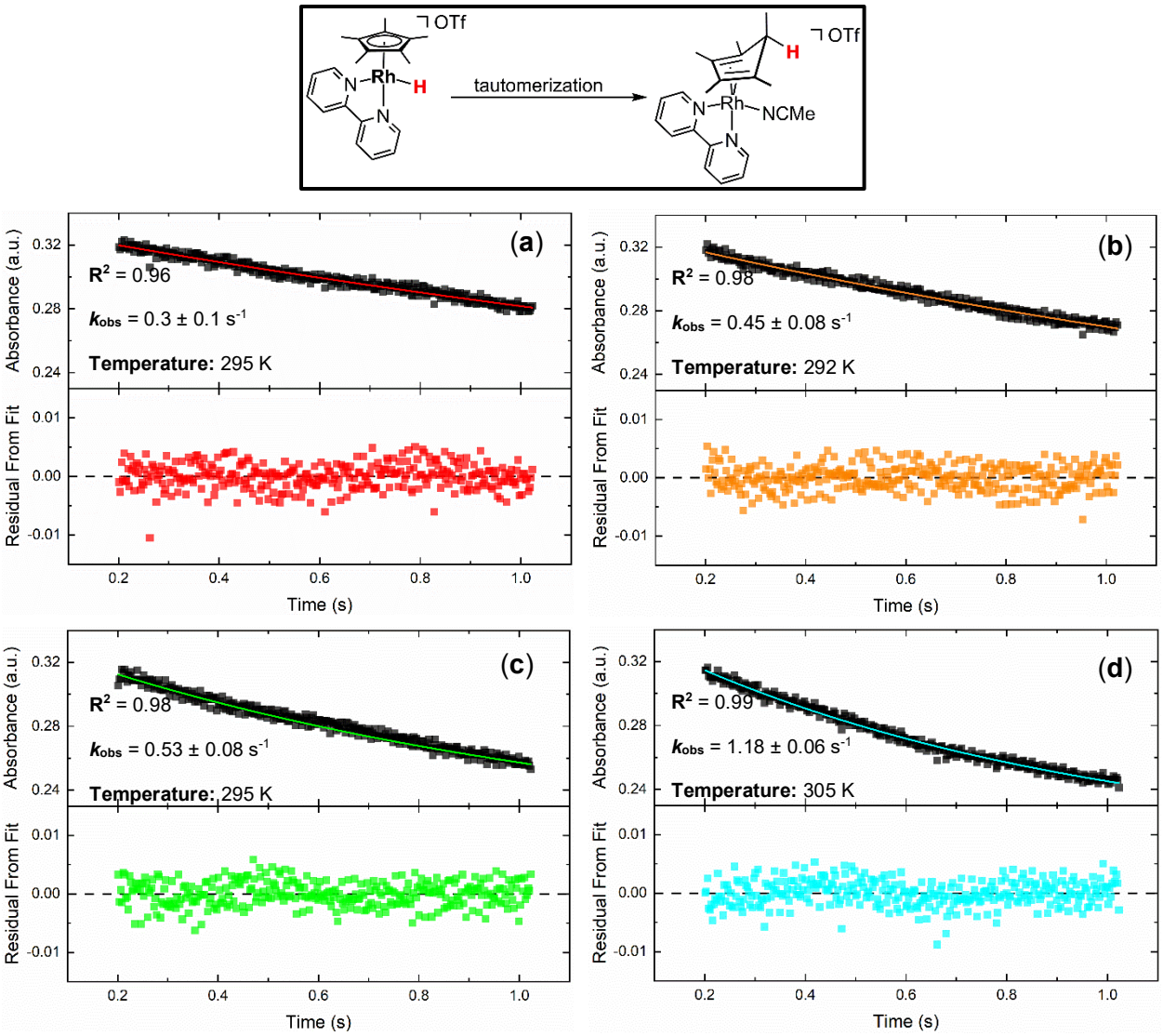

Figure B53: (**a-d**) Monitoring absorbance vs time at 399.8 nm for the tautomerization of **4** to generate **5** under pseudo-first order conditions while varying the temperature. The decay of the signal at 399.8 nm is fit with a monoexponential function to extract the observed rate constant (k_{obs}) at different temperatures. The residual from the fit monitored as a function of time rationalizes the use of a monoexponential fit here.

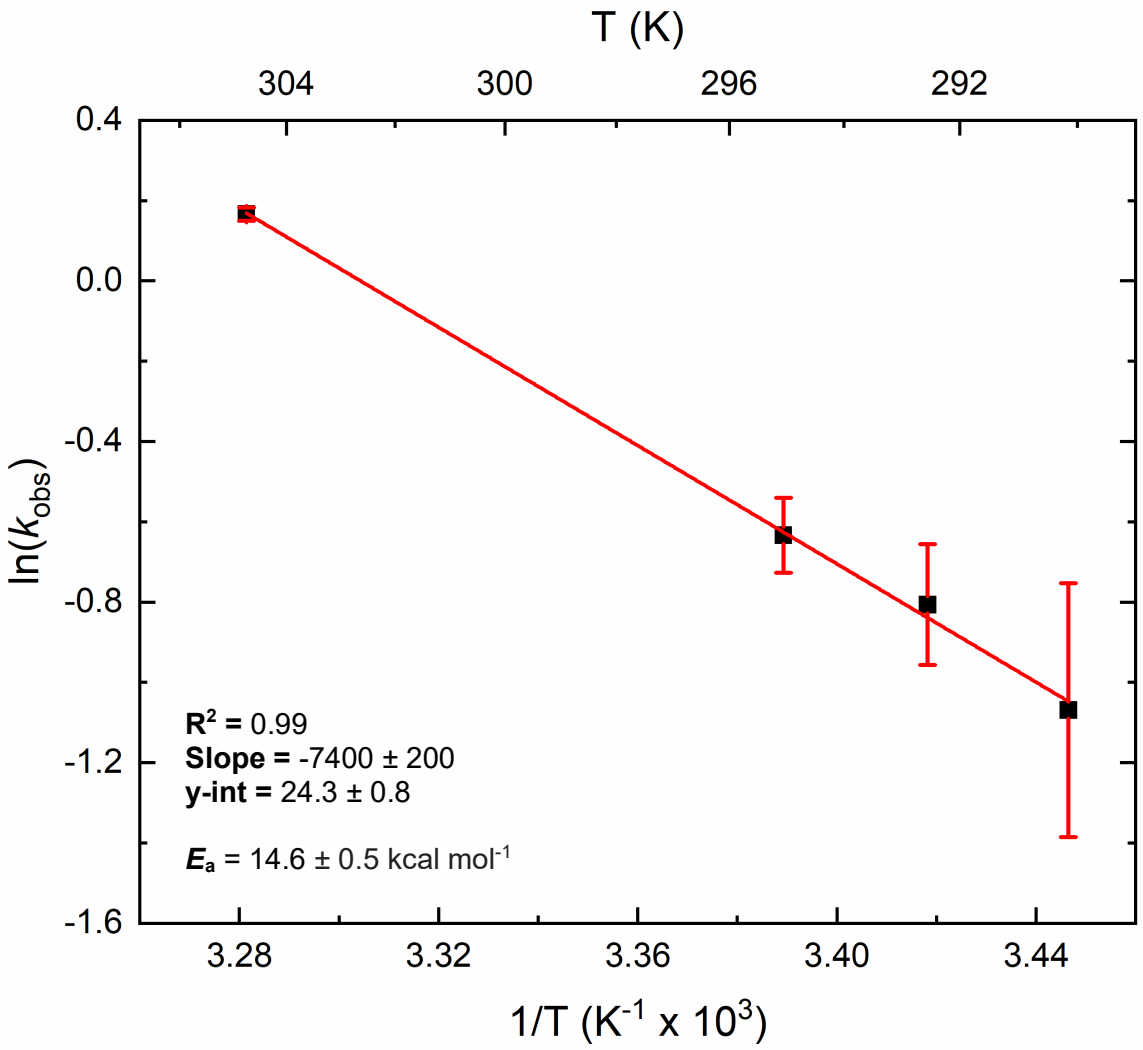

Figure B54: Arrhenius plot of variable temperature kinetic data to extract the activation energy (E_a) for the tautomerization of **4** to generate **5** monitored at 399.8 nm.

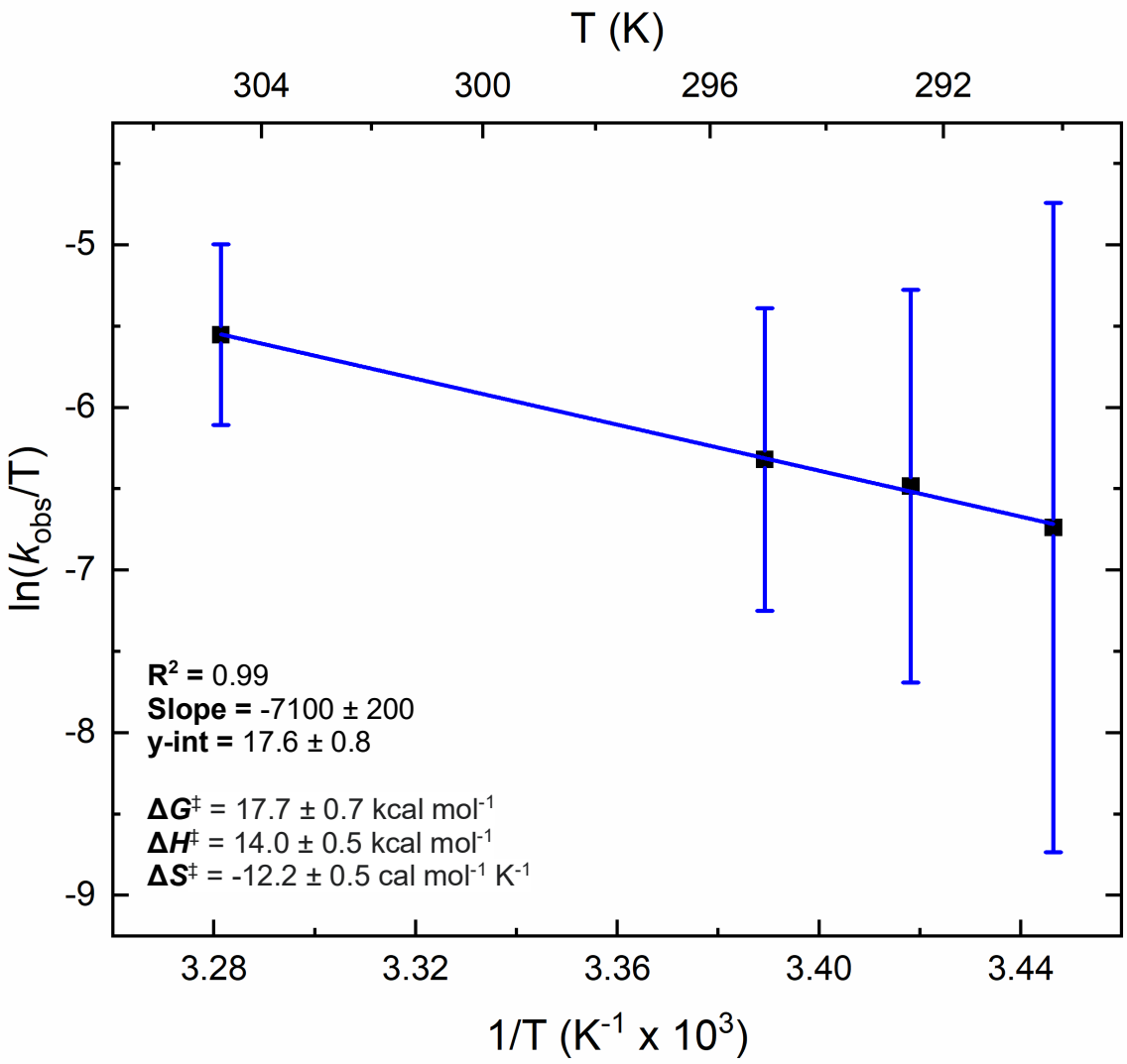

Figure B55: Eyring plot of variable temperature kinetic data to extract the activation enthalpy ($\Delta H^{\ddagger}$), entropy ($\Delta S^{\ddagger}$), and free energy ($\Delta G^{\ddagger}$) parameters, for the tautomerization **4** to generate **5** monitored at 399.8 nm.

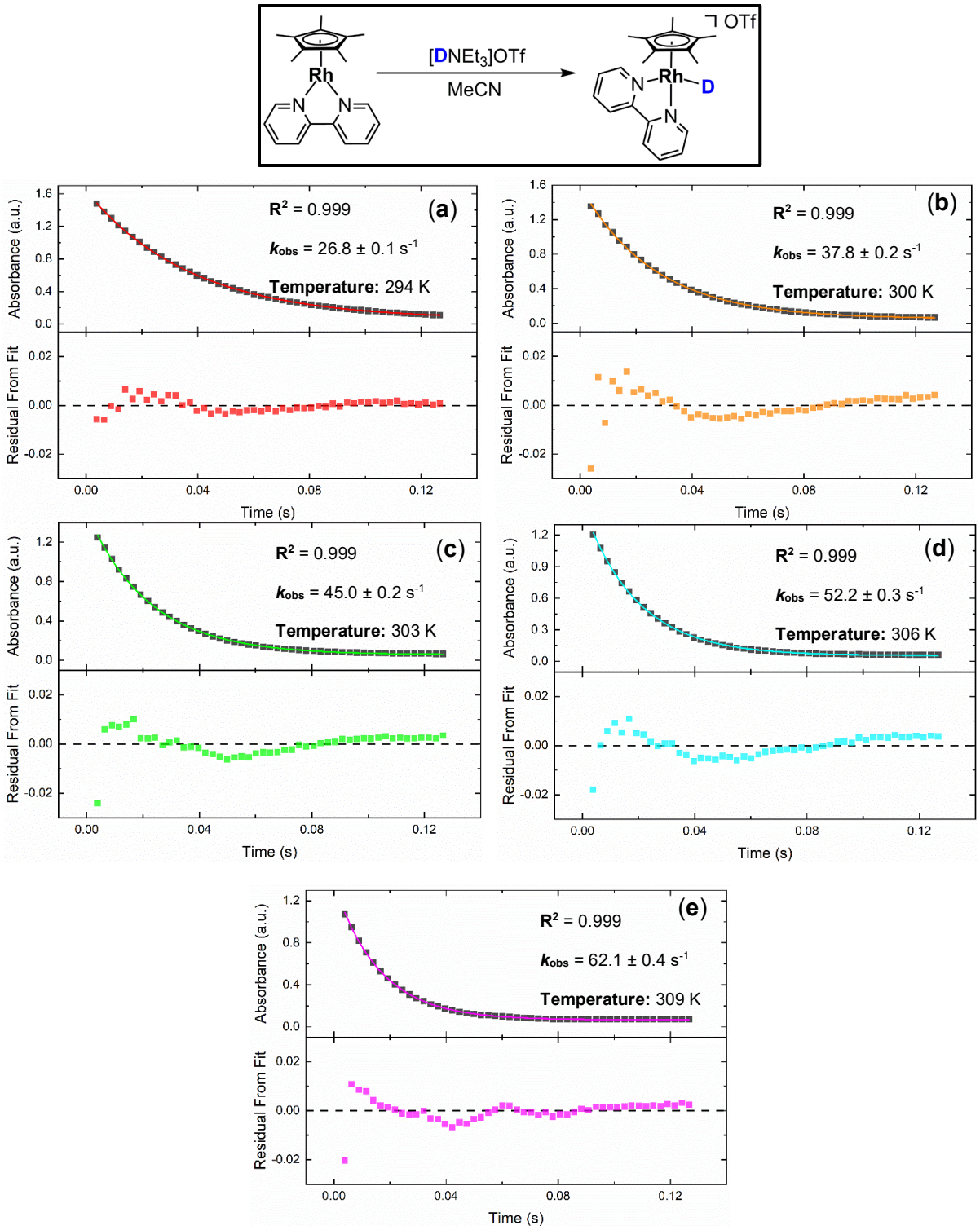

Figure B56: Monitoring absorbance vs time at 511.1 nm for the initial deuteration of **3** to generate **4D** with [DNEt$_3$]OTf under pseudo-first order conditions while varying the temperature. The decay of the signal at 511.1 nm is fit with a monoexponential function to extract the observed rate constant for the initial deuteration (k_{obs}) at different temperatures. The residual from the fit monitored as a function of time rationalizes the use of a monoexponential fit here.

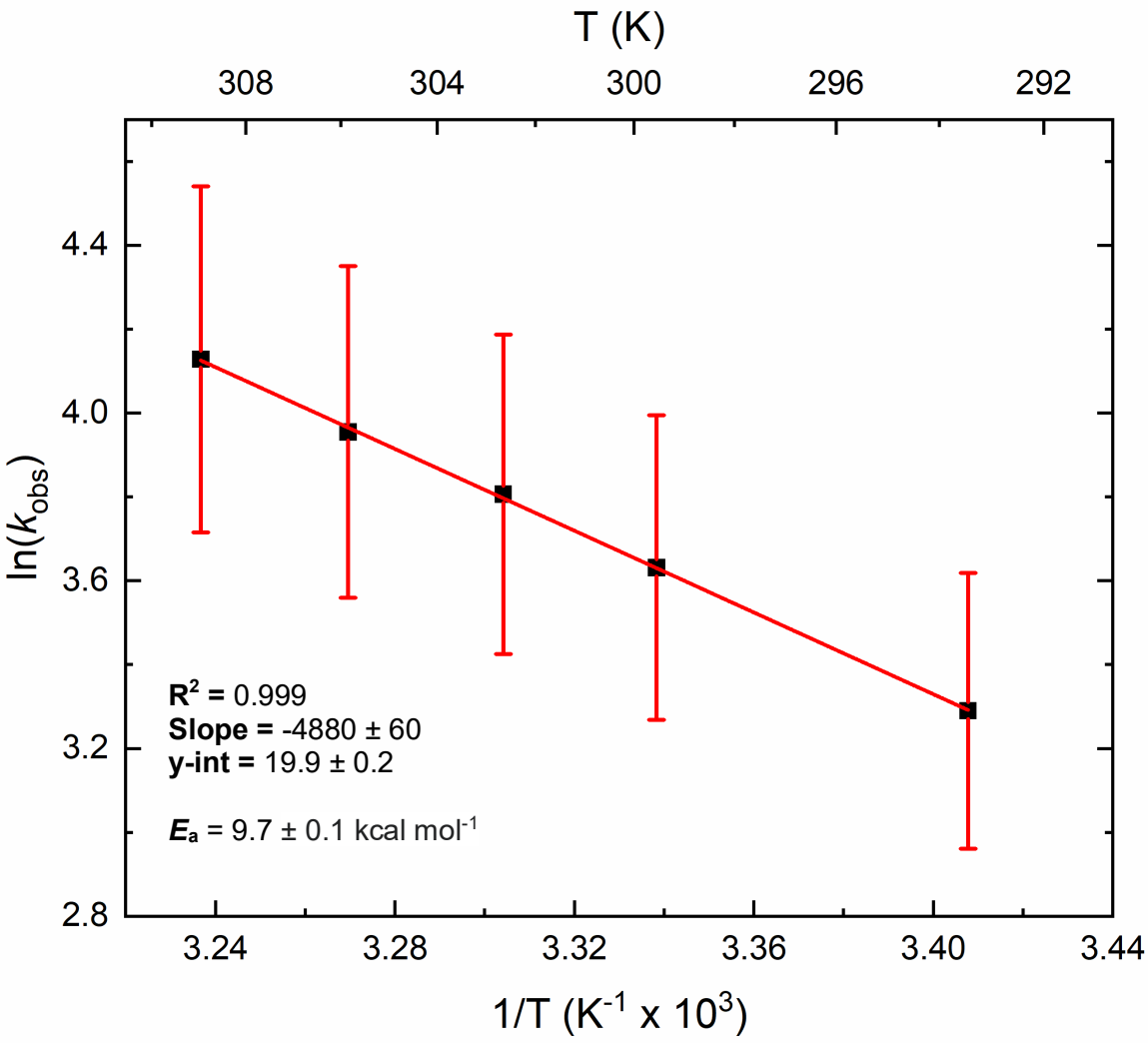

Figure B57: Arrhenius plot of variable temperature kinetic data to extract the activation energy (E_a) for the protonation of **3** to generate **4D** using [DNEt$_3$]OTf monitored at 511.1 nm.

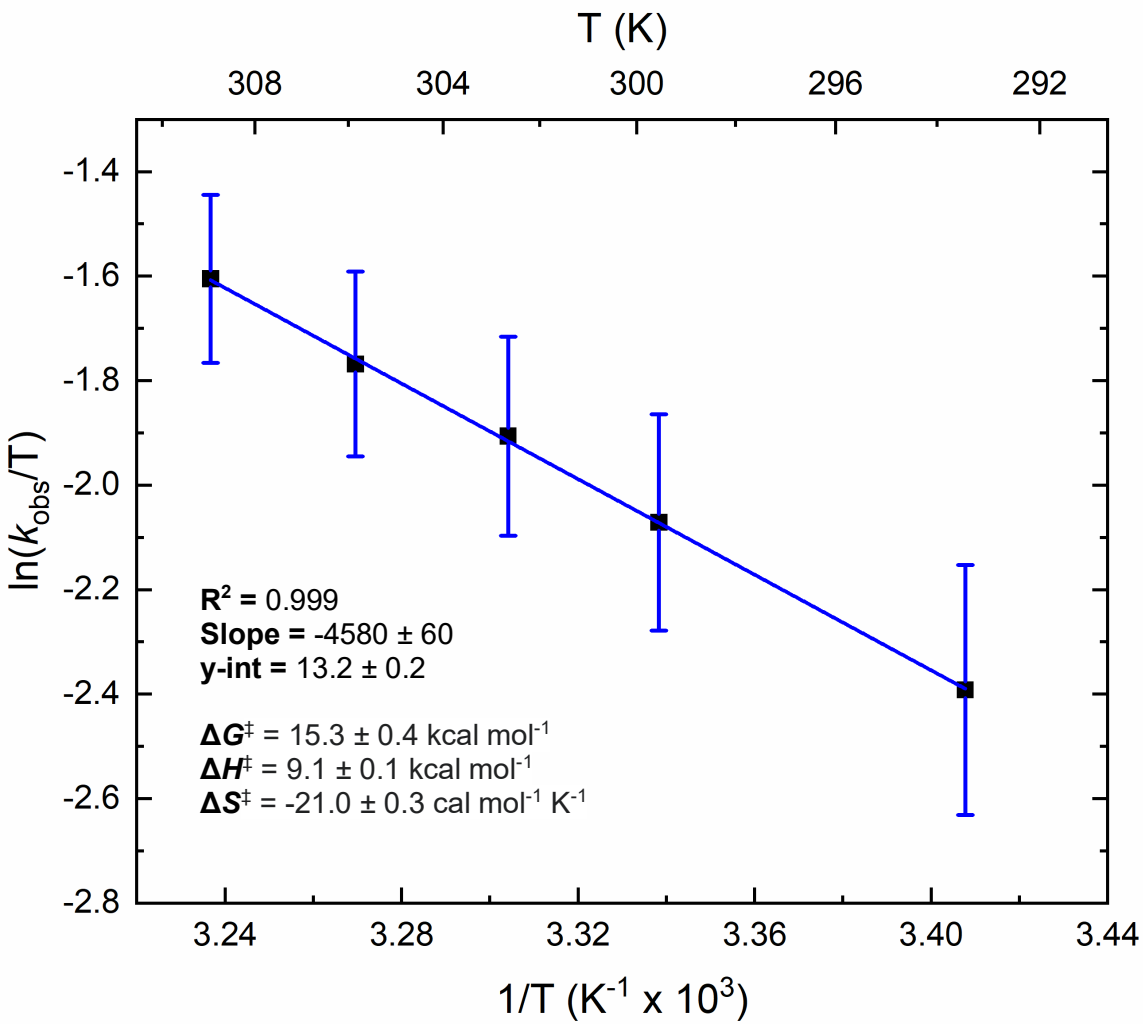

Figure B58: Eyring plot of variable temperature kinetic data to extract the activation enthalpy ($\Delta H^{\ddagger}$), entropy ($\Delta S^{\ddagger}$), and free energy ($\Delta G^{\ddagger}$) parameters, for the protonation of **3** using [DNEt$_3$]OTf monitored at 511.1 nm.

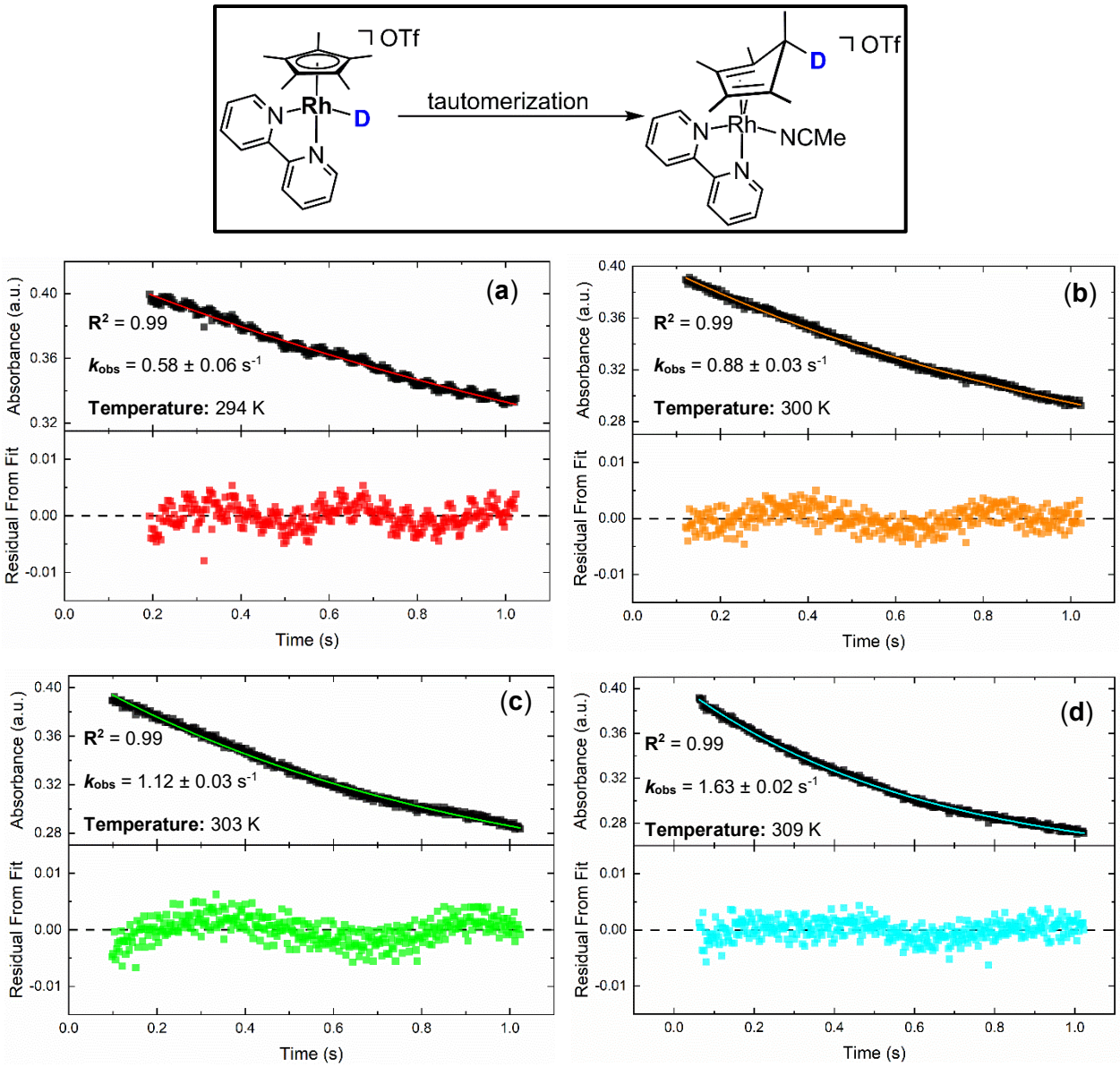

Figure B59: Monitoring absorbance vs time at 399.8 nm for the tautomerization of **4D** to generate **5D** under pseudo-first order conditions while varying the temperature. The decay of the signal at 399.8 nm is fit with a monoexponential function to extract the observed rate constant (k_{obs}) at different temperatures. The residual from the fit monitored as a function of time rationalizes the use of a monoexponential fit here.

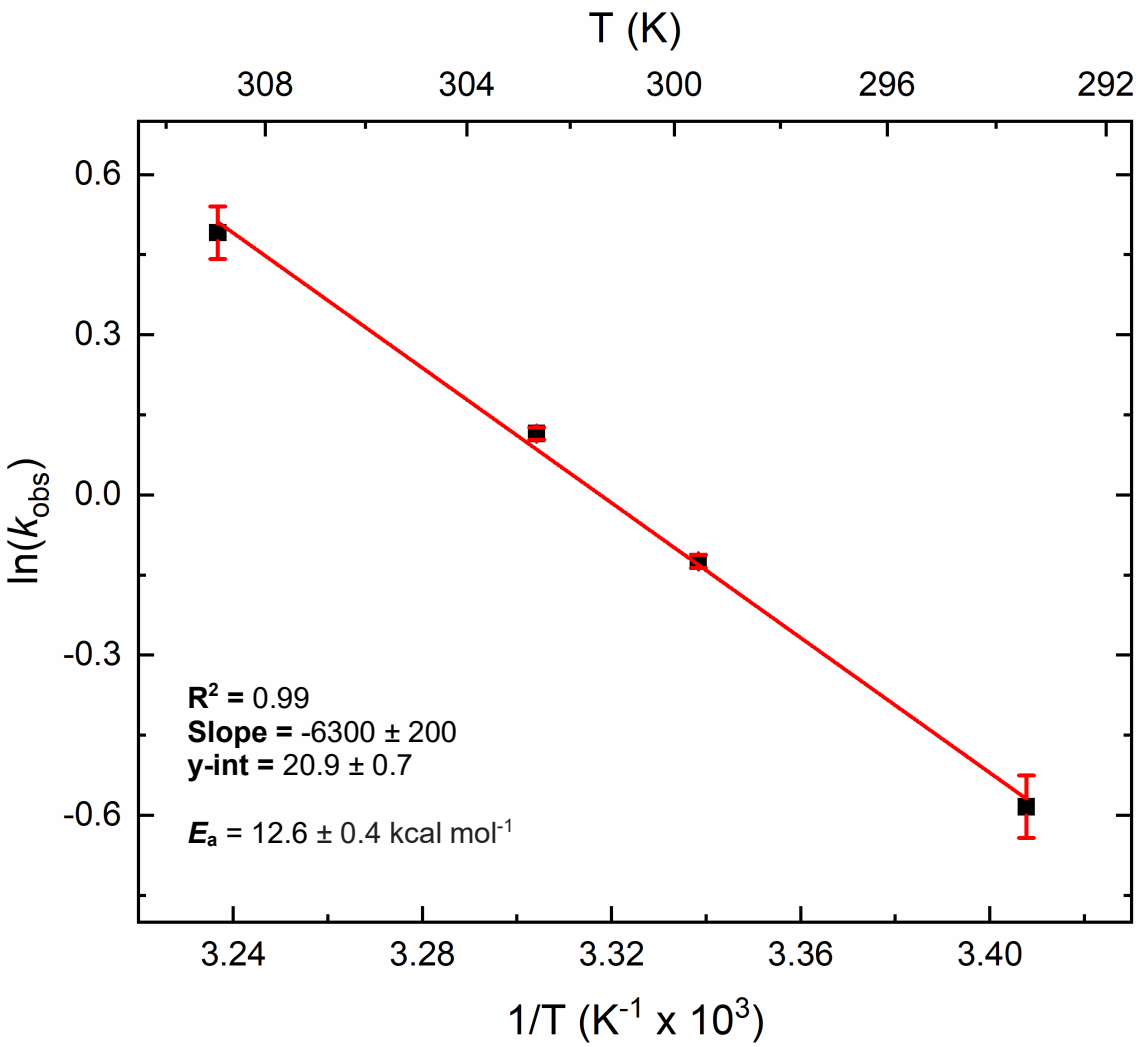

Figure B60: Arrhenius plot of variable temperature kinetic data to extract the activation energy (E_a) for the tautomerization of **4D** to generate **5D** monitored at 399.8 nm.

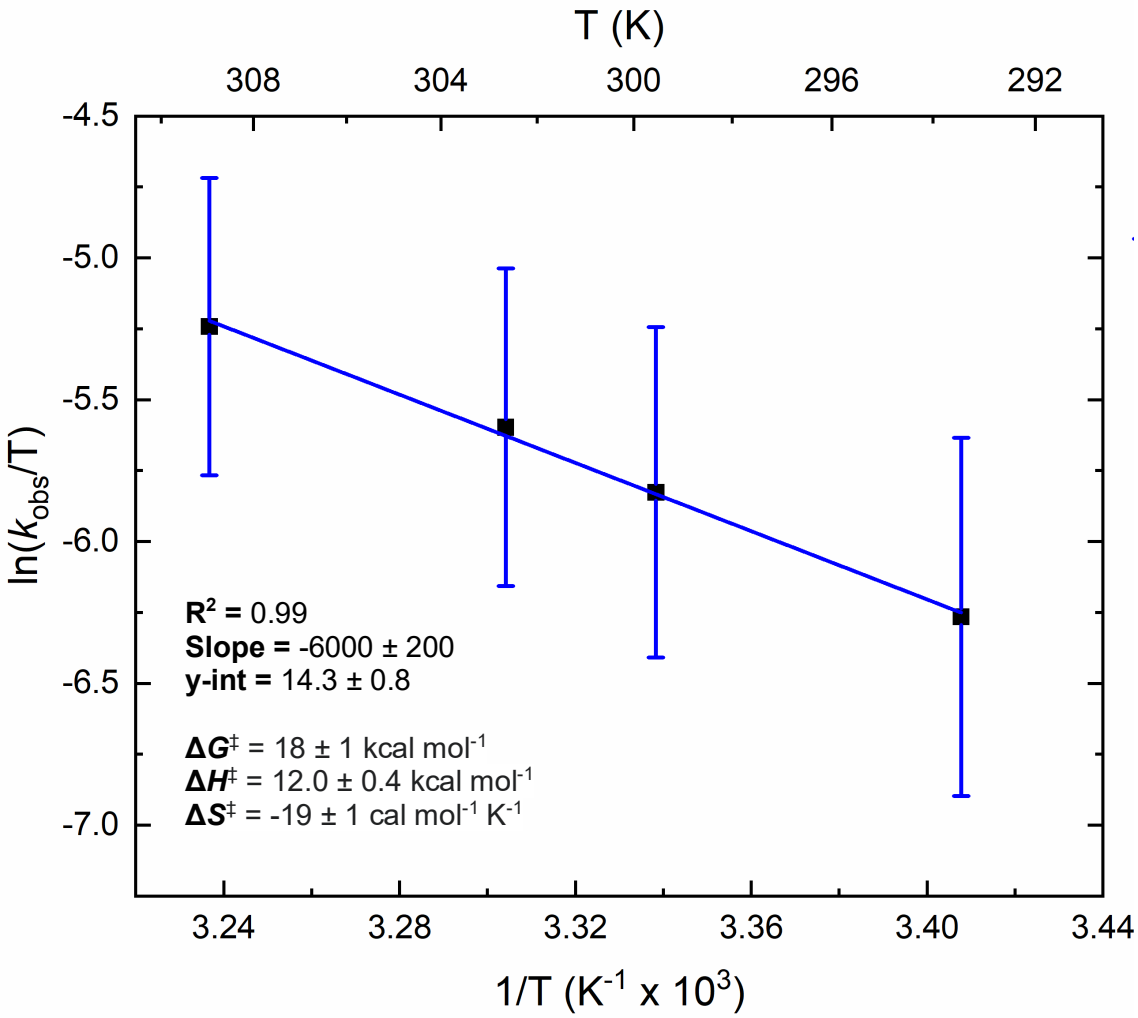

Figure B61: Eyring plot of variable temperature kinetic data to extract the activation enthalpy ($\Delta H^{\ddagger}$), entropy ($\Delta S^{\ddagger}$), and free energy ($\Delta G^{\ddagger}$) parameters for the tautomerization **4D** to **5D** monitored at 399.8 nm.

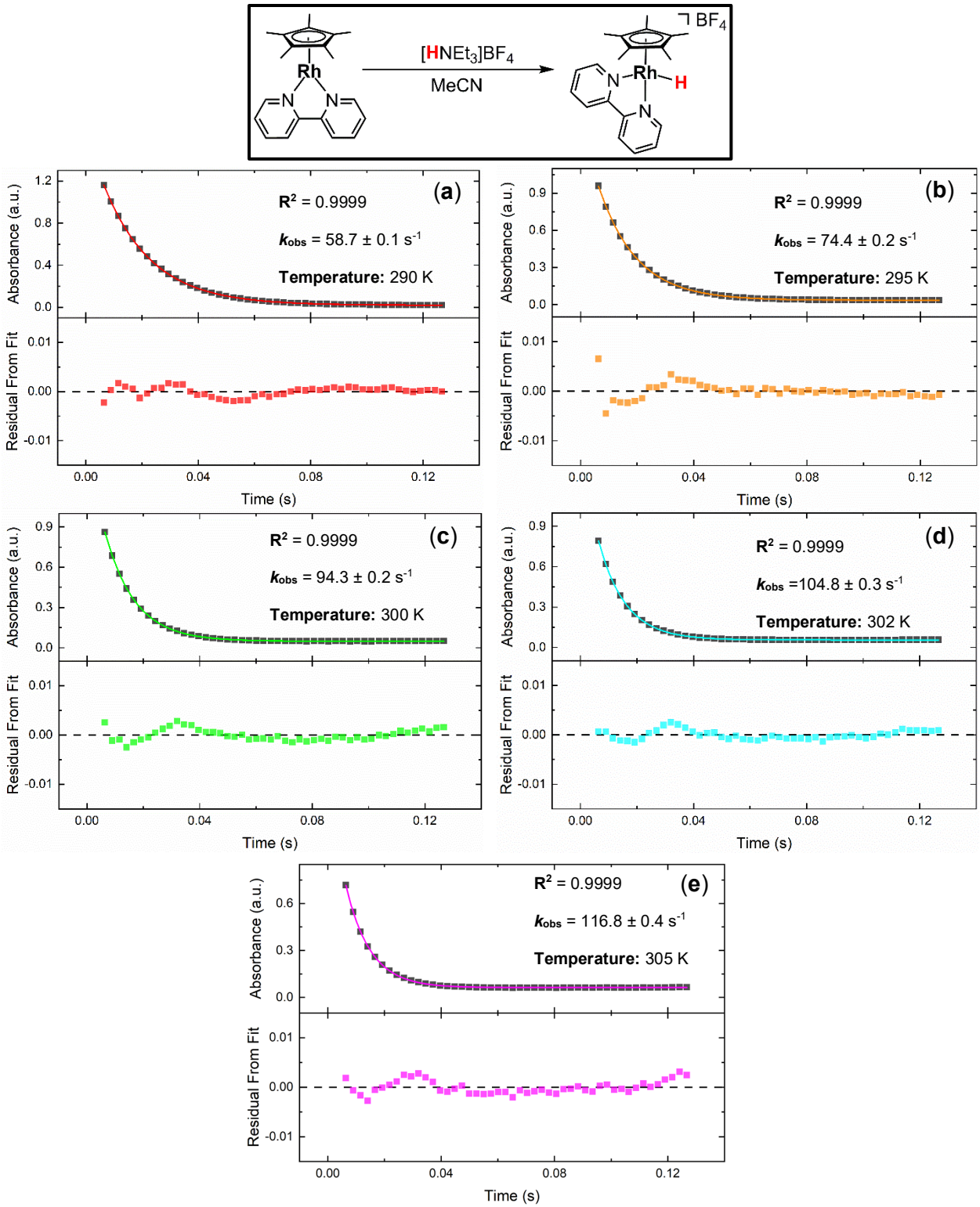

Figure B62: (**a-e**) Monitoring absorbance vs time at 511.1 nm for the initial protonation of **3** to generate **4-BF$_4$** with [HNEt$_3$]BF$_4$ under pseudo-first order conditions while varying the temperature. The decay of the signal at 511.1 nm is fit with a monoexponential function to extract the observed rate constant for the initial protonation (k_{obs}) at different temperatures. The residual from the fit monitored as a function of time rationalizes the use of a monoexponential fit here.

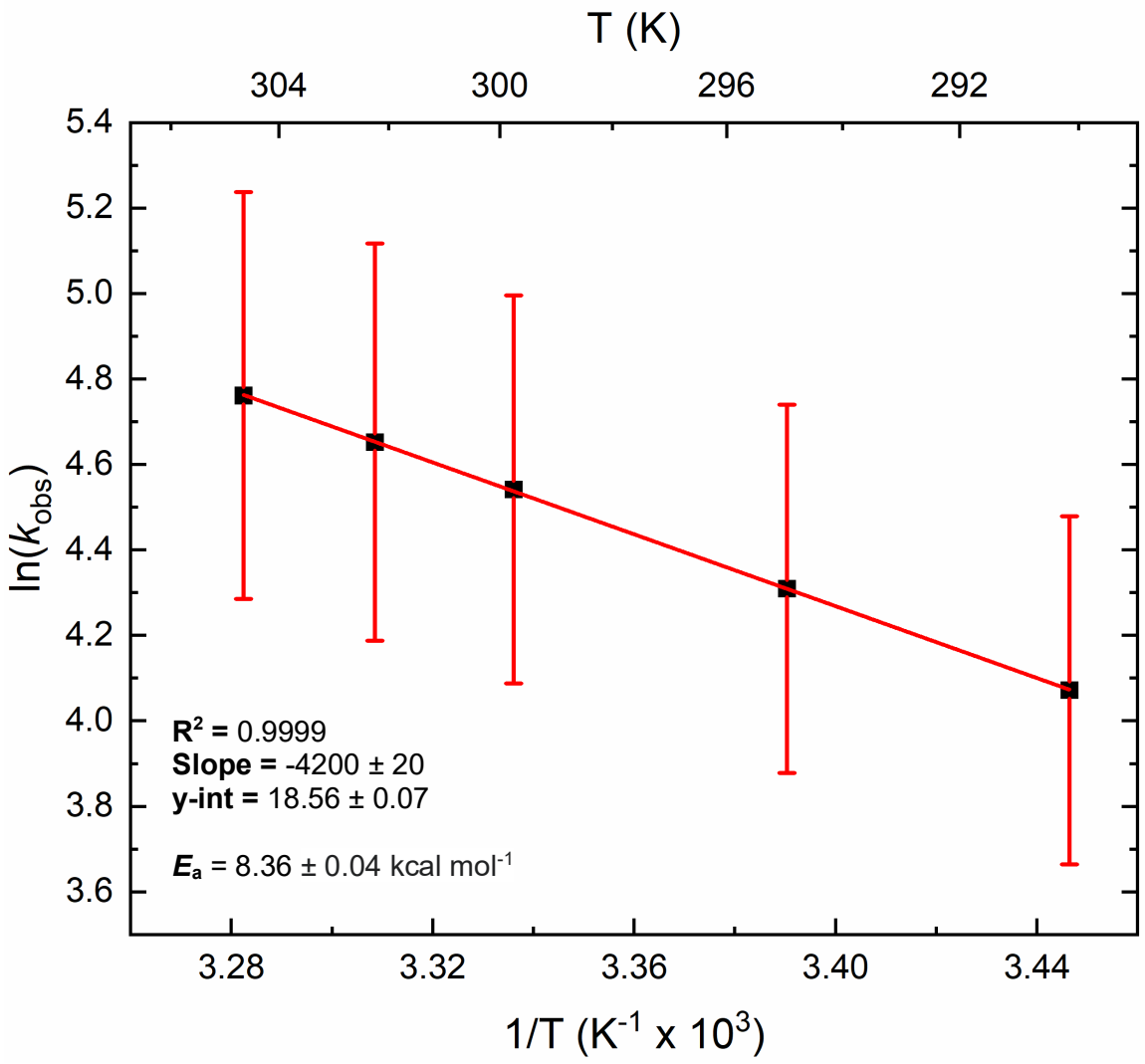

Figure B63: Arrhenius plot of variable temperature kinetic data to extract the activation energy (E_a) for the protonation of **3** to generate **4-BF$_4$** using [HNEt$_3$]BF$_4$ monitored at 511.1 nm.

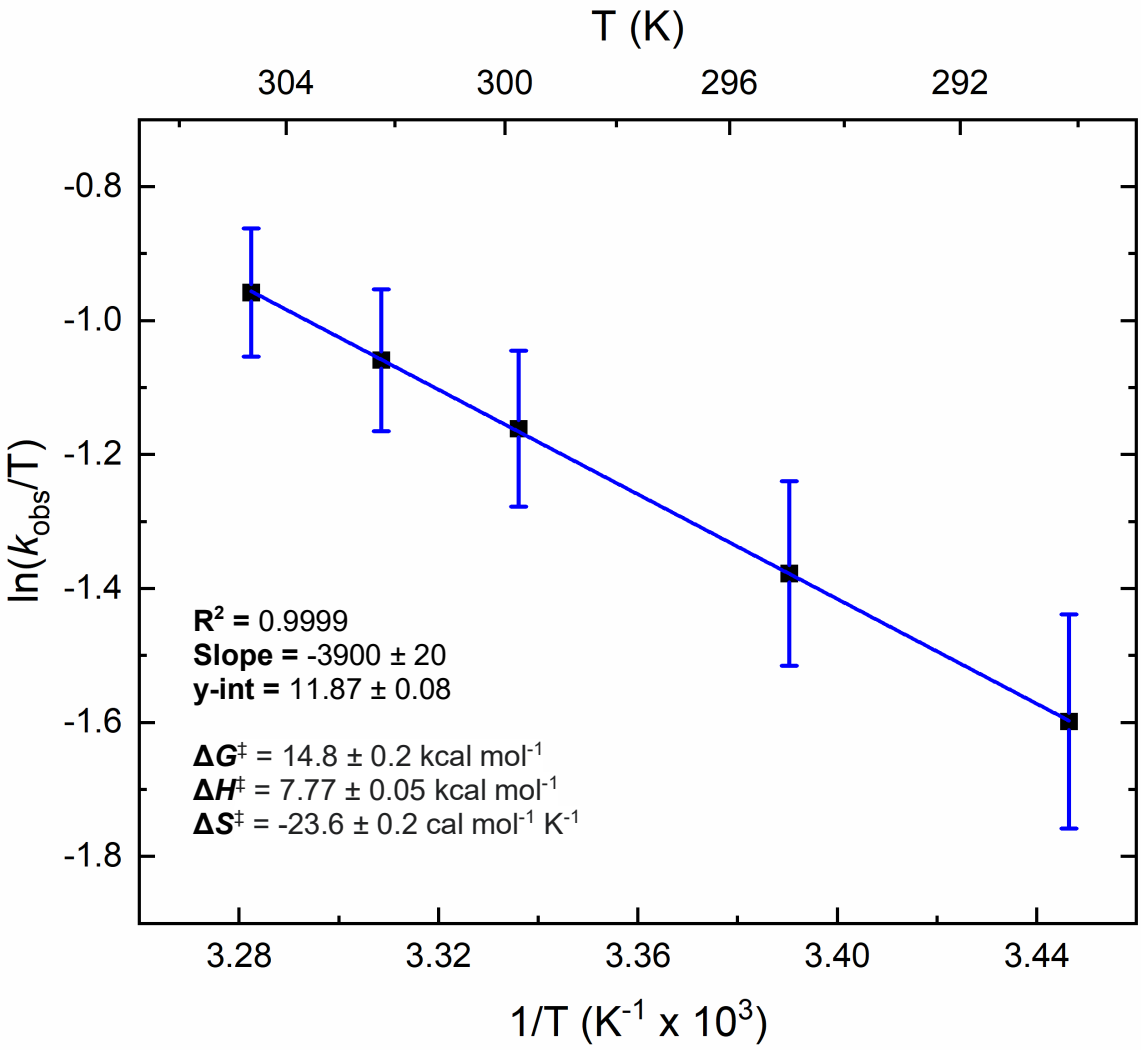

Figure B64: Eyring plot of variable temperature kinetic data to extract the activation enthalpy ($\Delta H^{\ddagger}$), entropy ($\Delta S^{\ddagger}$), and free energy ($\Delta G^{\ddagger}$) parameters, for the protonation of **3** to generate **4-BF$_4$** using [HNEt$_3$]BF$_4$ monitored at 511.1 nm.

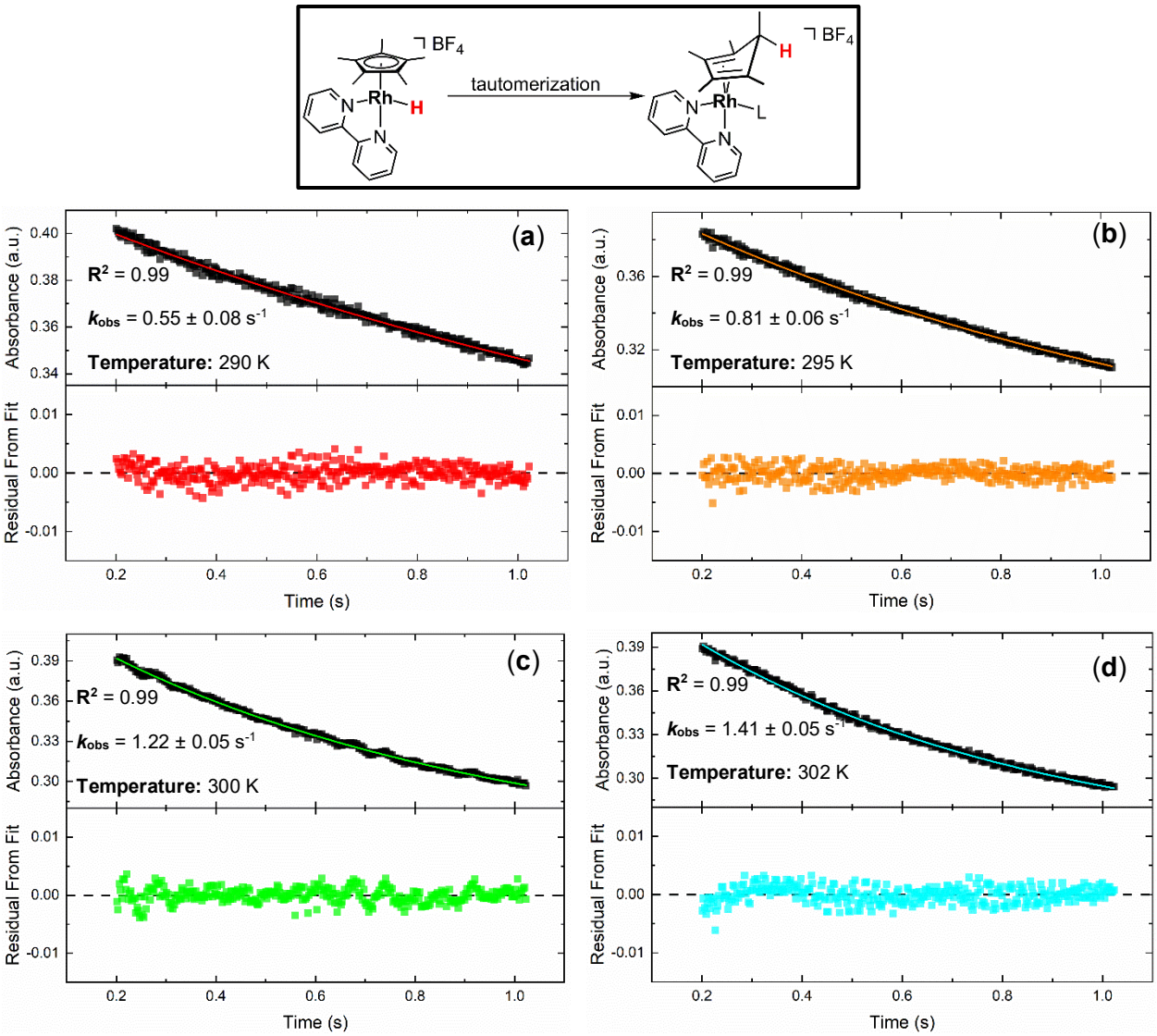

Figure B65: (**a-d**) Monitoring absorbance vs time at 399.8 nm for the tautomerization of **4-BF$_4$** to generate **5-BF$_4$** under pseudo-first order conditions while varying the temperature. The decay of the signal at 399.8 nm is fit with a monoexponential function to extract the observed rate constant (k_{obs}) at different temperatures. The residual from the fit monitored as a function of time rationalizes the use of a monoexponential fit here.

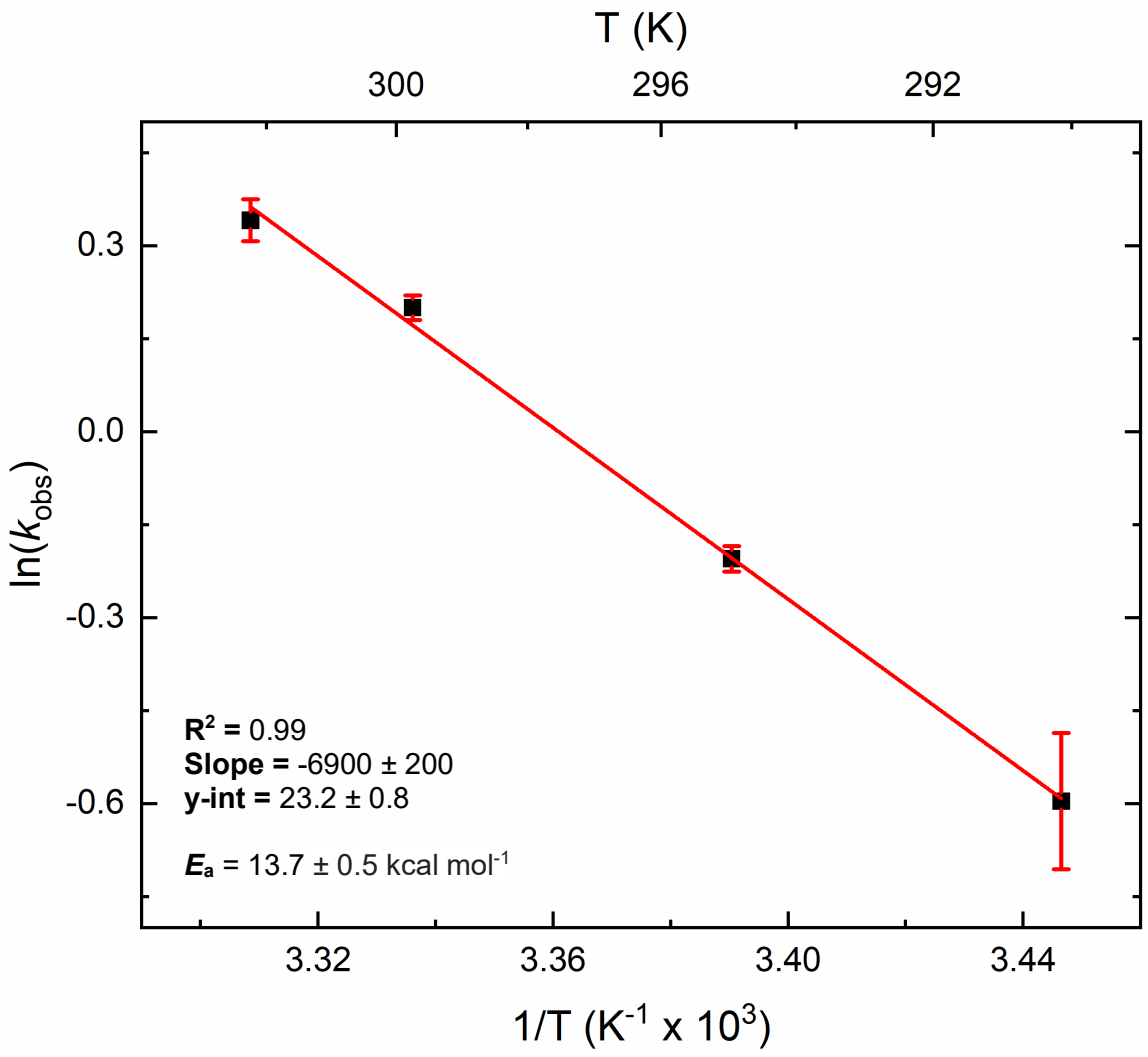

Figure B66: Arrhenius plot of variable temperature kinetic data to extract the activation energy (E_a) for the tautomerization of **4-BF$_4$** to generate **5-BF$_4$** monitored at 399.8 nm.

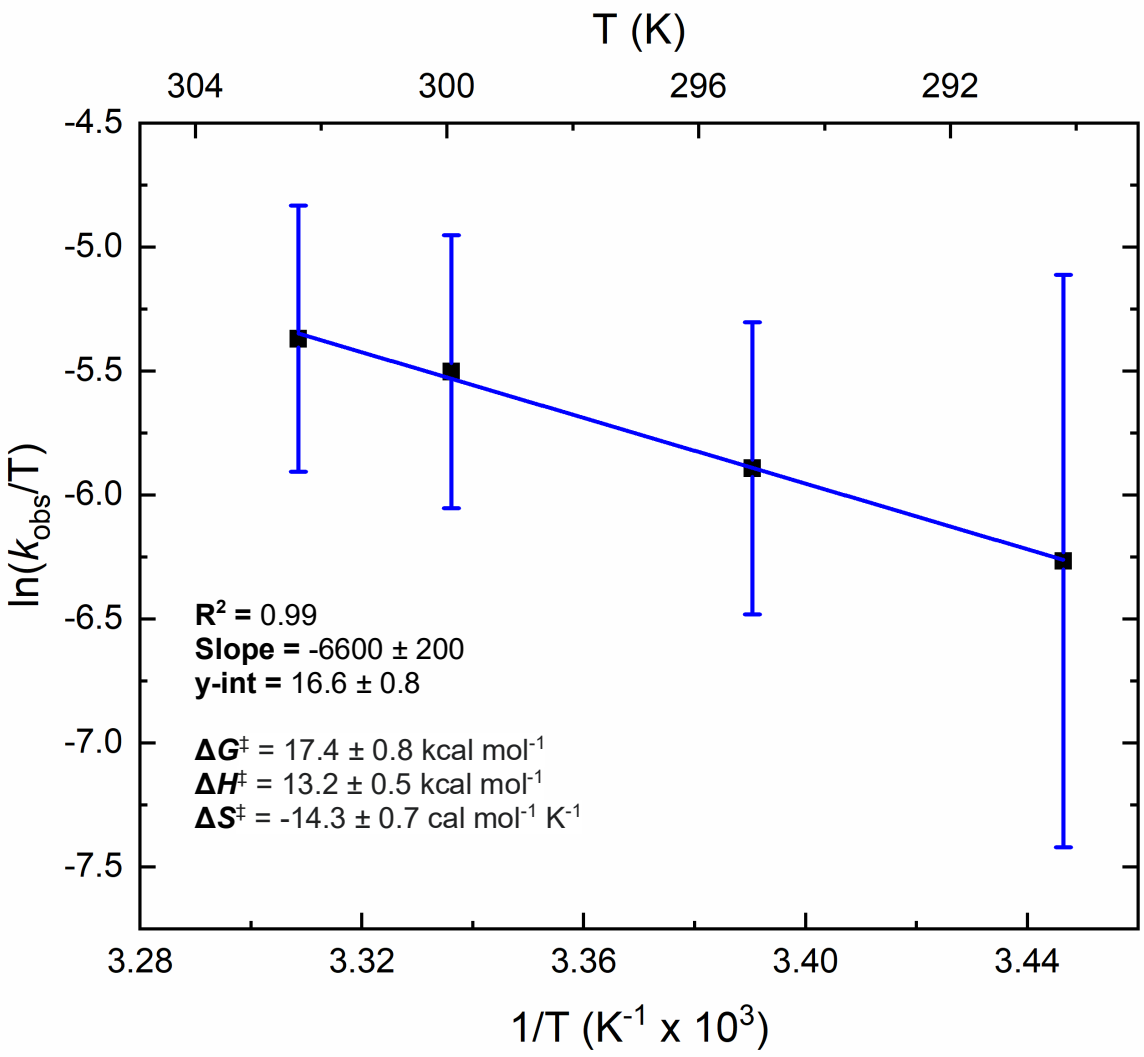

Figure B67: Eyring plot of variable temperature kinetic data to extract the activation enthalpy ($\Delta H^{\ddagger}$), entropy ($\Delta S^{\ddagger}$), and free energy ($\Delta G^{\ddagger}$) parameters, for the tautomerization **4-BF$_4$** to generate **5-BF$_4$** monitored at 399.8 nm

Stopped-Flow Kinetic Data for Second Protonation Order and Rate Constant Determination

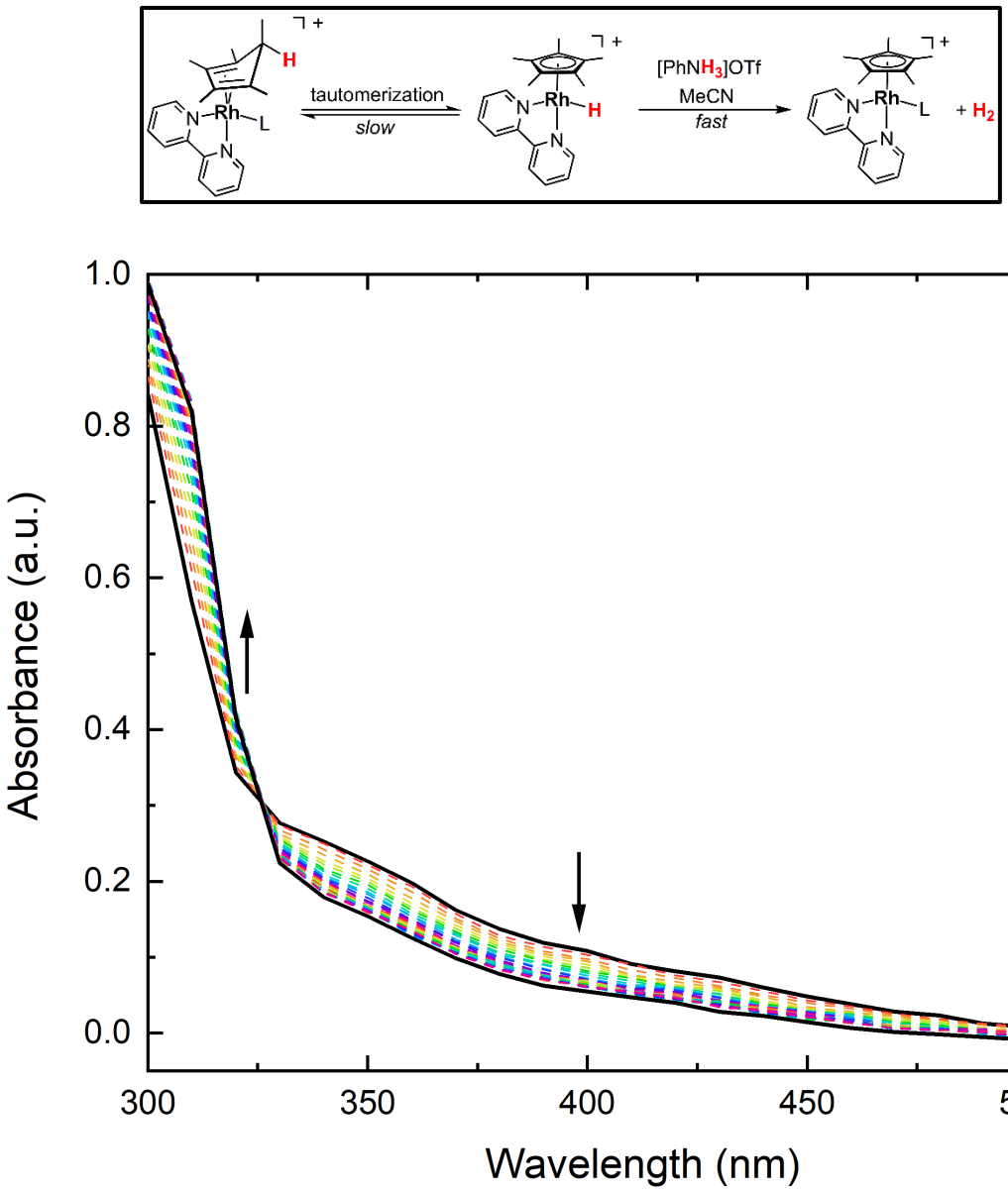

Figure B68: Stopped-flow UV-Vis absorbance vs wavelength plot of **5** with $[PhNH_3]OTf$ under pseudo-first order conditions. The isosbestic point present at 326 nm indicates clean conversion from one molecular species to another.

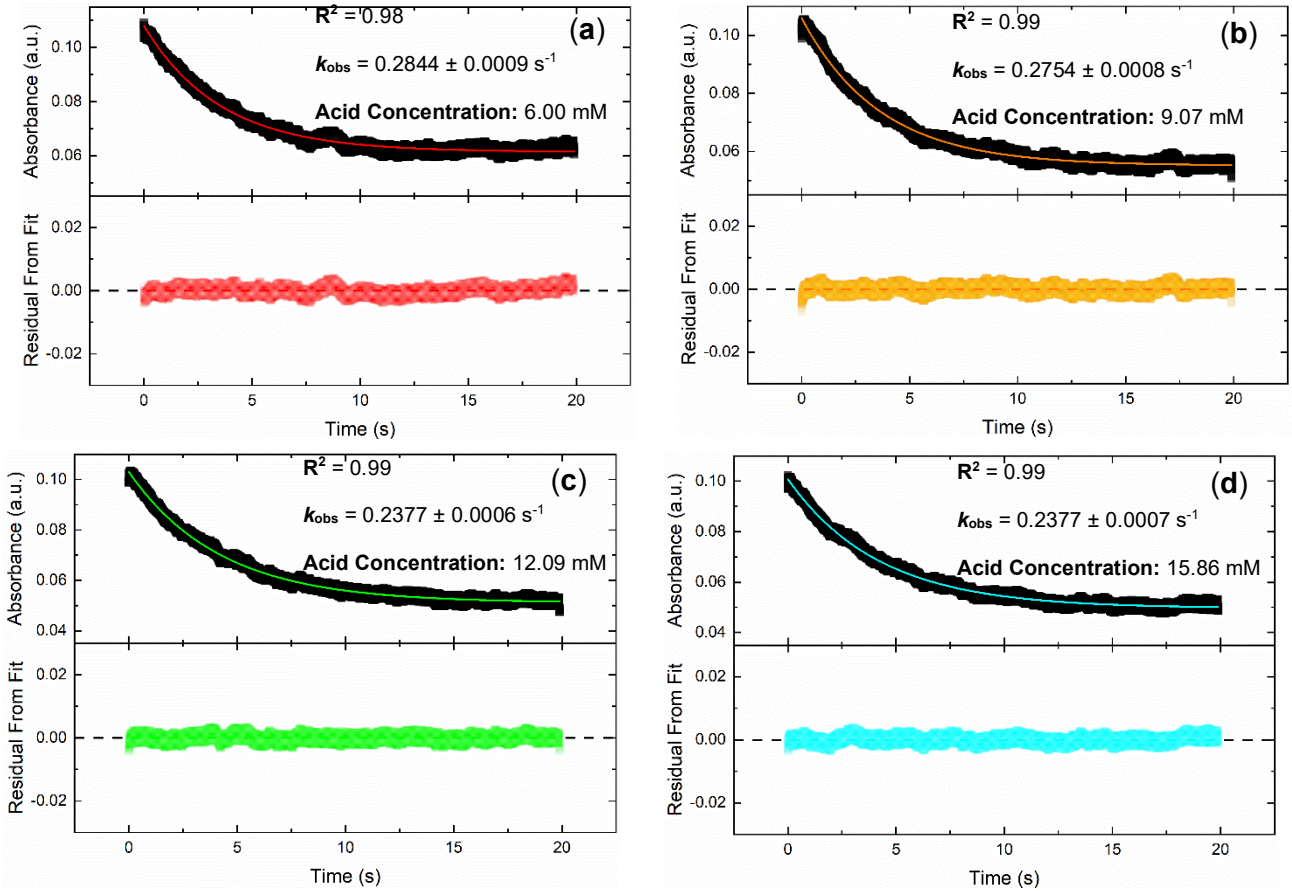

Figure B69: (a-d) Monitoring absorbance vs time at 400 nm for the protonation of **5** with [$PhNH_3$]OTf under pseudo-first order conditions. The decay of the signal at 400 nm is fit with a monoexponential function to extract the observed rate constant (k_{obs}). The residual from the fit monitored as a function of time rationalizes the use of a monoexponential fit here.

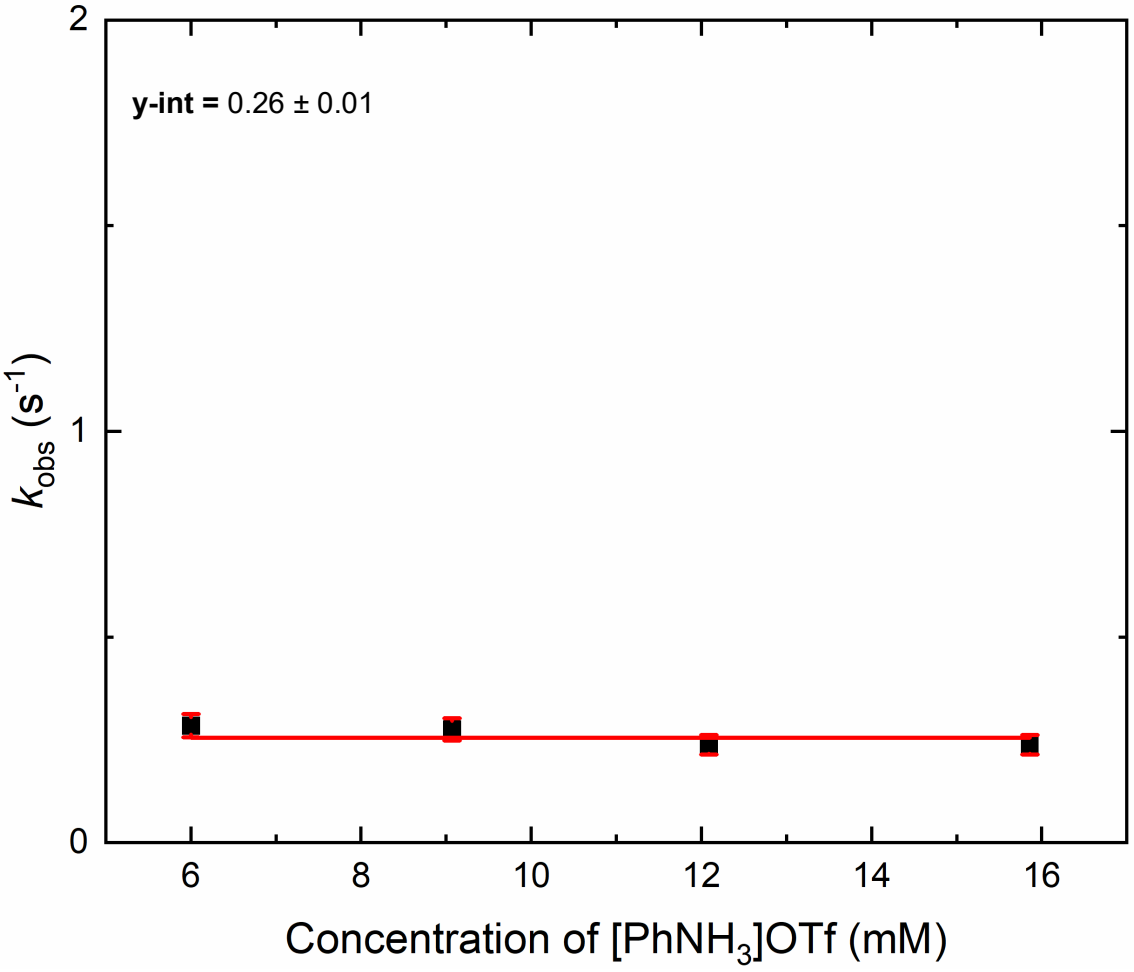

Figure B70: k_{obs} values (black squares) were obtained from the monoexponential fit of the decay signal at 400 nm in Figure B69 and are plotted here as a function of acid concentration. The k_{obs} values were measured at room temperature (298 K). The resulting plot is fit as a line with a fixed slope = 0 to extract the zero-order rate constant for the tautomerization of **5** back to **4**.

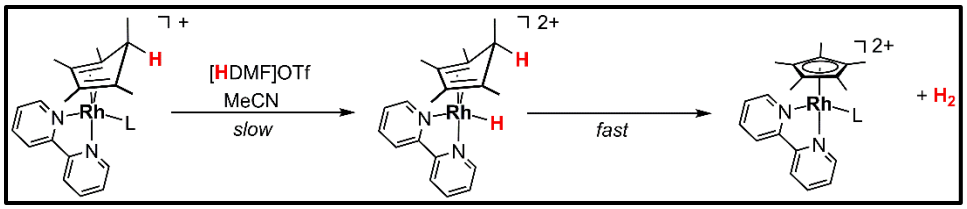

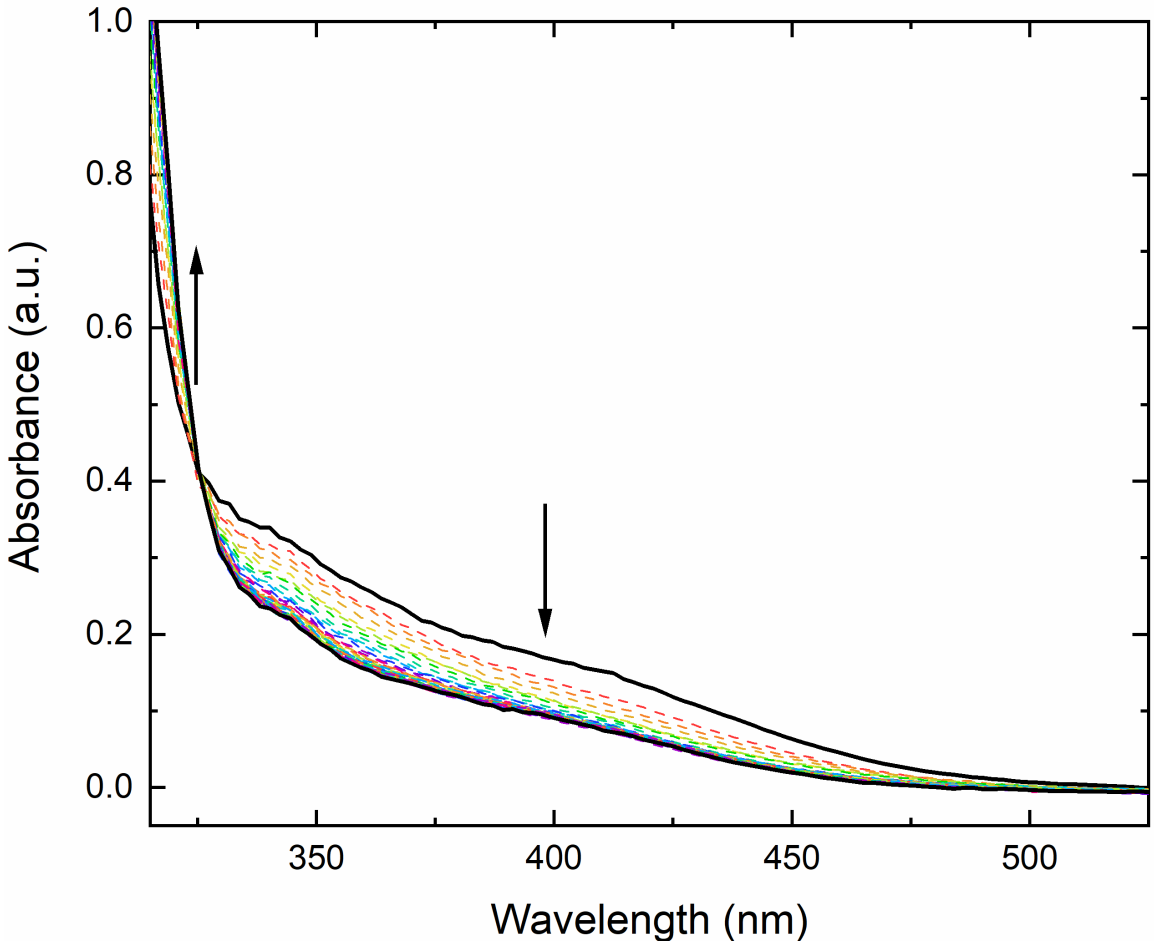

Figure B71: Stopped-flow UV-Vis absorbance vs wavelength plot of **5** and [DMFH]OTf under pseudo-first order conditions. The isosbestic point present at 325 nm indicates clean conversion from one molecular species to another.

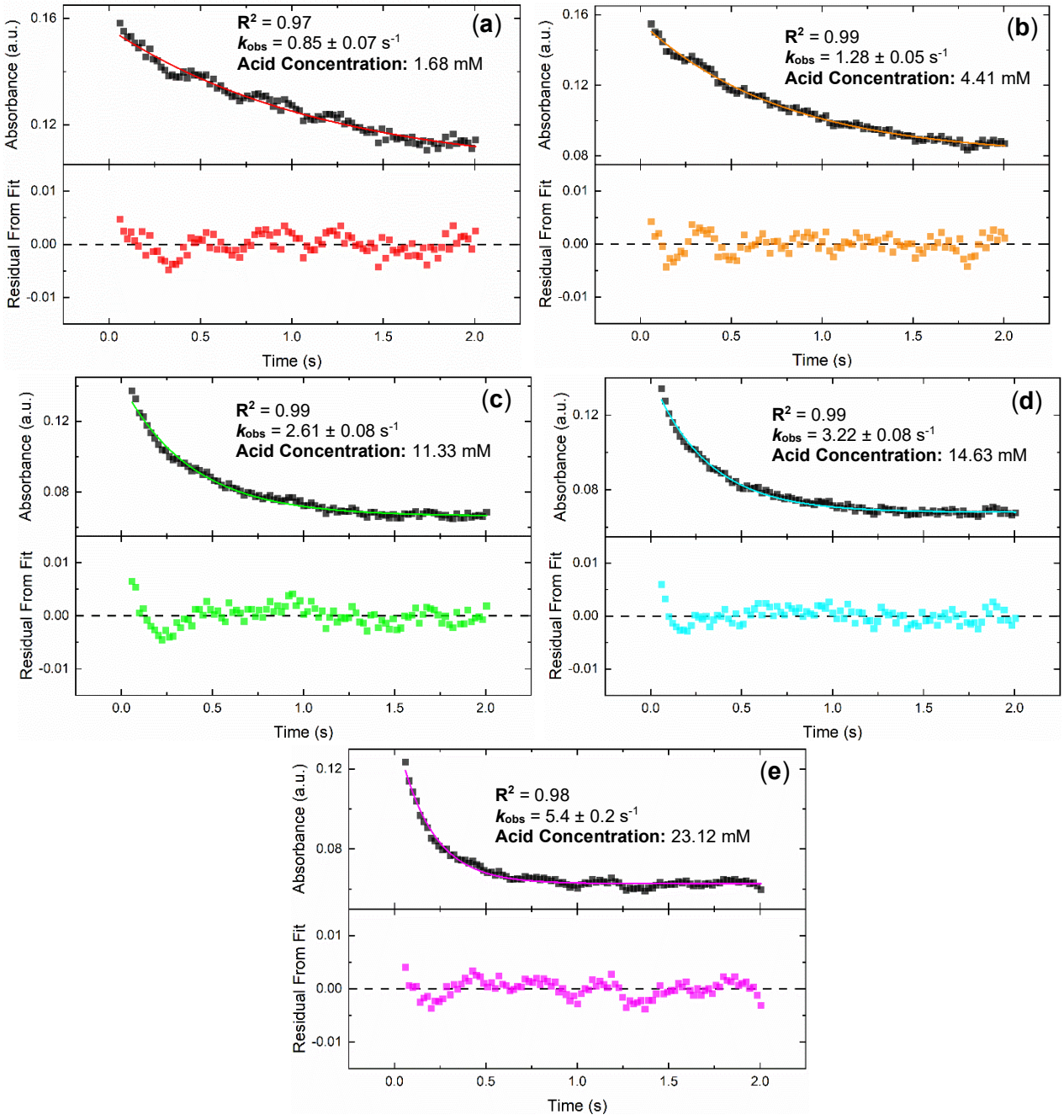

Figure B72: (a-e) Monitoring absorbance vs time at 399.8 nm nm for the protonation of **5** with [DMFH]OTf under pseudo-first order conditions. The decay of the signal at 399.8 nm is fit with a monoexponential function to extract the observed rate constant (k_{obs}). The residual from the fit monitored as a function of time rationalizes the use of a monoexponential fit here.

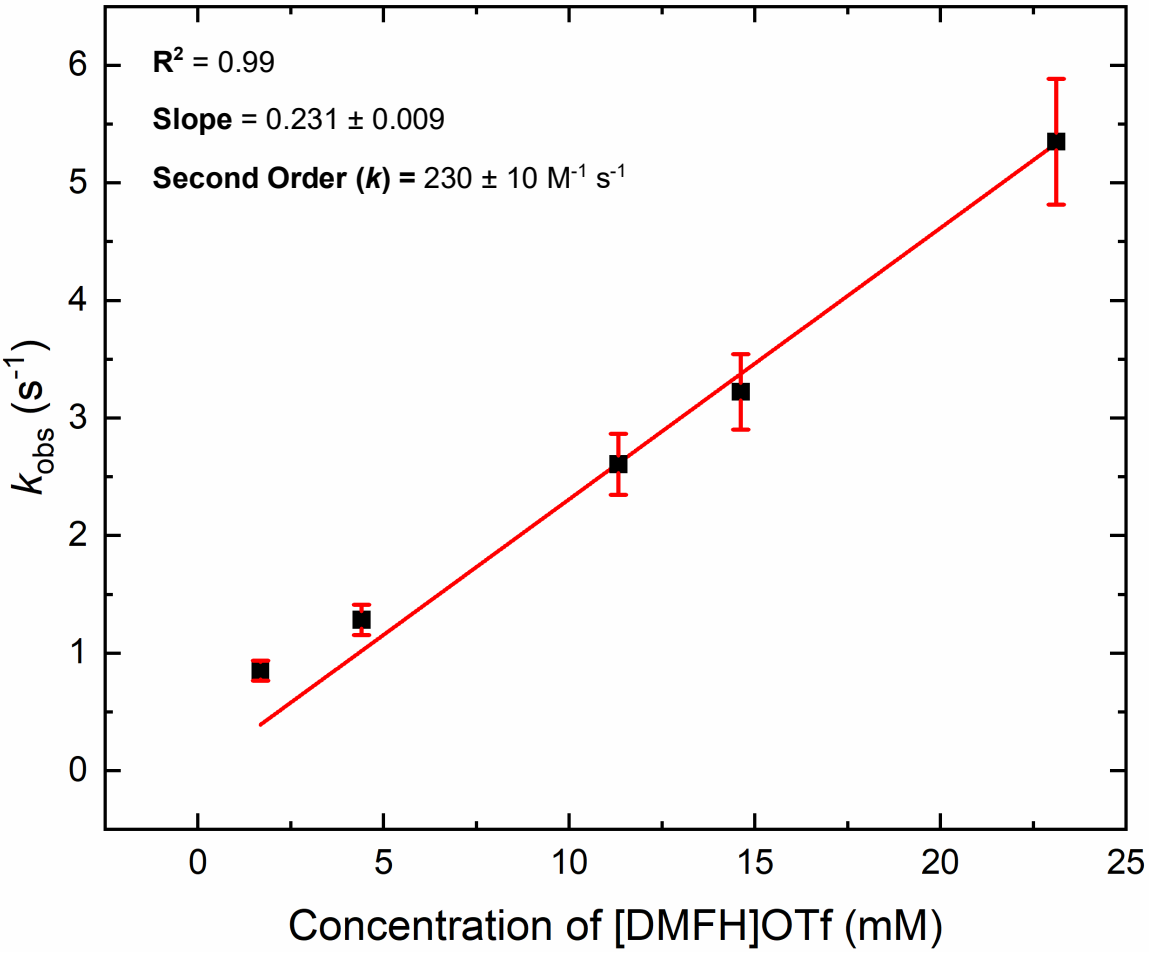

Figure B73: k_{obs} values (black squares), obtained from the monoexponential fits of the decay signal at 400 nm in Figure B72, plotted as a function of acid concentration. The resulting plot exhibits first-order dependence and is thus fit as a line through the origin to extract the overall second-order rate constant for the tautomerization of **5** to **6**, which results in the immediate generation of **1** and dihydrogen.

Comparison of Eyring Plots

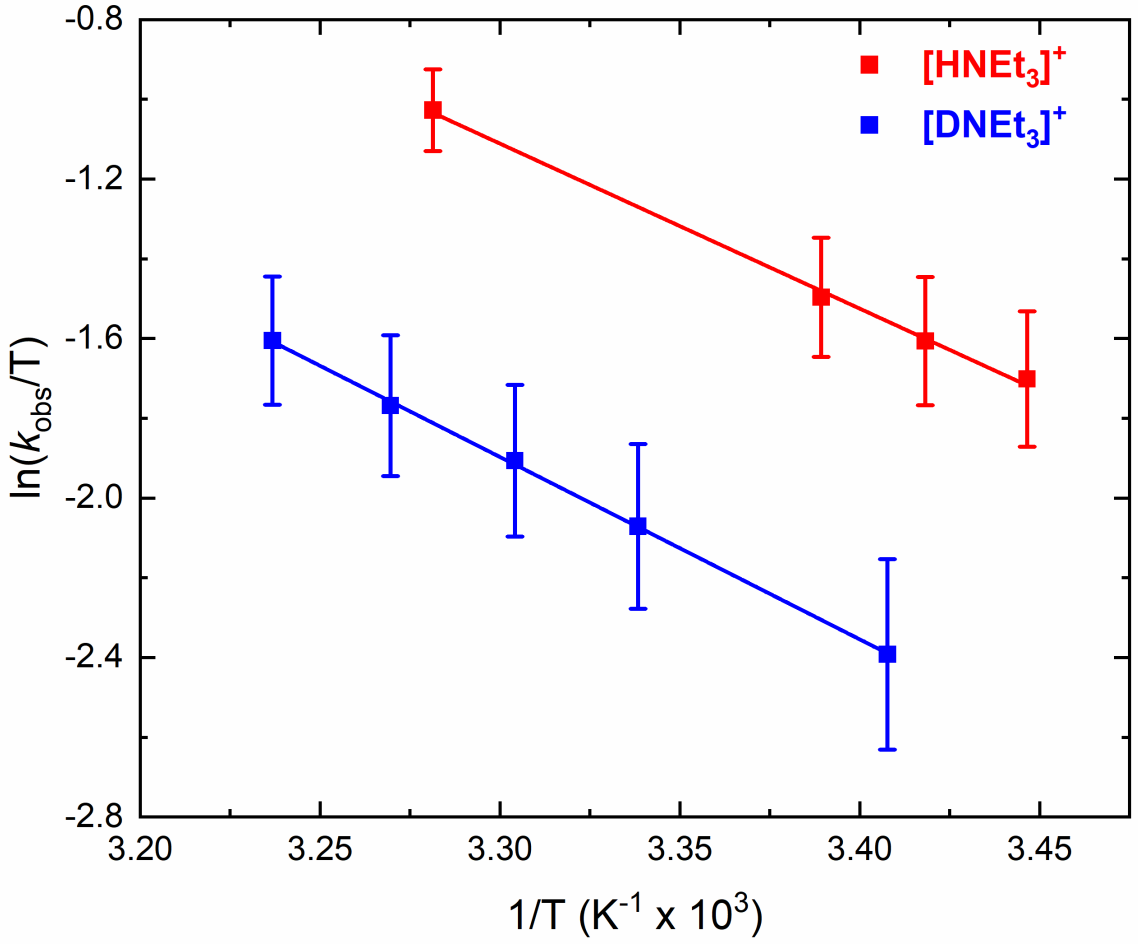

Figure B74: Comparison on the Eyring plots for the protonation of **3** using $[HNEt_3]^+$ or $[DNEt_3]^+$.

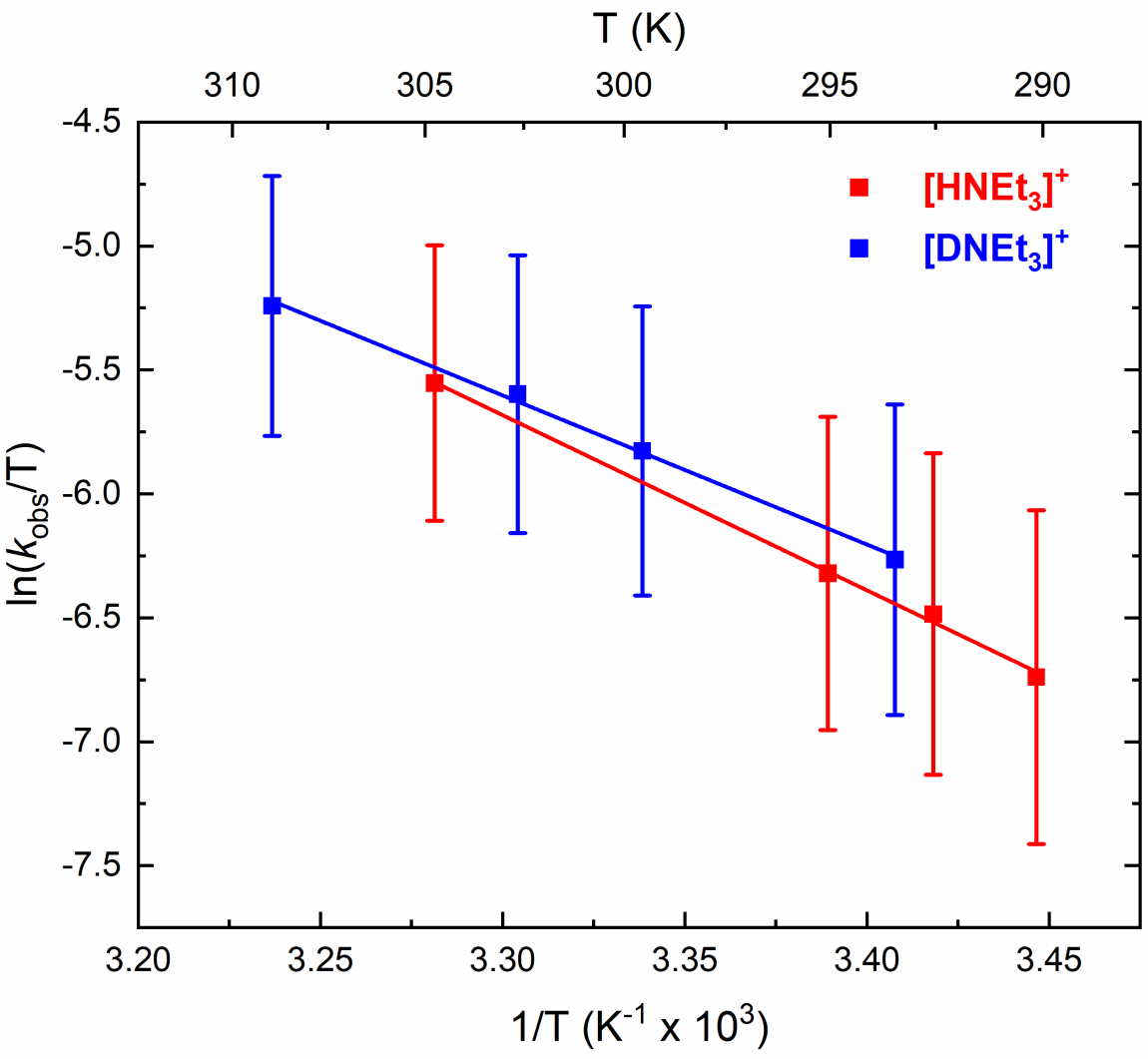

Figure B75: Comparison on the Eyring plots for the tautomerization of **4** or **4D**, respectively, using $[HNEt_3]^+$ or $[DNEt_3]^+$.

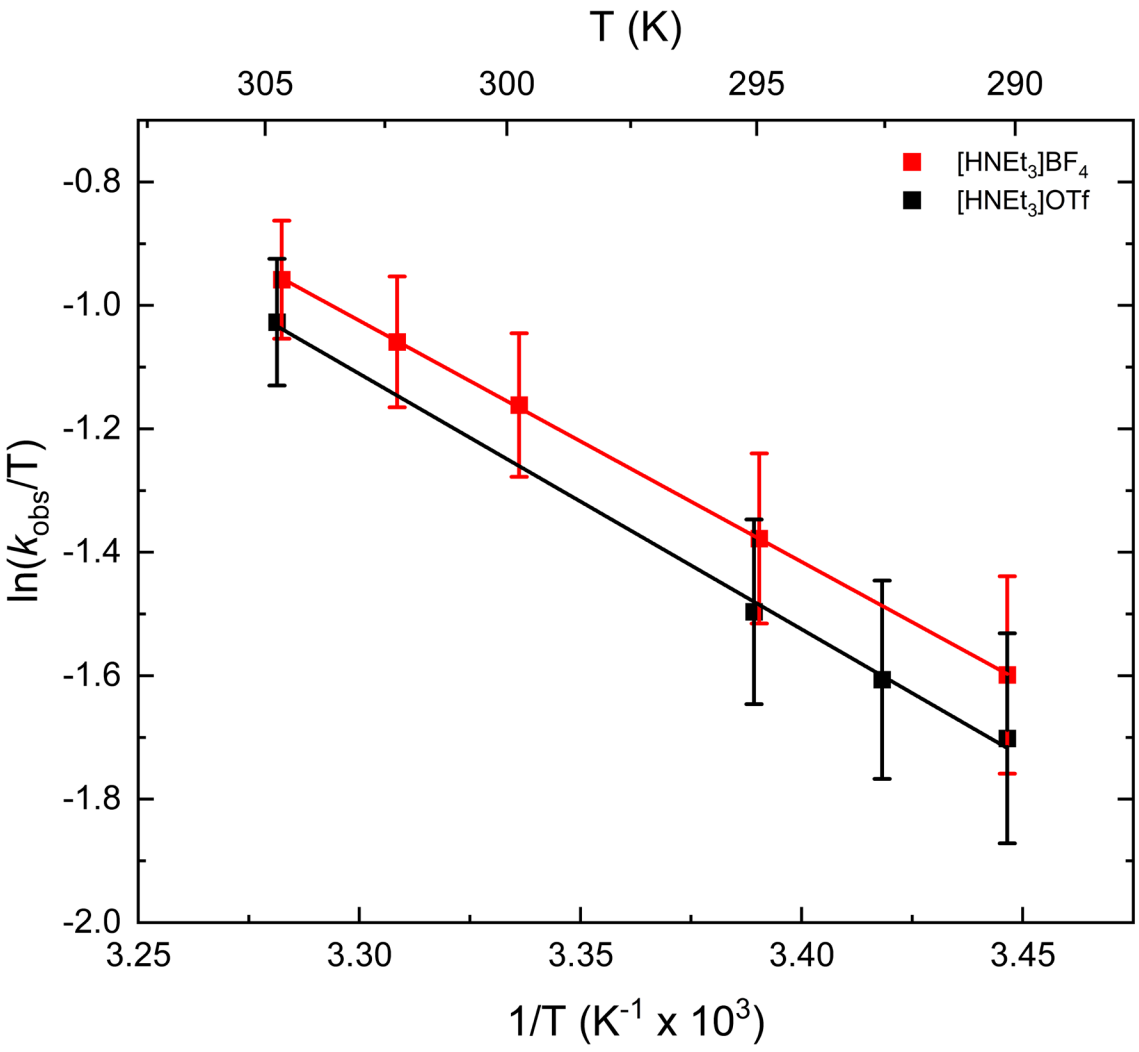

Figure B76: Comparison on the Eyring plots for the protonation of **3** using [$HNEt_3$]X, where X = BF_4 or OTf.

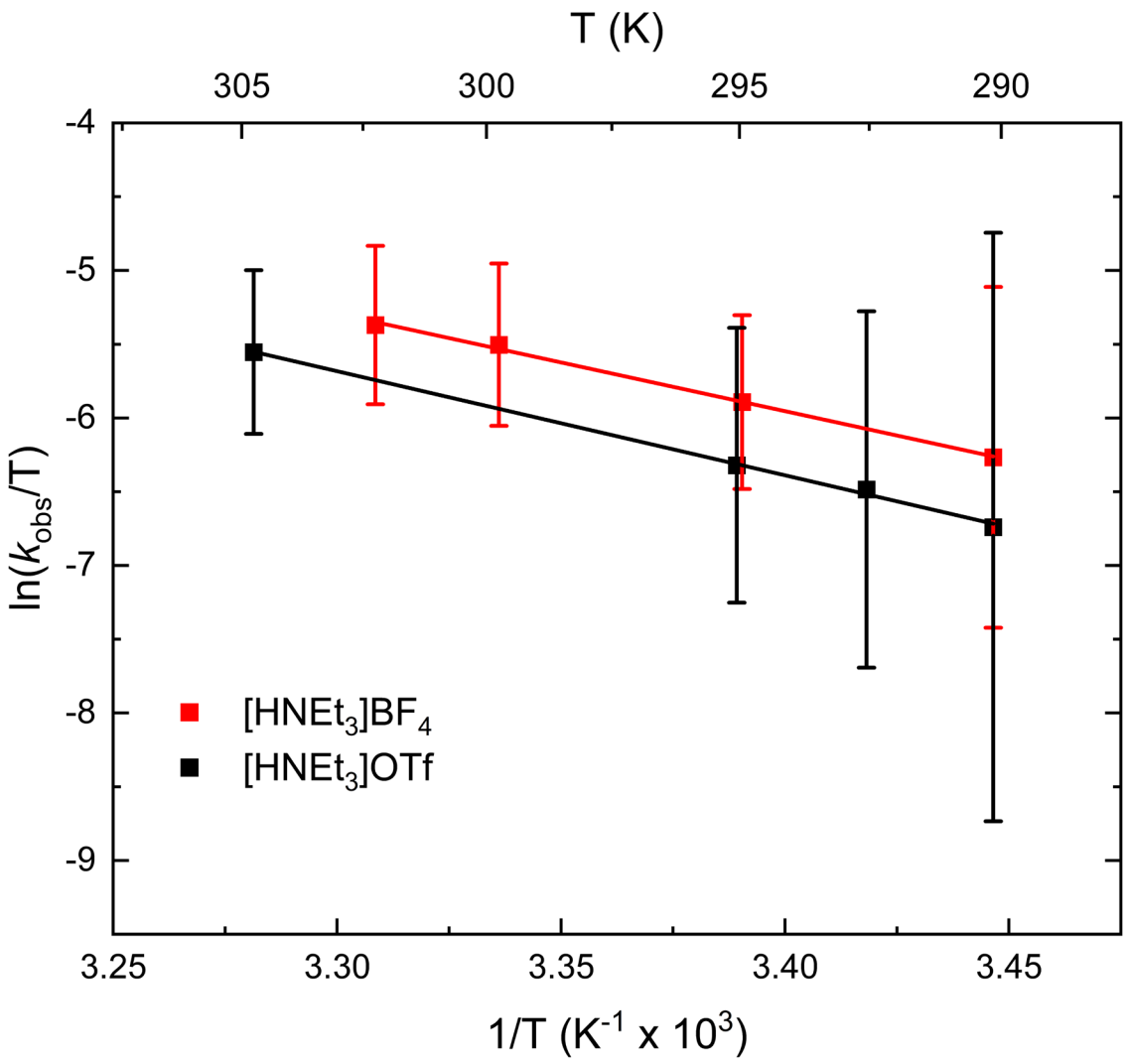

Figure B77: Comparison on the Eyring plots for the tautomerization of **4** or **4D**, respectively, in the presence of $[HNEt_3]X$, where X = BF_4 or OTf.

Summary of Rate Data

Table B1: Summary of rate constant data for the first protonation of **3**.

Starting Compound	Acid	Chemical Process	Temperature (K)	Second-Order Rate Constant (k, M^{-1} s^{-1})
3	$[HNEt_3]BF_4$	First Protonation	298	7100 ± 100
3	$[HNEt_3]OTf$	First Protonation	298	6400 ± 200
3	$[DNEt_3]OTf$	First Deuteration	298	2900 ± 200

Table B2: Summary of rate constant data for the tautomerization of **4** to **5**.

Starting Compound	Acid	Chemical Process	Temperature (K)	First-Order Rate Constant (k, s^{-1})
3	$[HNEt_3]BF_4$	Tautomerization	298	970 ± 20
3	$[HNEt_3]OTf$	Tautomerization	298	870 ± 30
3	$[DNEt_3]OTf$	Tautomerization	298	1000 ± 30

Table B3: Summary of rate constant data for the tautomerization or protonation of **5**.

Starting Compound	Acid	Chemical Process	Temperature (K)	Rate Constant (*k*)
5	$[PhNH_3]OTf$	Tautomerization	298	$260 \pm 10\ s^{-1}$
5	[DMFH]OTf	Protonation	298	$230 \pm 10\ M^{-1}\ s^{-1}$

Summary of Activation Energy Parameters from Arrhenius and Eyring Analyses

Table B4: Summary of Arrhenius and Eyring data for the first protonation of **3** with various acids.

Starting Compound	**Acid**	**Chemical Process**	**Activation Energy (kcal/mol)**	$\Delta G^{\ddagger}$ **(kcal/mol)**	$\Delta H^{\ddagger}$ **(kcal/mol)**	T **(K)**	$\Delta S^{\ddagger}$ **(cal mol^{-1} K^{-1})**
3	$[HNEt_3]BF_4$	First Protonation	8.4 ± 0.1	14.8 ± 0.2	7.8 ± 0.1	298	-23.6 ± 0.2
3	$[HNEt_3]OTf$	First Protonation	8.8 ± 0.3	14.9 ± 0.9	8.2 ± 0.3	298	-22.3 ± 0.8
3	$[DNEt_3]OTf$	First Deuteration	9.7 ± 0.1	15.3 ± 0.4	9.1 ± 0.1	298	-21.0 ± 0.3

Table B5: Summary of Arrhenius and Eyring data for the tautomerization of **4** to **5** with various acids.

Starting Compound	**Acid**	**Chemical Process**	**Activation Energy (kcal/mol)**	$\Delta G^{\ddagger}$ **(kcal/mol)**	$\Delta H^{\ddagger}$ **(kcal/mol)**	T **(K)**	$\Delta S^{\ddagger}$ **(cal mol^{-1} K^{-1})**
3	$[HNEt_3]BF_4$	Tautomerization	13.7 ± 0.5	17.4 ± 0.8	13.2 ± 0.5	298	-14.3 ± 0.7
3	$[HNEt_3]OTf$	Tautomerization	14.6 ± 0.5	17.7 ± 0.7	14.0 ± 0.5	298	-12.2 ± 0.5
3	$[DNEt_3]OTf$	Tautomerization	12.6 ± 0.4	18 ± 1	12.0 ± 0.4	298	-19 ± 1

Measuring stoichiometric dihydrogen production using gas chromatography (GC)

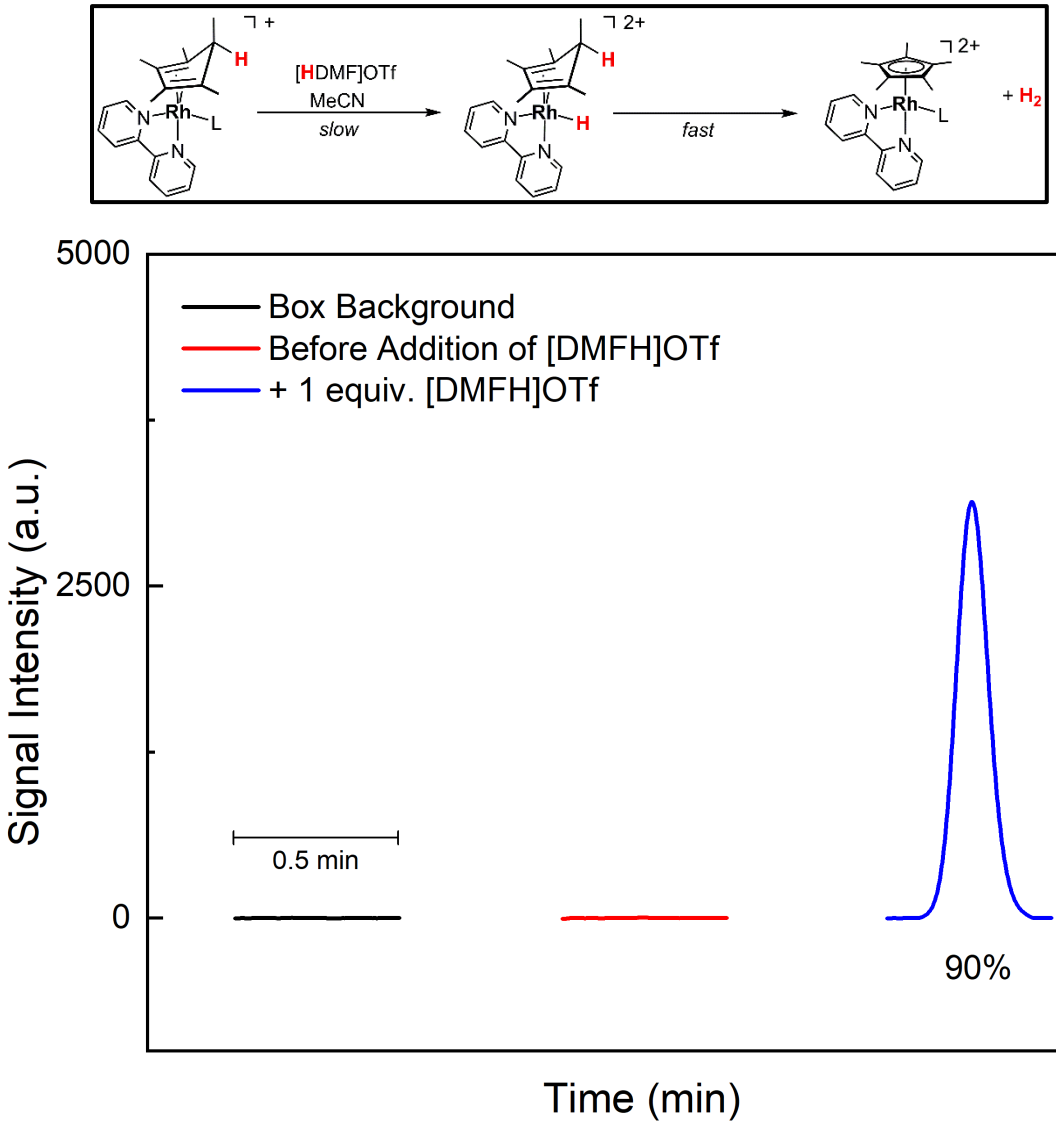

Figure B78: Gas chromatography data for the determination of evolved H_2 following the addition of 1 equiv. of [DMFH]OTf to **5**. The box background (black) and before addition (red) data was below our limit of quantitation (LOQ), while after addition of 1 equiv. of [DMFH]OTf (blue) results in generation of H_2.

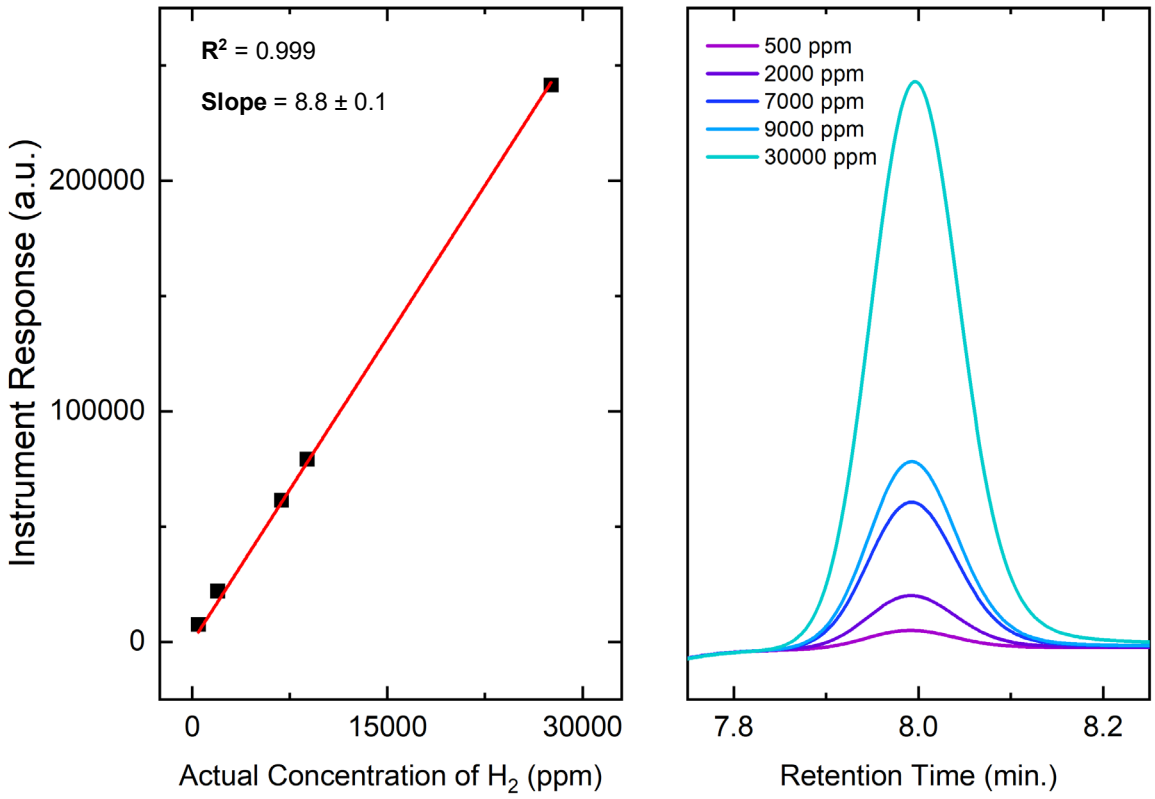

Figure B79: Calibration Curve (left) and chromatograms (right) obtained from injections of H_2 standards; this curve was used in the determination of H_2 evolved during addition of [DMFH]OTf to **5**.

Calculations

Table B6: Coordinates for the DFT optimized structure of **4.**

	X	Y	Z
Rh	12.95324	5.9388	8.88276
N	11.63394	6.58739	10.41154
C	10.30675	6.60149	10.28871
H	9.87706	6.25233	9.34521
C	9.46892	7.04965	11.30537
H	8.38508	7.04447	11.17003
C	10.04645	7.51162	12.48879
H	9.42161	7.87747	13.30803
C	11.43542	7.50488	12.60642
H	11.89601	7.87571	13.52435
C	12.20561	7.03261	11.54537

C	12.93286	5.35143	6.78623
C	11.79526	4.79152	7.44953
C	12.27031	3.8145	8.42239
C	11.381	2.98154	9.27306
H	10.86282	2.21766	8.66717
H	10.5954	3.58624	9.75633
H	11.9387	2.4583	10.06349
C	10.37334	4.98745	7.05849
H	10.11874	4.34419	6.19732
H	10.16809	6.02775	6.75998
H	9.68287	4.71467	7.87146
C	12.90573	6.26606	5.61411
H	12.89915	5.68107	4.6772
H	13.78938	6.92149	5.58619
H	12.00709	6.90146	5.61113
N	14.25758	6.55375	10.4285

C	15.59584	6.51815	10.34297
H	15.99626	6.16485	9.38864
C	16.41493	6.90826	11.38975
H	17.49739	6.85537	11.26239
C	15.83072	7.35758	12.56471
H	16.44349	7.67345	13.41197
C	14.45091	7.40868	12.65749
H	13.95596	7.76026	13.56451
C	13.6745	7.00154	11.56884
C	14.10352	4.82558	7.42138
C	13.67833	3.83678	8.40589
C	14.61311	3.04021	9.24159
H	15.12981	2.27763	8.63292
H	15.3989	3.67462	9.68572
H	14.0935	2.52067	10.06019
C	15.50811	5.05918	6.99212

H	15.75257	4.43455	6.11419
H	15.68305	6.10825	6.70517
H	16.22781	4.79304	7.78181
H	12.9672	7.48589	8.48402

Table B7: Frequencies for the DFT optimized structure of **4.**

Frequencies (cm^{-1})	**Intensities (km/mol)**
34.6722	0.151656
38.9899	0.209444
69.6319	0.099225
93.44	0.332339
101.491	0.215835
119.459	0.075373
124.63	0.09005
146.295	0.017643
149.523	0.287448
155.81	0.168265
160.061	0.059099
170.007	0.169241
176.551	0.057252

191.982	0.056803
194.69	0.031085
198.562	0.093954
225.151	1.28
236.762	0.230033
254.456	0.004918
259.197	0.138682
263.07	0.121135
271.841	0.12391
299.322	0.224417
309.544	0.079889
369.091	0.116983
383.371	4.32087
430.317	0.051818
437.865	0.01062
445.063	1.03062

448.517	0.560603
470.026	0.123623
477.122	0.190864
535.775	0.016045
540.67	0.16683
546.779	0.029019
571.066	0.009261
601.536	1.03425
606.369	1.66577
625.984	0.225833
639.638	0.502441
640.422	0.709312
656.386	0.81532
658.541	0.381947
749.317	3.20845
763.636	11.6189

767.913	0.406086
779.321	0.700682
784.811	6.44032
809.908	0.004822
812.01	0.081784
839.452	0.057769
907.939	0.039103
922.812	0.002315
932.967	0.004975
937.121	0.034596
992.699	0.470581
998.162	1.94672
1003.43	3.80708
1006.57	2.82563
1012.34	3.03076
1020.51	0.014533

1027.93	0.601753
1029.19	0.013682
1031.07	0.156784
1031.61	0.093437
1038.18	1.01154
1056.86	0.563999
1066.91	4.29167
1069.39	3.78852
1079.92	1.51242
1084.03	0.2447
1090.34	0.005501
1110.83	1.48946
1125.29	0.33608
1131.73	0.280627
1157.94	1.23989
1178.97	0.057836

1179.94	1.32533
1279.25	0.105856
1297.5	0.187362
1337.43	0.289678
1338.46	7.10288
1341.91	1.32652
1345.49	0.525442
1350.56	0.142433
1353.33	0.129784
1356.38	1.39495
1360.53	1.25071
1381.19	0.951859
1383.83	1.05986
1386.05	0.366888
1389.03	0.823759
1389.86	1.21376

1391.88	3.18642
1393.75	0.580207
1395.03	1.72857
1400.91	0.057176
1402	2.32913
1439.57	0.726323
1461.61	0.183028
1466.04	0.366295
1469.37	9.97987
1484.31	5.60907
1517.47	0.782772
1524.25	2.35854
1530.25	1.50676
1576.58	7.23278
1630.82	1.10694
1642.66	2.26687

1668.65	2.85444
1674.1	2.40686
1901.44	100
3013.25	6.9822
3013.76	4.07279
3014.51	1.23928
3016.04	3.79002
3016.9	0.749534
3101.41	0.957361
3102.83	1.24686
3103.88	0.97088
3104.09	0.21505
3111.13	0.37481
3137.12	0.963006
3137.72	0.609866
3138.24	0.923128

3140.76	1.39073
3143.53	1.01859
3182.46	0.682168
3183.77	0.73236
3190.64	0.110238
3191.96	0.1332
3202.3	0.064725
3206.73	0.114773
3207.94	0.570142
3212.86	0.223747

References

(1) C. White, A. Yates, P. M. Maitlis, D. M. Heinekey, "(η^5-Pentamethylcyclopentadienyl)Rhodium and -Iridium Compounds" in *Inorg. Synth.* 228-234 (1992).

(2) M. A. Mantell, J. W. Kampf, M. Sanford, Improved synthesis of $[Cp^RRhCl_2]_2$ complexes. *Organometallics* **37**, 3240-3242 (2018).

(3) U. Kölle, B.-S. Kang, P. Infelta, P. Comte, M. Grätzel, Elektrochemische und pulsradiolytische reduktion von (pentamethylcyclopentadienyl)(polypyridyl)rhodium-complexen. *Chem. Ber.* **122**, 1869-1880 (1989).

(4) H. Nakai, K. Jeong, T. Matsumoto, S. Ogo, Catalytic C–F bond hydrogenolysis of fluoroaromatics by [(η^5-C_5Me_5)RhI(2,2′-bipyridine)]. *Organometallics* **33**, 4349-4352 (2014).

(5) Y. Peng, M. V. Ramos-Garcés, D. Lionetti, J. D. Blakemore, Structural and electrochemical consequences of [Cp*] ligand protonation. *Inorg. Chem.* **56**, 10824-10831 (2017).

(6) K. Fumino, V. Fossog, K. Wittler, R. Hempelmann, R. Ludwig, Dissecting anion–cation interaction energies in protic ionic liquids. *Angew. Chem. Int. Ed.* **52**, 2368-2372 (2013).

(7) K. Fumino, V. Fossog, K. Wittler, R. Hempelmann, R. Ludwig, Dissecting anion–cation interaction energies in protic ionic liquids. *Angew. Chem. Int. Ed.* **52**, 2368-2372 (2013).

(8) J.-P. Belieres, C. A. Angell, Protic ionic liquids: preparation, characterization, and proton free energy level representation. *J. Phys. Chem.* **111**, 4926-4937 (2007).

(9) T. Gramstad, R. N. Haszeldine, 806. Perfluoroalkyl derivatives of sulphur. Part VII. Alkyl trifluoromethanesulphonates as alkylating agents, trifluoromethanesulphonic anhydride as a promoter for esterification, and some reactions of trifluoromethanesulphonic acid. *J. Chem. Soc.* 4069-4079 (1957).

(10) Favier, E. Duñach, New protic salts of aprotic polar solvents. *Tetrahedron Lett.* **45**, 3393-3395 (2004).

(11) G. R. Fulmer *et al.*, NMR chemical shifts of trace impurities: common laboratory solvents, organics, and gases in deuterated solvents relevant to the organometallic chemist. *Organometallics* **29**, 2176-2179 (2010).

(12) Y. Zhao, D. G. Truhlar, The M06 suite of density functionals for main group thermochemistry, thermochemical kinetics, noncovalent interactions, excited states, and transition elements: two new functionals and systematic testing of four M06-class functionals and 12 other functionals. *Theor. Chem. Acc.* **120**, 215-241 (2008).

(13) A. V. Marenich, C. J. Cramer, D. G. Truhlar, Universal Solvation Model Based on Solute Electron Density and on a Continuum Model of the Solvent Defined by the Bulk Dielectric Constant and Atomic Surface Tensions. *J. Phys. Chem. B* **113**, 6378-6396 (2009).

(14) F. Weigend, R. Ahlrichs, Balanced basis sets of split valence, triple zeta valence and quadruple zeta valence quality for H to Rn: Design and assessment of accuracy. *Phys. Chem. Chem. Phys.* **7**, 3297-3305 (2005).

(15) M. J. Frisch *et al.* (2016) Gaussian 16 Rev. C.01. (Wallingford, CT).

Appendices for Chapters in Part II

Appendix C

Supplementary Information for Chapter 5

NMR Spectra

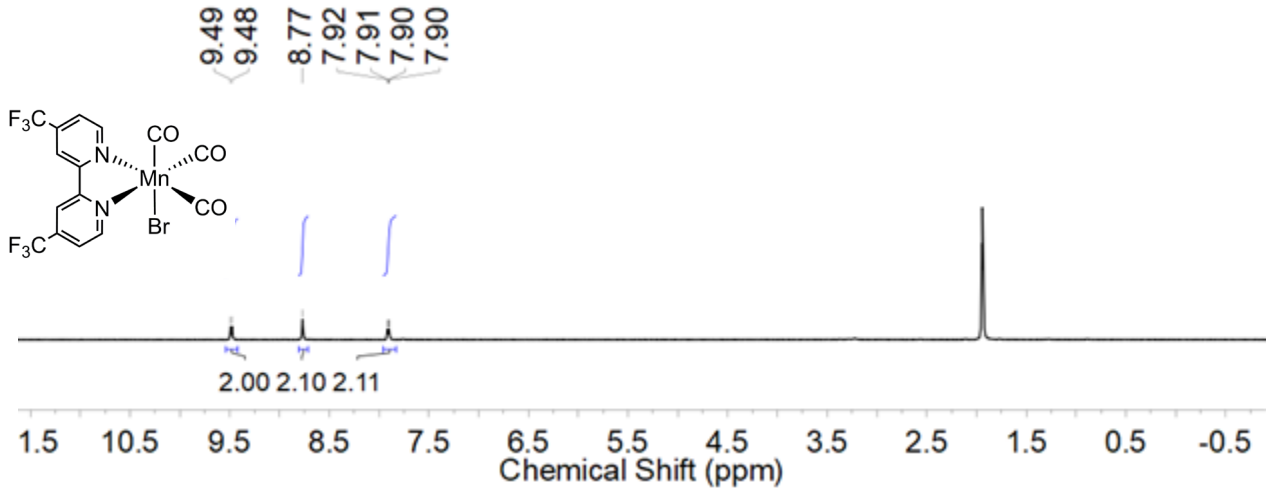

Figure C1: ^{1}H-NMR spectrum (400 MHz, CD3CN) of **3.**

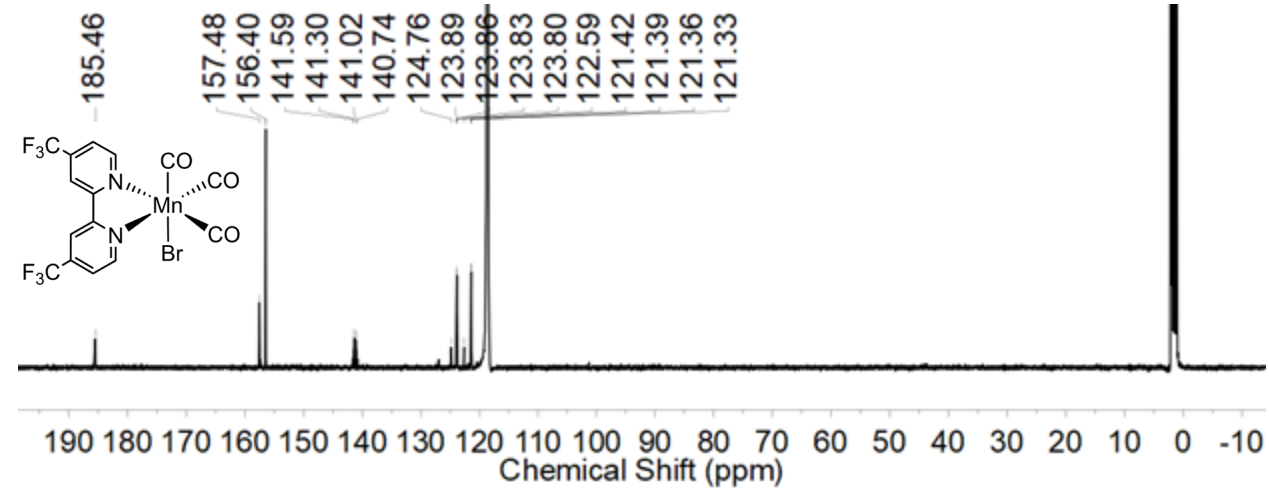

Figure C2: ^{13}C{^{1}H} NMR spectrum (126 MHz, CD_3CN) of **3.**

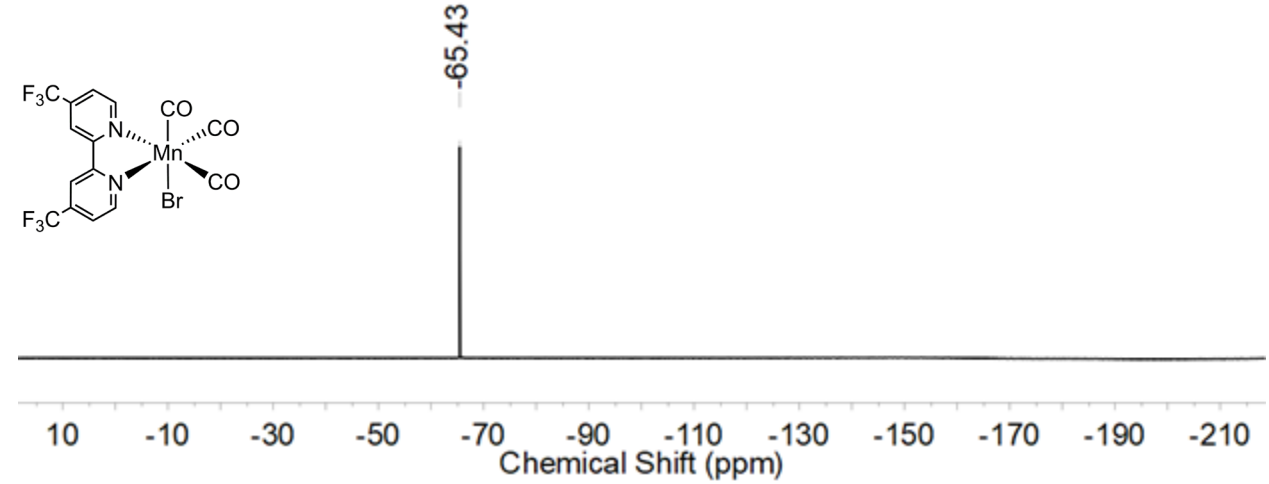

Figure C3: ^{19}F-NMR spectrum (376 MHz, CD_3CN) of **3.**

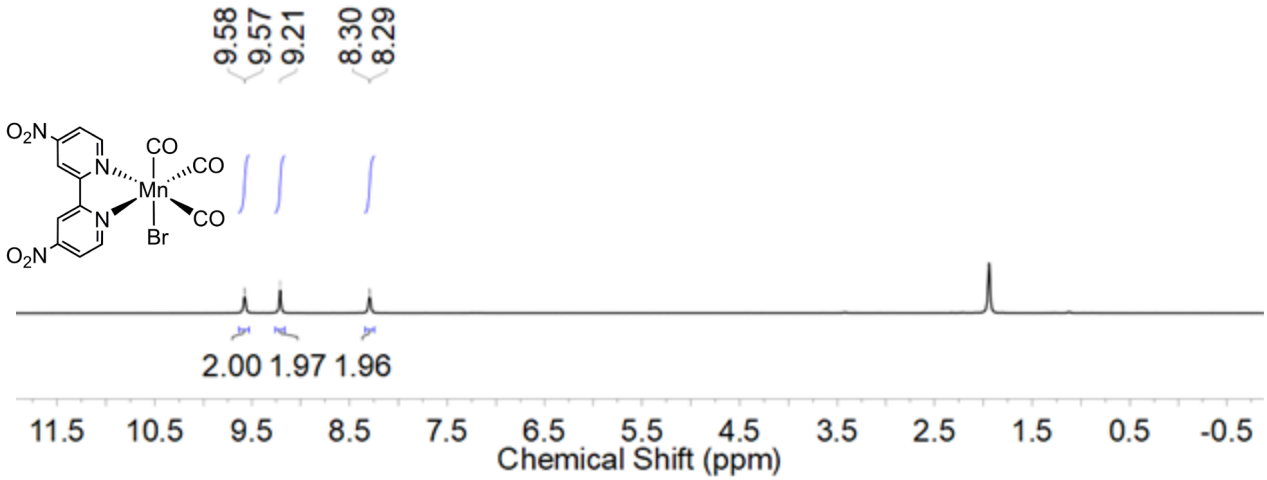

Figure C4: ^{1}H-NMR spectrum (400 MHz, CD3CN) of **4.**

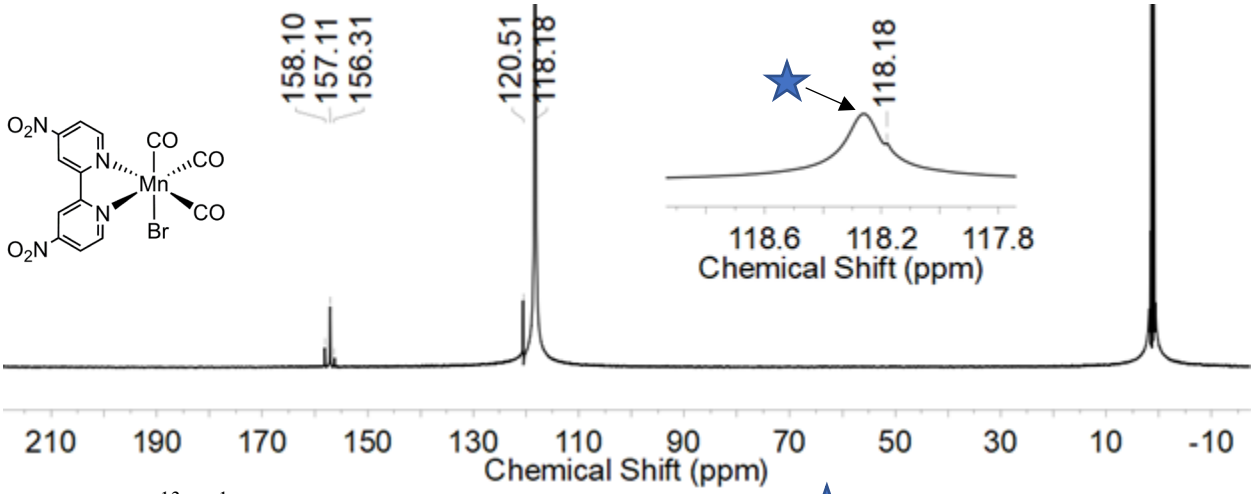

Figure C5: ^{13}C{^{1}H} NMR spectrum (126 MHz, CD_3CN) of **4**; ★ indicates the solvent residual.

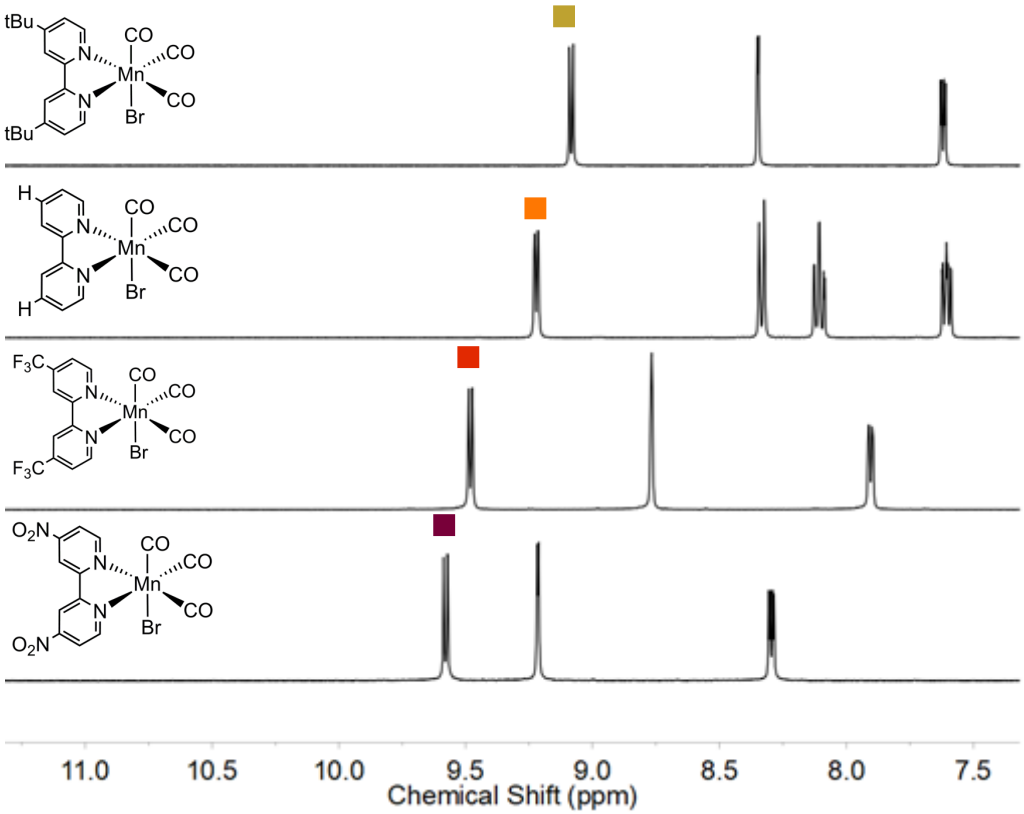

Figure C6: Stacked ^{1}H-NMR spectra (400 MHz, CD3CN) of **1**, **2**, **3**, and **4** in the aromatic region.

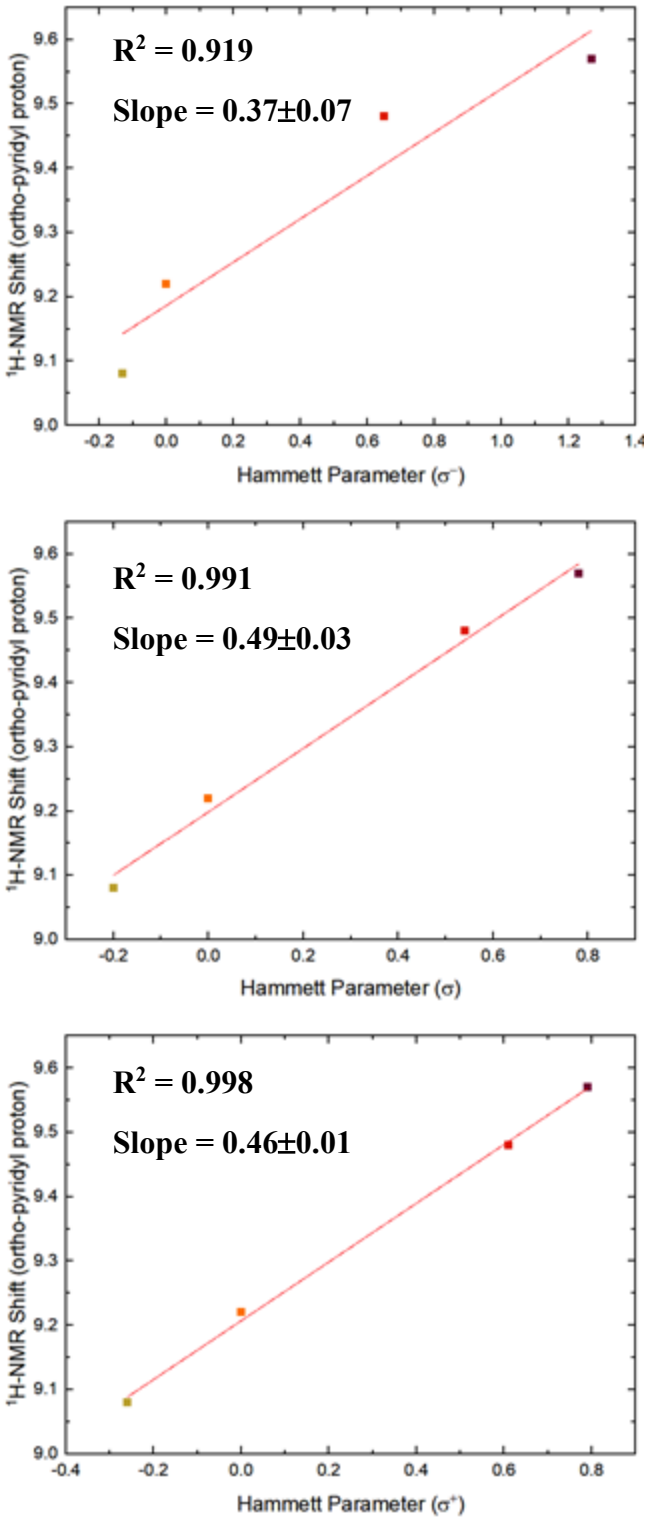

Figure C7: Hammett analyses showing the correlation between the ^{1}H-NMR shift of the ortho-pyridyl proton as a function of the various Hammett Parameters σ^{-} (top), σ (middle), and σ^{+} (bottom). The best fit is found when the data is plotted as a function of the σ^{+} Hammett Parameter.

IR Data

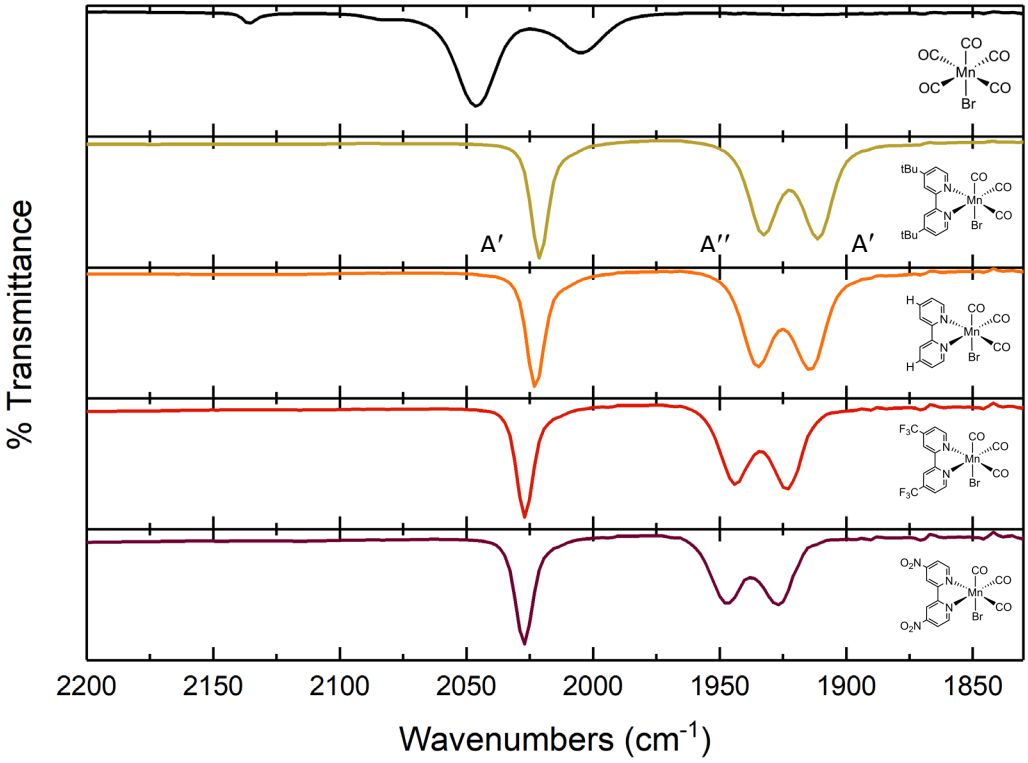

Figure C8: IR spectra of $Mn(CO)_5Br$, **1**, **2**, **3**, and **4** in THF in the CO stretching region. For a C_s symmetric molecule three CO stretches (Γ_{CO} = 2A′+A″) is expected, and the expected three features are observed for **1**, **2**, **3**, and **4**.

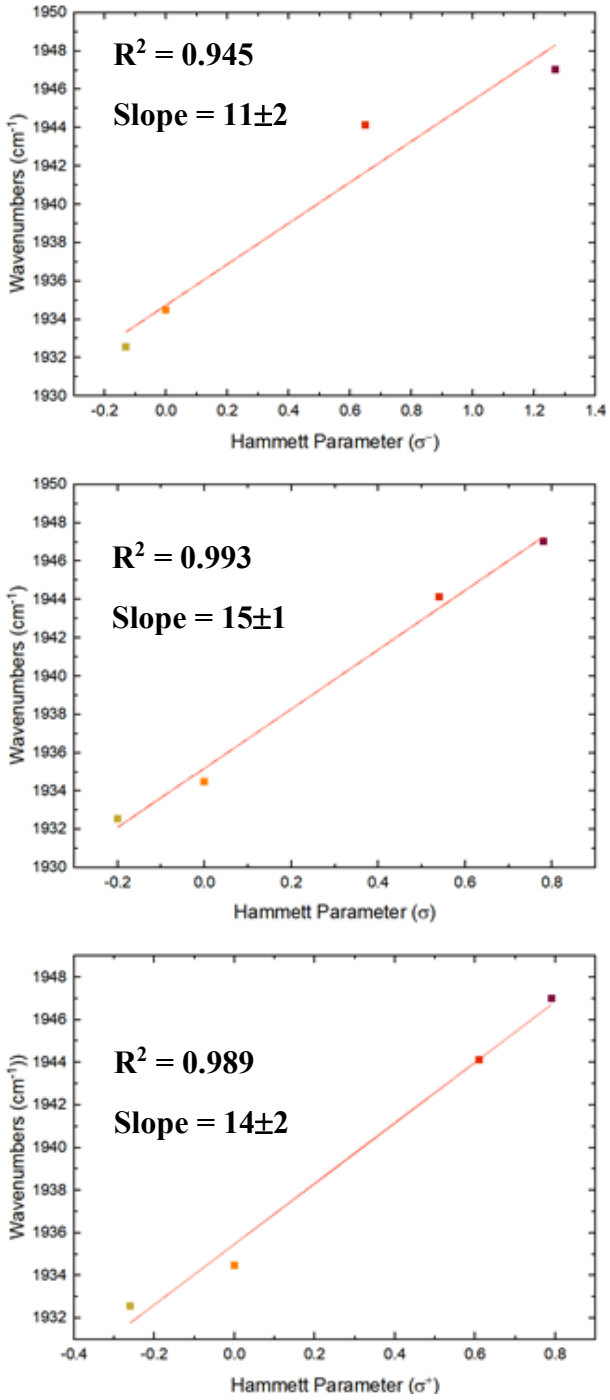

Figure C9: Hammett Analyses showing the correlation between the wavenumbers of the CO stretch as a function of the various Hammett Parameters σ^- (top), σ (middle), and σ^+ (bottom). The best fit is found when the data is plotted as a function of the σ Hammett Parameter.

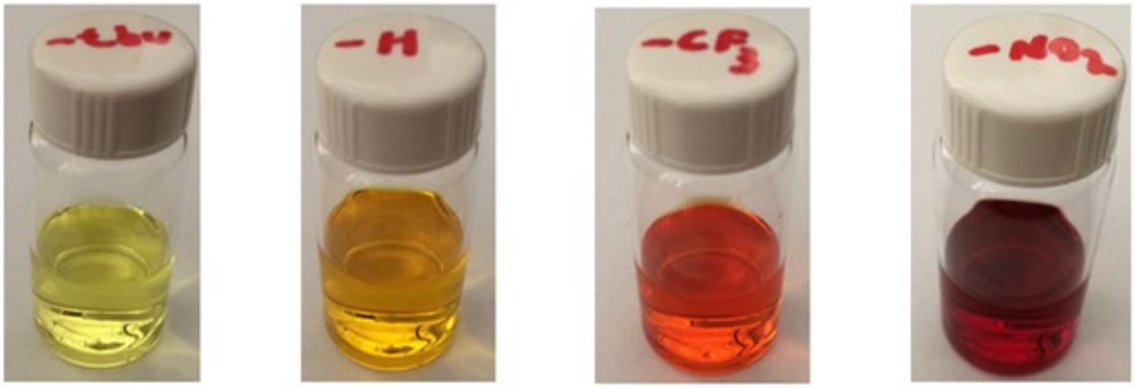

Figure C10: Prepared solutions of the $[Mn(CO)_3Br(^{R}bpy)]$ complexes in MeCN.

UV-Vis, Transient Absorption, and Gas Chromatography Data

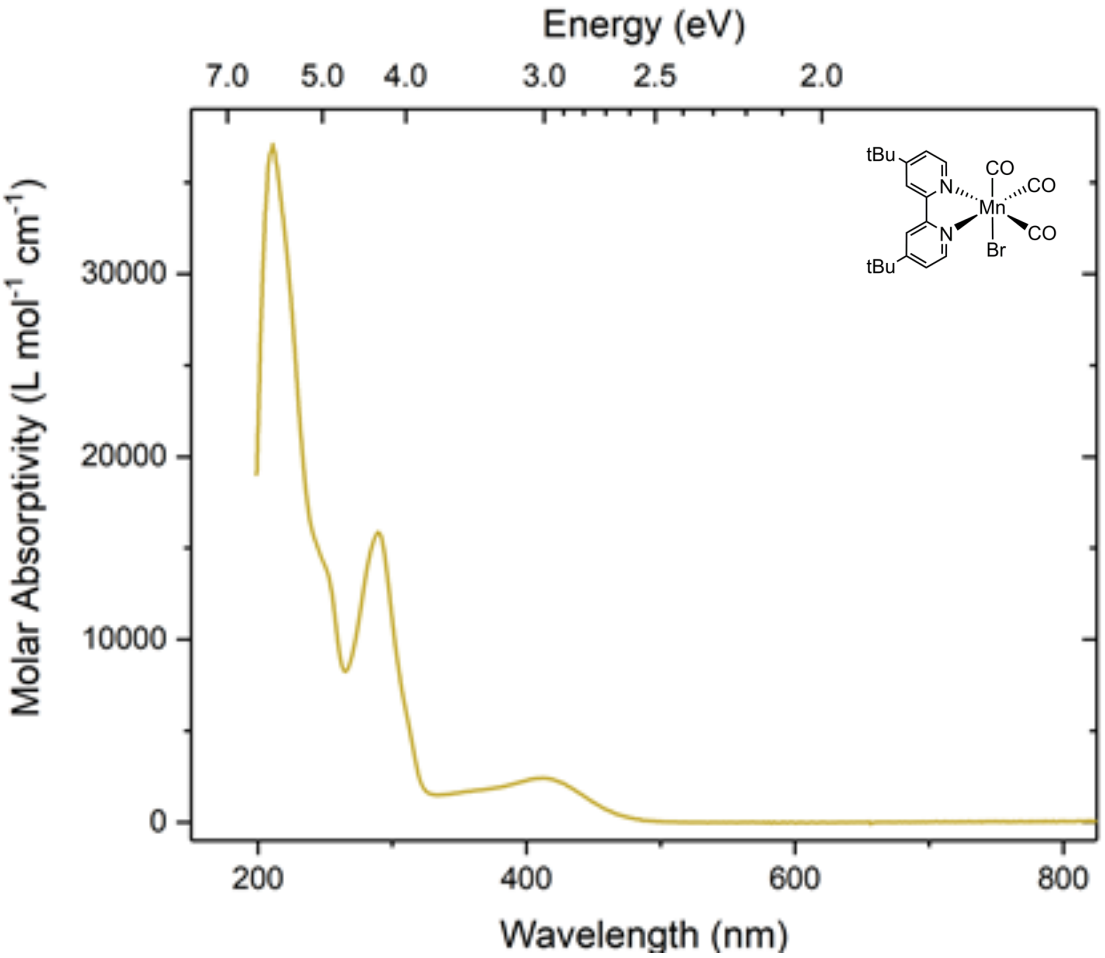

Figure C11: Electronic absorption spectrum of **1** in MeCN. The smaller tic marks are used to illustrate 0.1 eV increments.

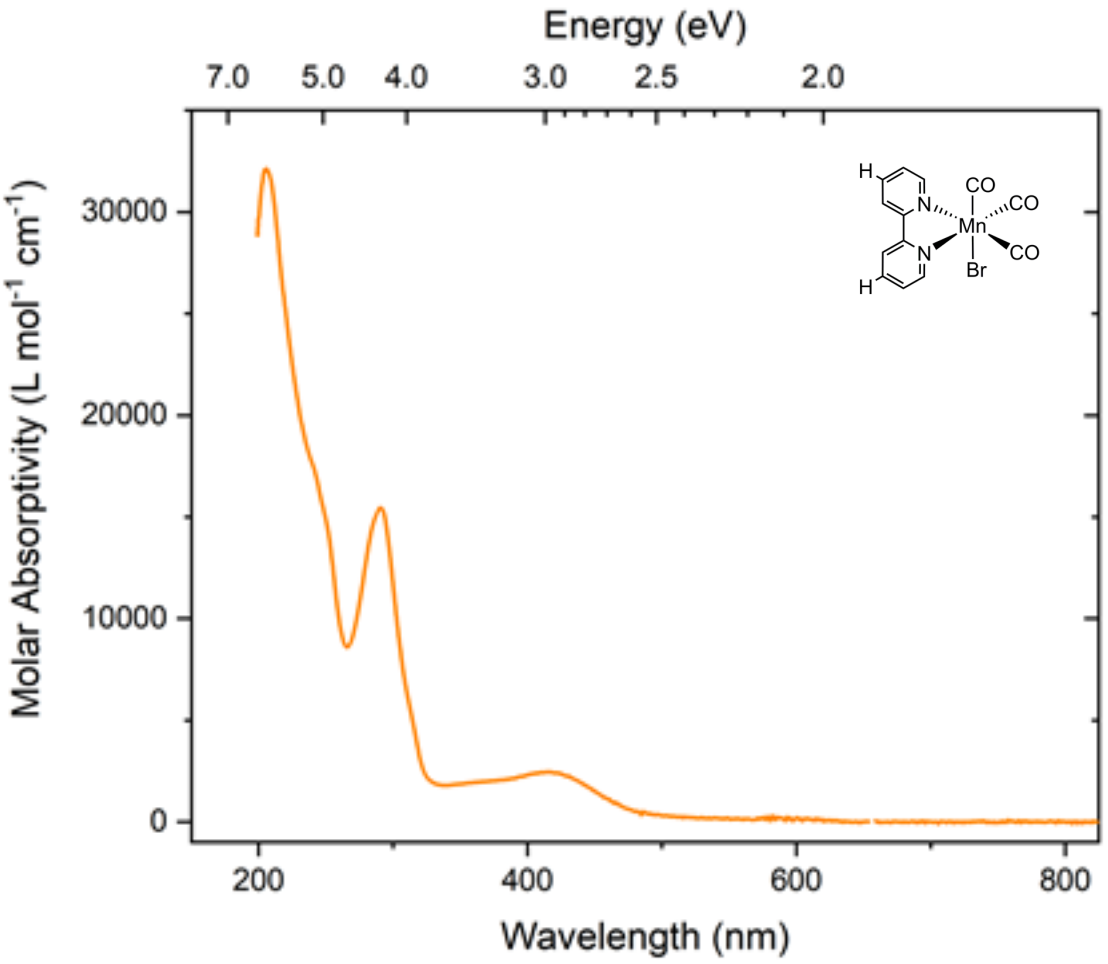

Figure C12: Electronic absorption spectrum of **2** in MeCN. The smaller tic marks are used to illustrate 0.1 eV increments.

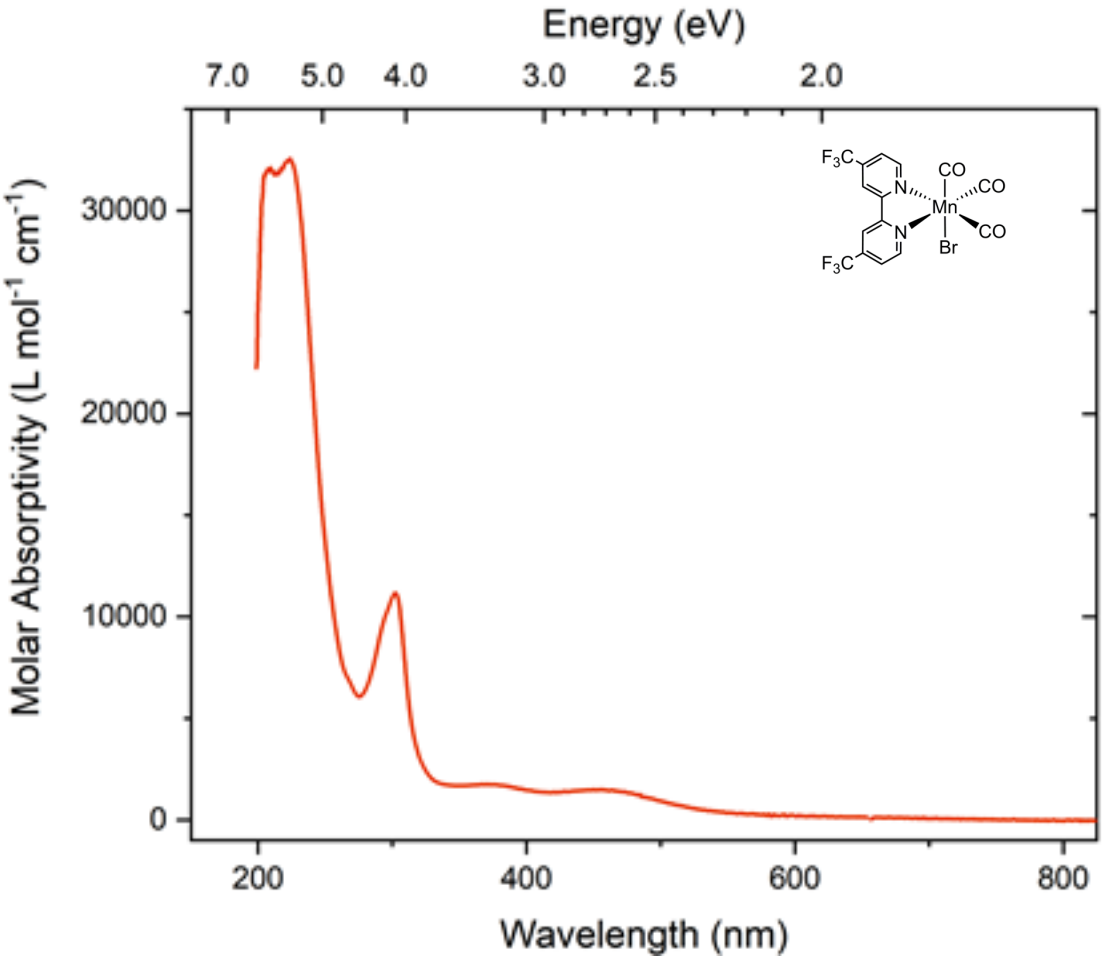

Figure C13: Electronic absorption spectrum of **3** in MeCN. The smaller tic marks are used to illustrate 0.1 eV increments.

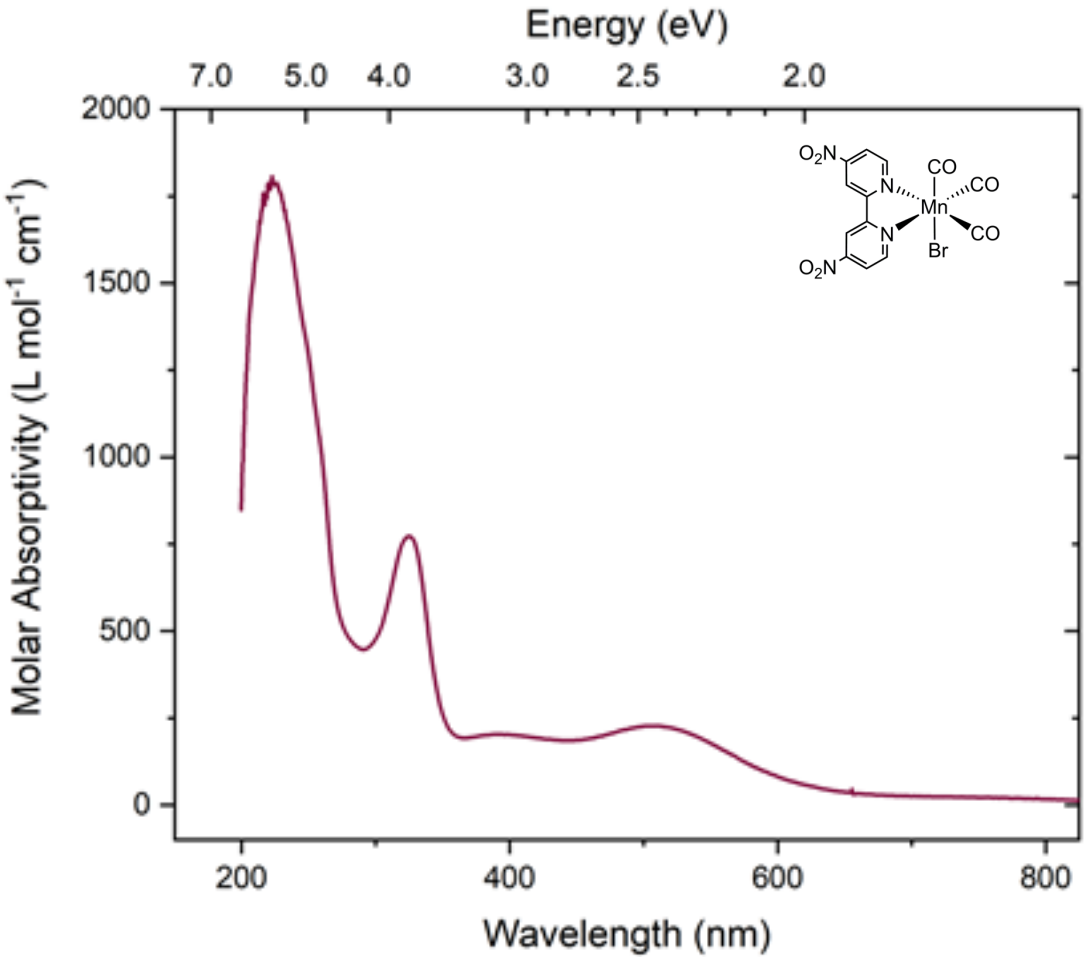

Figure C14: Electronic absorption spectrum of **4** in MeCN. The smaller tic marks are used to illustrate 0.1 eV increments.

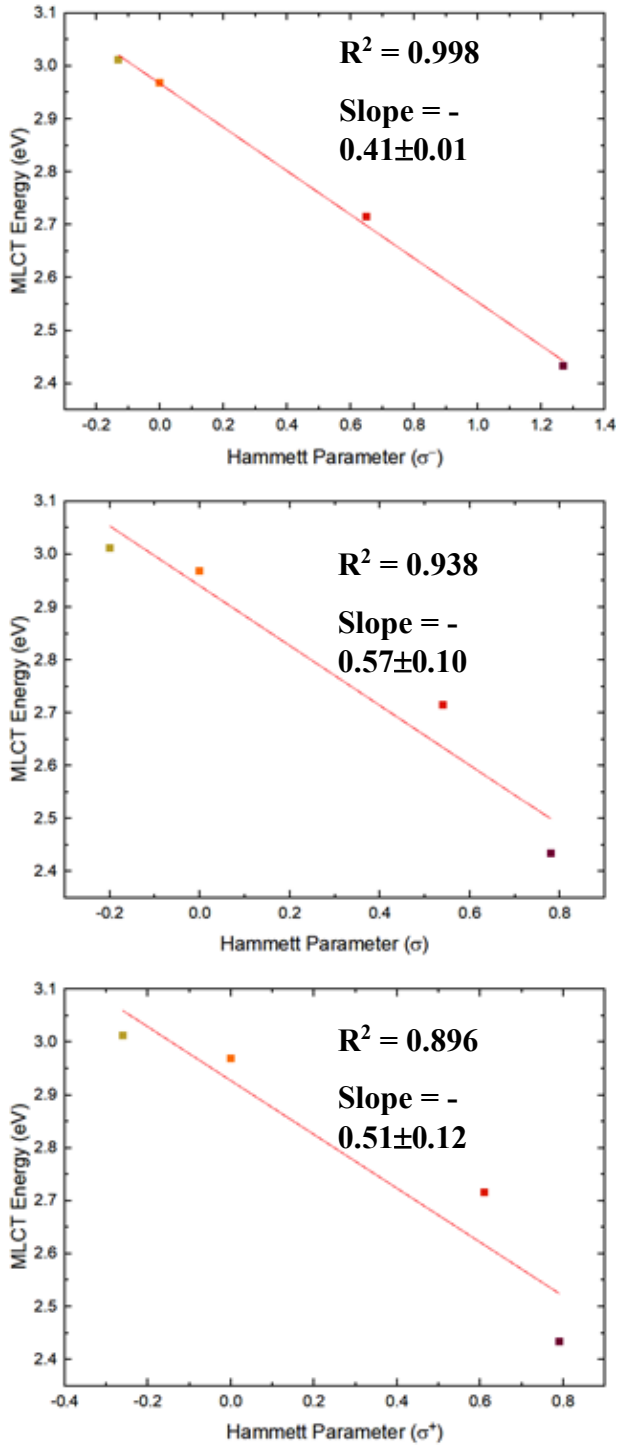

Figure C15: Hammett Analyses showing the correlation between the MLCT energy band as a function of the various Hammett Parameters σ^- (top), σ (middle), and σ^+ (bottom). The best fit is found when the data is plotted as a function of the σ^- Hammett Parameter.

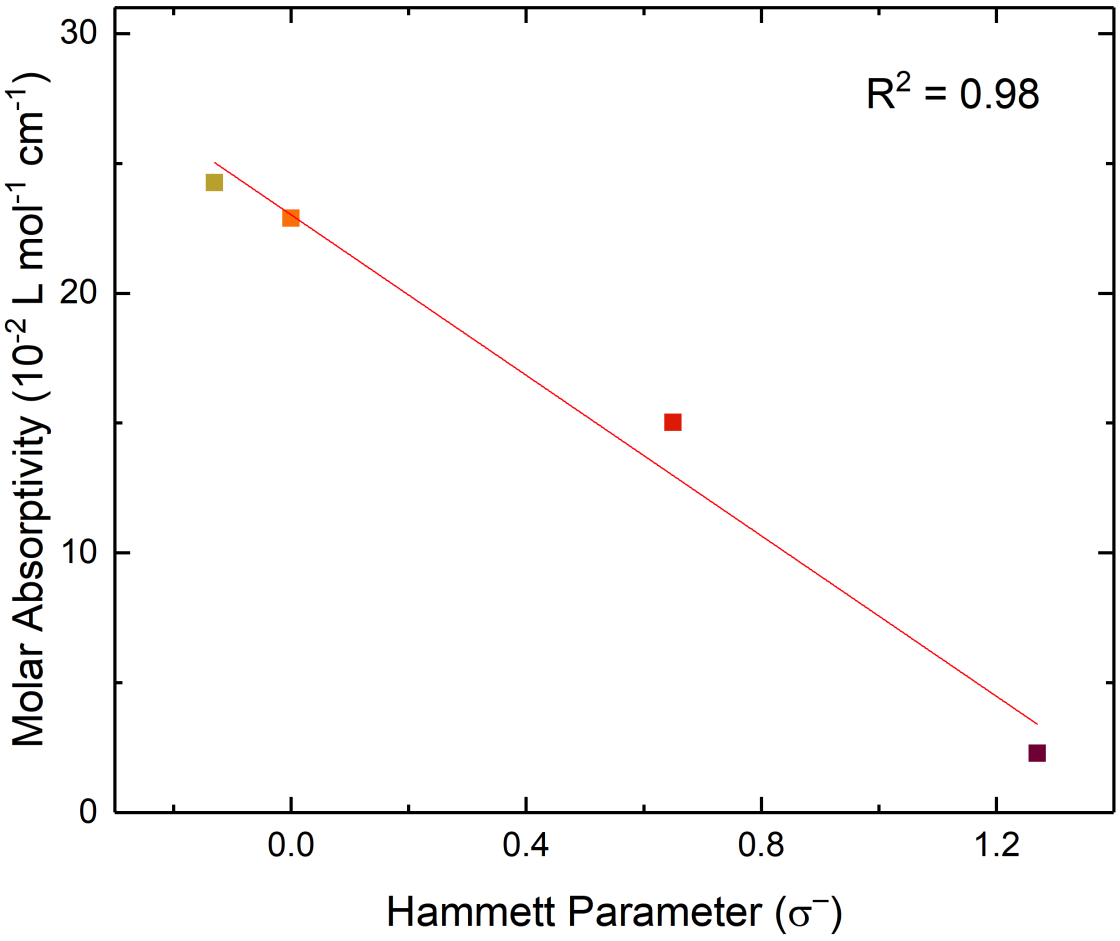

Figure C16: Molar absorptivity as a function of the Hammett Parameter for complexes **1-4**. The low molar absorptivity for **4** may be due to significant d-d character, but the trend established here may indicate that the absorption retains MLCT character.

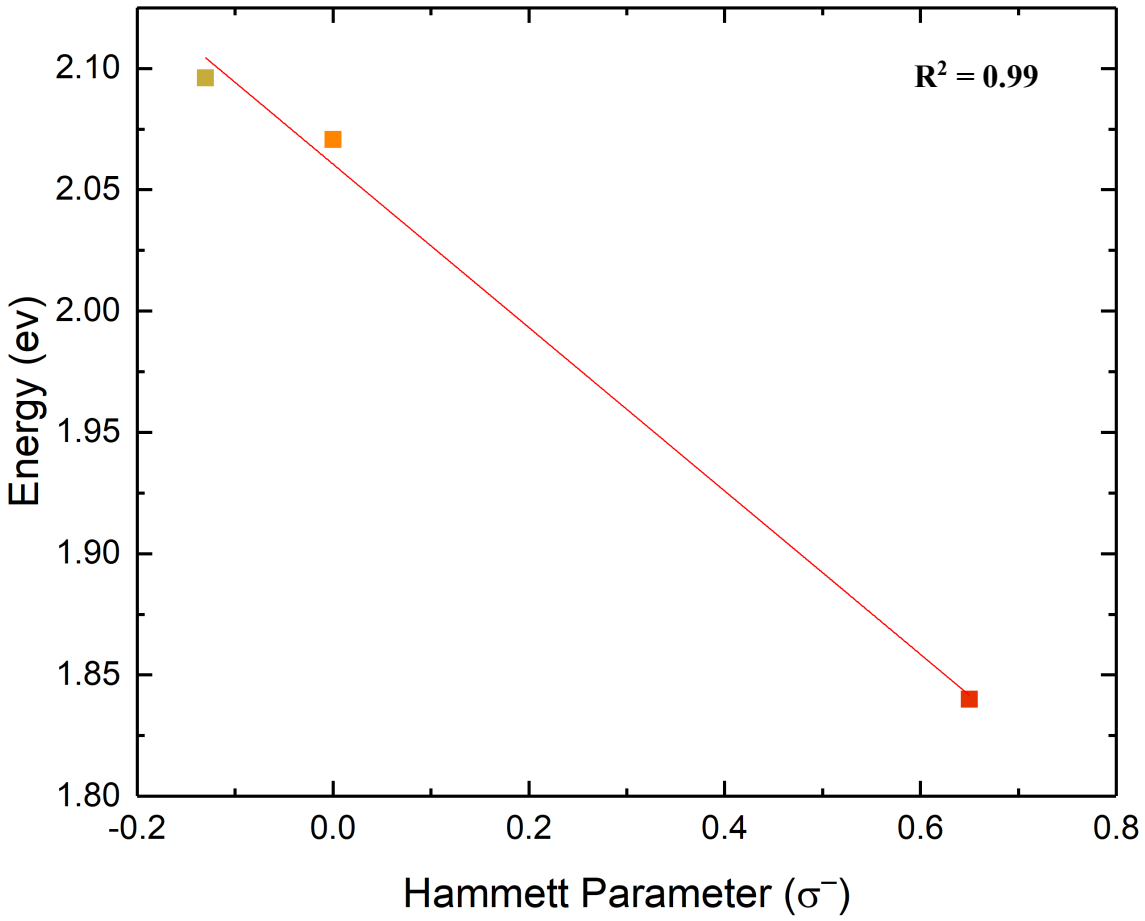

Figure C17: Hammett analysis of the excited state absorption maxima at longer wavelengths for the analogous solvent coordinated species arising from CO loss from **1**, **2**, and **3** correlating the lowest-energy band (an apparently shifted MLCT feature) as a function of Hammett Parameter (σ^{-}).

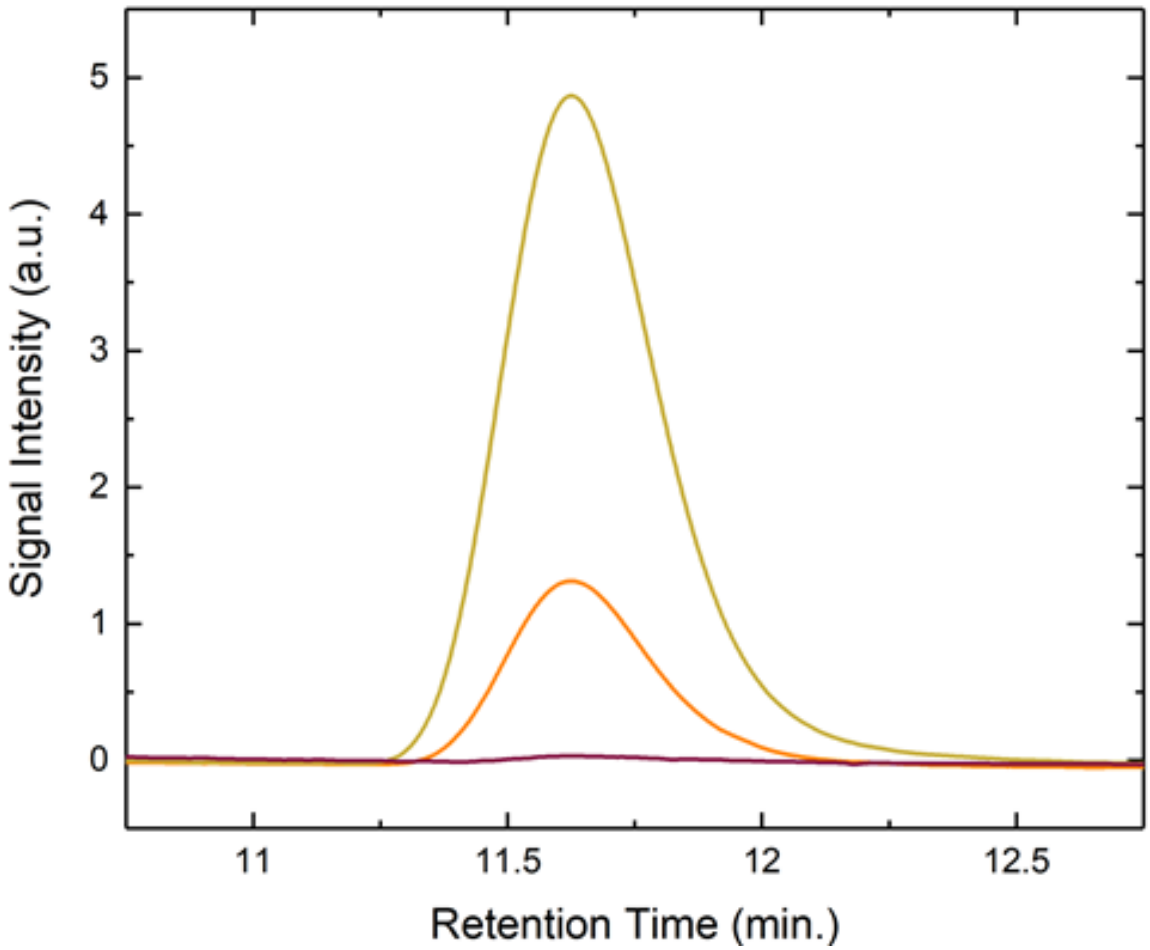

Figure C18: Monitoring of CO release by gas chromatography from photolysis of **1** (yellow; photolyzed at 420 nm), **2** (orange; photolyzed at 420 nm), and **4** (purple; photolyzed at 510 nm), for two hours. Signal intensity is normalized by solution concentration of complex in MeCN.

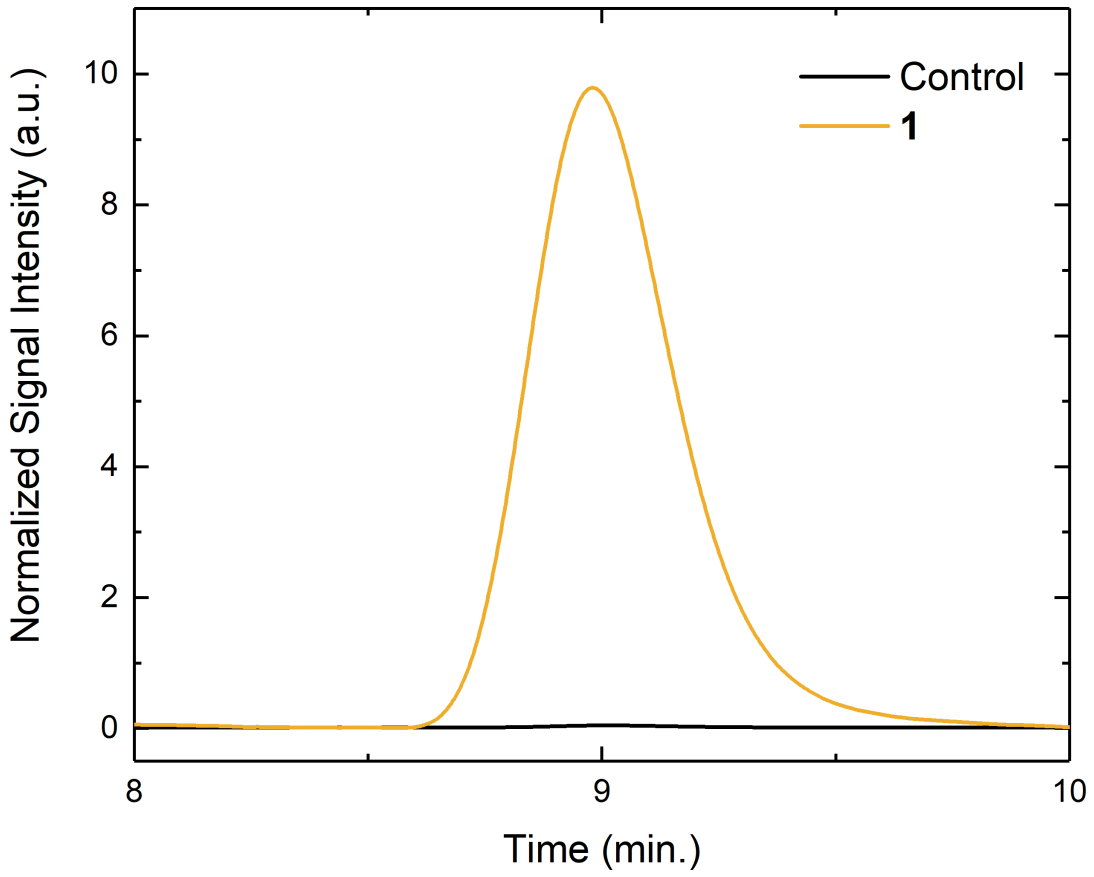

Figure C19: CO release measured by gas chromatography for photolysis of a 5-mL solution of **1** (dark yellow line; photolyzed at 420 nm) for 2 hours and comparison with a related control experiment with a 5-mL sample of **1** stored in the dark over a period of 10 hours. Signal intensity for yield of CO by gas chromatography is normalized by solution concentration of complex **1** in MeCN, headspace volume, and experiment time. Calculation of the apparent rates of CO loss show that the compound releases CO at a substantially faster rate upon irradiation (1.2 mol CO (mol Mn)$^{-1}$ day^{-1}) versus in the dark by slower thermal reactivity (0.003 mol CO (mol Mn)$^{-1}$ day^{-1}). [**1**] in each experiment was 10^{-3} M. Lamp characteristics are as described in the Experimental Section.

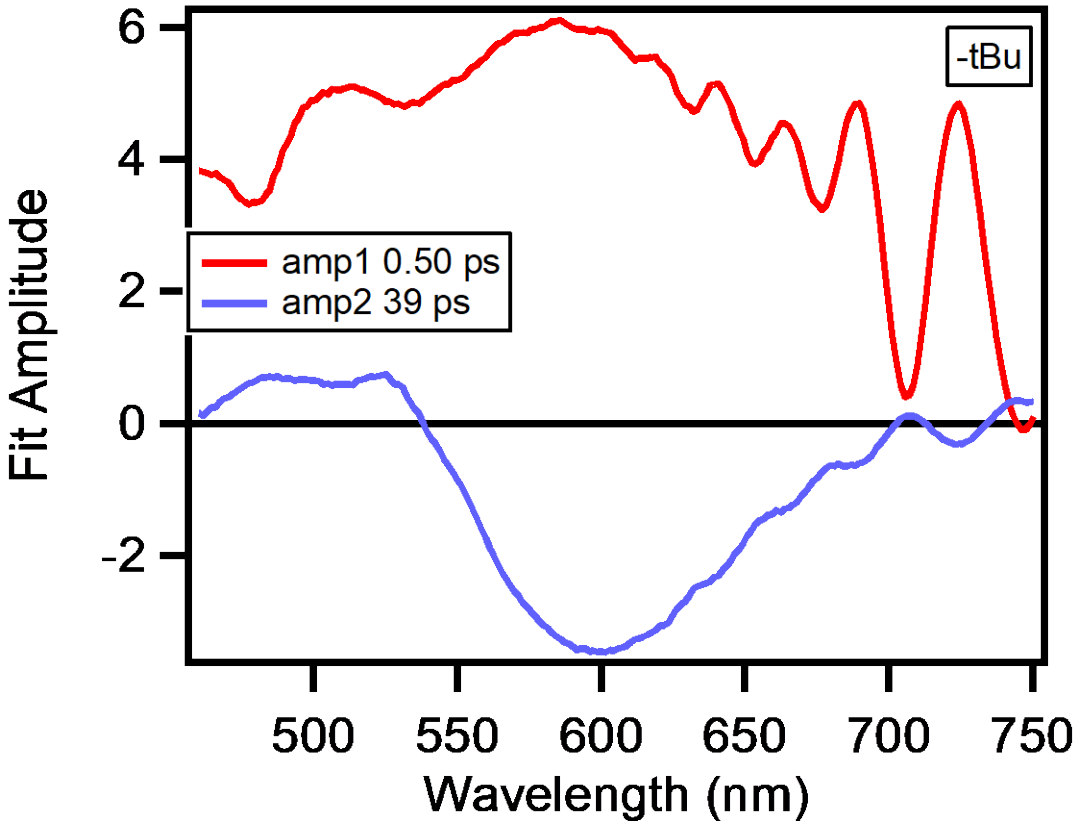

Figure C20: Fit of the decay associated spectrum for **1** to extract kinetic data.

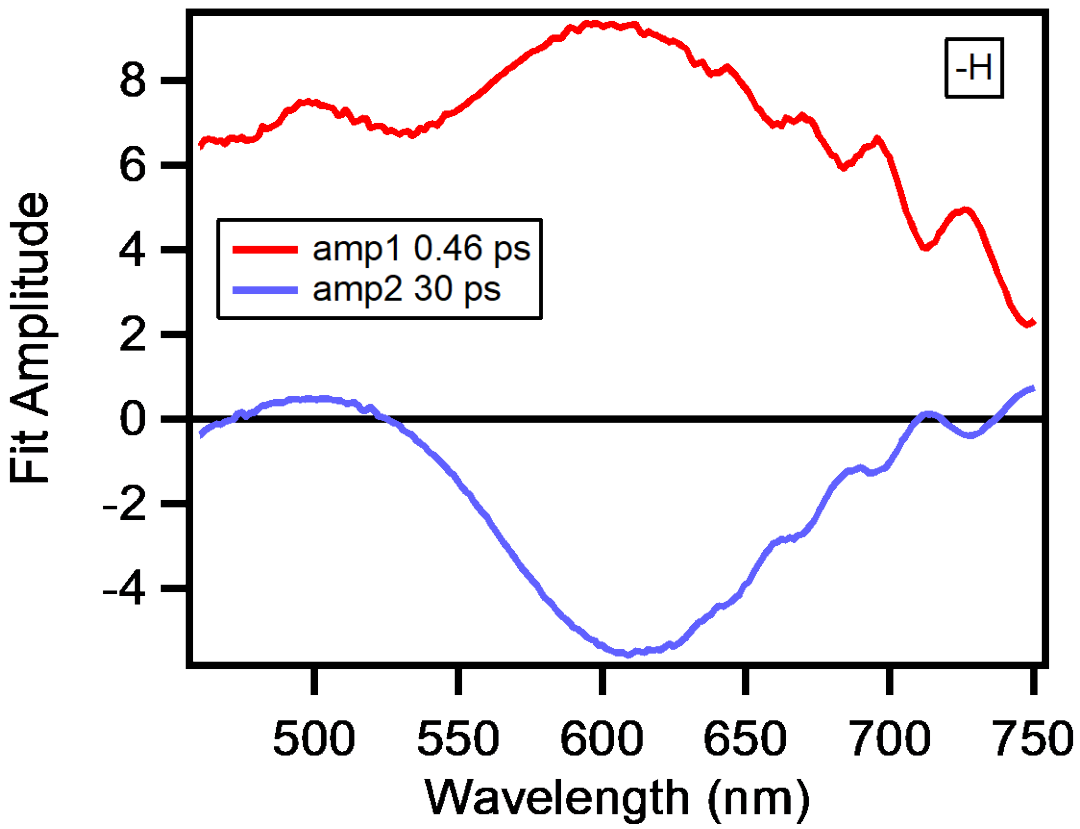

Figure C21: Fit of the decay associated spectrum for **2** to extract kinetic data.

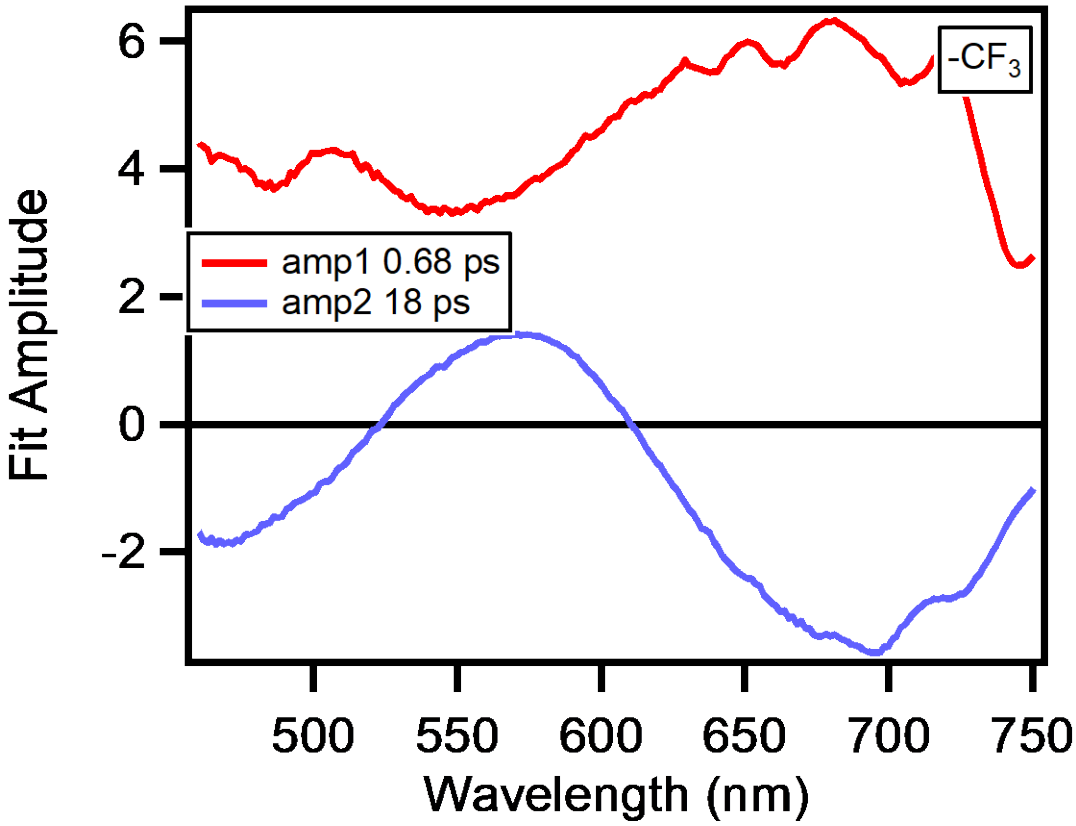

Figure C22: Fit of the decay associated spectrum for **3** to extract kinetic data.

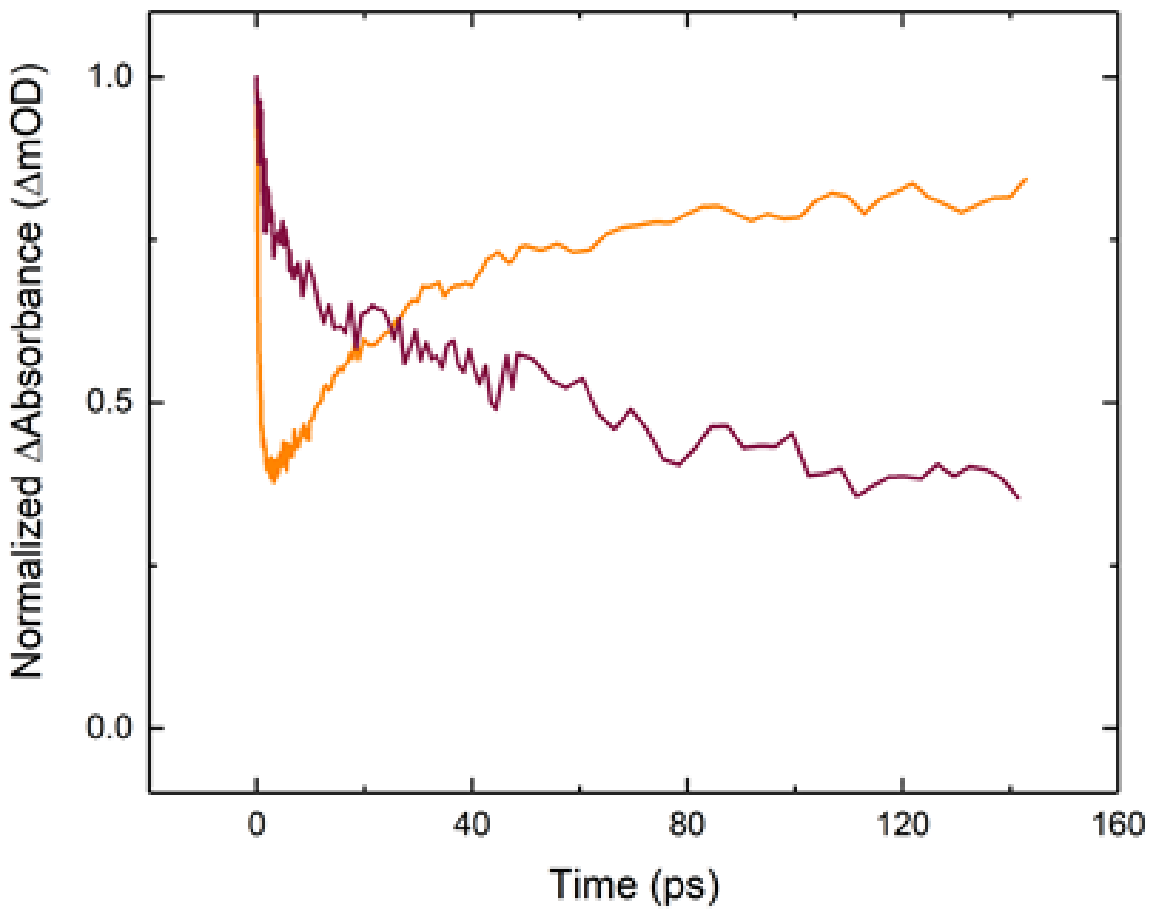

Figure C23: Comparison of the normalized ΔAbsorbance as a function of time for compounds **2** (monitored at 600nm—orange line) and **4** (monitored at 580nm—purple line); Complex **2** undergoes solvent coordination, while complex **4** undergoes vibrational cooling and forms an apparently long lived MLCT state.

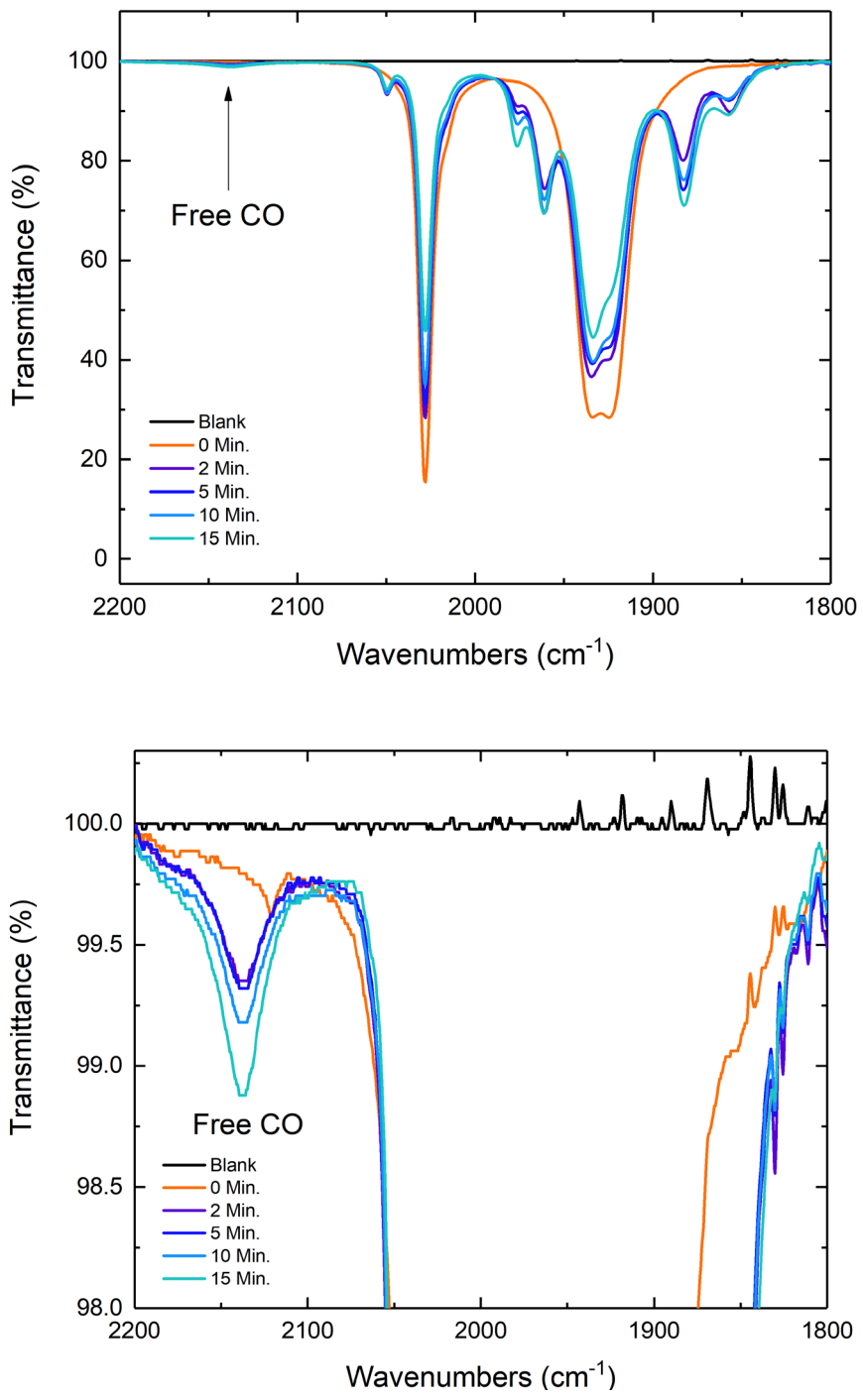

Figure C24: IR spectroscopic monitoring of a solution containing complex **2** irradiated over time with 415 nm light at 175 W. The irradiation results in follow-up chemical activity that is exhibited by the presence of new CO stretches in the IR spectrum after 2 min. of irradiation. The presence of free carbon monoxide is present after 2 min.

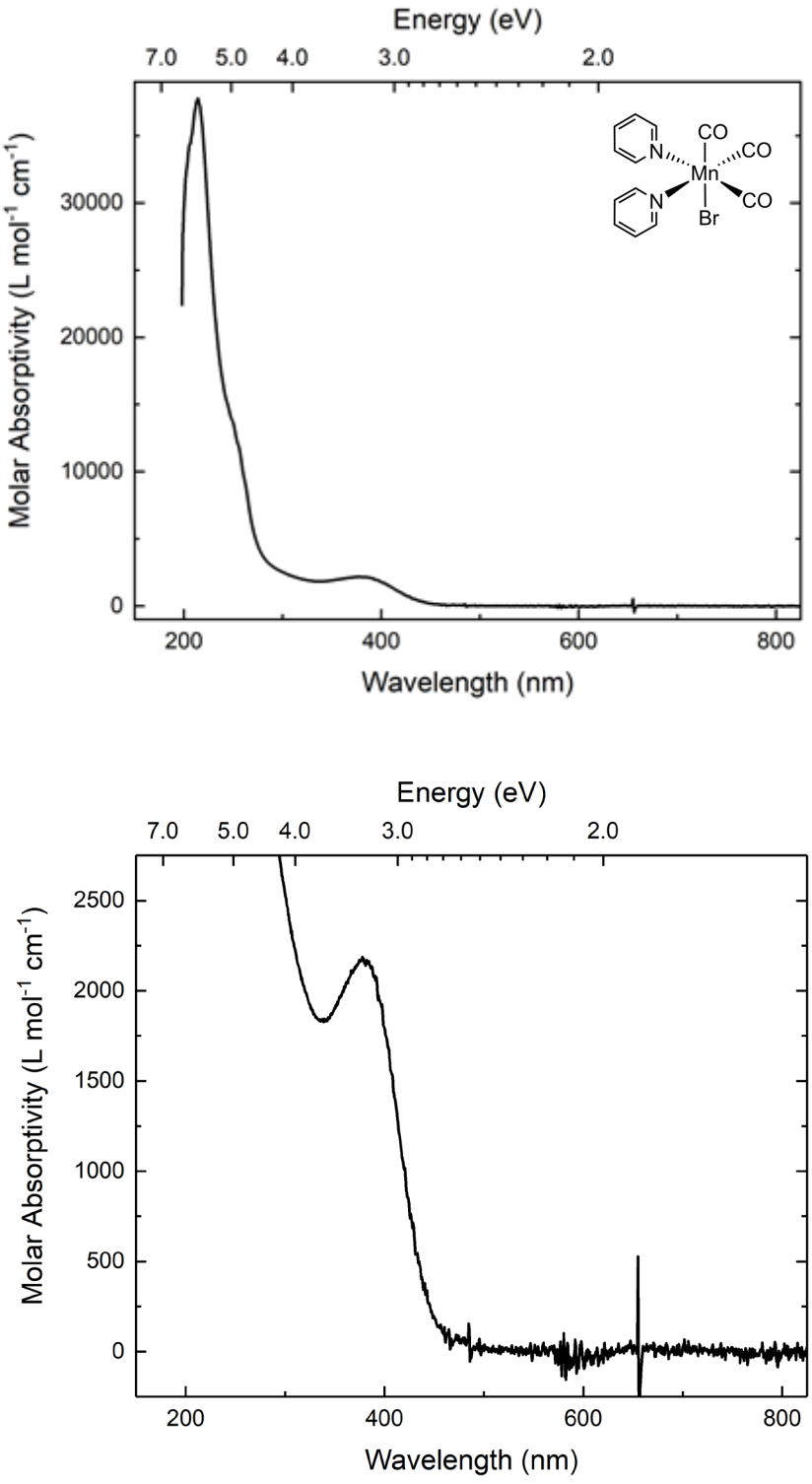

Figure C25: Electronic absorption spectrum of **5** in MeCN. The smaller tic marks are used to illustrate 0.1 eV increments.

Crystallographic Information

Refinement Details

Crystals were mounted on a nylon loop using Paratone oil under a nitrogen stream. Low temperature (200-296 K) X-ray data were obtained with a Bruker MicroStar microfocus rotating anode generator running at 50-60 mA and 45 kV (Cu Kα = 1.54178 Å; Apex II detector positioned at 50.0 mm and equipped with Helios multilayer mirror optics (Complexes **3** and **4**), or with a Bruker generator using a fine focus Mo sealed tube running at 30mA and 50kV (Mo Kα = 0.71073 Å; SMART APEX detector positioned at 50.0 mm and equipped with a MonoCap collimator and graphite monochromator (complex **5**). All diffractometer manipulations, including data collection, integration and scaling were carried out using the Bruker APEXII software.[1] Absorption corrections were applied using SADABS.[2] The space group was determined on the basis of systematic absences and intensity statistics and the structures were solved by intrinsic phasing using XT.[3] All non-hydrogen atoms were refined using anisotropic displacement parameters. Hydrogen atoms were placed in idealized positions and refined using a riding model. The structures was refined (weighted least squares refinement on F^2) to convergence using the Olex software package equipped with XL.[4]

Table C1: Crystal and Refinement Data

Compound	**3**	**4**	**5**
CCDC accession code	1922041	1922042	1922040
empirical formula	$C_{15}H_6BrF_6MnN_2O_3$	$C_{13}H_6N_4O_7MnBr$	$C_{13}H_{10}BrMnN_2O_3$
formula wt	510.07	465.07	377.08
T (K)	200	200	200
a, Å	19.666(2)	15.4742(7)	7.4387(17)
b, Å	10.4825(12)	9.8701(4)	14.408(3)
c, Å	17.0392(18)	21.8544(8)	13.148(3)
α, deg	90	90	90
β, deg	96.515(4)	107.363(3)	90.352(3)
γ, deg	90	90	90
V, $Å^3$	3489.9(7)	3185.8(2)	1409.1(6)
Z	8	8	4
cryst. syst	monoclinic	monoclinic	monoclinic
space group	C2/c	$P2_1/c$	Cc
ρ_{calcd}, g/cm^3	1.942	1.939	1.777
2θ range, deg	9.052 to 139.886	5.984 to 140.072	2.827 to 26.914
μ, mm^{-1}	9.594	10.143	3.779
abs corr	Multi-scan	Multi-scan	Multi-scan
GOOF[c]	1.042	1.052	1.014
R1,[a] wR2[b] (I > 2σ(I))	0.0654, 0.1734	0.0583, 0.1507	0.0277, 0.0602

[a] $R1 = \Sigma||F_o|-|F_c|| / \Sigma|F_o|$ [b] $wR2 = [\ \Sigma\ [w(F_o^2-F_c^2)^2] / \Sigma\ [w(F_o^2)^2]\ ]^{1/2}$ [c] $GOOF = S = [\ \Sigma\ [w(F_o^2-F_c^2)^2] / (n-p)\ ]^{1/2}$

Special Refinement Details for 5.

Diffraction data [6683 reflections using 1°-wide ω-scan frames with a scan time of 5 seconds] were collected[5] for a pseudomerohedrally-twinned crystal of **5** using graphite-monochromated MoKα radiation (λ= 0.71073 Å) on a Bruker SMART APEX CCD Single Crystal Diffraction System at 200 K. X-rays were provided by a fine-focus sealed X-ray tube operated at 50kV and 35mA. Lattice constants were determined with the Bruker SAINT software package using peak centers for 3524 reflections. The integrated data[6] were corrected empirically for variable absorption effects using equivalent reflections. The Bruker software package SHELXTL was used to solve the structure using "direct methods" techniques. All stages of weighted full-matrix least-squares refinement were conducted using F_o^2 data with the SHELXTL XL v2014 software package.[7] The final structural model incorporated anisotropic thermal parameters for all nonhydrogen atoms and isotropic thermal parameter for all hydrogen atoms. The pyridine hydrogen atoms were included in the structural model as idealized riding model atoms (assuming sp^2-hybridization of the carbon atoms and C-H bond lengths of 0.95 Å) and their isotropic thermal parameters were fixed at values 1.2 times the equivalent isotropic thermal parameter of the carbon atom to which they are covalently bonded. Final crystallographic details are summarized in Table C1.

Several aspects of the structure complicated its successful refinement. The similar size of a Br atom and a carbonyl ligand bonded to a Mn atom produced 83/17 "whole molecule" packing disorder of **5**. The major orientation is occupied 83% of the time and the minor is occupied 17% of the time. The structure is also pseudo-centrosymmetric: the fractional coordinates for the Mn atom coincide with those of a crystallographic C_2-axis in the centrosymmetric counterpart (C2/c)

of the noncentrosymmetric space group (Cc) utilized by **5**. Additionally, the coordinated pyridine ligands and two of the carbonyls are also related by this pseudo-C_2 axis. Finally, a monoclinic β angle of 90.35° promotes 93/7 pseudo-merohedral (orthorhombic) twinning with the major (93%) domain also being 85/15 racemically twinned.

It is therefore not surprising that restraints had to be imposed in order to obtain a reasonable refinement. Bond lengths and angles for the minor (17%) orientation of **5** were restrained to be similar to those of the major (83%) orientation. The anisotropic thermal parameters for the nonhydrogen atoms (except O1′) of the minor orientation of **5** were set to the same values as the corresponding atoms of the major orientation. O1′ was assigned its own anisotropic thermal parameter that was allowed to vary. Other mild restraints were needed for the minor orientation of **5** to ensure linear carbonyl coordination and planar pyridine ligands.

Solid-State Structure of 5

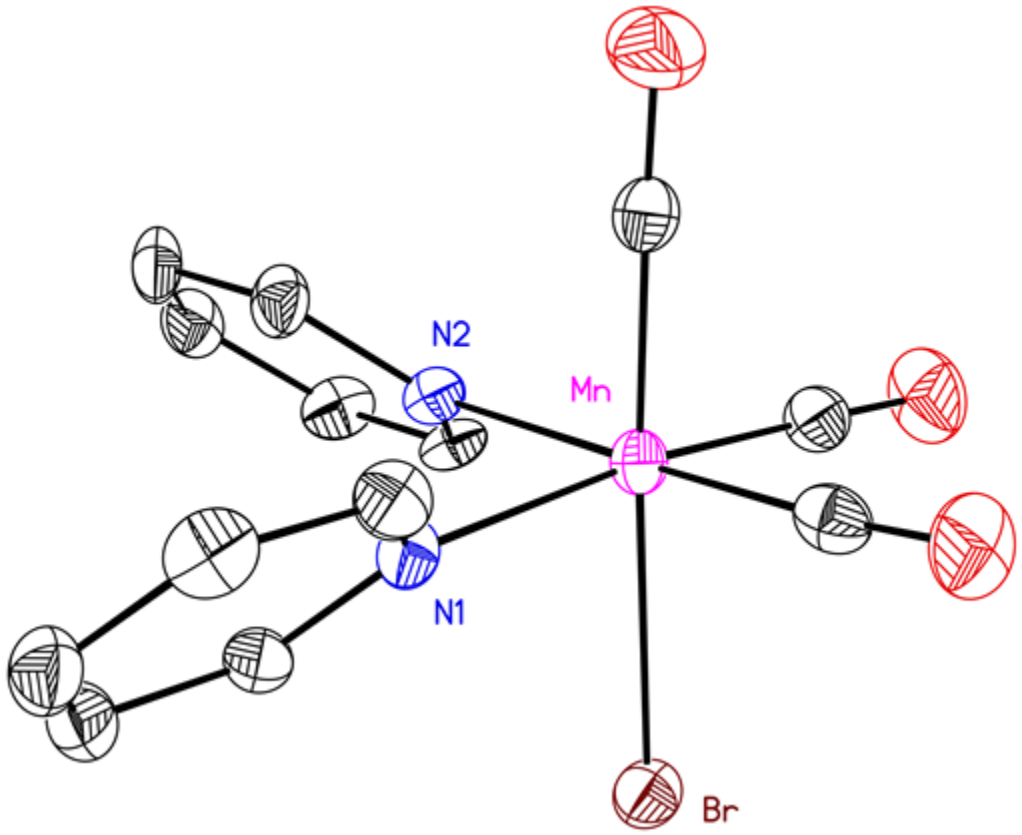

Figure C26: Solid-state structure of **5**. Hydrogen atoms and second molecule of **5** are omitted for clarity. Displacement ellipsoids shown at the 50% probability level.

Full Solid-State Structure of 5

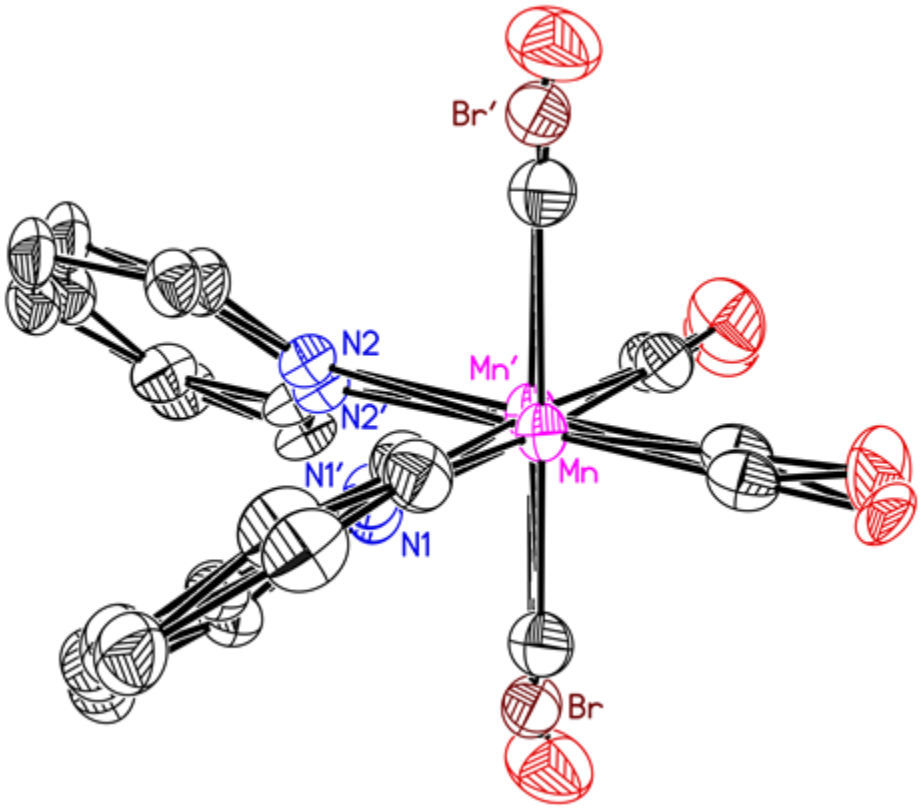

Figure C27: Full solid-state structure of **5**. Hydrogen atoms omitted for clarity. Displacement ellipsoids shown at the 50% probability level.

Full Solid-State Structure of 3

Special Refinement Details for 3.

No special refinement was required.

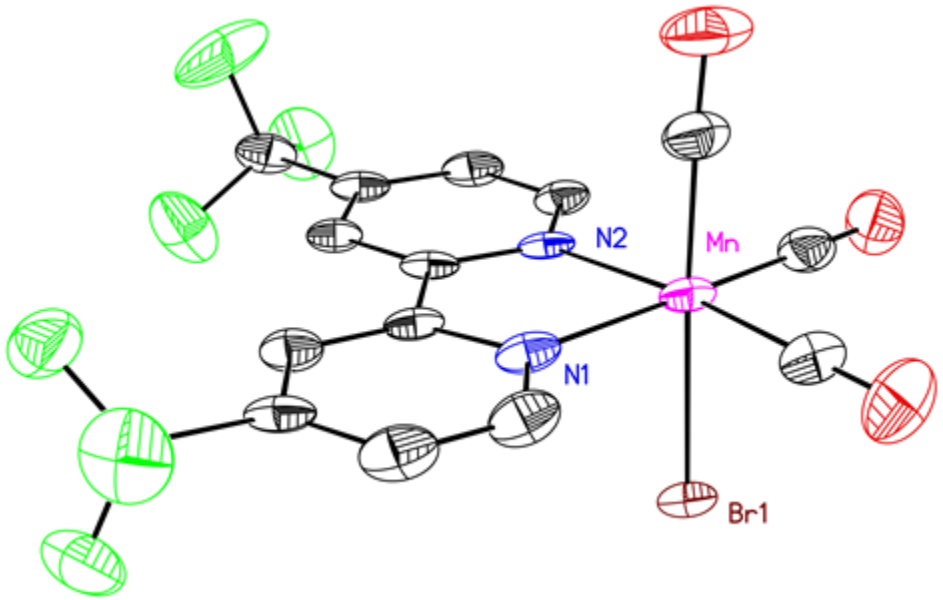

Figure C28: Full solid-state structure of **3**. Hydrogen atoms are omitted for clarity. Displacement ellipsoids shown at the 50% probability level.

Solid-State Structure of 4

Special Refinement Details for 4.

No special refinement was required.

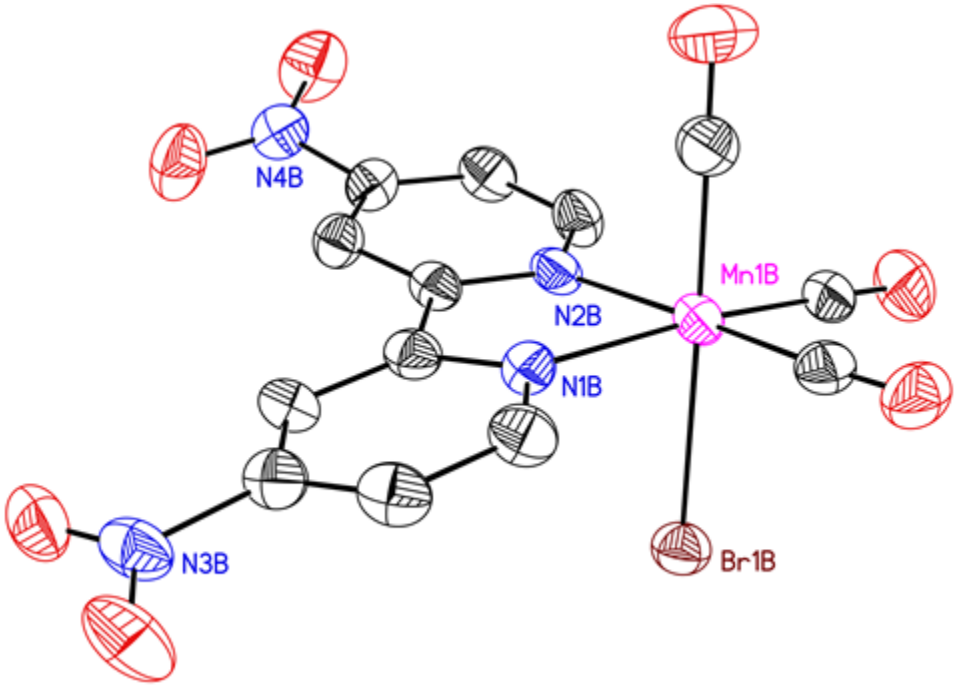

Figure C29: Solid-state structure of **4**. Hydrogen atoms and second molecule of **4** are omitted for clarity. Displacement ellipsoids shown at the 50% probability level.

Full Solid-State Structure of 4

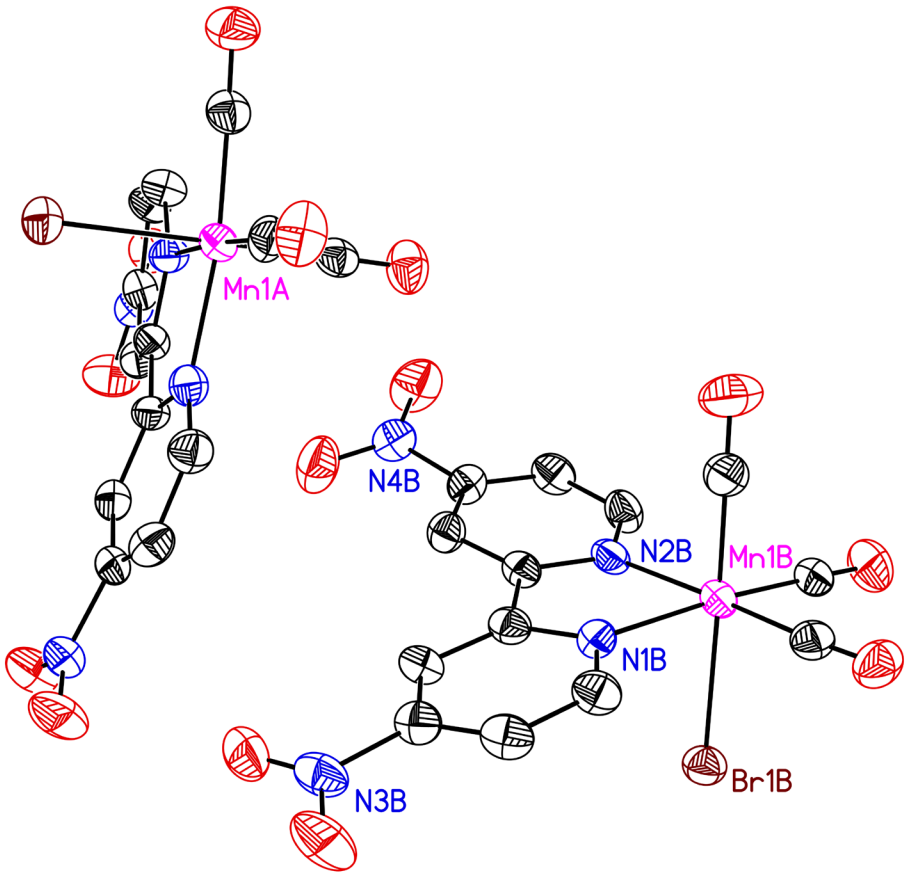

Figure C30: Full solid-state structure of **4**. Hydrogen atoms omitted for clarity. Displacement ellipsoids shown at the 50% probability level.

References

(1) *APEX2, Version 2 User Manual, M86-E01078,*; Bruker Analytical X-ray Systems: Madison, WI, June 2006.

(2) Sheldrick, G. M., SADABS (version 2008/1): Program for Absorption Correction for Data from Area Detector Frames, University of Göttingen, 2008.

(3) Sheldrick, G. Crystal structure refinement with SHELXL. *Acta Crystallogr., Sect. A: Found. Crystallogr.* **2015**, *71*, 3-8.

(4) Dolomanov, O. V.; Bourhis, L. J.; Gildea, R. J.; Howard, J. A. K.; Puschmann, H., *OLEX2*: A Complete Structure Solution, Refinement and Analysis Program, *J. Appl. Crystallogr.* **2009**, *42*, 339-341.

(5) Data Collection: SMART Software in APEX2 v2014.11-0 Suite. Bruker-AXS, 5465 E. Cheryl Parkway, Madison, WI 53711-5373 USA.

(6) Data Reduction: SAINT Software in APEX2 v2014.11-0 Suite. Bruker-AXS, 5465 E. Cheryl Parkway, Madison, WI 53711-5373 USA.

(7) Refinement: SHELXTL Software in APEX2 v2014.11-0 Suite. Bruker-AXS, 5465 E. Cheryl

Appendix D

Supplementary Information for Chapter 6

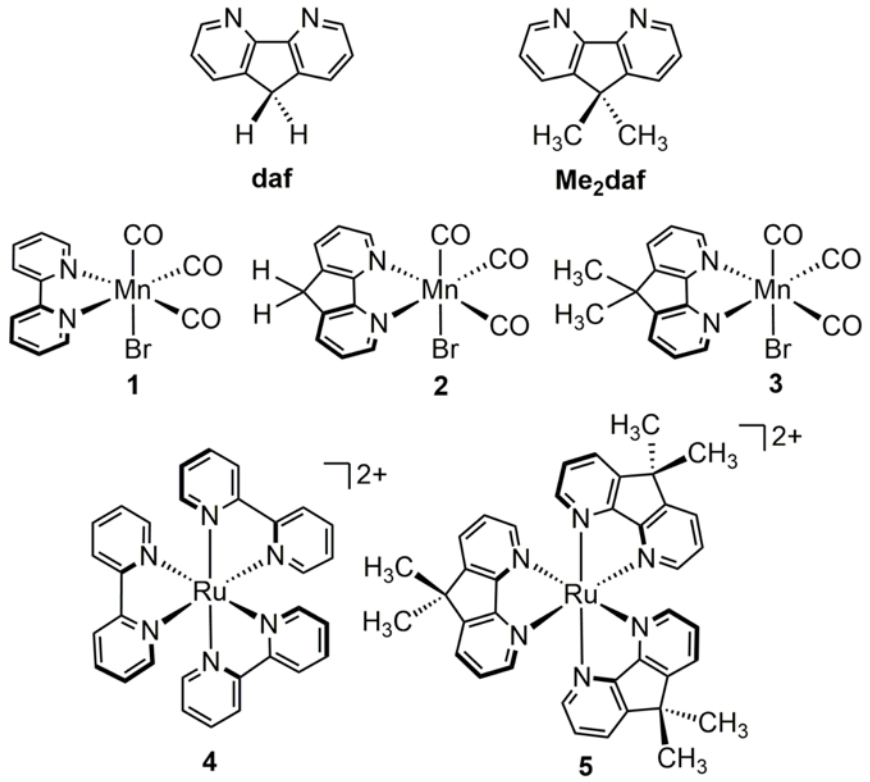

Chart D1: Ligands and complexes described in this study.

NMR Spectra

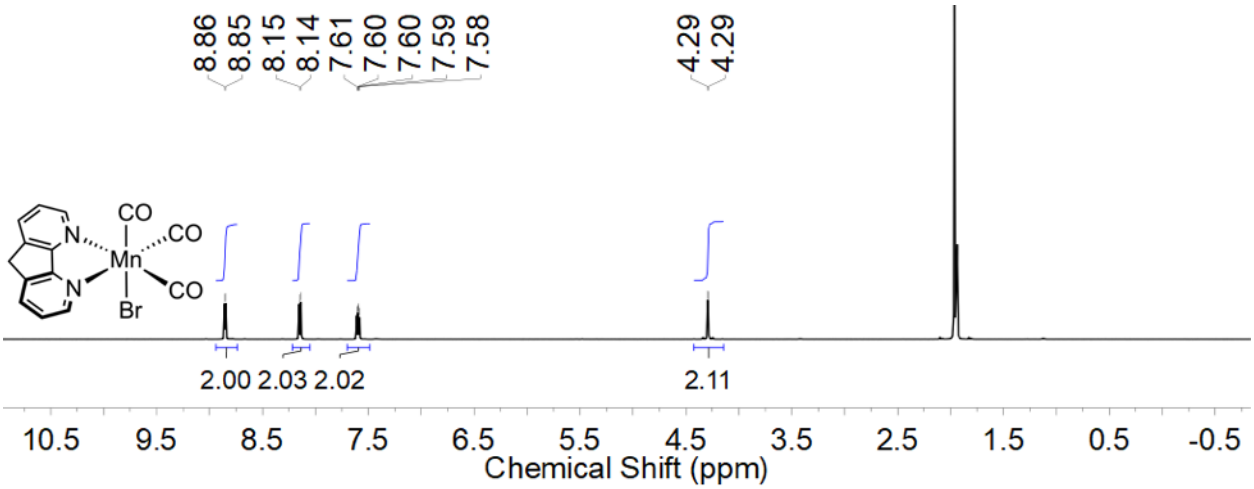

Figure D1: ^{1}H-NMR spectrum (500 MHz, CD_3CN) of **2**.

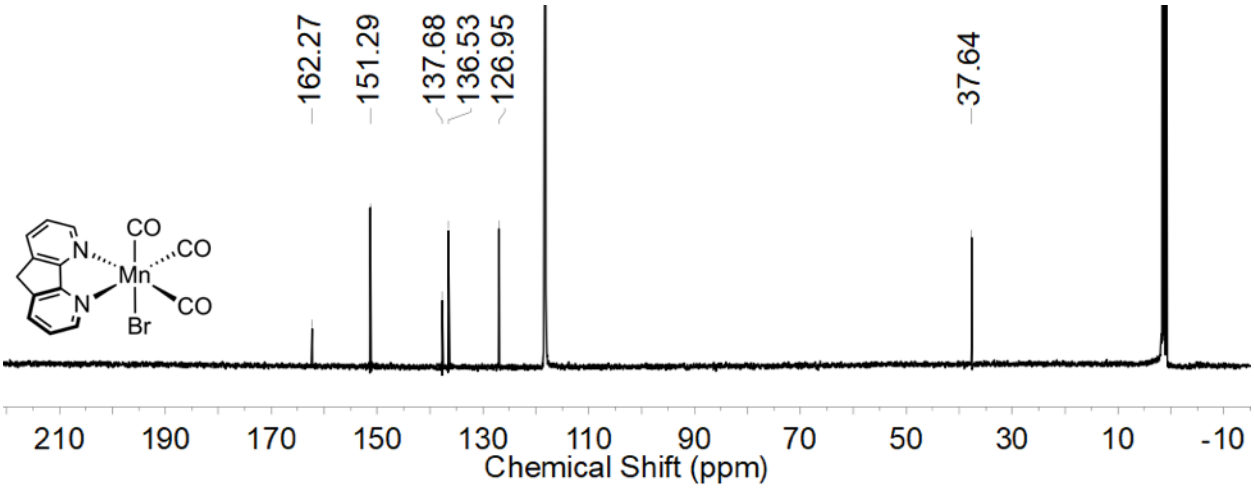

Figure D2: ^{13}C{^{1}H}-NMR spectrum (126 MHz, CD_3CN) of **2**.

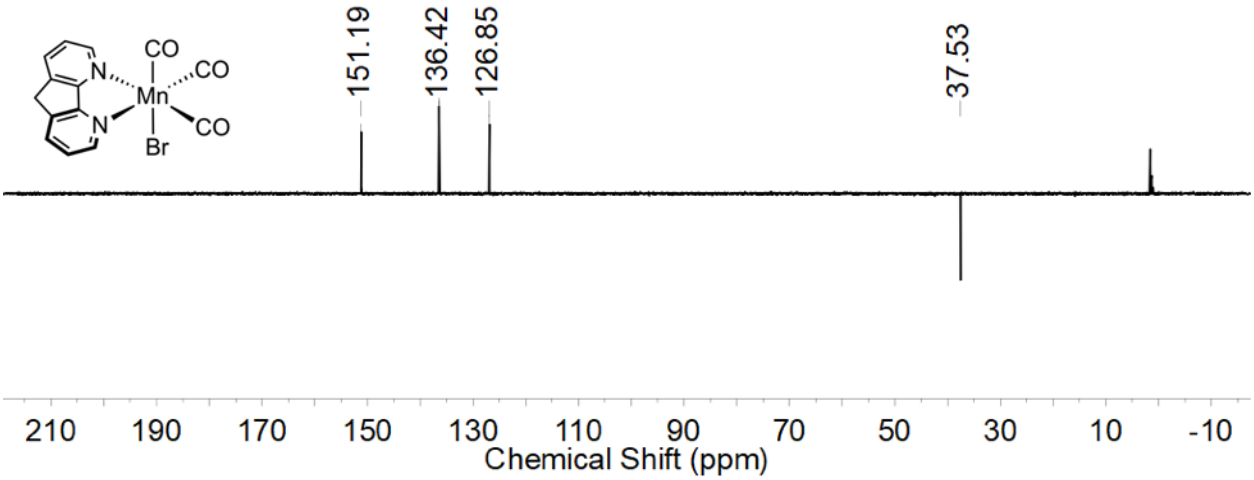

Figure D3: ^{13}C{^{1}H} DEPT-NMR spectrum (126 MHz, CD_3CN) of **2**.

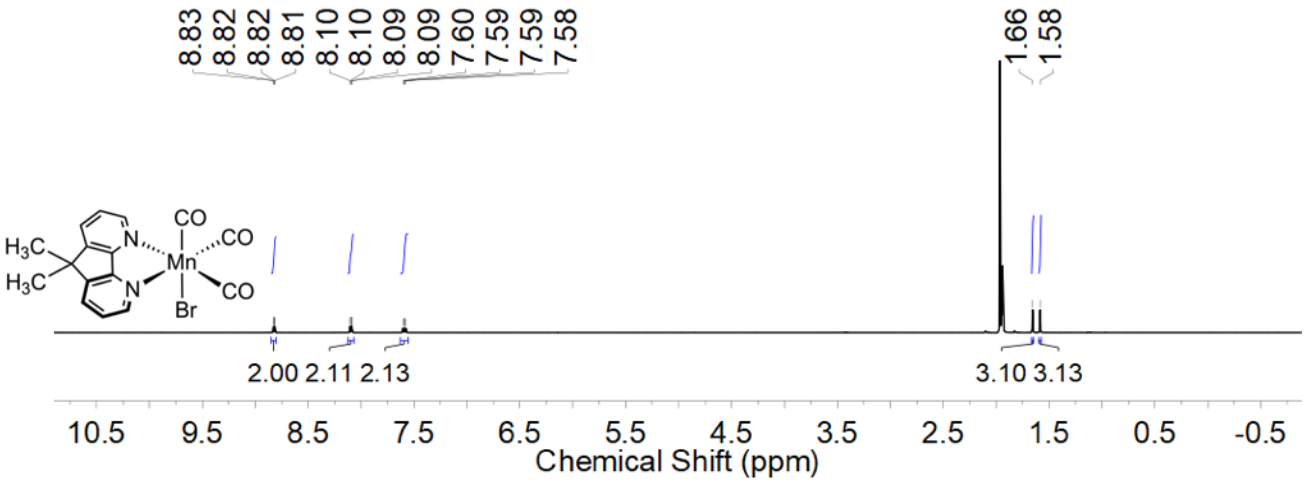

Figure D4: ^{1}H-NMR spectrum (400 MHz, CD_3CN) of **3**.

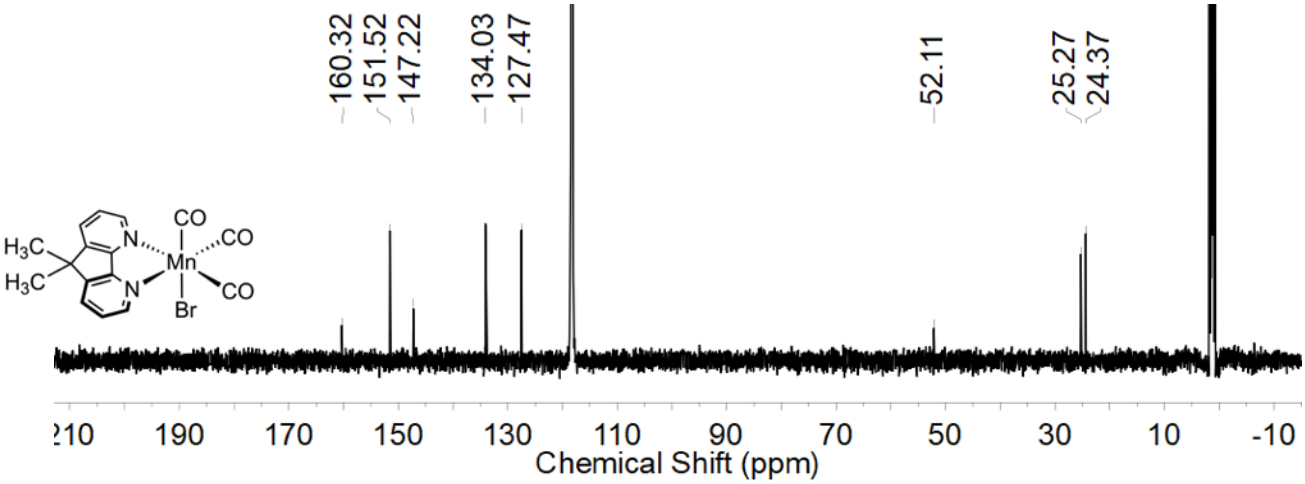

Figure D5: ^{13}C{^{1}H}-NMR spectrum (126 MHz, CD_3CN) of **3**.

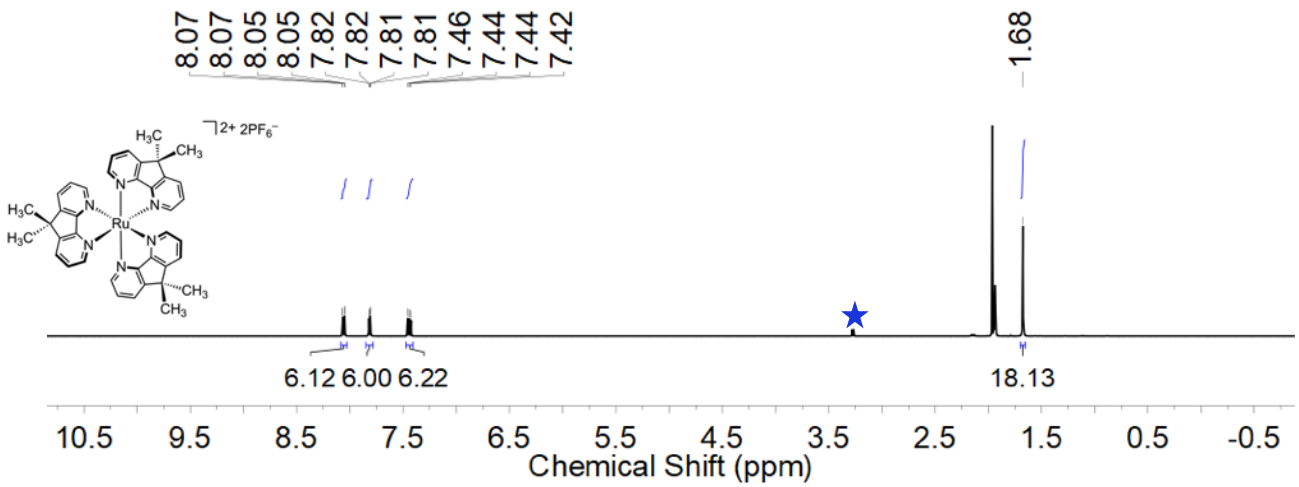

Figure D6: ^{1}H-NMR spectrum (500 MHz, CD_3CN) of **5**; The blue star (★) corresponds to adventitious methanol.

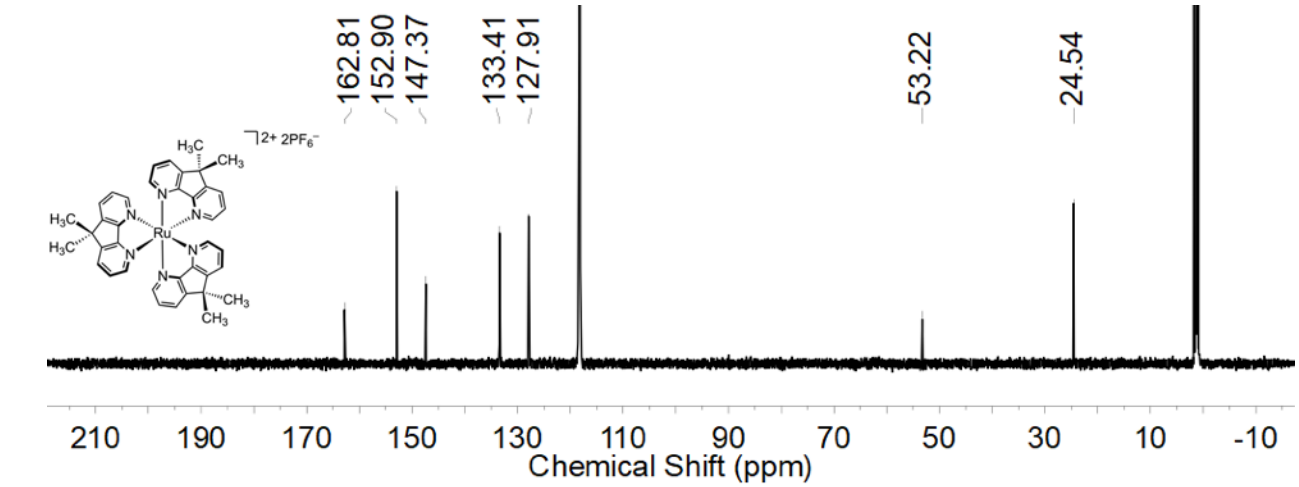

Figure D7: ^{13}C{^{1}H}-NMR spectrum (126 MHz, CD_3CN) of **5**.

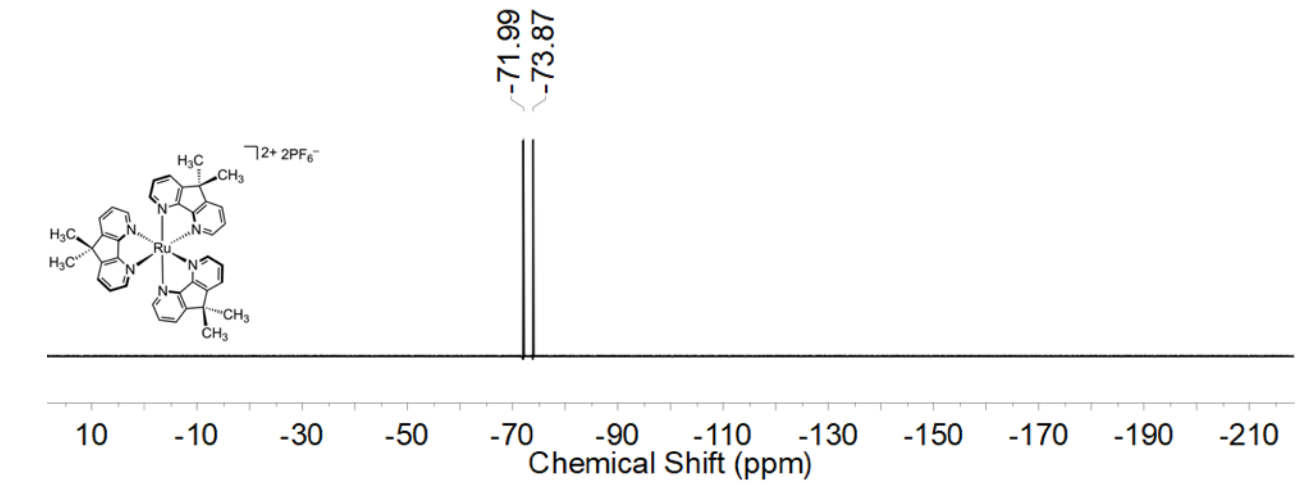

Figure D8: ^{19}F-NMR spectrum (376 MHz, CD_3CN) of **5**.

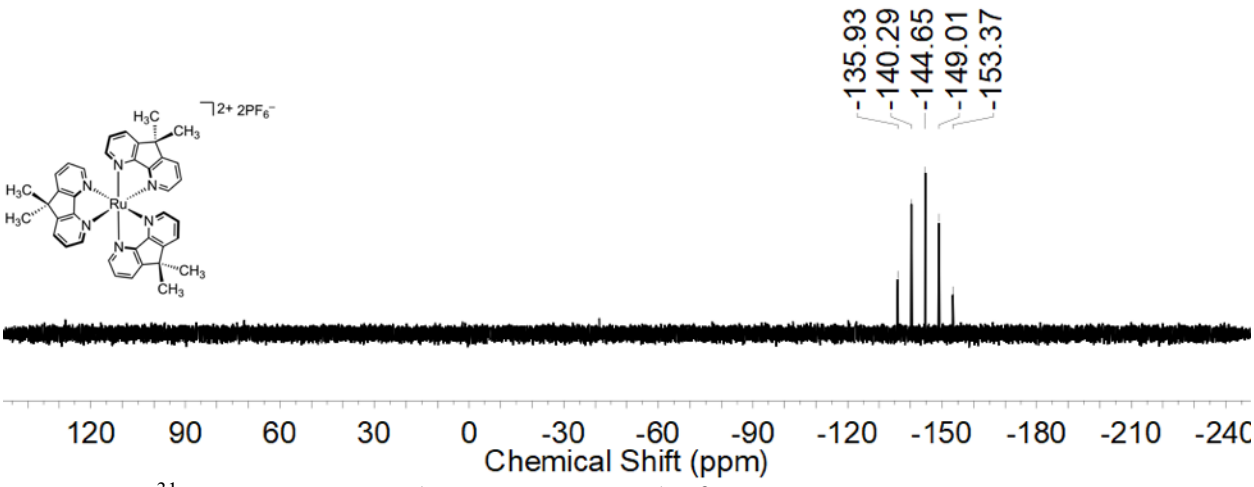

Figure D9: ^{31}P-NMR spectrum (162 MHz, CD_3CN) of **5**.

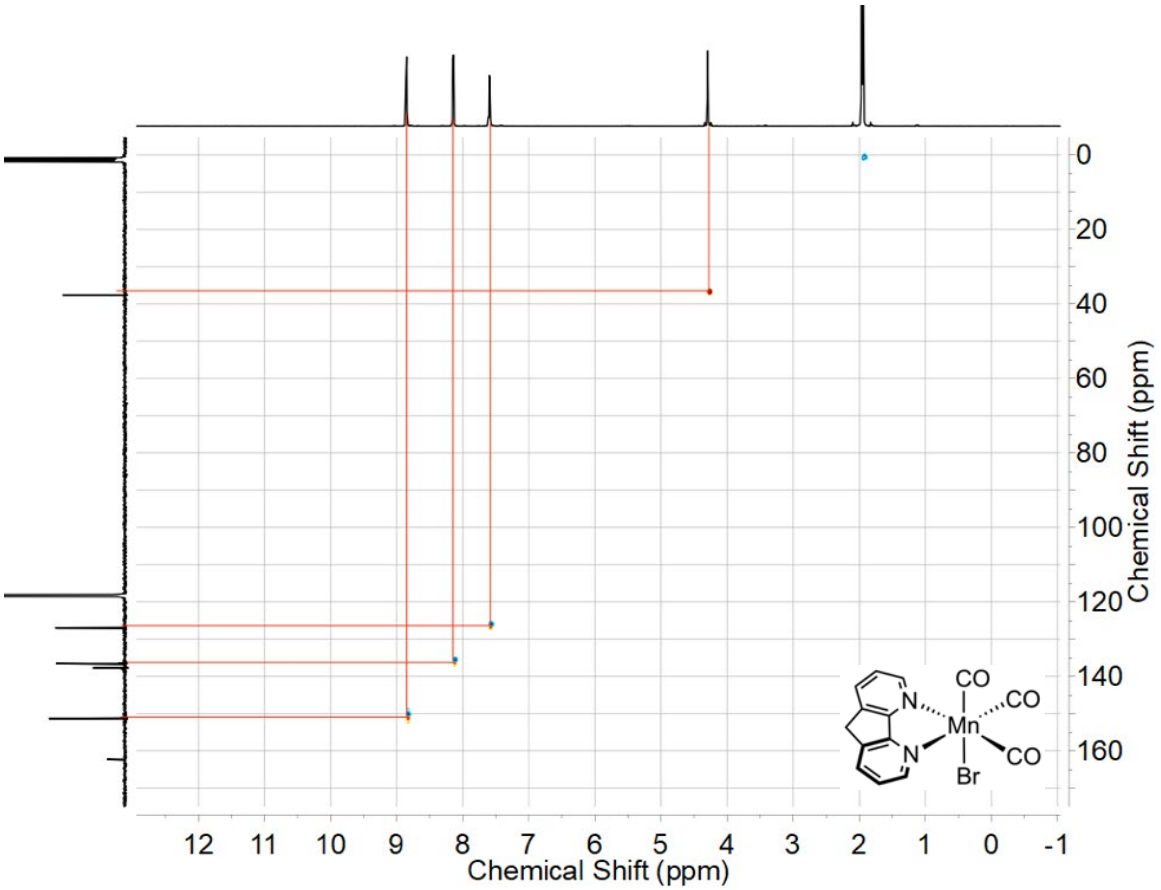

Figure D10: ^{1}H-^{13}C HSQC of complex **2** in CD_3CN depicting the methylene protons indicated by the opposite phasing (red) compared to the methyl and methine protons (blue).

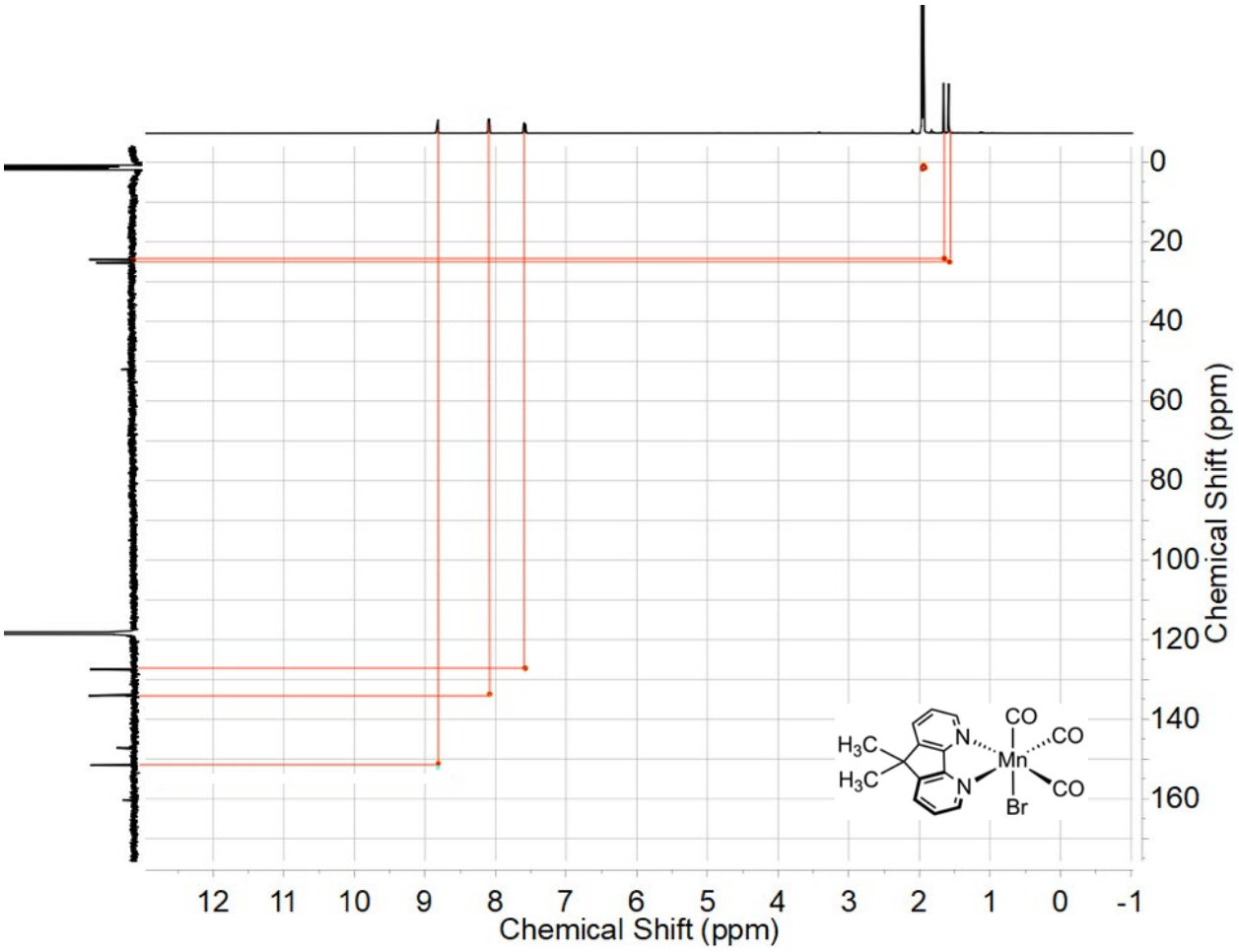

Figure D11: ^{1}H-^{13}C HSQC of complex **3** in CD_3CN depicting the diastereotopic methyl groups. Methyl and methine protons (red) and methylene protons (blue).

IR Spectra

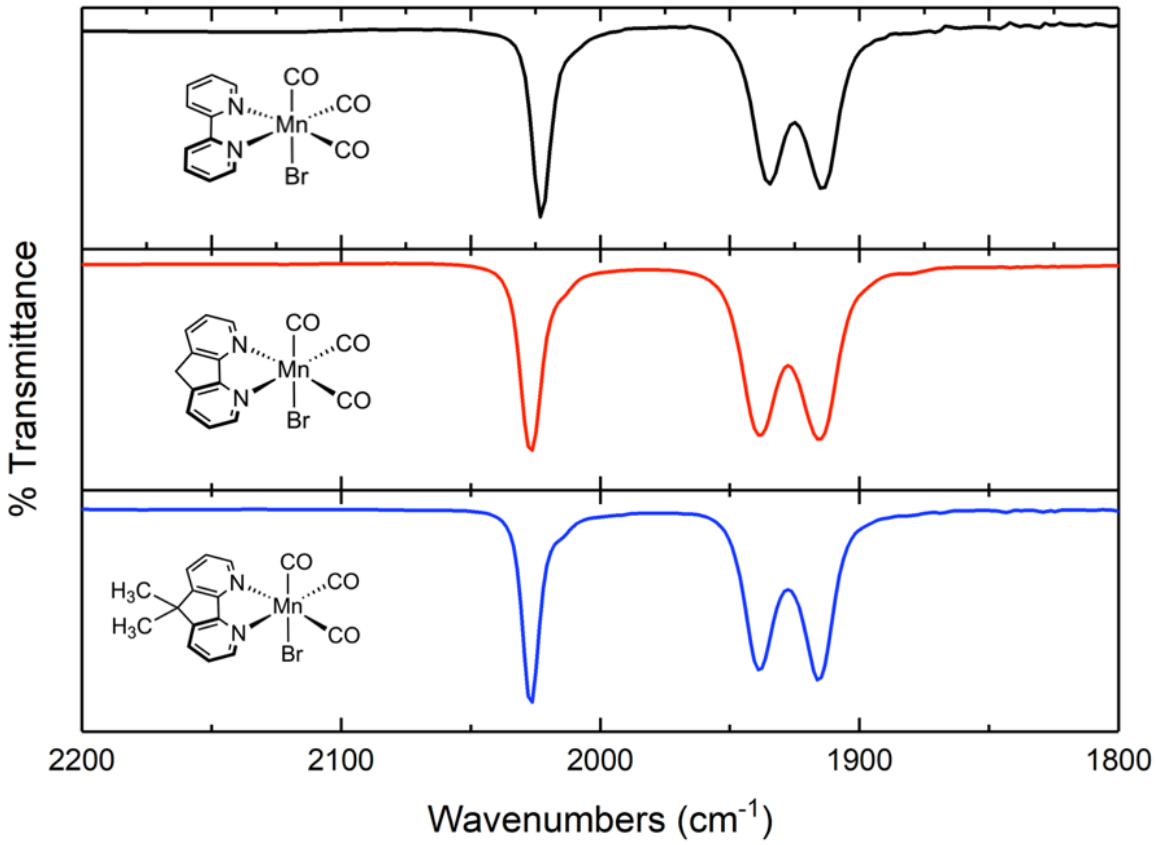

Figure D12: IR spectra of the carbonyl stretches for **1**, **2**, and **3** in THF solution; focusing on the CO stretching region. For a *fac*-tricarbonyl, C_s symmetric molecule, three CO stretches (Γ_{CO} = 2A′+A″) would be expected and are observed for complexes **1, 2,** and **3.**

Mass Spectra

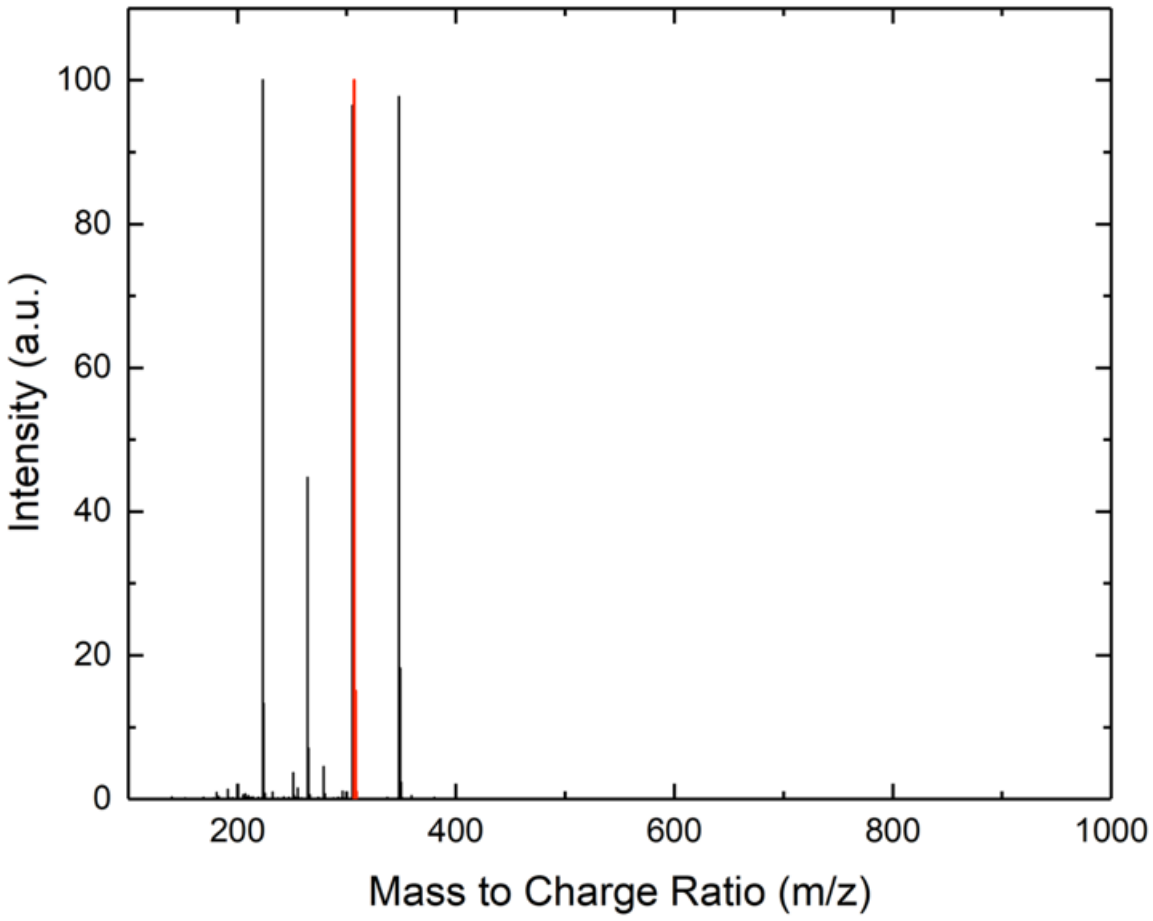

Figure D13: Full ESI-Mass spectrum of **2**. The experimental data is shown in **black** and the predicted data is shown in **red**. The other peaks in the spectrum correspond to fragments that are identified below.

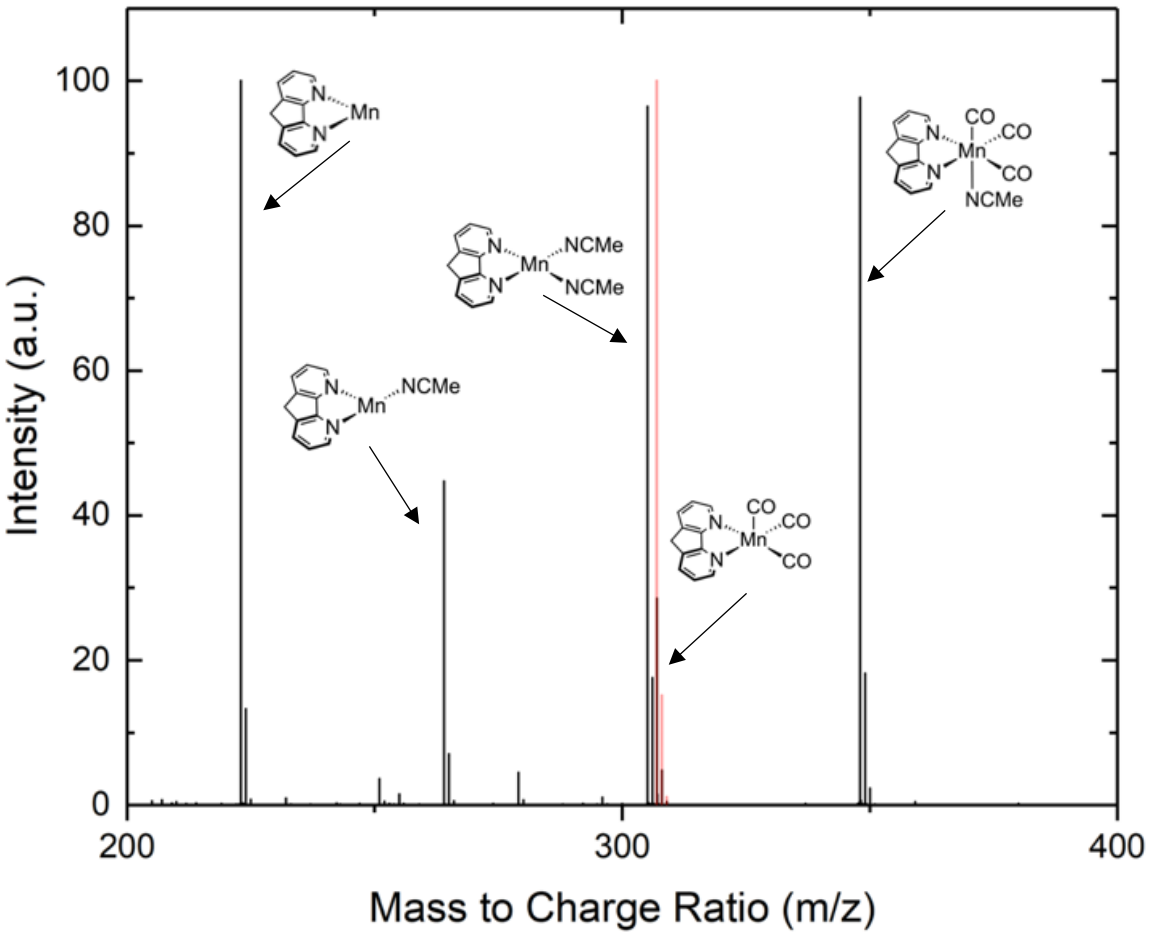

Figure D14: Zoomed in mass spectrum of **2** with fragment assignment. The experimental data is shown in **black** and the predicted data is shown in **red**.

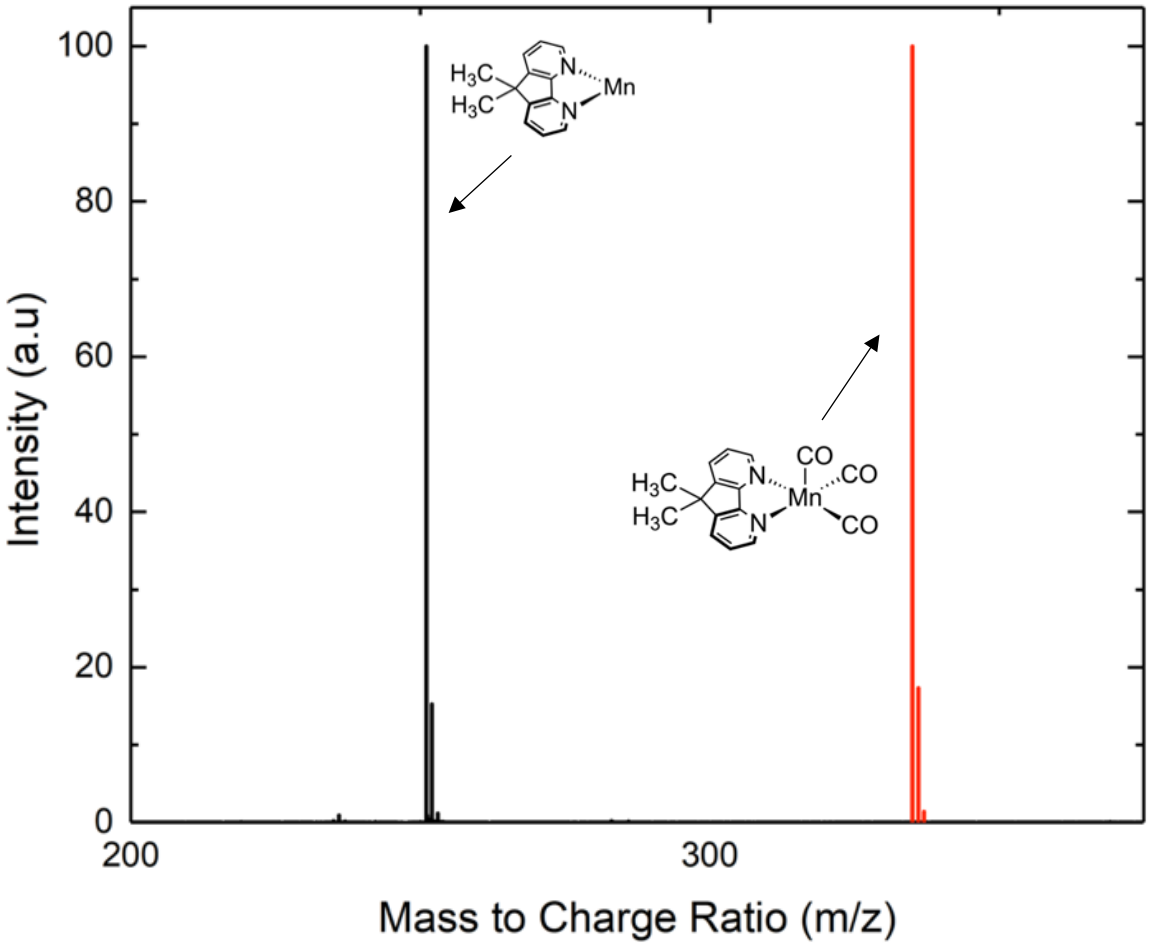

Figure D15: Full ESI-Mass spectrum of **3**. The experimental data is shown in **black** and the predicted data is shown in **red**. The expected parent peak was not present, but a corresponding fragment is identified in Figure D16.

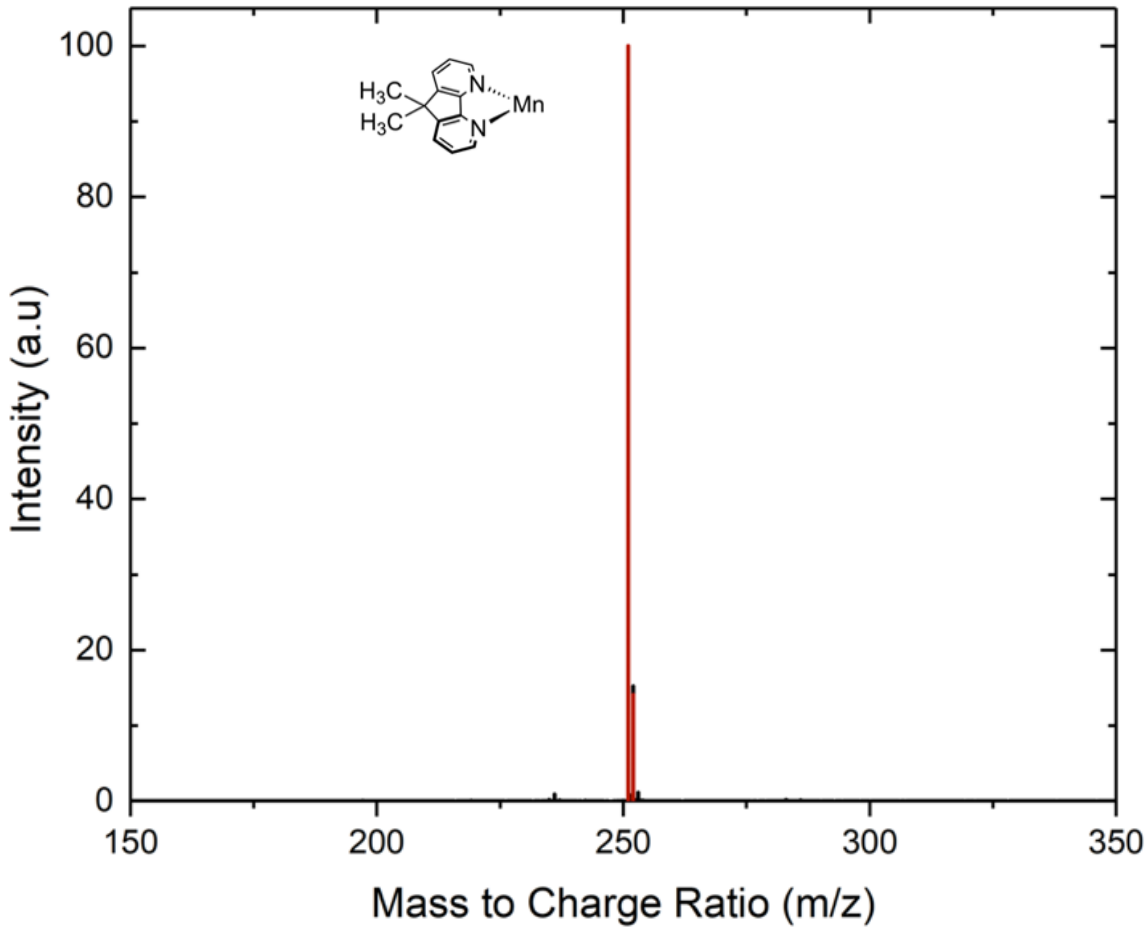

Figure D16: Zoomed in mass spectrum of **3** with fragment assignment. The experimental data is shown in **black** and the predicted data is shown in **red** for this specific fragment.

Electronic Absorption Spectra

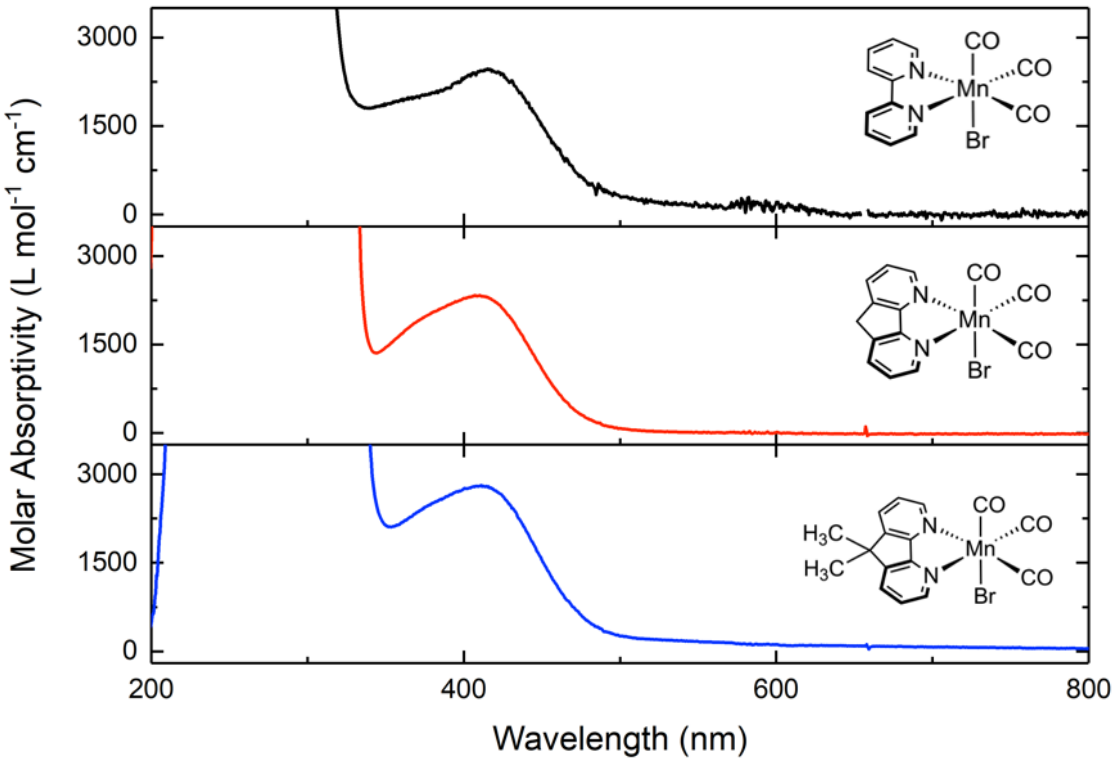

Figure D17: Stacked electronic absorption spectrum of **1**, **2**, and **3** featuring the MLCT transition in the visible region.

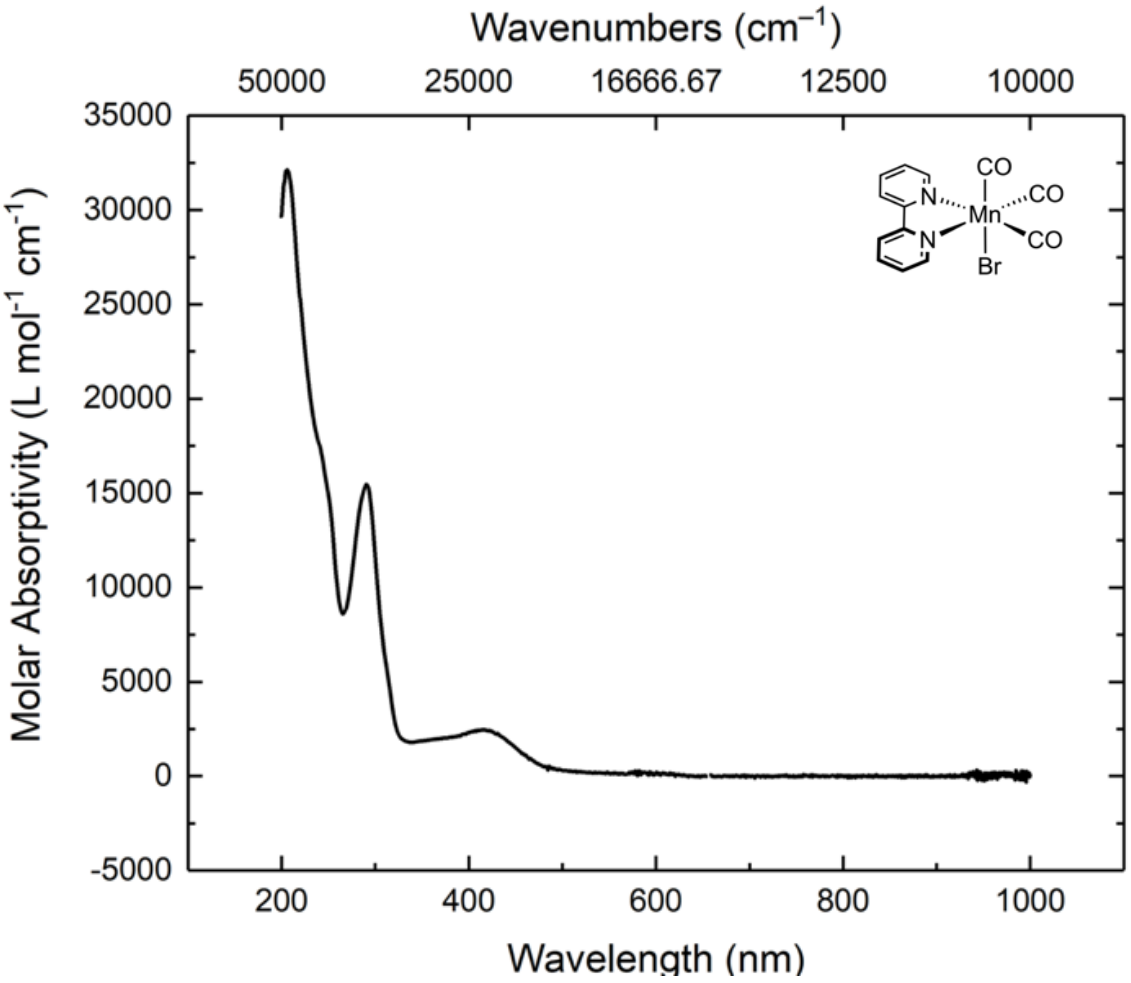

Figure D18: Electronic absorption spectrum of **1** in MeCN**.**

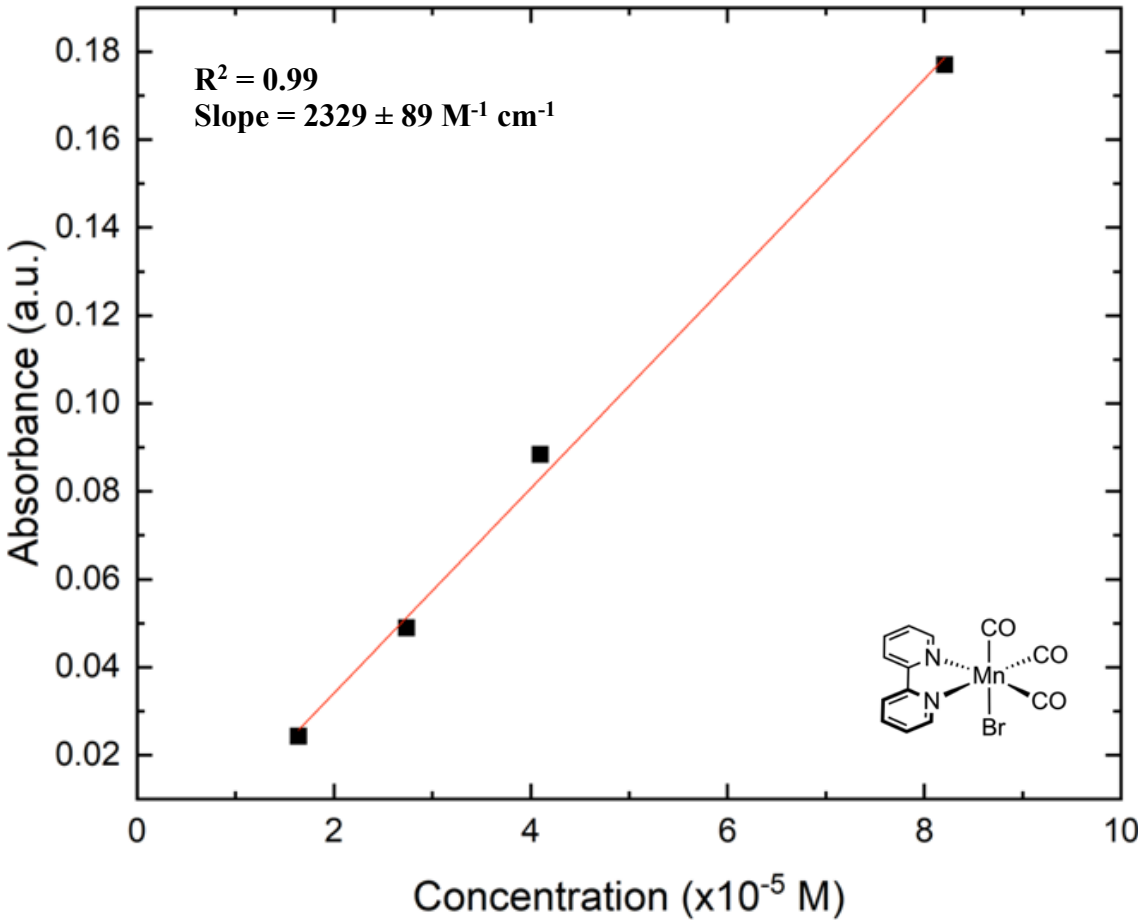

Figure D19: Absorbance vs. concentration plot of complex **1** in MeCN to obtain the molar absorptivity.

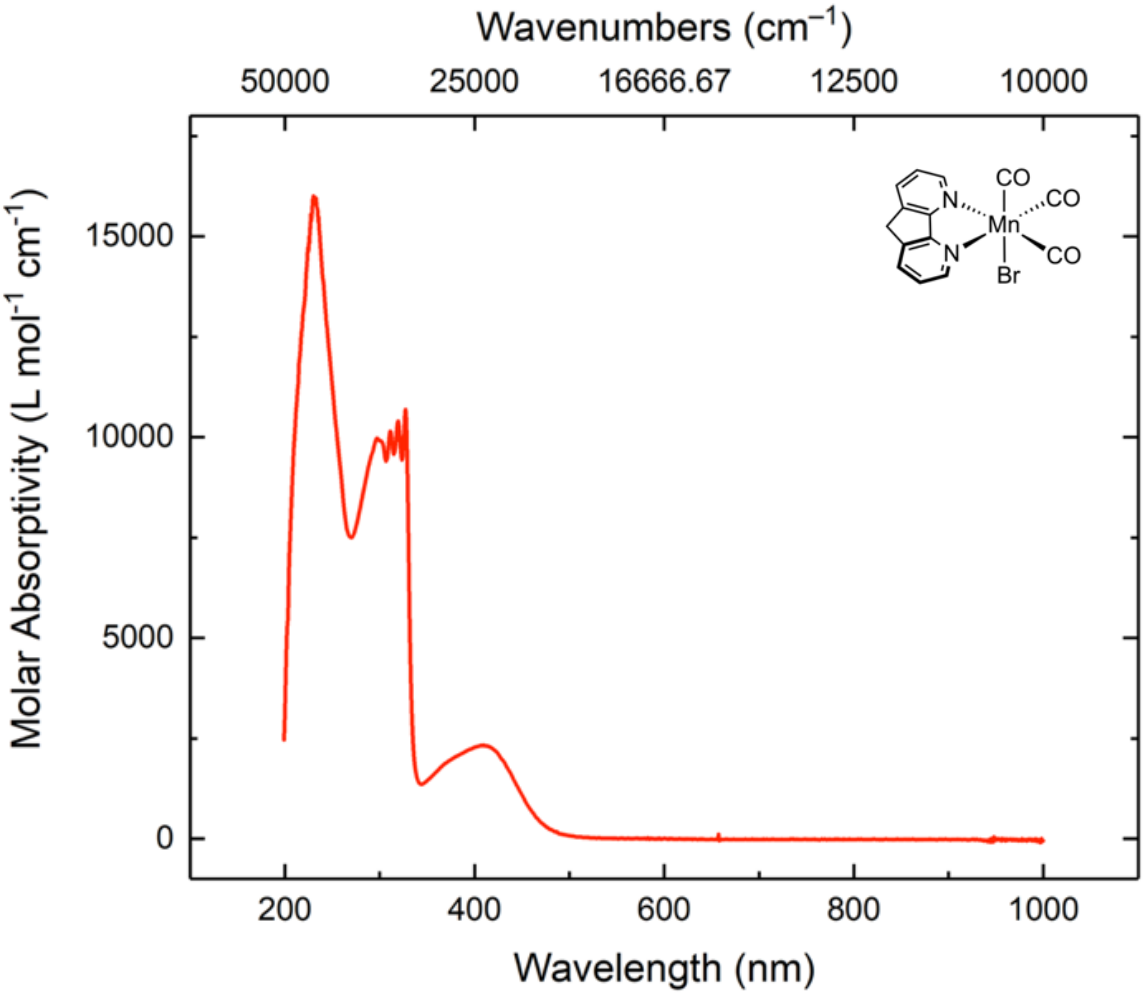

Figure D20: Electronic absorption spectrum of **2** in MeCN**.**

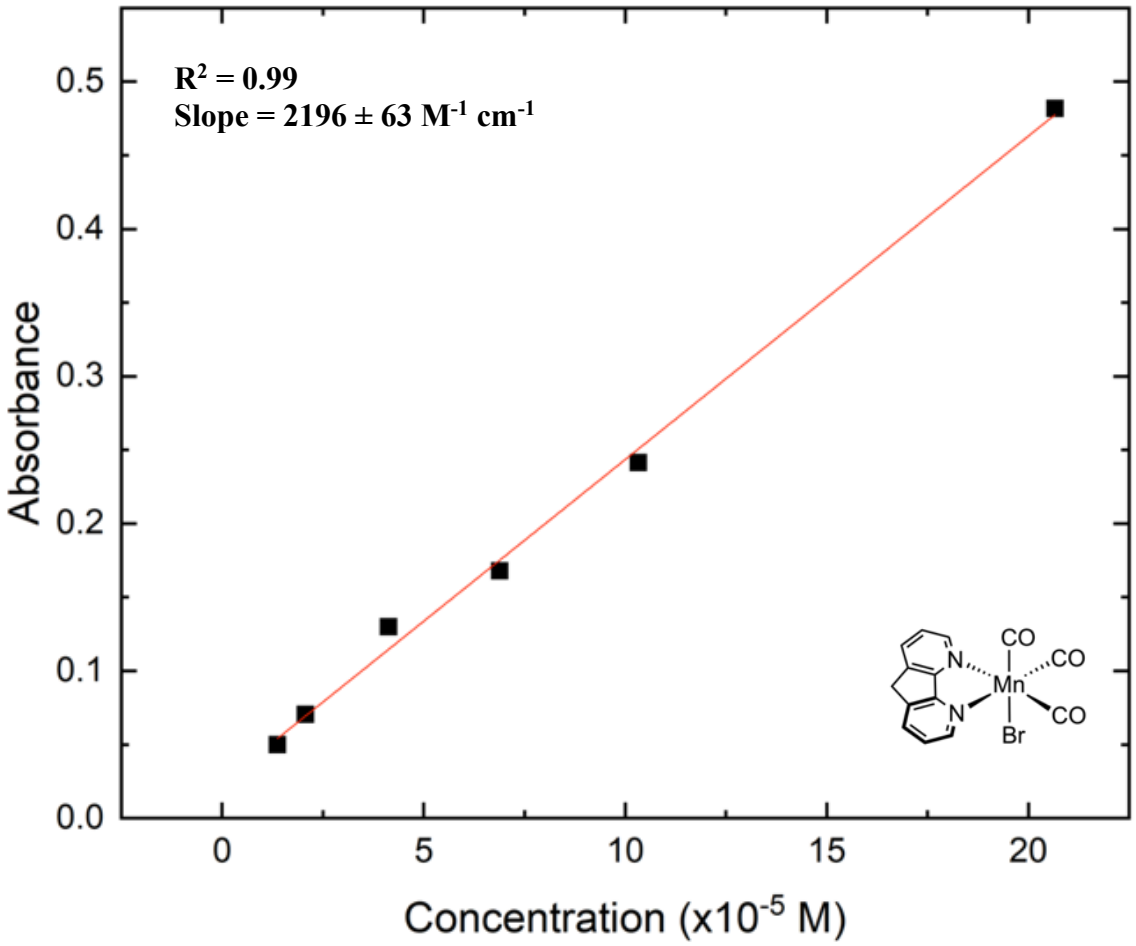

Figure D21: Absorbance vs. concentration plot of complex **2** in MeCN to obtain the molar absorptivity.

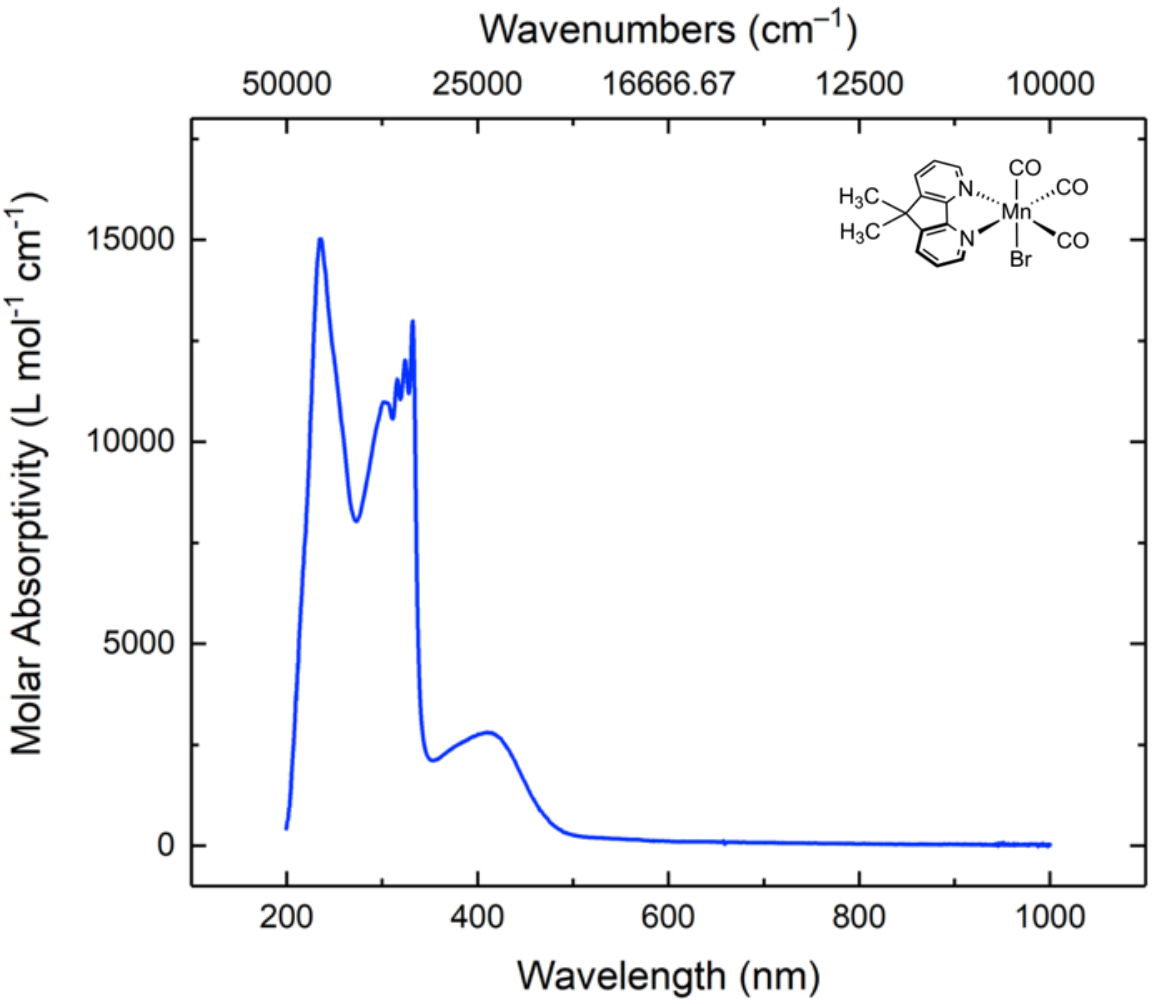

Figure D22: Electronic absorption spectrum of **3** in MeCN**.**

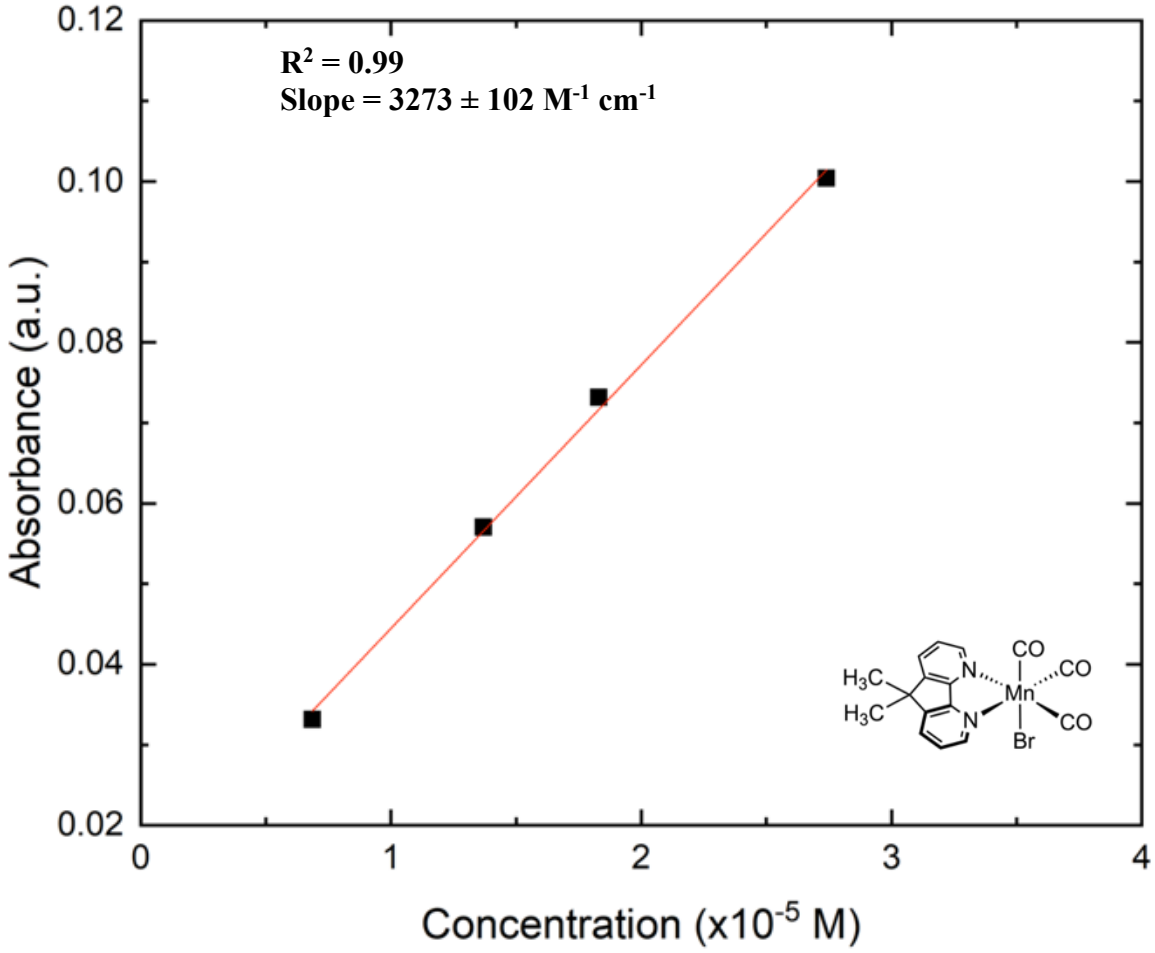

Figure D23: Absorbance vs. concentration plot of complex **3** in MeCN to obtain the molar absorptivity.

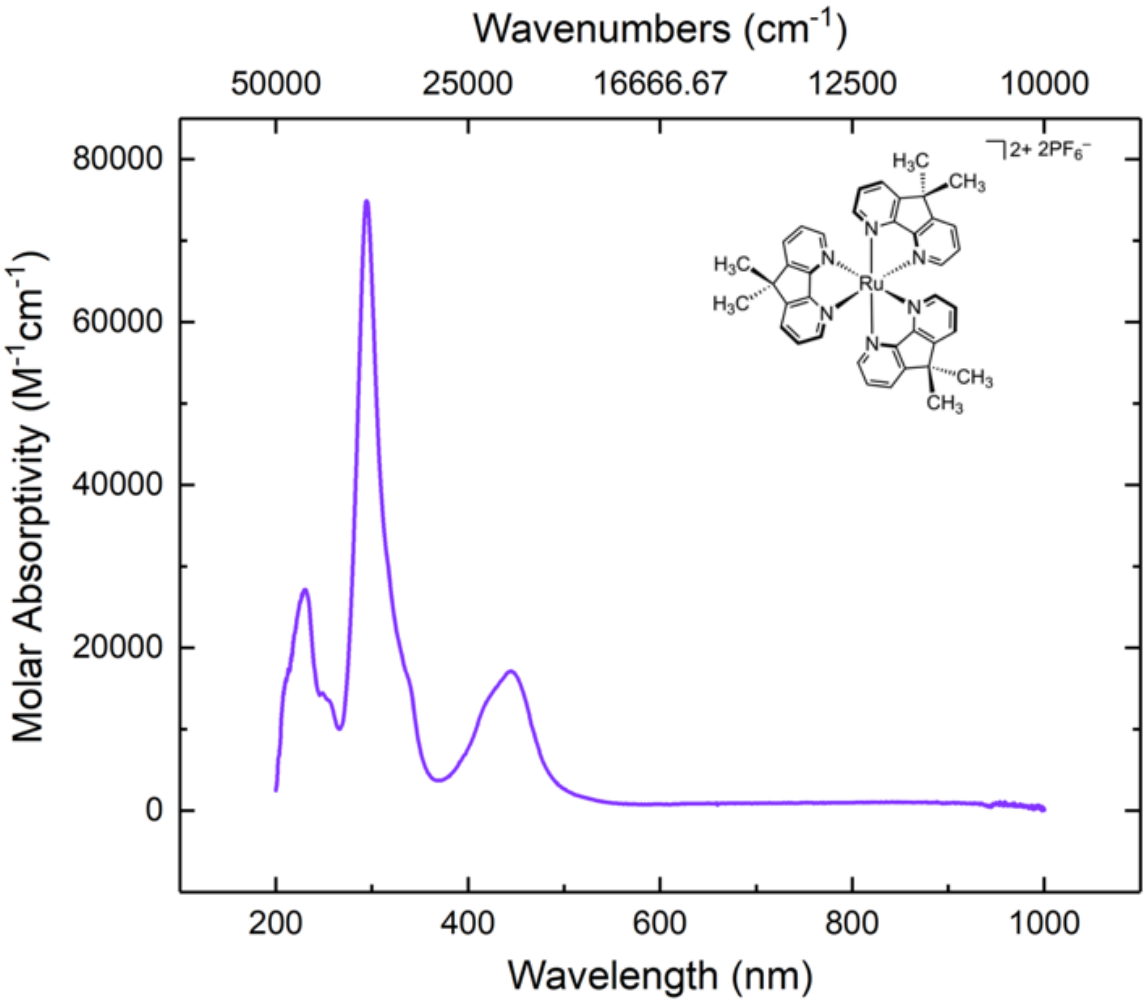

Figure D24: Electronic absorption spectrum of **5** in MeCN**.**

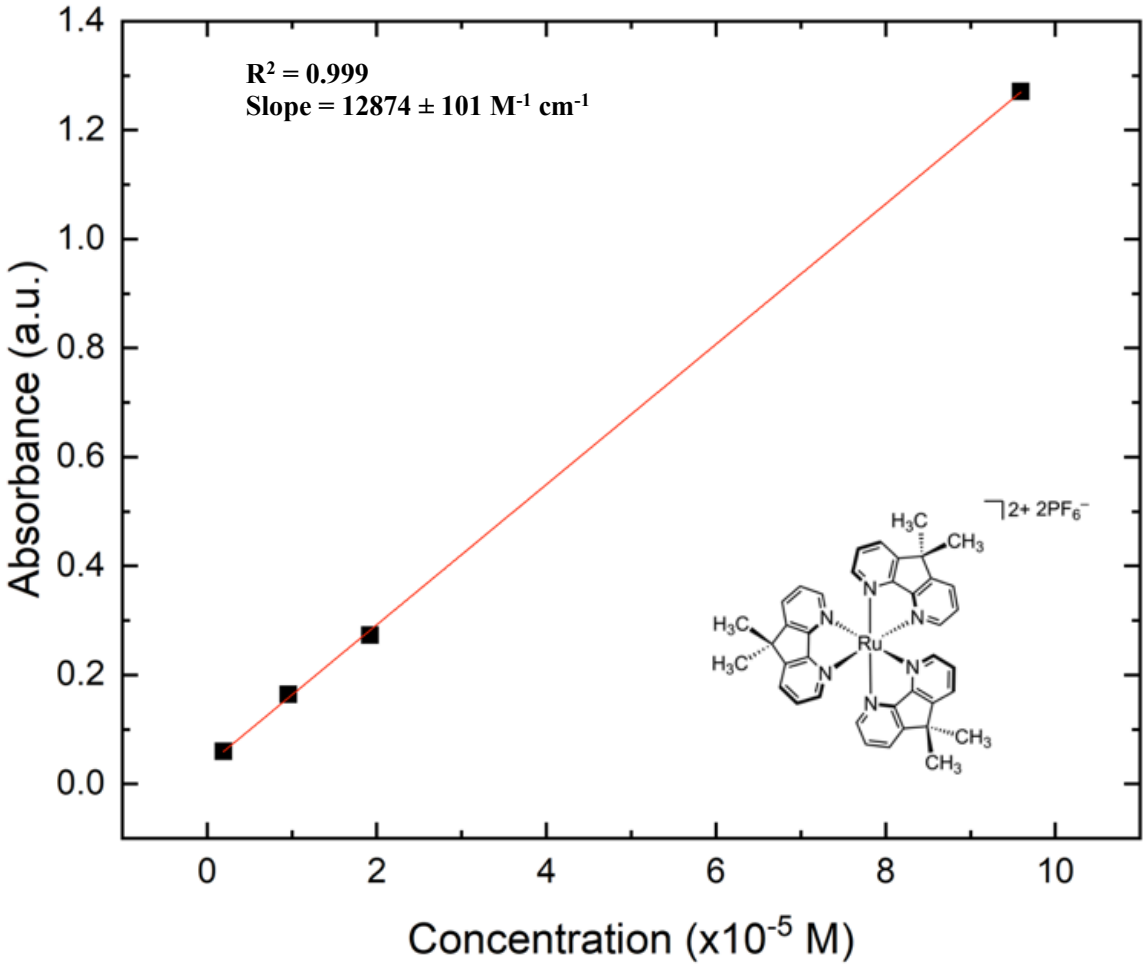

Figure D25: Absorbance vs. concentration plot of complex **5** in MeCN to obtain the molar absorptivity.

Cyclic Voltammetry Data

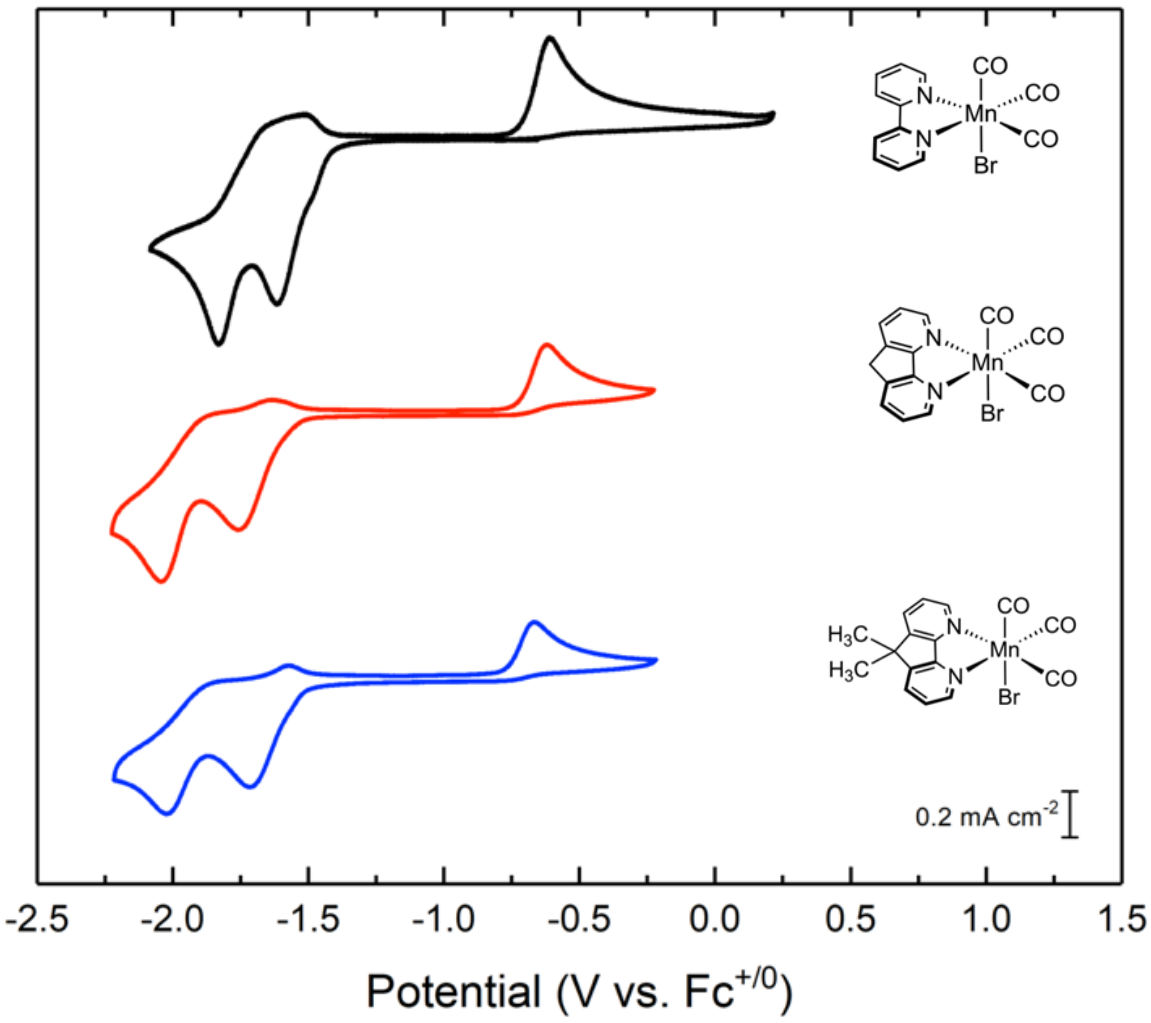

Figure D26: Stacked cyclic voltammograms of **1**, **2**, and **3** in 0.1 M $TBAPF_6$/MeCN solution.

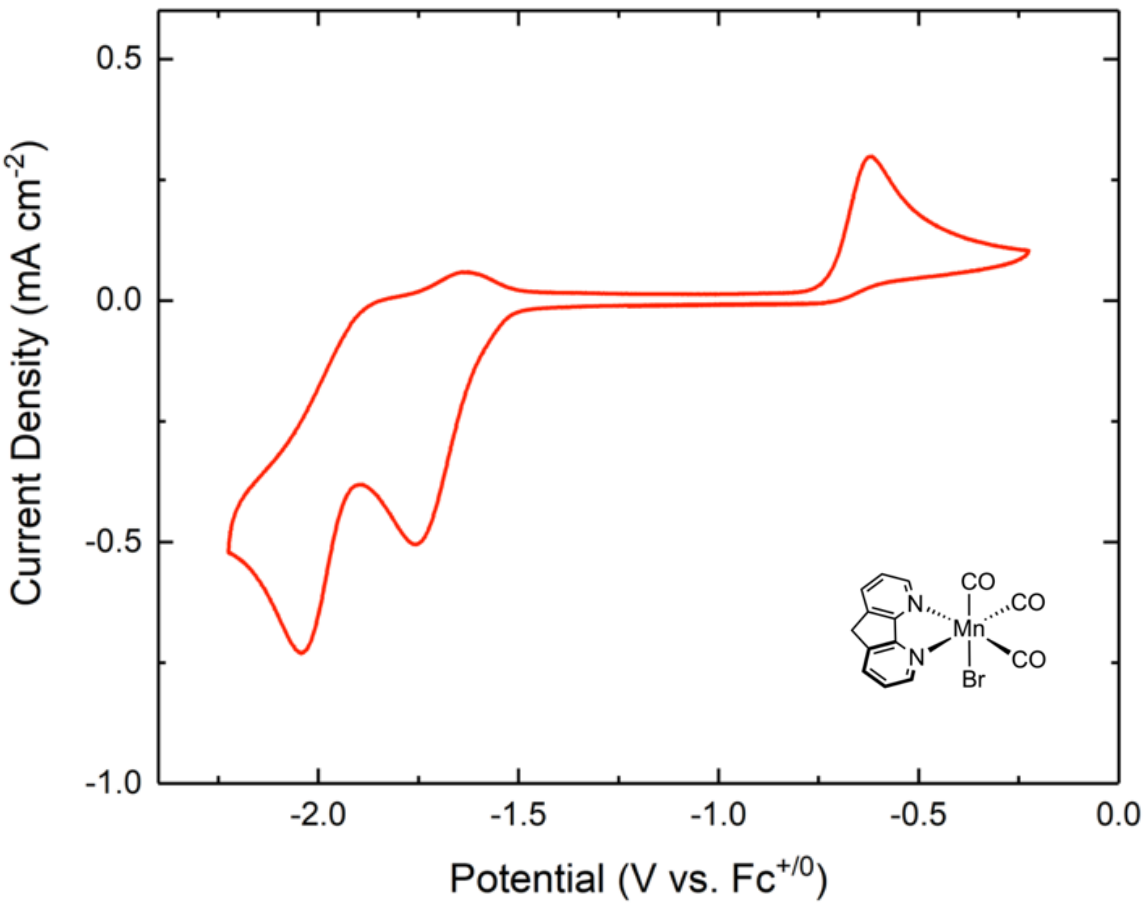

Figure D27: Cyclic voltammogram of **2** in 0.1M $TBAPF_6$/MeCN solution.

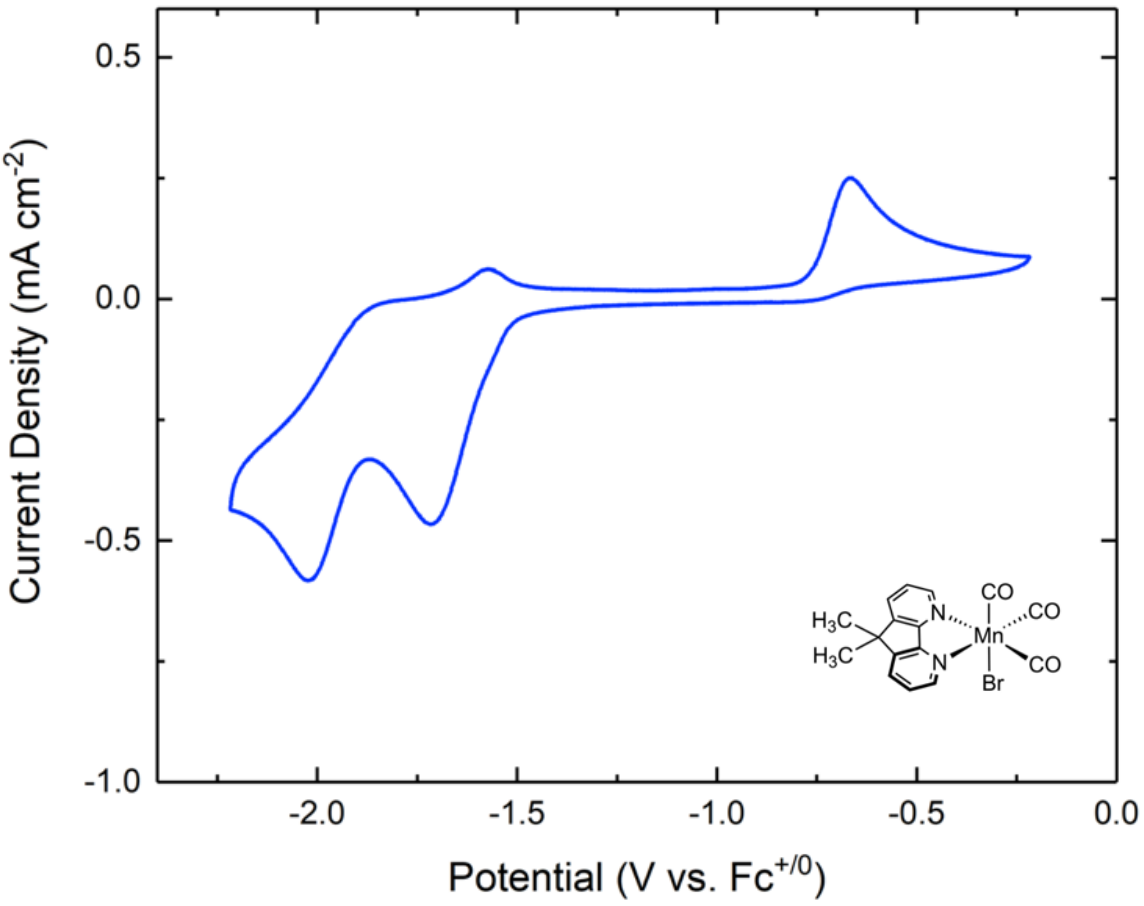

Figure D28: Cyclic voltammogram of **3** in 0.1M $TBAPF_6$/MeCN solution.

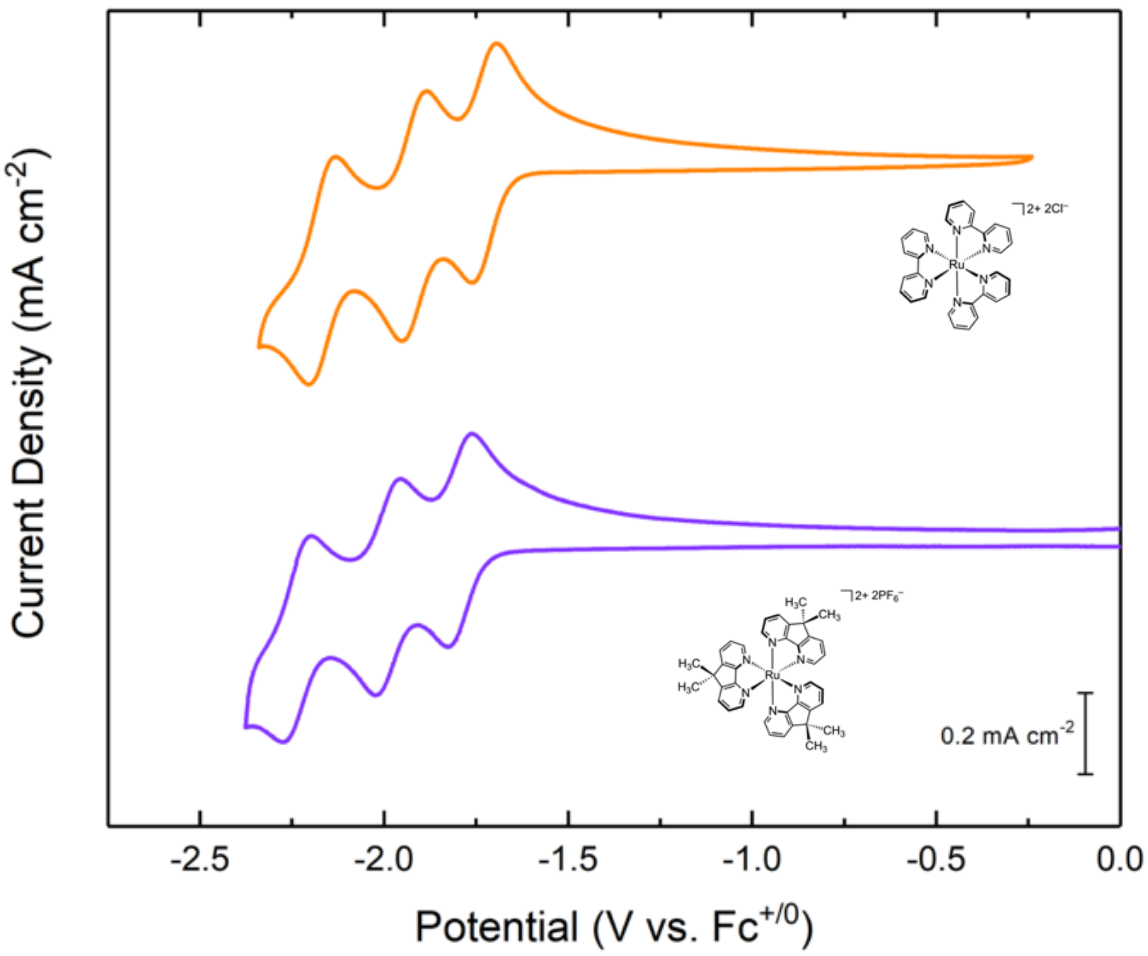

Figure D29: Stacked cyclic voltammograms of **4** and **5** in 0.1M $TBAPF_6$/MeCN solution.

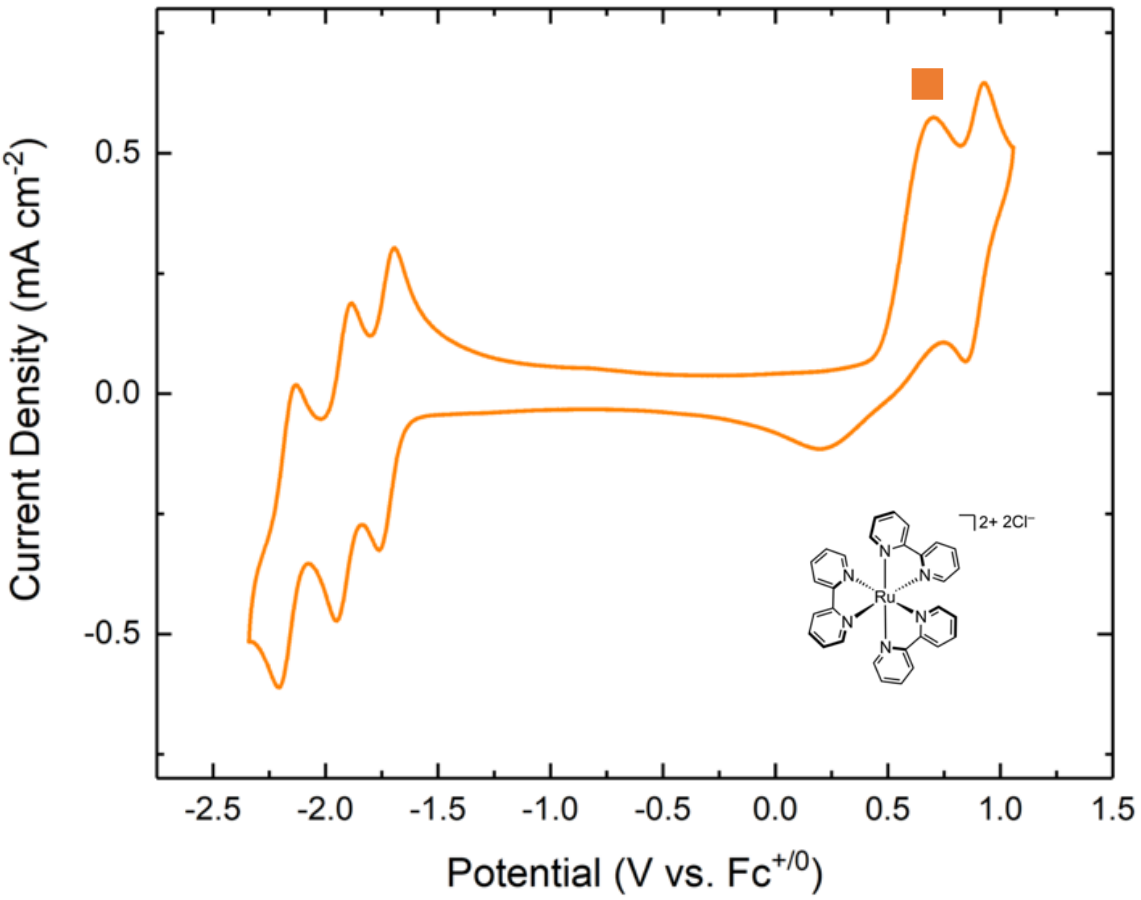

Figure D30: Cyclic voltammograms of **4** in 0.1M $TBAPF_6$/MeCN solution. The orange square (■) indicates chloride oxidation, which is a result of follow up chemical reactivity observed upon reduction.

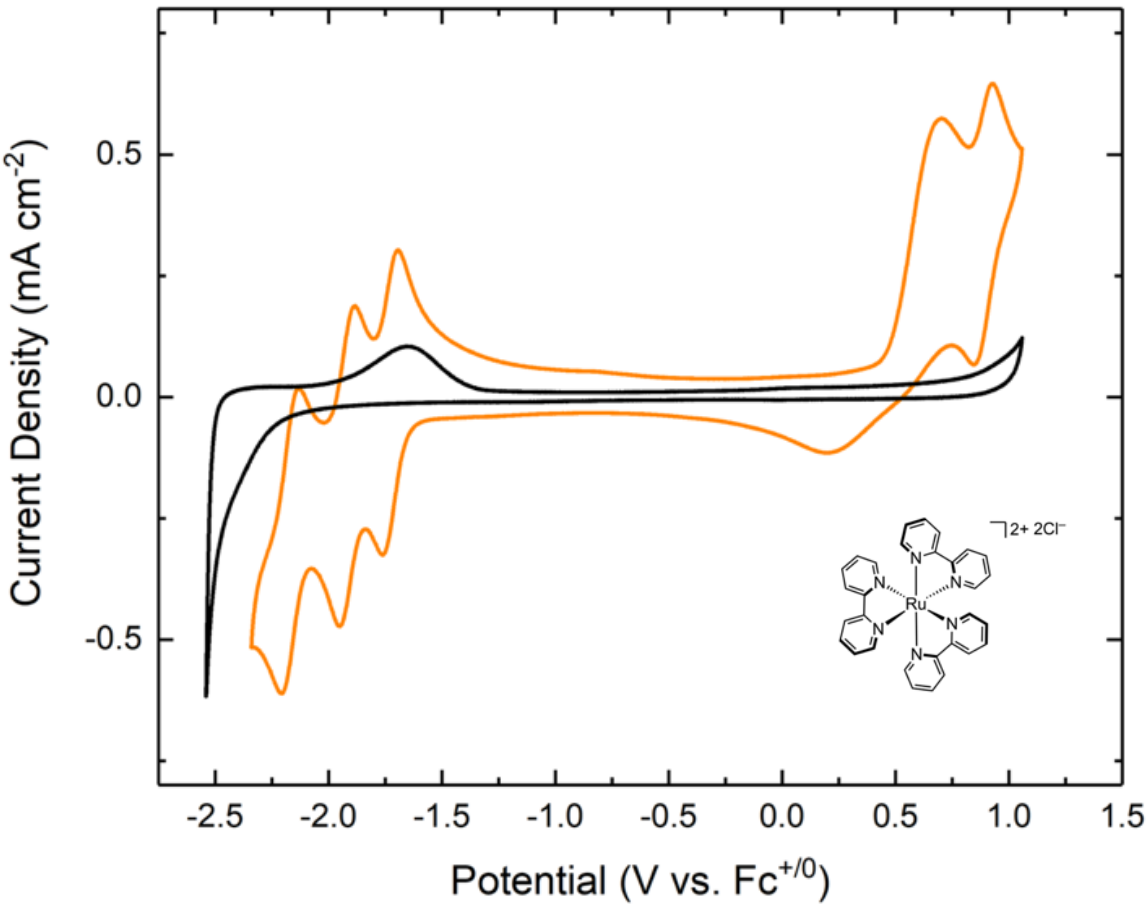

Figure D31: Cyclic voltammograms of **4** overlaid with **blank** in 0.1M $TBAPF_6$/MeCN solution.

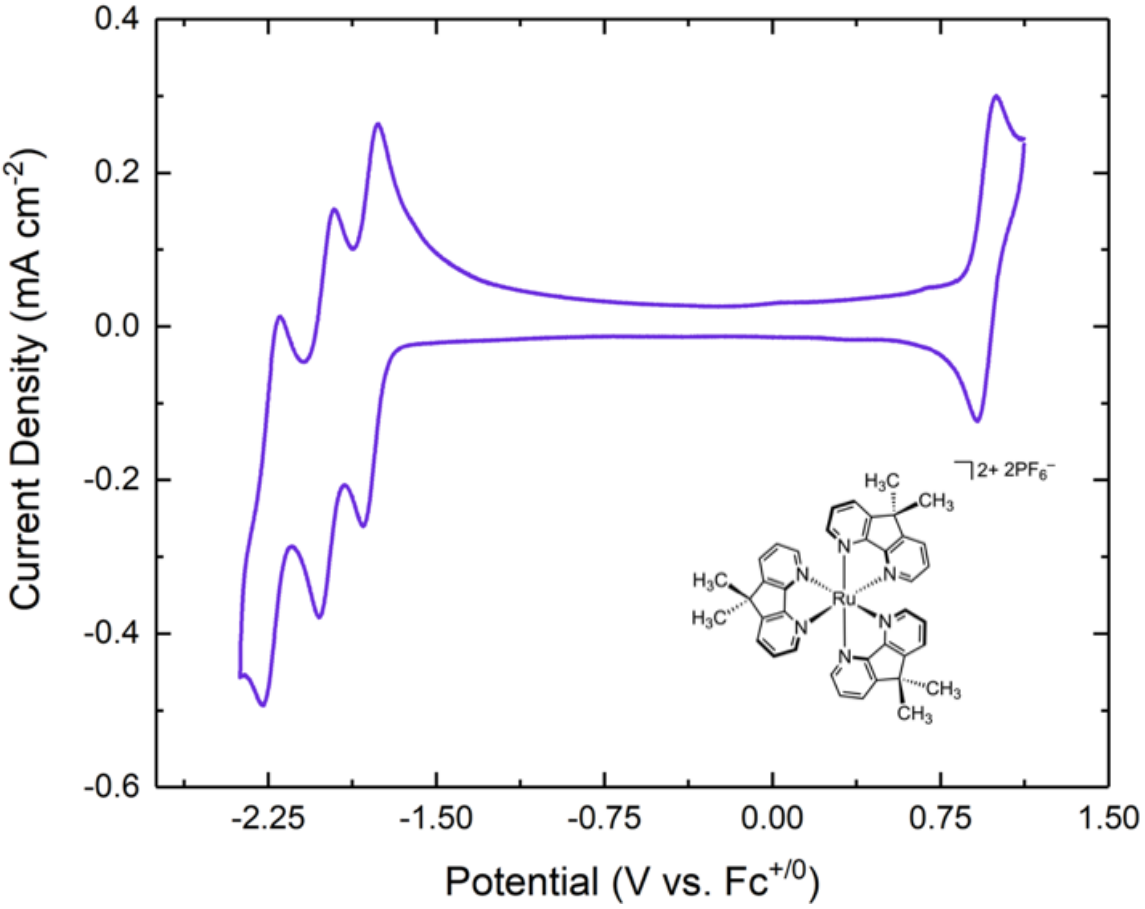

Figure D32: Cyclic voltammograms of **5** in 0.1M $TBAPF_6$/MeCN solution.

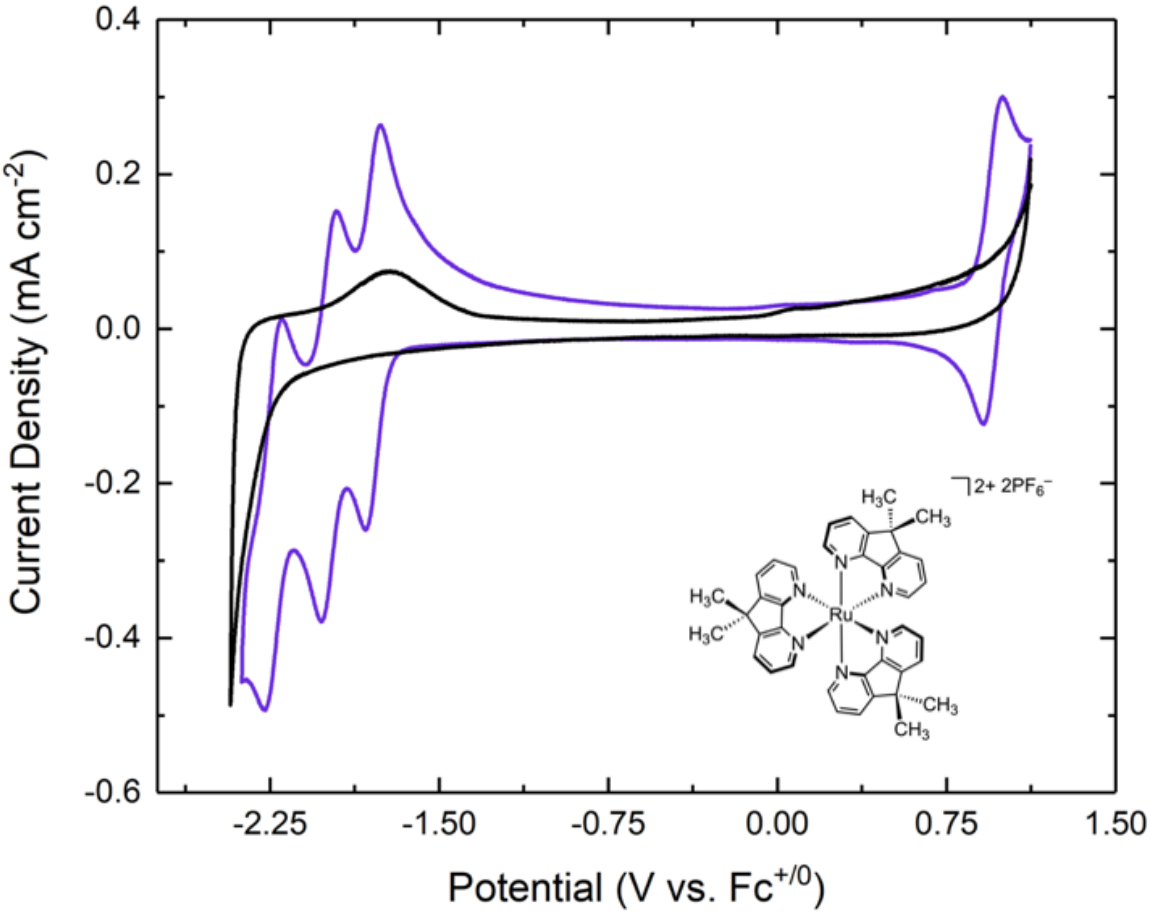

Figure D33: Cyclic voltammogram of **5** overlaid with a **blank** in 0.1M $TBAPF_6$/MeCN solution.

Cyclic Voltammetry with Acid Data

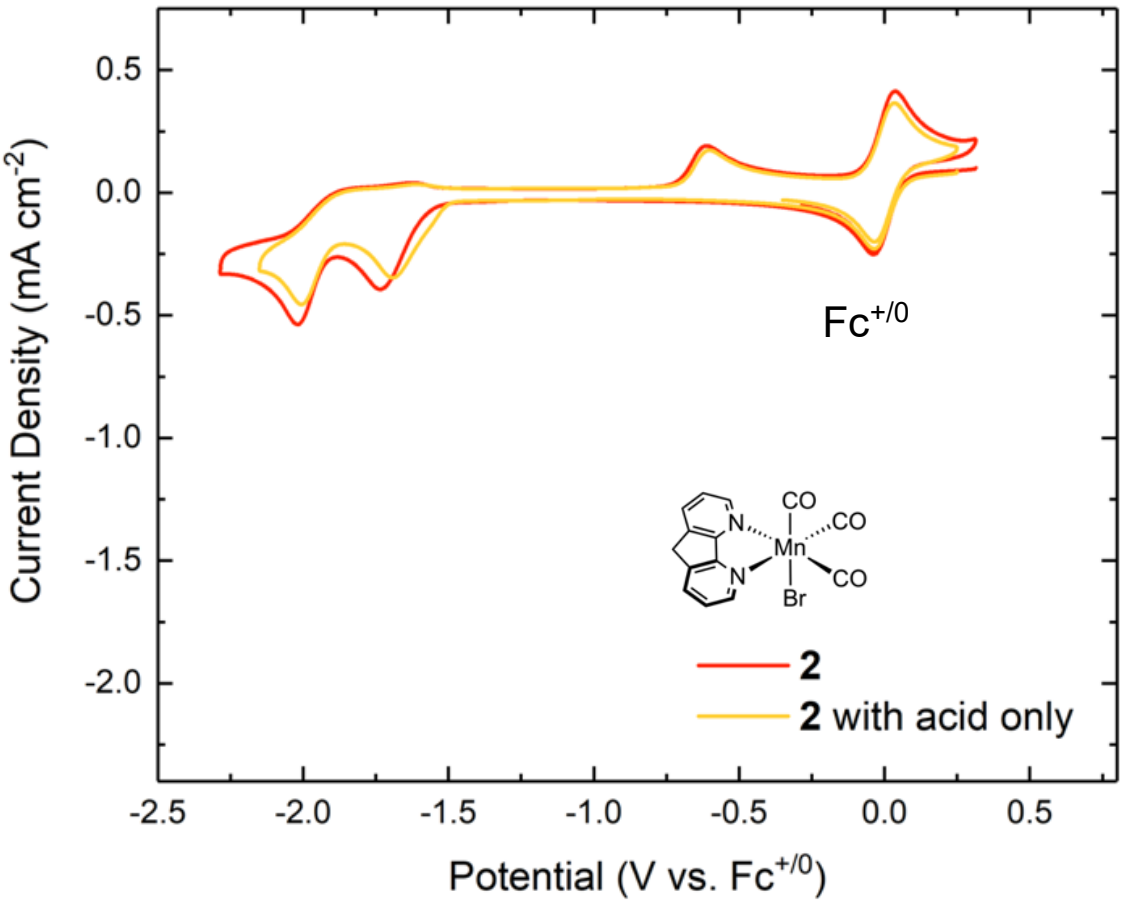

Figure D34: Cyclic voltammetry of **2** (red) in 0.1M $TBAPF_6$/MeCN solution followed by the addition of a 5% H_2O solution (yellow). The diminished current density is a result of dilution.

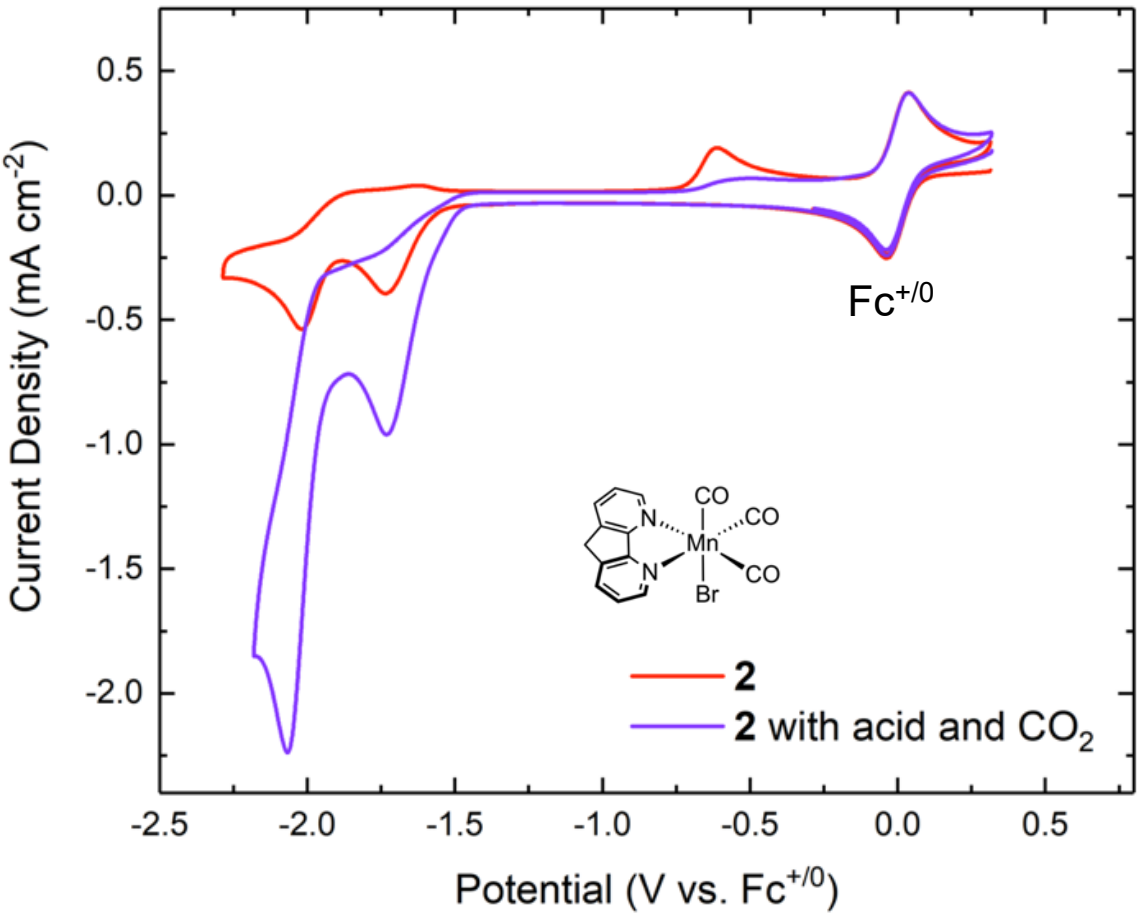

Figure D35: Cyclic voltammetry of **2** (red) in the presence of a 5% H_2O solution and a CO_2 atmosphere (purple).

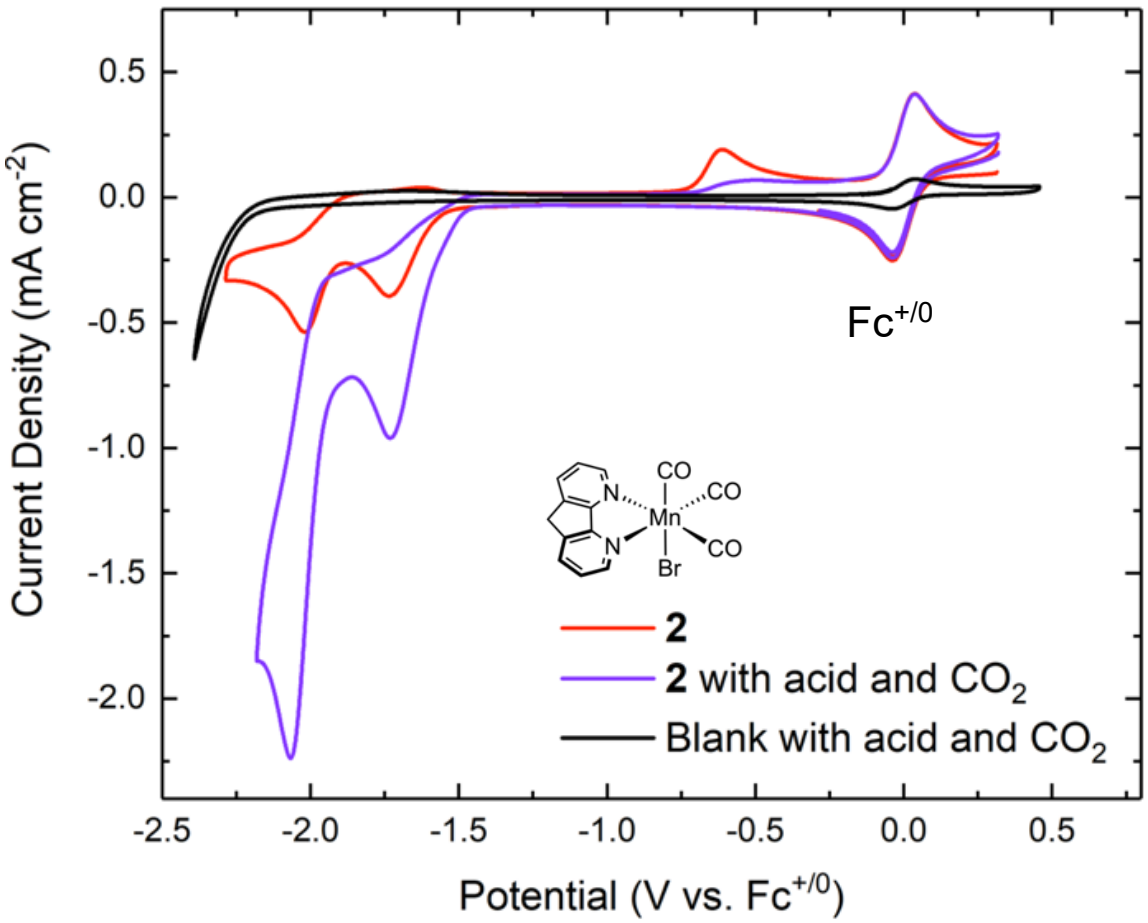

Figure D36: Cyclic voltammetry of **2** (red) and in the presence of a 5% H_2O solution and a CO_2 atmosphere (purple). The black trace illustrates a blank in the presence of a 5% H_2O solution and a CO_2 atmosphere.

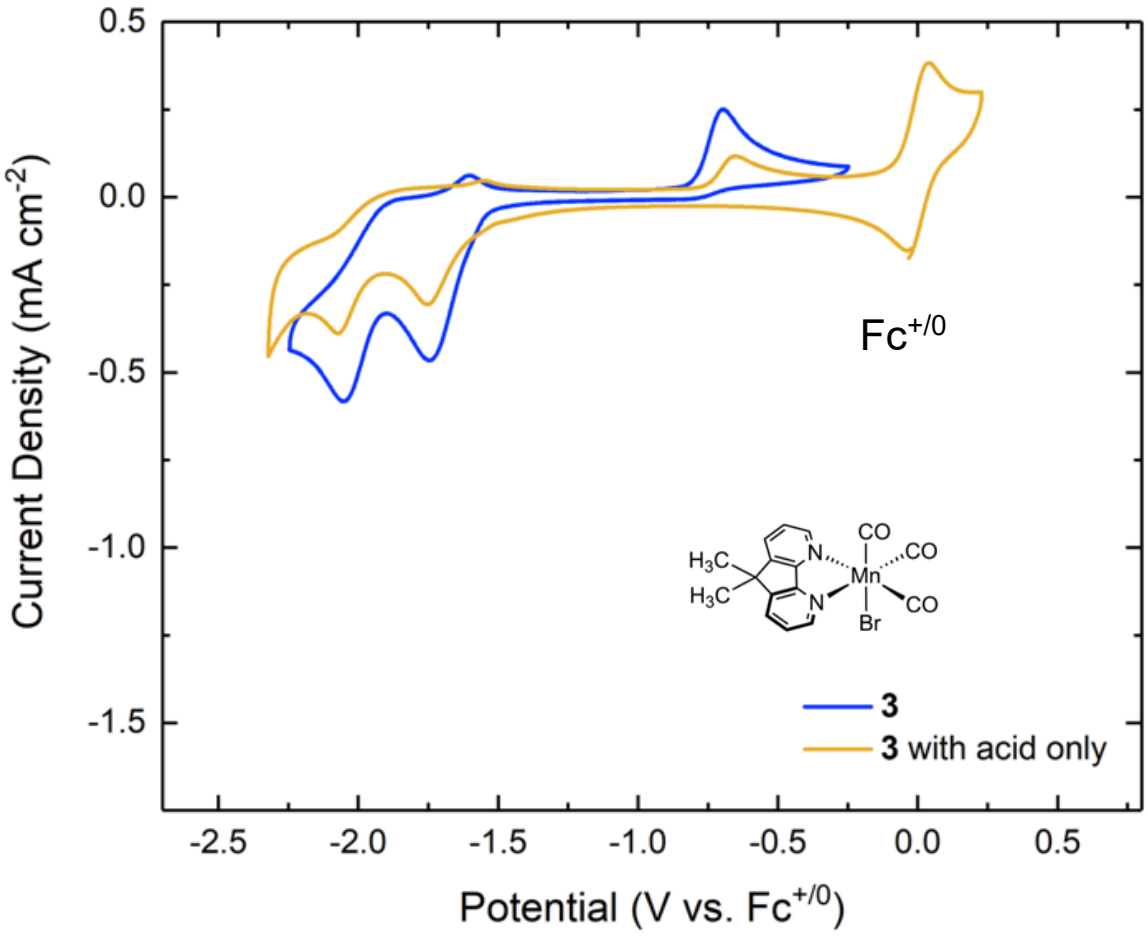

Figure D37: Cyclic voltammetry of **3** (blue) in 0.1M $TBAPF_6$/MeCN solution followed by the addition of a 5% H_2O solution (yellow). The diminished current density is a result of dilution.

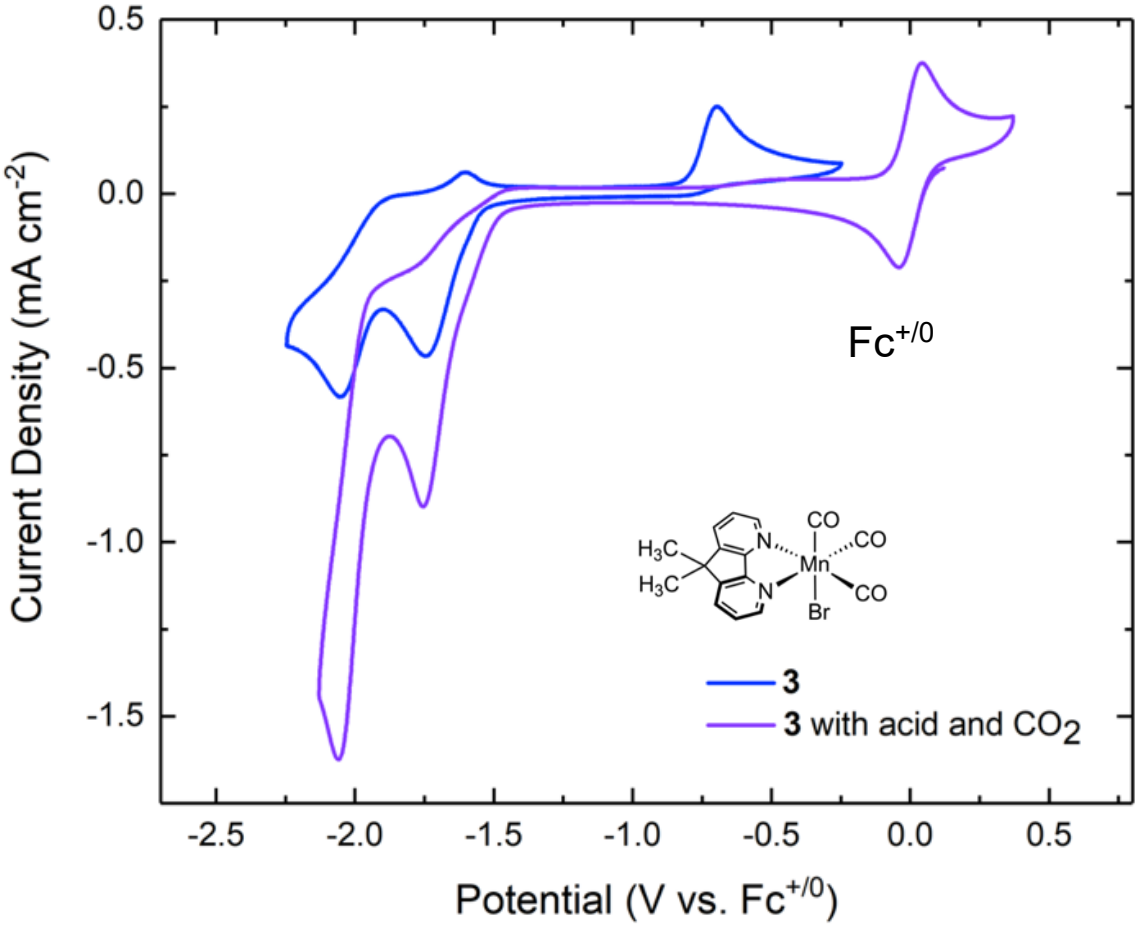

Figure D38: Cyclic voltammetry of **3** (blue) in the presence of a 5% H_2O solution and a CO_2 atmosphere (purple).

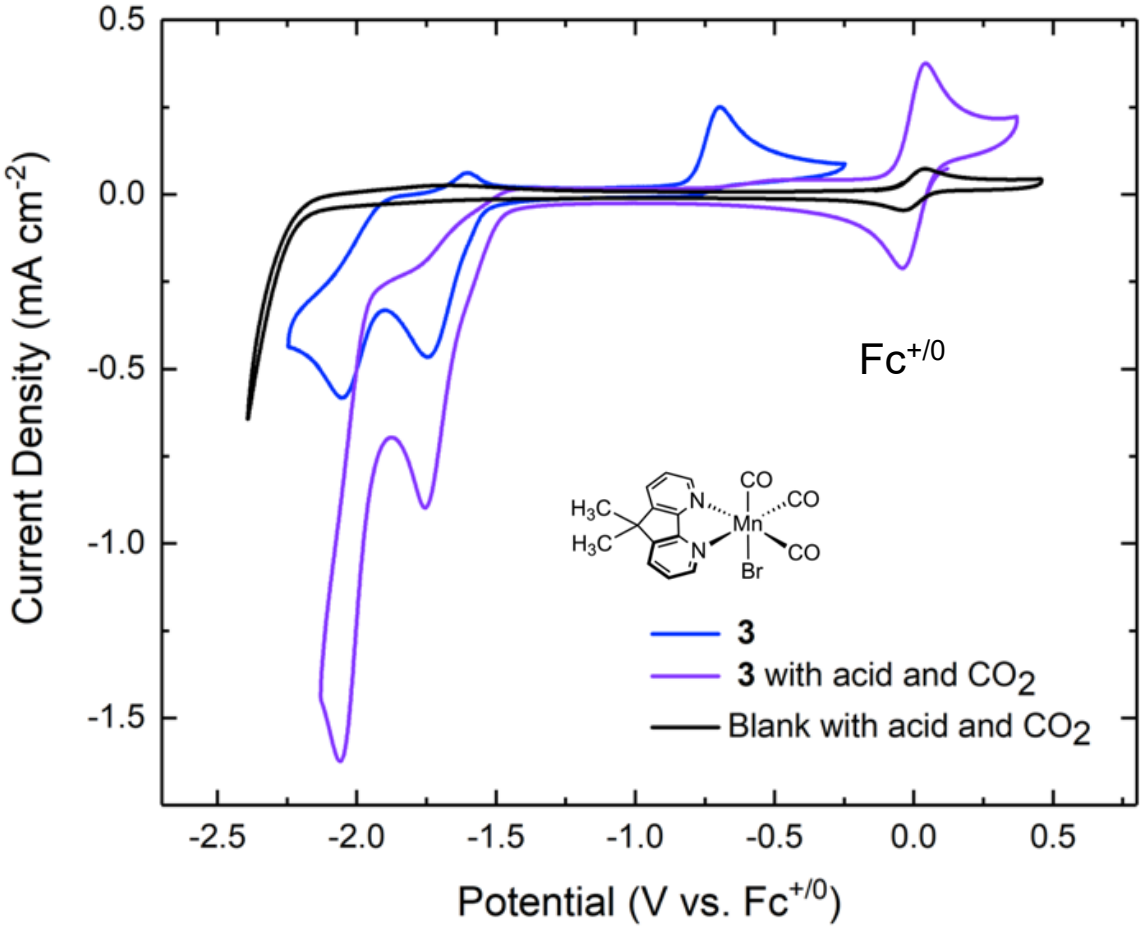

Figure D39: Cyclic voltammetry of **3** (blue) and in the presence of a 5% H_2O solution and a CO_2 atmosphere (purple). The black trace illustrates a blank in the presence of a 5% H_2O solution and a CO_2 atmosphere.

Bulk Electrolysis Data

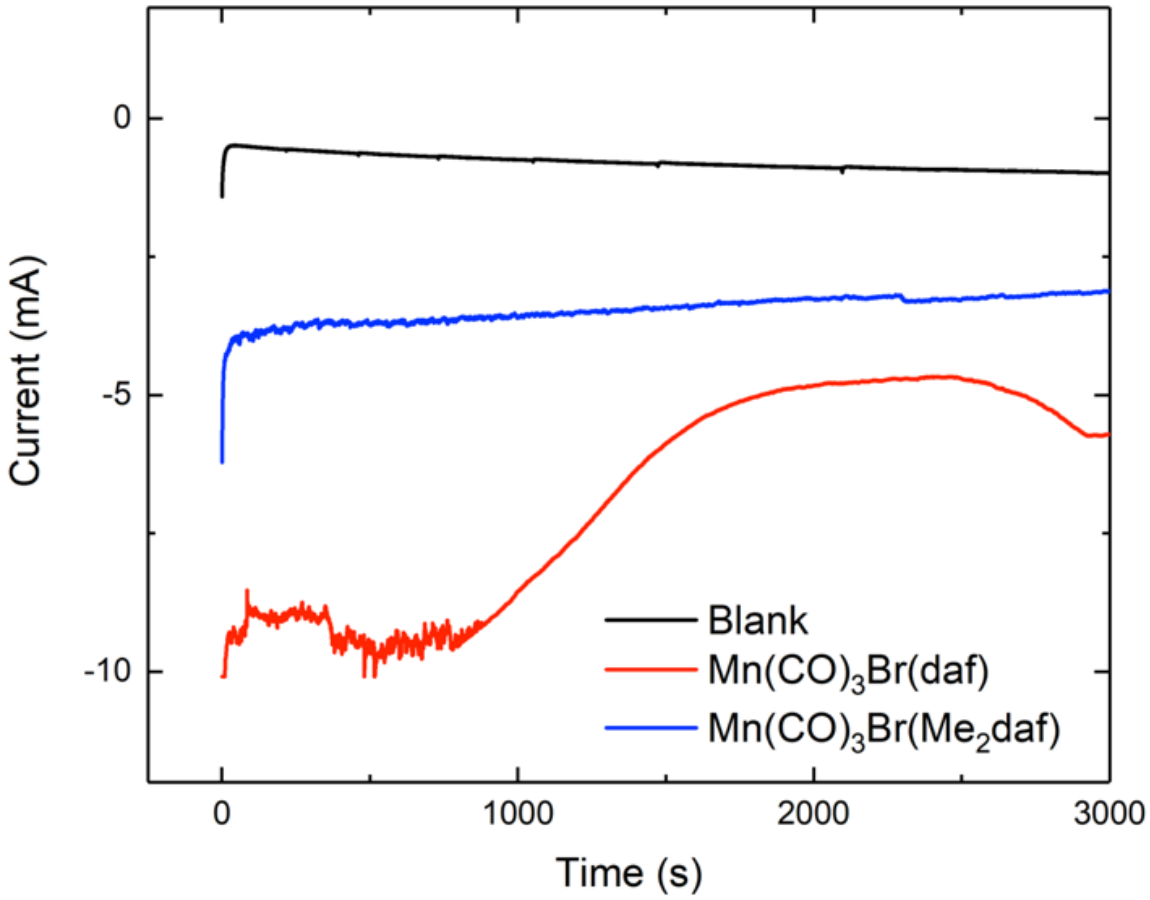

Figure D40: Chronoamperograms demonstrating current passed as a function of time for complexes **2**, **3**, and a **blank** polarized at –2.05 V vs $Fc^{+/0}$ in the presence of a 5% H_2O solution and a CO_2 atmosphere in 0.1M $TBAPF_6$/MeCN electrolyte.

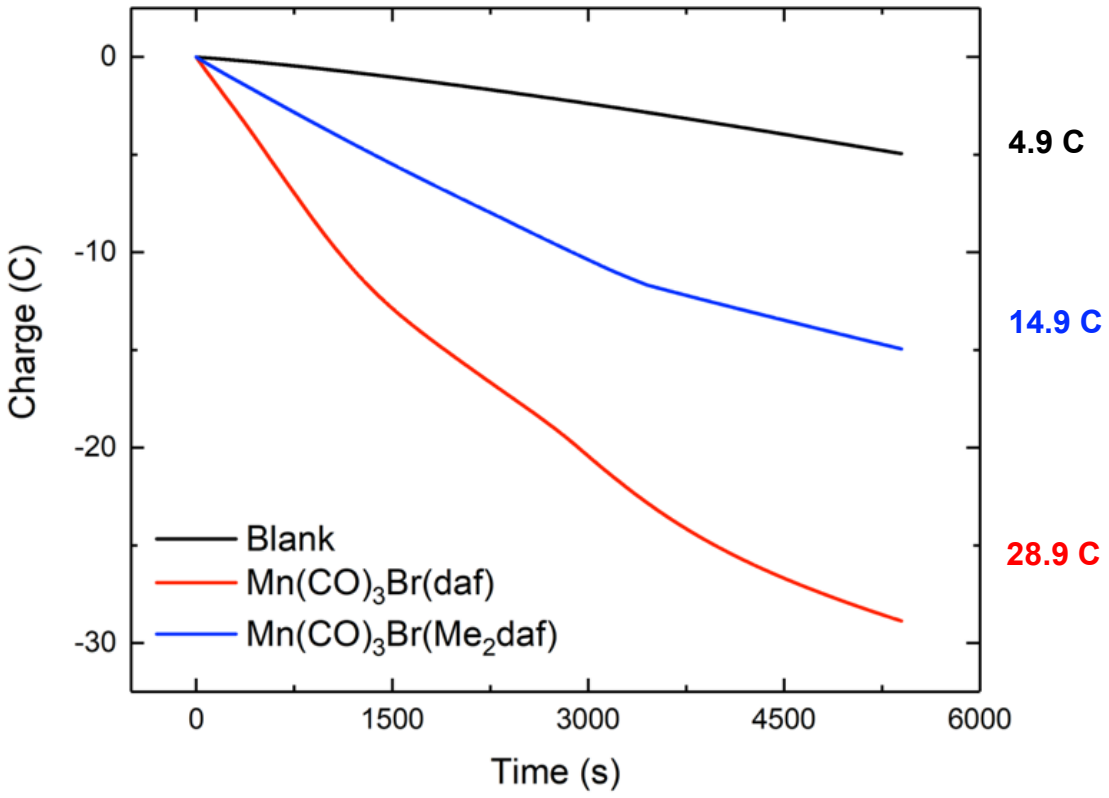

Figure D41: Charge passed as a function of time for complexes **2**, **3**, and a **blank** polarized at –2.05 V vs $Fc^{+/0}$ in the presence of a 5% H_2O solution and a CO_2 atmosphere in 0.1M $TBAPF_6$/MeCN electrolyte.

Table D1: Yield and Faradaic efficiencies for complexes **2** and **3** following a 90 minute controlled potential electrolysis polarized at -2.05 V vs. $Fc^{+/0}$ in in the presence of a 5% H_2O solution and a CO_2 atmosphere in 0.1M $TBAPF_6$/MeCN electrolyte. Water serves as the proton source and Fc is used as the sacrificial reductant.

Complex	H_2 yield (ppm)	CO yield (ppm)	Faradaic efficiency for H_2 (%)	Faradaic efficiency for CO (%)	Faradaic Efficiency Total (%)	TON H_2	TON CO
Blank	1882	271	—	—	—	—	—
2	190	8271	1	27	28	0.02	0.82
3	137	5484	1	34	35	0.02	0.62

Crystallographic Information

Refinement Details

X-ray Crystallographic Studies for (2, q51h), (3, q72j), (5, v74e), and (5, q36k).

Crystals of **2**, **3**, **5 (v74e)**, and **5 (q36k)** were mounted with Paratone N oil in MiteGen nylon loops under a cold nitrogen stream and placed on a Bruker Proteum diffractometer equipped with two CCD detectors (Apex II and Platinum 135) sharing a common MicroStar microfocus Cu rotating anode generator running at 45 mA and 60 kV (Cu Kα = 1.54178 A). Complete sets of low temperature (200 K) x-ray diffraction data were obtained for all three compounds using monochromated Cu radiation with the Apex II detector (**2**, **3, 5(q36k)**) positioned at 50.0 mm and equipped with Helios high brilliance multilayer mirror optics or the Platinum 135 detector (**5(v74e)**) positioned at 80.0 mm and equipped with Helios high- brilliance multilayer mirror optics. Totals of 7281 (**2**), 1958 (**3**), 2217 (**5(v74e**)), and 2291 (**5(q36k)**) 1.0°-wide ω- or ϕ-scan frames were collected with counting times of 5-8 seconds (**2**), 10-60 seconds (**3)** 8-30 seconds (**5(v74e)**), and 4-6 seconds (**5(q36k)**). Preliminary lattice constants were obtained with SMART in the Bruker Apex2 Software Suite.[1] Integrated reflection intensities for all three compounds were produced using SAINT in the Bruker Apex2 Software Suite.[1] Each data set was corrected empirically for variable absorption effects with SADABS[2] using equivalent reflections. The Bruker software package SHELXTL was used to solve each structure using intrinsic direct methods phasing. Final stages of weighted full-matrix least-squares refinement were conducted using Fo^2 data with SHELXTL[3] or the Olex software package equipped with XL.[4] The relevant crystallographic and structure refinement data for all three structures compounds are given in Table D2.

The final structural model for each structure incorporated anisotropic thermal parameters for all full-occupancy nonhydrogen atoms. The final structural model for each structure incorporated anisotropic thermal parameters for all full-occupancy nonhydrogen atoms. Isotropic thermal parameters were used for all included hydrogen atoms as well as disordered partial-occupancy carbonyl atoms O1′ and C1′ in **3**. Nonmethyl hydrogen atoms were fixed at idealized riding model sp^2- or sp^3-hybridized positions with C-H bond lengths of 0.95 – 0.99 Å. Both methyl groups for the ligands in **3** were incorporated into the structural model as fixed sp^3-hybridized riding-model rigid groups with one methyl hydrogen in the crystallographic mirror plane and C-H bond lengths of 0.96 Å. The six methyl groups in the ligands of **5(v74e)** were refined as idealized riding model rigid rotors (with a C-H bond length of 0.98 Å) that were allowed to rotate freely about their C-C bonds in least-squares refinement cycles.

Table D2: Crystal Refinement Data

	2 (q51h)	**3 (q72j)**
CCDC accession code	1977431	1994285
Empirical formula	$C_{14}H_8BrMnN_2O_3$	$C_{16}H_{12}BrMnN_2O_3$
Formula weight	387.07	415.13
Temperature	200(2) K	200(2) K
Wavelength	1.54178 Å	1.54178 Å
Crystal system	Triclinic	Orthorhombic
Space group	$P\bar{1}$ - C_i^1 (No. 2)	Cmca - D_{2h}^{18} (No. 64)
a	7.1682(7) Å	11.2628(5) Å
b	10.0797(10) Å	19.4283(13) Å
c	10.5015(7) Å	15.0920(10) Å
a	77.757(6)°	90°
β	73.507(5)°	90°
γ	75.228(6)°	90°
Volume	695.47(11) $Å^3$	3302.4(3) $Å^3$
Z	2	8
Density (calculated)	1.848 g/cm^3	1.670g/cm^3
Absorption coefficient	11.193 mm^{-1}	9.473 mm^{-1}
F(000)	380	1648
Crystal size	0.04 x 0.04 x 0.04 mm^3	0.085 x 0.065 x 0.010 mm^3
Number of data frames/time	7281/5-8 seconds	1958/10-60 seconds
Theta range	4.44 to 70.32°	4.55 to 70.39°
Index ranges	$-8\leq h\leq 8$, $-12\leq k\leq 11$, $-12\leq l\leq 11$	$-12\leq h\leq 13$, $-23\leq k\leq 20$, $-18\leq l\leq 18$
Reflections collected	17866	10636
Independent reflections	2484 [R_{int} = 0.035]	1635 [R_{int} = 0.073]
Completeness/θ_{max}	99.2%/66.00°	99.9%/66.00°
Absorption correction	Multi-scan	Multi-scan
Max. and min. transmission	1.000 and 0.811	1.000 and 0.659
Refinement method	Full-matrix least-squares on F^2	Full-matrix least-squares on F^2
Data / restraints / parameters	2484 / 0 /190	1635 / 9 / 128
Goodness-of-fit on F^2	1.105	1.181
Final R indices [I>2σ(I)]	R_1 = 0.030, wR_2 = 0.081	R_1 = 0.070, wR_2 = 0.179
R indices (all data)	R_1 = 0.032, wR_2 = 0.082	R_1 = 0.083, wR_2 = 0.187
Largest diff. peak and hole	0.86 and -0.34 $e^-/Å^3$	1.13 and -1.01 $e^-/Å^3$

	5 (v74e)	5(q36k)
CCDC accession code	1982214	#####
Empirical formula	$C_{42.41}H_{36}F_{12}N_6O_4P_2Ru$	$C_{45}H_{45}F_{12}N_9O_{0.5}P_2Ru$
Formula weight	1084.70	1110.91
Temperature	200(2) K	200(2) K
Wavelength	1.54178 Å	1.54178 Å
Crystal system	Monoclinic	Monoclinic
Space group	$P2_1$ - C_2^2 (No. 4)	$P2_1$ - C_2^2 (No. 4)
a	11.7917(10) Å	11.7769(5) Å
b	19.7081(14) Å	19.6256(8) Å
c	12.3211(11) Å	12.3972(5) Å
a	90°	90°
β	110.665(5)°	110.8508(17)°
γ	90°	90°
Volume	2697.1(4) $Å^3$	2677.70(19) $Å^3$
Z	2	2
Density (calculated)	1.345 g/cm^3	1.398 g/cm^3
Absorption coefficient	3.682 mm^{-1}	3.661 mm^{-1}
F(000)	1093	1128
Crystal size	0.540 x 0.097 x 0.060 mm^3	0.204 x 0.051 x 0.027 mm^3
Number of data frames/time	2217/8-30 seconds	2291/4-6 seconds
Theta range	4.44 to 68.72°	3.82 to 70.23°
Index ranges	$-13\leq h\leq 13$, $-16\leq k\leq 23$, $-14\leq l\leq 14$	$-14\leq h\leq 13$, $-21\leq k\leq 23$, $-14\leq l\leq 14$
Reflections collected	17556	19973
Independent reflections	7199 [R_{int} = 0.069]	7988 [R_{int} = 0.053]
Completeness/θ_{max}	99.0%/66.00°	99.5%/66.00°
Absorption correction	Multi-scan	Numerical face-indexed
Max. and min. transmission	1.000 and 0.500	0.823 and 0.265
Refinement method	Full-matrix least-squares on F^2	Full-matrix least-squares on F^2
Data / restraints / parameters	7199 / 43 / 640	7988 / 1 / 641
Goodness-of-fit on F^2	1.057	1.072
Final R indices [I>2σ(I)]	R_1 = 0.112, wR_2 = 0.294	R_1 = 0.053, wR_2 = 0.141
R indices (all data)	R_1 = 0.125, wR_2 = 0.309	R_1 = 0.055, wR_2 = 0.143
Largest diff. peak and hole	1.84 and -1.05 $e^-/Å^3$	1.18 and -0.95 $e^-/Å^3$

Special Refinement Details for 2.

No special refinement was required

Full Solid-state Structure of 2.

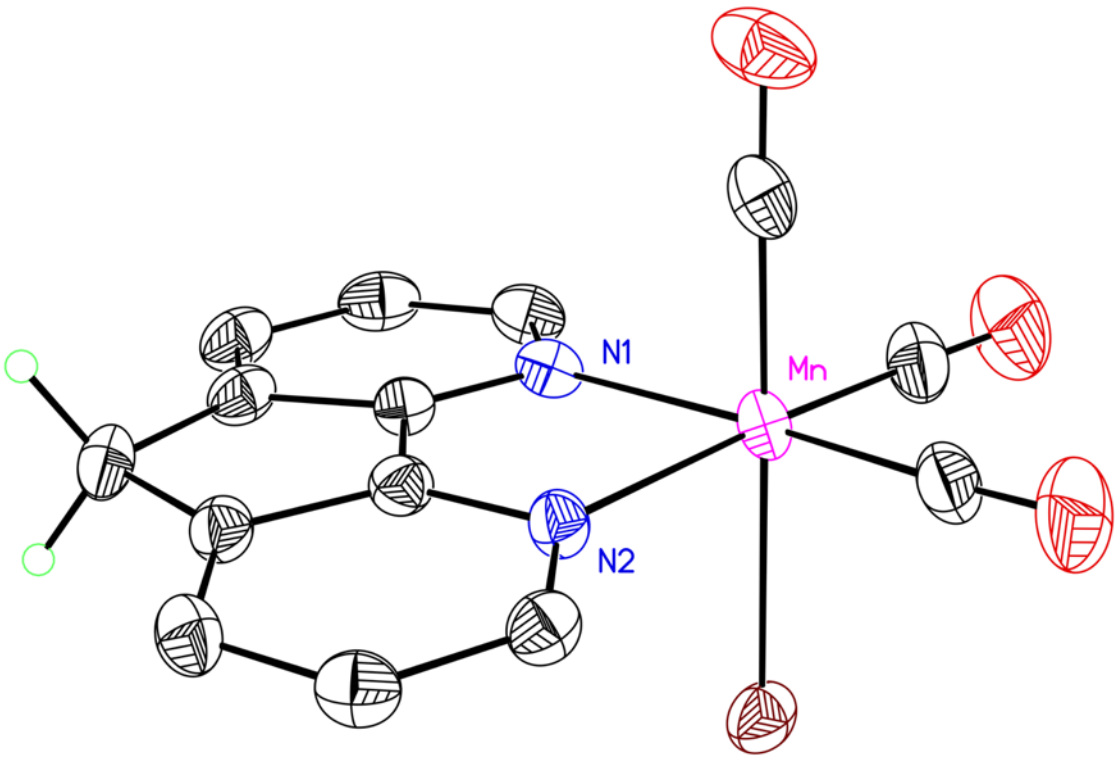

Figure D42: Full solid-state structure of **2**. Hydrogen atoms are omitted for clarity except on the methylene backbone. Displacement ellipsoids shown at the 50% probability level.

Special Refinement Details for 3.

Since Br and trans-coordinated CO ligands bonded to Mn have similar sizes and shapes, it is not surprising that the C_s- $Mn(CO)_3(N_2C_{13}H_{12})Br$ molecule (**3**) might pack in a disordered fashion with the Br and trans-coordinated CO ligands interchanged 31% of the time. This disorder necessitated mild bond length and angle restraints for this disordered group of atoms. The Mn-Br, Mn-Br′, Mn-O1, Mn-O1′, Mn-C1, Mn-C1′, C1-O1, C1′-O1′and C2-O2 bond lengths in **3** were all mildly restrained to have values which were appropriate multiples of the Mn-Br bond length that was included as a free variable in the least-squares refinement and refined to a final value of 2.406(7)Å. When the isotropic thermal parameter for C1′ refined to an unrealistically high value, it was fixed at a value equal to the average of Mn and O1′.

Solid-state Structure of 3.

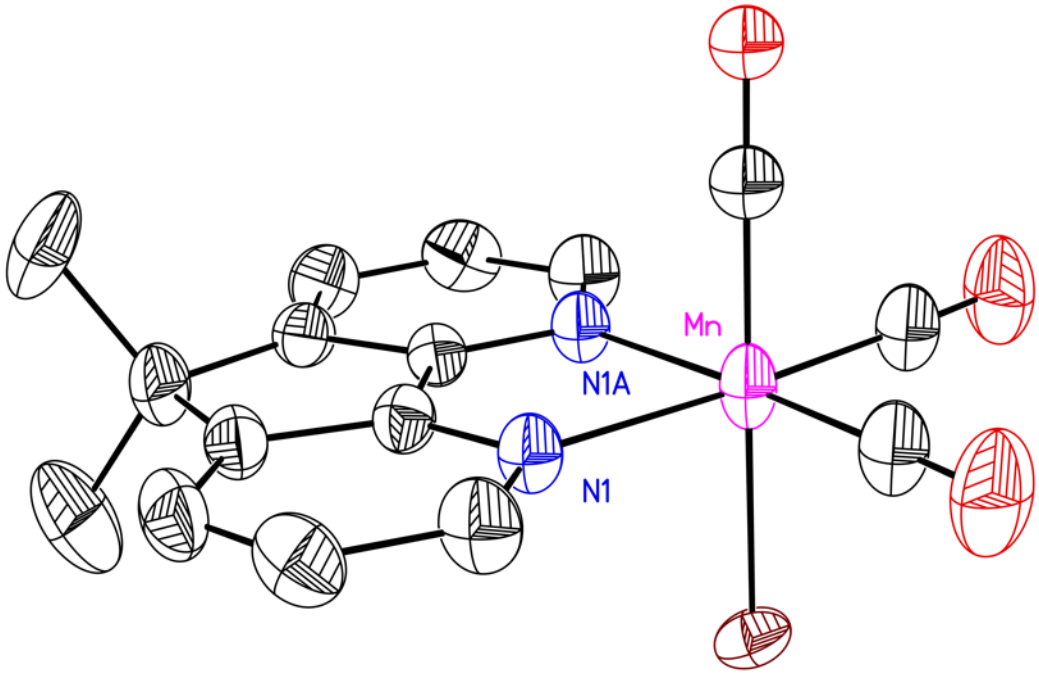

Figure D43: Solid-state structure of **3**. Hydrogen atoms, a second molecule of **3** is omitted for clarity. Displacement ellipsoids shown at the 50% probability level.

Full Solid-state Structure of 3.

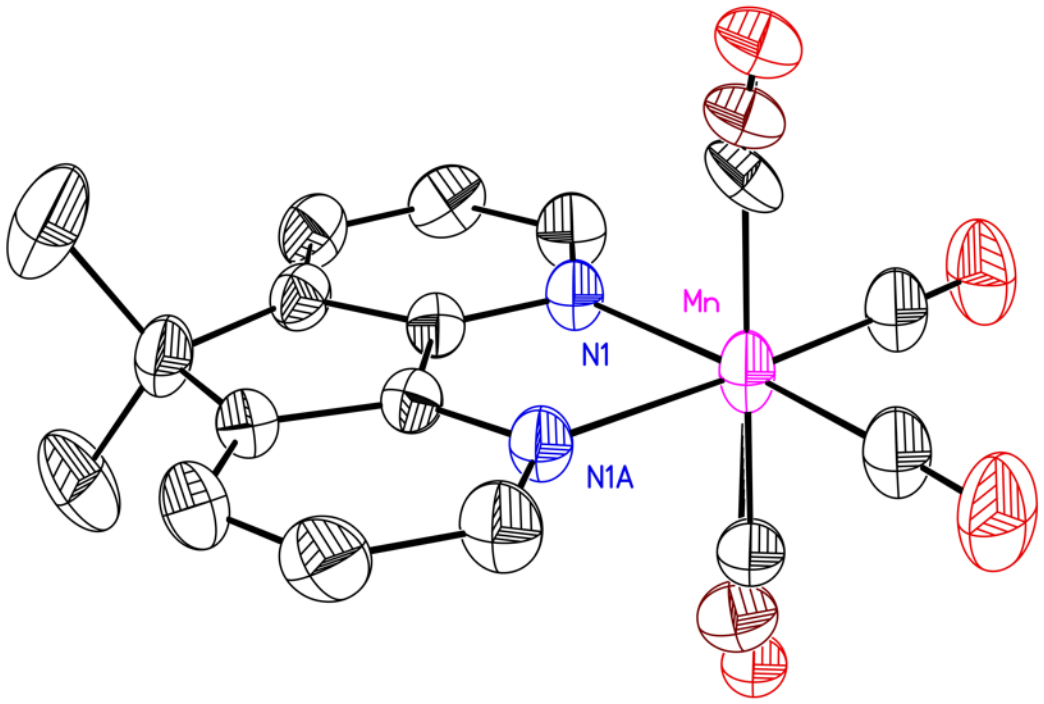

Figure D44: Full solid-state structure of **3**. Hydrogen atoms are omitted for clarity.

Displacement ellipsoids shown at the 50% probability level.

Special Refinement Details for 5 (v74e).

The solvent molecules of crystallization in **5(v74e)** are disordered and hydrogen atoms were not included for them in the structural model. A methanol molecule (atoms O3S and C4S) is present 41% of the time and a nearby water molecule (oxygen O1W) is present the remaining 59% of the time. A second water molecule is 77/23 disordered over two closely-spaced sites (oxygen atoms O2W and O2W'). We note explicitly here that no rigorous H-bonding scheme could be detected for these solvent molecules of crystallization, and thus the structural details of the solvent molecules of crystallization remain elusive. However, these details do not impact the assignment and structural details associated with the $[Ru(Me_2daf)_3]^{2+}$ core.

The structure of **5(v74e)** was refined as a 52/48 racemic twin.

Solid-state Structure of 5 (v74e).

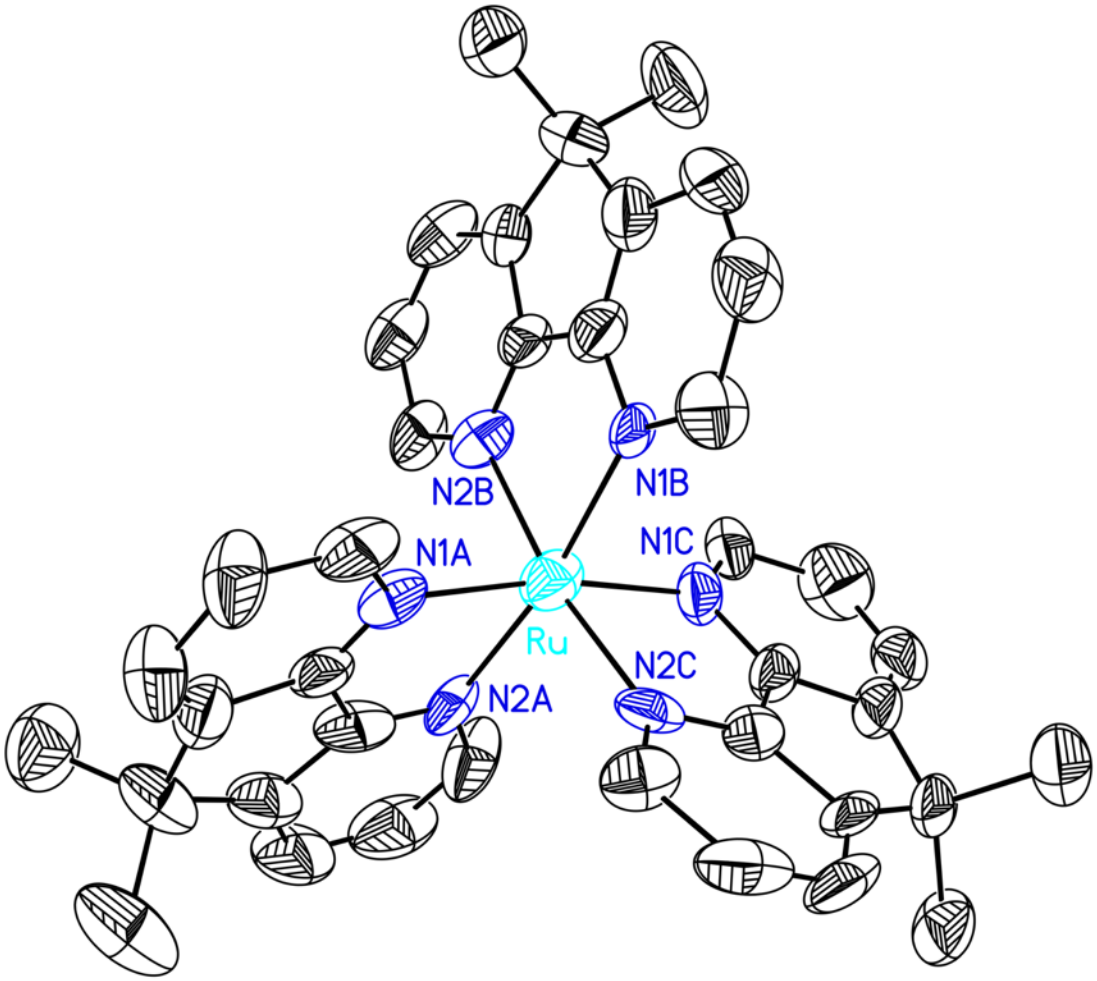

Figure D45: Solid-state structure of **5(v74e)**. Hydrogen atoms and co-crystalized water, methanol, and ethanol are omitted for clarity. Displacement ellipsoids shown at the 50% probability level.

Full Solid-state Structure of 5 (v74e).

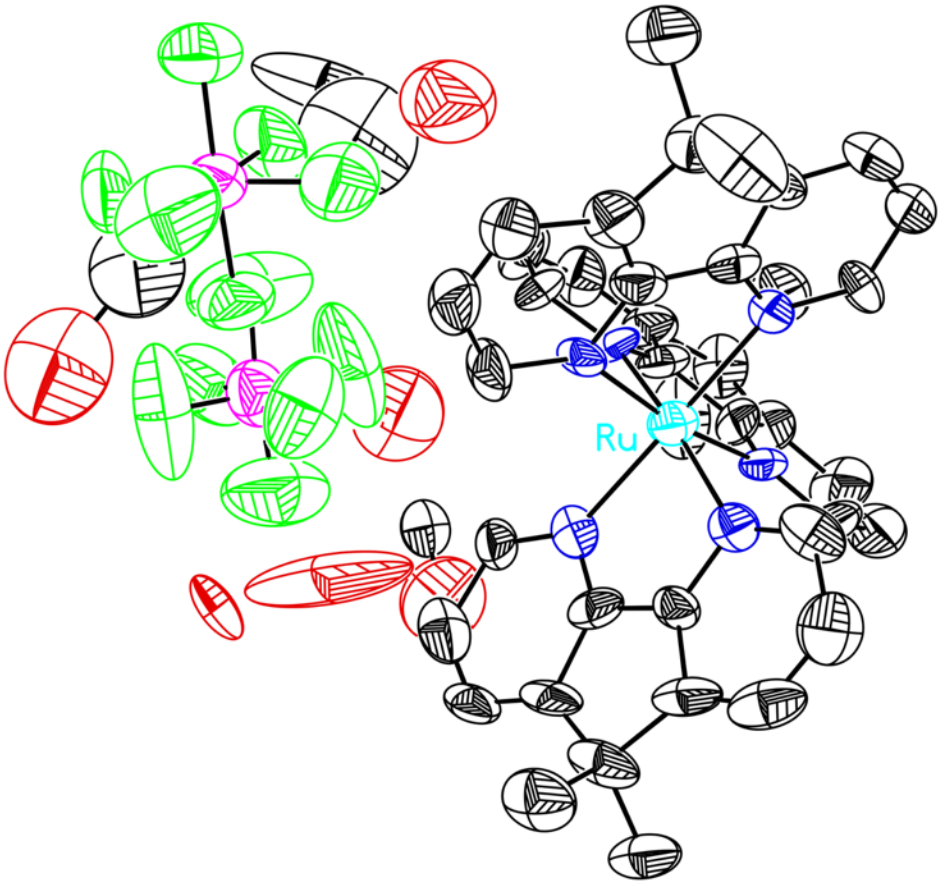

Figure D46: Full solid-state structure of **5(v74e)**. Hydrogen atoms omitted for clarity. Displacement ellipsoids shown at the 50% probability level. Atoms attributable to co-crystalized water, methanol, and ethanol are present.

Special Refinement Details for 5 (q36k).

No special refinement was required

Solid-state Structure of 5(q36k).

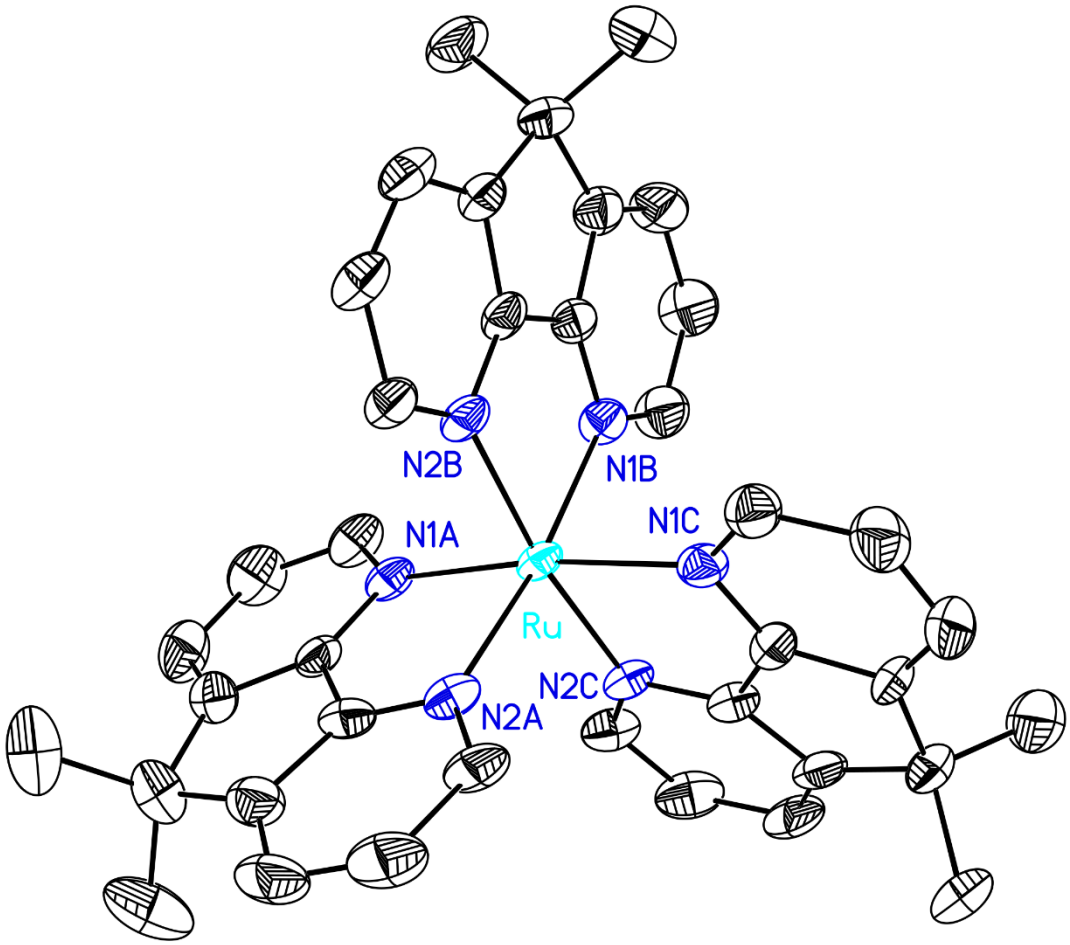

Figure D47: Solid-state structure of **5(q36k)**. Displacement ellipsoids shown at the 50% probability level. Hydrogen atoms, atoms attributable to three co-crystalized acetonitrile molecules, and a water molecule are omitted for clarity.

Full Solid-state Structure of 5 (q36k).

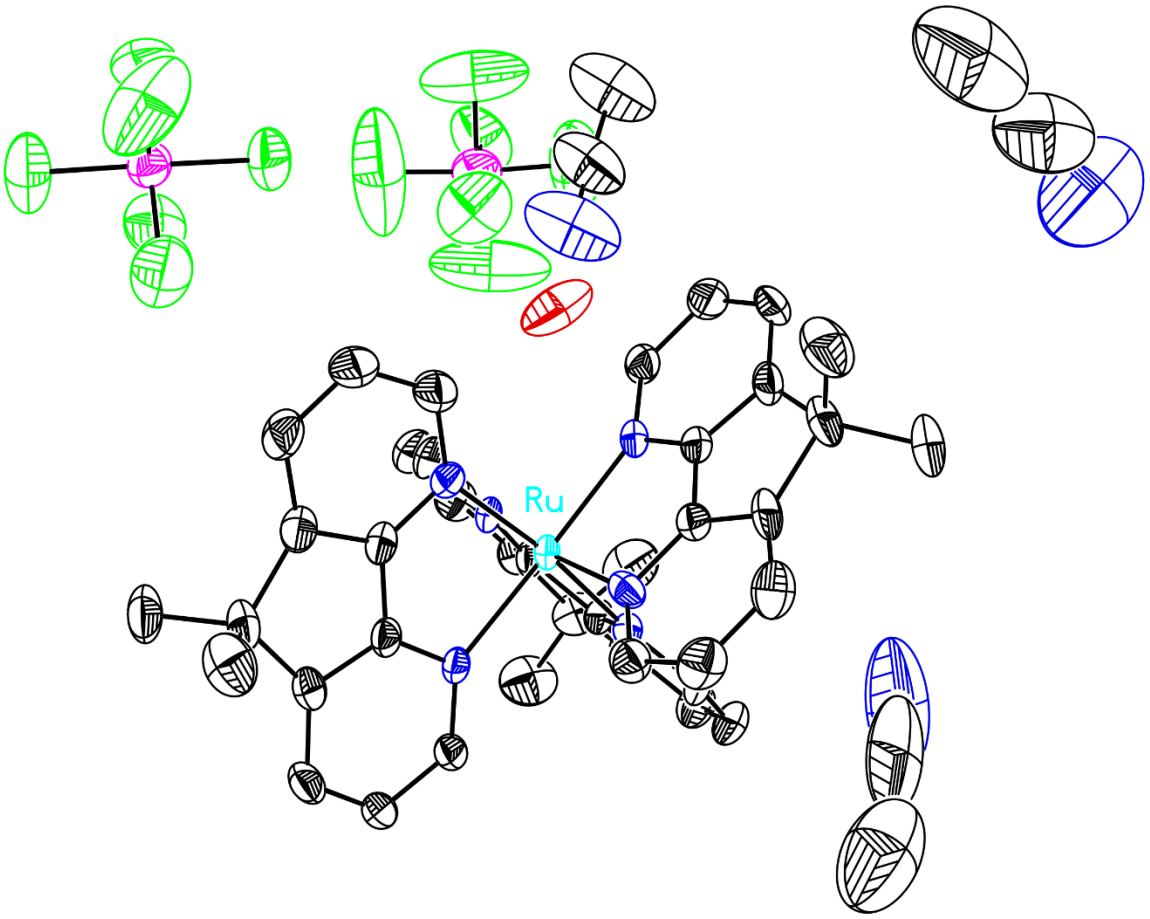

Figure D48: Full solid-state structure of **5(q36k)**. Hydrogen atoms omitted for clarity. Displacement ellipsoids shown at the 50% probability level. Atoms attributable to three co-crystalized acetonitrile molecules and a water molecule are also present.

Table D3: Selected bond lengths.

Bond Lengths (Å)	5 (v74e)	5 (q36k)
Ru–N	2.090(14)	2.104(5)
	2.143(15)	2.108(5)
	2.150(14)	2.114(6)
	2.154(14)	2.123(6)
	2.158(12)	2.125(5)
	2.159(15)	2.130(5)
Ru–N (avg.)	**2.142(34)**	**2.117(13)**
C5-C6	1.39(2)	1.416(9)
	1.40(3)	1.420(9)
	1.43(2)	1.425(9)
C5-C6 (avg.)	**1.41(4)**	**1.420(16)**

Table D4: Selected bond angles.

Bond Angles (°)	**5 (v74e)**	**5 (q36k)**
N–Ru–N	79.5(5)	82.2(2)
	81.7(5)	83.1(2)
	82.1(6)	83.3(2)
N–Ru–N (avg.)	**81.1(9)**	**82.9(3)**
CH_3–C–CH_3	108(2)	109.4(7)
	112(2)	109.9(7)
	109.5(17)	111.9(8)
CH_3–C–CH_3 (avg.)	**110(3)**	**110.4(13)**

References

(1) *APEX2, Version 2 User Manual, M86-E01078,*; Bruker Analytical X-ray Systems: Madison, WI, June 2006.

(2) Sheldrick, G. M., SADABS (version 2008/1): Program for Absorption Correction for Data from Area Detector Frames, University of Göttingen, 2008.

(3) Sheldrick, G. Crystal structure refinement with SHELXL. *Acta Crystallogr., Sect. A: Found. Crystallogr.* **2015**, *71*, 3-8.

(4) Dolomanov, O. V.; Bourhis, L. J.; Gildea, R. J.; Howard, J. A. K.; Puschmann, H. *J. Appl. Crystallogr.* **2009**, *42*, 339-341.

Appendix E

Supplementary Information for Chapter 7

NMR Spectra

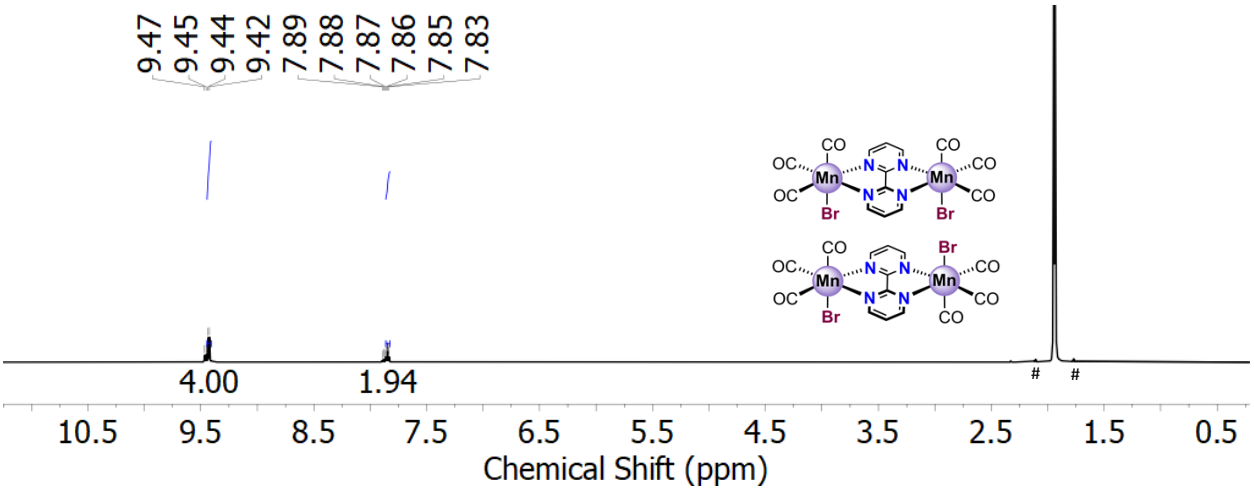

Figure E1: ^{1}H-NMR spectrum (400 MHz, CD_3CN) of **5-syn + 5-anti**. The # symbols denote ^{13}C satellites on the CD_3CN protio-solvent residual.

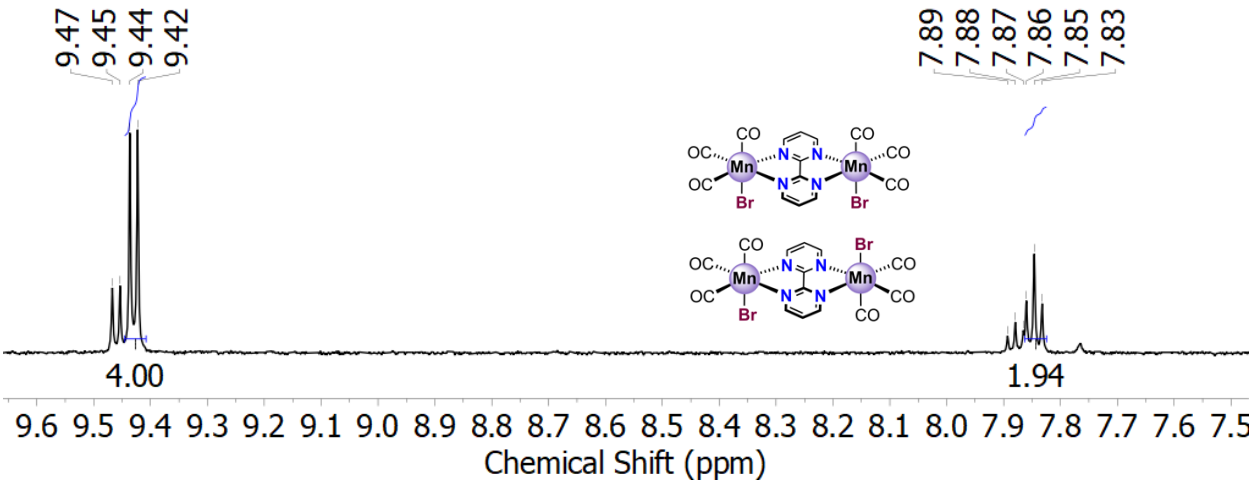

Figure E2: Zoomed-in ^{1}H-NMR spectrum (400 MHz, CD_3CN) of **5-syn + 5-anti** highlighting the aromatic region.

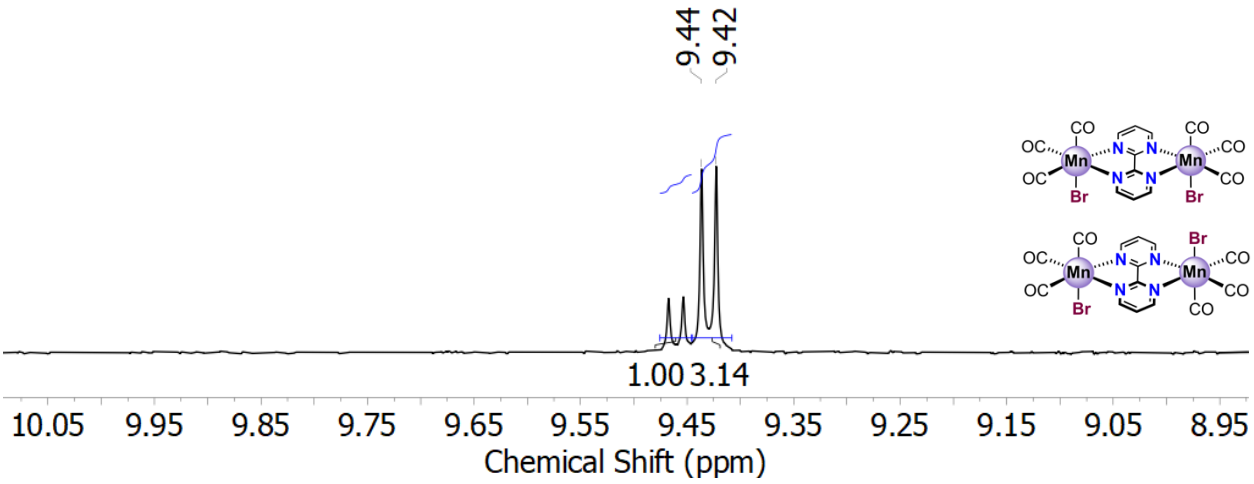

Figure E3: ^{1}H-NMR spectrum (400 MHz, CD_3CN) comparing the ratio of **5-syn** + **5-anti**.

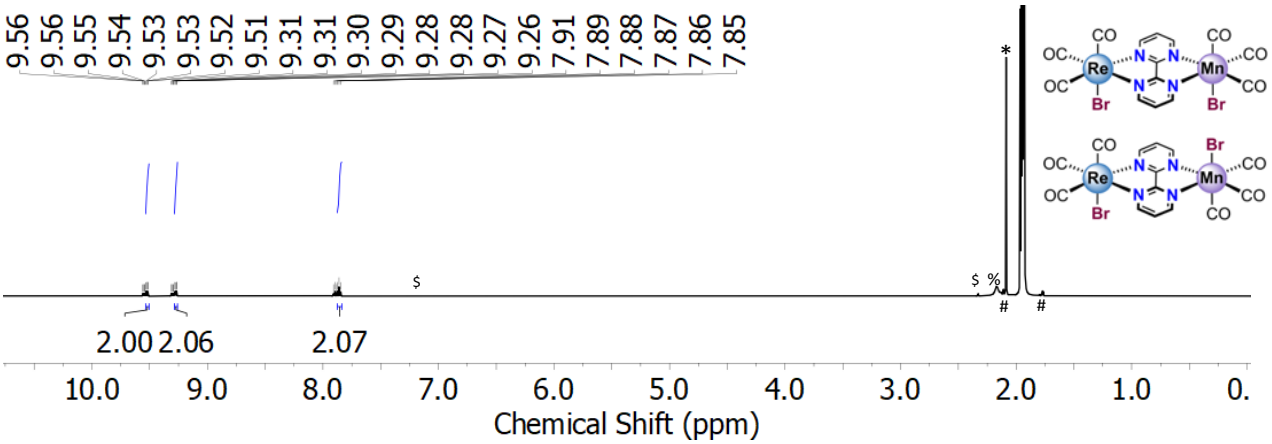

Figure E4: ^{1}H-NMR spectrum (400 MHz, CD_3CN) of **6-syn + 6-anti**. The symbols denote the ^{13}C satellites on the CD_3CN protio-solvent residuals (#), toluene ($), water (%), and adventitious acetone (*).

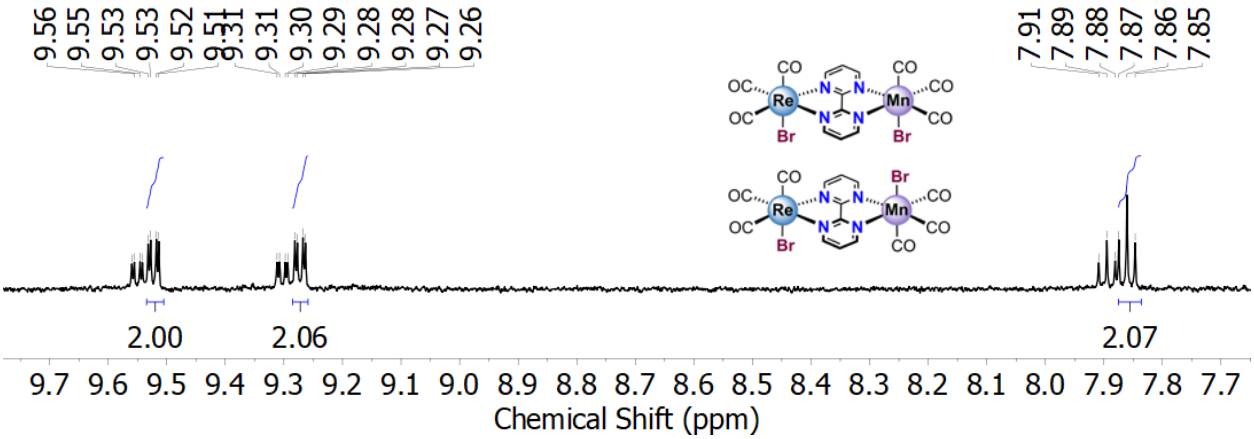

Figure E5: Zoomed-in ^{1}H-NMR spectrum (400 MHz, CD_3CN) of **6-syn + 6-anti**

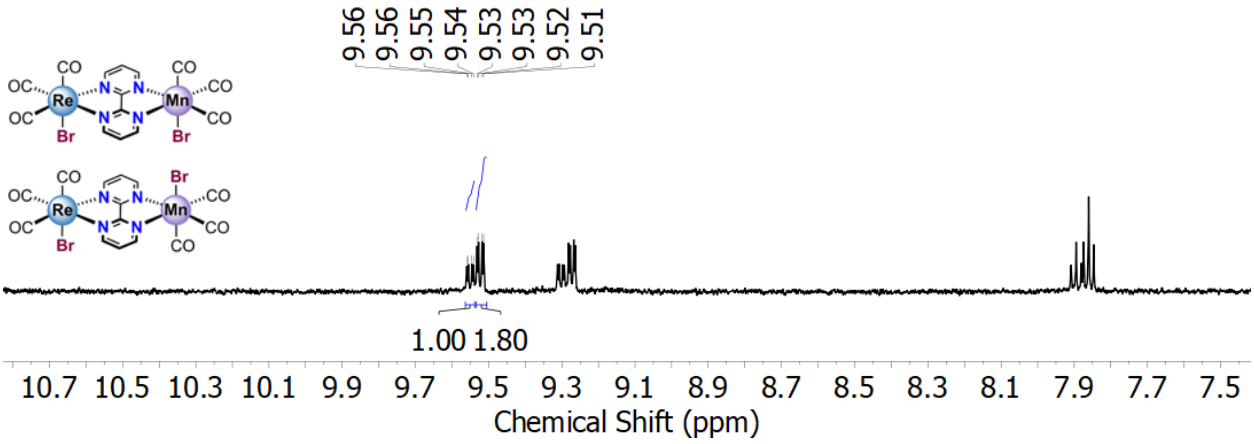

Figure E6: ^{1}H-NMR spectrum (400 MHz, CD_3CN) comparing the ratio of **6-syn** + **6-anti**.

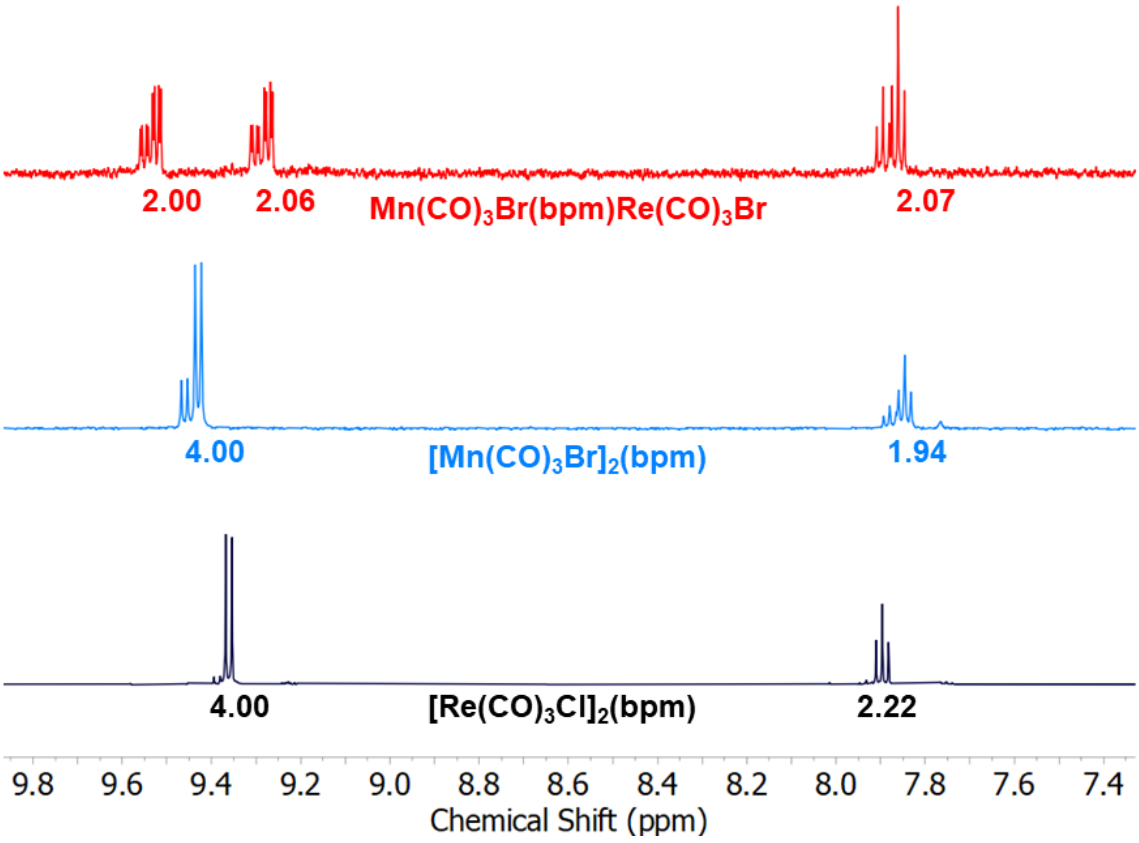

Figure E7: Stacked ^{1}H-NMR spectra (400 MHz, CD_3CN) of **2-syn + 2-anti (black), 5-syn + 5-anti (blue), and 6-syn + 6-anti (red)**. The presence of both **syn-** and **anti**-isomers give rise to the additional resonances in the spectra.

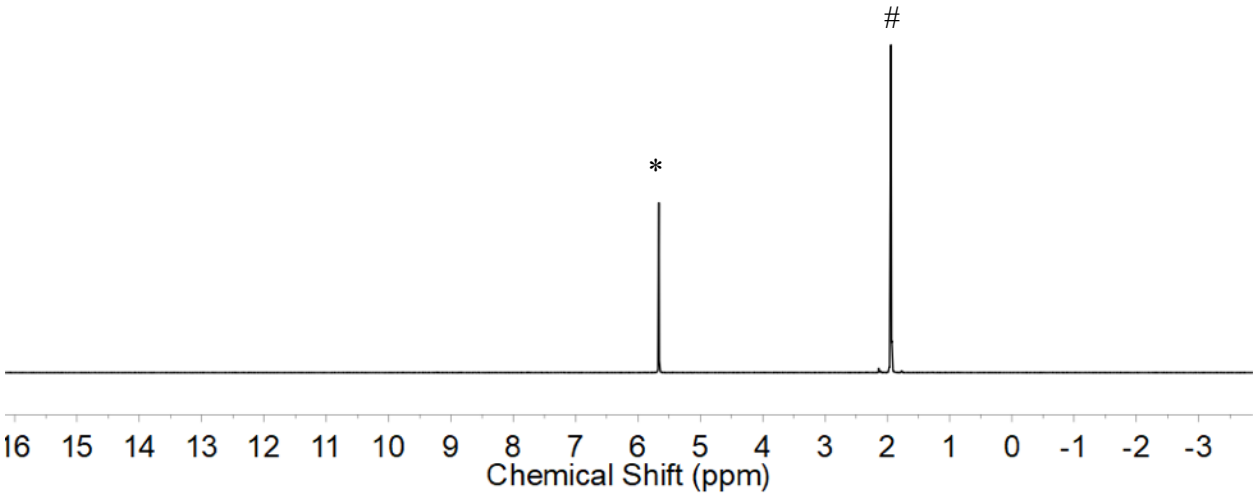

Figure E8: The resulting ^{1}H-NMR spectrum (400 MHz, CD_3CN) following the *in situ* one e^- reduction of complex **2-syn + 2-anti** using the stoichiometric reductant Cp_2Co. The resulting complex is NMR silent, consistent with the presence of an expected paramagnetic species. The presence of $[Cp_2Co]Cl$ (*, 5.66 ppm) and the solvent residual $CD_2(H)CN$ (#).

IR Spectra

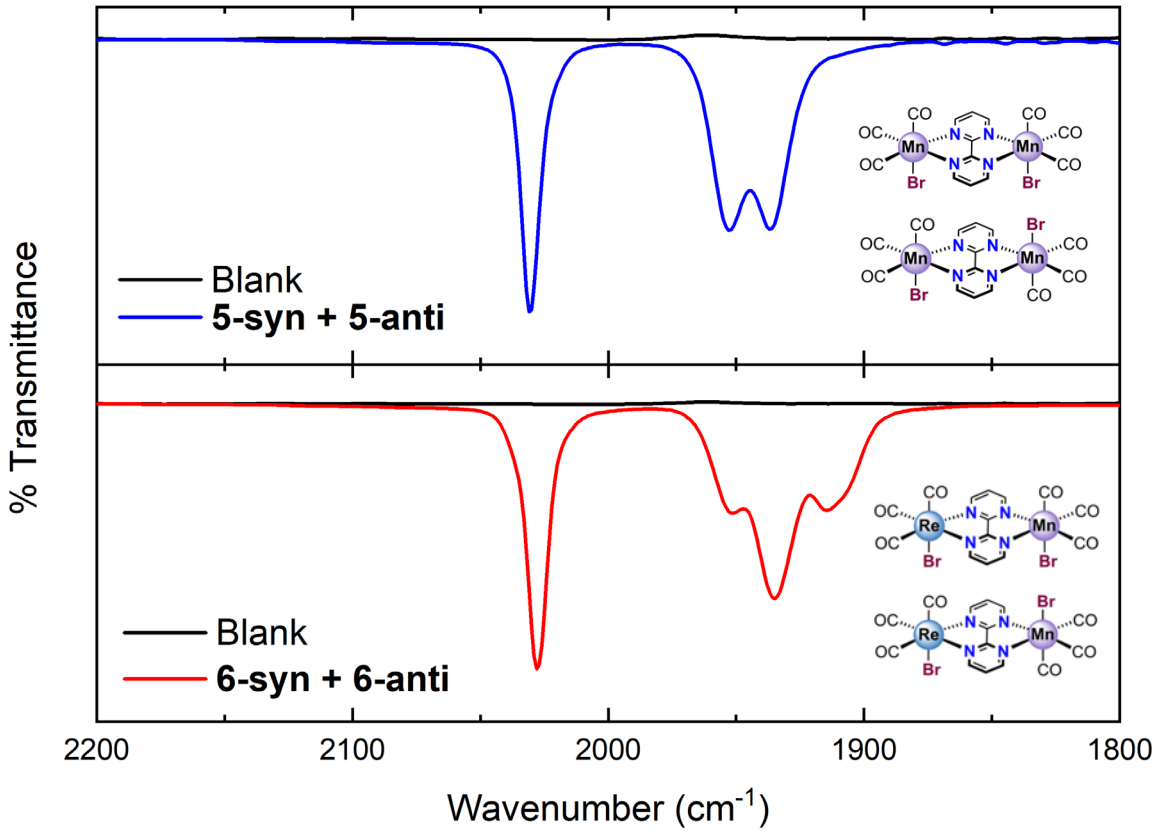

Figure E9: IR spectra for the CO stretching region showing the carbonyl stretches for **5-syn** + **5-anti** (upper panel) and **6-syn** + **6-anti** (lower panel) in THF solution. The greater number of CO stretches for **6-syn** + **6-anti** in comparison to **5-syn** + **5-anti** can be attributed to the lower symmetry of the heterobimetallic compound. The symmetries of **5-syn** + **5-anti** are C_{2v} and C_{2h}, respectively. Group theory analysis predicts that **5-syn** should have six IR active bands while **5-anti** should have three IR active bands. Experimentally, there is likely significant overlap of bands for the CO stretches, as they should have very similar energies, resulting in only three apparent bands. The symmetries of **6-syn** + **6-anti** are both C_s. Group theory analysis thus predicts that both compounds should each have six IR-active CO stretching modes. Experimentally, the observation

of a greater number of overlapping bands is consistent with the decreased symmetry as well as the anticipated electronic difference between the $[Mn(CO)_3]$ and $[Re(CO)_3]$ motifs in both isomers.

High Resolution Mass Spectra

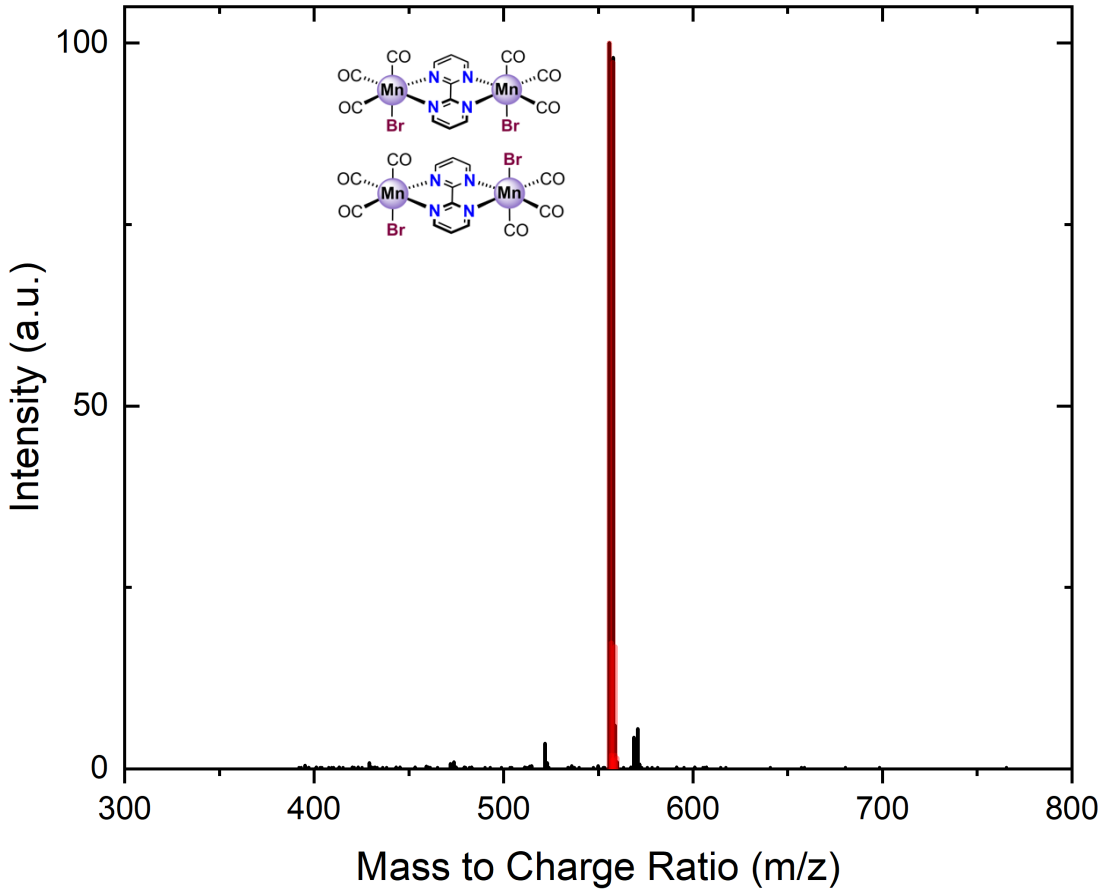

Figure E10: Full high-resolution mass spectrum of **5-syn** + **5-anti**. Both syn and anti isomers could be present and the resulting acetonitrile ligand could bind to either Re or Mn. The experimental data is shown in **black** and the predicted data is shown in **red**. The identified fragment is given in detail below.

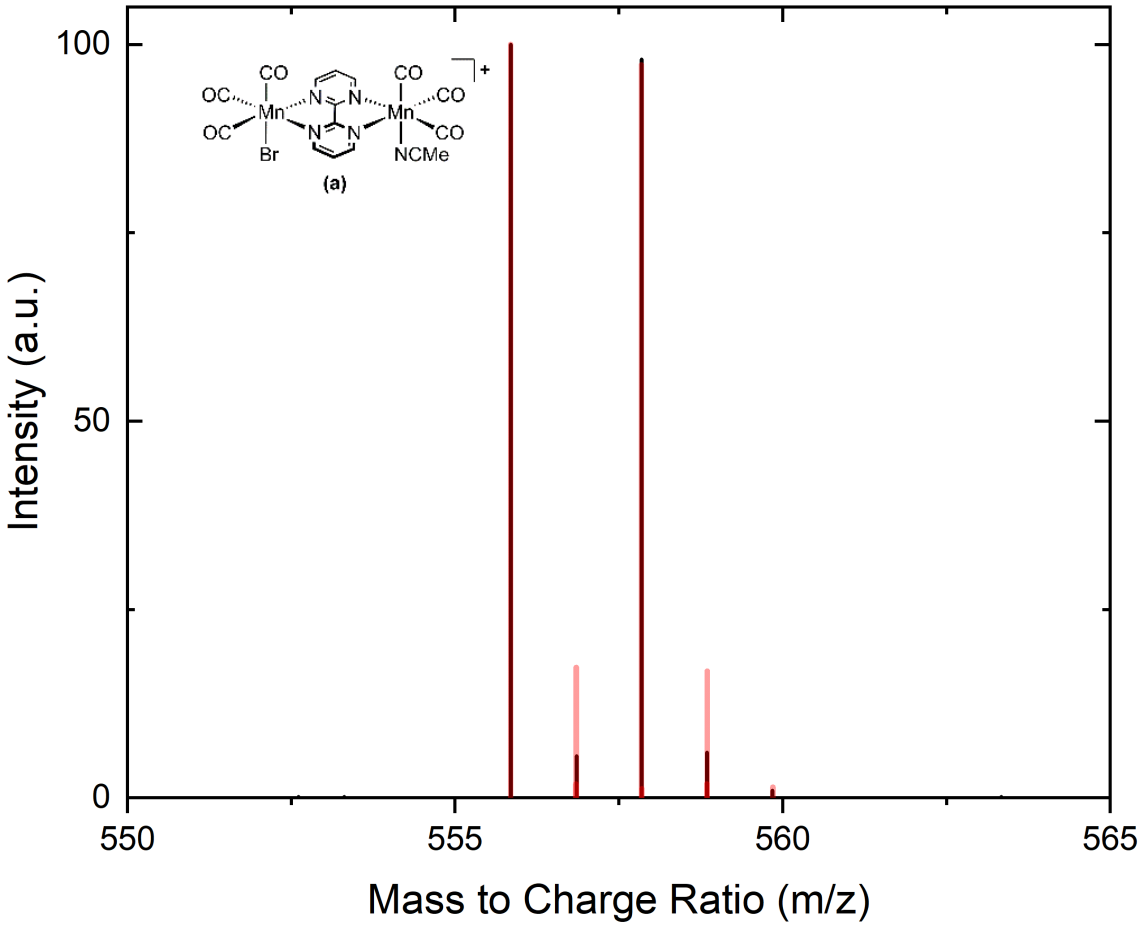

Figure E11: Fragment **(a)** was the identified fragement in the data from Figure S10 (**Experimental: 555.8495; Theoretical: 555.8497**).

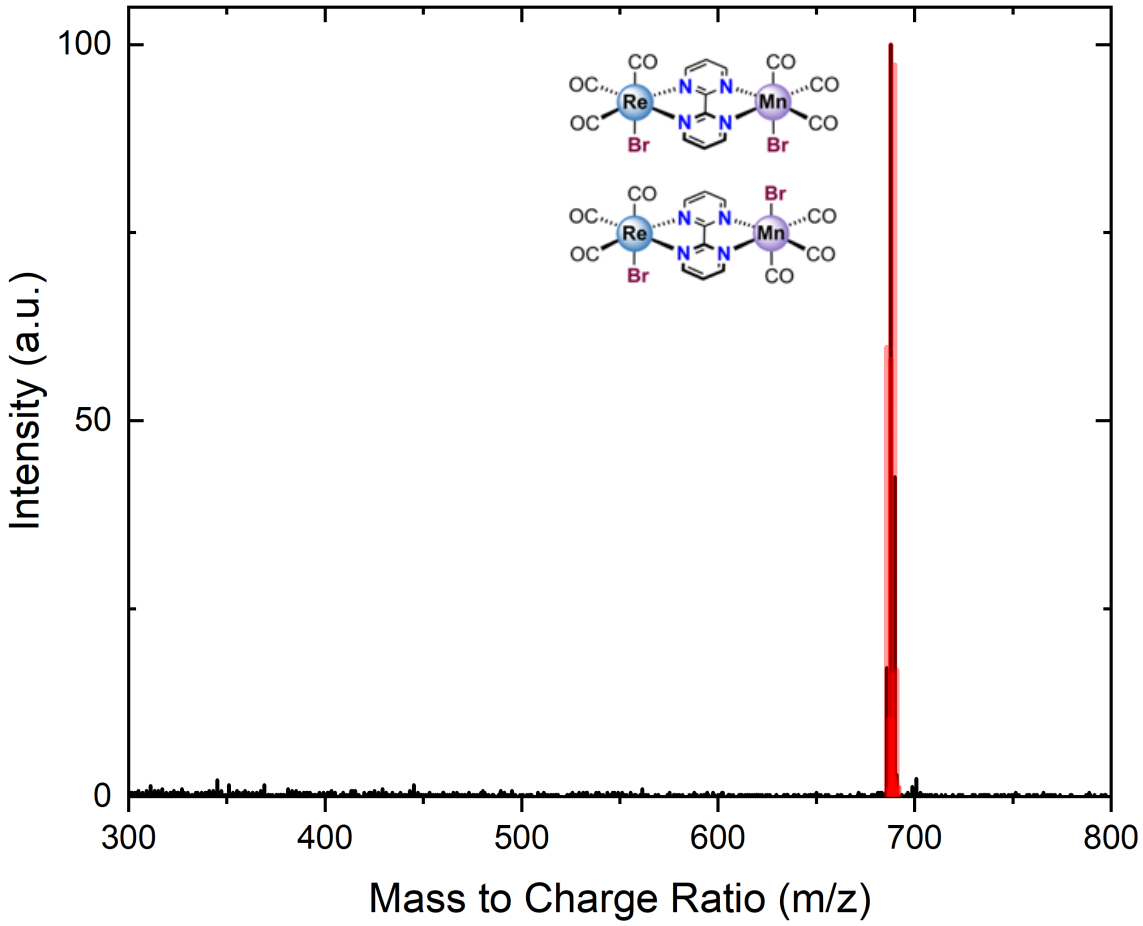

Figure E12: Full high-resolution mass spectrum of **6-syn** + **6-anti**. Both syn and anti isomers could be present, and the resulting acetonitrile ligand could bind to Re or Mn. The experimental data is shown in **black** and the predicted data is shown in **red**. The identified fragment is investigated below.

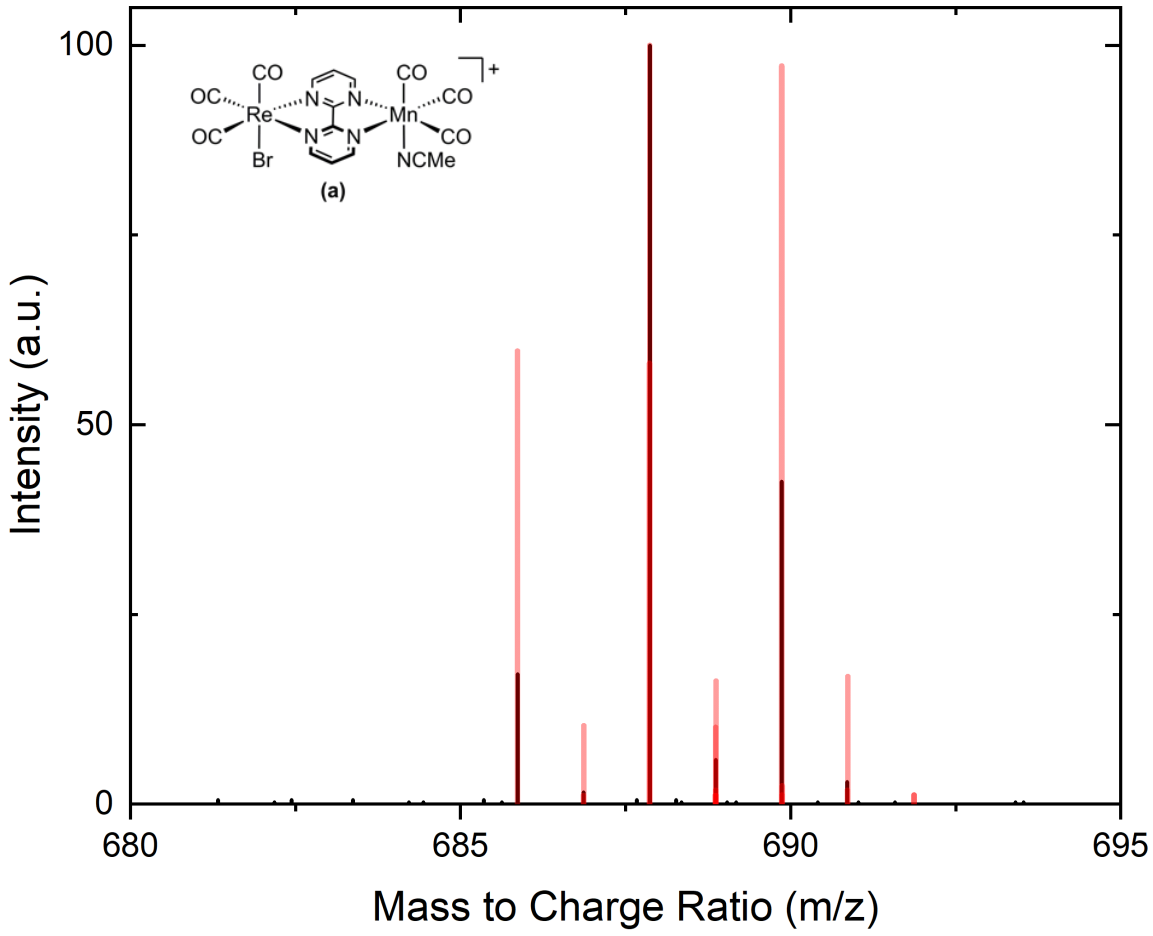

Figure E13: Fragment **(a)** was the identified fragment in the data from Figure S12 (**Experimental: 687.8672; Theoretical: 687.8674**).

Electronic Absorption Spectra

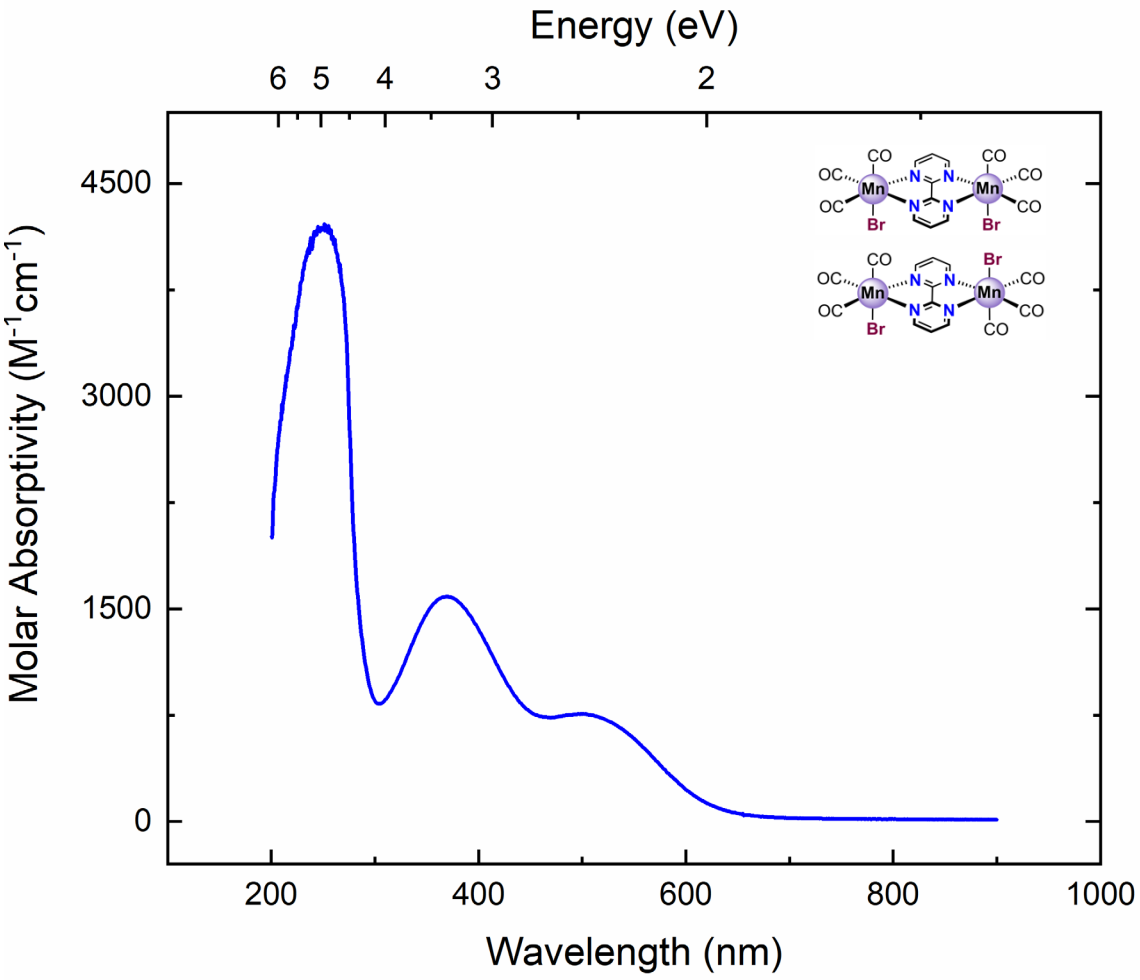

Figure E14: Electronic absorption spectrum of **5-syn** + **5-anti** in MeCN.

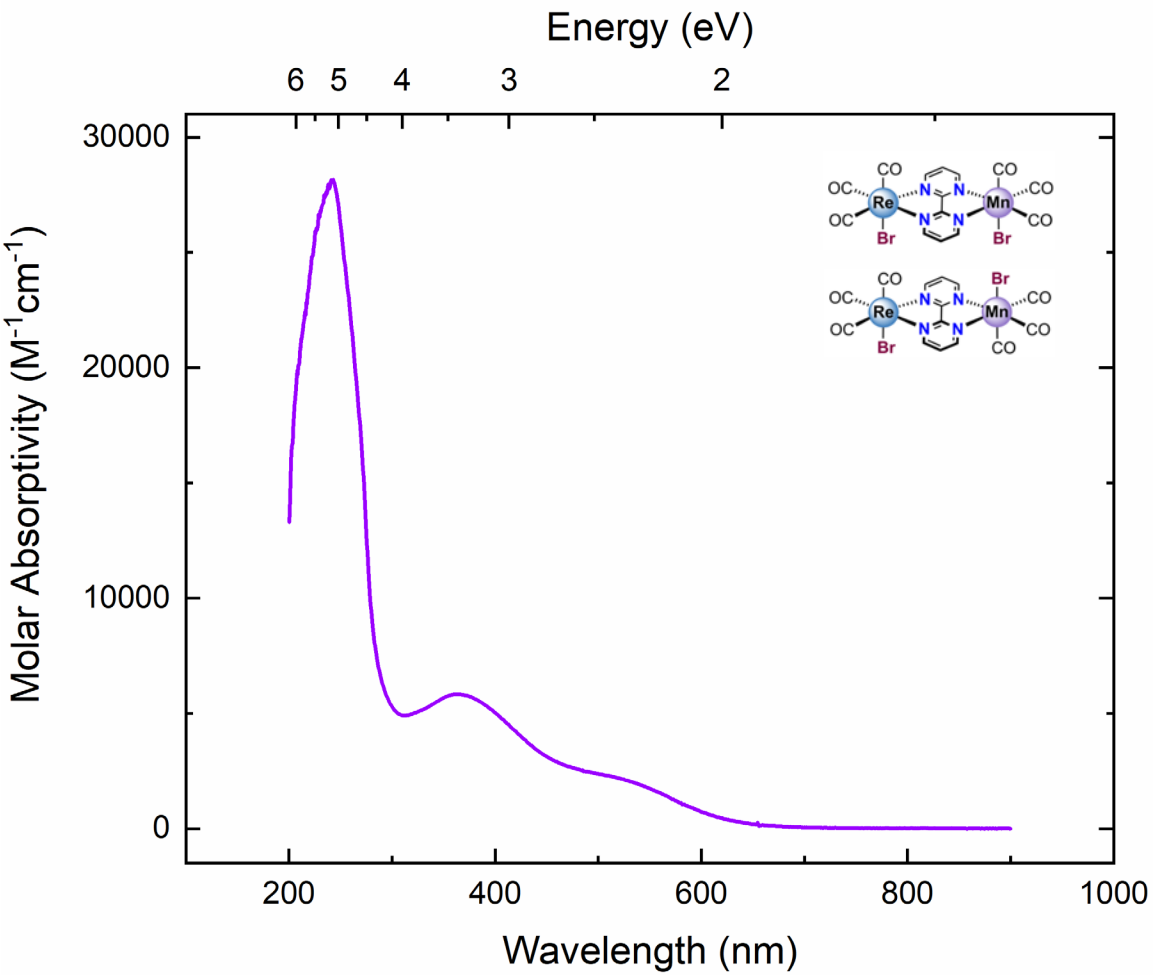

Figure E15: Electronic absorption spectrum of **6-syn** + **6-anti** in MeCN.

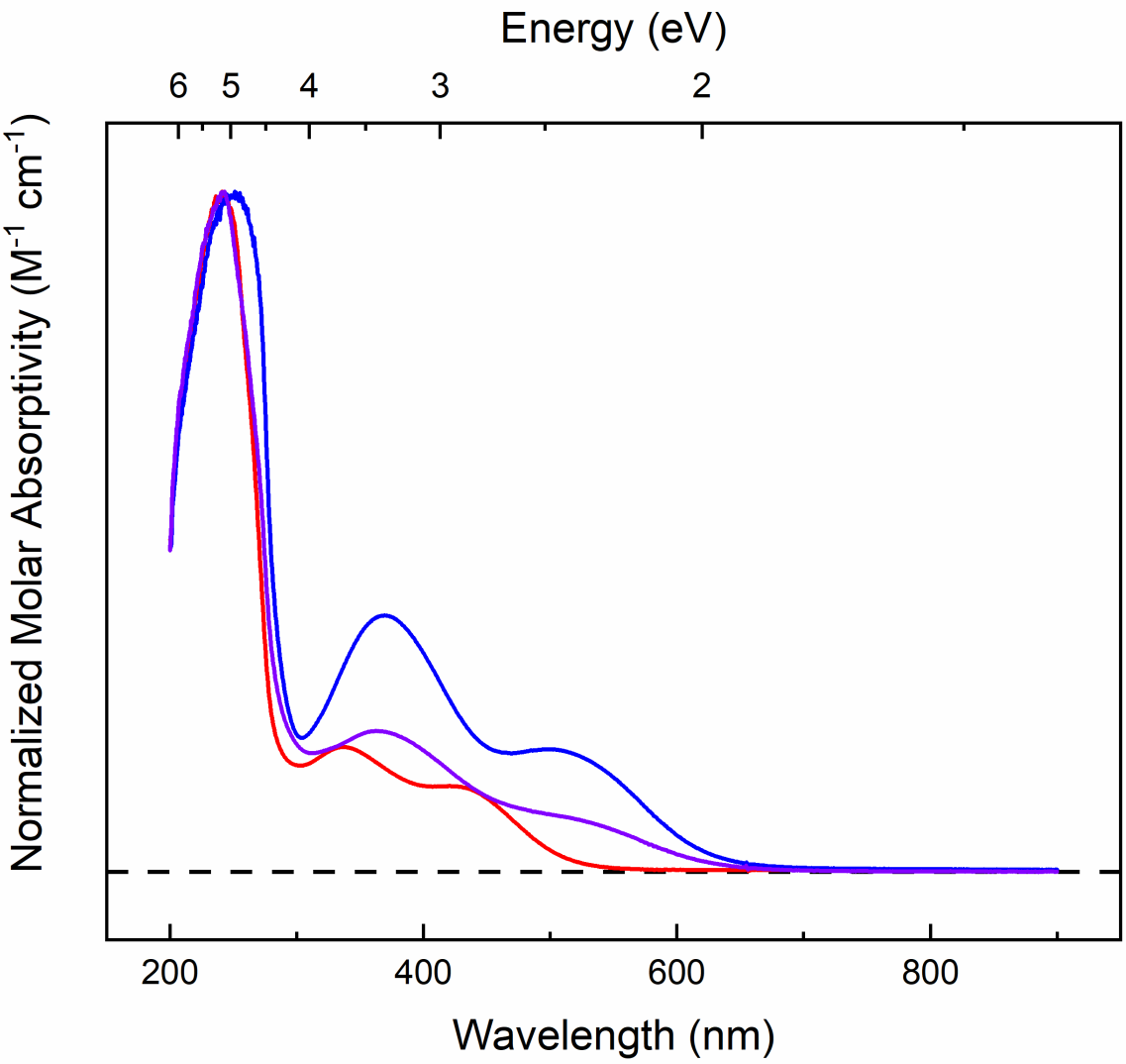

Figure E16: Normalized stacked electronic absorption spectra of **4 (red)**, **5-syn + 5-anti (blue),** and **6-syn + 6-anti (purple)** in MeCN.

Cyclic Voltammetry Data

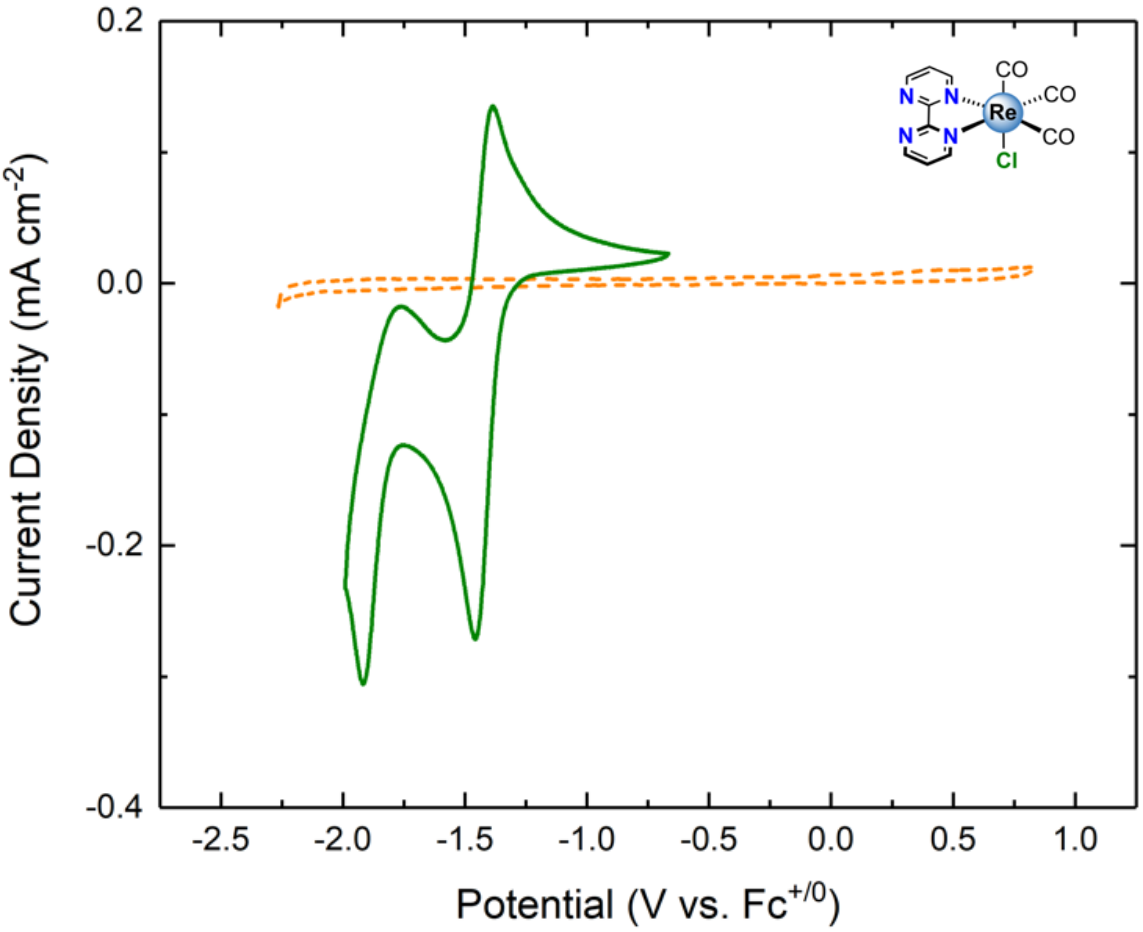

Figure E17: Cyclic voltammogram (100 mV/s) of **1** (**green**) in 0.1M $TBAPF_6$/MeCN solution. The **orange** trace is the blank taken prior to beginning the experiment.

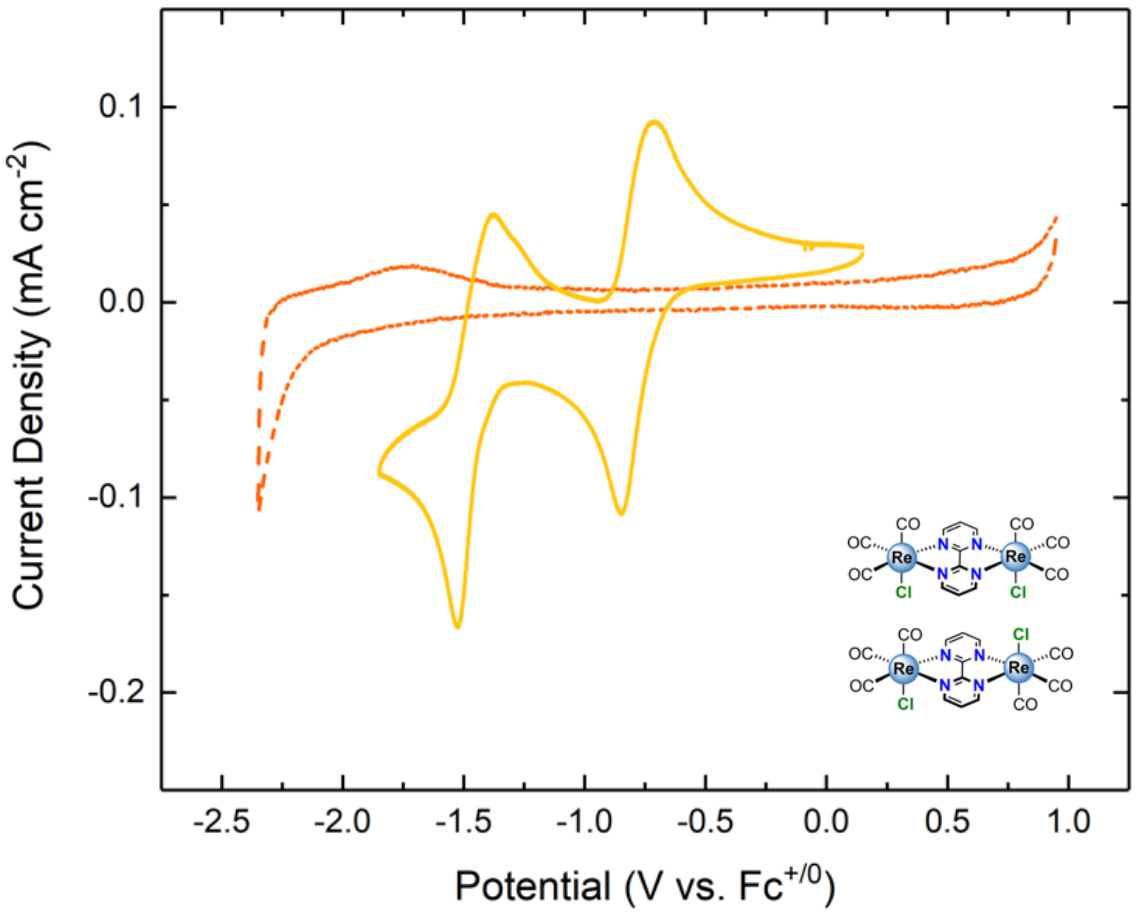

Figure E18: Cyclic voltammogram (100 mV/s) of **2-syn** + **2-anti** (yellow) in 0.1M $TBAPF_6$/MeCN solution. The **orange** trace is the blank taken prior to beginning the experiment.

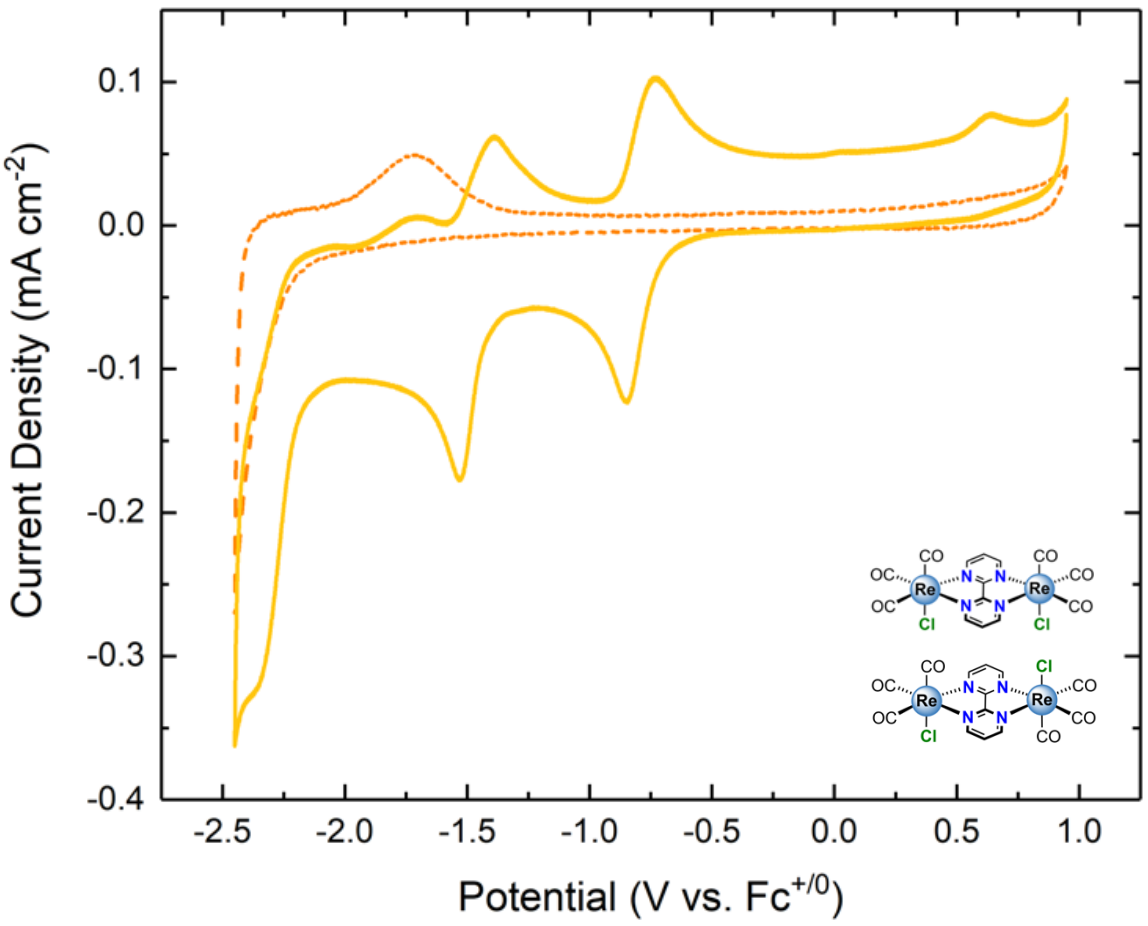

Figure E19: Extended cyclic voltammogram (100 mV/s) of **2-syn** + **2-anti** (yellow) in 0.1M $TBAPF_6$/MeCN solution. The **orange** trace is the blank taken prior to beginning the experiment.

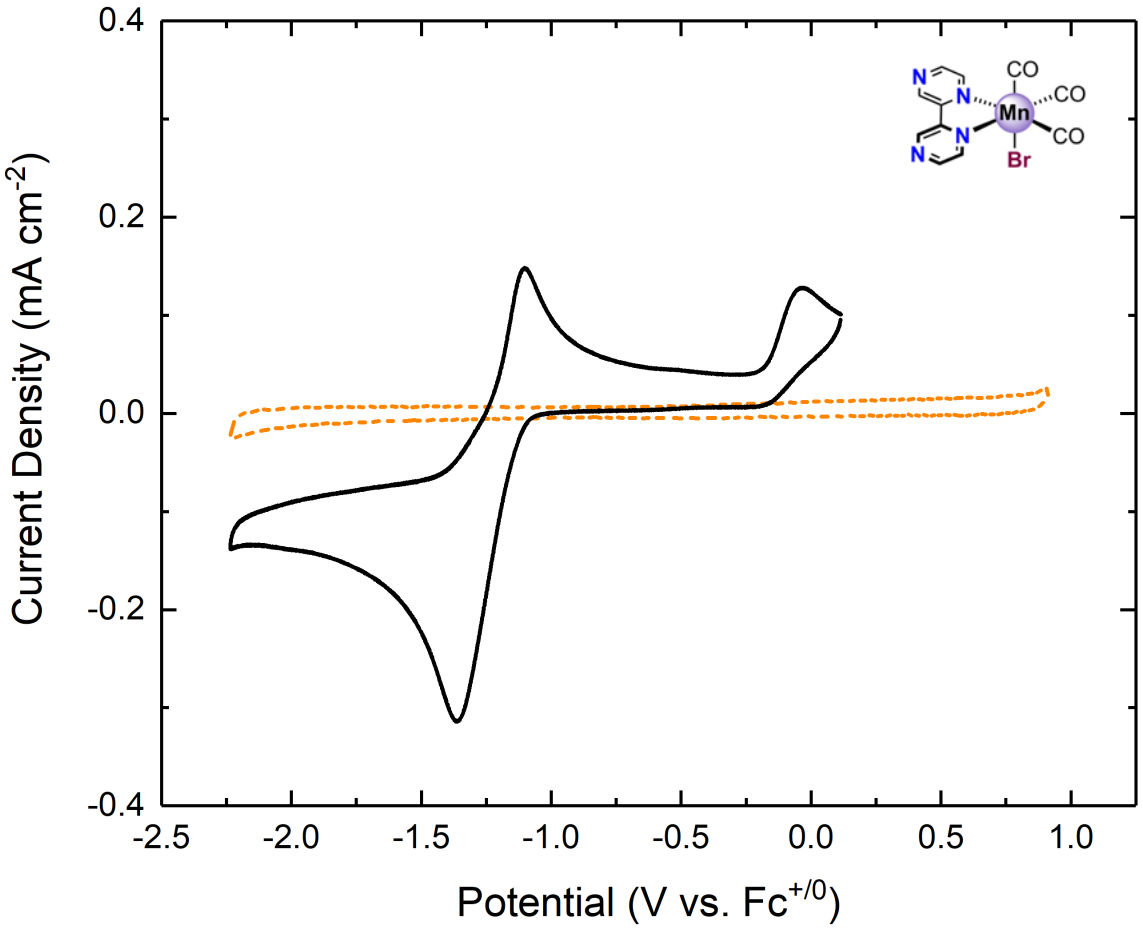

Figure E20: Cyclic voltammogram (100 mV/s) of **3** (**black**) in 0.1M $TBAPF_6$/MeCN solution. The **orange** trace is the blank taken prior to beginning the experiment.

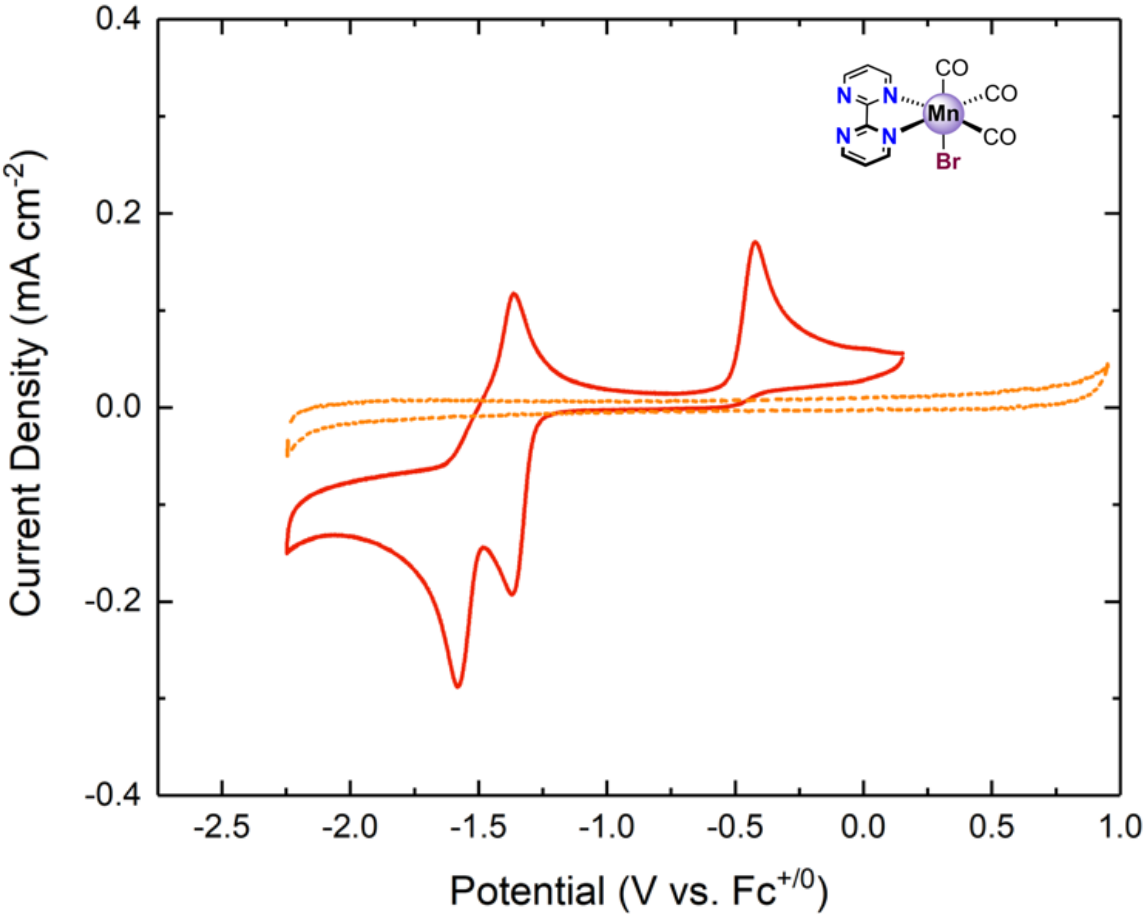

Figure E21: Cyclic voltammogram (100 mV/s) of **4** (**red**) in 0.1M $TBAPF_6$/MeCN solution. The **orange** trace is the blank taken prior to beginning the experiment.

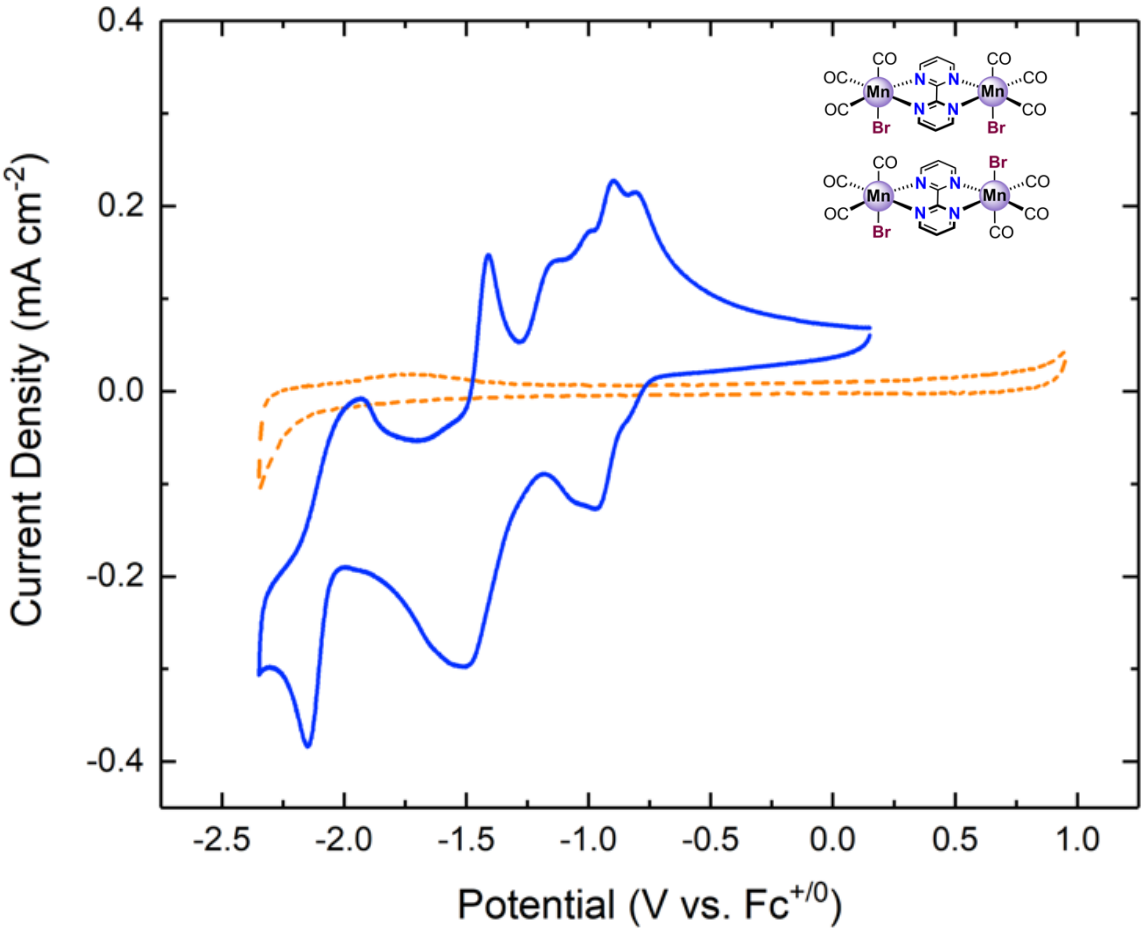

Figure E22: Cyclic voltammogram (100 mV/s) of **5-syn** + **5-anti** (**blue**) in 0.1M $TBAPF_6$/MeCN solution. The **orange** trace is the blank taken prior to beginning the experiment.

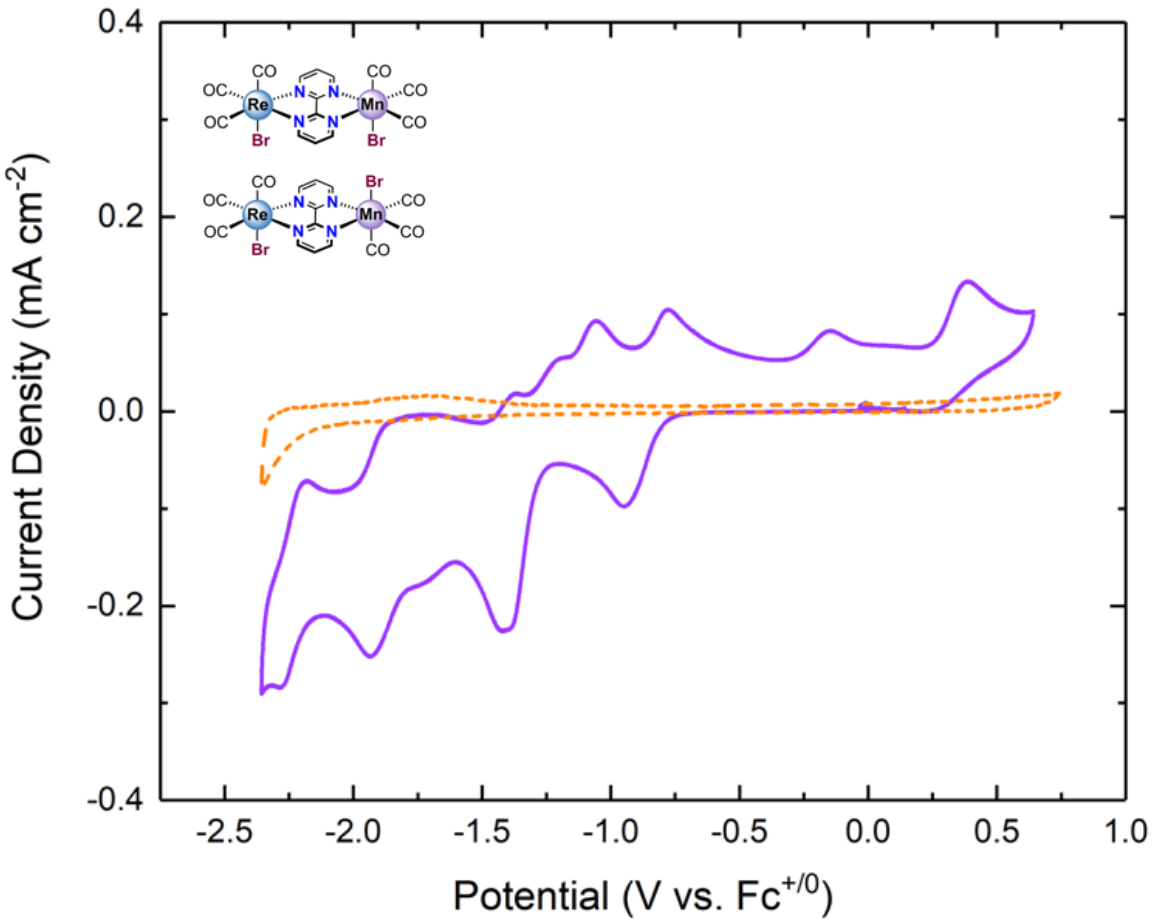

Figure E23: Cyclic voltammogram (100 mV/s) of **6-syn** + **6-anti** (**purple**) in 0.1M $TBAPF_6$/MeCN solution. The **orange** trace is the blank taken prior to beginning the experiment.

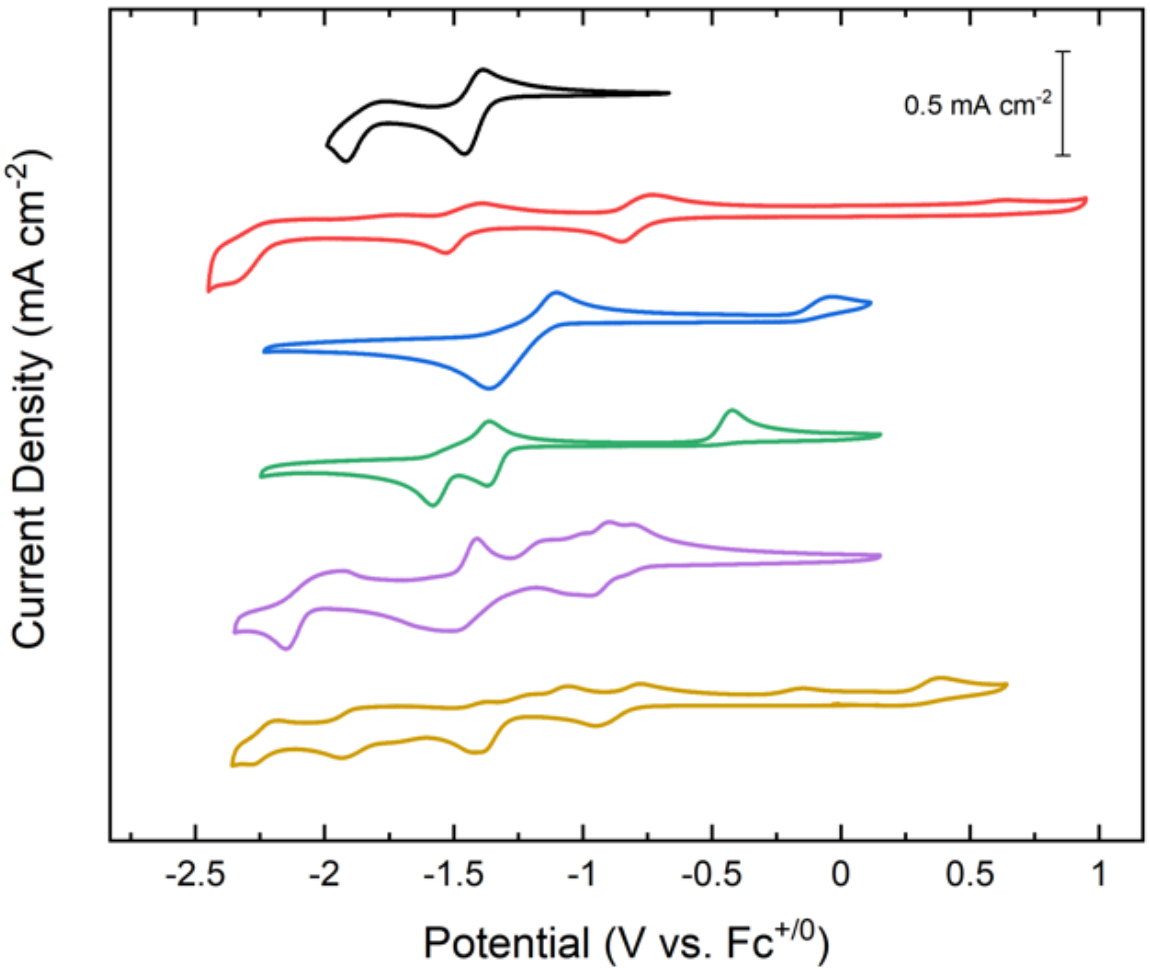

Figure E24: Stacked cyclic voltammograms (100 mV/s) of complexes **1-6** in 0.1M $TBAPF_6$/MeCN solution. **1** (**black**), **2-syn** + **2-anti** (**red**), **3** (**blue**), **4** (**green**), **5-syn** + **5-anti** (**purple**), **6-syn** + **6-anti** (**gold**).

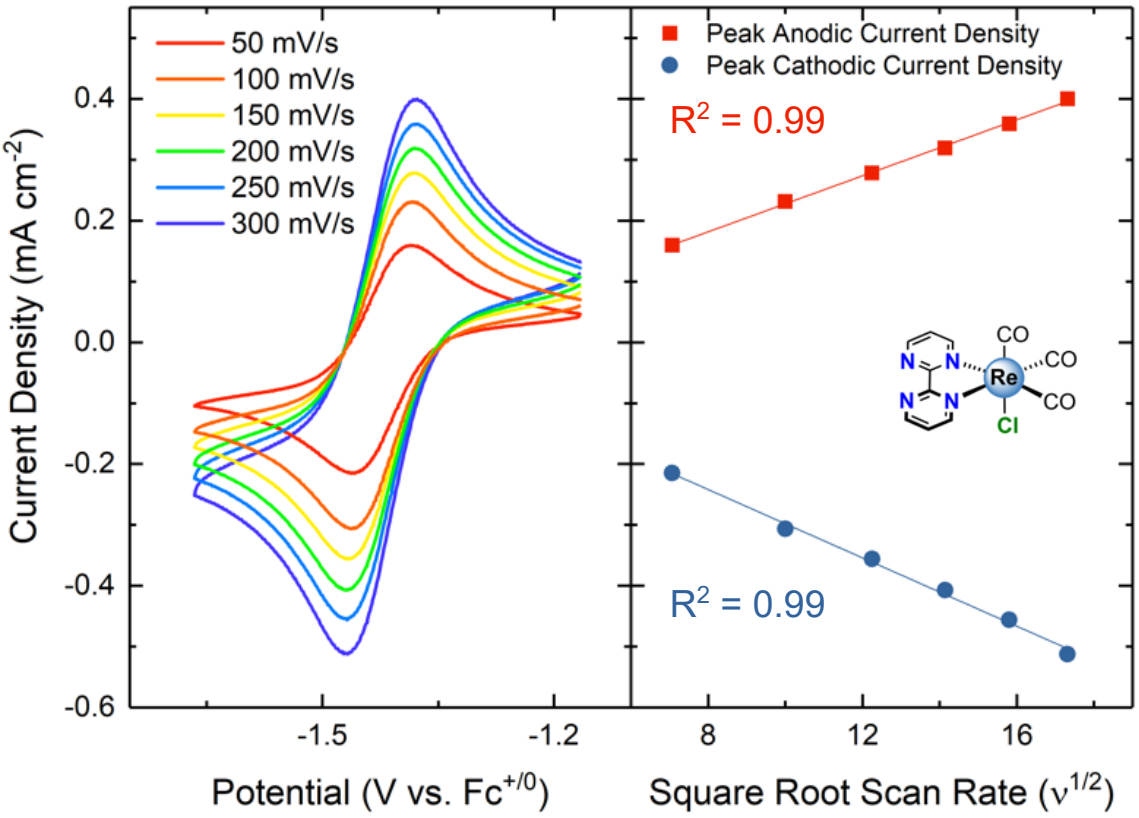

Figure E25: Scan rate dependence studies (left) and peak anodic and cathodic current density as a function of the square root of scan rate (right) for the first redox couple of complex **1**.

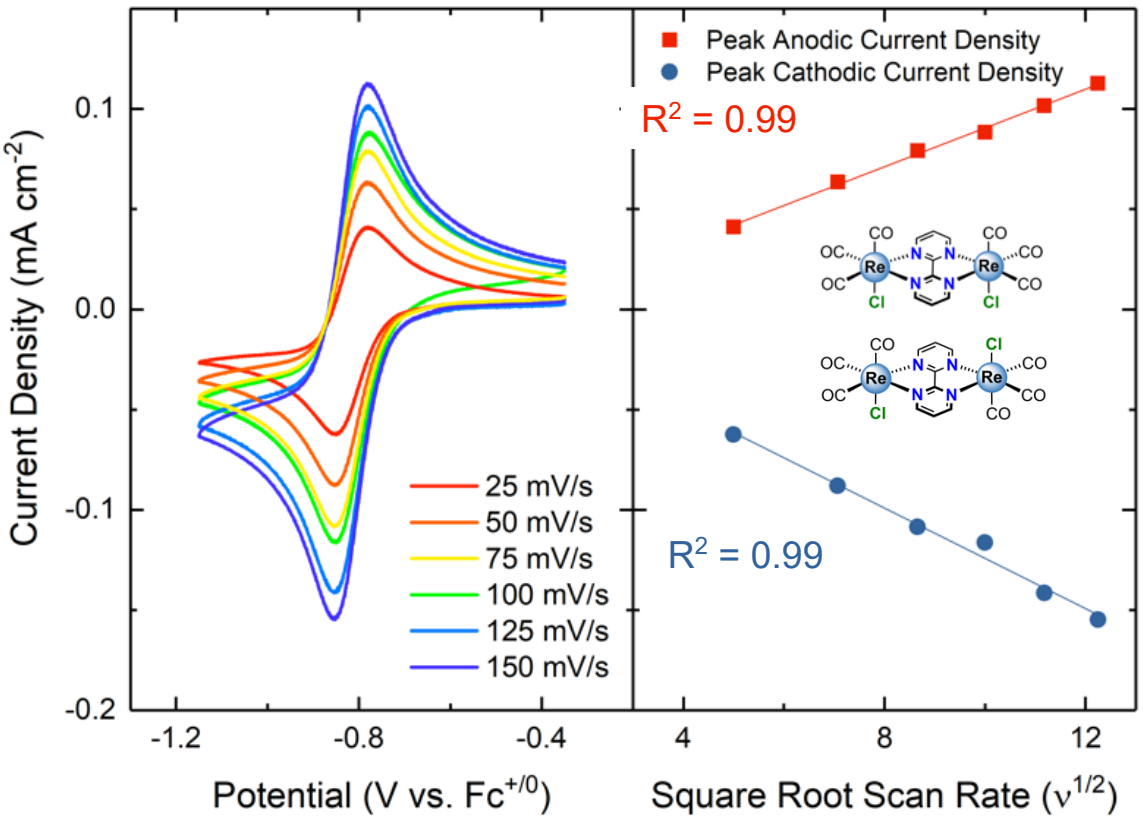

Figure E26: Scan rate dependence studies (left) and peak anodic and cathodic current density as a function of the square root of scan rate (right) for the first redox couple of complex **2-syn** + **2-anti**.

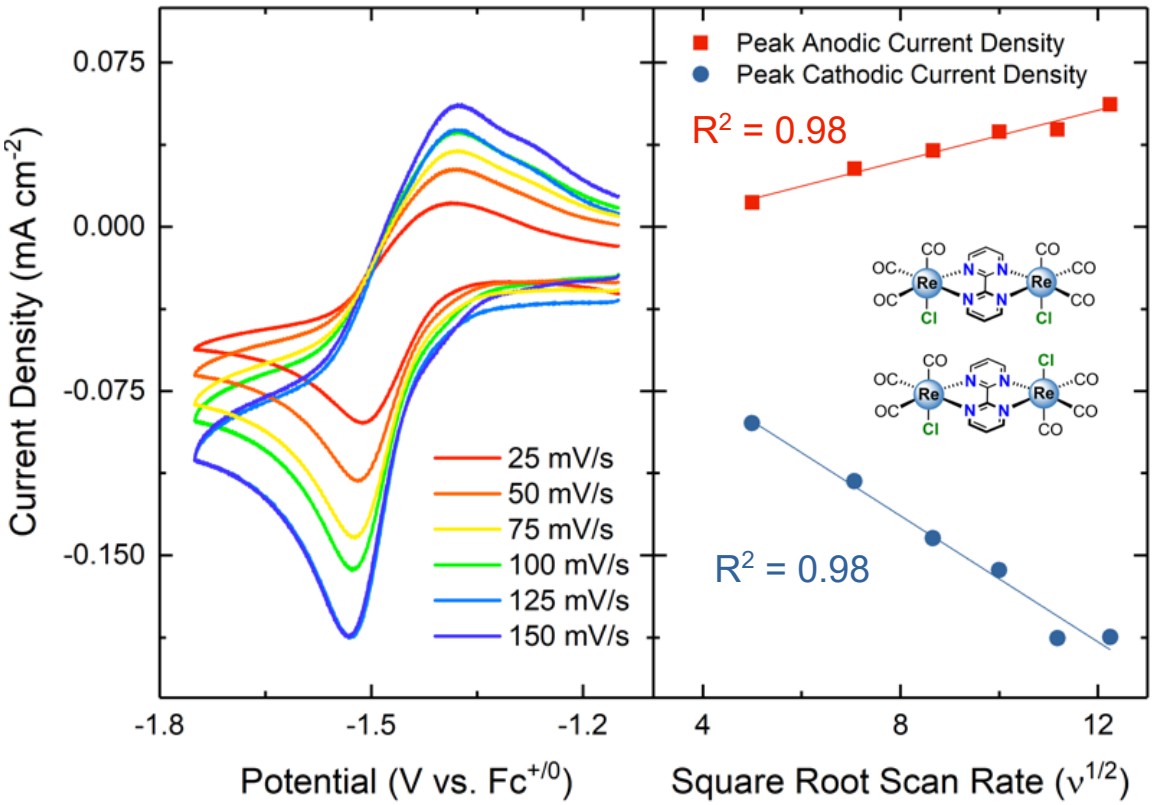

Figure E27: Scan rate dependence studies (left) and peak anodic and cathodic current density as a function of the square root of scan rate (right) for the second redox couple of complex **2-syn** + **2-anti**.

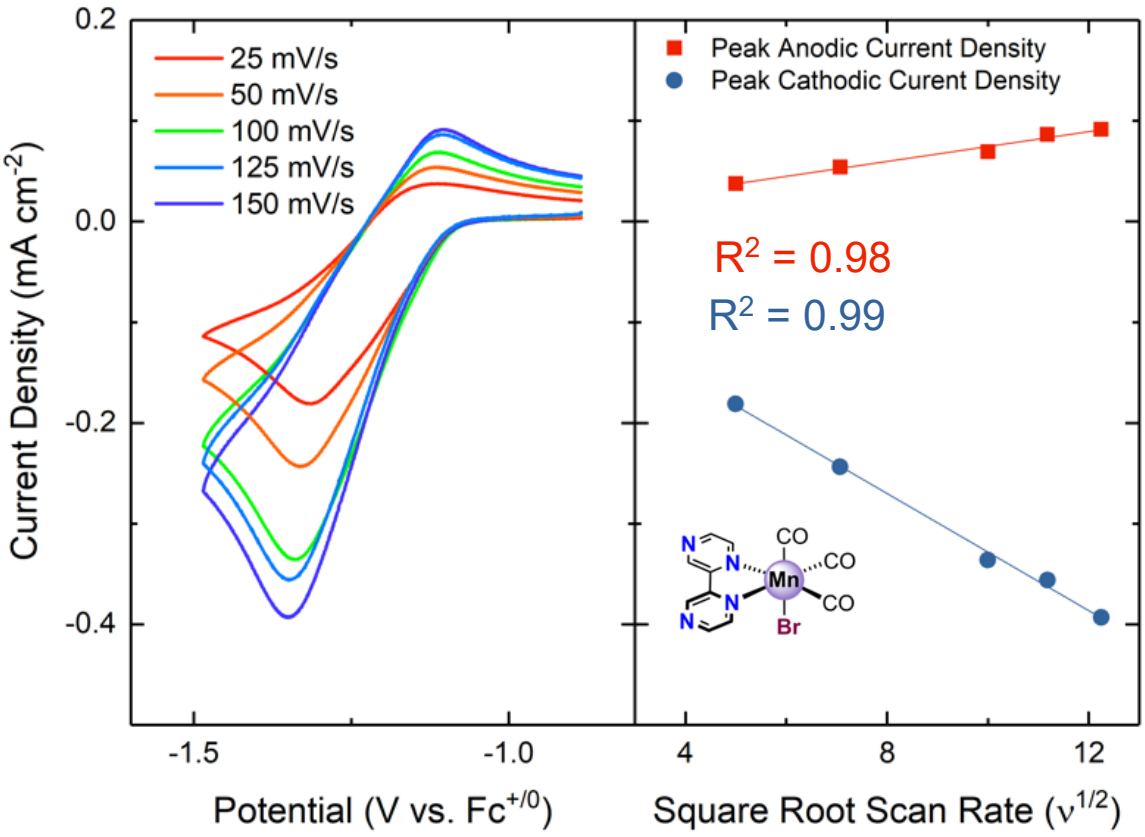

Figure E28: Scan rate dependence studies (left) and peak anodic and cathodic current density as a function of the square root of scan rate (right) for complex **3**.

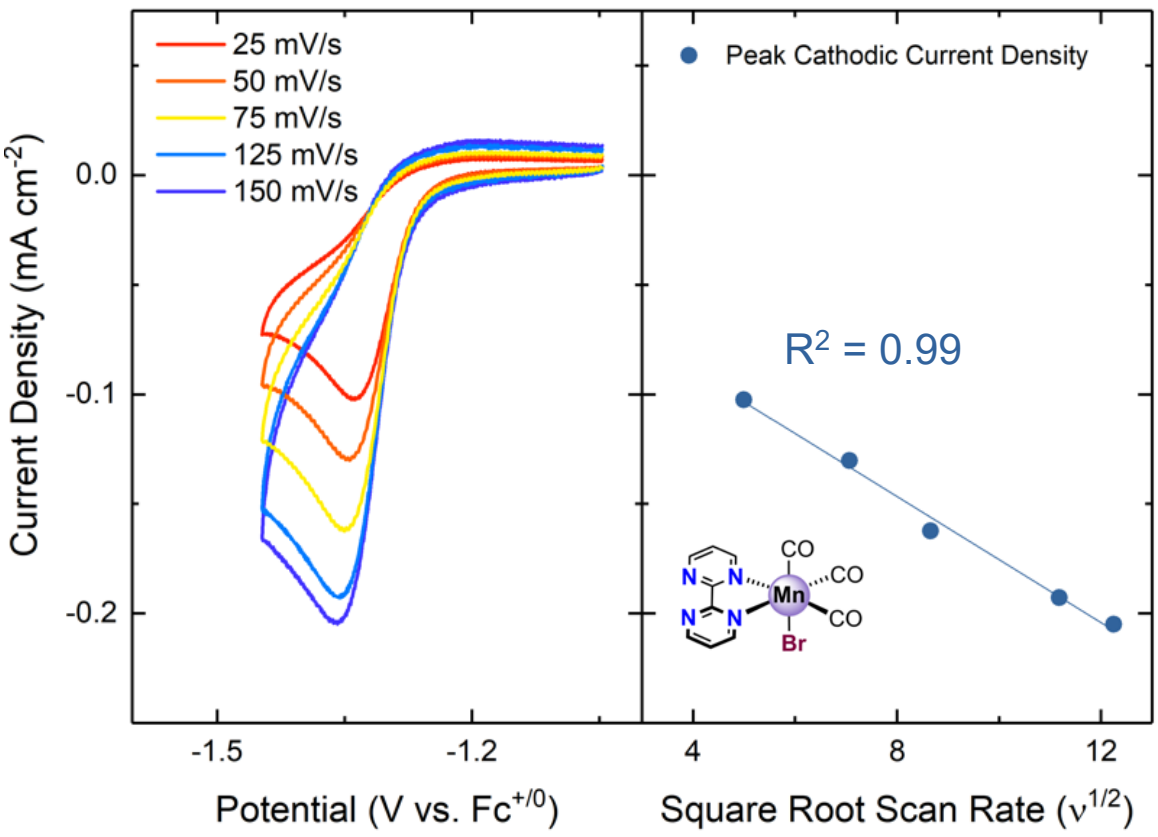

Figure E29: Scan rate dependence studies (left) and peak anodic and cathodic current density as a function of the square root of scan rate (right) for complex **4**.

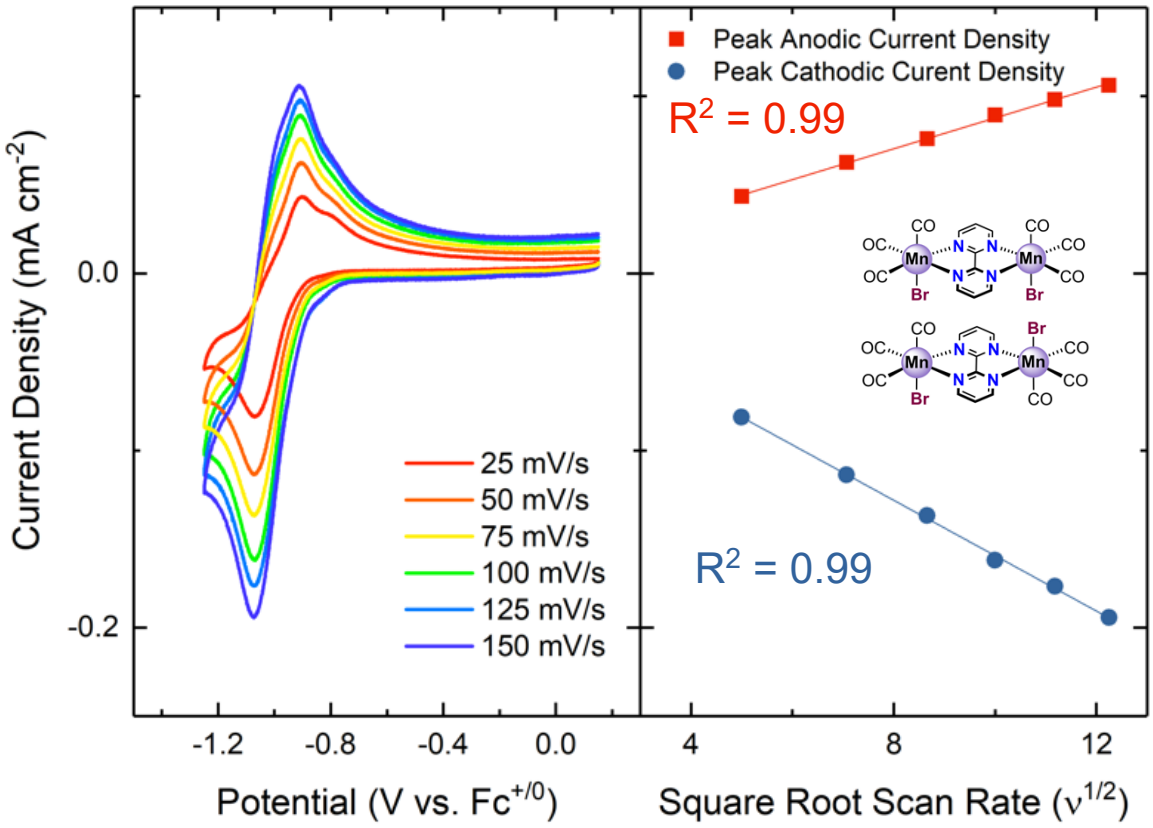

Figure E30: Scan rate dependence studies (left) and peak anodic and cathodic current density as a function of the square root of scan rate (right) for complex **5-syn** + **5-anti**.

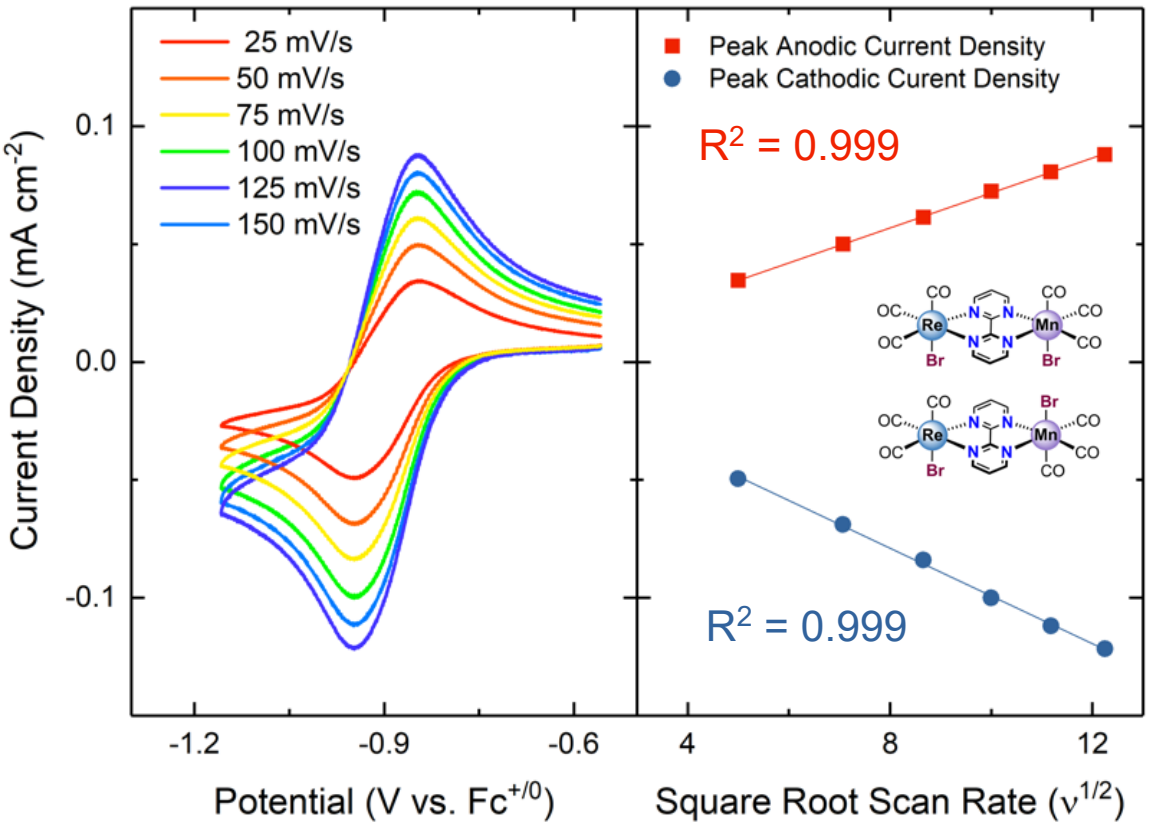

Figure E31: Scan rate dependence studies (left) and peak anodic and cathodic current density as a function of the square root of scan rate (right) for complex **6-syn** + **6-anti**.

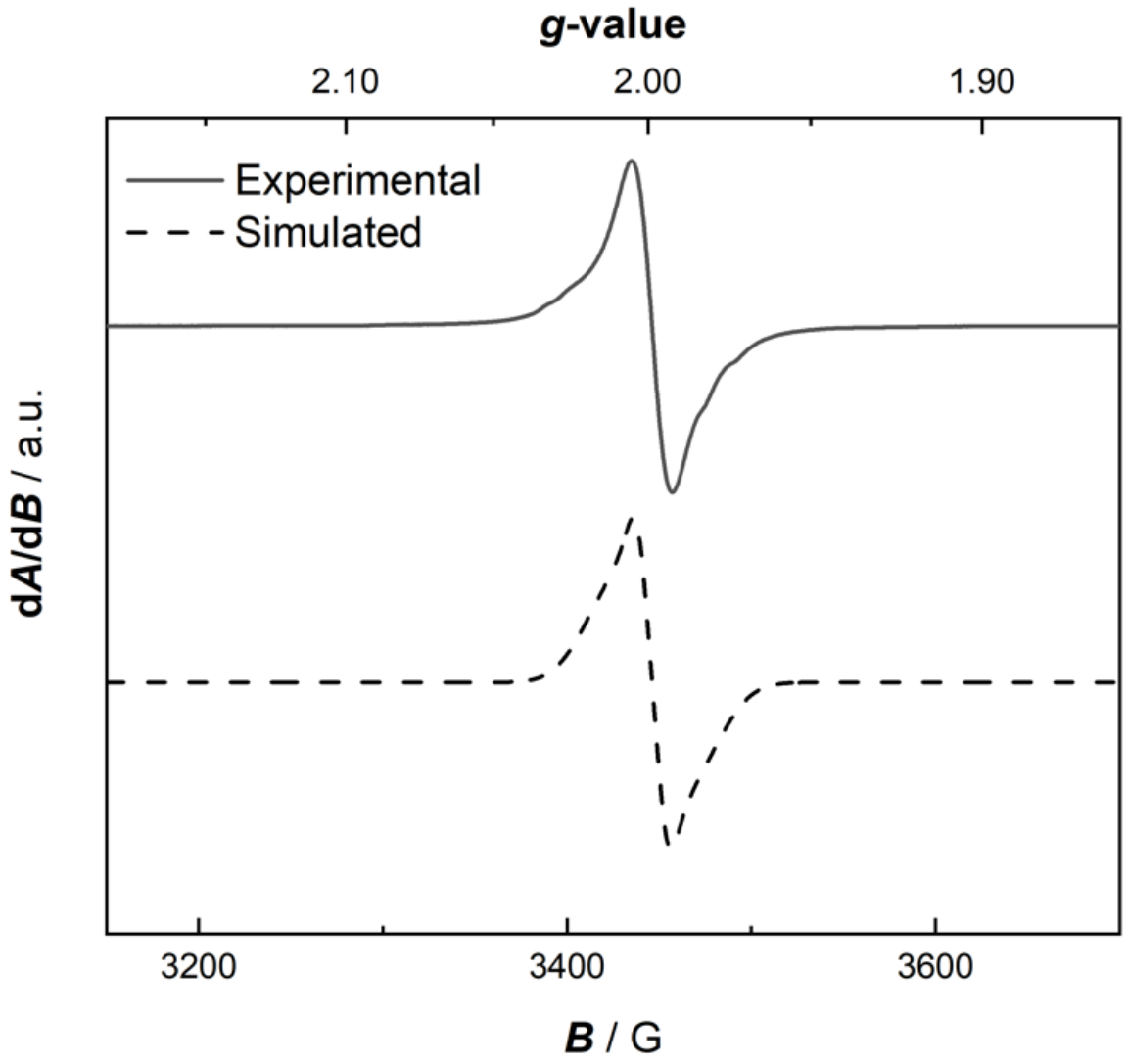

Figure E32: Experimental: perpendicular-mode X-band EPR spectrum of **2-syn** + **2-anti** after reduction by one e^- using Cp_2Co to generate a singly reduced paramagnetic species *in situ* (toluene, Temperature = 20 K, Frequency = 9.6405 GHz, Power = 2 mW). Simulated: Easyspin simulation of EPR data; Best values: g_x = 1.99, g_y = 2.01, g_z = 1.98, A_x = 43 MHz, A_y = 50 MHz, A_z = 15 MHz, HStrain(x) = 1 MHz, HStrain(y) = 100 MHz, HStrain(z) = 100 MHz, peak to peak line width (lwpp) = 0.75, weight = 1.

Crystallographic Information

Refinement Details

X-ray Crystallographic Studies for 1, 2-anti, 3, 4, 5-syn, 5-anti, and 6-syn

Crystals were mounted on polyimide MiTeGen loops with STP Oil Treatment and placed under a nitrogen stream. Low temperature (100 K) X-ray data were collected on a Bruker AXS D8 KAPPA diffractometer with an APEX II CCD detector and TRIUMPH graphite monochromator running at 50 kV and 30 mA with Mo radiation (K_α = 0.71073 Å) for **1** and on a Bruker AXS D8 VENTURE KAPPA diffractometer with PHOTON 100 CMOS detector and Helios focusing multilayer mirror optics running at 50 kV and 1 mA using Cu radiation (K_α = 1.54178 Å) for **5-syn** and **5-anti** and using Mo radiation (K_α = 0.71073 Å) for **2-anti**, **3**, **4**, and **6-syn.** Totals of 2374 (**1**), 2053 (**2-anti**), 2444 (**3**), 1206 (**4**), 1338 (**5-syn**), 2013 (**5-anti**), 884 (**6-syn**), 0.5° or 1.0° -wide ω- *or* ϕ-scan frames were collected with counting times of 10-20 seconds (**1**), 4-30 seconds (**2**), 1-10 seconds (**3**), 1-20 seconds (**4**), 5-60 seconds (**5-syn**), 1-15 seconds (**5-anti**), and 2-60 seconds (**6-syn**). Preliminary lattice constants were obtained with the Bruker Apex2 Software Suite.[1] Integrated reflection intensities for all compounds were produced using SAINT in the Bruker Apex2 Software Suite. Each data set was corrected empirically for variable absorption effects with SADABS[2] using equivalent reflections. The Bruker software package SHELXTL was used to solve each structure using intrinsic direct methods phasing. Final stages of weighted full-matrix least-squares refinement were conducted using F_o^2 data with SHELXTL[3] or the Olex2 software package equipped with XL[4]. All non-hydrogen atoms were refined anisotropically. All hydrogen atoms were included into the model at geometrically calculated positions and refined using a riding model. The isotropic displacement

parameters of all hydrogen atoms were fixed to 1.2 times the *U* value of the atoms they are linked to. The relevant crystallographic and structure refinement data for all seven structures are given in Table S1.

Table E1: Crystal Refinement Data

	1 (a15100)	**2-anti** (p15249)	**3** (p15315)
CCDC accession code	2005316	2005317	2005320
Empirical formula	$C_{11}H_6ClN_4O_3Re$	$C_{14}H_6Cl_2N_4O_6Re_2$	$C_{11}H_6BrMnN_4O_3$
Formula weight	463.85	769.53	377.05
Temperature	100 K	100 K	100 K
Wavelength	0.71073 Å	0.71073 Å	0.71073 Å
Crystal system	monoclinic	monoclinic	triclinic
Space group	*P2₁/c* (No. 14)	*P2₁/c* (No. 14)	*P-1* (No. 2)
a	6.2872(3) Å	6.3386(3) Å	6.6093(3) Å
b	14.9679(7) Å	11.9351(6) Å	6.6618(3) Å
c	13.4775(7) Å	12.3347(6) Å	14.8504(8) Å
α	90°	90°	102.3575(17)°
β	102.408(2)°	97.6407(17)°	93.1195(18)°
γ	90°	90°	102.3828(17)°
Volume	1238.69(11) $Å^3$	924.86(8) $Å^3$	620.40(5) $Å^3$
Z	4	2	2
Density (calculated)	2.487 g/cm^3	2.763 g/cm^3	2.018 g/cm^3
Absorption coefficient	10.038 mm^{-1}	13.406 mm^{-1}	4.296 mm^{-1}
F(000)	864	700	368
Crystal size	0.4 x 0.06 x 0.02 mm^3	0.06 x 0.04 x 0.02 mm^3	0.300 x 0.150 x 0.100 mm^3
Number of data frames/time	2374/10-20 seconds	2053/4-30 seconds	2444/1-10 seconds
Theta range	2.06 to 29.992°	2.385 to 24.992°	3.173 to 36.362°
Index ranges	$-8\le h\le 8$, $-21\le k\le 21$, $-18\le l\le 18$	$-7\le h\le 7$, $-14\le k\le 14$, $-14\le l\le 14$	$-10\le h\le 10$, $-10\le k\le 11$, $-24\le l\le 24$
Reflections collected	32945	21581	31855
Independent reflections	3602 [R_{int} = 0.039]	1634 [R_{int} = 0.055]	5964 [R_{int} = 0.038]
Completeness/θ_{max}	100%/25.000°	100%/24.992°	99.9%/25.242°
Absorption correction	Multi-scan	Multi-scan	Mulit-scan
Max. and min. transmission	1.000 and 0.630	1.000 and 0.852	0.7471 and 0.5920
Refinement method	Full-matrix least-squares on F^2	Full-matrix least-squares on F^2	Full-matrix least-squares on F^2
Data / restraints / parameters	3602 / 0 / 193	1634 / 0 / 145	5964 / 0 / 181
Goodness-of-fit on F^2	1.252	1.401	1.040
Final R indices [I>2σ(I)]	R_1 = 0.0212, wR_2 = 0.0453	R_1 =0.0267, wR_2 = 0.0478	R_1 =0.0289, wR_2 = 0.0572
R indices (all data)	R_1 = 0.0226, wR_2 = 0.0457	R_1 = 0.0304, wR_2 = 0.0485	R_1 = 0.0411, wR_2 = 0.0605
Largest diff. peak and hole	1.19 and -0.91 $e^-/Å^3$	1.57 and -1.79 $e^-/Å^3$	0.778 and -0.778 $e^-/Å^3$

	4 (p15260)	**5-syn** (p15288)	**5-anti** (p15287)
CCDC accession code	2005318	2005315	2005321
Empirical formula	$C_{11}H_6BrMnN_4O_3$	$C_{17}H_{12}Br_2Mn_2N_4O_7$	$C_{14}H_6Br_2Mn_2N_4O_6$
Formula weight	377.05	647.96	595.93
Temperature	100 K	100 K	100 K
Wavelength	0.71073 Å	1.54178 Å	1.54178 Å
Crystal system	monoclinic	orthorhombic	triclinic
Space group	*P2₁ /c* (No. 14)	*Cmcm* (No. 63)	*P-1* (No. 2)
a	6.4216(2) Å	17.597(3) Å	6.4380(6) Å
b	14.7565(6) Å	10.830(2) Å	8.3336(7) Å
c	13.5124(5) Å	11.8313(18) Å	9.4980(9) Å
α	90°	90°	98.880(7)°
β	102.0331(12)°	90°	100.604(7)°
γ	90°	90°	96.117(7)°
Volume	1252.30(8) $Å^3$	2254.8(7) $Å^3$	490.08(8) $Å^3$
Z	4	4	1
Density (calculated)	2.000 g/cm^3	1.909 g/cm^3	2.019 g/cm^3
Absorption coefficient	4.257 mm^{-1}	13.687 mm^{-1}	15.626 mm^{-1}
F(000)	736	1248.0	286
Crystal size	0.250 x 0.100 x 0.050 mm^3	0.1 x 0.03 x 0.03 mm^3	0.070 x 0.050 x 0.030 mm^3
Number of data frames/time	1206/1-20 seconds	1338/5-60 seconds	2013/1-15 seconds
Theta range	3.083 to 36.307°	4.794 to 74.214°	4.814 to 72.057°
Index ranges	$-10\le h\le 10$, $-24\le k\le 24$, $-22\le l\le 22$	$-21\le h\le 19$, $-13\le k\le 11$, $-14\le l\le 9$	$-6\le h\le 7$, $-10\le k\le 10$, $-11\le l\le 11$
Reflections collected	28709	4267	5479
Independent reflections	6048 [R_{int} = 0.039]	1178[R_{int} = 0.109]	1911[R_{int} = 0.092]
Completeness/θ_{max}	99.9%/25.242°	97.9%/66.00°	99.7%/67.679°
Absorption correction	Multi-scan	None	Multi-scan
Max. and min. transmission	0.7474 and 0.5901	0.7538 and 0.5415	0.7538 and 0.5580
Refinement method	Full-matrix least-squares on F^2	Full-matrix least-squares on F^2	Full-matrix least-squares on F^2
Data / restraints / parameters	6048 / 0 / 181	1178 / 29 / 93	1911 / 0 / 127
Goodness-of-fit on F^2	1.045	1.065	1.062
Final R indices [I>2σ(I)]	R_1 =0.0309, wR_2 = 0.0638	R_1 = 0.0616, wR_2 = 0.1333	R_1 = 0.0702, wR_2 = 0.1569
R indices (all data)	R_1 =0.0476, wR_2 = 0.0687	R_1 = 0.1106, wR_2 = 0.1538	R_1 = 0.1034 wR_2 = 0.1759
Largest diff. peak and hole	0.969 and -0.693 $e^-/Å^3$	0.97 and -1.13 $e^-/Å^3$	1.451 and -0.966 $e^-/Å^3$

	6-syn (p15317)
CCDC accession code	2005319
Empirical formula	$C_{17}H_{12}Br_2MnN_4O_7Re$
Formula weight	785.27
Temperature	100 K
Wavelength	0.71073 Å
Crystal system	orthorhombic
Space group	*Cmcm* (No 63)
a	17.6165(8) Å
b	10.9052(5) Å
c	11.8240(6) Å
α	90°
β	90°
γ	90°
Volume	2271.53(19) $Å^3$
Z	4
Density (calculated)	2.296 g/cm^3
Absorption coefficient	9.444 mm^{-1}
F(000)	1472
Crystal size	0.100 x 0.030 x 0.030 mm^3
Number of data frames/time	884/2-60 seconds
Theta range	2.196 to 30.501°
Index ranges	$-22 \leq h \leq 25$, $-14 \leq k \leq 14$, $-16 \leq l \leq 15$
Reflections collected	15274
Independent reflections	1811[R_{int} = 0.056]
Completeness/θ_{max}	99.9%/25.242°
Absorption correction	Multi-scan
Max. and min. transmission	0.7466 and 0.5762
Refinement method	Full-matrix least-squares on F^2
Data / restraints / parameters	1811 / 199 / 126
Goodness-of-fit on F^2	1.060
Final R indices [I>2σ(I)]	R_1 = 0.0286, wR_2 = 0.0489
R indices (all data)	R_1 = 0.0448, wR_2 = 0.0519
Largest diff. peak and hole	0.892 and -1.442 $e^-/Å^3$

Special Refinement Details for 1.

Complex **1** crystalizes in the monoclinic space group $P2_1/c$. The crystal exhibits disorder in regard to the axial CO and axial Cl. Specifically, the disorder was modeled by refining the relative occupancies of Cl1 and Cl1a, giving a ratio of 94:6. Additionally, refinement of the relative occupancies of O3 and O3a revealed a ratio of 94:6.

Solid-State Structure of Complex 1.

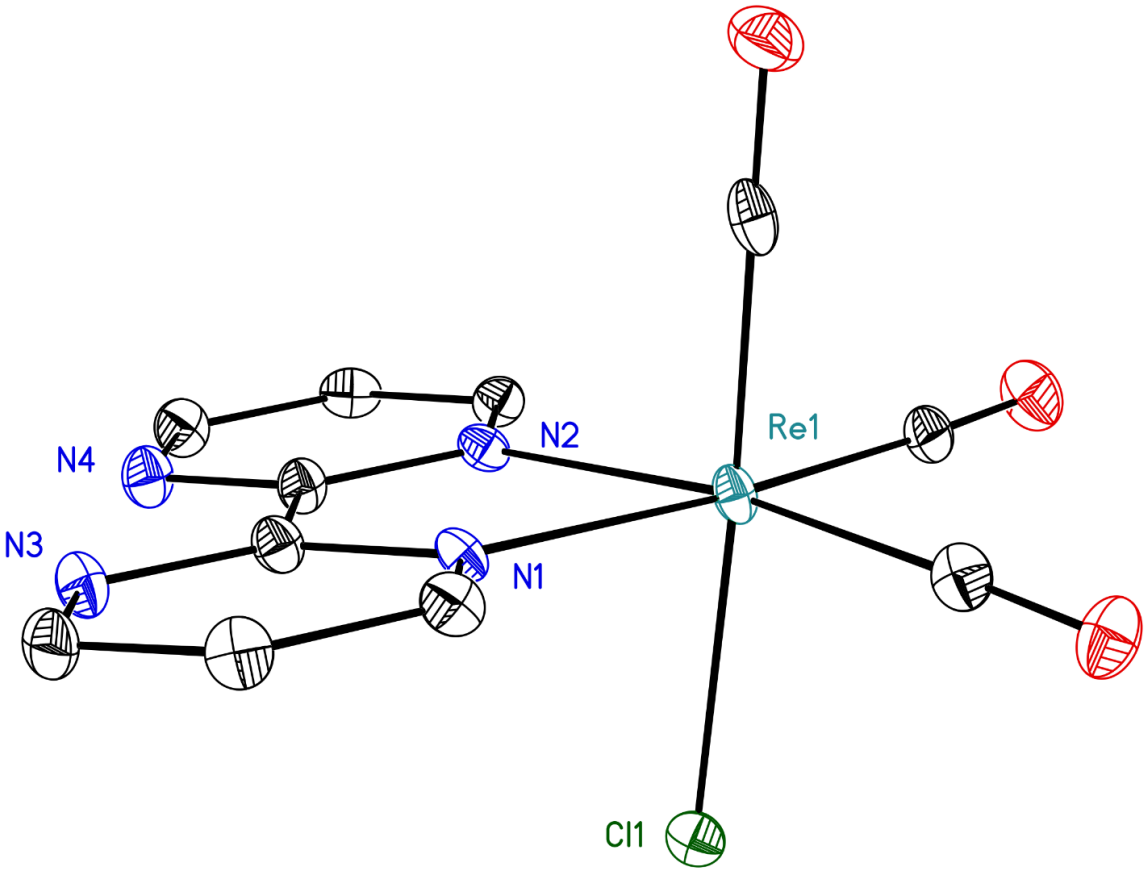

Figure E33. Solid-state structure of complex **1**. Partial occupancy CO and Cl omitted for clarity. Hydrogen atoms are omitted for clarity. Displacement ellipsoids are shown at the 50% probability level.

Full Solid-state Structure of Complex 1.

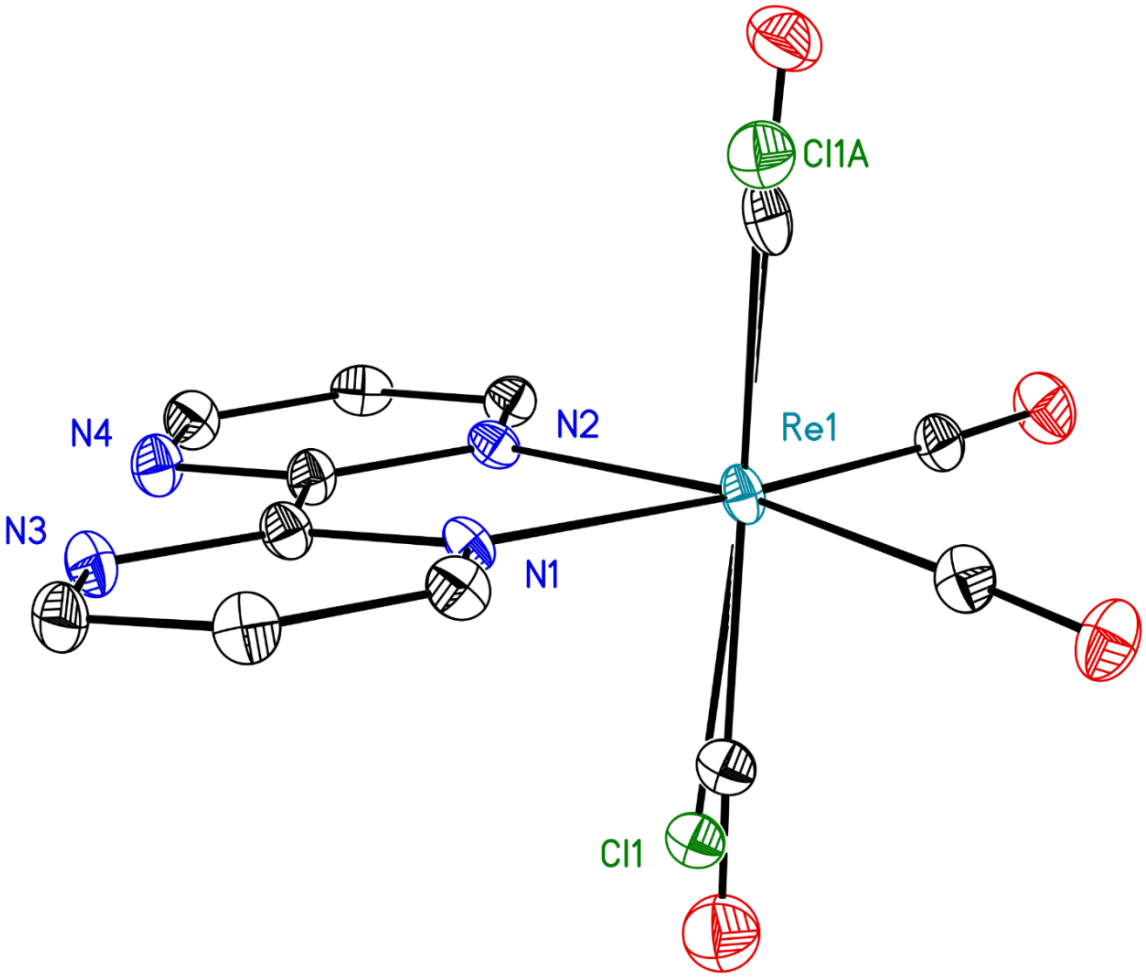

Figure E34. Full solid-state structure of complex **1**. Hydrogen atoms are omitted for clarity. Displacement ellipsoids are shown at the 50% probability level.

Special Refinement Details for 2-anti.

Complex **2-anti** crystalizes in the monoclinic space group $P2_1/C$. The crystal exhibits disorder in regard to the axial CO and axial Cl ligands. Specifically, the disorder was modeled by refining the relative occupancies of Cl1 and Cl1A, giving a ratio of 80:20. Additionally, refinement of the relative occupancies of C7 and C7A, as well as O3 and O3A, revealed a ratio of 80:20.

Solid-State Structure of Complex 2-anti.

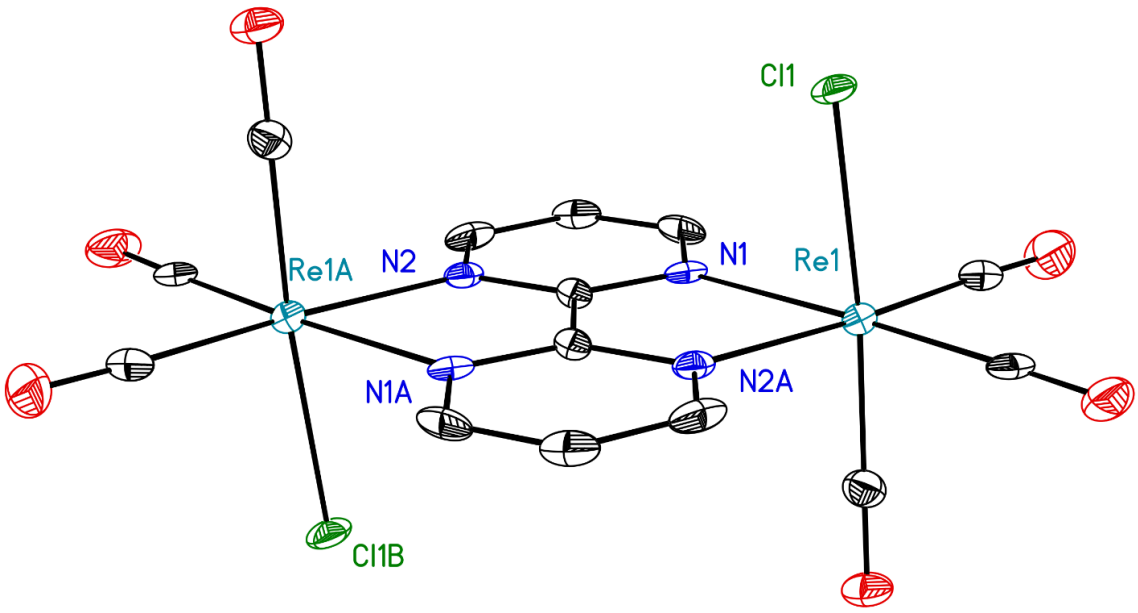

Figure E35: Solid-state structure of complex **2-anti**. Partial occupancy Cl1A, Cl1C, C7A, O3A, C7AA, and O3AA atoms are omitted for clarity. Hydrogen atoms are omitted for clarity. Displacement ellipsoids are shown at the 50% probability level.

Full Solid-State Structure of Complex 2-anti.

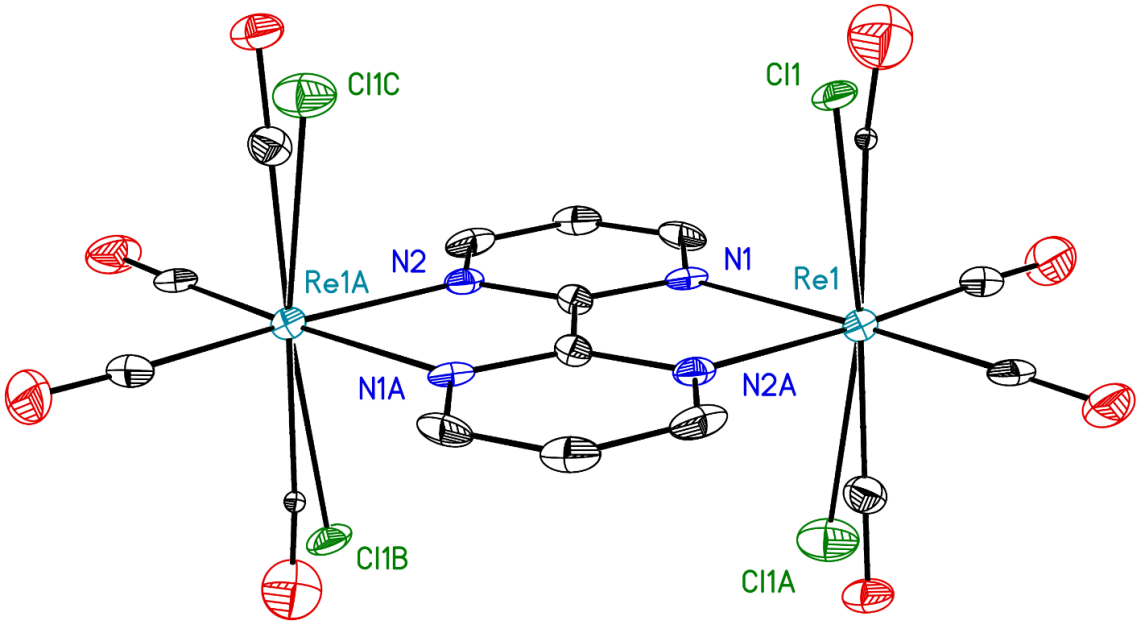

Figure E36: Full solid-state structure of complex **2-anti**, showing admixture of **2-syn** that is also present in the unit cell due to packing disorder. Hydrogen atoms are omitted for clarity. Displacement ellipsoids are shown at the 50% probability level.

Special Refinement Details for 3.

No special refinement was required.

Full Solid-State Structure of Complex 3.

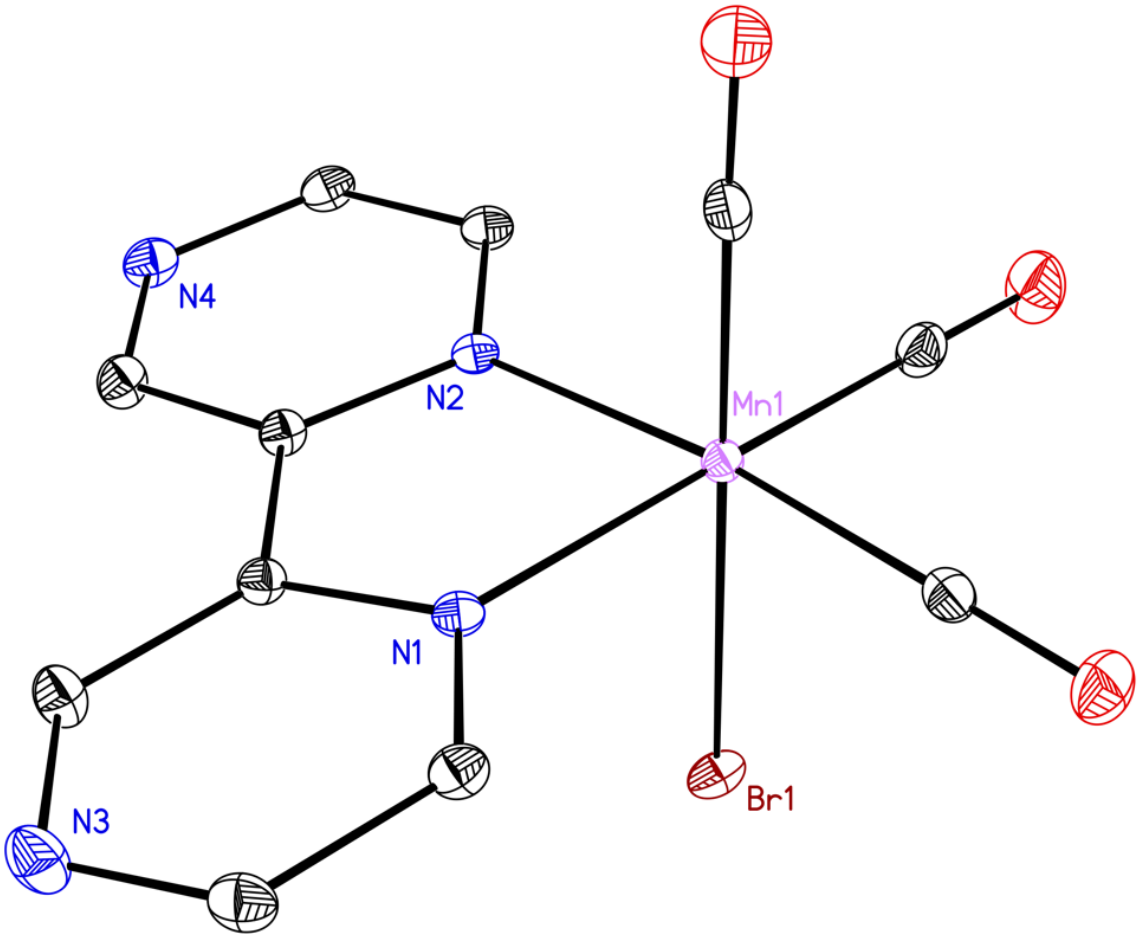

Figure E37. Full solid-state structure of complex **3**. Hydrogen atoms are omitted for clarity. Displacement ellipsoids are shown at the 50% probability level.

Special Refinement Details for 4.

Complex **4** crystallizes in the monoclinic space group $P2_1/c$ with one molecule in the asymmetric unit. The highest electron density maximum is located in a position consistent with a bromine disordered with carbon monoxide (C1 and O11). This disorder was not modeled because the occupancy of this bromine refined to less than 5% and no partially occupied carbon monoxide could be located in the bromine position (Br1).

Full Solid-State Structure of Complex 4.

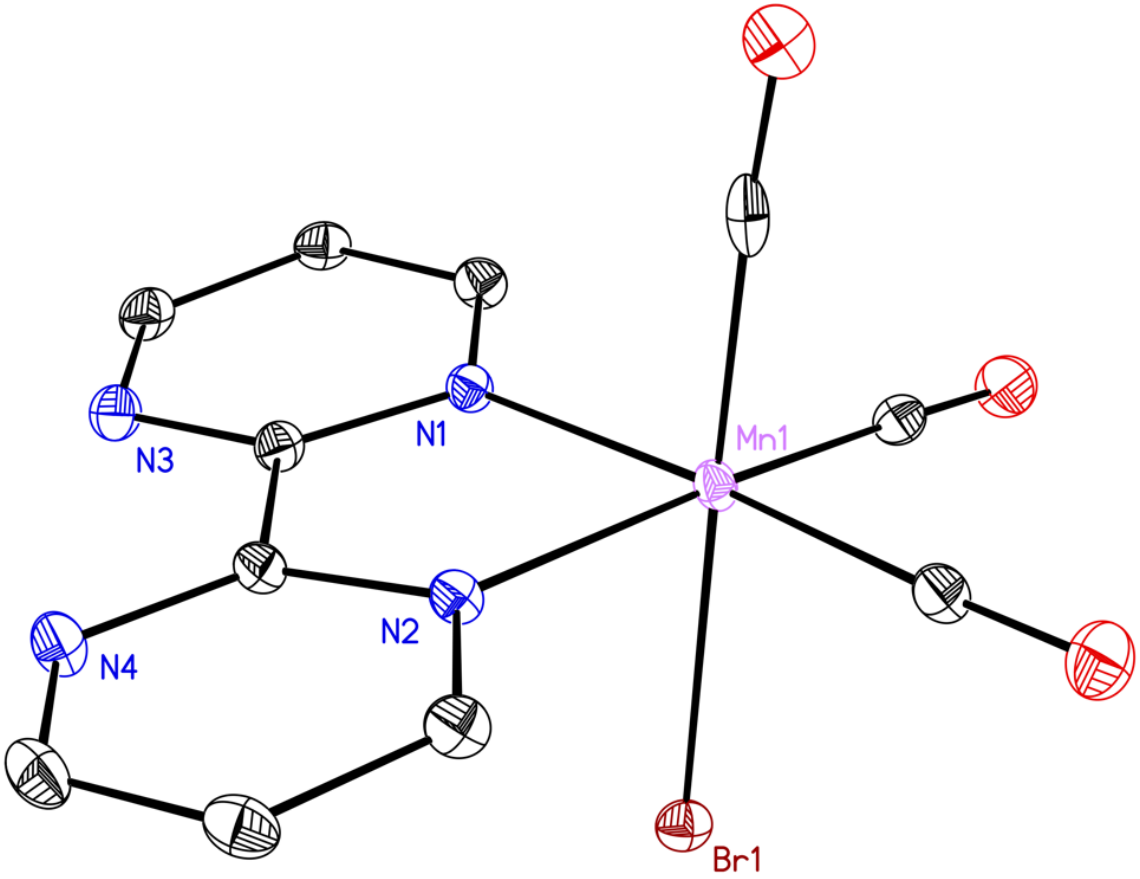

Figure E38: Full solid-state structure of complex **4**. Hydrogen atoms are omitted for clarity. Displacement ellipsoids are shown at the 50% probability level.

Special Refinement Details for 5-syn.

Complex **5-syn** crystallizes in the orthorhombic space group *Cmcm* with one quarter of a molecule in the asymmetric unit along with a quarter of an acetone. The occupancy of the acetone molecule was decreased to a quarter because it is located on multiple symmetry elements (mirrors and two-fold rotation axis). The acetone was refined with the help of similarity restraints on the 1,2- and 1,3-distances and displacement parameters as well as rigid bond restraints for anisotropic displacement parameters. In addition, the C-C distances were restrained to be 1.51(4) Å and all atoms were restrained to be flat. The quality of this crystal is relatively poor because is appeared to decompose over the course of data collection, possibly due to light exposure.

Solid-State Structure of Complex 5-syn.

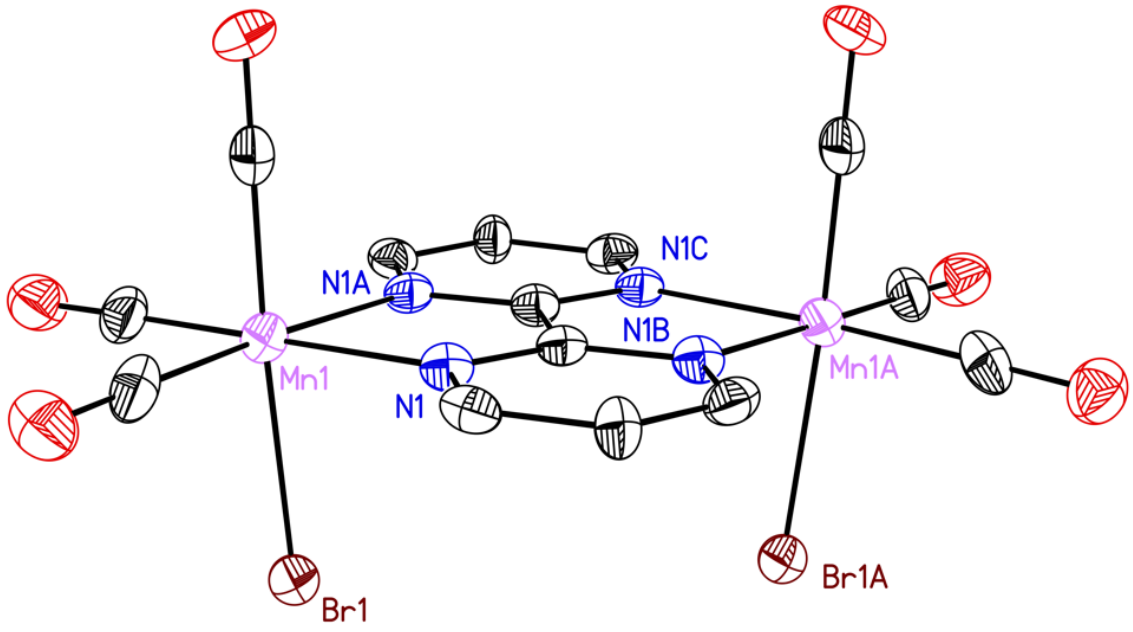

Figure E39: Solid-state structure of complex **5-syn**. Hydrogen atoms and a disordered acetone molecule are omitted for clarity. Displacement ellipsoids are shown at the 50% probability level.

Full Solid-State Structure of Complex 5-syn.

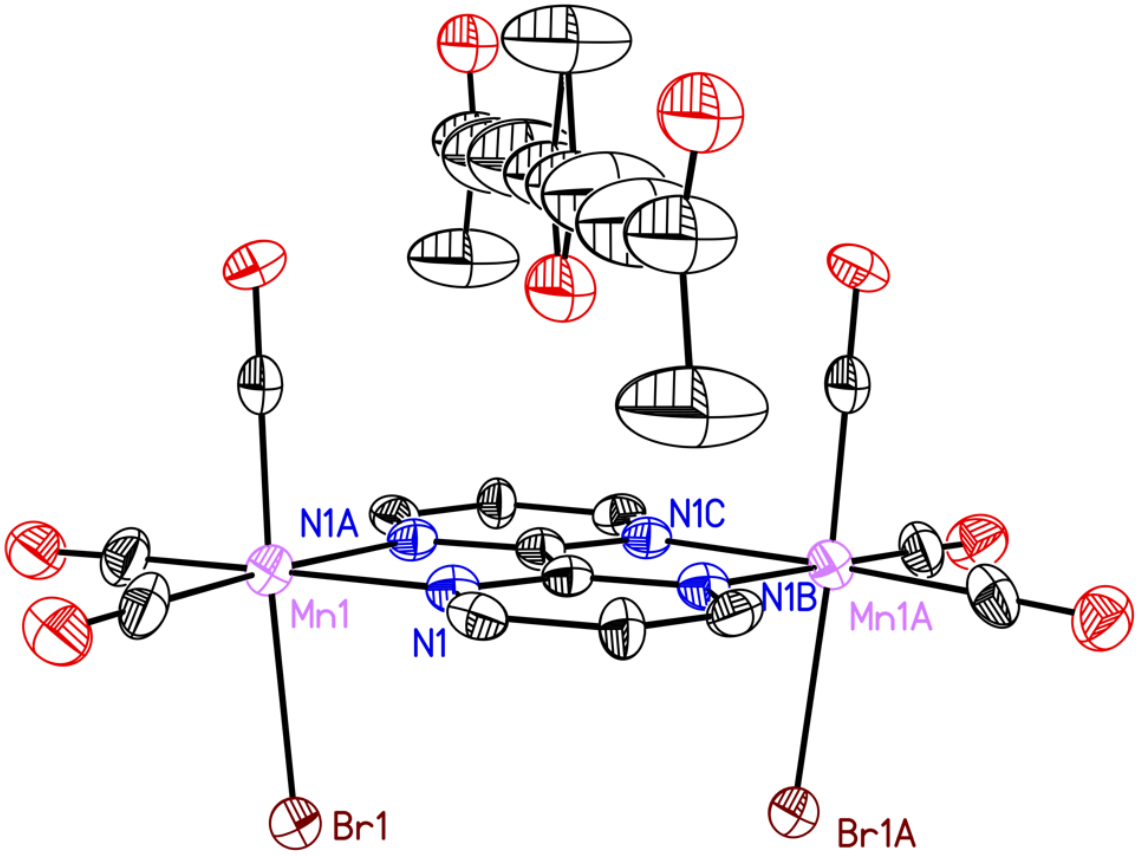

Figure E40: Solid-state structure of complex **5-syn**. Hydrogen are omitted for clarity. Displacement ellipsoids are shown at the 50% probability level.

Special Refinement Details for 5-anti.

No special refinement was required.

Full Solid-State Structure of Complex 5-anti.

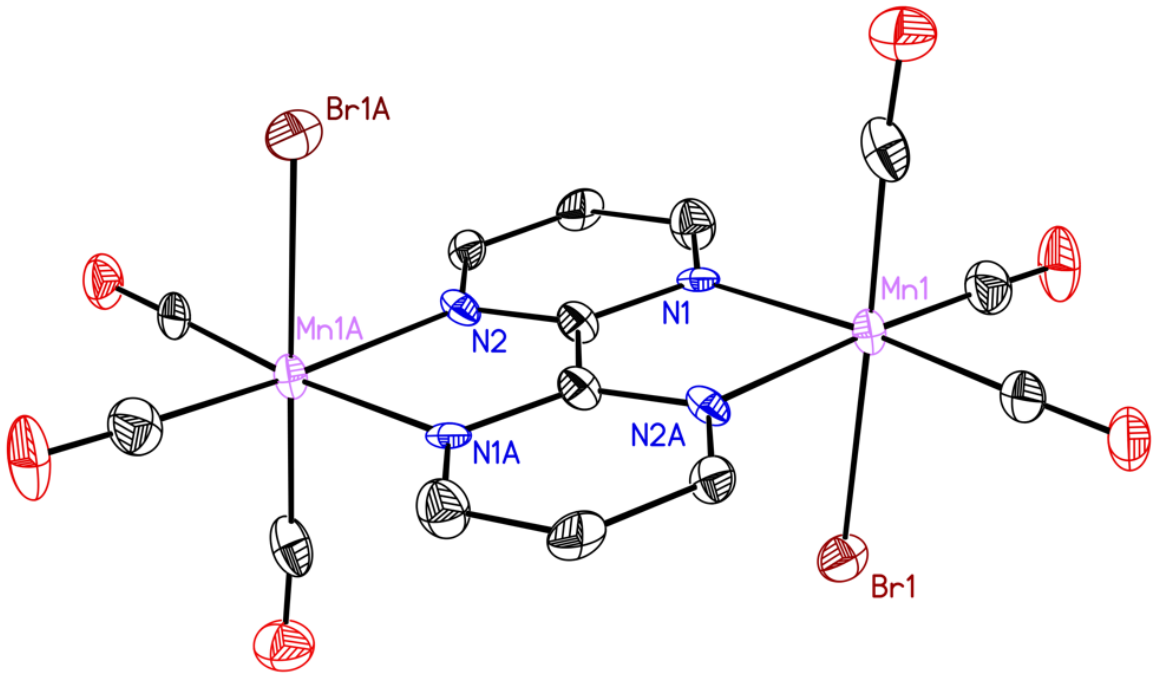

Figure E41: Full solid-state structure of **5-anti.** Hydrogen are omitted for clarity. Displacement ellipsoids are shown at the 50% probability level.

Special Refinement Details for 6-syn.

Compound **6-syn** crystallizes in the orthorhombic space group *Cmcm* with a quarter of a molecule in the asymmetric unit along with a quarter of an acetone. All disordered atoms were refined with the help of similarity restraints on the 1,2- and 1,3-distances and displacement parameters as well as rigid or enhanced rigid bond restraints for anisotropic displacement parameters. The molecule is located on multiple symmetry elements (mirror planes and a 2-fold rotation axis). Due to this situation, only one metal position is present in the asymmetric unit which was modeled as a mixture of Mn and Re. Refinement of the relative occupancies of Mn and Re gave a ratio of approximately 49.4:50.6. For the final refinement the occupancies of Mn and Re were constrained to be 50:50 and the anisotropic displacement parameters were constrained to be equal. As a result of the Mn-Re disorder, the carbonyl ligands were also disordered.

The occupancy of the acetone molecule was decreased to a quarter because it is located on multiple symmetry elements (mirror planes and two-fold rotation axis). The acetone was refined with the help of similarity restraints on the 1,2- and 1,3-distances and displacement parameters as well as rigid bond restraints for anisotropic displacement parameters. In addition, the C-C distances were restrained to be 1.51(4) Å and all atoms were restrained to be flat.

Solid-State Structure of Complex 6-syn.

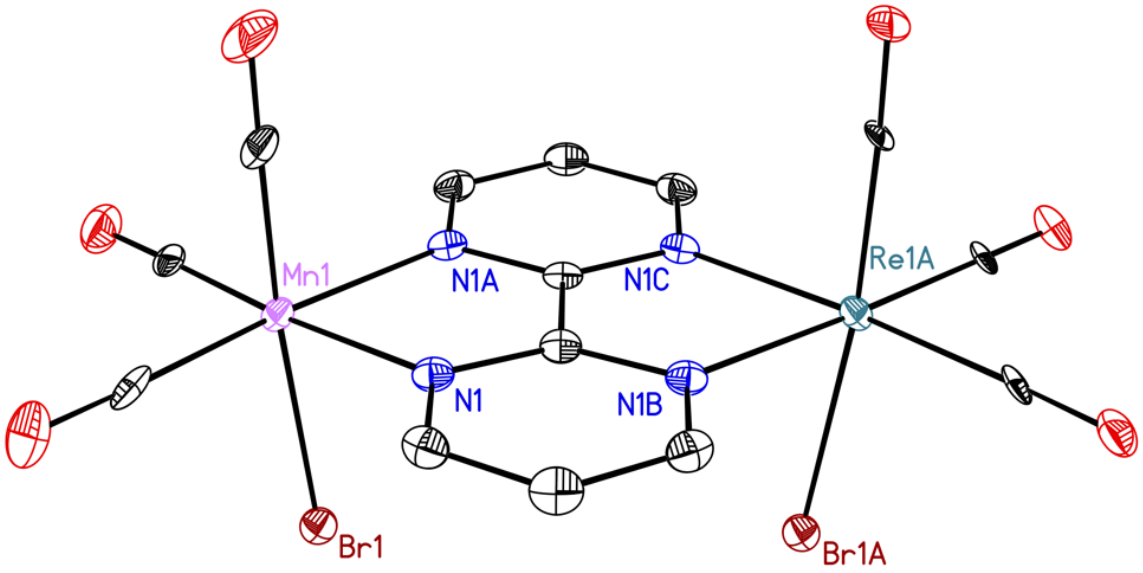

Figure E42: Solid-state structure of complex **6-syn**. Hydrogen atoms, a disordered acetone molecule, and a disordered molecule of **6-syn** are omitted for clarity. Displacement ellipsoids are shown at the 50% probability level.

Full Solid-State Structure of Complex 6-syn.

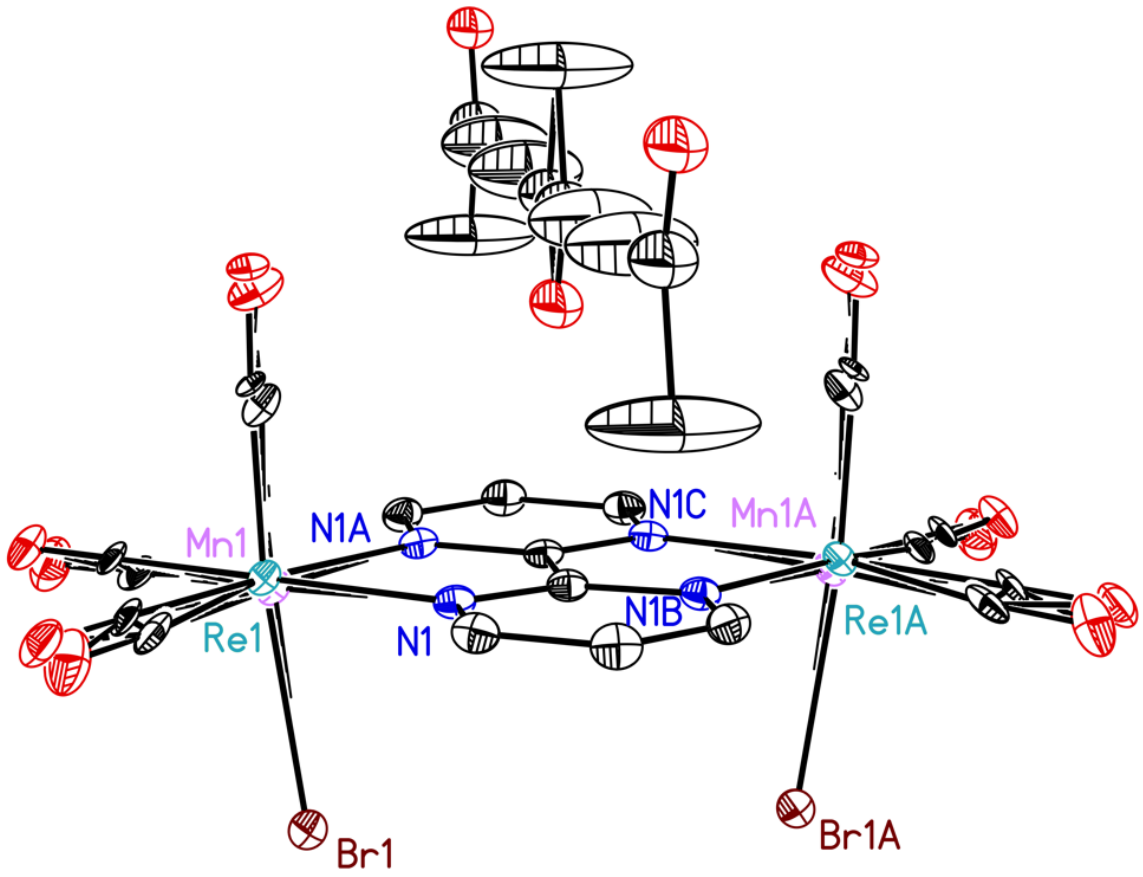

Figure E43: Solid-state structure of complex **6-syn**. Hydrogen atoms are omitted for clarity. Displacement ellipsoids are shown at the 50% probability level.

References

(1) APEX2, Version 2 User Manual, M86-E01078, Bruker Analytical X-ray Systems: Madison, WI, June 2006.

(2) G. M. Sheldrick, SADABS (version 2008/1): Program for Absorption Correction for Data from Area Detector Frames, University of Göttingen, 2008.

(3) G. M. Sheldrick, Crystal structure refinement with SHELXL. *Acta Crystallogr., Sect. A: Found. Crystallogr.* 2015, **71**, 3-8.

(4) O. V. Dolomanov, L. J. Bourhis, R. J. Gildea, J. A. K. Howard, H. J. Puschmann, *Appl. Crystallogr.* 2009, **42**, 339-341.

Appendix F

Evidence for Redox Chemistry Following Photoinduced CO Release from $[Mn(CO)_3]$ Complexes

Complexes of Interest

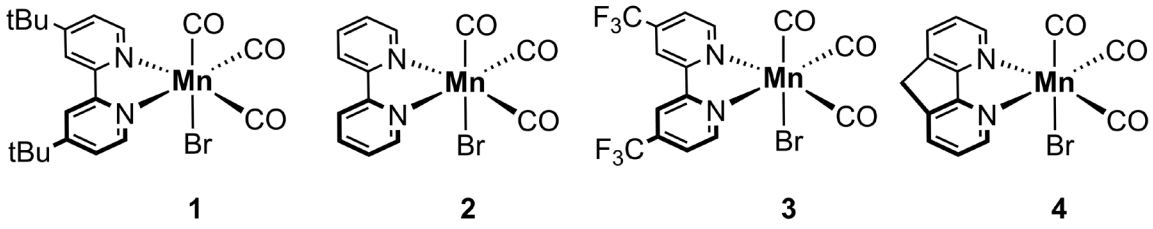

Chart F1: Complexes of interest.

Electrochemical Data

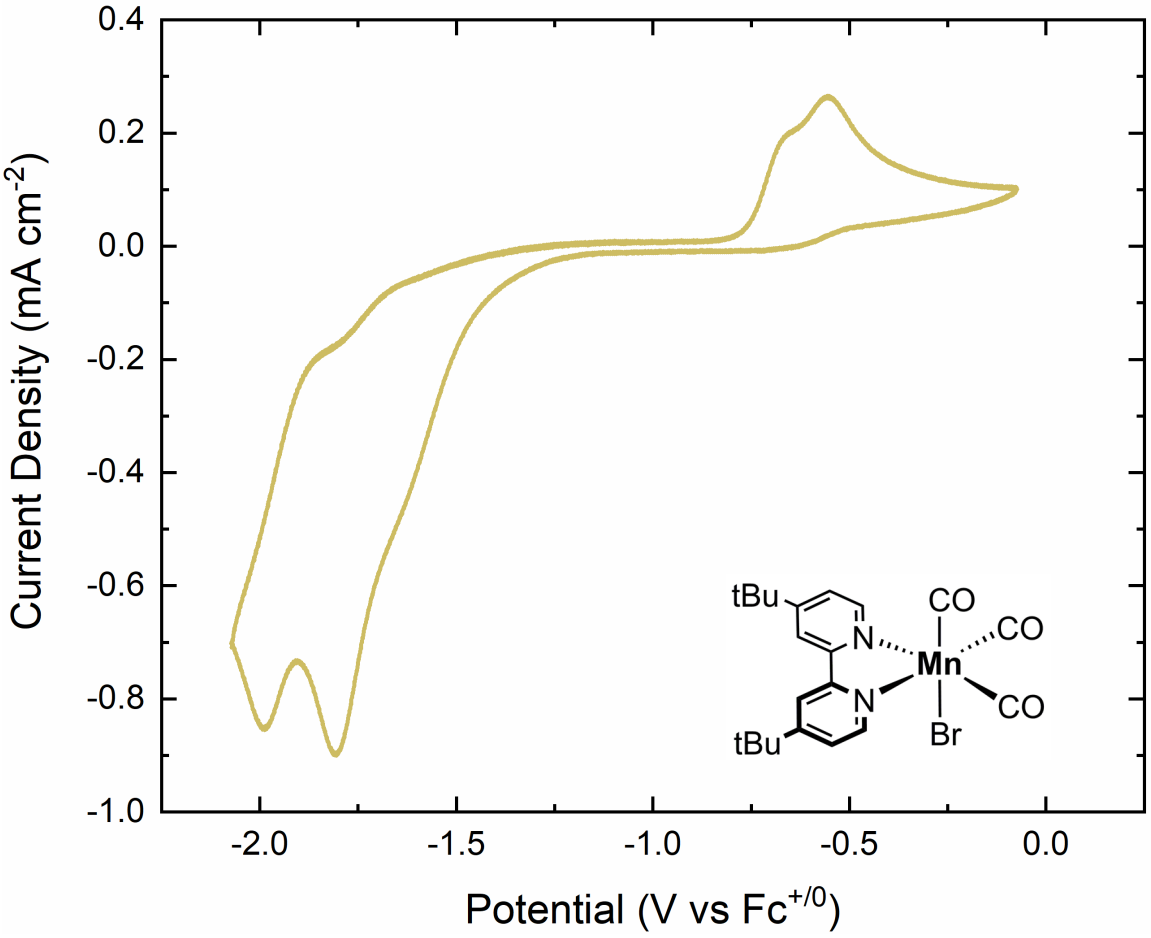

Figure F1: Cyclic voltammogram (100 mV/s) of **1** in 0.1M $TBAPF_6$/MeCN solution.

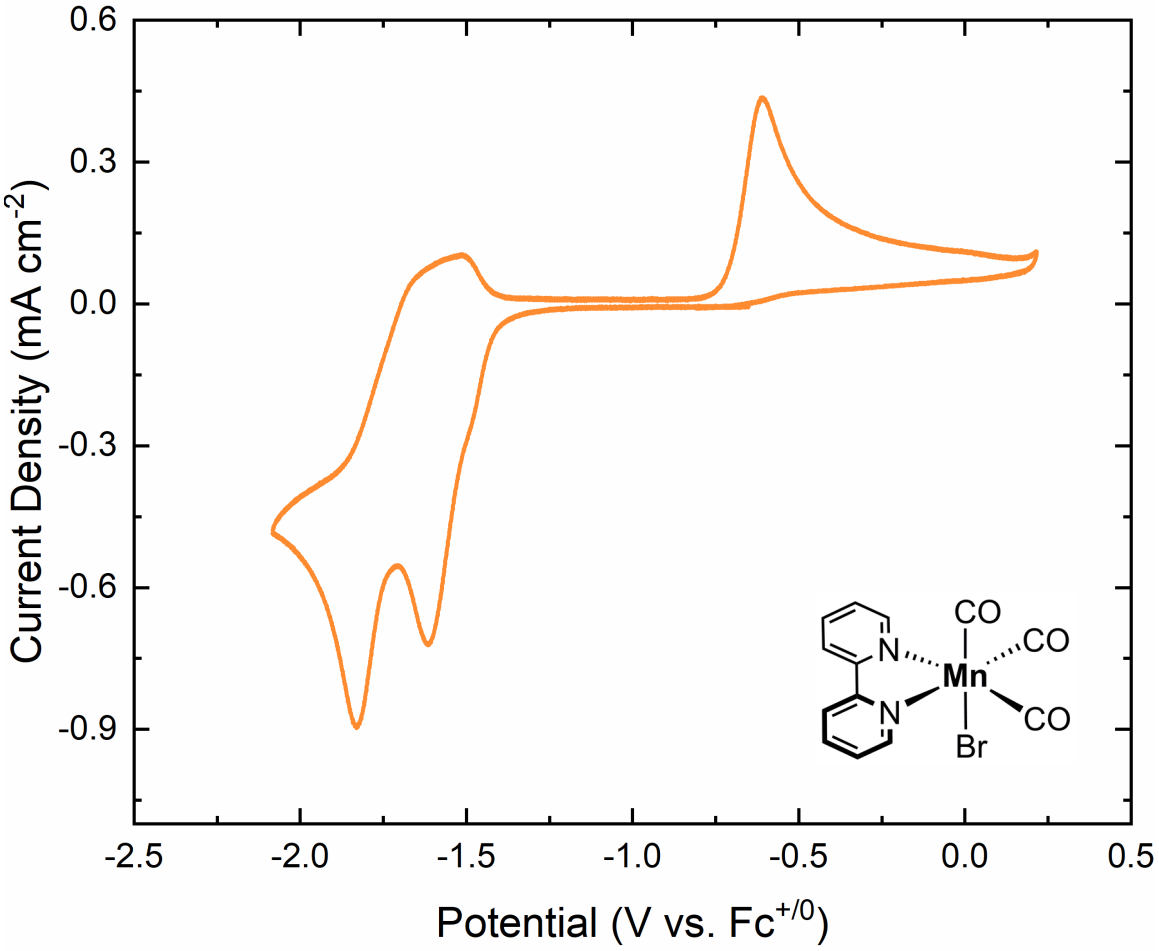

Figure F2: Cyclic voltammogram (100 mV/s) of **2** in 0.1M $TBAPF_6$/MeCN solution.

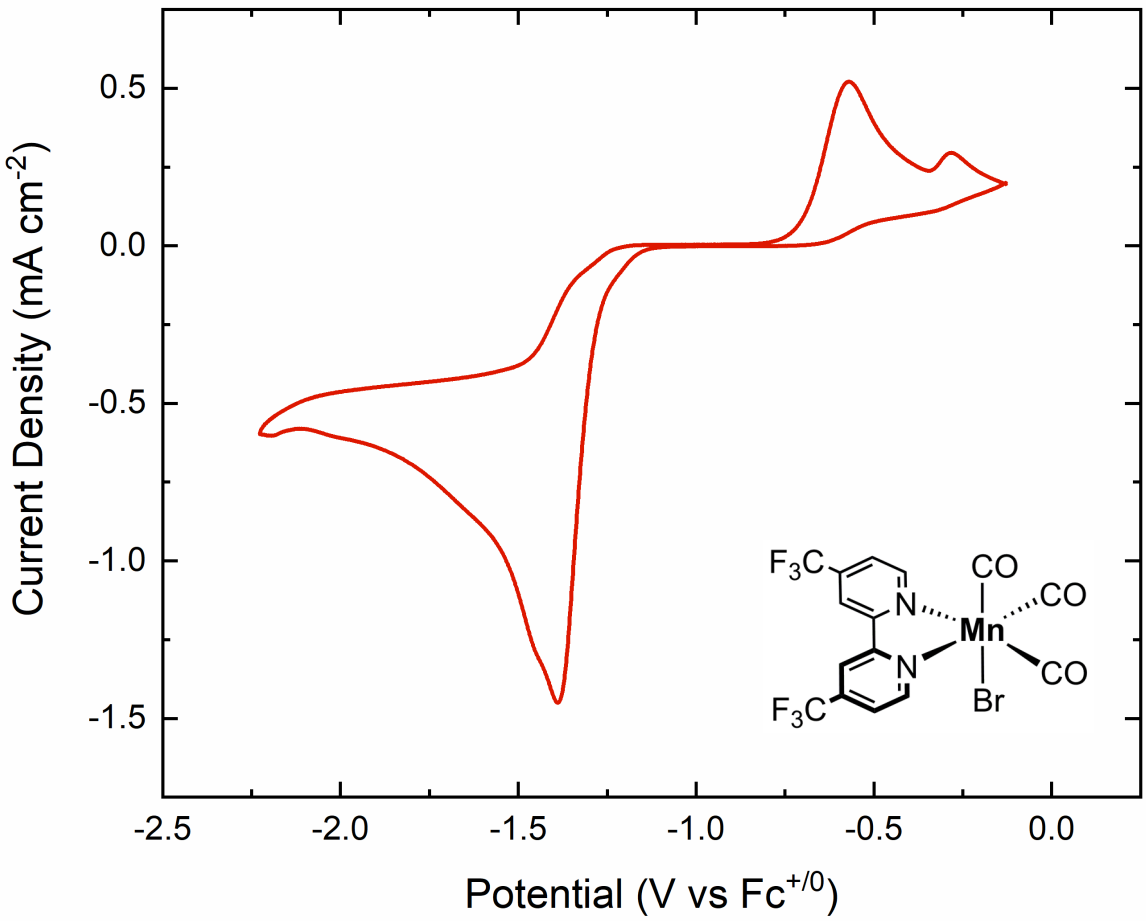

Figure F3: Cyclic voltammogram (100 mV/s) of **3** in 0.1M $TBAPF_6$/MeCN solution.

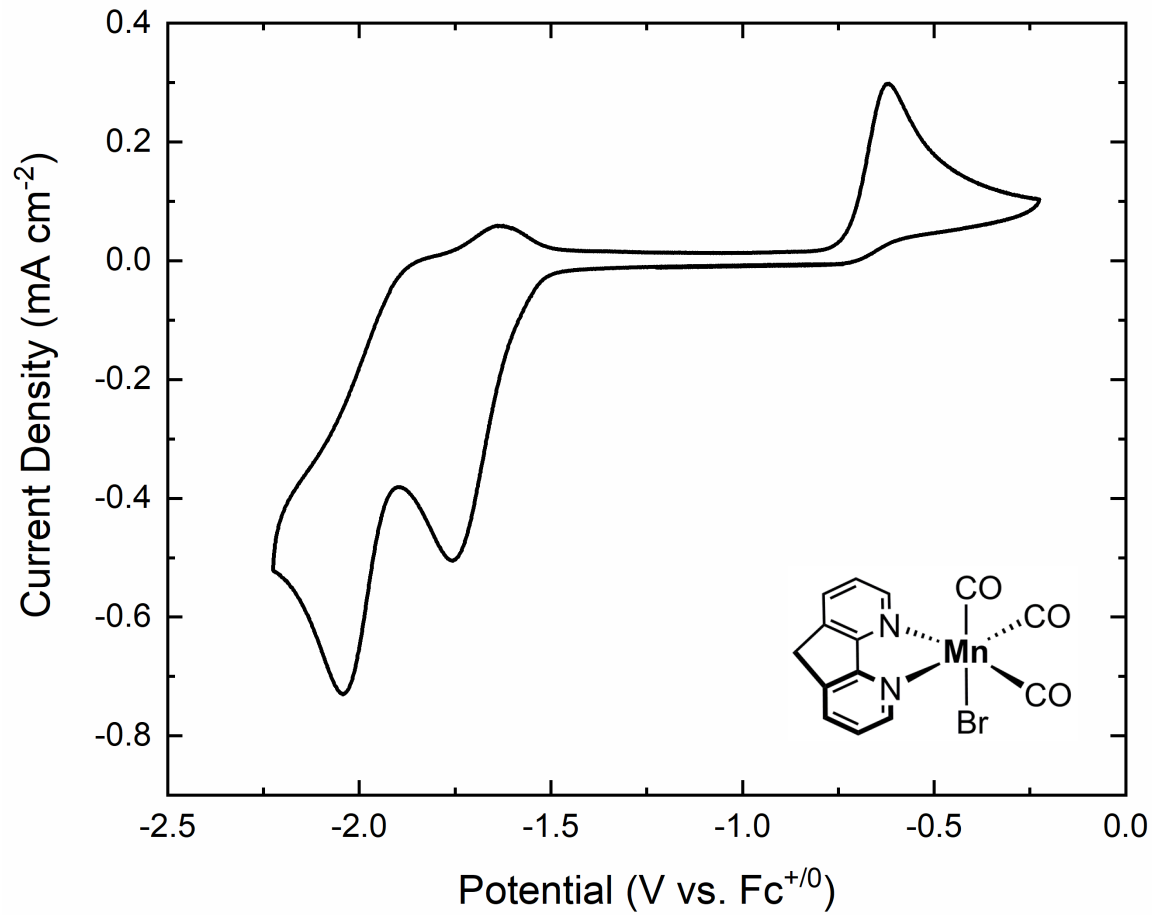

Figure F4: Cyclic voltammogram (100 mV/s) of **4** in 0.1M $TBAPF_6$/MeCN solution.

Spectrochemical Redox Titration

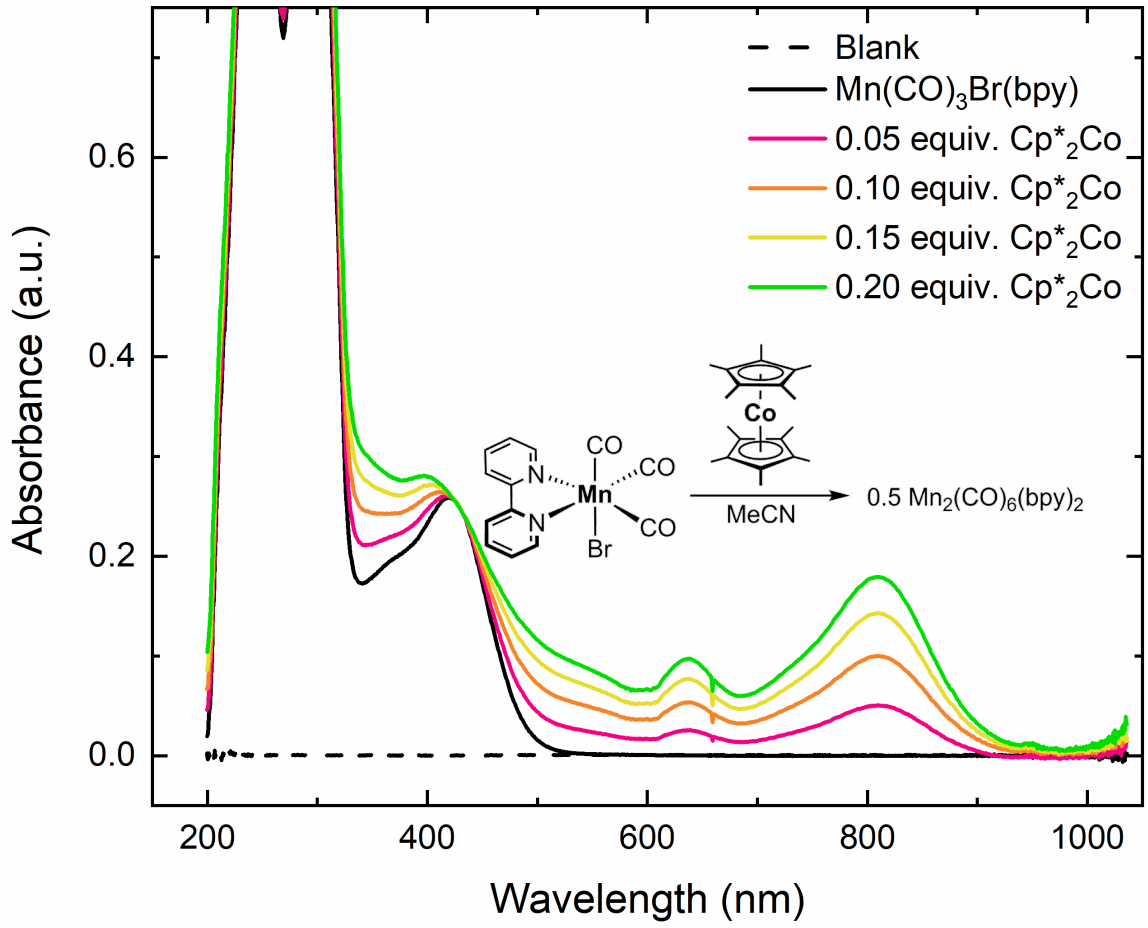

Figure F5: A solution of **2** in MeCN is titrated with increasing equivalents of Cp^*_2Co to generate $Mn_2(CO)_6(bpy)_2$.

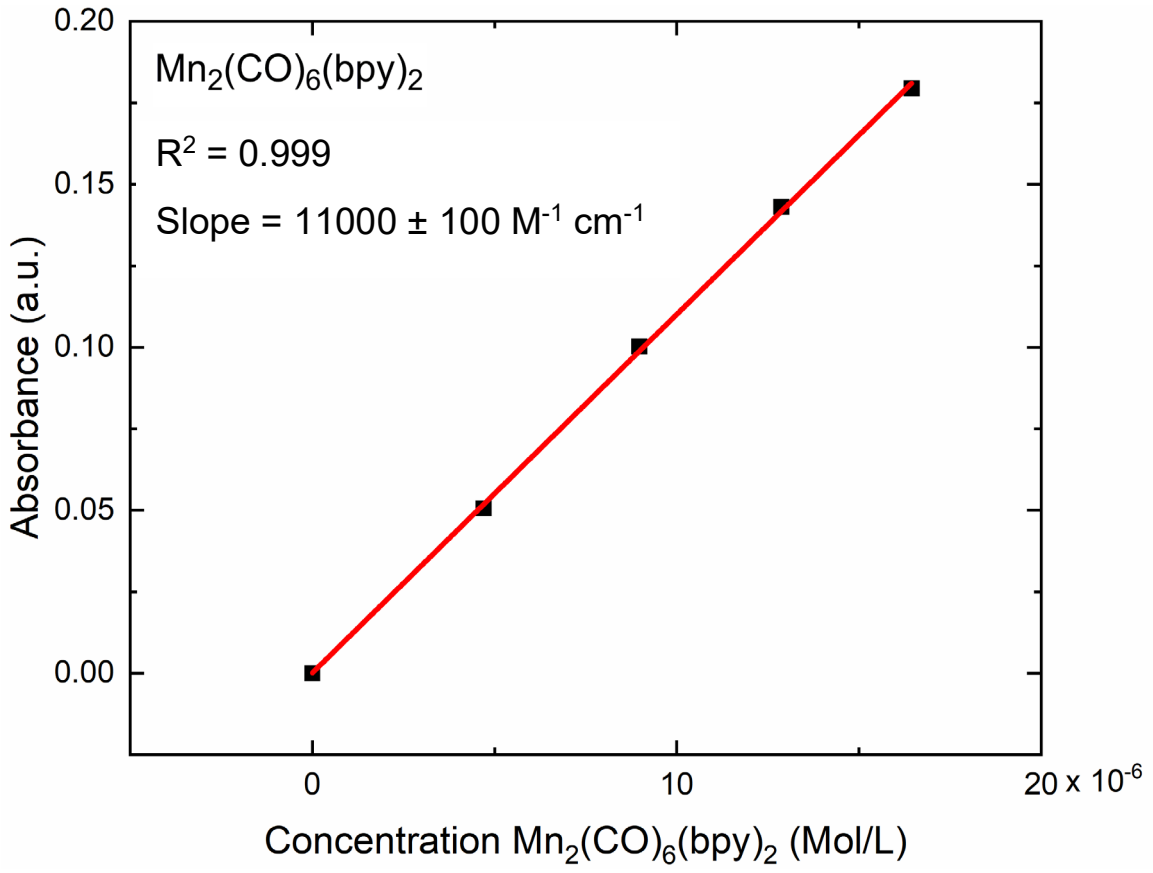

Figure F6: From the titration shown in Figure F5, an absorbance vs. concentration of $Mn_2(CO)_6(bpy)_2$ plot is constructed to extract the molar absorptivity of $Mn_2(CO)_6(bpy)_2$ at 810 nm.

Photolysis Data with NMR Monitoring

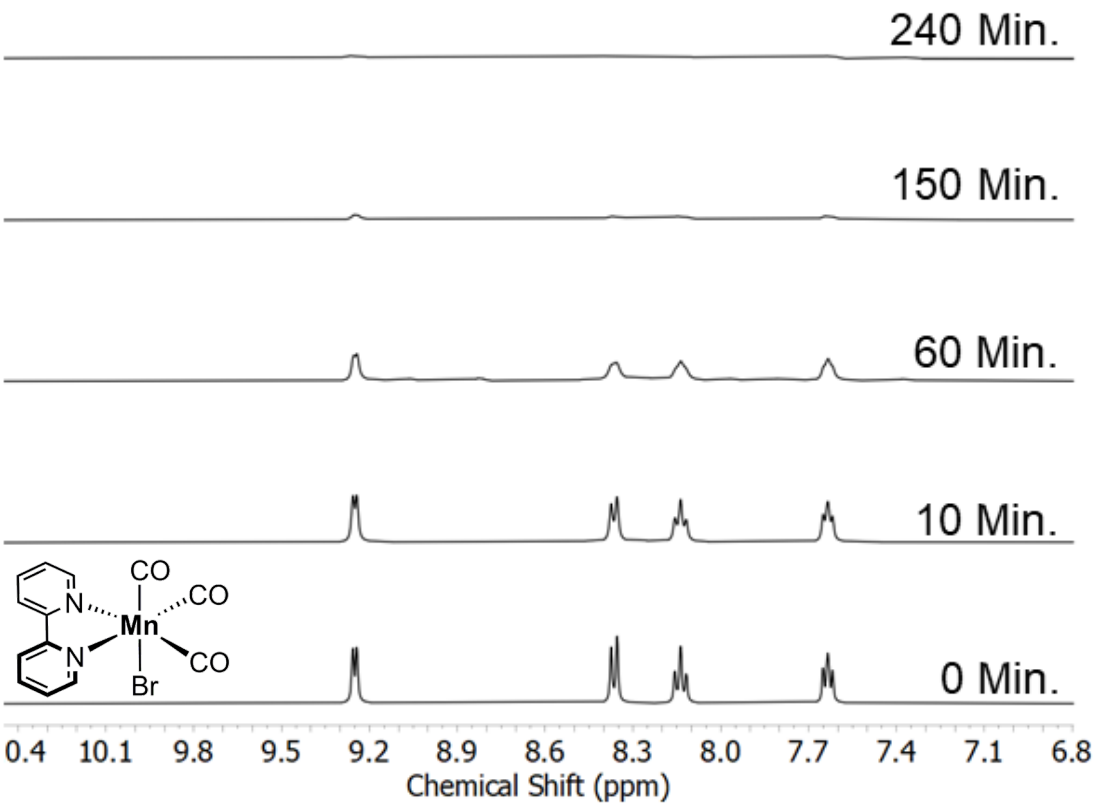

Figure F7: NMR spectroscopic monitoring of a solution containing complex **2** irradiated over time with 415 nm light at 175 W. The irradiation results in the disappearance of the starting material. Broadening of the resonances in the spectra can be observed after 10 min. of irradiation.

Photolysis Data with IR Monitoring

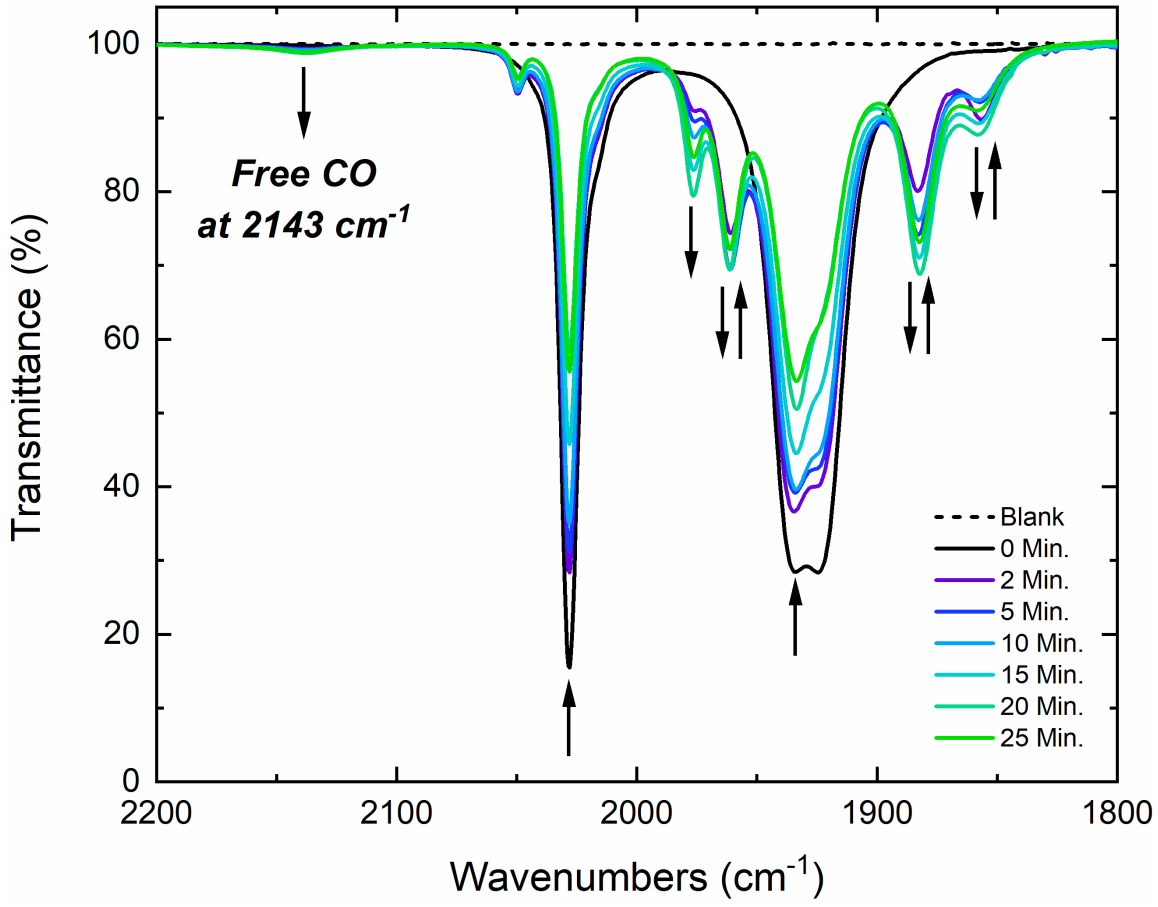

Figure F8: Full IR spectra. IR monitoring of a solution containing complex **2** irradiated over time with 415 nm light at 175 W. The irradiation results in follow-up chemical activity that is exhibited by the presence of new CO stretches in the IR spectrum after 2 min. of irradiation. The presence of free carbon monoxide is present after 2 min.

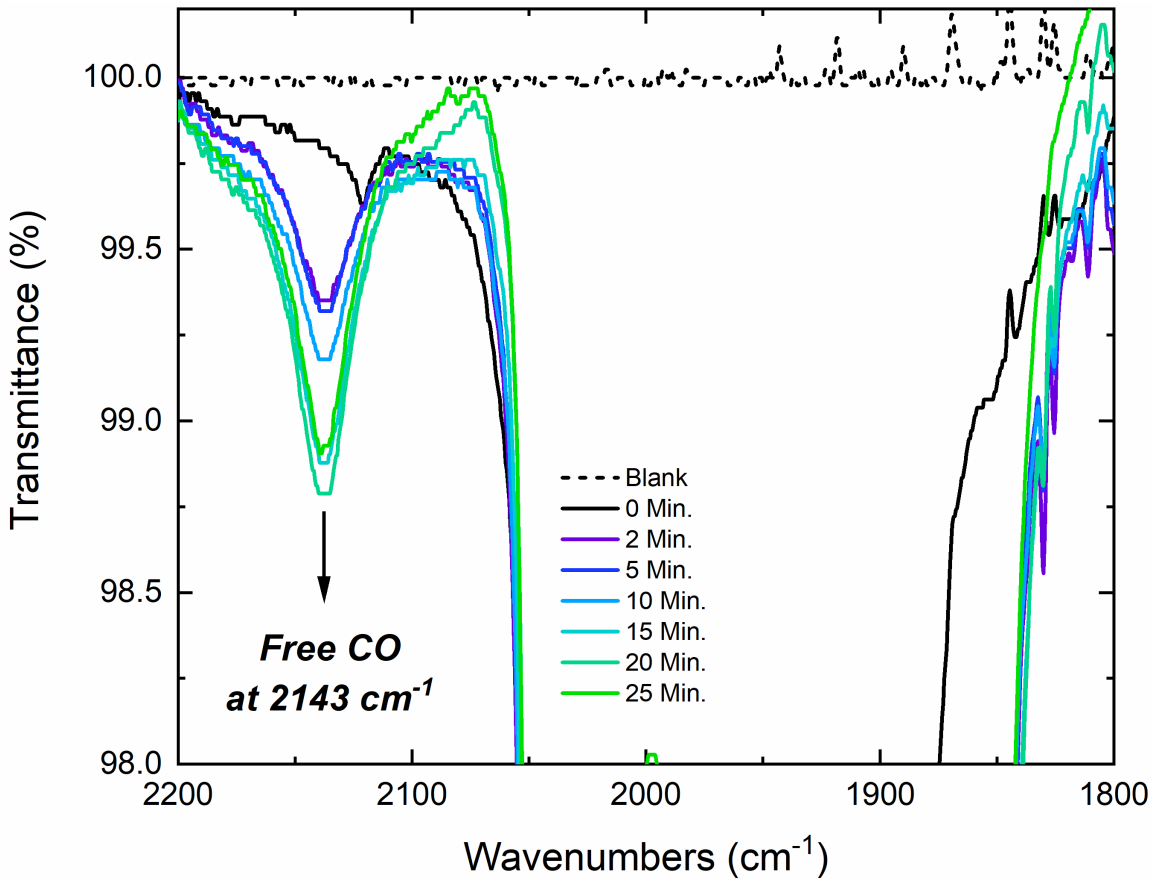

Figure F9: Zoomed in IR spectra. IR monitoring of a solution containing complex **2** irradiated over time with 415 nm light at 175 W. The presence of free carbon monoxide is present after 2 min and continues to increase during the course of irradiation.

Photolysis Data with UV-Vis Monitoring

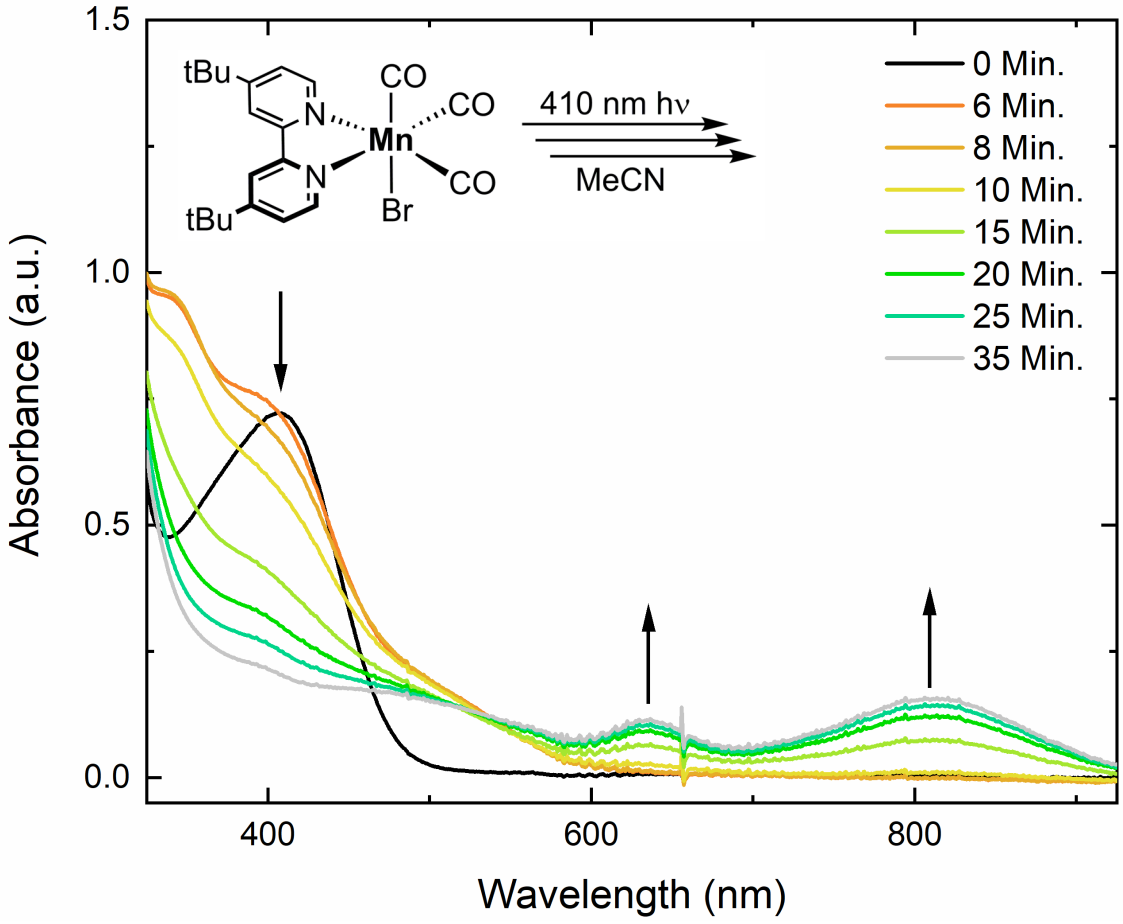

Figure F10: UV-Vis monitoring of a solution containing complex **1** irradiated over time with 410 nm light at 175 W. The irradiation results in follow-up chemical activity that is exhibited by the presence of new transitions in the UV-Vis spectrum after 2 min. of irradiation. The long wavelength absorptions resemble those observed in **2**.

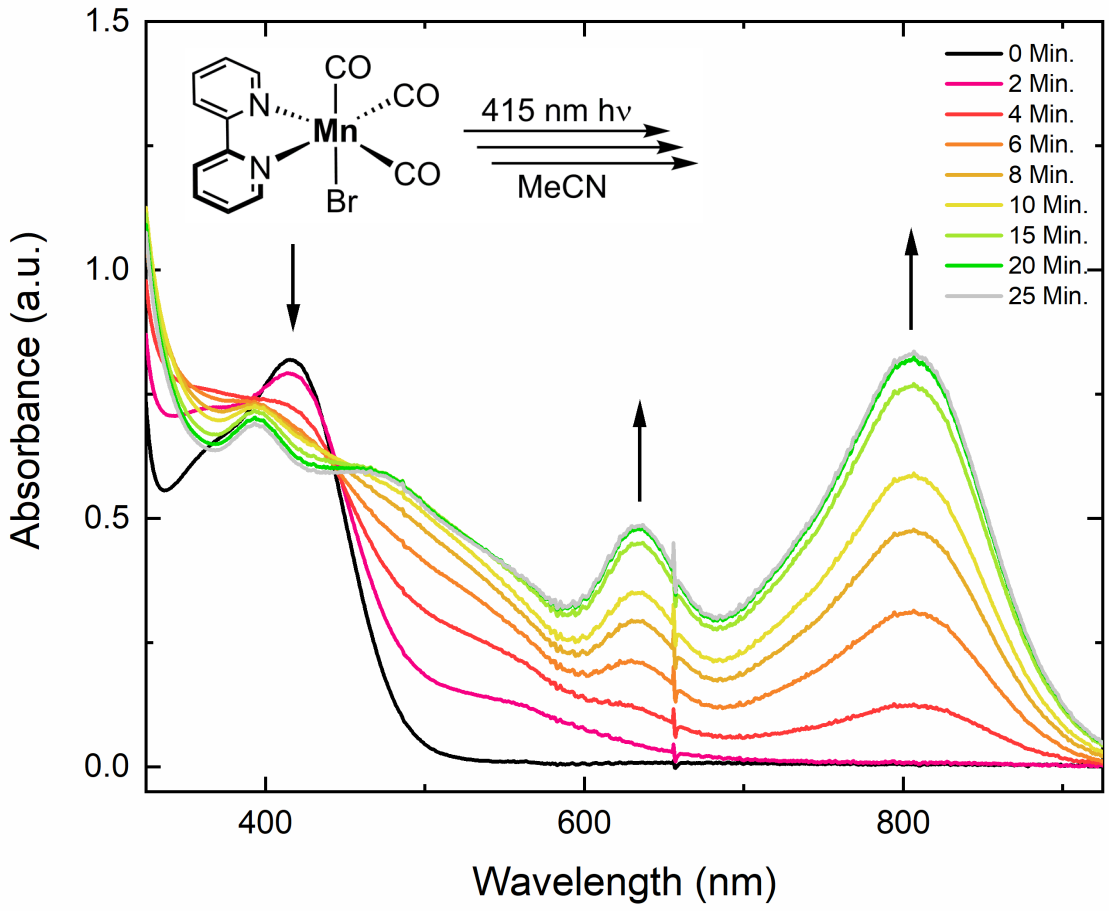

Figure F11: UV-Vis monitoring of a solution containing complex **2** irradiated over time with 415 nm light at 175 W. The irradiation results in follow-up chemical activity that is exhibited by the presence of new transitions in the UV-Vis spectrum after 2 min. of irradiation. The spectrum is consistent with the generation of $Mn_2(CO)_6(bpy)_2$, closely resembling the spectroelectrochemical data provided by Deronzier and co-workers.[1]

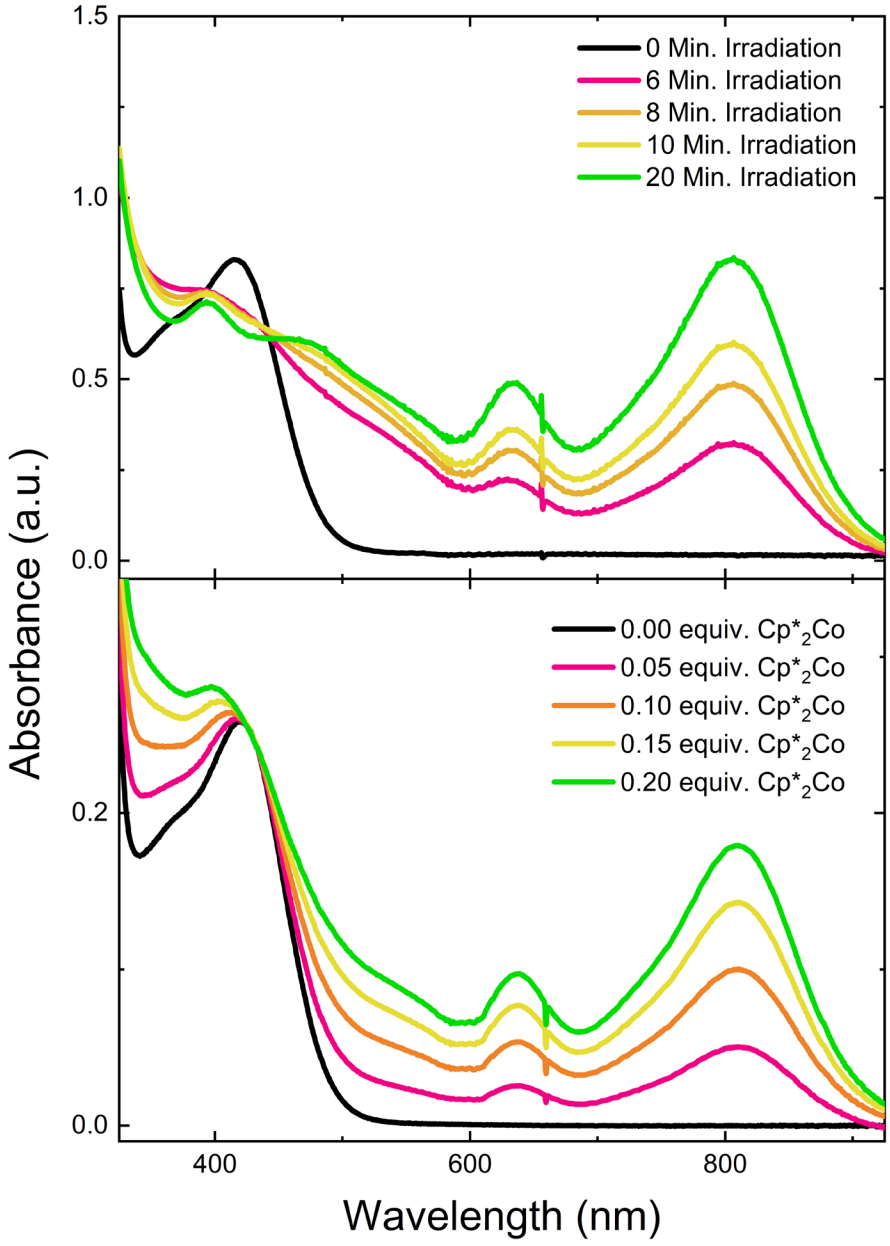

Figure F12: The spectrum obtained by irradiation of **2** is consistent with the generation of $Mn_2(CO)_6(bpy)_2$, closely resembling the spectroelectrochemical data provided by Deronzier and co-workers (upper panel).[1] The data in the upper panel also closely resembles the spectrochemical titration data provided here (lower panel). This supports the generation of an *in situ* reductant. Using the molar absorptivity of $Mn_2(CO)_6(bpy)_2$ obtained in Figure F6, the conversion of **2** to $Mn_2(CO)_6(bpy)_2$ was determined to be 42 ± 5%.

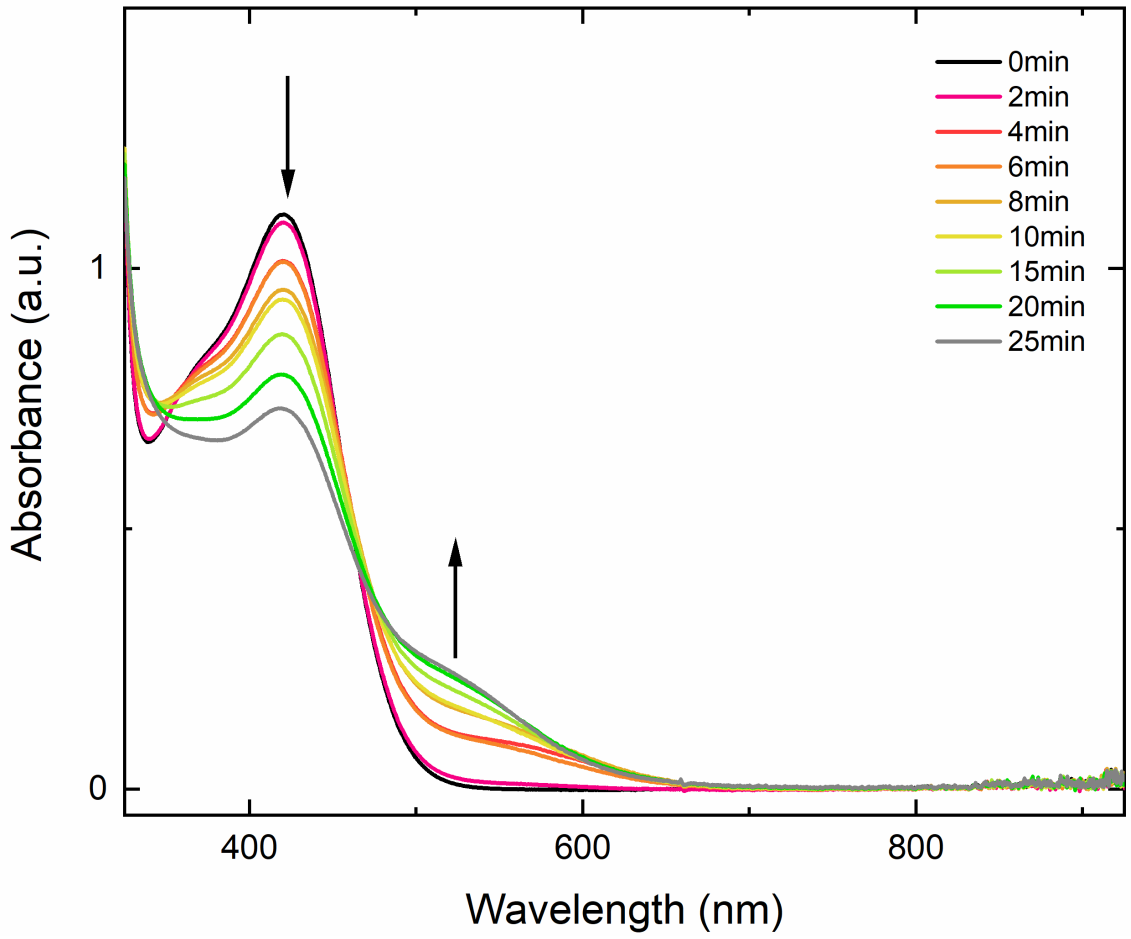

Figure F13: UV-Vis monitoring of a solution containing complex **2** irradiated over time with 415 nm light at 175 W under ambient atmosphere. The irradiation results in follow-up chemical activity that is exhibited by the presence of new transitions in the UV-Vis spectrum after 2 min. of irradiation. Notably, the transitions corresponding to the generation of $Mn_2(CO)_6(bpy)_2$ are not observed, confirming the air sensitivity of $Mn_2(CO)_6(bpy)_2$, a result that is further supported by the reduction potential of **2** ($E_{p,a} = -1.62$ V vs $Fc^{+/0}$).

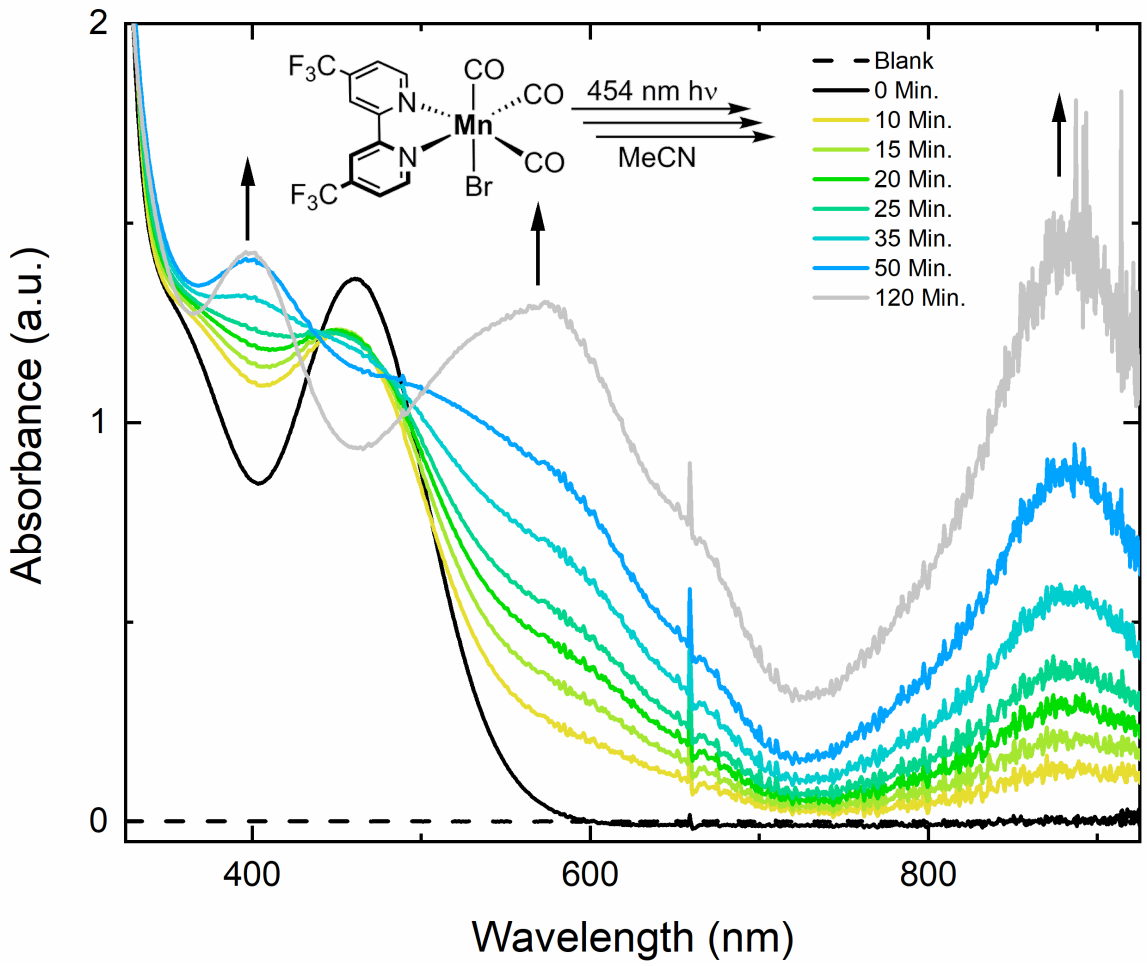

Figure F14: UV-Vis monitoring of a solution containing complex **3** irradiated over time with 454 nm light at 175 W. The irradiation results in follow-up chemical activity that is exhibited by the presence of new transitions in the UV-Vis spectrum after 2 min. of irradiation. The long wavelength absorptions resemble those observed in **2**, and the shift of the absorption features suggests that the ^{CF3}bpy ligand is still bound in the newly generated compound.

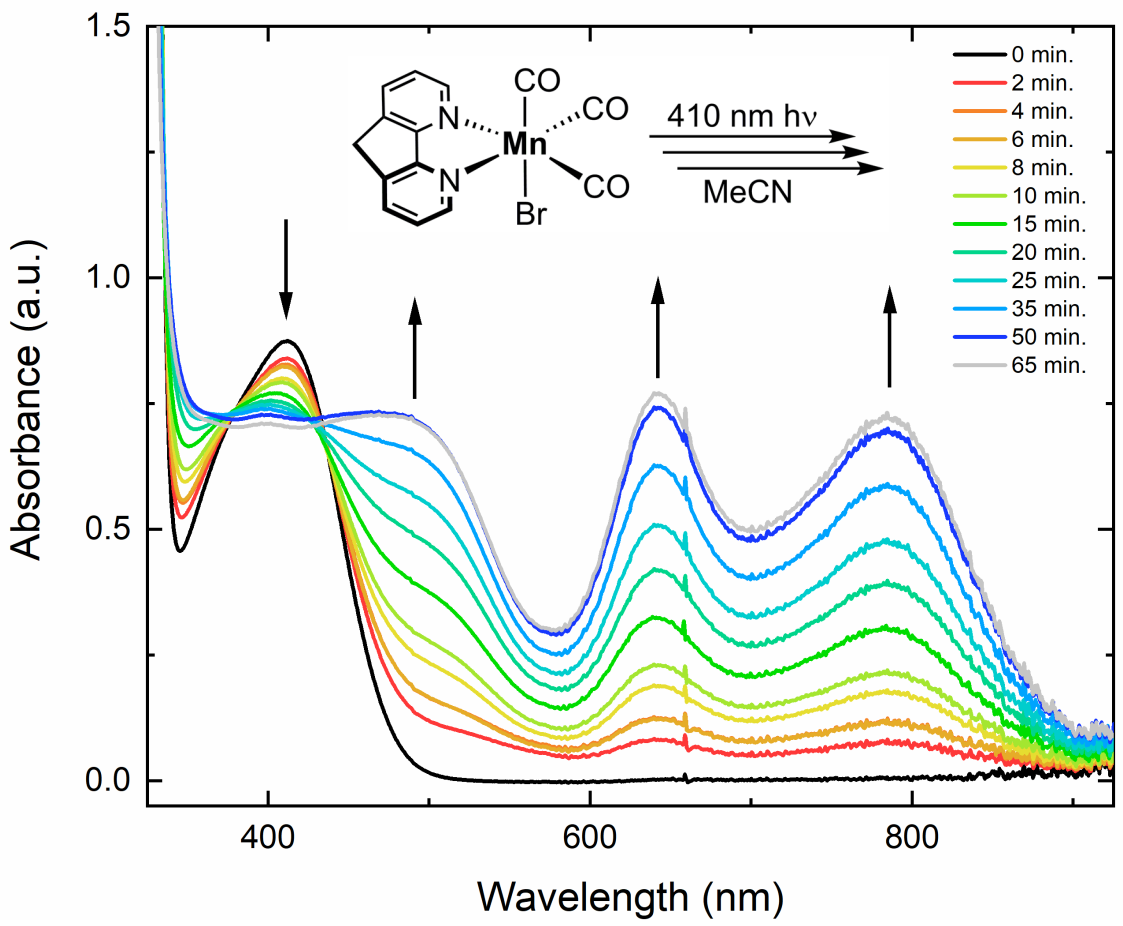

Figure F15: UV-Vis monitoring of a solution containing complex **2** irradiated over time with 410 nm light at 175 W. The irradiation results in follow-up chemical activity that is exhibited by the presence of new transitions in the UV-Vis spectrum after 2 min. of irradiation. The long wavelength absorptions resemble those observed in **2**.

Photolysis Data with EPR Monitoring

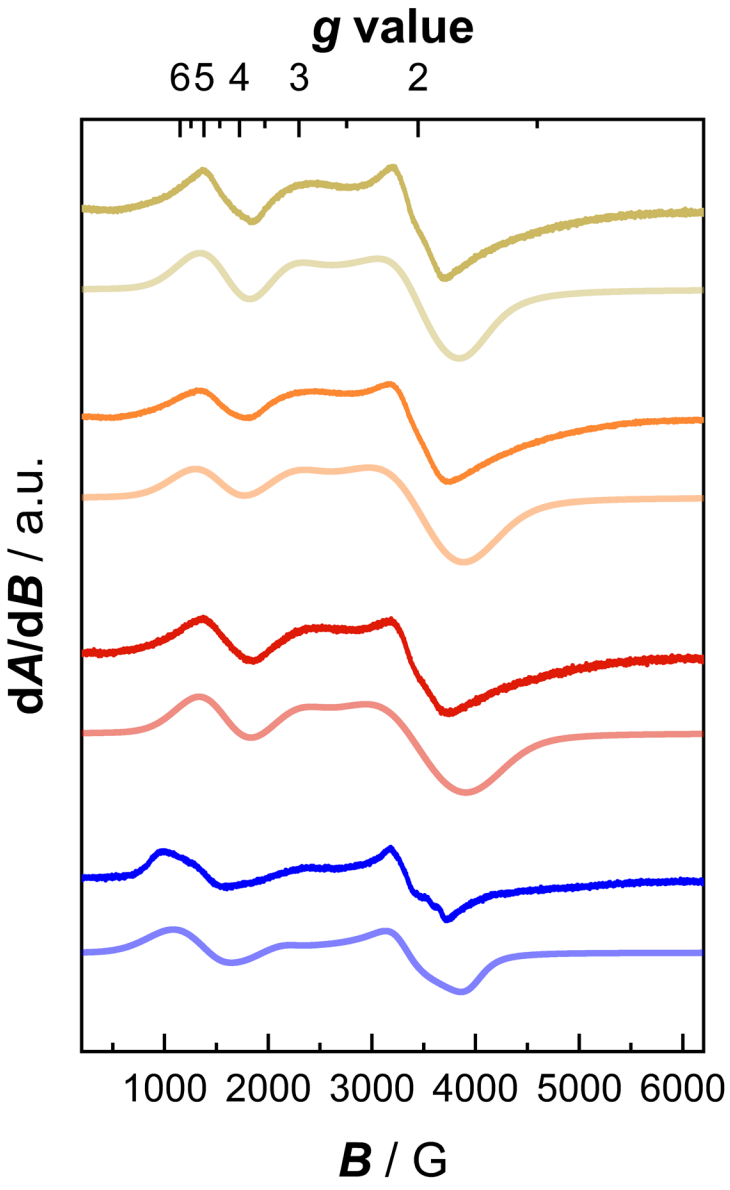

Figure F16: Two component X-band continuous wave EPR spectra of *in situ* generated Mn^{II} species following the irradiation of a solution of **1** (gold; simulated spectrum in light yellow), **2** (orange; simulated spectrum in light orange), **3** (red; simulated spectrum in light red), and **4** (blue; simulated spectrum in light blue) in frozen MeCN.

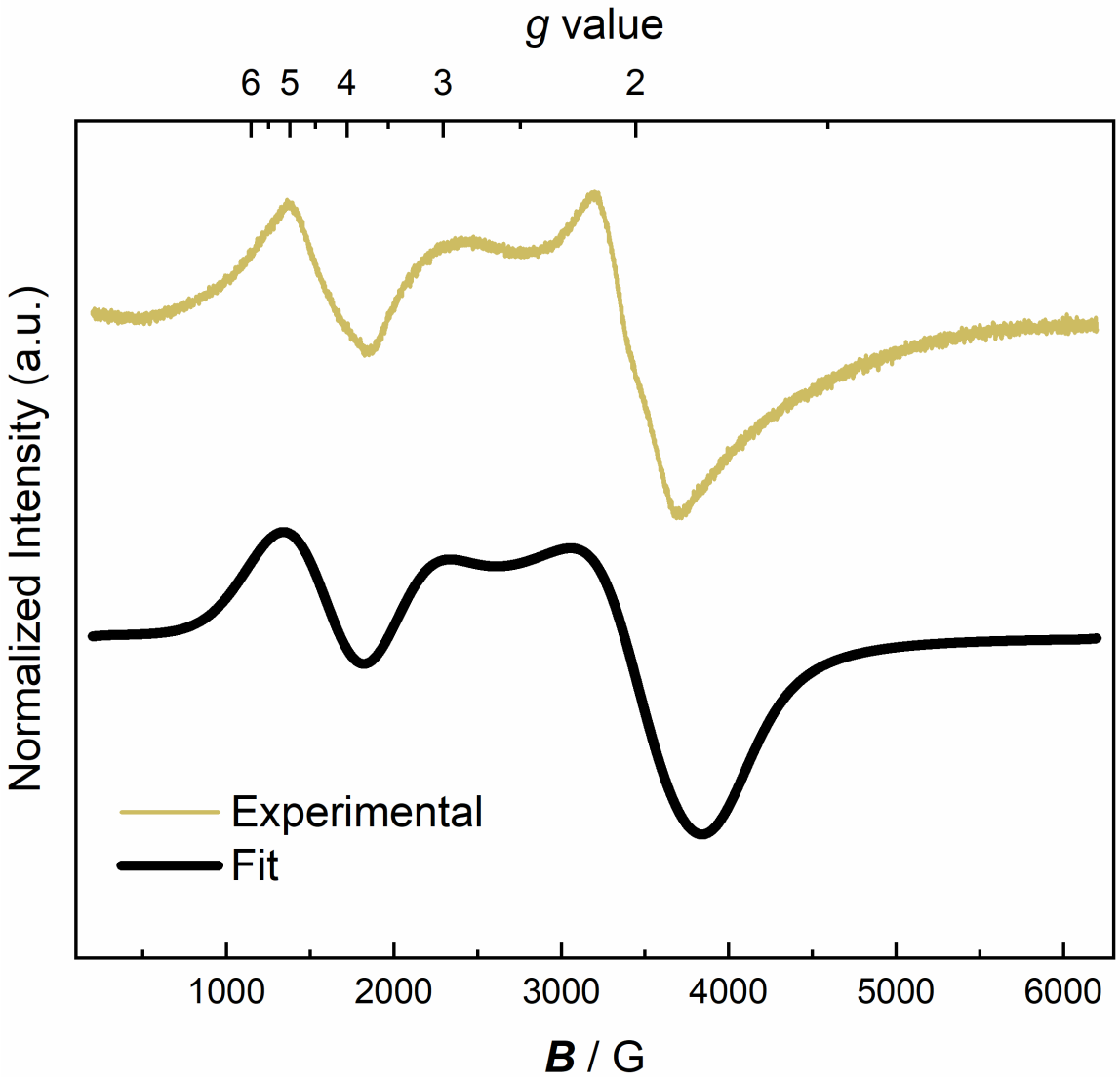

Figure F17: Experimental spectrum (gold): Following irradiation of **1** with ambient light for 24 hours, a perpendicular-mode, X-band EPR spectrum of two Mn^{II} species was measured in MeCN at 7.4 K (frequency = 9.6418 GHz; power = 2 mW; attenuation= 20 dB; time constant = 5.12 ms; modulation amplitude = 8.000G). Simulated spectrum (black): Easyspin simulation of the EPR data; simulations parameters for **Component A**: nucleus: Mn, S = 5/2, g = [1.88 3.23], A = [273 300], HStrain = [705 490], lwpp = [10 30], DStrain = [5.1 5.0], and weight = [0.94]. **Component B**: Mn, S = 5/2, g = [4.27], A = [72], HStrain = [73], lwpp = [57], DStrain = [5.0], and weight = [0.06].

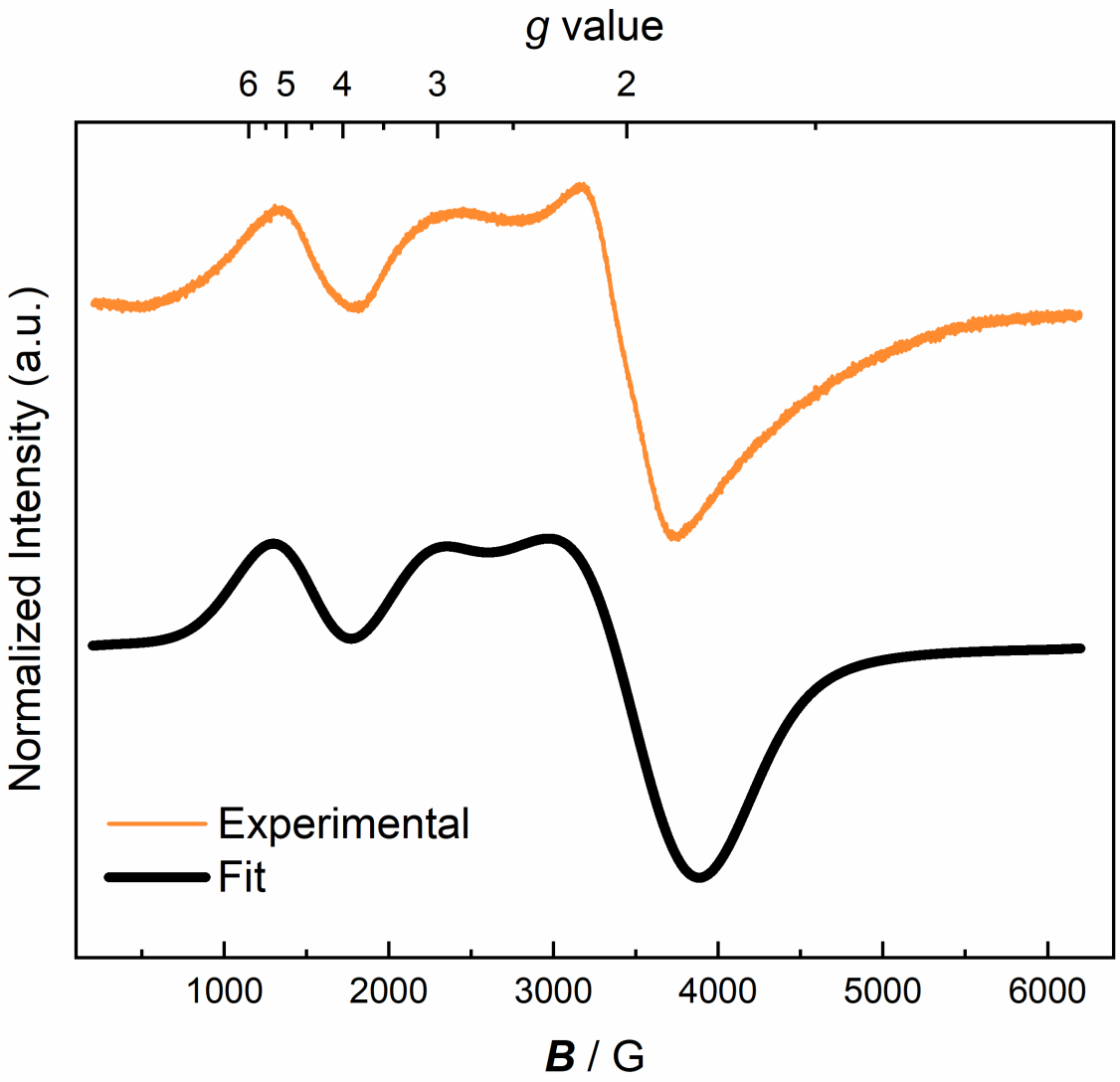

Figure F18: Experimental spectrum (orange): Following irradiation of **2** with ambient light for 24 hours, a perpendicular-mode, X-band EPR spectrum of two Mn^{II} species was measured in MeCN at 7.4 K (frequency = 9.6427 GHz; power = 2 mW; attenuation= 20 dB; time constant = 2.56 ms; modulation amplitude = 8.000G). Simulated spectrum (black): EasySpin simulation of the EPR data; simulations parameters for **Component A**: nucleus: Mn, S = 5/2, g = [1.87 3.32], A = [283 536], HStrain = [1284 308], lwpp = [20 25], DStrain = [5.0 5.0], and weight = [0.95]. **Component B**: Mn, S = 5/2, g = [4.39], A = [81], HStrain = [73], lwpp = [59], DStrain = [1.0], and weight = [0.05].

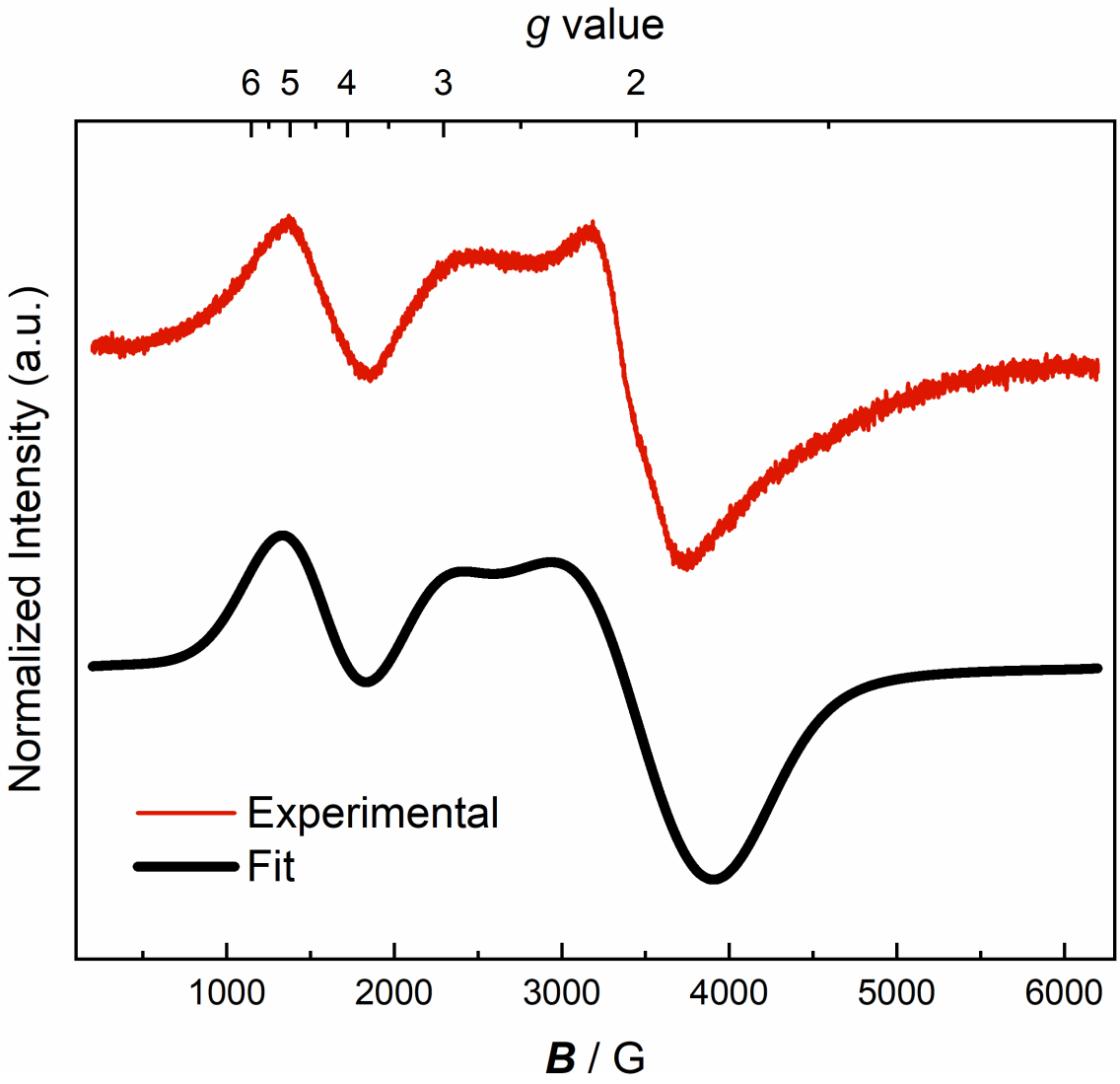

Figure F19: Experimental spectrum (orange): Following irradiation of **2** with ambient light for 24 hours, a perpendicular-mode, X-band EPR spectrum of two Mn^{II} species was measured in MeCN at 7.4 K (frequency = 9.6415 GHz; power = 2 mW; attenuation= 20 dB; time constant = 5.12 ms; modulation amplitude = 8.000G). Simulated spectrum (black): EasySpin simulation of the EPR data; simulations parameters for **Component A**: nucleus: Mn, S = 5/2, g = [1.87 3.29], A = [339 534], HStrain = [1300 315], lwpp = [21 22], DStrain = [5.0 5.0], and weight = [0.94]. **Component B**: Mn, S = 5/2, g = [4.29], A = [191], HStrain = [74], lwpp = [59], DStrain = [5.0], and weight = [0.06].

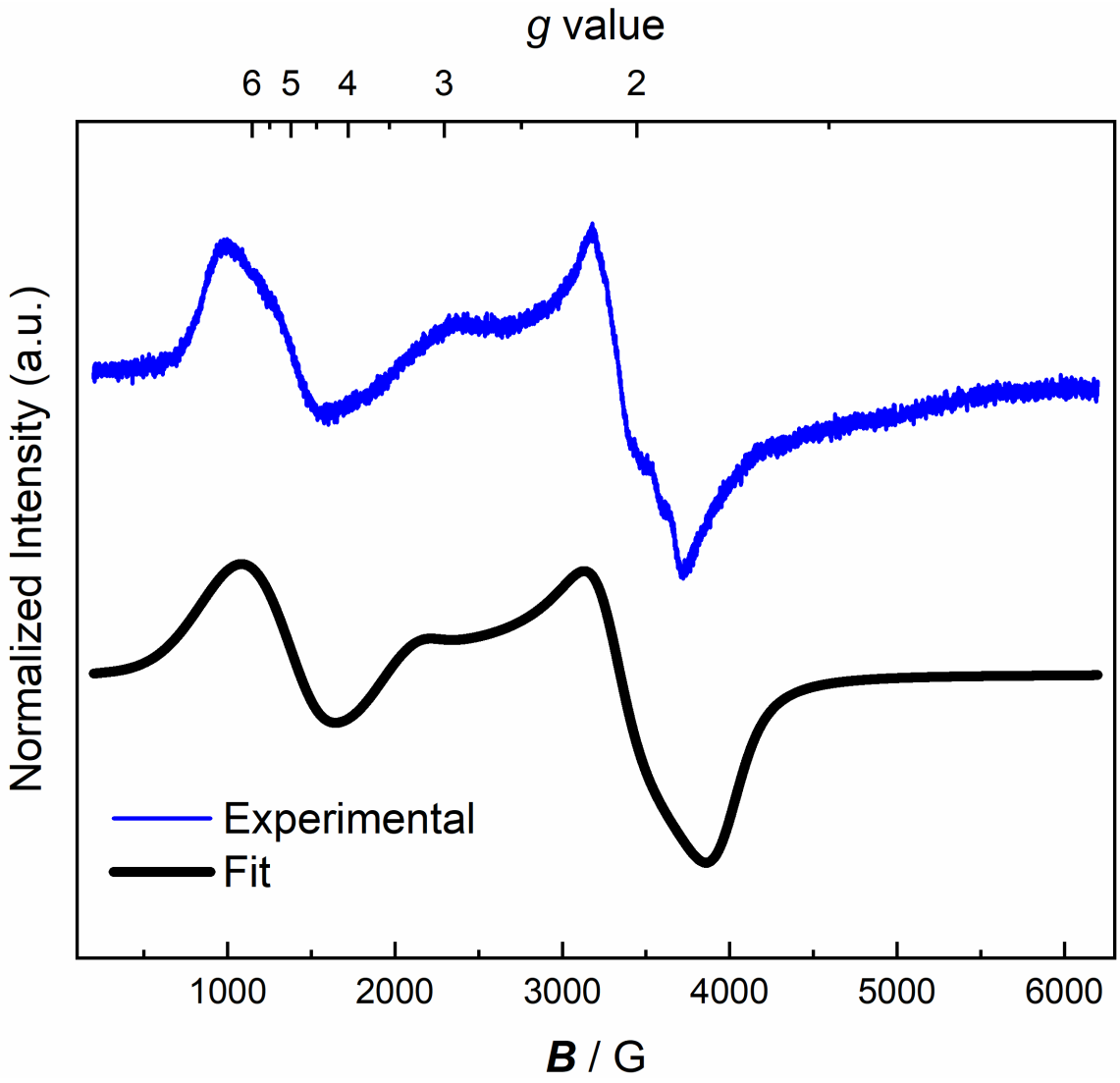

Figure F20: Experimental spectrum (orange): Following irradiation of **2** with ambient light for 24 hours, a perpendicular-mode, X-band EPR spectrum of two Mn^{II} species was measured in MeCN at 7.4 K (frequency = 9.6407 GHz; power = 2 mW; attenuation= 20 dB; time constant = 5.12 ms; modulation amplitude = 8.000G). Simulated spectrum (black): EasySpin simulation of the EPR data; simulations parameters for **Component A**: nucleus: Mn, S = 5/2, g = [1.90 3.60], A = [314 529], HStrain = [400 230], lwpp = [9 16], DStrain = [1.0 1.0], and weight = [0.89]. **Component B**: Mn, S = 5/2, g = [4.91], A = [194], HStrain = [83], lwpp = [64], DStrain = [1.0], and weight = [0.11].

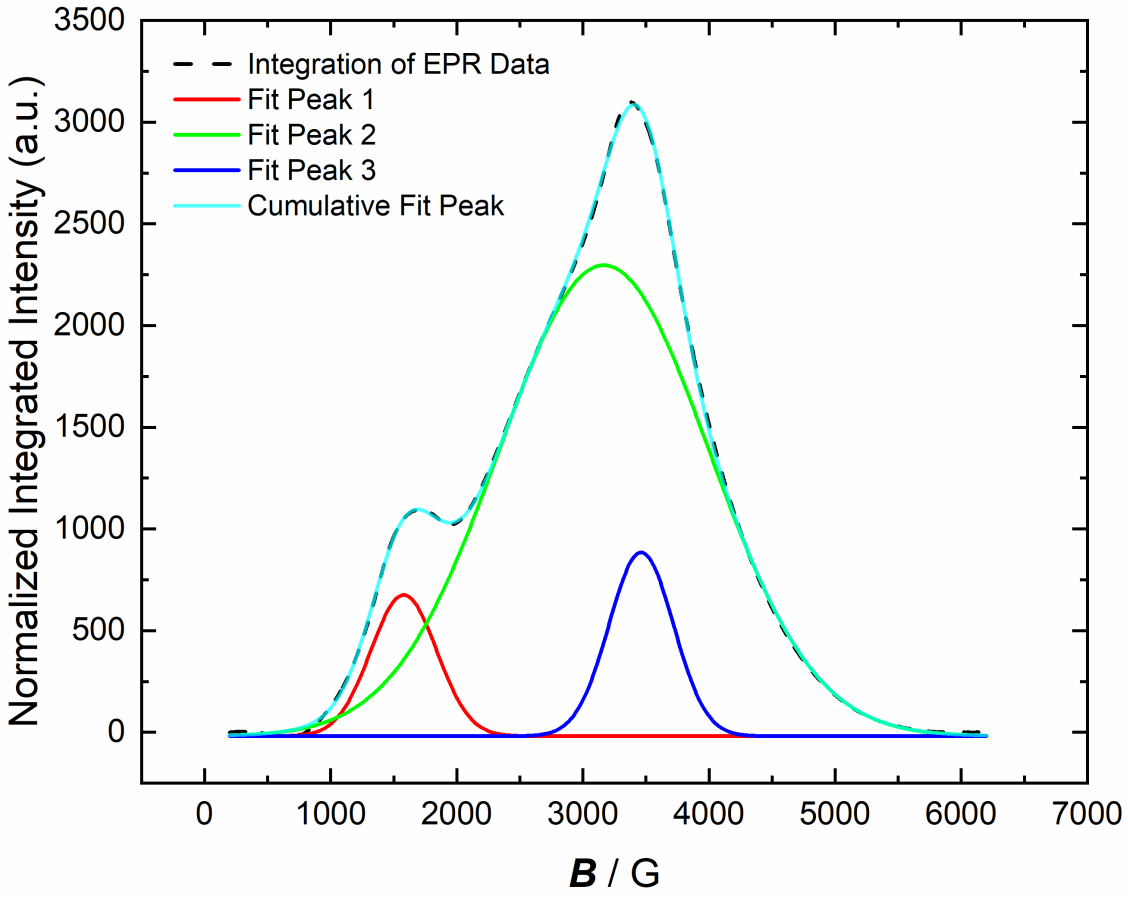

Figure F21: Peak deconvolution of the integrated EPR spectrum of **1**. The overall signal was fit with three separate gaussians, where peaks 2 and 3 correspond to Component A and peak 1 corresponds to component B. Based on the integration, the weighting of Components A and B are 0.92 and 0.8, respectively.

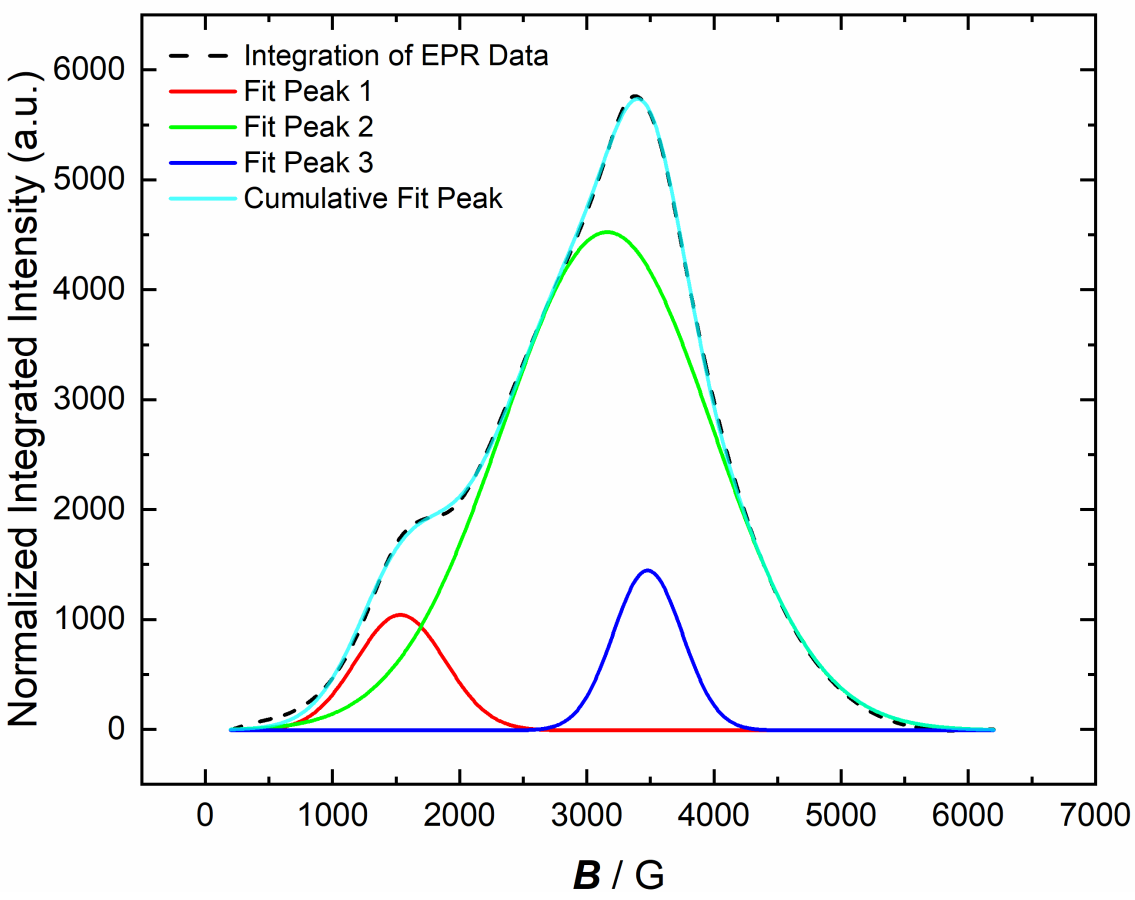

Figure F22: Peak deconvolution of the integrated EPR spectrum of **2**. The overall signal was fit with three separate gaussians, where peaks 2 and 3 correspond to Component A and peak 1 corresponds to component B. Based on the integration, the weighting of Components A and B are 0.92 and 0.8, respectively.

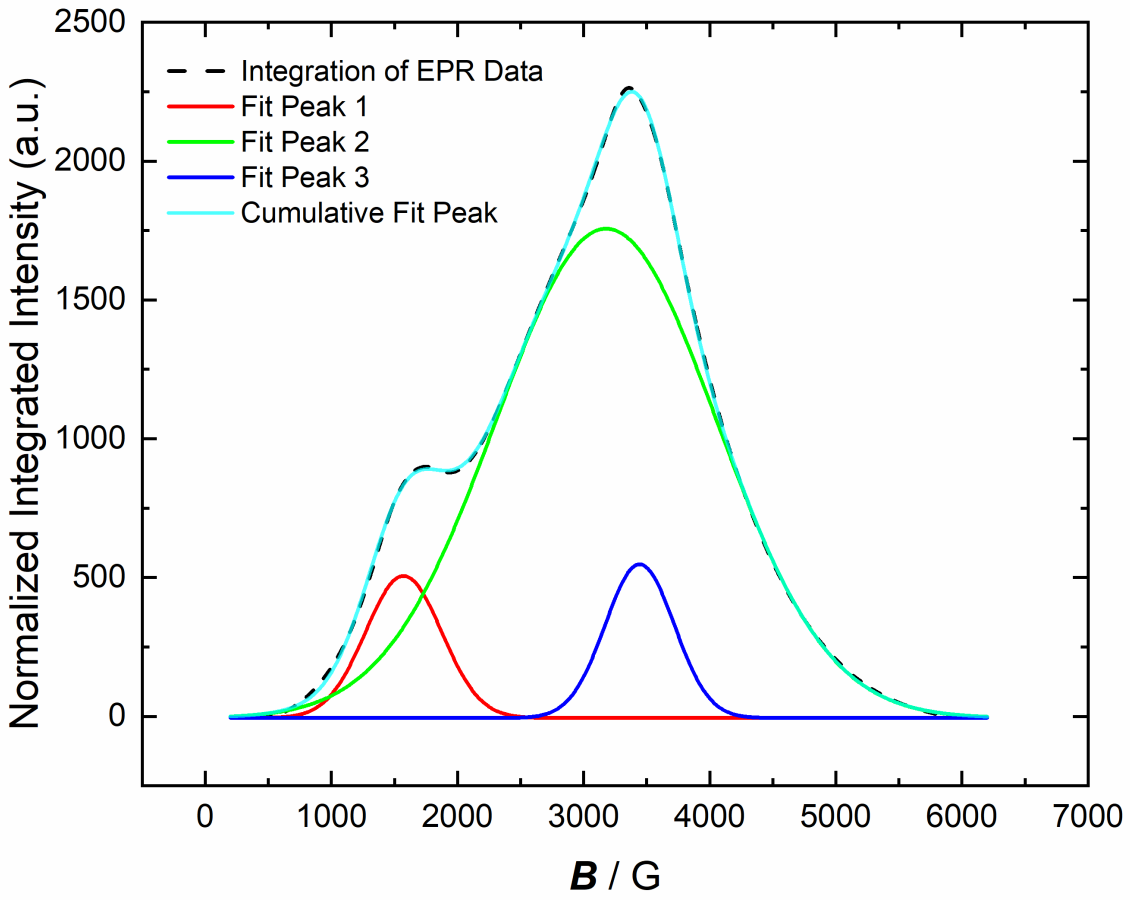

Figure F23: Peak deconvolution of the integrated EPR spectrum of **3**. The overall signal was fit with three separate gaussians, where peaks 2 and 3 correspond to Component A and peak 1 corresponds to component B. Based on the integration, the weighting of Components A and B are 0.92 and 0.8, respectively.

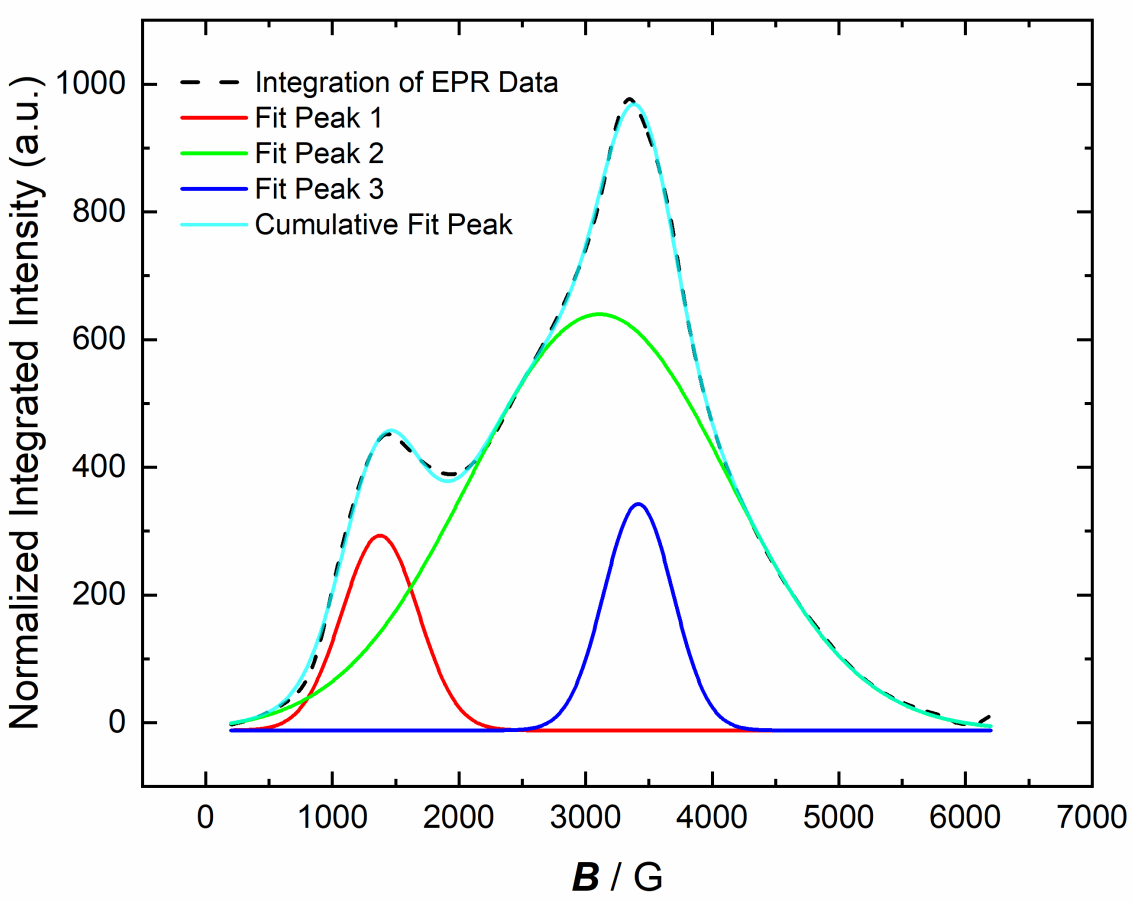

Figure F24: Peak deconvolution of the integrated EPR spectrum of **4**. The overall signal was fit with three separate gaussians, where peaks 2 and 3 correspond to Component A, and peak 1 corresponds to component B. Based on the integration, the weighting of Components A and B are 0.89 and 0.11, respectively.

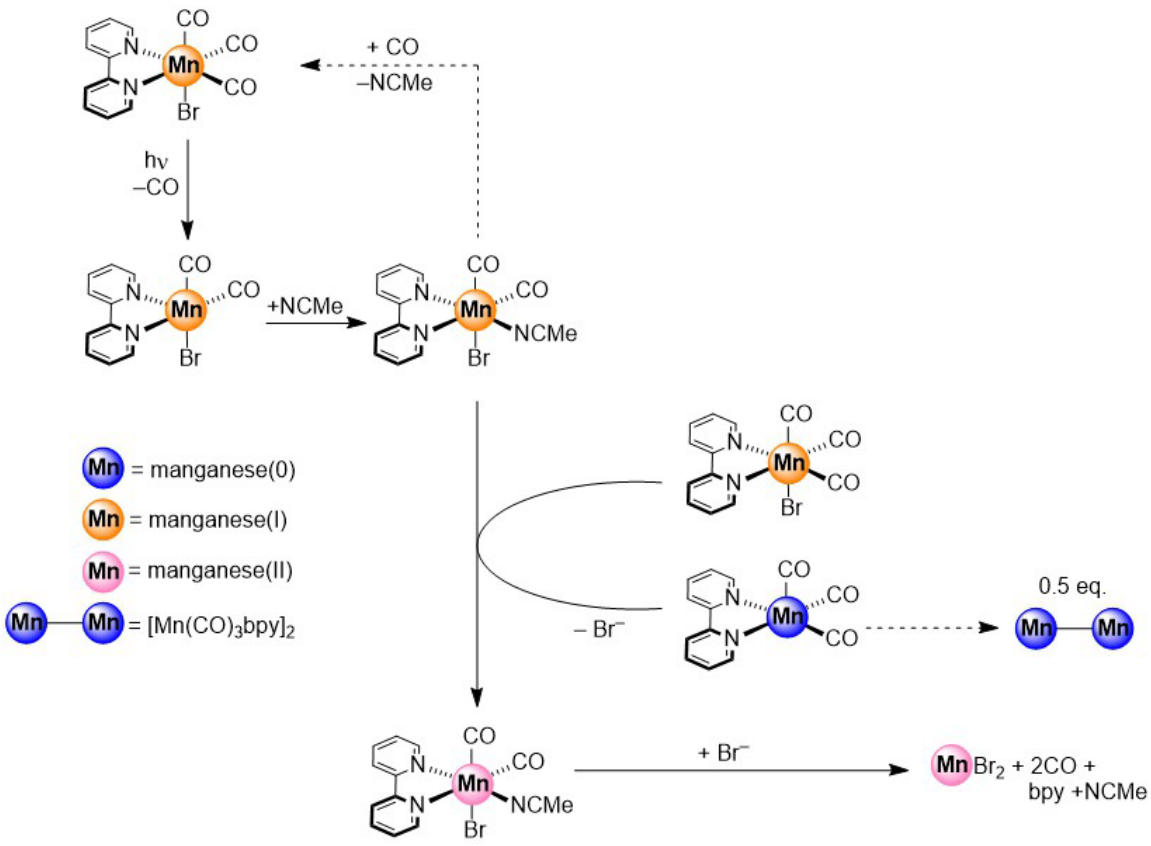

Scheme F1: Proposed mechanism for the speciation of $[Mn(CO)_3Br(diimine)]$ complexes **1-3**. Initial carbon monoxide release and solvent coordination were proposed in a prior publication based on ultrafast transient absorption spectroscopy with UV-visible monitoring.[2] After loss of an MeCN ligand, the proposed Mn solvento species would be a much better reductant than the starting material. The *in situ* generated reductant then reacts with an equivalent of the starting material, and the resulting redox chemistry then generates Mn(0) and Mn(II) species. The $17e^-$ Mn(0) species can then react with an equivalent of itself to generate $[Mn(CO)_3(bpy)]_2$, which is supported by the UV-vis and IR studies. The initial Mn(II) species that is generated would be labile and could lose its supporting ligands. The generation of Mn(II) and loss of its surrounding ligands is supported by experimental EPR measurements and theoretical modeling with EasySpin, as well as IR and gas chromatography measurements.[2,3]

References:

(1) Bourrez, M.; Molton, F.; Chardon-Noblat, S.; Deronzier, A., *Angew. Chem. Int. Ed.* **2011,** *50* (42), 9903-9906.

(2) Henke, W. C.; Otolski, C. J.; Moore, W. N. G.; Elles, C. G.; Blakemore, J. D., *Inorg. Chem.* **2020,** *59* (4), 2178-2187.

(3) S. Stoll and A. Schweiger, *J. Magn. Reson.*, **2006**, *178*, 42-55.